Addressing two missing problems of Modern Astrophysics: From the missing number of Galactic Supernova Remnants to the missing mass of the Universe

Dissertation
der Mathematisch-Naturwissenschaftlichen Fakultät
der Eberhard Karls Universität Tübingen
zur Erlangung des Grades eines
Doktors der Naturwissenschaften
(Dr. rer. nat.)

vorgelegt von Miltiadis Michailidis
aus Thessaloniki/Griechenland

Tübingen
2024

Gedruckt mit Genehmigung der Mathematisch-Naturwissenschaftlichen
Fakultät der Eberhard Karls Universität Tübingen.

Tag der mündlichen Qualifikation: 30.07.2024
Dekan: Prof. Dr. Thilo Stehle
1. Berichterstatter/-in: Prof. Dr. Andrea Santangelo
2. Berichterstatter/-in: Prof. Dr. Kostas Kokkotas
3. Berichterstatter/-in: Prof. Dr. Giorgio Matt

Multiwavelength studies of Galactic Supernova Remnants

Spaghetti nebula

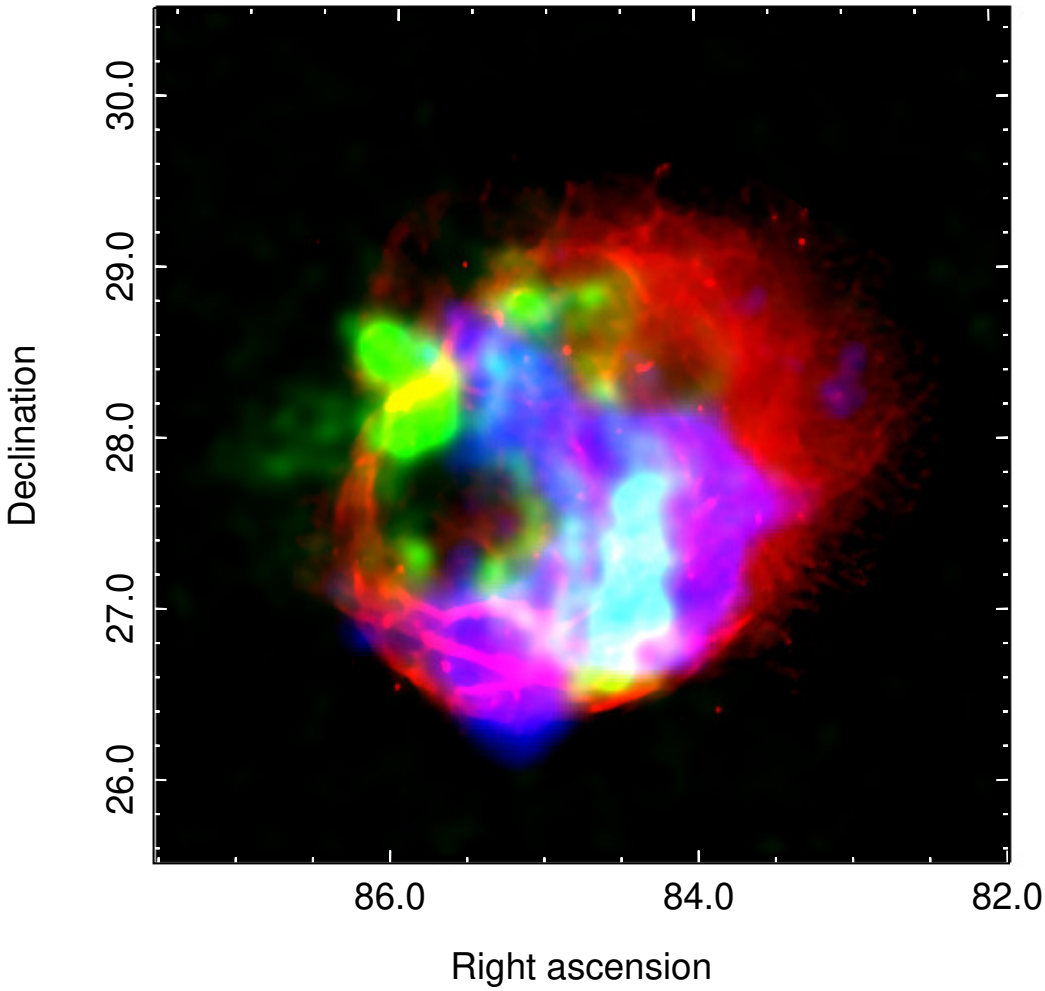

G279.0+01.1

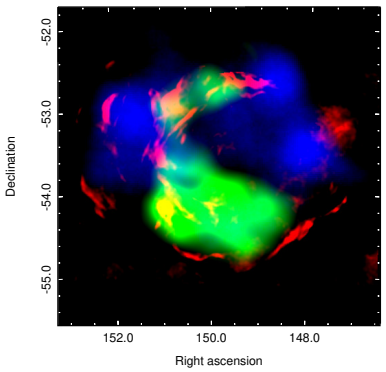

G309.8+00.0

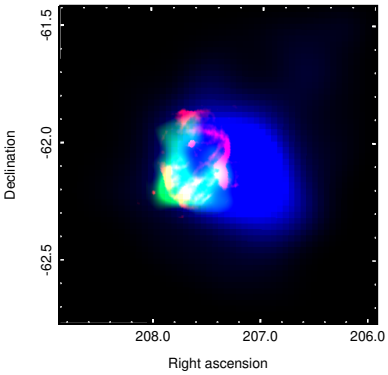

HESSJ1614-518

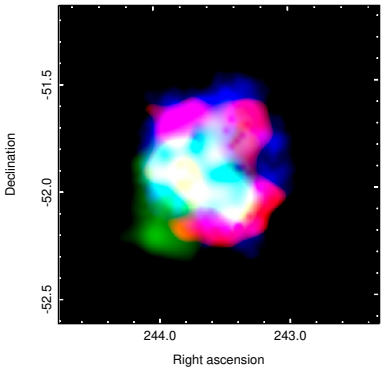

Dark Matter studies

Sample of Dark Matter density profiles across a host of different objects spanning a wide range of size and mass ($DM_\rho cat$)

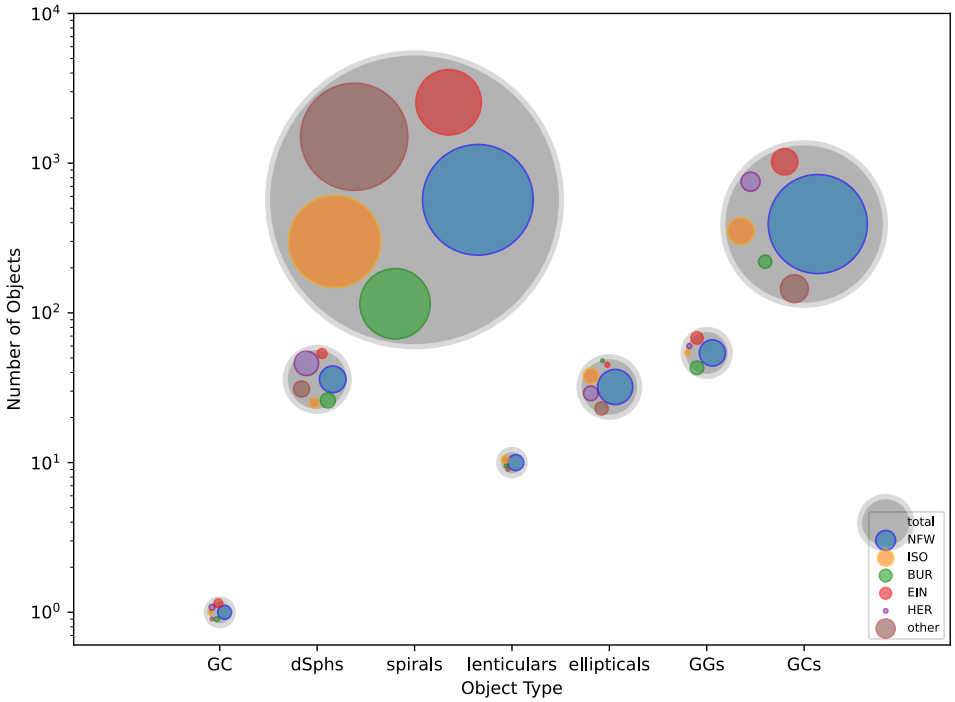

CTA sensitivity for annihilating Dark Matter signal from nearby spiral galaxies

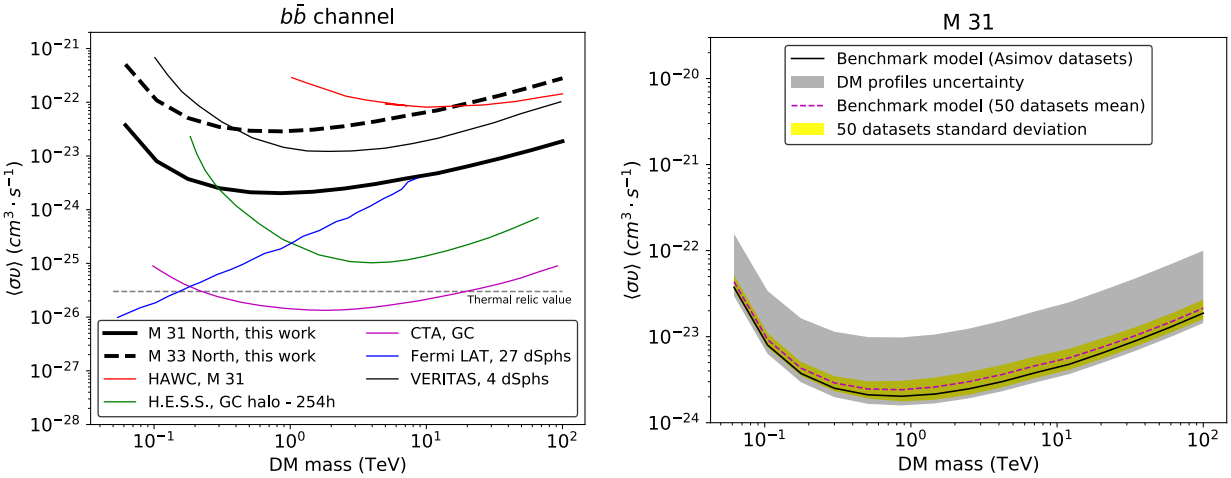

Abstract

Between end of 2019 and 2022, the seven eROSITA telescopes onboard the Russian-German Spectrum-Roentgen-Gamma satellite (SRG) were used to perform an All-Sky X-ray survey in the soft to medium energy X-ray band (0.2-10.0 keV). The eROSITA All-Sky Survey (eRASS) surpasses the ROSAT All-Sky Survey (its predecessor) sensitivity by more than an order of magnitude. At the same time, current X-ray instruments that are used for pointed observations, such as *XMM-Newton*, *Chandra*, *Suzaku*, and NuSTAR are unable to cover the entire sky, even after decades of operation, and can therefore not be used to conduct a comprehensive Galactic Supernova remnant (SNR) population study. In addition, SNRs in close proximity to Earth (hundreds of parsecs), that can reach degree-scale sizes in X-rays, are difficult to be studied with pointed X-ray instruments. Proposing blind observations aiming to cover the whole sky for potential new remnants is not an option. As it appears, a large fraction of the missing number between the expected Galactic SNRs and detected Galactic SNRs is a result of not having properly covered the whole sky in all distinct energy bands that SNRs are detectable. Given eROSITA's CCD-type sensitivity and energy coverage well beyond the ROSAT XRT's upper energy range (2 keV), eRASS is ideally suited to discover and investigate the X-ray emission from a variety of astrophysical objects including SNRs which are highly absorbed and/or exhibit non-thermal spectral components. The corresponding X-ray data, therefore, permit to study the known population of both thermal and non-thermal sources and to search for new such sources, especially the latter ones (i.e., non-thermal) which are potential accelerators of cosmic-rays (CRs). The thorough screening of the first four eRASS surveys (eRASS:4), accessible to the German eROSITA consortium, that we conducted has revealed several tens of new SNR candidates and new X-ray counterparts to known SNRs, out of which we have identified compelling candidates for being previously unknown accelerators of ultra-relativistic particles.

The first part of this dissertation is a compilation of five publications resulting from a detailed and deep multiwavelength analysis of three SNRs (Michailidis et al. 2024a, Michailidis et al. 2024b, Khabibullin et al. 2024, Michailidis et al. 2024c) that we have detected for the first time in X-rays with eROSITA (G279.0+01.1 SNR, the Spaghetti nebula (S147 or G180.0-01.7 SNR), and the G309.8+00.0 SNR) and the identification of the SNR nature of the HESS J1614-518 SNR candidate (Pühlhofer et al. 2024), as suggested

by H.E.S.S. data, using eROSITA and GLEAM radio data. For all the above SNRs/targets we have conducted a detailed analysis to probe the individual remnant's properties such as (if detected in the respective source): X-ray thermal plasma temperature, ionization age, chemical composition of both the local ISM and the progenitor star (elemental abundances), thermal plasma state (equilibrium or not), powerlaw shape (indices) that characterizes the spectrum of non-thermal particle populations (both in X-rays and γ-rays), plasma density, distance, and age determination. The goal of this study is to inspect the properties of those SNRs that can efficiently accelerate particles to GeV/TeV energies (non-thermal SNRs). Its results also contribute towards the reduction and explanation of the gap between the total number of detected Galactic SNRs and the number of Galactic SNRs detected in X-rays and ultimately close the gap between the expected and the detected number of Galactic SNRs.

The second part of this dissertation is a compilation of two publications in the field of Indirect detection of Dark Matter (DM) using γ-ray instruments (The Cherenkov Telescope Array (CTA) and *Fermi*-LAT). Specifically, we focus on the Weakly Interacting Massive Particles (WIMPs) annihilation signal in the diffuse halo of M31 and M33 neighboring spiral galaxies (not that frequently selected targets for DM studies), for which a large variety of DM profiles and a detailed baryonic mass characterization are reported in the literature mainly due to their close proximity to Earth that permits extensive studies in the context of their astrophysical nature. In particular, our study (Michailidis et al. 2023) provides the expected sensitivity of CTA to an annihilation signal from WIMPs from M31 and M33. We show that a 100 h long observation campaign will allow CTA to probe annihilation cross-sections up to $\langle \sigma v \rangle \approx 5 \cdot 10^{-25}$ cm^{3}s^{-1} for the $\tau^+\tau^-$ annihilation channel (for M31, at a DM mass of 0.3 TeV), improving the current limits derived by HAWC by up to an order of magnitude. For the derivation of the expected CTA sensitivity to the annihilating DM signal we analysed uncertainties connected to *(i)*: the potential astrophysical background contamination within the Field of View (FoV) of CTA, *(ii)* the presence of DM substructures, *(iii)*: the imperfect knowledge of the instrument itself and/or misidentification of CRs, i.e. systematic uncertainties, and *(iv)*: the lack of knowledge of the actual DM density distribution. Thus, we argue that our study provides an excellent basis for the specifics (i.e., exposure time) of the upcoming observation of M31 with CTA that has already been planned. We suggest that taking into account the possible effects of the highly uncertain astrophysical

background and DM density distribution, the observations of the selected targets could provide important constraints on the WIMP DM parameter space. Driven by our result that the uncertainties on the DM density profiles result in the highest uncertainty (among the four aforementioned causes of uncertainty) in the derived prospects, we provide an excellent review of the DM distribution to commonly studied astrophysical objects (1095 objects and 5659 DM density profiles in total plus seventy-four thousand DM density profiles from thirty-two thousand nearby galaxies provided by two recent studies that employed Sloan Digital Sky Survey (SDSS) and ALFALFA survey data) spanning many orders of magnitude in mass (from dSphs to Galaxy Clusters) that can provide a valuable guide for colleagues seeking to inspect the unseen mass component on individual targets (Michailidis et al. 2024d). The latter study also provides evidence for a new universal property of DM at all observed masses that we are addressing in detail in an upcoming publication where we put all different DM density profiles collected into context (in the form of the DM column density (S) as a function of the halo mass) to introduce a new scaling relation that allows direct comparison of observations with theoretical predictions/numerical simulations.

Zusammenfassung

Zwischen Ende 2019 und 2022 wurden die sieben eROSITA-Teleskope an Bord des russisch-deutschen Spectrum-Roentgen-Gamma-Satelliten (SRG) genutzt, um eine All-Sky-X-ray-Survey im weichen bis mittelenergetischen Röntgenbereich (0,2-10,0 keV) durchzuführen. Die eROSITA-All-Sky-Survey (eRASS) übertrifft die Empfindlichkeit der ROSAT-All-Sky-Survey (seines Vorgängers) um mehr als eine Größenordnung. Gleichzeitig sind die derzeitigen Röntgeninstrumente, die für gezielte Beobachtungen verwendet werden, wie *XMM-Newton*, *Chandra*, *Suzaku* und NuSTAR, selbst nach Jahrzehnten des Betriebs nicht in der Lage, den gesamten Himmel abzudecken, und können daher nicht für eine umfassende Untersuchung der Population der galaktischen Supernova-Überreste (SNR) verwendet werden. Darüber hinaus sind SNRs in Erdnähe (hunderte von Parsec), die im Röntgenbereich Größenordnungen von einem Grad erreichen können, mit gezielten Röntgeninstrumenten nur schwer zu untersuchen. Blindbeobachtungen mit dem Ziel, den gesamten Himmel nach potenziellen neuen Überresten absuchen, sind keine Option. Wie es scheint, ist ein großer Teil der Differenz zwischen der erwarteten Anzahl galaktischer SNRs und der Anzahl entdeckten galaktischen SNRs darauf zurückzuführen, dass nicht der gesamte Himmel in allen verschiedenen Energiebereichen, in denen SNRs nachweisbar sind, erfasst wurde. Angesichts der Empfindlichkeit des von eROSITA verwendeten CCD-Typs und dessen Energieabdeckung, die weit über den oberen Energiebereich von ROSAT XRT (2 keV) hinausgeht, ist eRASS ideal geeignet, um die Röntgenemission einer Vielzahl von astrophysikalischen Objekten zu entdecken und zu untersuchen, einschließlich SNRs, die stark absorbiert sind und/oder nicht-thermische Spektralkomponenten aufweisen. Die entsprechenden Röntgendaten ermöglichen es daher, die bekannte Population thermischer und nicht-thermischer Quellen zu untersuchen und nach neuen Quellen zu suchen, insbesondere nach letzteren (d.h. nicht-thermischen), die potenzielle Beschleuniger kosmischer Strahlung sind. Das von uns durchgeführte gründliche Screening der ersten vier eRASS-Durchmusterungen (eRASS:4), die dem deutschen eROSITA-Konsortium zugänglich sind, hat mehrere Dutzend neuer SNR-Kandidaten und neuer Röntgen-Gegenstücke zu bekannten SNRs aufgedeckt, von denen wir überzeugende Kandidaten für

bisher unbekannte Beschleuniger ultra-relativistischer Teilchen identifiziert haben.

Der erste Teil dieser Dissertation ist eine Zusammenstellung von fünf Publikationen, die aus einer detaillierten und tiefgreifenden Multiwellenlängenanalyse von drei SNRs (Michailidis et al. 2024a, Michailidis et al. 2024b, Khabibullin et al. 2024, Michailidis et al. 2024c) resultieren, die wir zum ersten Mal mit eROSITA im Röntgenbereich nachgewiesen haben (G279.0+01.1 SNR, der Spaghetti-Nebel (S147 oder G180.0-01.7 SNR) und der G309.8+00.0 SNR) und die Identifizierung der SNR-Natur des HESS J1614-518 SNR-Kandidaten (Pühlhofer et al. 2024), wie von den H.E.S.S.-Daten nahegelegt, unter Verwendung von eROSITA- und GLEAM-Radiodaten. Für alle oben genannten SNRs/Ziele haben wir eine detaillierte Analyse durchgeführt, um die Eigenschaften der einzelnen Überreste zu untersuchen, wie z. B. (falls in der jeweiligen Quelle entdeckt): Temperatur des thermischen Röntgenplasmas, Ionisationsalter, chemische Zusammensetzung des lokalen ISM und des Vorläufersterns (Elementhäufigkeiten), thermischer Plasmazustand (Gleichgewicht oder nicht), Powerlaw-Form (Indizes), die das Spektrum der nicht-thermischen Teilchenpopulationen (sowohl in Röntgen- als auch in γ-Strahlen) charakterisiert, Plasmadichte, Entfernung und Altersbestimmung. Ziel dieser Studie ist es, die Eigenschaften derjenigen SNRs zu untersuchen, die Teilchen effizient auf GeV/TeV-Energien beschleunigen können (nicht-thermische SNRs). Die Ergebnisse tragen auch dazu bei, die Diskrepanz zwischen der Gesamtzahl der entdeckten galaktischen SNRs und der Anzahl der im Röntgenlicht entdeckten galaktischen SNRs zu verringern und zu erklären, sowie letztlich die Lücke zwischen der erwarteten und der entdeckten Anzahl der galaktischen SNRs zu schließen.

Der zweite Teil dieser Dissertation ist eine Zusammenstellung von zwei Veröffentlichungen auf dem Gebiet des indirekten Nachweises von Dunkler Materie (DM) mit Hilfe von Gammastrahlen-Instrumenten (dem Cherenkov-Telescope-Array (CTA) und *Fermi*-LAT). Im Besonderen konzentrieren wir uns auf das Annihilationssignal der sogenannten Weakly Interacting Massive Particles (WIMPs) im diffusen Halo der benachbarten Spiralgalaxien M31 und M33 (nicht allzu häufig gewählte Ziele für DM-Studien), für die in der Literatur eine große Vielfalt an DM-Profilen und eine detaillierte Charakterisierung der baryonischen Masse berichtet wird, hauptsächlich aufgrund ihrer Nähe zur Erde, was umfangreiche Studien im Kontext ihrer astrophysikalischen Natur ermöglicht. Unsere

Studie (Michailidis et al. 2023) im Besonderen liefert die erwartete Empfindlichkeit von CTA für ein Annihilationssignal von WIMPs aus M31 und M33. Wir zeigen, dass CTA bei einer 100 h langen Beobachtungskampagne Annihilationsquerschnitte bis zu $\langle \sigma v \rangle \approx 5 \cdot 10^{-25}$ cm^{3}s^{-1} für den $\tau^+\tau^-$-Annihilationskanal (für M31, bei einer DM-Masse von 0.3 TeV) nachweisen kann, was die aktuellen, von HAWC abgeleiteten Grenzwerte um bis zu einer Größenordnung verbessert. Für die Ableitung der erwarteten CTA-Empfindlichkeit für das Annihilations-DM-Signal analysierten wir Unsicherheiten im Zusammenhang mit *(i)*: der potenziellen astrophysikalischen Hintergrundkontamination im Sichtfeld (FoV) von CTA, *(ii)* dem Vorhandensein von DM-Substrukturen, *(iii)*: der unvollkommenen Kenntnis des Instruments selbst und/oder der falschen Identifizierung von CRs, d. h. systematische Unsicherheiten, und *(iv)*: die fehlende Kenntnis der tatsächlichen DM-Dichteverteilung. Daher argumentieren wir, dass unsere Studie eine ausgezeichnete Grundlage für die Spezifikation (d. h. die Belichtungszeit) der bevorstehenden Beobachtung von M31 mit CTA bietet, welche bereits geplant ist. Wir gehen davon aus, dass die Beobachtungen der ausgewählten Ziele unter Berücksichtigung der möglichen Auswirkungen des höchst unsicheren astrophysikalischen Hintergrunds und der DM-Dichteverteilung wichtige Hinweise auf den WIMP-DM-Parameterraum liefern könnten. Angetrieben von unserem Ergebnis, dass die Unsicherheiten der DM-Dichteprofile zu den größten Unsicherheiten (unter den vier oben genannten Ursachen für Unsicherheiten) in den abgeleiteten Werten führen, bieten wir einen ausgezeichneten Überblick über die DM-Verteilung in häufig untersuchten astrophysikalischen Objekten (1095 Objekte und 5659 DM-Dichteprofile insgesamt, plus vierundsiebzigtausend DM-Dichteprofile von zweiunddreißigtausend nahen Galaxien, die in zwei neueren Studien unter Verwendung von Daten des Sloan Digital Sky Survey (SDSS) und der ALFALFA-Durchmusterung erstellt wurden), die sich über viele Größenordnungen der Masse erstrecken (von dSphs bis hin zu Galaxienhaufen) und einen wertvollen Anhaltspunkt für Kollegen darstellen können, welche die Komponente Dunkler Materie einzelner Ziele untersuchen wollen (Michailidis et al. 2024d). Die letztgenannte Studie liefert auch Beweise für eine neue universelle Eigenschaft von DM bei allen beobachteten Massen, die wir in einer bevorstehenden Veröffentlichung detailliert behandeln, in der wir alle verschiedenen gesammelten DM-Dichteprofile in einen Kontext stellen (in Form der DM-Säulendichte (S) als Funktion der Halomasse), um eine

neue Skalierungsbeziehung einzuführen, die einen direkten Vergleich der Beobachtungen mit theoretischen Vorhersagen/numerischen Simulationen ermöglicht.

List of original publications

The following is a list of all publications written during my Doctoral program (in chronological order). My contribution to the publication/s not first-authored by me is/are explicitly stated.

I **M. Michailidis**, L. Marafatto, D. Malyshev, F. Iocco, G. Zaharijas, O. Sergijenko, M.I. Bernardos, C. Eckner, A. Boyarsky, A. Sokolenko, A. Santangelo. Prospects for annihilating dark matter from M31 and M33 observations with the Cherenkov Telescope Array. In: Journal of Cosmology and Astroparticle Physics (JCAP) 2023.8, 073 (Aug. 2023).

II **M. Michailidis**, G. Pühlhofer, A. Santangelo, W. Becker, M. Sasaki. X-ray counterpart detection and γ-ray analysis of the SNR G279.0+01.1 with eROSITA and *Fermi*-LAT. In: Astronomy & Astrophysics (A&A), 685 (2024) A23 (Apr. 2024).

III **M. Michailidis**, G. Pühlhofer, W. Becker, M. Freyberg, A. Merloni, A. Santangelo, M. Sasaki, A. Bykov, N. Chugai, E. Churazov, I. Khabibullin, R. Sunyaev, V. Utrobin, I. Zinchenko. Study of X-ray emission from the S147 nebula by *SRG*/eROSITA: X-ray imaging, spectral characterization and a multiwavelength picture. In: Astronomy & Astrophysics (A&A), accepted (May 2024).

IV I. Khabibullin, E. Churazov, N. Chugai, A. Bykov, R. Sunyaev, V. Utrobin, I. Zinchenko, **M. Michailidis**, G. Pühlhofer, W. Becker, M. Freyberg, A. Merloni, A. Santangelo, M. Sasaki. Study of X-ray emission from the S147 nebula by *SRG*/eROSITA: supernova-in-the-cavity scenario. In: Astronomy & Astrophysics (A&A), accepted (May 2024).

- **My contribution**: eROSITA imaging, spectral analysis, and characterization of the S147 SNR. I am leading the German team in this project (since it is a joint project between a German and a Russian team of scientists) and I have also contributed significantly to developing ideas and participating in discussions that determined the paper's contexts and shaped its final version.

V **M. Michailidis**, G. Pühlhofer, A. Santangelo, W. Becker, M. Sasaki. A look at the high energy aspects of the supernova remnant G309.8+00.0 with eROSITA and *Fermi*-LAT. In: Astronomy & Astrophysics (A&A), accepted (June 2024).

VI G. Pühlhofer, **M. Michailidis**, N. Nguyen, A. Santangelo, W. Becker, M.

Sasaki, G. Ponti. Identification of HESS J1614-518 as Supernova remnant using GLEAM, eROSITA and *Fermi*-LAT survey data. In: Astronomy & Astrophysics (A&A), to be submitted.

• **My contribution**: I am the second and corresponding author of this paper. The discovery, the large majority of the analysis (80%) as well as a large part of the writing (at least 50%) has been conducted by me. I have used eROSITA (X-rays), Fermi-LAT (γ-rays), and GLEAM (radio) data to identify the SNR nature of the SNR candidate HESS J1614-518. I have run the entire multiwavelength analysis of the remnant (imaging and spectral analysis in all three aforementioned energy ranges) and its modeling (in terms of distance and age estimates).

VII **M. Michailidis**, C. Thorpe-Morgan, D. Malyshev, A. Santangelo, J. Jochum. Dark Matter Density Profiles (DM_ρcat): A Review. In: Astronomy & Astrophysics (A&A), to be submitted.

List of publications not included in this work

The subjects discussed in these papers are not covered in this dissertation since they are pertaining a larger discipline of high-energy astrophysics with smaller contributions from my side.

I The Cherenkov Telescope Array Consortium [including **M. Michailidis**]. Prospects for γ-ray observations of the Perseus galaxy cluster with the Cherenkov Telescope Array. In: Journal of Cosmology and Astroparticle Physics (JCAP), submitted (Sep. 2023), arXiv.2309.03712.

II The Cherenkov Telescope Array Consortium [including **M. Michailidis**]. Prospects for a survey of the Galactic plane with the Cherenkov Telescope Array. In: Journal of Cosmology and Astroparticle Physics (JCAP), submitted (Oct. 2023), arXiv.2310.02828.

III The eROSITA Consortium [including **M. Michailidis**]. The SRG/eROSITA all-sky survey: X-ray catalogues of the Western Galactic Hemisphere and first data release. In: Astronomy & Astrophysics (A&A), (Jan. 2024), DOI: 10.1051/0004-6361/202347165, arXiv.2401.17274.

IV The Cherenkov Telescope Array Consortium [including **M. Michailidis**]. Dark Matter Line Searches with the Cherenkov Telescope Array. In: Journal of Cosmology and Astroparticle Physics (JCAP), submitted (Mar. 2024), arXiv.2403.04857.

V The Cherenkov Telescope Array Consortium [including **M. Michailidis**]. Galactic transient sources with the Cherenkov Telescope Array. In: Monthly Notices of the Royal Astronomical Society (MNRAS), submitted (May 2024), arXiv.2405.04469.

Declaration

The first objective of this two-phase collective work is the detection of new X-ray counterparts of non-thermal Galactic SNRs and/or the identification of the SNR nature of SNR candidates (and/or unidentified objects) that are potential sources of CR acceleration with eROSITA, aiming at investigating the properties of the highest shock velocities in our Milky Way and shedding light on important questions of Modern Astrophysics (e.g., what fraction of X-ray emitting SNRs are of non-thermal nature, what fraction of all observed Galactic SNRs are of non-thermal nature in the high energy and very high energy domain (X-rays and γ-rays), up to what age SNRs can efficiently accelerate particles?). In such a way this work indirectly contributes toward gaining further insight into universal unresolved problems of Modern Astrophysics that have been addressed before but are not yet solved: is there a missing problem of Galactic SNRs, up to which energies Galactic SNRs can efficiently accelerate particles, and what is the contribution of the Galactic CRs to the total CR spectrum? The second part of this work deals with the study of the expected sensitivity of CTA to an annihilation signal of WIMPs from nearby spiral galaxies and the systematic study of the distribution of the DM in objects spanning many orders of magnitude in mass (from dSphs to Galaxy Clusters). I hereby declare that all findings presented in this dissertation are the result of research I conducted independently, based on my own ideas and new findings, and all collaborators who contributed to this research are listed in the corresponding articles. To the best of my knowledge, I have not used any additional sources besides those mentioned in the corresponding bibliography sections.

Tübingen, August 4, 2024

Michailidis Miltiadis

Abbreviations

AI Artificial Intelligence

ASKAP Australian Square Kilometre Array Pathfinder

BH Black Hole

CC Core-Collapse

CMB Cosmic Microwave Background

CTA Cherenkov Telescope Array

CR Cosmic-rays

DES Dark Energy Survey

DM Dark Matter

dSphs dwarf spheroidal satellite galaxies

EGRET Energetic Gamma Ray Experiment Telescope

EM Electromagnetic

eV electron volt

FoV Field of View

GB6 The Green Bank 6cm radio survey

GC Galactic Center

GLEAM GaLactic and Extragalactic All-sky MWA Survey

HAWC High-Altitude Water Cherenkov Observatory

HE High Energy

H.E.S.S. High Energy Stereoscopic System

HGPS H.E.S.S. Galactic Plane Survey

HYB Hybrid profile

IACT Imaging Atmospheric Cherenkov Telescope

IC Inverse Compton

IR Infrared

ISM Interstellar Medium

ISO Isothermal profile

LHAASO Large High Altitude Air Shower Observatory

LST Large Sized Telescope

MAGIC Major Atmospheric Gamma Imaging Cherenkov Telescopes

MC Molecular clouds

MOND Modified Newtonian Dynamics

MST Medium Sized Telescope

MW Milky Way

NFW Navarro, Frenk and White

PBH Primordial Black Holes

pc parsec

PWN Pulsar Wind Nebula

PMN Parkes-MIT-NRAO

SED Spectral Energy Distribution

SHASSA Southern H-Alpha Sky Survey Atlas

SIS Singular Isothermal Sphere

SM Standard Model

SN Supernova

SNR Supernova remnant

SST Small Sized Telescope

TS Test Statistic

VERITAS Very Energetic Radiation Imaging Telescope Array System

VHE Very High Energy

WD White Dwarfs

WIMP Weakly Interacting Massive Particle

3FHL Third catalogue of Hard Fermi-LAT sources

4FGL Fourth catalogue of Fermi-LAT sources

3ML Multi-Mission Maximum Likelihood framework

Contents

Chapter 1

Introduction

1.1 Multiwavelength analysis of Supernova remnants

1.1.1 What are Supernovae and Supernova remnants?

Supernova remnants (SNRs) are the residua of Supernova (SN) explosions, one of the most energetic processes in the Universe. SNe mark the death of stars with violent blasts that release $\sim 10^{51}$ ergs of kinetic energy into space. Their byproducts, i.e., SNRs, heat, compress, kick, and enrich the surrounding interstellar medium (ISM). Thus, SNRs are responsible for the chemical enrichment of the ISM, which in turn triggers star formation. The shock waves of those bursts can efficiently accelerate charged particles from radio to X-ray emitting energies (Koyama et al., 1995), and as of recently confirmed up to GeV/TeV energies (e.g., Esposito et al. (1996); Aharonian et al. (2001, 2004); Acero et al. (2016); Abdalla et al. (2018)). SNRs are also responsible for neutrino emission and can be characterized as particle-accelerating laboratories. They are believed to be cosmic-rays (CRs) accelerators, i.e., they are thought to accelerate charged particles, mainly protons and atomic nuclei but also electrons, to the highest energies ($> 10^{14}$ eV).

By definition, SNRs, along with neutron stars and black holes, are considered to be the stars' graveyards. Yet, they were initially named after the interpretation of the detection of a new star in the sky (SN explosion) and they provide some of the most beautiful images in our Galaxy. SNR images demonstrate the violent and chaotic-looking mass from gas and dust bounded by the SNR shock-waves. In fact, SNRs are the gleaming fusion of the processed and ejected progenitor stellar material and the heated and compressed surrounding ISM. SNe and subsequently SNRs are rare events of a rate of 1-2 per century in our Galaxy, even though we have not directly

observed an SN in our Galaxy for the past ~ 400 years. However, in contrast to SNe, events that occur in a short period of time and are observable only within a few years of occurrence, their remnants can remain visible for several thousand to ten-thousands of years as they go through several stages of development as described in detail in section 1.1.5.

1.1.2 SN classification

SNe can be broadly categorized into two distinct classes: i) type Ia or ii) type Ib,c/II mainly due to the presence or absence of hydrogen lines in their optical spectrum. Individual sub-categories exist based on broadly observed characteristics (refer to Weiler & Sramek (1988) for a more detailed study on the subclasses of SN). Type Ia SNe are the result of the thermonuclear runaway of a white dwarf (WD) accreting material from a donor star (binary companion) or a binary system of WDs. Type Ib,c/II SNe are the result of the gravitational core-collapse (CC) of massive stars that happens at the end of their life when the nuclear fusion produced by the star is no longer strong enough to oppose gravity (and thus massive stars collapse under their own gravity). In the first case, no compact object is left behind. However, type Ib,c/II SNe leave behind neutron stars or black holes (BH) as their legacy. Since the progenitors of type Ib,c/II SNe are massive stars, that are more abundant in the Galactic plane compared to higher Galactic latitudes, the highest concentration of SNRs is expected to be found along the Galactic plane.

SNRs serve as tracers of SN explosions and can provide valuable insight into their progenitors (both on the type of the SN and on the composition of the progenitor star). In particular, the resulting SNR spectrum in X-rays serves as an identifier of their progenitor. The X-ray spectrum of SNRs originating from type Ia explosions exhibits a low O/Fe ratio, with a characteristic Fe-L peak ($\sim 0.7 - 1$ keV), and the presence of some intermediate heavier elements such as Si, S, Ar, and Fe. On the contrary, the X-ray spectrum of SNRs of type Ib,c/II progenitor origin is characterized by a high O/Fe ratio and it is dominated by light emission line elements (i.e., O, Ne, and Mg) (refer to Vink (2012) and references therein).

1.1.3 The multiwavelength picture of SNRs

The kinetic energy released by the SN explosion heats up both the swept-up ISM and the ejected material up to $10^6 - 10^7$ K. Therefore, SNRs are

emitting in X-rays for a large fraction of their lifetime (yet such a timescale is significantly shorter than the lifetime of radio SNRs as discussed below) and thus studies of SNRs in X-rays come as a natural consequence. However, the primary criterion for the classification of an object as an SNR is the detection of its radio counterpart (radio synchrotron emission). The reasoning behind the latter assertion is that SNRs efficiently accelerate electrons up to GeV energies (responsible for non-thermal radio synchrotron emission). The lifetime of the latter relativistic particles exceeds the lifetime of SNRs and thus SNRs are considered to be "bright" in radio wavelengths from the very first moments of the shockfront creation until they merge with the local medium, get dissolved in the surrounding ISM, and dissipate completely when eventually the shock runs out of steam. Thus, SNRs have been most extensively cataloged in radio (Green, 2019), with a total number of ~ 300 Galactic SNRs ever detected. Recent catalogs, i.e., SNRcat[1] (Ferrand & Safi-Harb, 2012), contain a somewhat larger number (by a few tens) of Galactic SNRs. Therefore, the main criteria for the classification of an object as an SNR is a non-thermal spectrum (radio synchrotron emission with a negative spectral index) and an angular extent that exceeds the instrument's resolution (Clark et al., 1973). Additional proof such as a shell-type morphology (not necessarily in radio but also in X-rays and/or γ-rays) and a location at the Galactic plane complement the above criteria well but they are insufficient to identify an object as an SNR by themselves. However, a non-thermal X-ray shell or a γ-ray shell confirms the non-thermal nature of the source. Objects that meet one or more complementary features but do not satisfy the main criteria are classified as SNR candidates, e.g., the detection of three new SNR candidates purely based on their shell-type appearance in the TeV band (H. E. S. S. Collaboration et al., 2018).

SNRs are also detectable in different wavelengths across the entire electromagnetic (EM) spectrum. Optical identification of SNRs permits observation of the correlation of the shock wave and the surrounding ISM as the shocks propagate through the ISM material of different densities, especially cool regions that exhibit bright Hα emission triggered by the passage of the Supernova blast wave. The radiative shock (shock slowed down < 200 km/s – SNR at the border of phase II and III as described in detail in section 1.1.5) of the SNR passing through ambient medium also causes Fe II line emission (1.27, 1.64 μm) which is detected in Infrared (IR) and has its origin in thermal dust (Oliva et al., 1989). Additionally, the shocks of these

[1] http://snrcat.physics.umanitoba.ca

explosions are, as of recently probed, capable of accelerating particles up to very high energies (VHE) (acceleration of electrons at TeV energies, compared to GeV electrons that trigger radio synchrotron emission, and protons (CRs)). Thus, since the last decade, SNRs have been established as γ-ray sources (as confirmed by currently operating GeV and TeV observatories, e.g., Abdo et al. (2011); Tanaka et al. (2011); Acero et al. (2010); Carrigan et al. (2013)) and sources of high energy CRs (Ackermann et al., 2013). Some SNRs have been confirmed to accelerate electrons up to $\sim$100 TeV, e.g., SN1006 (Koyama et al., 1995). Whether SNRs are responsible for the "bulk" of CRs in the PeV energy band (up to 10^{17} eV) is debatable. Among the Galactic objects, SNRs are widely considered to be the best candidates for particle acceleration to such very high energies. However, definitive proof that SNRs can accelerate particles to the highest energies (PeVatrons) in our Galaxy is still lacking (Helder et al., 2012). As confirmed by X-ray observatories in the last three decades (ROSAT, *XMM-Newton*, *Chandra*, *Suzaku*, NuSTAR, e.g., Koyama et al. (1995); Allen et al. (1997); Aschenbach (1998)) as well as by γ-ray observatories (*Fermi*-LAT, H.E.S.S., HAWC, LHAASO) as mentioned above, SNRs are capable of accelerating electrons up to TeV energies (Vink, 2012). The latter can emit in X-rays through X-ray synchrotron emission (non-thermal X-rays, first confirmed in X-ray studies of the SN1006 SNR (Koyama et al., 1995)) or in γ-rays through Inverse Compton (IC). Though, this is not the end of the story. The nature of γ-ray emission from SNRs can either be leptonic (as introduced above) or hadronic. Relativistic hadrons can interact with subrelativistic nuclei likely originating from nearby molecular clouds (MCs) creating neutral pions that decay to two γ-ray photons. To conclude, SNRs are detectable across the entire EM spectrum and thus studying them at different wavelengths offers a unique opportunity to gain further insight into the extreme physical processes taking place within those objects. The results of multiwavelength studies can help to break the hadron/lepton ambiguity. Although hadrons are only visible in γ-rays, X-ray synchrotron emission originating from TeV electrons (the same TeV electron population responsible for leptonic γ-ray emission) can provide constraints on the leptonic part of γ-rays.

1.1.4 SNR classification

SNRs can be distinguished into three main categories based on their observational characteristics (imaging and spectral analysis results): i) shell-type SNRs that exhibit a shell-type structure in radio, optical, and

X-rays. The X-ray emission is found to be thermal in the majority of the cases, however, non-thermal X-ray emission might be present, ii) composite SNRs that vary in appearance in radio and X-rays, however, they all share a common feature; they host a Pulsar Wind Nebula (PWN), and iii) mixed-morphology SNRs that are characterized by a radio shell that is center-filled in X-rays. Fig. 1.1 demonstrates the observational characteristics of the three distinct classes of SNRs.

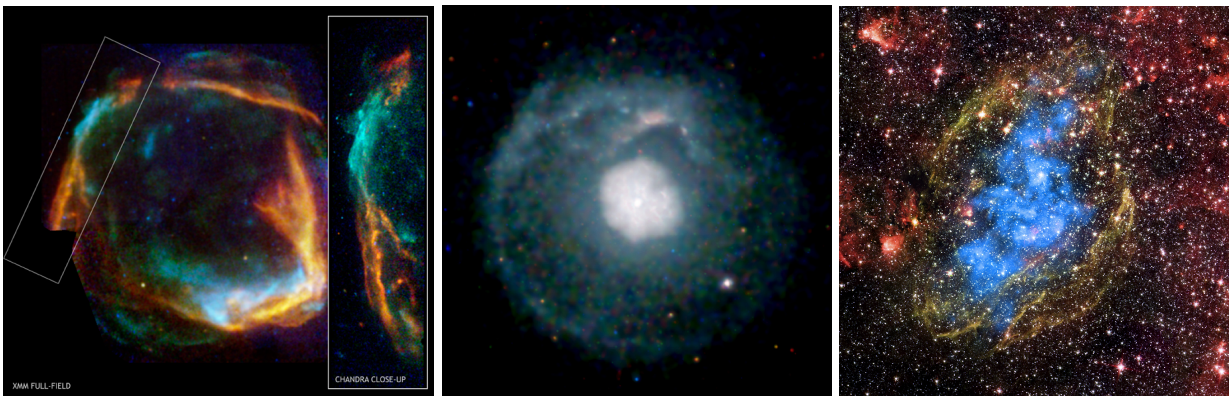

Figure 1.1: The three distinct classes of SNRs based on observational characteristics. Right: Shell type SNR. Middle: Composite SNR (hosts a PWN). Right: Mixed-morphology SNR (radio shell (yellow) filled with X-rays (blue))[2].

1.1.5 Evolutionary stages of SNRs

The simple and broadly accepted, and subsequently adopted, model for the SNR evolution consists of four main phases (Woltjer, 1972): i) free expansion phase (a few tens to a few hundreds of years), in which the mass of the remnant is dominated by the ejected material from the progenitor star. The whole explosion energy is contained in the ejected material, the shockfront propagates with a supersonic velocity ($>$ 3000 km/s) sweeping up most of the ambient medium material in its passage, ii) adiabatic expansion or Sedov phase (Sedov, 1959; Taylor, 1950) (a few hundreds to several thousands of years), in which the swept up mass becomes comparable or exceeds the ejecta mass. At this phase, the pressure difference between the ejecta and the swept-up mass actuates the creation of a reverse shock that propagates toward the center of the explosion. The kinetic energy is now transferred to internal energy (heating) but as of recently suggested up to 50% of the initial energy can be released in the form of CRs. The shock velocity drops below 3000 km/s but it remains well above 200 km/s, iii) radiative or "snow plough" phase (several thousands to several tens of thousands of years), in

[2] https://chandra.harvard.edu

which the energy can no longer be conserved. The remnant slowly dissipates its thermal energy through strong radiative cooling and the shock velocity drops to several tens of km/s, and iv) the merging phase, in which the shock velocity drops to the level of the turbulent motion of the surrounding ambient medium. The remnant gets dissolved and is no longer discernible from the surrounding ISM. However, real SNRs exhibit ample evidence that the exact physical processes taking place in individual remnants differ and are strongly dependent on the irregularities of the surrounding ISM (Tsunemi & Inoue, 1980; Cowie et al., 1981; Shull et al., 1985; Kesteven & Caswell, 1987). A classic example is SNRs originating from type Ib,c/II SNe of massive stellar progenitors that can strongly disturb the surrounding ISM through strong stellar winds. The latter results in the formation of low-density bubbles of hot gas that can affect the standard evolution of SNRs as described above.

1.1.6 The missing number of Galactic SNRs

There are about 300 SNRs detected in our Galaxy, mainly cataloged from radio searches as mentioned before (Green, 2019). Taking into account the age of the Milky Way (MW) and the occurrence rate of SNe (and SNRs) there is a huge discrepancy (by a factor of 4 to 6) between the expected and detected number of Galactic SNRs at any given moment under the assumption of at least a 60 kyrs lifetime for radio SNRs (Frail et al., 1994; Becker et al., 2021) (since older SNRs are expected to not be observable after they get dissolved in the surrounding ISM). Even if we exclude the type Ib,c/II SNe that leave behind a black hole and thus are not luminous, a significant mismatch remains. Apparently, the age (and consequently evolutionary phase) of the SNRs plays a critical role in their detection since extremely evolved SNRs are expected to not be discernible from the surrounding Interstellar Medium (ISM). The sensitivity of our instruments could also play a key role since fainter remnants would not be detected. Finally, the size which is a function of the distance of each remnant is also an unavoidable factor in the proper instrument selection (pointing observations versus All-Sky Surveys). Depending on their evolutionary state and distance from Earth, the angular sizes of Galactic SNRs can range from a few arcmin to several degrees. Only a handful of Earth-adjacent remnants, a few tens of hundreds of parsecs away, which are found in their most evolved state and with sizes of several degrees, have been detected to date.

In the X-ray band particularly, even fewer findings have been reported. A large discrepancy between the total number of detected Galactic SNRs and the

number of SNRs detected in the X-ray band also exists. Although the lifetime of the X-ray emission originating from Galactic SNRs is smaller compared to radio SNRs which explains the apparent gap, tens of known SNRs (from radio observations) and new SNR candidates have already been discovered with eROSITA (refer to section 1.1.7 for a detailed description of the instrument). Current imaging X-ray instruments, such as *XMM-Newton*, *Chandra*, and *Suzaku* have a limited field of view (FoV). Proposing blind observations aiming to cover the whole sky for potential remnants that are not observable in radio and could potentially emit in higher energies is not an option. In many cases, imaging survey data is the only option. The concentration of dust in the Galactic Plane also prohibits the detection of many SNRs that are located close to the Galactic Plane in X-rays (highly absorbed SNRs). The improved sensitivity (that is significant at soft X-rays, 0.2-2 keV, where many SNRs in the Galactic plane are likely to be partially or totally absorbed) of the eROSITA All-Sky Survey, the main X-ray instrument used in this work, as described in detail in the next paragraph, offers a unique chance to detect such SNRs that *XMM-Newton*/*Chandra*/*Suzaku* and ROSAT (eROSITA provides a 25-fold or higher sensitivity compared to ROSAT depending on the sky region observed) could not have seen due to their limited Field of View (FoV).

1.1.7 eROSITA

The eROSITA (extended ROentgen Survey Imaging Telescope Array) instrument operating at the soft X-ray energy regime, 0.2-10.0 keV (Predehl et al., 2021), and the Russian X-ray concentrator `MIKHAIL PAVLINSKY` ART-XC (Astronomocial Roentgen Telescope-X-ray Concentrator) working complementary in the harder X-ray energy band of 4.0-30.0 keV (Pavlinsky et al., 2021), are the two instruments mounted on the Russian-German Spektrum Roentgen Gamma (SRG) observatory (Sunyaev et al., 2021). The mission was launched on the 13th of July 2019 towards L2 Lagrangian point, whereas the survey began on the 13th of December 2019.

Equipped with seven parallel aligned X-ray telescopes TM1-7, having a 1° field of view each, and with an objective to achieve an 26″ average spatial resolution in survey mode after the completion of 8 All-Sky Surveys, eRASS:8, in a duration of six years (Merloni et al., 2012; Predehl et al., 2021) the German-Russian eROSITA telescope (Predehl et al., 2021) offers the opportunity to search for X-ray sources in the 0.2-2.0 keV energy band (soft X-rays) with a 25-fold sensitivity improvement in comparison to the RASS All-Sky Survey data (Voges et al., 1999) provided by the ROSAT instrument.

In the hard X-ray band (2.0-10.0 keV), eROSITA is the first ever true imaging survey of the sky (Merloni et al., 2012). A preliminary analysis of the in-flight PSF calibration presented in Merloni et al. (2023) shows an $\sim$ 30" average spatial resolution in survey mode (with only 4 out of the 8 all-sky surveys having been completed), compared to the expected value by Predehl et al. (2021). Overall, the corresponding X-ray data in the broadband 0.2-10 keV energy range permit the study of the known population of both thermal and non-thermal SNRs and the search for new such sources.

1.1.8 X-ray spectroscopy of SNRs

X-rays is a natural and characteristic wavelength to study SNRs, as discussed above, since the shock of the burst heats the surrounding ISM (shock-front) and the ejecta material (reverse shock) to temperatures greater than a million Kelvin. At those temperatures, Hydrogen and Helium are completely ionized while a large number of heavier-Z elements are also strongly ionized. Despite the amount of the ejected stellar material and the compressed ISM falling within the SNRs extensions, the latter are low-density objects since the corresponding blast expands to distances that can reach hundreds of parsecs, and thus collision processes are far less frequent than radiative processes responsible for X-ray emission (optically thin plasma). The thermal X-ray spectrum of SNRs is a mixture of a continuum component (thermal bremsstrahlung) and line emission mainly dominant at lower energies. The plasma is usually in a non-equilibrium state for younger SNRs (for which a short period of time, this usually applies to SNRs in phase I and II as discussed in section 1.1.5, has passed after the plasma was shocked) since only a few collisions that cause ionization have taken place, whereas it usually reaches equilibrium for the most evolved SNRs since the latter have undergone a sufficient amount of interactions at larger timescales that permits reaching an equilibrium state. Thus, a global temperature, the ionization parameter, the elemental abundances, and the normalization are all needed for a detailed characterization of the spectrum. The non-thermal X-ray spectrum originating from a population of electrons accelerated to TeV energies that emit X-ray photons through synchrotron radiation is well described by only two parameters, the powerlaw index and the normalization. A SNR can be characterized by the presence of either a thermal, a non-thermal component, or a mixture of both in its spectrum.

1.1.9 *Fermi*-LAT

Fermi-LAT is a γ-ray telescope, launched on June 11, 2008, and is sensitive from 20 MeV to greater than 300 GeV. As eROSITA, *Fermi*-LAT provides all-sky coverage (Atwood et al., 2009), including the Galactic Plane, but at higher energies (γ-rays). With *Fermi*-LAT, extended emission from various SNRs has been spatially resolved for the first time (Giuliani et al., 2011; Katagiri et al., 2011; Ackermann et al., 2013; Acero et al., 2016). Previous γ-ray instruments (e.g., EGRET) were incapable of distinguishing high-energy (HE) photons that are SNR-produced from those originating from the background due to their limited spatial and spectral resolution (Sturner & Dermer, 1995; Esposito et al., 1996). In addition, a large number of studies confirm the presence of nearby Molecular clouds (MCs) interacting with SNRs (refer to e.g., Chen & Jiang (2013) and references therein for a list of such remnants which are considered to be interacting with MCs based on reasonable selection criteria as established by previous studies). The remnants that exhibit such characteristics (interacting with MCs) are accompanied by a high probability of emitting in γ-rays, as seen by *Fermi*-LAT (Thompson et al., 2012). The latter connection is luckily attributed to the higher chance of hadronic CRs, produced by the SNR, interacting with the lower energy nuclei of dense MCs resulting in the production of γ-ray photons. A surprising finding, however, is that γ-rays appear bright in a number of old SNRs (e.g., Araya (2020)). Ultrarelativistic particles are expected to have escaped the shell of old SNRs. Thus, γ-ray emission from some of those old SNRs could also be a result of the interaction of "sea CR" particles with nearby MCs giving the false impression that γ-ray emission originates from the SNR. The discrimination between the different particle populations responsible for the extended γ-ray emission is obtained by inspecting their GeV-spectrum. In particular, GeV-TeV electrons emitting in γ-rays through IC are expected to produce a characteristic peak in the γ-ray spectrum (usually toward TeV energies) of the SNR whereas the interaction of hadrons (accelerated protons from the SNR) with subrelativistic nuclei from the surrounding medium (and/or nearby MCs) produces neutral pions, among other particles, that decay in γ-rays. The spectral energy distribution of this radiation has a characteristic bell-type shape (π^0-decay bump) (Ackermann et al., 2013). Being able to analyze SNRs non-thermal emission from radio to X-rays and γ-rays provides us with the opportunity to set tight constraints on individual SNR properties such as the energy budget of protons and electrons as well as the magnetic field strength in the case of leptonic GeV-TeV spectra.

1.2 Indirect Detection of Dark Matter

1.2.1 Evidence that point out the existence of DM

Since the start of the 20th century, there is ample evidence for the existence of a "dark" component in our Universe. The Dutch Astronomer J. Kapteyn (Kapteyn, 1922), and Oort (Oort, 1932) presented the first evidence for the existence of an unseen mass component, erroneous as proved later in Kuijken & Gilmore (1989), by measurements of stellar velocities in the MW. At the same epoch, 1933, the Swiss-American astronomer Fritz Zwicky (who is now considered one of the most popular and widely cited pioneers in studies of DM) found similar indications for the existence of DM but on a much larger scale. Zwicky studied the Coma cluster and he was able to calculate the velocity dispersion of galaxies in the cluster by using observed Doppler shifts of the galactic spectra (Zwicky, 1933, 1937). As a result, he concluded that galaxies only account for a small fraction of the total mass and thus a missing component of matter exists. At first, Zwicky's discovery in the Coma cluster was largely ignored. It was only 40 years later that V. Rubin and collaborators conducted an extended research on the rotation curves of 60 isolated spiral galaxies that exhibit similar features to the MW (Rubin, 1983). The collected data gave a flat appearance of the rotation curve of the galaxies which largely deviated from the expected decreasing curve as seen in Fig 1.2. Rotational curves are not the only evidence for the existence of the dark component of matter. The movement of galaxies in Galaxy Clusters, gravitational lensing, and the spectrum of fluctuations of Cosmic Microwave Background (CMB) are amongst the most relevant evidences for the existence of DM.

The newest pieces of evidence come from 2006 (Clowe et al., 2006) when the Bullet cluster, the result of the clash of two galaxy clusters (a collision between a subcluster with the cluster 1E 065756), was observed (as seen on the right pane of Fig 1.2). Analyzing the individual spectral regions it was realized that the clash had caused a strong separation of the individual components of the clusters. The stars and galaxies passed each other without strong interaction but the baryonic mass, which exists in the extremely hot gas clouds in between the galaxies emitting X-rays, was compressed and a shock was created as detected by the *Chandra* X-ray Observatory[4] (baryonic matter shown in red color on the right panel of Fig 1.2). The blue areas of the right picture of Fig 1.2 show where one finds most of the mass of the

[3] https://chandra.harvard.edu/photo/2006/1e0657/
[4] https://chandra.harvard.edu/

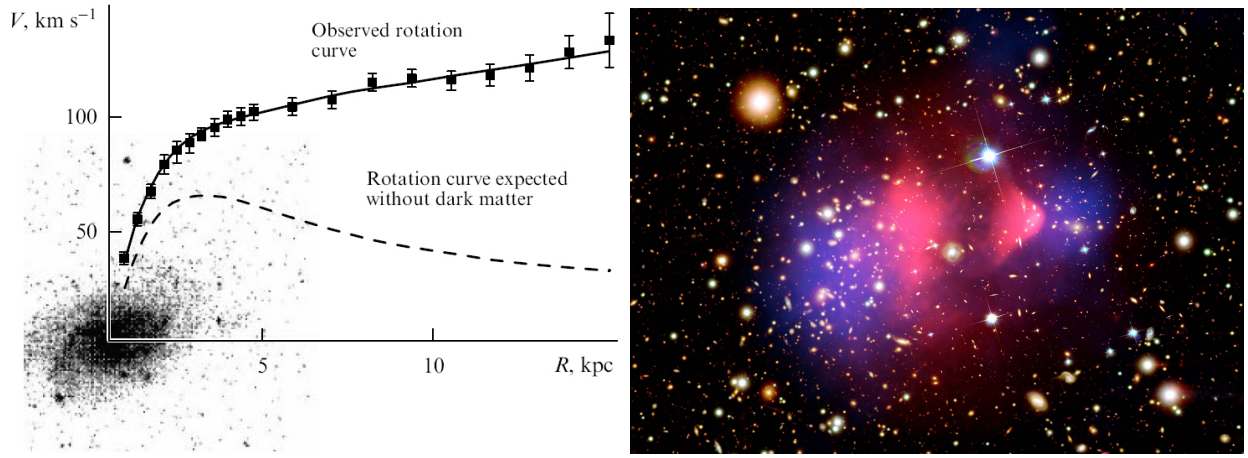

Figure 1.2: Evidence for DM. Left: Comparison of the expected with the observed rotation curve of M 33 (Zasov et al., 2017). Right: Colour image of Bullet Cluster 1E0657-558. The red colour represents the X-ray emitting hot gas and contains most of the baryonic matter in the two clusters. The blue colour represents the total mass contours. Image is adopted from the *Chandra* X-ray Observatory[3].

clusters which is clearly separated from the baryonic matter (red colour). The final conclusion was that the areas of strong X-ray emission significantly differ from the area of the largest concentration of mass seen through gravitational lensing and consequently most of the mass in clusters is not baryonic. Since the first evidences of the existence of DM by searches in the Bullet cluster (Clowe et al., 2006), other studies have found similar evidences for missing mass in galaxy clusters (Bradač et al., 2008; Ragozzine et al., 2012; Jee et al., 2016).

1.2.2 The nature of DM

By today we have managed to calculate the DM density with great accuracy ($\Omega_{DM}h^2 = 0.11933 \pm 0.00091$ (Akrami et al., 2020)). However, the nature of DM continues to be a mystery. Different scenarios for the nature of the DM have been proposed throughout the years. Among those scenarios, some suggest that the missing matter can be explained within the Standard Model (SM) Cosmology (e.g., Primordial Black Holes (PBH)) whereas in other theories, such as Modified Newtonian Dynamics (MOND), DM does not even have to exist. MOND is a paradigm proposed to account for the mass discrepancies in galaxies and galaxy systems. In 1983, Milgrom proposed MOND as an alternative theory of gravity (Milgrom, 1983) by introducing an acceleration constant ($\alpha_0 = 2 \cdot 10^{-8}$ cm s^{-2}) to modify Newton's second law. However, the vast majority of scenarios keep holding around the fact that DM is non-baryonic and thus it applies to Physics beyond the SM (Bertone et al., 2005; Zyla et al., 2020). Among the broadly adopted SM extensions trying to

explain the missing mass problem (DM), Weakly Interacting Massive Particles (WIMPs) are among the DM candidates that have been extensively explored. They are considered to be stable, electrically neutral, and have a cross-section of the order of the weak interaction, therefore satisfying all the requirements for a Dark Matter particle. The latter candidates belong to the cold dark matter census, i.e., particles that were moving slowly during the formation of the pre-galactic clumps. Warm and hot dark matter particles moving at faster speeds and nearly at the speed of light respectively, when the clumps were formed, have also been proposed as non-baryonic candidates. However, the cold DM alternative supported by the bottom-up process (confirmed by observations that contradict with DM particles of high velocities, e.g., *Chandra* observations showing cluster formation from Galaxy groups and Galaxy sub-clusters merging) is broadly accepted to date.

1.2.3 IACTs and CTA

Self-annihilating WIMPs at mass scales ranging from MeV to TeV have a weak-scale cross-section (velocity averaged annihilation cross-section $\langle \sigma \upsilon \rangle_{th} = 3 \cdot 10^{-26} \mathrm{cm}^3 \mathrm{s}^{-1}$ for DM particles) which naturally generates the observed abundance of the DM as an outcome of thermal freeze-out in the early Universe (Lee & Weinberg, 1977; Feng & Kumar, 2008; Profumo, 2013; Baer et al., 2015). Assuming that WIMPs constitute the entirety of the DM, their annihilation into SM particles and consequently the production of γ-ray photons (see e.g., Cirelli et al., 2011, for a review) makes WIMPs suitable for searches for annihilation signals from certain DM-dominated objects using indirect methods. During the last decade, several IACTs (e.g., MAGIC, VERITAS, H.E.S.S.) and more recent γ-ray instruments (i.e., HAWC and LHAASO) performed a number of dedicated WIMP DM search campaigns in the TeV band, in the context of WIMPs annihilation to γ-ray photons. The non-detection of a DM annihilation signal in the MW halo (Abeysekara et al., 2018), dSphs (Albert et al., 2018a), DM sub-halos (Coronado-Blázquez & Sánchez-Conde, 2020) and nearby galaxies (Albert et al., 2018b) imposes the tightest constraints on the parameters of annihilating DM as provided by these facilities.

Despite considerable efforts, current WIMP DM searches fall short of the thermal annihilation cross-section scale. The upcoming CTA observatory on the other hand, consisting of arrays of imaging atmospheric Cherenkov telescopes in both the southern (Chile) and the northern (La Palma)

hemisphere, with telescopes of three distinct sizes (Small Size Telescopes (SSTs), Medium Size Telescopes (MSTs), and Large Size Telescopes (LSTs)), operating in the 20 GeV to 300 TeV energy range, will be able to provide a full sky coverage and achieve a sensitivity improved by up to an order of magnitude (Acharya et al. (2019)) compared to already existing instruments, such as those mentioned above. This way CTA provides us with the opportunity to search for WIMPs in the TeV mass range with unprecedented sensitivity. The first telescope, Large Size Telescope 1 (LST1, 23 meters in diameter), has been successfully built and commissioned since 2018. It is now transitioning into scientific operation along with the MAGIC telescopes in stereo observation. Currently, three additional large-size telescopes (LST2-4) are under construction and are expected to be completed in 2026. CTA is set to revolutionize our understanding of the high-energy Universe by providing unprecedented sensitivity for DM searches and many other aspects of VHE Astrophysics.

1.2.4 DM targets and corresponding density profiles

The main criteria for the classification of an object as an ideal target for DM studies are: i) high expected DM concentration, ii) low astrophysical background contamination, and iii) large angular size/proximity (in-depth knowledge of its baryonic component from observations). There are a number of classes of DM objects currently being explored with indirect detection techniques including DM-dominated objects such as the Galactic center (GC), dSphs, and Galaxy Clusters. However, other targets such as nearby spiral galaxies that have been studied in detail in terms of their baryonic nature due to their proximity, and the MW diffuse halo are also prominent targets for DM searches. The latter targets offer an opportunity to gain deeper insight into the uncertainty of the DM constraints derived.

Among the DM properties considered for determining an object as a viable target for DM studies is the dark matter density profile. However, the latter is perhaps the most complex to derive. Since it is complicated to measure a "model-independent" DM profile in different objects because of the imperfect knowledge of the DM density distribution in objects, a variety of analytic approximations based on theoretical estimations (ISO), N-body simulations (NFW, Einasto) or empirical fit to the data (Burkert) were proposed. The NFW profile (Navarro et al., 1997), steeply rising (r^{-1}) towards the object's center and thus characterized as "cuspy" halo, is a traditional

benchmark choice motivated by N-body simulations. A generalized NFW profile was also proposed by Zhao (Zhao (1996)). In more recent numerical simulations, a profile that is not converging to a power-law at the GC but is a bit more chubby at kpc scales, is emerging as a better fit to the galaxies in the Spitzer Photometry and Accurate Rotation Curves (SPARC) catalog (Lelli et al., 2016) compared to an NFW profile. The above profile, which is called Einasto profile (Einasto, 1965, 1968), is characterized by a shape parameter α which can take several values, but 0.17 is the central, fiducial value that we adopt. More recently, it has been discovered that simulated DM halos match with the Einasto distribution over a wider range of radii in comparison to the NFW profile (Merritt et al. (2006), Navarro et al. (2010) and Chemin et al. (2011)). Cored or Isothermal profiles, such as the Burkert (Burkert, 1995) or Isothermal/Pseudo-Isothermal (ISO/PIS) (King (1966), Bahcall & Soneira (1980), Carignan & Freeman (1985)) may be instead more motivated by the observations of galactic rotation curves. Alternately, there are also profiles steeper than NFW like those proposed by Moore and collaborators (Moore et al., 1999). More recently a modified Einasto profile has been proposed, reflecting the baryonic feedback effects. In particular, this profile is denoted as EinastoB (Cirelli et al., 2011), it is a profile which is steeper in the center with respect to DM-only simulation which follows the above mathematical expression of Einasto profile with an α parameter of 0.11. Last but not least other profiles can be derived by combining two or more of the profiles listed above. Such an example is the HYB profile which is a mixture of SIS and NFW (hence hybrid profile (Hayashi & Chiba, 2014)). In general, the profiles differ most in the inner region of the galactic halo, close to GC, while they are rather alike above a few kpc. Consequently, DM signals from the innermost galaxy regions will be more sensitive to the choice of the DM profile.

The uncertainty on the DM distribution in those objects largely impacts the derived constraints on the DM parameters, therefore, detailed studies of the DM distribution in prominent DM targets are a requirement for the precise estimate of WIMPs (but also of any other valid DM particle candidate) annihilation detection within these objects.

Chapter 2

Objectives and expected outcome of the Doctoral research

The goal of the work carried out in the context of this Doctoral study is i) the detection and study of the population of non-thermal Galactic SNRs using telescopes observing in radio, X-rays, and γ-rays, which adds to closing the gap between the radio and X-ray/γ-ray emitting SNRs and indirectly contributes in resolving the topic of the missing population of Galactic SNRs, and ii) provide further insights on what can be achieved in the field of Indirect DM research with the next generation γ-ray facility CTA and highlight the shortcomings and uncertainties that need to be considered on the derivation of future constraints on the DM parameter space.

i) research rationale: Unveiling the nature of the non-thermal Galactic Supernova remnant (SNR) population by means of High-Energy (HE: X-rays) and Very-High-Energy (VHE: γ-rays, GeV/TeV/PeV) detailed/deep observations and subsequent data analysis, using eROSITA/*XMM-Newton* and *Fermi*-LAT/H.E.S.S. surveys. Radio observations with the GLEAM radio telescope working complementary to HE and VHE observations were also employed. Understanding the nature of the problem of the missing number of expected SNRs in the Milky Way (MW), investigating the properties of the highest shock velocities in our Milky Way, and gaining insight into important but unresolved problems of CR Physics: up to what age SNRs can efficiently accelerate particles and what is the SNRs contribution to the Galactic component of the CR spectrum? Aside from the detailed study of individual interesting cases, a more quantitative assessment of the selected sample of relevant sources needs to be carried out in order to address the following questions: What are they (confirm their nature) and how do they look like (morphology and information of the surrounding Interstellar Medium-ISM)? What is the expected (X-ray) energy spectrum? Do they

carry potential signatures for young SNRs with HE-lepton component: non-thermal X-ray spectrum (pure/dominant/subdominant component)? Are they considered non-thermal because of γ-ray (GeV-TeV) signal but no corresponding (non-thermal) X-ray emission: HE protons vs. HE relic leptons? Could the absence of non-thermal X-rays when combined with a non-thermal population of γ-ray particles be interpreted as a sensitivity issue (e.g., lack of deep enough exposure time toward a faint target) or does it point towards a physical explanation? Is it meaningful to derive upper limits in the latter cases? And most importantly, could a quantitative evaluation of the correlation between TeV source catalogs and H.E.S.S., *Fermi*-LAT sky maps and eROSITA maps be derived? Those are the main questions addressed in this thesis that set the groundwork for the studies I plan to undertake shortly. In the near future, investigating a much larger fraction of the detected SNR population but also examining new findings (new SNRs and SNR candidates) detected with eROSITA, but not analyzed in detail in this work, when combined with deep follow-up studies with *XMM-Newton*, *Chandra*, and XRISM and a detailed assessment of the γ-ray emission from the corresponding locations with *Fermi*-LAT could provide answers on the fundamental question of CR Physics such as: up to which energies SNRs efficiently accelerate particles, and what is the Galaxy's contribution to the total CR spectrum? Finally, searching for a potential correlation between the shock speed (from X-rays and other information) and the γ-ray spectral cutoff (signature for particle escape) would be of great importance in further understanding the nature of the physical processes taking place in SNRs,

ii) research rationale: Estimating the expected sensitivity of CTA to the annihilating DM signal from detailed studies of not that frequently considered targets for DM studies (i.e., nearby spiral galaxies), which have been extensively studied (in terms of their astrophysical component - baryonic mass) mainly due to their proximity. Thus, great emphasis needs to be given to the uncertainties of the derived results originating from astrophysical background contamination, lack of knowledge of a concrete DM density distribution in the targets, and systematic uncertainties connected to the imperfect knowledge of the instrument itself. Show that the imperfect knowledge of the actual DM density distribution, on prominent targets for DM studies (from small scales: dSphs to large scales: Galaxy Clusters), exhibits the most significant cause of uncertainty and provide a complete sample of all DM density profiles reported in the literature before; that every fellow colleague should take into consideration when deriving constraints on

DM properties. We additionally try to provide more accurate evidence (due to the larger sample of collected data) for a universal relation, proposed more than a decade ago (Boyarsky et al., 2009), that is satisfied by all different DM density distributions at all observed scales (i.e., the insensitivity of the DM column density to the type of DM density profile that is observed from dSphs to Galaxy Clusters - still an ongoing work).

Chapter 3

Multiwavelength study of Galactic SNR

Published works are presented here as originally published, with the permission of the publishers. Publications that are either submitted or in a "to be submitted" stage are reprinted with permission from the co-authors. Copyright holders with the corresponding copyright notices are listed below.

3.1 M. Michailidis, G. Pühlhofer, A. Santangelo, W. Becker, M. Sasaki. X-ray counterpart detection and γ-ray analysis of the SNR G279.0+01.1 with eROSITA and *Fermi*-LAT. In: Astronomy & Astrophysics (A&A), 685 (2024) A23 (Apr. 2024)

A&A, 685, A23 (2024)
https://doi.org/10.1051/0004-6361/202348491

Astronomy & Astrophysics

X-ray counterpart detection and γ-ray analysis of the supernova remnant G279.0+01.1 with eROSITA and *Fermi*-LAT

Miltiadis Michailidis[1], Gerd Pühlhofer[1], Andrea Santangelo[1], Werner Becker[2,3], and Manami Sasaki[4]

[1] Institut für Astronomie und Astrophysik Tübingen (IAAT), Sand 1, 72076 Tübingen, Germany
e-mail: michailidis@astro.uni-tuebingen.de
[2] Max-Planck-Institut für extraterrestrische Physik, Gießenbachstraße 1, 85748 Garching, Germany
[3] Max-Planck-Institut für Radioastronomie, Auf dem Hügel 69, 53121 Bonn, Germany
[4] Dr. Karl Remeis Observatory, Erlangen Centre for Astroparticle Physics, Friedrich-Alexander-Universität Erlangen-Nürnberg, Sternwartstraße 7, 96049 Bamberg, Germany

Received 4 November 2023 / Accepted 19 February 2024

ABSTRACT

A thorough inspection of known Galactic supernova remnants (SNRs) along the Galactic plane with SRG/eROSITA yielded the detection of the X-ray counterpart of the SNR G279.0+01.1. The SNR is located just 1.5° above the Galactic plane. Its X-ray emission emerges as an incomplete, partial shell of ∼3° angular extension. It is strongly correlated to the fragmented shell-type morphology of its radio continuum emission. The X-ray spatial morphology of the SNR seems to be linked to the presence of dust clouds in the surroundings. The majority of its X-ray emission is soft (exhibiting strong O, Ne, and Mg lines), and it occurs in a narrow range of energies between 0.3 and 1.5 keV. Above 2.0 keV the remnant remains undetected. The remnant's X-ray spectrum is purely of a thermal nature. Constraining the X-ray absorption column to values which are consistent with optical extinction data from the remnant's location favors nonequilibrium over equilibrium models. A nonequilibrium two-temperature plasma model of $kT \sim 0.3$ keV and $kT \sim 0.6$ keV, as well as an absorption column density of $N_{\rm H} \sim 0.3$ cm^{-2} describe the spectrum of the entire remnant well. Significant temperature variations across the remnant have been detected. Employing 14.5 yr of *Fermi*-LAT data, we carried out a comprehensive study of the extended giga-electronvolt source 4FGL J1000.0-5312e. By refining and properly modeling the giga-electronvolt excess originating from the location of the remnant, we conclude that the emission is likely related to the remnant itself rather than being colocated by chance. The remnant's properties as determined by the X-ray spectra are consistent with the ∼2.5 kpc distance estimates from the literature, which implies a source diameter of ∼140 pc and an old age of $>7 \times 10^5$ yr. However, if the source is associated with any of the pulsars previously considered to be associated with the SNR, then the updated nearby pulsar distance estimates from the YMW16 electron density model rather place the SNR at a distance of ∼0.4 kpc. This would correspond to a ∼20 pc linear size and a younger age of $10^4 - < 7 \times 10^5$ yr, which would be more in line with the nonequilibrium state of the plasma.

Key words. acceleration of particles – cosmic rays – ISM: supernova remnants – gamma rays: ISM – X-rays: ISM – X-rays: individuals: G279.0+01.1

1. Introduction

Supernova remnants (SNRs) are the residua of supernova (SN) explosions, one of the most energetic processes in the Universe. The shock waves of those bursts can efficiently accelerate charged particles from radio to X-ray emitting energies (Koyama et al. 1995), and also up to giga-electronvolt/tera-electronvolt energies (Aharonian et al. 2004; Acero et al. 2016; H.E.S.S. Collaboration 2018a). In contrast to SNe, that is to say events that occur in a short period of time observable within a few years of occurrence, their remnants can remain visible for several thousand to tens of thousands of years. Depending on their evolutionary state and distance from Earth, their angular sizes (assuming Galactic SNRs) can range from a few arcmin to several degrees. Only a select number of low surface brightness Earth-adjacent remnants, a few tens of hundreds of parsecs away, which are found in their most evolved state and with sizes of several degrees, have been detected. In the X-ray band particularly, even fewer findings have been reported. The improved sensitivity of the eROSITA All-Sky Survey offers a unique chance to detect such SNRs that *XMM-Newton/Chandra/Suzaku* and ROSAT could not have seen (Becker et al., in prep.).

The majority of detected SNRs fall in the Galactic plane, where massive stars are most abundant. Even though they are extended objects, particularly in their evolved states, they can be partially or totally obscured (e.g., in optical and X-ray wavebands) due to the prevalence of absorbing dust in the Galactic plane. In the radio band, the sensitivity limitation of current instruments as well as the potential confusion or contamination of the emission from brighter nearby sources is another inhibitory factor in the localization of the emission originating from SNRs. G279.0+01.1 is such a case of a remnant. According to current literature, it is possibly located near the tangent point to the nearby Carina spiral arm, which would place it at a distance of 2.7 ± 0.3 kpc (Shan et al. 2019). Its center is located just 1.5° above the Galactic plane, and it has a size of 2.3° in the radio band (Stupar & Parker 2009). Its spatial appearance in the optical is morphologically consistent with the high concentration of dust on the three sides (i.e., the southern, western, and eastern sides) of the remnant as reported in

Stupar & Parker (2009). The bright radio sources at and around the remnant's vicinity make it challenging to determine its true radio extent. A giga-electronvolt source, seemingly correlated with the remnant, has recently been discovered (Araya 2020), whereas no X-ray counterpart had been found to date. In this work, we report on the first X-ray counterpart detection of G279.0+01.1 by utilizing data of the first four completed eROSITA All-Sky Surveys, in other words eRASS:4 (Merloni et al. 2024).

In 1988, the remnant was detected for the first time in the radio continuum band (Woermann & Jonas 1988). The SNR appears as a circular shell of ∼1.6° angular extension, quite distinguished from the radio emission related to the nearby Carina spiral arm. The northern and eastern limbs appear to be the brightest parts of the remnant, whereas the fainter western limb is characterized by a region of enhanced radio emission. The latter is likely attributed to an unrelated point source, which in later studies was determined to be a powerful extragalactic point-like radio emitter (G278.0+0.8) (Duncan et al. 1995). The northern, radio-bright limb of the remnant lies along the line of sight of an HI region. However, the latter is highly unlikely to be interacting with the remnant given that their kinematic distances differ significantly, by 8 kpc. Moreover, Duncan et al. (1995) confirmed the detection of two CO clouds likely interacting with the SNR.

There are ten pulsars within less than a 3.0° angular separation from the remnant's redefined center (refer to Sect. 2.1). Three of these pulsars – B0953-52, B0959-54, and B1014-53 – have been discussed as potential associations with the remnant. B0953-52 was initially considered the most plausible counterpart, given its 0.64° angular distance from the remnant's center and alignment with the SNR's circular morphology (Woermann & Jonas 1988). However, Duncan et al. (1995) suggested that the pulsar B0959-54, currently named J1001-5507, is more likely associated with the remnant, despite being 1.6° away from the remnant's center and outside the radio emission region. We examined the implications of potential pulsar associations with G279.0+01.1, considering a recent update to the electron density model (Yao et al. 2017). This update reduces, by about an order of magnitude, distance estimates to all pulsars potentially associated with the remnant compared to values derived using the earlier model in Cordes & Lazio (2002).

In addition, more recent radio studies showcase the detection of previously missed broad filamentary structures in the northeastern and southwestern parts of the SNR, and strong polarization at 1.4 GHz and 2.4 GHz frequencies (Duncan et al. 1995; Whiteoak & Green 1996). In particular, while typical SNRs do not exceed radio polarization levels of 10%, Duncan et al. (1995) detected strong polarization up to 50% at 2.4 GHz. The remnant has also been classified among the barrel shape SNRs as introduced in Kesteven & Caswell (1987). A reassessment of the remnant's radio morphology was conducted in Stupar & Parker (2009), revealing a larger – compared to previous studies (Woermann & Jonas 1988; Duncan et al. 1995) – radio image of the SNR at 843 MHz and 4.85 GHz. A 2.3° angular size was obtained from observations of the remnant at both frequencies (Cram et al. 1998; Stupar & Parker 2009).

Optical Hα emission, originating from G279.0+01.1, was detected for the first time by Stupar & Parker (2009). The detailed optical analysis revealed 14 small-scale fragmented groups of Hα filaments spread over a 2° area within the SNR's radio shell. Those structures are concentrated at the central and northeastern parts of the remnant, suggesting that the high dust concentration toward the south and west of the remnant prevents optical detection. Even though the strong radio source G278.0+0.8 does not have an optical Hα counterpart, a strong enhancement in Hα emission is being observed just to the west of the remnant. The latter Hα excess is consistent with diffuse radio emission of the size of 24 arcmin. The emission is concluded to be unrelated to the remnant itself and is more likely an illuminated HII region. More recent infrared (IR) Galactic surveys – that is, the Wide-Field Infrared Survey Explorer (WISE) – confirmed the shell-type morphology of the object and classified it as an HII region that can be found under the name G277.731+00.647 in the WISE HII catalog Ver. 2.4 (Anderson et al. 2014).

A distance estimation based on the interaction of the SNR's blast wave with interstellar clouds resulted in a 3 kpc distance (McKee & Cowie 1975; Stupar & Parker 2009) consistent with the $\Sigma - D$ estimation. A consistent distance estimation of 2.7 ± 0.3 kpc was obtained using optical extinction from red clump stars (Shan et al. 2019).

A giga-electronvolt source positionally coincident to the remnant has been detected utilizing Pass 8 *Fermi*-LAT data (Araya 2020). The γ-ray emission region above 5 GeV has an ∼2.8° angular size, seemingly surpassing the radio synchrotron (Stupar & Parker 2009) toward the northeastern parts of the remnant. Both a leptonic and a hadronic scenario of the γ-ray origin are discussed in Araya (2020). However, Zeng et al. (2021) ruled out the leptonic scenario possibility by fitting the remnant's multiwavelength spectra with hard γ-ray spectra, extending up to 0.5 TeV, mainly due to the remnant's evolved state. There are no signs of softening of the γ-ray spectrum at higher energies, >0.5 TeV, but the remnant is undetected in the tera-electronvolt band (H.E.S.S. Collaboration 2018b).

The paper is organized as follows. In Sect. 2, we report on the outcomes of eROSITA observations and X-ray data analysis of the remnant utilizing eRASS:4 data. We also checked archival ROSAT survey data and *XMM-Newton* pointings toward the southwest of the remnant and briefly report those results. In Sect. 3, we provide a multiwavelength study of the remnant employing archival radio synchrotron and giga-electronvolt γ-ray data, as well as dust tracers. In Sect. 4 we report on the X-ray spectral analysis of the remnant, utilizing both eROSITA and *XMM-Newton* data. An updated giga-electronvolt spectrum is also provided. Closing remarks are reported in Sect. 5.

2. X-ray observations and data analysis

The main parameters of all X-ray observations employed in this work are summarized in Table 1.

2.1. eROSITA data

In this work, we use data from the eROSITA (extended ROentgen Survey Imaging Telescope Array) instrument operating in the 0.2–4.0 keV energy range (Merloni et al. 2012; Predehl et al. 2021). eROSITA is one of the two scientific instruments aboard the Russian-German Spektrum Roentgen Gamma (SRG) observatory (Sunyaev et al. 2021). It hosts seven parallel-aligned X-ray telescopes (TM1-7). Each telescope has a field of view of 1°. The All-Sky Surveys started December 13, 2019. A (preliminary) analysis of the in-flight PSF calibration (Merloni et al. 2024) showed a ∼30″ average spatial resolution in survey mode.

In the current analysis, only data from the first four completed All-Sky Surveys (eRASS:4), were exploited, in the `c020` processing version. Data reduction and analysis was conducted utilizing the `eSASSusers_201009` version (Brunner et al. 2022)

Table 1. eROSITA, *XMM-Newton* (MOS1, MOS2, and PN), and ROSAT observations analyzed in this work.

Instrument	ObsID	Year	Mode	Exposure (ks)	Pointing
eROSITA	eRASS:4 (150144, 145144,150141,145141)	2019–2021	survey	25.9 [(a)]	–
MOS1, MOS2, PN	0823031001	2018	Full frame (×3)	17.7/17.7/15.8	South West
MOS1, MOS2, PN	0823030401	2018	Full frame (×3)	16.7/16.7/14.8	South West
MOS1, MOS2, PN	0823030301	2018	Full frame (×3)	9.0/9.0/7.1	North
ROSAT	RASS (932618, 932619,932716,932717)	1990	Survey	14.0 [(b)]	–

Notes. The pointing column describes the position of the *XMM-Newton* observations with respect to the remnant's center. [(a)]Total on-source exposure time. [(b)]Livetime, on time.

of eSASS (eROSITA Standard Analysis Software). All events that were flagged as corrupt either individually or as a whole corrupt frame were filtered out. All four legal patterns were sustained while bad patterns were identified and excluded (`pattern=15`). Disordered GTIs were recognized and repaired. In addition, eRASS:4 data were inspected for flares. The affected regions were reprocessed and corrected, thus preventing possible contamination of the event files.

The eROSITA All-Sky map consists of 4700 sky tiles. Each one of them has a square morphology of ∼3.6° × 3.6° size. The majority of the X-ray emission from the SNR is contained in a single sky tile. However, a total of four sky tiles were exploited in order to obtain complete coverage of the remnant and sufficient background control area. Fitting an annulus to the outermost X-ray emission ring of the remnant's fragmented shell structure, resulted in a geometrical center position of: RA: 9:58:27.23, Dec: –53:35:46.95. We verified the above result by performing a Minkowski tensor analysis, which is an automatic bubble-recognition routine for parametrizing the shapes of bodies (Collischon et al. 2021). The detection routine is based on the drawing of perpendicular lines to the detected structures. In our work, we perform the latter routine to the SNR fragmented shell, in the 0.3–1.1 keV energy band. Aiming to avoid contamination of our data sets and distortion of the obtained results, only X-ray diffuse structures encapsulated within the extension of the remnant's radio counterpart (see Sect. 3) were employed. Nearby structures unrelated to the remnant (e.g., the diffuse X-ray emission situated in the south of the remnant) were excluded from this analysis. All lines of the shell should meet in a small region inside the shell, thus creating high-line-density regions. The reconstructed center is shown in Fig. 1 in green. The obtained result (central coordinates in X-rays: RA: 9:59:45.48, Dec: –53:33:11.91) is consistent with the one derived above. Consequently, to explore the remnant's X-ray spatial morphology, we construct mosaic sky maps with a size of 4° × 4° and a 10″ pixel size centered on the best-fitted coordinates from the Minkowski tensor analysis.

In particular, the mosaic sky maps from the location of the remnant were produced by employing the `evtool` task of the eSASS software, combining the four aforementioned individual eROSITA sky tiles and using data from all instrument's telescopes TM1-7. We find a strong detection of the SNR G279.0+01.1 in the narrow energy range from 0.3 to 1.1 keV, as depicted in Fig. 1. Individual regions of the remnant, positioned mainly to the south and west, exhibit X-ray emission up to 1.5 keV. However, the remnant remains totally undetected above

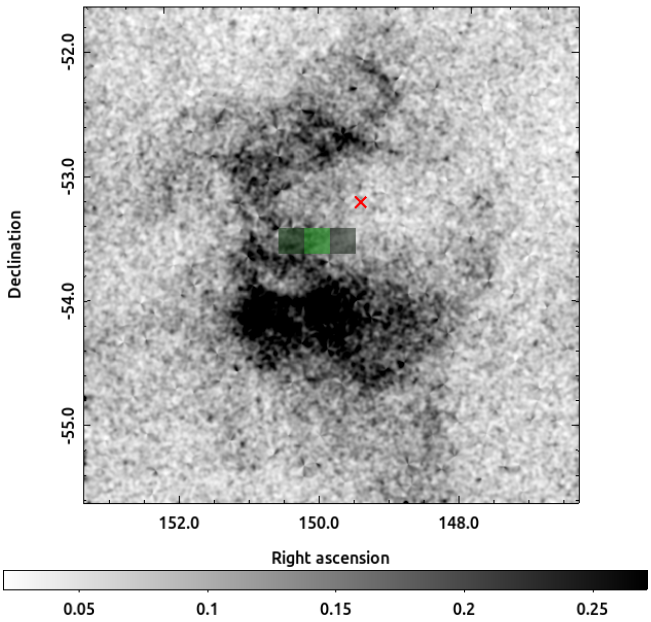

Fig. 1. eRASS:4 exposure-corrected intensity sky map in the 0.3–1.1 keV energy band, in units of counts per pixel with a pixel size of 10″. Point sources have been filtered out, and the image has been convolved with a $\sigma = 45''$ Gaussian to enhance the visibility of the diffuse X-ray emission originating from the source. The geometrical center of the X-ray emission from a Minkowski tensor analysis is shown by the green boxes. A brighter box means a higher probability to represent the center. The red cross indicates the remnant's center based on previous radio measurements.

2.0 keV. In addition to the soft X-ray emission that the image analysis reveals, the spatial morphology of the remnant matches with an incomplete shell (since the western part of the shell is not observable in X-rays), or a fragmented annulus of highly asymmetric width, of ∼3° angular size. The two enhanced regions of X-ray emission, in particular the two brightest X-ray "blobs" found at the southeastern part of the remnant (saturated blobs in Fig. 1), are not associated with any known astrophysical object that could account for such a type of diffuse X-ray emission. Therefore, we strongly suggest that they are part of the diffuse emission originating from the remnant itself. Further imaging analysis, color-coded RGB image (0.3–0.7 keV: red, 0.7–1.1 keV: green, 1.1–2.3 keV: blue) displayed in Fig. 2, indicates potential

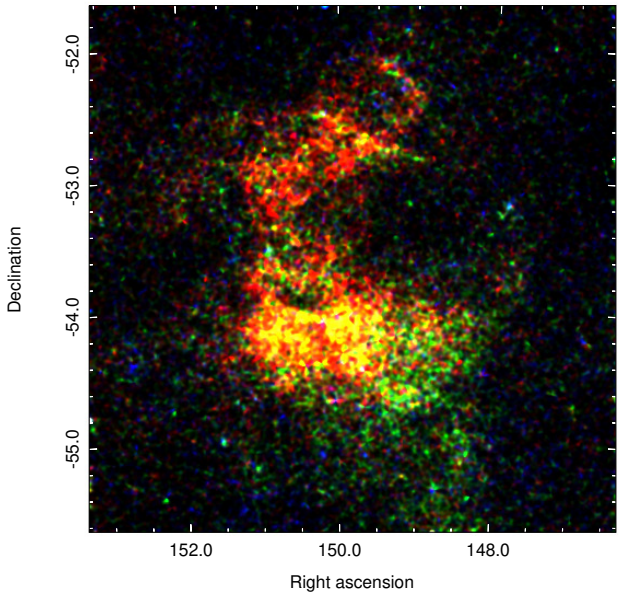

Fig. 2. eRASS:4 RGB exposure-corrected intensity sky map, with the energy color-coded as follows: R, 0.3–0.7 keV; G, 0.7–1.1 keV; and B, 1.1–2.3 keV, in units of counts per pixel with a pixel size of 10″. A squared-colored distribution is chosen for visual purposes. Point sources are filtered out, and the image is convolved with a $\sigma = 45''$ Gaussian to enhance the visibility of the diffuse X-ray emission.

temperature variation, that is to say plasmas of different temperatures across the remnant. This is confirmed by the spectral analysis results in Sect. 4. Additionally, Fig. 2 confirms the lack of X-ray emission at hard X-rays by the absence of blue color, the majority of the X-ray emission is confined in the 0.3–1.1 keV energy band (red and green colors).

2.2. ROSAT data

After the very significant detection of G279.0+01.1 in X-rays with eROSITA for the very first time we checked why the remnant has escaped detection in the ROSAT All-Sky-Survey (RASS data). We exploited publicly available data from the RASS Position Sensitive Proportional Counter detector in survey mode (PSPC; Voges et al. 2000). The medium, 0.4–2.4 keV, energy band, yielded a better signal-to-noise ratio in comparison to the narrower 0.3–1.1 keV energy range selected for eROSITA. As shown on the right panel of Fig. 3, the incomplete shell-type structure of the remnant, with much lower statistical quality in comparison to eROSITA, is visible above a strongly structured background. Both images of Fig. 3 are smoothed using a Gaussian function as described in the caption of the corresponding figure to enhance the visibility of the source. 5125 counts (of which 1444 are source counts) are detected with ROSAT from the location of the remnant, that is to say a circular region centered at the X-ray coordinates derived in Sect. 2.1 with a radius of 1.7°, to make sure that it encircles the entire X-ray excess originating from the remnant. The corresponding numbers for the eRASS:4 data in the same energy range are 205 077 counts (of which 76 651 are source counts). eRASS:4 has a ∼53 times higher collection area than the previous ROSAT survey (as expected), and the limited photon statistics plus the uneven background has apparently prevented a discovery with ROSAT.

2.3. XMM-Newton data

The *XMM-Newton* data archive was inspected to see whether relevant observations exist toward the direction of G279.0+01.1 that could enhance or complement (on limited regions) the eROSITA imaging and spectral results. Indeed, two *XMM-Newton* observations that overlap with the SNR and one very adjacent toward the north of the SNR are found in the *XMM-Newton* archive (see the left panel of Fig. 3 for the locations of these pointings with respect to G279.0+01.1). These observations (PI: Bettina Posselt, ObsId 0823031001, 0823030401, 0823030301) were targeted on nearby pulsars (J0957-5432, J0954-5430, J1000-5149, respectively), and no analysis on potential diffuse emission in the FoVs has been reported in the literature. We therefore analyzed these data to check for consistency with the eRASS results. Indeed, the two observations overlapping the SNR (one partially, one fully) exhibit significant diffuse emission consistent in morphology with the eRASS sky map (see Fig. B.1 and the left panel of Fig. 3). We therefore extracted source spectra from the two *XMM-Newton* pointings from the respective on-source areas, using the source-free region and the third, off-source pointing as background control regions. eRASS spectra were extracted from the same on-source regions. Overall, there is good consistency between the spectral results of the two instruments. The *XMM-Newton* data were useful to verify the applicability of the spectral model ultimately chosen for the eRASS data, but did not permit to put further constraints on the ambiguities that remained in the choice of models from the eRASS spectral data analysis. Refer to Appendices A and B for further details on the specifics of the *XMM-Newton* pointings and the *XMM-Newton* spectral analysis process.

3. G279.0+01.1 multiwavelength study

3.1. Radio continuum and Hα

Figure 4 demonstrates the spatial correlation between the X-ray emission as seen with eROSITA, using eRASS:4 data in the 0.3–1.1 keV energy range, with 4850 MHz radio data from the PMN southern survey (Condon et al. 1993) as blue contours, and full-sky Hα data of 6′ FWHM resolution (Finkbeiner 2003), as magenta contours. The remnant appears as a fragmented shell of comparable radius in all three energy bands. The radio angular size seems to extend even further compared to the latest estimate of ∼2.3° (Stupar & Parker 2009) matching its X-ray counterpart size of ∼3°, derived in this work. In particular, the bright radio limb to the north of the SNR is well complemented with a region of enhanced X-ray emission, which could possibly be associated with the presence of a CO cloud at that location of the remnant, as reported in Duncan et al. (1995). An excellent visual correlation is found between the radio and X-ray data at the location of the two bright blobs that stand out in the eRASS:4 sky maps. The bright radio source G278.0+0.8, which is most probably of Extragalactic origin, is also detected in eRASS:4 data but masked out since this work focuses on diffuse X-ray emission from the location of the remnant. A diffuse radio emission region, of 24″ size, observed just to the west of G278.0+0.8 is absent in the X-ray band (or too faint to be observed with eROSITA – eROSITA detects only two point sources from that area).

No particular association between the 14 bright optical filaments detected toward G279.0+01.1 (Stupar & Parker 2009) with the eRASS:4 data has been found, whatsoever. However, collectively, they are nicely enclosed within the remnant's extension. In

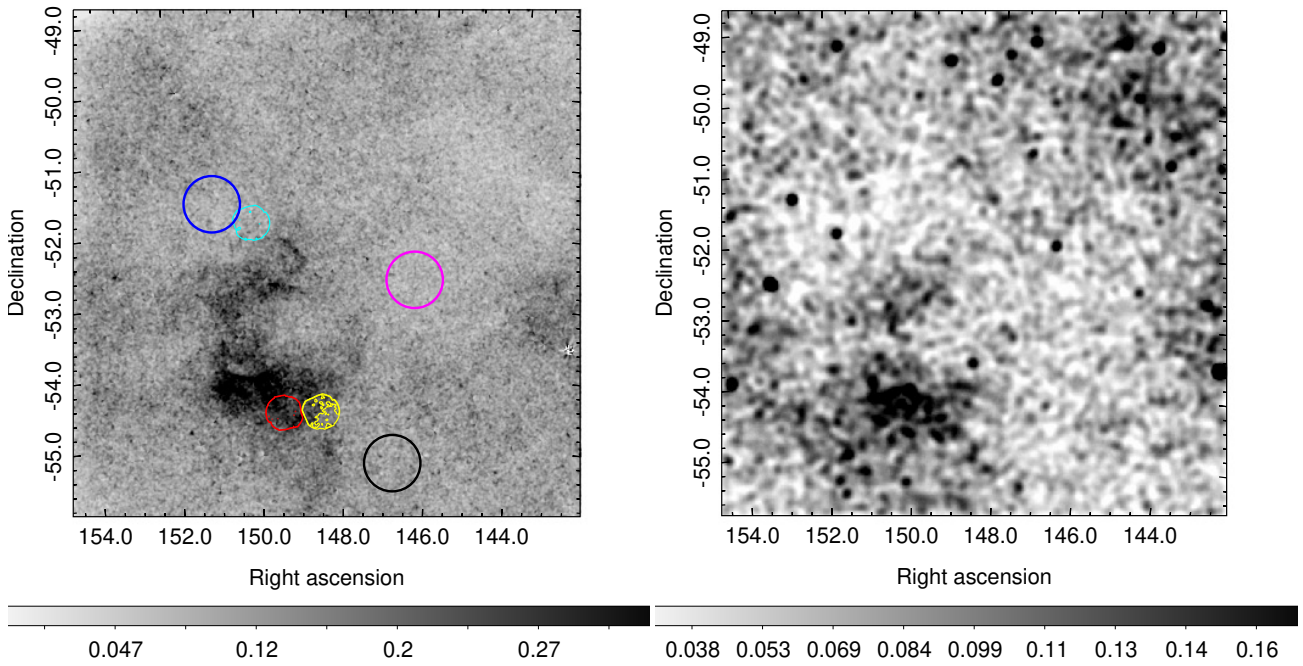

Fig. 3. Comparison of eROSITA and ROSAT view of the remnant. Left panel: eRASS:4 exposure-corrected intensity sky map in the 0.4–2.4 keV energy band, in units of counts per pixel with a pixel size of 10″. Point sources are filtered out, and the image is convolved with a $\sigma = 45''$ Gaussian. The black, magenta, and blue circles represent the three background control regions that we have selected to inspect potential background variations in the remnant's Galactic vicinity. Among those, the black circle was selected as the representative background used for the spectral analysis of the on-source regions, see Sect. 4.1 for more details. Red, yellow, and cyan circles mark the positions of the 0823031001, 0823030401, and 0823030301 *XMM-Newton* pointings, respectively. Within each circle one level contours are used, of identical scale for all three pointings, aiming at illustrating regions of enhanced X-ray emission. Right panel: ROSAT intensity sky map in the 0.4–2.4 KeV energy band (medium RASS band). The image, with a 45″ pixel size, is convolved with a $\sigma = 3'$ Gaussian to enhance the visibility of the diffuse emission from the location of the remnant. Point sources are not removed since their proper masking requires a substantially larger extraction radius than for eROSITA, which heavily affects the faint diffuse emission originating from the remnant.

this work, we additionally exploited the optical Hα data obtained from the full-sky Hα map (of 6′ FWHM resolution; Finkbeiner 2003), which is a conglomerate of the Virginia Tech Spectral line Survey (VTSS) in the north and the Southern Hα Sky Survey Atlas (SHASSA) in the south, to examine such an association. Two enhanced regions, in terms of Hα emission, become clearly apparent. Both seem to be partially spatially coincident with parts of the remnant that appear bright in the eRASS:4 sky maps and well-aligned with the small-scale fragmented groups of Hα filaments (Stupar & Parker 2009). This association is depicted in Fig. 4. The Hα contours overlaid in the aforementioned image were constructed by omitting nearby, bright optical (Hα) sources, which do not seem to be associated with the remnant. Therefore, due to the fact that the remnant falls in a highly contaminated Hα galactic neighborhood, the available data did not allow us to perform further spectral analysis. Confirmatory spectral results are presented in Stupar & Parker (2009) which are well-aligned with the shock excitation expected from such an old remnant and provide evidence for prominent [OII] and [OIII] lines (a potentially O-rich remnant).

3.2. Giga-electronvolt γ-rays

Araya (2020) carried out a detailed *Fermi*-LAT data analysis from the location of the remnant, which revealed a 2.8° wide extended giga-electronvolt source, currently found under the name 4FGL J1000.0-5312e. The giga-electronvolt source is found to be spatially coincident with the remnant and extends slightly further to the north and east in comparison to the radio shell. γ-ray emission, likely associated with the remnant, is detected up to 0.5 TeV with no indication of softening at higher energies. The remnant is, however, not detected in the VHE (Very-High-Energy) band, but the available data is limited (2.7 hours of observational live time with H.E.S.S. H.E.S.S. Collaboration 2018b). Later on, Zeng et al. (2021) attempted to fit the multiwavelength spectra of the remnant, as a part of detailed spectral modeling of a sample of 13 SNR characterized by hard giga-electronvolt γ-ray. Araya (2020) discusses both a leptonic and a hadronic scenario for the origin of the giga-electronvolt γ-ray emission. However, the detailed spectral modeling of G279.0+01.1 performed by Zeng et al. (2021) challenges the leptonic processes, claiming that the giga-electronvolt emission cannot be attributed to leptonic mechanisms due to the evolved state of the remnant, which is of age >100 kyr. Thus, a hadronic scenario for the production of gamma-rays is favored.

In this work, we reanalyzed Pass 8 *Fermi*-LAT data (P8R3) from the location of the remnant, using `fermitools` Ver. 2.0.8 standard analysis software and employing ∼4 additional years of data (August 2008 to March 2023) in comparison to the previous studies (Araya 2020). In more detail, we performed the data reduction and analysis in a similar manner to what is reported in Araya (2020). A region of the size of 40° centered on the remnant's coordinates (identical to those employed by Araya 2020) was analyzed. Source event class data, front, and back interactions included (evclass=128, evtype=3), were exploited. The

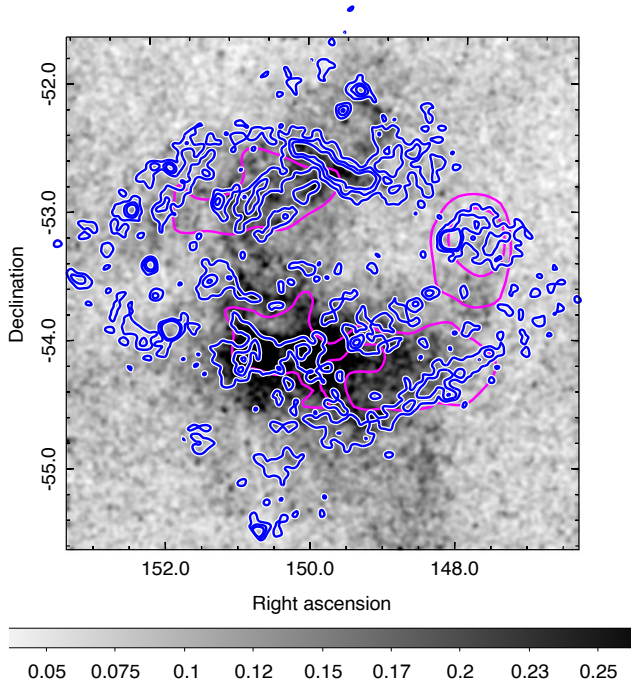

Fig. 4. eRASS:4 exposure-corrected intensity sky map, with identical parameters as the one displayed in Fig. 1. The blue contours mark the 4850 MHz radio data obtained from PMN (Condon et al. 1993) southern and tropical surveys, and GB6 (Condon et al. 1991, 1994). The magenta contours mark the optical Hα data obtained from the full-sky Hα map of Finkbeiner (2003), with 6′ FWHM resolution.

maximum data zenith angle was set to 90°. An angular bin size of 0.025° was selected, in comparison to 0.1° used in Araya (2020), in order to secure a good sampling of the *Fermi*-LAT Point Spread Functions (PSF). Modeling of the *Fermi*-LAT background was performed by including the Galactic diffuse component `(gll_iem_v07.fits)`, the isotropic diffuse component `(iso_P8R3_SOURCE_V3_v1.txt)` and all sources included in the *Fermi*-LAT 12 year source catalog (4FGL-DR3). In more detail, the normalization spectral parameter of sources within 5° of the center of the region of interest was left to vary keeping the remaining spectral parameters fixed to default catalog values. In comparison to Araya (2020), the 4FGL J1000.0-5312e extended giga-electronvolt source, seemingly associated with the remnant, appears in the 4FGL-DR3 catalog with different spectral features. In particular, a LogParabola spectrum instead of a simple powerlaw appears to provide the best fit model for the giga-electronvolt source.

A series of binned analysis procedures for extended *Fermi*-LAT sources was carried out. Both residual count map and Test Statistic (TS) maps were produced in different energy ranges to thoroughly inspect and refine the gamma-ray emission originating from the remnant's location. Below 5 GeV, γ-ray emission is barely distinguished from nearby giga-electronvolt emission originating from the Galactic plane. Therefore, for the construction of both types of sky maps, we restricted ourselves to >5 GeV to make use of the improved spatial resolution that the *Fermi*-LAT PSF provides at higher energies. On the left panel of Fig. 5, the residual count map above 5 GeV is depicted, which is in good agreement with the corresponding image obtained by Araya (2020). For the TS map production, the detection significance calculation was carried out based on the maximum likelihood test statistic. In particular, the TS maps were obtained by moving an ostensible point source through the grid and obtaining the maximum likelihood fit at each position of the grid. From the inspection of the 5–500 GeV TS map at the location of the remnant, which is shown on the left panel of Fig. 6, we identified 3 main regions of significant giga-electronvolt emission with 4.6σ, 5.5σ, and 5.8σ detection significance, respectively. Moreover, 3σ significance detections are obtained at multiple regions where the remnant extends over. As displayed on the right panel of Fig. 5, the giga-electronvolt emission encircles well both the radio and X-ray fragmented shells. It also exhibits an angular extension of ∼3°, a result obtained by fitting an annulus to the outermost part of the emission. The above value is in agreement with the findings by Araya (2020).

Comparing eRASS:4 to *Fermi*-LAT data strongly suggests that the emission at the remnant site spatially anticorrelates in those two energy bands. One obtains such a result by overlaying the TS map contours to the eRASS:4 data, as seen on the right panel of Fig. 5. However, the absence of X-ray emission accompanying the detection of significant giga-electronvolt emission to the west of the remnant can be easily interpreted when taking a look at the combined eRASS1-4 (red), IRAS 25 μm (green), and IRAS 100 μm (blue) data depicted as an RGB image that is displayed in Fig. 7. Here, it becomes apparent that the SNR's structure is a fragmented shell in X-rays because it is partially occluded by dust. The surrounding dust clouds encircle the remnant, absorbing the majority of the X-ray emission to its western part, and thus forcing this fragmented shell-type appearance of the remnant in the X-ray band. The above claim is confirmed by the X-ray spectral analysis of the remnant, performed in Sect. 4. When fitting an appropriate model to the data, a significantly increased absorption column density is obtained to the west of the remnant as shown in Fig. 8. The infrared emission to the east of the remnant appears weakened in comparison to the southern and western regions, and spectral analysis results do not reveal strong absorption in comparison to its neighboring regions, that are found to be bright in X-rays. Concluding, the prevalence of dust clouds in the surroundings of the remnant seems to be responsible for the morphological anti-colleration of the remnant in the two wavebands. Unlike gamma-ray emission, X-ray emission is subject to absorption.

The origin of the gamma-ray emission is complex to derive. While there is strong absorption of the X-rays to the western part of the SNR, *Fermi*-LAT data reveal two regions of enhanced giga-electronvolt emission of unclear origin. The giga-electronvolt blob in the southwest of the remnant overlaps only partially with the G277.731+00.647 HII region and the strong radio source G278.0+0.8, making a possible association unlikely. The giga-electronvolt blob in the northwest of the remnant spatially coincides with the western faint CO cloud reported in Duncan et al. (1995), but it is not consistent with the overall spatial morphology of the cloud. Similarly, the region of bright giga-electronvolt emission in the northeast of the remnant partially overlaps with the eastern CO cloud reported in Duncan et al. (1995). Therefore, it could be the case that the two faint CO clouds, reported in Duncan et al. (1995), account for two of the three aforementioned, significantly giga-electronvolt-emitting, regions by interacting with the remnant at the west and thus yielding giga-electronvolt emission. Overall, at first glance, it is unclear whether the gamma-ray emission there originates from the remnant itself or if it occurs randomly (point source related). A combination of all of the above scenarios may apply.

To inspect in detail whether the three regions of enhanced giga-electronvolt emission belong to the diffuse

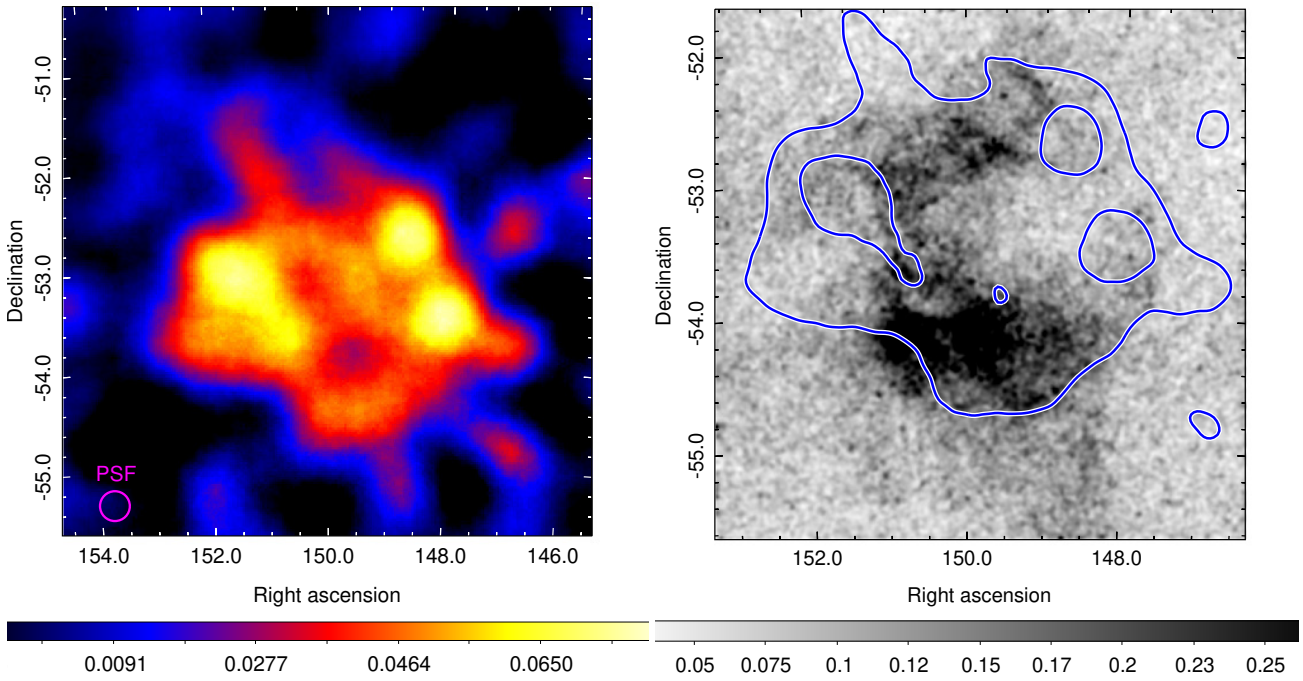

Fig. 5. Spatial correlation between X-ray and γ-ray emission from the remnant. Left panel: $5.3^\circ \times 5.3^\circ$ *Fermi*-LAT residual count map > 5 GeV centered at the coordinates used in Araya (2020), in units of counts per pixel. The image, of 90″ pixel size, is convolved with a $\sigma = 15'$ Gaussian. The magenta thick circle represents the 68% containment PSF size at 5 GeV energy threshold used for the construction of the residual count map. Right panel: eRASS:4 exposure-corrected intensity sky map, with the same parameters as the one displayed in Fig. 1. The blue contours mark the giga-electronvolt extension of 4FGL J1000.0-5312e as displayed on the *Fermi*-LAT residual count map on the left panel of the figure.

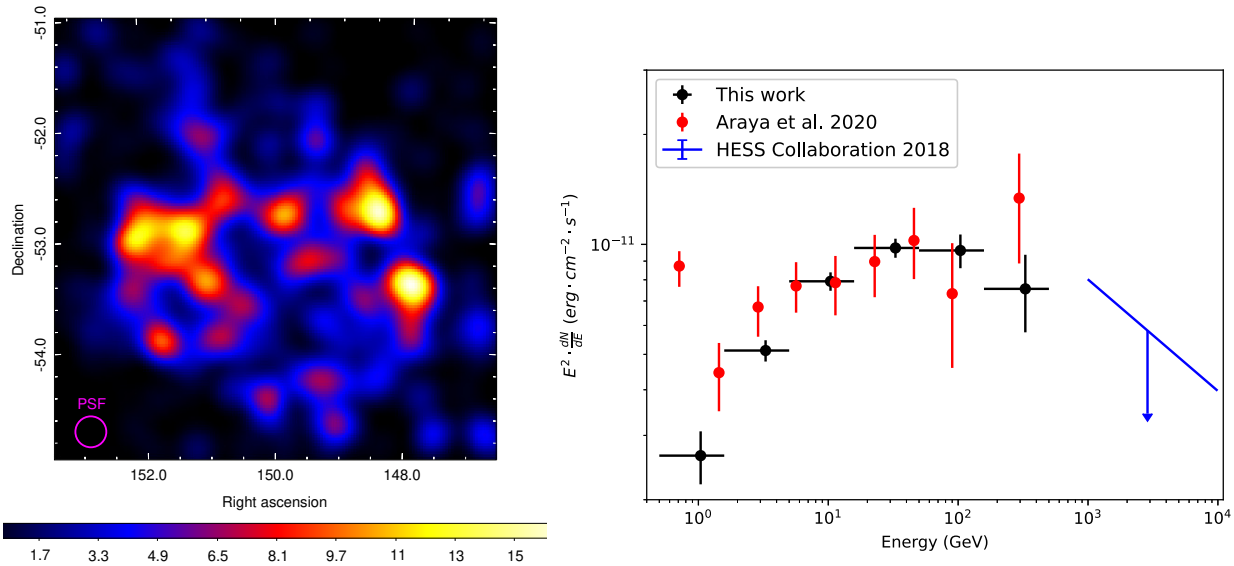

Fig. 6. γ-ray imaging and spectral analysis results of G279.0+01.1. Left panel: $4^\circ \times 4^\circ$ *Fermi*-LAT TS map >5 GeV centered at the coordinates used in Araya (2020). The image, of 90″ pixel size, is convolved with a $\sigma = 6.75'$ Gaussian. The magenta thick circle represents the 68% containment PSF size, applied at the 5 GeV energy threshold used for the construction of the TS map. Right panel: 4FGL J1000.0-5312e *Fermi*-LAT SED. Black dots correspond to the *Fermi*-LAT spectrum in the 0.5–500 GeV band, obtained in this work. Red and blue dots correspond to giga-electronvolt *Fermi*-LAT data reported in Araya (2020) and TeV-H.E.S.S. upper limits reported in H.E.S.S. Collaboration (2018b), respectively.

giga-electronvolt emission originating from the remnant or if they can be attributed to three distinct unknown point sources, we added to the spectral model three new point sources. The new point sources were centered at the location of the three regions which are bright in giga-electronvolt. By adopting a simple powerlaw spectra for all three sources, we performed the same fitting process and extracted the spectrum from the location of the remnant. The computed spectral shape does not change

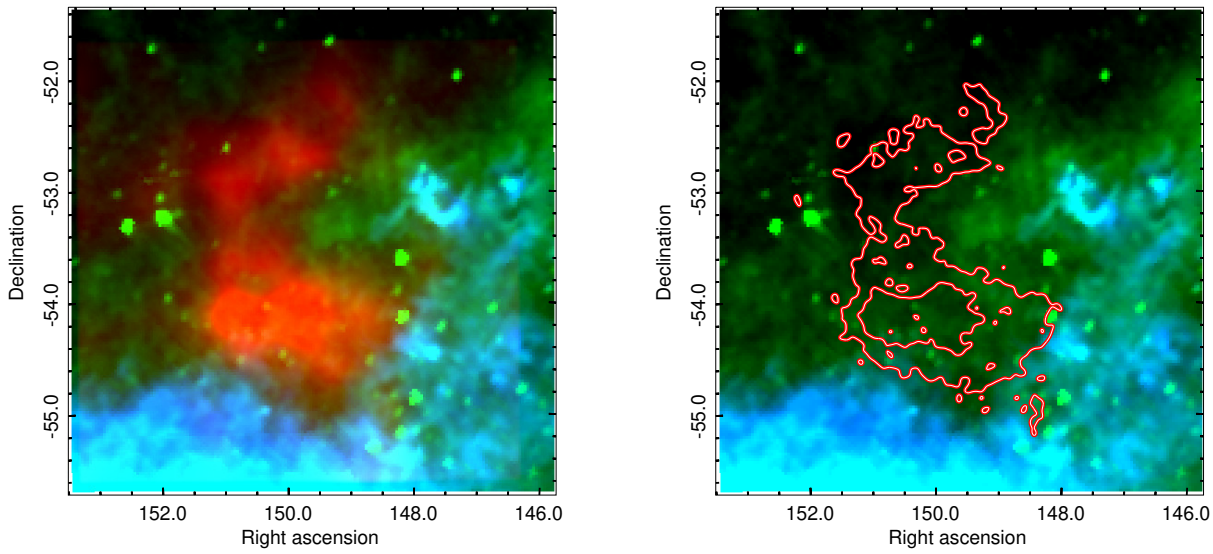

Fig. 7. Spatial correlation between X-ray and IR data from the remnant's location. Left panel: RGB image, displaying combined eRASS:4 X-ray data in the 0.3–1.1 keV energy band (red), IRAS 25 μm data (green), and IRAS 100 μm data (blue) from the location of the remnant. Right panel: Combined IRAS 25 μm data (green) and IRAS 100 μm data (blue) from the location of the remnant. The red contours represent two levels of eRASS:4 X-ray data in the 0.3–1.1 keV energy band which we overlaid to IRAS data sets, aiming at inspecting the IR emission at the location of the X-ray excess, as observed with eROSITA, and enhancing the apparent anti-correlation in the two distinct energy bands, that is to say how the IR emission "respects" the X-ray excess emanating from the remnant in the south and west.

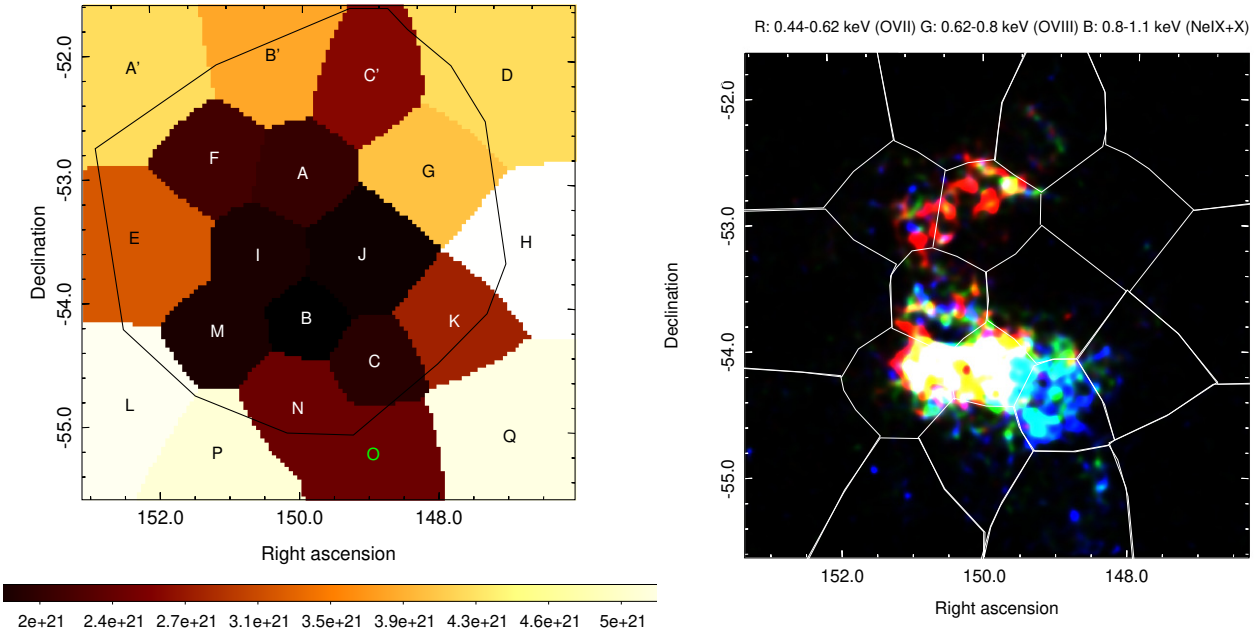

Fig. 8. Absorption features and elemental abundance distribution across the remnant's area. Left panel: absorption column density map (in units of cm^{-2}) from the location of the remnant, as computed by the best-fit absorption column density. Values are obtained from each distinct subregion defined by the Voronoi binning algorithm. The region selected for spectral analysis of the entire remnant is shown as a black line. Regions of significant diffuse X-ray emission from the remnant are displayed in white letters whereas those surrounding regions containing faint diffuse X-ray emission from the remnant are displayed in black letters. Finally, in green the region which contains diffuse X-ray emission unrelated to the remnant is shown. Right panel: eRASS:4 RGB image (R: 0.44–0.62 keV (O VII), G: 0.62–0.80 keV (O VIII), B: 0.80–1.10 keV (Ne IX+X)), identical to the lower right panel of Fig. 9 but in power scale aiming to reveal the strongest elemental abundance at each subregion where we perform spectral analysis. It displays the distribution of the different elemental abundances detected across the remnant. White contours represent the 20 distinct regions obtained from the Voronoi binning analysis to be used for further spectral analysis.

while the derived flux is only marginally lower. Thus, we are strongly convinced that the three bright blobs are part of the diffuse giga-electronvolt emission emanating from the remnant and not the result of several point source emission regions. Regardless, the hard giga-electronvolt spectral component, detected up to 0.5 TeV, as reported in Araya (2020) and confirmed in this work with a slightly modified spectral shape (see Sect. 4.2 for details on the giga-electronvolt spectral analysis), supports the hypothesis that the extended giga-electronvolt emission, or at least a good fraction of it, is the result of particle acceleration in the remnant. We note that the age of the remnant of 10^6 yr (when adopting a distance of 2.7 kpc) implies that particles at TeV energies should already have escaped the SNR. A possible solution to this apparent contradiction with the above findings might come from a revised age estimate as discussed later in the paper.

4. Spectral analysis and modeling

4.1. eROSITA spectra

Figure 2 indicates potential temperature variation across the remnant, as described in Sect. 2.1. Therefore, aiming to assess the nature of the X-ray emission emanating from the remnant in detail, a spectral extraction process was performed from 20 distinctive regions, which are shown in the right panel of Fig. 8 by using `SAOIMAGE DS9` (Joye & Mandel 2003). The selection of the regions was optimized based on the Cappellari & Copin (2003) Voronoi binning algorithm that we run on the 0.3–1.1 keV intensity map of the remnant, depicted in Fig. 1. Here, the image was rebinned to 2′ pixel size so that a single pixel contains sufficient number of counts. A signal-to-noise ratio of $S/N = 110$ was set given the relatively faint appearance of the SNR in the X-ray energy band. The obtained regions are shown on both panels of Fig. 8. We also extracted the spectrum from the entire remnant. The selected polygonal region that combines the emission from the whole remnant is overlaid on the left panel of Fig. 8 with black contours. Additionally, we extracted the spectrum from a region identical to the 0823031401 *XMM-Newton* observation, to be able to directly compare the X-ray spectra obtained from the two distinct instruments from the exact same location of the remnant. The X-ray spectra comparison between the two instruments is presented in Appendix. B. eRASS:4 data were utilized in the spectral analysis procedure, excluding data recorded by TM5 and TM7 since the light peak suffering of those cameras (Predehl et al. 2021) strongly affects the lower energy regime where the SNR is observable. In addition, the spectra were grouped, using the grppha FTOOLS[1] task, to achieve a minimum of 50 counts per single bin. Spectral extraction was also performed from three additional regions representative of the background, aiming at inspecting potential background variations. The regions are shown on the left panel of Fig. 3. Their selection was optimized based on the contamination of the surrounding regions. In particular, regions located toward the south of the remnant were excluded since they exhibit strong X-ray emission of unknown origin. However, we speculate that the nature of the emission could potentially be associated with another remnant since there is an apparent radio arc in the PMN data that seems to encapsulate nicely the X-ray excess. Despite the differences, one obtains compatible results when modeling the spectrum obtained from each of those off-source regions, mainly discrepancies in the normalization value of the astrophysical background components. The obtained spectral source parameters for the best-fit models are consistent within 1σ errors for all background regions when applied to the simultaneous fitting of the on-source regions, as discussed below. Therefore, the black circled region was chosen to represent the background X-ray emission from the whole remnant. For the background model, the best-fit model spectral parameters used in the simultaneous fitting of the source and background emission are fixed to the best-fit values. The normalization values are rescaled according to the area of the corresponding on-source regions. The fitting of the background regions is performed by adopting the following model in Xspec notation: `apec+tbabs(apec+apec+pow) + gaussian + expfac(bkn2pow + powerlaw + powerlaw) + powerlaw + gaussian + gaussian + gaussian+ gaussian + gaussian + gaussian`. This can be broken down to the contribution from the astrophysical background (`apec+tbabs(apec+apec+pow)`) that includes the Local Hot Bubble (LHB) low temperature plasma, the Galactic Halo (GH) plasma, and the Cosmic X-ray Background (CXB) originating from the combined emission of unresolved Active Galactic Nuclei (AGN), and to the particle or instrumental background of eROSITA which can be best described by a combination of power law and Gaussian model components in the particular energy range that the X-ray fitting is performed: `gaussian + expfac(bkn2pow + powerlaw + powerlaw) + powerlaw + gaussian + gaussian + gaussian+ gaussian + gaussian + gaussian`. To avoid likely spectral contamination from point sources that fall within the extension of the remnant, we masked out with a 110 arcsec mask radius all point sources detected with a 3σ significance level or higher, based on the latest eROSITA point source catalog. The `srctool` eSASS task was employed for the spectral extraction procedure, while Xspec (X-ray spectral fitting package; Ver. 12.12.1) was utilized to perform the spectral fitting. Given the relatively faint appearance of the remnant in the X-ray band, C-statistics (Cash 1979) were selected in the fitting procedure. A simultaneous fit of the on-source and background emission is favored over the subtraction of the background emission from the on-source spectra. As a cross-check, we also performed a spectral analysis on the background-subtracted spectra. Given that the normalization of the background models in the simultaneous fitting procedure was not left to vary, both methods yield, as expected, consistent results. The methodology that we employed for the fitting process of each individual region is as follows. We started by obtaining the best fit of the background subtracted spectra which give us a rough estimate of the emission nature originating from the remnant. We then proceeded to the simultaneous fitting process using as initial input parameters, of the source emission, the ones obtained from the background subtraction strategy. Since the emission emanating from the remnant is purely thermal, one can describe the optically thin plasma either in a nonequilibrium ionization state (NEI), which usually applies to young and middle-age remnants, or in collisionally ionization equilibrium (CIE) which is representative of older remnants. In our analysis, even if the remnant is considered to be old, we tested both types of models. In particular, the VAPEC model of collisionally ionized diffuse gas as a CIE model, and the nonequilibrium ionization collisional plasma (VNEI) as well as the constant temperature plane parallel shock plasma (VPSHOCK Borkowski et al. 2001), as NEI model representatives in Xspec notation, were employed in the fitting process. The Galactic absorption toward the source was modeled with the TBABS absorption model by Wilms et al. (2000). Finally,

[1] `http://heasarc.gsfc.nasa.gov/ftools/`

the spectral fitting is performed in the 0.3–1.7 keV energy range since above 1.7 keV the background becomes strongly dominant. For the majority of the selected regions, when one tries to fit the emission spectrum with one of the aforementioned single-component models by keeping the elemental abundances fixed to solar values results in a poor fit. On the contrary, varying Oxygen (O), Neon (Ne), and Magnesium (Mg) significantly improves the fitting results. The latest assertion is confirmed by the clear identification of O VII (~0.56 keV), O VIII Lyα (~0.65 keV), and Ne IX (~0.905 keV) emission line features in the source spectrum. The Ne X Lyα line (~1.02 keV), as well as the He-like Mg XI unresolved triplet (~1.35 keV), and the Mg XII Lyα line (~1.47 keV) are also present for some of the regions. Finally, some Fe L-transitions are prominent in a number of regions selected for spectral analysis, in the 0.7–1.2 keV energy band, but a definitive identification of the latter is beyond the scope of this work. Since those Fe-L lines do not leave strong residuals, as is the case in Kamitsukasa et al. (2015), for example, due to the errors in Fe-L modeling in current version of Xspec code (Borkowski et al. 2006; Yamaguchi et al. 2011), we did not add any additional Gaussian lines around those energies. On Fig. 9 we display eRASS:4 intensity sky maps in narrower, spectrally motivated energy bands: 0.3–0.44 keV (N), 0.44–0.62 keV (OVII), 0.62–0.80 keV (OVIII), 0.80–1.10 keV (NeIX+X), and 1.10–2.10 keV (Mg). As can be seen in Fig. 9, the northeastern parts of the remnant contain high abundances of OVII and OVIII, whereas the southwestern parts contain high abundances of OVIII, Ne, and Mg. It is interesting to note that the two bright blobs contain high abundances of all three elements. A similar pattern is evident in the spectra as displayed in Fig. 10 which displays significant changes in the spectral shape. In particular, the OVII abundance declines whereas the Ne and Mg abundances increase, as one moves across the remnant from the northeast (region A) to the southwest (region C).

For the on-source regions with significant diffuse X-ray excess, the obtained reduced chi-squared values of the single-component model, after letting the above elemental abundances vary, might indicate that a single-component model does not sufficiently describe the source's emission. In particular, for the majority of the regions significant residuals are apparent at the Ne X Lyα line energy (at ~1.02 keV) which cannot be improved neither when switching from an equilibrium to a nonequilibrium model nor when varying the elemental abundances of the corresponding model. Strong residuals are also present in the 0.7–1.0 keV energy range. Therefore, multiple-component models were also employed for those regions, aimed at improving the quality of the fit and effectively describing the source emission. In Fig. 10 we show the X-ray spectral fitting results obtained from three representative regions of the remnant (in a simultaneous fitting of the source and background emission). The regions were chosen to depict the substantial X-ray spectral variation found across the remnant, in particular, how the X-ray spectral shape changes as one moves from the northeast to the southwest of the SNR. Figure 11 depicts the X-ray spectral fitting results that one obtains when extracting the spectrum from the entire SNR. The letters A, B, and C are used to identify these three regions in Fig. 8. For the rest of the regions, the X-ray spectral fitting results are summarized in Appendix D, and displayed in Fig. D.1. For each individual region, we started the fitting procedure attempting to fit the data with the simplest possible model for an evolved SNR, that is to say the VAPEC model (CIE). We then switched to nonequilibrium models (NEI), which provide a much higher temperature plasma and a significantly lower absorption column density compared to CIE models, as shown in Table 2. Therefore, we conclude that NEI models are necessary at least in some regions since the derived absorption column density based on the known distance of the remnant is well-aligned with the spectral fit results of NEI models whereas it falls short of the CIE model (see Sect. 4.3 for a detailed discussion). This is even more true when a revised distance estimate to the SNR is considered (refer to Sect. 4.3). We stress, however, that a `tbabs(vpshock)` model for regions A and C and a `tbabs(vapec)` model (ignoring $N_{\rm H}$ constraints) for region B seem to describe the remnant's spectral data relatively well. Even if in both cases (single CIE or single NEI model) acceptable fits were derived for specific subregions (under certain adjustments which are described in detail in Appendix C), the obtained results point toward the fact that multi-temperature models further improve the fitting process.

Therefore, as a next step, we considered multiple component models, and in particular two temperature plasmas, aiming at improving our fitting results. We note that the best-fit spectral results for each subregion are reported in Table D.1. Here, we give an overview of the most important findings. In this work, we attempted to model the remnant's spectrum with all possible combinations of two temperature plasma models (i.e., equilibrium models (`tbabs(vapec+vapec)`), nonequilibrium models (`tbabs(vnei+vnei)`, `tbabs(vpshock+vpshock)`), and mixed models (`tbabs(vapec+vnei)`, `tbabs(vapec+vpshock)`). As shown in Table 2, no strong preference among the aforementioned models was obtained. However, it is worth to note that a significantly improved fit is obtained for regions A and B compared to single-component models, whereas region C can be sufficiently described by single-component models. All best-fit results are described in detail in Appendix C and reported in Table 2. Finally, when fitting the spectrum of the entire remnant, two temperature plasma components provide by far better fit quality compared to single-temperature models (either CIE or NEI). In particular, among all models mentioned above, a two-temperature plasma component in nonequilibrium (`tbabs(vphock+vpshock)`), letting O and Ne to vary, provides a fit of χ^2/d.o.f. = 1.19 (with a total flux of $F_{\rm total} = 1.48^{+0.61}_{-0.42} \times 10^{-9}$ erg cm^{-2} s^{-1}). The best fit parameters of this model are reported in Table 2.

An identical spectral fitting approach was employed for the rest of the regions obtained from the Voronoi binning algorithm, when the source and background emission were simultaneously fitted with independent models. The obtained spectral fits for the rest of the subregions are summarized in Appendix D. The main parameters of the best-fit for the three representative regions, as well as those obtained from the entire remnant, are summarized in Table 2. The best-fit models from each distinct region used for the spectral fitting process confirm that the X-ray emission originating from the remnant is purely thermal. Figure 8, left panel, shows the absorption column density variation across the remnant as derived from the spectral analysis of individual subregions. We note that this map is not obtained by employing a consistent model for all subregions but rather by individual "preferred" models. A similar figure illustrating the temperature variation across the remnant would not be that instructive since some regions of the remnant are sufficiently fitted with one plasma temperature model while others require two distinct temperature plasma components. Therefore, we did not include such an image in this work. The southwestern part of the remnant appears to be the hottest, and well-described by a single

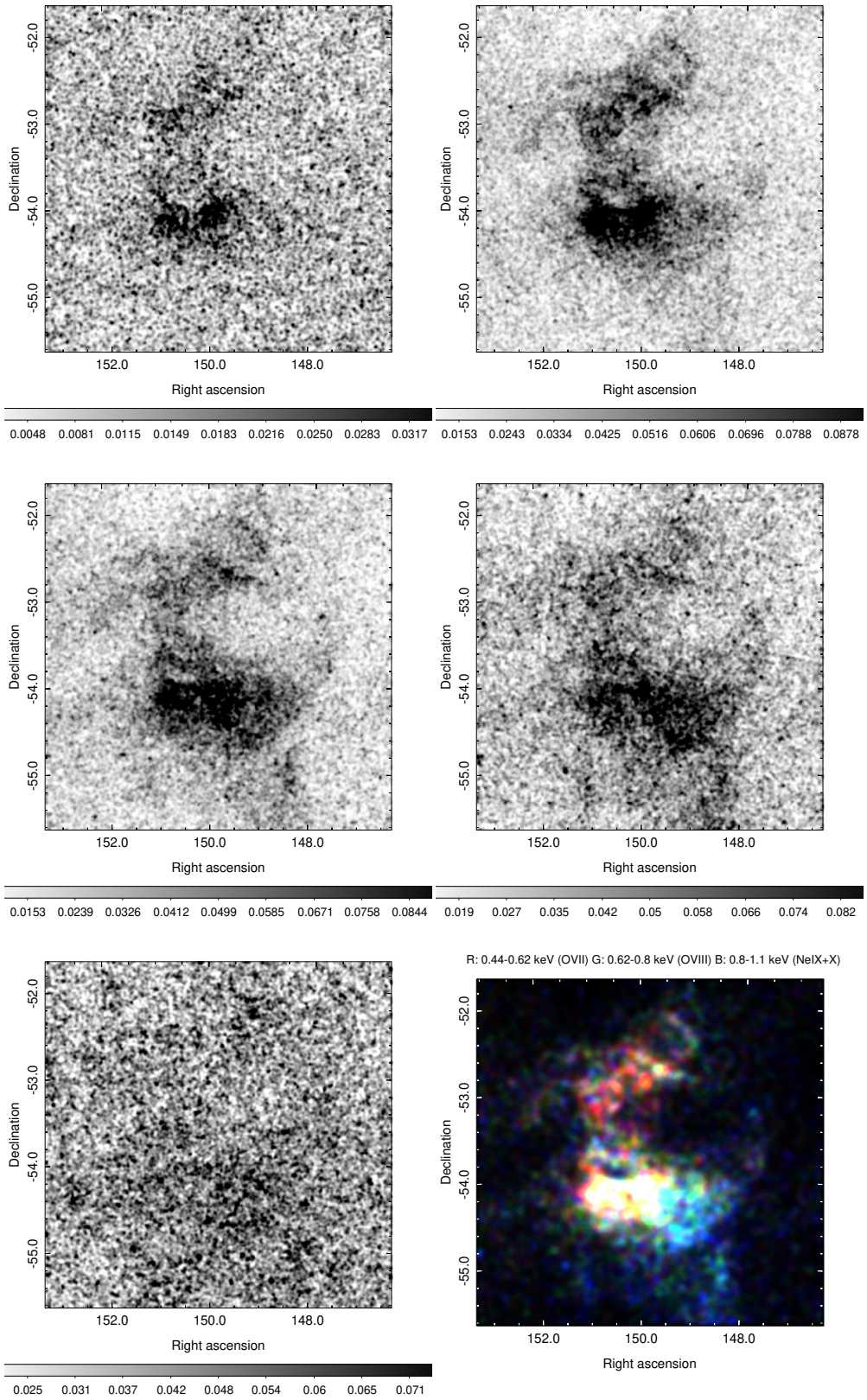

Fig. 9. eRASS:4 exposure-corrected intensity sky maps in units of counts per pixel. The five distinct panels depict narrow, spectrally motivated energy bands: 0.3–0.44 keV (N, upper left), 0.44–0.62 keV (OVII, upper right), 0.62–0.80 keV (OVIII, middle left), 0.80–1.10 keV (NeIX+X, middle right), and 1.10–2.10 keV (Mg, lower left). The sixth one (RGB, lower right) displays the distribution of the different elemental abundances detected across the remnant.

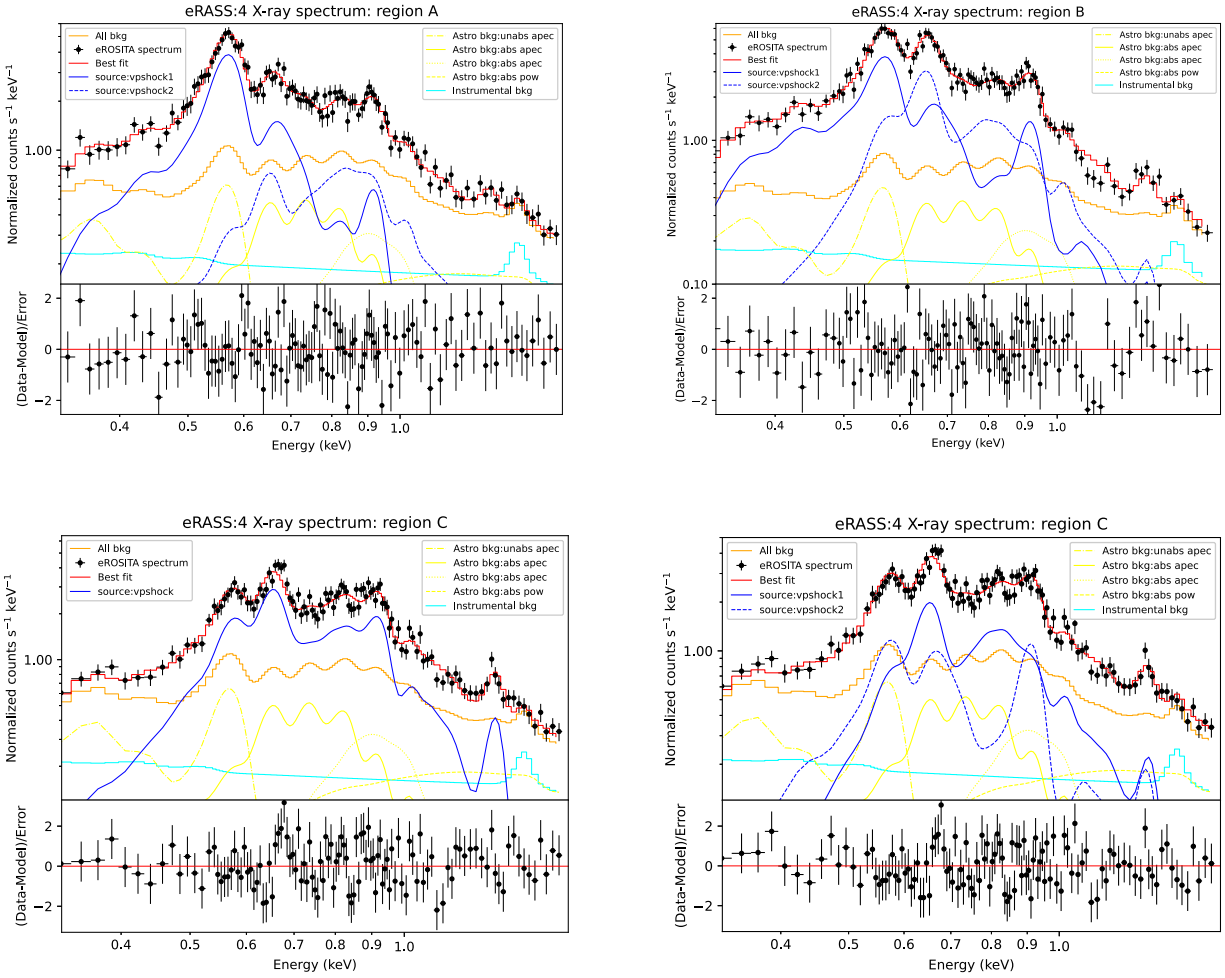

Fig. 10. X-ray spectrum, eRASS:4 data in the 0.3–1.7 keV energy band, from the selected representatives regions of the remnant, which demonstrate the spectral shape change detected across the remnant. Upper left: region A, `tbabs(vpshock+vpshock)`. Upper right: region B, `tbabs(vpshock+vpshock)`. Lower left: region C, `tbabs(vpshock)`. Lower right: region C, `tbabs(vpshock+vpshock)`.

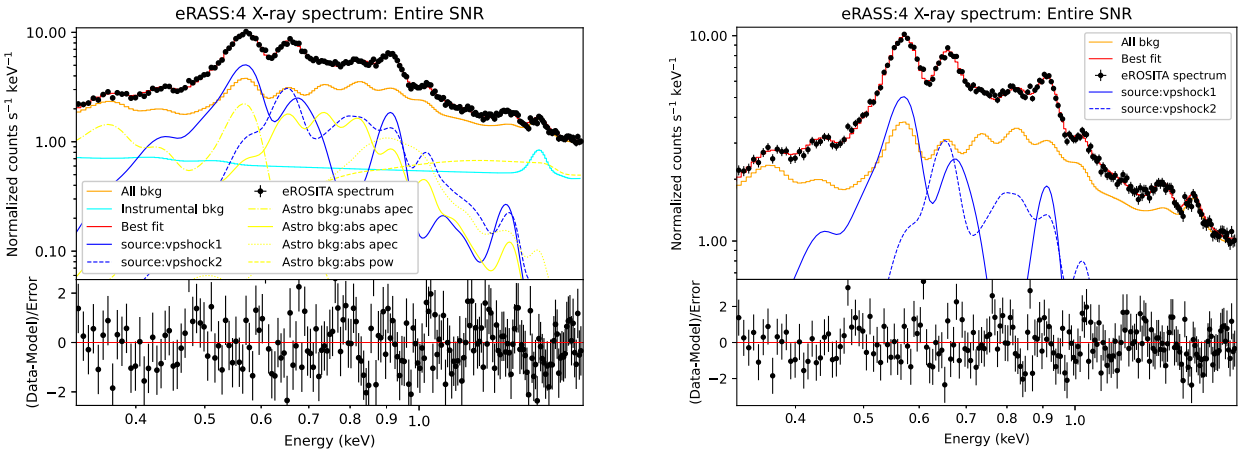

Fig. 11. X-ray spectrum, eRASS:4 data in the 0.3–1.7 keV energy band, from the entire remnant. Left panel: all distinct components contributing to the spectrum (yellow: astrophysical background, cyan: instrumental background, and blue: source). Right panel: source components, in blue, and total background contribution to the spectrum, in orange.

Table 2. Best-fit parameters derived from the X-ray spectral analysis of three representative subregions and the entire remnant.

Region	A region	B region	C region	Entire remnant
Area (10^6 arcs^2)	7.13	4.23	5.23	104.36
Surf_bri (10^{-3} c arcs^{-2})	1.92	3.36	2.25	1.66
Model	vapec+vapec			
kT(keV)	$0.62^{+0.05}_{-0.08}$ $0.16^{+0.01}_{-0.01}$	$0.54^{+0.08}_{-0.09}$ $0.19^{+0.01}_{-0.01}$	$0.16^{+0.01}_{-0.01}$ NaN	–
$N_{\rm H}(10^{22}{\rm cm}^{-2})$	$0.20^{+0.03}_{-0.03}$	$0.13^{+0.02}_{-0.01}$	$0.63^{+0.03}_{-0.04}$	–
O	1.0 $0.83^{+0.09}_{-0.08}$	1.0 $0.71^{+0.07}_{-0.06}$	$1.38^{+0.41}_{-0.30}$	–
Ne	$3.08^{+1.02}_{-0.92}$ 1.0	$8.52^{+9.42}_{-3.44}$ $1.69^{+0.24}_{-0.21}$	$1.17^{+0.32}_{-0.23}$	–
Mg	–	$9.32^{+9.40}_{-3.25}$ 1.0	$2.46^{+0.92}_{-0.67}$	–
Fe	–	–	$3.30^{+2.78}_{-1.47}$	–
χ^2/d.o.f.	1.03	1.01	1.19	–
Model	vnei+vnei			
kT(keV)	$0.68^{+0.32}_{-0.08}$ $0.29^{+0.10}_{-0.06}$	$0.66^{+0.14}_{-0.12}$ $0.58^{+0.26}_{-0.17}$	$15.30^{+7.96}_{-4.53}$ NaN	–
$N_{\rm H}(10^{22}{\rm cm}^{-2})$	$0.20^{+0.04}_{-0.04}$	$0.16^{+0.02}_{-0.02}$	$0.20^{+0.03}_{-0.03}$	–
O	–	$3.51^{+2.48}_{-1.36}$ $0.59^{+0.07}_{-0.07}$	$1.15^{+0.13}_{-0.11}$	–
Ne	–	$1.55^{+0.67}_{-0.48}$ $0.94^{+0.29}_{-0.22}$	$1.43^{+0.17}_{-0.15}$	–
Mg	–	–	–	–
Ionization time (10^{10}s cm^{-3})	$9.78^{+4.00}_{-0.81}$ $1.53^{+3.02}_{-5.03}$	$10.23^{+5.86}_{-3.82}$ $0.48^{+0.45}_{-0.10}$	$0.78^{+0.10}_{-0.07}$	–
χ^2/d.o.f.	0.88	1.06	1.26	–
Model	vpshock+vpshock			
kT(keV)	$0.85^{+0.23}_{-0.16}$ $0.26^{+0.11}_{-0.05}$	0.70 $0.54^{+0.27}_{-0.24}$	$1.00^{+0.34}_{-0.21}$ NaN	$0.60^{+0.07}_{-0.05}$ $0.34^{+0.03}_{-0.07}$
$N_{\rm H}(10^{22}{\rm cm}^{-2})$	$0.20^{+0.03}_{-0.03}$	$0.16^{+0.02}_{-0.02}$	$0.19^{+0.04}_{-0.03}$	$0.31^{+0.04}_{-0.02}$
O	–	$3.93^{+5.91}_{-1.75}$ $0.51^{+0.06}_{-0.05}$	$1.30^{+0.16}_{-0.14}$	$4.47^{+1.30}_{-0.84}$ $0.66^{+0.04}_{-0.05}$
Ne	–	$1.65^{+0.90}_{-0.51}$ $1.1^{+0.47}_{-0.23}$	$1.82^{+0.35}_{-0.34}$	$2.52^{+0.38}_{-0.39}$ $1.48^{+0.26}_{-0.22}$
Mg	–	–	$1.88^{+0.50}_{-0.46}$	1.0 $5.85^{+4.27}_{-1.43}$
Ionization time (10^{11}s cm^{-3})	$1.57^{+1.16}_{-0.69}$ $0.52^{+0.79}_{-0.36}$	$2.31^{+2.14}_{-0.95}$ $0.09^{+0.34}_{-0.04}$	$0.41^{+0.19}_{-0.14}$	$2.34^{+0.97}_{-0.69}$ $0.06^{+0.02}_{-0.01}$
χ^2/d.o.f.	0.87	1.06	1.16	1.19
Model	vnei+vapec			
kT(keV)	$0.65^{+0.04}_{-0.05}$ $0.16^{+0.01}_{-0.01}$	$0.63^{+0.15}_{-0.12}$ $0.19^{+0.01}_{-0.01}$	–	–
$N_{\rm H}(10^{22}{\rm cm}^{-2})$	$0.18^{+0.04}_{-0.03}$	$0.13^{+0.01}_{-0.02}$	–	–
O	–	1.0 $0.71^{+0.07}_{-0.06}$	–	–
Ne	–	$4.12^{+6.26}_{-1.88}$ $1.59^{+0.25}_{-0.24}$	–	–
Mg	–	$6.50^{+6.48}_{-2.72}$ 1.0	–	–
Ionization time (10^{11}s cm^{-3})	$2.16^{+1.22}_{-0.92}$ NaN	2.43 NaN	–	–
χ^2/d.o.f.	1.03	0.99	–	–

Notes. The best-fit parameters are reported with 1σ errors. The three subregions (defined via the Voronoi analysis process) have been selected as representatives to exhibit best the spectral variation detected across the remnant. Where not defined, elemental abundances were set to solar values.

component model. The region of enhanced X-ray emission positioned at the southeastern part of the remnant, which contains the two bright blobs, appears to be moderately cooler. The northern part of the remnant is the coolest of all. The presence of O- and Ne-enriched ejecta material, along with the presence of strong [OII] and [OIII] lines in its optical spectrum (Dopita et al. 1981; Goss et al. 1979; LASKER 1979; Mathewson et al. 1980), forces us to propose the identification of G279.0+01.1, as a new O-rich SNR. However, the dominance of oxygen over hydrogen, [OIII]/Hβ > 3, is not that strong compared to typical O-rich remnants. Further studies of the remnant's optical spectrum are required to explore in detail the nature of its optical counterpart. Until now, only a small number of the detected optical filaments have been spectrally studied. If confirmed, G279.0+01.1 will be the first known evolved Galactic SNR that exhibits such features. It is worth noting that even if ejecta detection was expected only from young SNR, such a feature has been detected in a small number of middle-aged SNR (e.g., G292.0+1.8 Murdin & Clark 1979; Winkler et al. 2009, Puppis A Hwang et al. 2008). Such a finding would make G279.0+01.1 the first evolved O-rich SNR and the fourth O-rich SNR in the Milky Way (MW): Cassiopeia A (Kamper & van den Bergh 1976; Thorstensen et al. 2001; Fesen et al. 2006; Hammell & Fesen 2008), Puppis A (Winkler & Kirshner 1985), and G292.0+1.8 (Murdin & Clark 1979; Winkler et al. 2009) are the remaining three O-rich remnants. None of the aforementioned remnants are found in evolved states. In fact, only four such (young) remnants are known outside the MW: 0102.2-272.9, and 0103-72.6 (Park et al. 2003; Finkelstein et al. 2006; Banovetz et al. 2021) in the Small Magellanic Clouds (SMC) and N132D (Hughes 1987), and 0540-69.3 (Mathewson et al. 1980; Park et al. 2010) in the Large Magellanic Clouds (LMC). A second evolved Galactic SNR, S 147 or Spaghetti nebula, has recently been discovered to exhibit similar characteristics (i.e., ejecta material in the X-ray spectrum Michailidis et al. 2024; Khabibullin et al. 2024). However, the latter lacks the presence of [OIII] lines in its optical spectrum. Thus it cannot be classified as O-rich as of now.

4.2. Fermi-LAT spectra and multiwavelenght SED

As a final part of the binned likelihood analysis of the extended giga-electronvolt source 4FGL J1000.0-5312e, which is spatially coincident to the remnant, we report on the obtained spectral energy distribution (SED) computed in the 0.5–500 GeV energy range. Data are divided into 6 equally spaced logarithmic energy bins. The best-fit spatial template reported in Araya (2020) was used. The spectral fitting procedure reveals that a LogParabola model emerges as the best fit to the data, instead of a simple power law as reported in Araya (2020). During the fitting process, the normalization of all 4FGL-DR3 sources falling within 5° distance from the source of interest was let to vary. The same approach was applied to the normalization values of the Galactic diffuse and isotropic background. In addition, the normalization of the LogParabola model of G279.0+01.1 was left free, with the goal of obtaining the best fit. Our results are found to be in good agreement with the updated spectral plot of the remnant[2] as illustrated in Fig. 6 and there is a discrepancy to the giga-electronvolt spectrum derived by Araya (2020) toward the low-energy end (refer to Fig. 6, right panel). We stress that the SED results are largely independent of the adopted spectral model (i.e., a Log-parabola or a power-law) used to construct the SED. This discrepancy is likely caused by the updated model used in 4FGL-DR3 to model the Galactic diffuse component (`gll_iem_v07.fits`) and the isotropic diffuse component (`iso_P8R3_SOURCE_V3_v1.txt`).

The interpretation of the gamma-ray data remains challenging. Our spectral results are less compatible with the expected gamma-ray emission from a hadronic hard-spectrum particle component given the flux decrease toward 1 GeV (e.g., Yang et al. 2018, for the expected spectral shape). However, given the age of the SNR, a leptonic, Inverse Compton (IC) emission scenario continues to be questionable as well (Zeng et al. 2021). Additionally, no nonthermal (electron synchrotron) component has been detected in the X-ray data from the remnant, data from both eROSITA and *XMM-Newton* are fully consistent with pure thermal emission. A relic electron scenario (i.e. emission from giga-electronvolt/tera-electronvolt electrons outside of high magnetic-field areas) might explain giga-electronvolt IC emission without detectable (with current sensitivity) nonthermal X-ray emission, but a quantitative exploration is beyond the scope of this work.

4.3. Distance, age, and plasma density estimation

A kinematic distance calculation of the remnant is difficult to be implemented due to the uncertainty of the spatial distribution of the radiative shock. However, three distinct distance estimation methodologies have been carried out so far. McKee & Cowie (1975) introduced a distance estimation technique on the basis of the blast wave energy and associated cloud parameters, which when employed for G279.0+01.1 resulted in a ∼3 kpc distance. The $\Sigma - D$ relation for distance calculation has also been applied in the case of the remnant, converging toward a similar distance of ∼3 kpc (Woermann & Jonas 1988). The distance estimation of CO-emitting clouds possibly associated with the remnant, reported in Woermann & Jonas (1988), is also placing the remnant at the same distance. More recently, Shan et al. (2019) utilized Red Clump (RC) stars to build an extinction-to-distance relation in the direction of remnants from the fourth Galactic quadrant, reporting a 2.7 ± 0.3 kpc distance for G279.0+01.1, based on the computed optical extinction.

We perform an additional distance consistency check based on the estimated absorption column density parameter obtained from the best fit of the eRASS:4 X-ray spectra. In particular, we made use of the Galactic mean color excess spatial distribution, established in Lucke (1978), and the 3D extinction maps obtained from the combination of *Gaia* and 2MASS photometric data reported in Lallement et al. (2019, 2022). Using the statistical relation between the observed absorption in X-rays with the mean color excess (Predehl & Schmitt 1995),

$$\begin{matrix} N_{\rm H}/E_{\rm B-V} & = 5.3 \times 10^{21}\ {\rm cm}^{-2} \cdot {\rm mag}^{-1} \\ N_{\rm H}[{\rm cm}^{-2}/A_{\nu}] & = 1.79 \times 10^{21} \end{matrix}, \quad (1)$$

we derived $A_{\nu} = 1.73^{+0.23}_{-0.11}$ in the direction of the remnant. The error in the latter estimate is computed based on the 1σ error of the absorption column density as obtained by the X-ray spectral fitting of the entire remnant. Compared to the *Gaia* data set (Lallement et al. 2019), this places G279.0+01.1 at a distance larger than 3 kpc ($A0 \equiv A(550\ {\rm nm})$). Making use of the updated (Lallement et al. 2022) data sets, which extend up to ∼5 kpc, a distance constraint of $4.9^{>+0.17}_{-1.0}$ kpc is obtained, as shown on the right panel of Fig. 12 in yellow.

[2] https://fermi.gsfc.nasa.gov/ssc/data/access/lat/12yr_catalog/

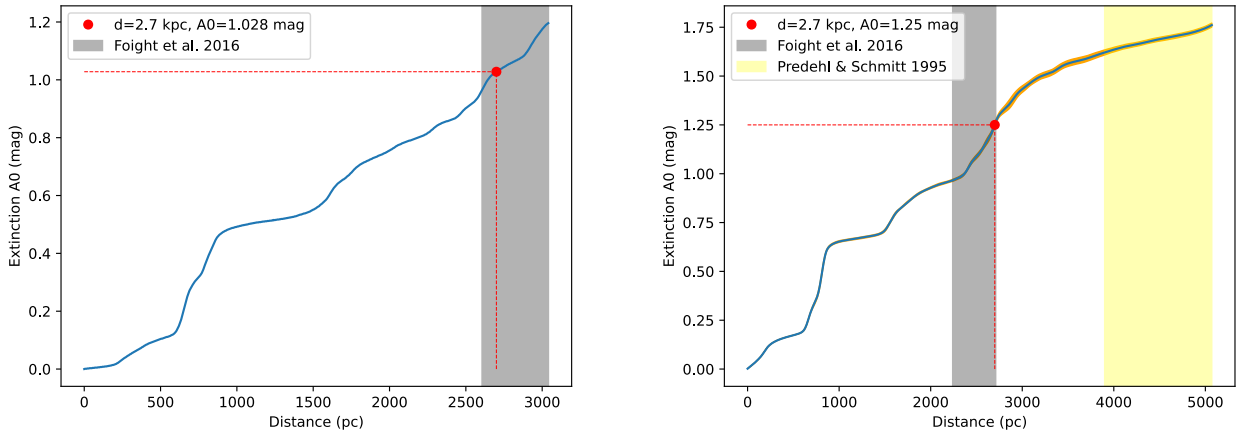

Fig. 12. Cumulative extinction in the direction of G279.0+01.1. Left panel: one-dimensional cumulative extinction graph as a function of the distance up to ∼3 kpc (Lallement et al. 2019 data sets) toward G279.0+01.1 SNR, obtained by using the *Gaia*-2MASS tool for one-dimensional extinction computation https://astro.acri-st.fr/gaia_dev/. Right panel: one-dimensional cumulative extinction graph as a function of the distance up to ∼5 kpc (updated Lallement et al. 2022 data sets) toward G279.0+01.1 SNR, obtained by using the EXPLORE G-Tomo tool for one-dimensional extinction computation https://explore-platform.eu/. In both panels, the gray-shaded areas correspond to the distance uncertainty estimation when employing Eq. (2) and the obtained best-fit value of the absorption column density derived from the spectral analysis. The yellow area indicates the distance uncertainty range when employing Eq. (1). The red point represents the obtained extinction when assuming that the remnant is located at a distance of 2.7 kpc.

However, more recent observations of SNRs employing *Chandra* data have resulted in a modified statistical relation between X-ray absorption and mean color excess (Foight et al. 2016). A significantly higher proportionality factor compared to previous reports was derived:

$$\begin{array}{l} N_{\rm H}/E_{\rm B-V} \quad = 8.9\times10^{21}\ {\rm cm}^{-2}\cdot{\rm mag}^{-1} \\ N_{\rm H}[{\rm cm}^{-2}/A_v] = 2.87(\pm0.12)\times10^{21} \end{array}. \tag{2}$$

Using this relation, the obtained X-ray absorption column density yields an expected extinction of $A_v = 1.08^{+0.19}_{-0.12}$. Employing the Lallement et al. (2019) data sets the latter estimate results in a $2.9^{>+0.14}_{-0.30}$ kpc distance for G279.0+01.1, as shown on the left panel of Fig. 12 in grey. Compared to the most recent Lallement et al. (2022) data sets, a $2.49^{+0.22}_{-0.25}$ kpc distance is derived, as shown on the right panel of Fig. 12 in grey. These distance values (using the Foight et al. 2016 values) are consistent with earlier estimations of the remnant's distance.

Using the data sets by Lallement et al. (2019, 2022), one can also perform the inverse, cross-check, procedure considering as known the remnant's distance, 2.7 ± 0.3 kpc. In this case, as shown in Fig. 12 in red, an extinction of A0=1.03 mag or A0=1.25 mag is obtained, depending on the *Gaia*-2MASS data sets utilized. Employing Eq. (2) results in $N_{\rm H} = 0.29^{+0.06}_{-0.06}\times10^{22}{\rm cm}^{-2}$ or $N_{\rm H} = 0.36^{+0.07}_{-0.08}\times10^{22}{\rm cm}^{-2}$, respectively, for the two different data sets. These values are consistent with the best-fit values obtained from the X-ray spectral fitting. One derives even smaller $N_{\rm H}$ values when employing the empirical relation implemented in Predehl & Schmitt (1995). In particular, when employing Eq. (1) for the two distinct data sets by Lallement et al. (2019, 2022), one derives $N_{\rm H} = 0.18^{+0.03}_{-0.03}\times10^{22}{\rm cm}^{-2}$ and $N_{\rm H} = 0.22^{+0.04}_{-0.04}\times10^{22}{\rm cm}^{-2}$, respectively. To summarize, based on all the above measurements one expects a maximum $N_{\rm H}\sim 0.3$–$0.35\times10^{22}\,{\rm cm}^{-2}$ toward the remnant, except for the parts of the remnant which are spatially coincident with dense dust clouds. In the latter case, the aforementioned value could easily be exceeded.

Adopting now a distance to the remnant of 2.7 kpc, and taking into account the remnant's angular size of ∼3°, one derives a 140 pc diameter (or 70 pc radius). Hence, assuming a spherical distribution, one derives a total plasma volume of $V = 4.32\times10^{61}\ {\rm cm}^{-3}$. The emission measure of the lower and higher temperature components, using the corresponding normalization values from the two-temperature spectrum best-fit and assuming a uniform density distribution across a spherical volume of fully ionized plasma($n_{\rm e} = 1.2n_{\rm H}$), was estimated to:

$$\boldsymbol{EM} = \int n_{\rm e}\cdot n_{\rm H}{\rm d}V = \eta\cdot1.2\cdot n_{\rm H}^2\cdot V. \tag{3}$$

Here, $n_{\rm e}$ is the electron density, $n_{\rm H}$ is the proton density, η is a filling factor and V the volume occupied by both plasmas, as computed above.

At the same time, one can employ the following equation for the emission measure calculation:

$$EM = \frac{\boldsymbol{norm}\times4\pi D^2}{10^{-14}}, \tag{4}$$

where D is the remnant's distance in cm. Combining Eqs. (3) and (4) one obtains the following formula for the plasma density computation:

$$n_{\rm H} = \sqrt{\frac{norm\times4\pi\cdot D^2}{1.2\cdot\eta\times10^{-14}\cdot V}}. \tag{5}$$

From the best-fit model of the spectrum from the entire remnant, we obtained: $norm_{\rm Hot} = 0.013^{+0.002}_{-0.001}$ for the hot temperature plasma component. The filling factor of the two components is unknown. Assuming uniform diffuse emission covering the entire spherical volume, the filling factor is of order unity. However, given that a portion of the computed volume is free of emission (i.e., the central part of the remnant where the spectral analysis results does not suggest X-ray absorption), we estimated the fraction of the area free of plasma emission to be $\eta = 0.92$. Taking into account the error on the distance of the remnant (2.7 ± 0.3 kpc, Shan et al. 2019 utilizing Red Clump (RC) stars), the resulting local density is: $n_{\rm H} = 4.9^{+0.54}_{-0.54}\times10^{-3}\ {\rm cm}^{-3}$ (or

Table 3. Pulsars within 3° of the remnant's center.

Pulsar	Ang. sep. (°)	DM (pc cm^{-3})	D_1 (kpc)	D_2 (kpc)	Age (Myr)	$v_{\rm transv}$ (km s^{-1})
J0955-5304 (B0953-52)	0.83	156.9	0.40(3.31)	–	3.87	1.5
J0957-5432	0.88	226.1	0.45(4.33)	–	1.66	4.1
J0954-5430	1.13	201.57	0.43(3.96)	–	0.17	48.8
J1001-5507 (B0959-54)	1.48	130.32	0.41(2.78)	$0.30^{+1.1}_{-0.3}$	0.44	23.5
J1000-5149	1.85	72.8	0.13(1.93)	–	4.22	1.0
J1001-5559	2.32	159.3	0.43(3.32)	–	30.6	0.6
J1002-5559	2.37	426.0	3.27(9.83)	–	7.84	16.9
J1016-5345 (B1014-53)	2.55	66.8	0.12(1.94)	–	6.33	0.8
J0941-5244	2.80	157.94	0.40(3.14)	–	9.17	2.1
J0940-5428	2.81	134.55	0.38(2.95)	–	0.04	455.5

Notes. The table is split into two halves: the upper half contains the first three pulsars which lie within the remnant's extension. The rest of the pulsars that lie well outside the remnant's structure are displayed in the lower half of the table. The first and second columns give the pulsar's name and angular separation from the remnant's center (as redefined in this work). The third column gives the dispersion measure (DM). The fourth and fifth columns give the pulsar's distance from Earth based on DM measurements and potential associations, respectively. The values within parentheses correspond to older distance estimates based on the NE2001 electron density model (Cordes & Lazio 2002). Since 2017, YMW16 has been considered the default model for DM-based distance calculations (Yao et al. 2017). The sixth column corresponds to the pulsar's spin-down age. The seventh column displays the transverse velocity required for each pulsar to move from the remnant's center to its present location.

$n_{\rm e} = 5.9^{+0.65}_{-0.65} \times 10^{-3}$ cm^{-3}). The normalization error is negligible here, and the error on the filling factor is unknown.

The remnant is considered to be amongst the oldest Galactic SNR. An estimated age on the order of 10^6 yr has been reported by Woermann & Jonas (1988). One can estimate the age of the remnant by employing the same relation as in Giacani et al. (2009): $t \sim \frac{\tau}{n_e}$, where τ is the ionization timescale of the emission plasma. Making use of the derived $n_{\rm e}$ value and the ionization timescale of the hot plasma component for the entire remnant (as shown in Table 2), we compute the remnant's age to be $1.26^{+0.66}_{-0.51}$ Myr. We additionally applied the evolutionary models of SNR as provided in Leahy & Williams (2017) to perform an updated age estimation. For the obtained absorption column density of the entire remnant, $N_{\rm H} = 0.31^{+0.04}_{-0.02} \times 10^{22}$ cm^{-2} (as shown in Table 2) and a distance of 2.7 ± 0.3 kpc, one derives a local[3] interstellar medium (ISM) number density of $n_{\rm H} = 0.37^{+0.09}_{-0.07}$ cm^{-3}. Considering as inputs the derived local plasma density as calculated above, a typical explosion energy on the order of 10^{51} erg and keeping the remaining parameters to default input values, we derived an age of $9.25^{+1.85}_{-1.55} \times 10^5$ yr. This value is again in great agreement with previous reports.

All the estimates reported above yield a consistent picture for the SNR, using an adopted distance of ∼2.7 kpc. Nevertheless, all distance estimates are based on empirical relations with substantial scatter, and a critical assessment may be justified. Specifically, it is noteworthy that an update of the electron density model from NE2001 (Cordes & Lazio 2002) to YMW16 (Yao et al. 2017) has reduced the dispersion-measure based distances of all pulsars in projected vicinity to G279.0+01.1 by typically a factor of ∼8. While this withdraws the basis of all proposed pulsar associations in the literature which are based on the compatibility of the SNR's distance estimate with the respective pulsar's distances estimate, it is a useful exercise to consider whether a typical (as of today) distance that would be derived from a pulsar's dispersion measure together with a proposed association with the SNR would also yield a consistent picture. To this end, we list in Table 3 all pulsars that are in reasonable (within 3° of the remnant's center) angular distance to G279.0+01.1, together with their properties from the ATNF pulsar catalog[4] (Manchester et al. 2005). Three pulsars fall within the remnant's extension (J0955-5304 (B0953-52), J0957-5432, J0954-5430), whereas seven pulsars lie outside of the remnant's structure (J1001-5507 (B0959-54), J1000-5149, J1001-5559, J1002-5559, J1016-5345 (B1014-53), J0941-5244, J0940-5438). Amongst the above pulsars, J0940-5428 is the only one categorized as a giga-electronvolt emitter, namely 4FGL J0941.1-5429 as a giga-electronvolt point source (Abdollahi et al. 2020), and it exhibits the highest spin-down power (1.9×10^{36} erg s^{-1}). A potential association with any of the aforementioned pulsars (except for J1002.5559) would place the remnant at a much closer distance of 0.12–0.45 kpc, based on the YMW16 electron density model (Yao et al. 2017). In particular, assuming that the pulsar J1001-5507 (0959-54) is associated with the remnant (as suggested by Duncan et al. 1995), the dispersion-measure based distance is 0.41 kpc and the pulsar's spin-down age (which would then be a measure for the SNR's age) is 0.4 Myr.

Assuming thus a 0.4 kpc remnant distance one can perform the same computation series as for the case of an assumed remnant's distance of 2.7 ± 0.3 kpc. Such a closer distance results in a 21 pc remnant diameter. A $V = 1.42 \times 10^{59}$ cm^{-3} volume can then be derived assuming spherical geometry. For identical values of η and $norm_{\rm Hot}$ one then derives (using Eq. (5)) $n_{\rm H} = 1.26^{+0.09}_{-0.05} \times 10^{-2}$ cm^{-3} (or $n_{\rm e} = 1.52^{+0.11}_{-0.06} \times 10^{-2}$ cm^{-3}) local density. Employing the Giacani et al. (2009) relation: $t \sim \frac{\tau}{n_e}$, the remnant is found to have an age of $4.9^{+2.4}_{-1.7} \times 10^5$ yr. Similarly, one can also employ the evolutionary models of SNR as provided in Leahy & Williams (2017) to derive an age estimate. With default inputs (identical to those employed for an age estimate assuming a 2.7 ± 0.3 kpc remnant's distance) except for the local ISM number density which is computed to be $n_{\rm H} = 2.51^{+0.33}_{-0.16}$ cm^{-3} (for $N_{\rm H} = 0.31^{+0.04}_{-0.02} \times 10^{22}$ cm^{-2} and a distance of 0.4 kpc), one obtains a remnant's age of $1.01^{+0.09}_{-0.03} \times 10^4$ yr. Such an age would

[3] Local in the sense that the average density toward the SNR is representative of the density at the SNR.

[4] https://www.atnf.csiro.au/research/pulsar/psrcat/

actually favor an association with the pulsar J0940-5428, the pulsar J0954-5430, or the pulsar J1001-5507, since the rest of the pulsars appear to be considerably older. It is noteworthy that whereas a 0.38 kpc pulsar's J0940-5428 distance makes the latter object a compelling candidate to be associated with the remnant given its computed transverse velocity, its young age (0.04 Myr), its large spin-down power, and its giga-electronvolt counterpart (4FGL J0941.1-5429). A 2.7 kpc distance forbids such an association with the remnant given the extremely unrealistic transverse velocity of ∼3236 km s^{-1} which would be required to reach its present position.

5. Summary

We report on the discovery of the X-ray counterpart of the SNR G279.0+01.1, which is found to be of ∼3° in size, using eRASS:4 data. We performed a comprehensive X-ray imaging and spectral analysis, using eRASS:4 data, and complement the findings with archival data from ROSAT and *XMM-Newton*. The obtained results from all X-ray datasets were found to be in excellent agreement, taking into account the restrictions to which the ROSAT and *XMM-Newton* data are subject.

The majority of the remnant's X-ray emission is restricted to the 0.3–1.1 keV energy band. In the 1.1–1.5 keV band, only portions of the remnant are observable; whereas, above 2 keV, no emission from the remnant is detected at all. The emission from the remnant can be described with thermal, thin-plasma emission. No sign for nonthermal emission was detected. The data from the entire remnant can be described by a two-temperature plane-parallel shocked plasma in nonequilibrium, with temperatures of kT∼0.6 keV and ∼0.3 keV, respectively, and an average absorption column density of $N_{\rm H} \sim 0.3 \times 10^{22}$ cm^{-2}. However, significant X-ray temperature variations have been detected across the 3° angular extension of the SNR, and also the absorption column differs at different regions. Still, also when analyzing individual subregions, defined for example with a Voronoi binning analysis, most of the regions require more than one temperature for a satisfactory fit (see Table 2 and Appendices C, D). Whether the plasma is in equilibrium or in nonequilibrium can however not be decided from the X-ray data alone.

However, significantly enhanced (above solar) abundances for O, Ne, and Mg seem to be required for an adequate description of the individual spectra and the total spectrum, when the simplest two-temperature models are adopted. No high-Z elements are observed. This is noteworthy since only a small number of such O- Ne- dominated SNRs have been observed as of yet. The latter characteristics, that is to say exhibiting clear O VII, O VIII Lyα, and Ne IX lines with an ejecta origin as well as the Ne X Lyα line and the He-like Mg XI unresolved triplet all across its surface, along with the detection of strong [OIII] lines in its optical spectra suggests that the SNR can be classified as O-rich. However, only a limited number of its optical filaments have been spectrally studied. Therefore, a more detailed analysis of its optical spectrum is essential to confirm its O-rich nature. If the SNR is confirmed to be O-rich, it would be the fourth known SNR of this class in our Galaxy, and the first evolved Galactic remnant that demonstrates such features. Two O-rich remnants have been observed in the SMC, 0102.2-272.9 (Finkelstein et al. 2006; Banovetz et al. 2021) and 0103-72.6 (Park et al. 2003), another two in the LMC, N132D (Hughes 1987) and 0540-69.3 (Mathewson et al. 1980; Park et al. 2010), and three have been identified in the Milky Way, Cassiopeia A (Kamper & van den Bergh 1976; Thorstensen et al. 2001; Fesen et al. 2006; Hammell & Fesen 2008), Puppis A (Winkler & Kirshner 1985), and G292.0+1.8 (Murdin & Clark 1979; Winkler et al. 2009). Even though the above remnants have the presence of O-enriched ejecta in common, their nature varies significantly. Such O-rich remnants, and in general SNRs exhibiting X-ray spectral line emission dominated by O, Ne, and Mg, are considered to be the remnants of core-collapse SNe of the stars of the highest mass. Such massive progenitor stars can reach masses of 20 $M_\odot$ or greater, and are objects of major importance for the study of SN nucleosynthesis.

The SNR's X-ray spatial morphology is in agreement with the radio continuum data as depicted in Fig. 4. The radio continuum image of the remnant, using 4850 MHz data from the PMN (Condon et al. 1993) southern surveys, yields a 2.5–3° extension almost identical to its X-ray size and larger than what previously was reported in Woermann & Jonas (1988) and Stupar & Parker (2009). The remnant appears as an incomplete shell in both wavebands. The regions of enhanced emission positioned to the north and southeast of the SNR are spatially identical in both radio and X-rays. Further X-ray spectral analysis revealed a strong X-ray absorption to the west, likely linked to the presence of enhanced IR emission originating from dust clouds (as seen in Fig. 7). This is also supported by the obtained absorption column density parameter of the X-ray spectral fit (as seen in Fig. 8). The results suggest that the SNR is characterized by a peculiar limb-brightened morphology in the X-ray energy band since no enhanced absorption column density values were derived from its central region (region J). However, strong absorption column density values were derived from the western part of the remnant accompanied by the absence or very weak X-ray diffuse emission, and thus we argue that the remnant is partially occluded to the west.

Fermi-LAT giga-electronvolt data analysis from the location of the remnant using all available data yields consistent imaging results with earlier findings reported in Araya (2020). We confirm the detection of an extended giga-electronvolt source spatially coincident with the remnant, named 4FGL J1000.0-5312e. In particular, three individual regions of enhanced γ – ray emission were detected with 4.6σ, 5.5σ, and 5.8σ significance, respectively, as shown in Fig. 6. The modeling of the giga-electronvolt excess favors the scenario in which those three regions are part of the diffuse giga-electronvolt emission from the SNR. A strong spatial anticorrelation is observable between X-ray and giga-electronvolt emission without any clear explanation. However, the spatial morphology of the extended giga-electronvolt source (which is highly coincident with the location of the remnant), the high detection significance of three prominent regions, and its hard giga-electronvolt spectral component (extending up to 0.5 TeV without any indications of spectral softening) strongly suggest that 4FGL J1000.0-5312e is likely the remnant's giga-electronvolt counterpart.

The results obtained in this work cast some doubt on the so far prevailing interpretation that G279.0+01.1 is located at a distance of ∼2.7 kpc and has an age of ∼1 Myr. On the one hand, we could obtain a consistent picture for the state of the SNR under this assumption, specifically also considering an independent, consistent distance estimate using the derived X-ray absorption column and matching it to the latest *Gaia*-2MASS extinction maps (Lallement et al. 2019, 2022). If taken at face value, the SNR has a 140 pc linear diameter and an age of 0.75–1.92 Myr, exploiting either the formula employed in Giacani et al. (2009) ($t \sim \frac{\tau}{n_e}$) or evolutionary models by Leahy & Williams (2017). Then, the remnant would be categorized among

the oldest Galactic SNRs, if not the oldest, and would as of now be the oldest SNR in which swept-up ISM and ejecta contributions are apparently detected. On the other hand, some of our observational results would be better consistent with a much smaller distance, for example ~ 0.4 kpc, if one assumes that the SNR is associated with one of the potentially associated pulsars and their revised distance estimate from the YMW16 electron density model. The SNR would then have a ~ 20 pc linear diameter and a much younger age of $\sim 1 \times 10^4$–5×10^5 yr, using again the same evolutionary models as above. The best-fit nonequilibrium X-ray models would be better in line with this younger age. Also, the association with a morphologically associated giga-electronvolt counterpart argues in favor of a younger age. Further studies are required to resolve this ambiguity regarding the SNR's estimated distance and age.

Acknowledgements. M.M. and G.P. acknowledge support from the Deutsche Forschungsgemeinschaft through grant PU 308/2-1. This work is based on data from eROSITA, the soft X-ray instrument aboard SRG, a joint Russian-German science mission supported by the Russian Space Agency (Roskosmos), in the interests of the Russian Academy of Sciences represented by its Space Research Institute (IKI), and the Deutsches Zentrum für Luft- und Raumfahrt (DLR). The SRG spacecraft was built by Lavochkin Association (NPOL) and its subcontractors, and is operated by NPOL with support from the Max Planck Institute for Extraterrestrial Physics (MPE). The development and construction of the eROSITA X-ray instrument was led by MPE, with contributions from the Dr. Karl Remeis Observatory Bamberg & ECAP (FAU Erlangen-Nuernberg), the University of Hamburg Observatory, the Leibniz Institute for Astrophysics Potsdam (AIP), and the Institute for Astronomy and Astrophysics of the University of Tübingen, with the support of DLR and the Max Planck Society. The Argelander Institute for Astronomy of the University of Bonn and the Ludwig Maximilians Universität Munich also participated in the science preparation for eROSITA. The eROSITA data shown here were processed using the eSASS/NRTA software system developed by the German eROSITA consortium. We thank the EXPLORE team which provided us access to the G-TOMO tool of the EXPLORE platform `https://explore-platform.eu/` allowing us to exploit updated *Gaia*-2MASS data. We also thank Denys Malyshev, Victor Doroshenko and Lorenzo Ducci for fruitful discussions. We thank the referee, Knox Long for his insightful comments and recommendations.

References

Abdollahi, S., Acero, F., Ackermann, M., et al. 2020, ApJS, 247, 33
Acero, F., Ackermann, M., Ajello, M., et al. 2016, ApJS, 224, 8
Aharonian, F. A., Akhperjanian, A. G., Aye, K. M., et al. 2004, Nature, 432, 75
Anderson, L. D., Bania, T. M., Balser, D. S., et al. 2014, ApJS, 212, 1
Araya, M. 2020, MNRAS, 492, 5980
Banovetz, J., Milisavljevic, D., Sravan, N., et al. 2021, ApJ, 912, 33
Borkowski, K. J., Lyerly, W. J., & Reynolds, S. P. 2001, ApJ, 548, 820
Borkowski, K. J., Hendrick, S. P., & Reynolds, S. P. 2006, ApJ, 652, 1259
Brunner, H., Liu, T., Lamer, G., et al. 2022, A&A, 661, A1
Cappellari, M., & Copin, Y. 2003, MNRAS, 342, 345
Cash, W. 1979, ApJ, 228, 939
Collischon, C., Sasaki, M., Mecke, K., Points, S. D., & Klatt, M. A. 2021, A&A, 653, A16
Condon, J. J., Broderick, J. J., & Seielstad, G. A. 1991, AJ, 102, 2041
Condon, J. J., Griffith, M. R., & Wright, A. E. 1993, AJ, 106, 1095
Condon, J. J., Broderick, J. J., Seielstad, G. A., Douglas, K., & Gregory, P. C. 1994, AJ, 107, 1829
Cordes, J. M., & Lazio, T. J. W. 2002, arXiv e-prints [arXiv:astro-ph/0207156]
Cram, L. E., Green, A. J., & Bock, D. C. J. 1998, PASA, 15, 64
Dopita, M. A., Tuohy, I. R., & Mathewson, D. S. 1981, ApJ, 248, L105
Duncan, A. R., Haynes, R. F., Stewart, R. T., & Jones, K. L. 1995, MNRAS, 277, 319
Fesen, R. A., Hammell, M. C., Morse, J., et al. 2006, ApJ, 645, 283
Finkbeiner, D. P. 2003, ApJS, 146, 407
Finkelstein, S. L., Morse, J. A., Green, J. C., et al. 2006, ApJ, 641, 919
Foight, D. R., Güver, T., Özel, F., & Slane, P. O. 2016, ApJ, 826, 66
Giacani, E., Smith, M. J. S., Dubner, G., et al. 2009, A&A, 507, 841
Goss, W. M., Shaver, P. A., Zealey, W. J., Murdin, P., & Clark, D. H. 1979, MNRAS, 188, 357
H.E.S.S. Collaboration (Abdalla, H., et al.) 2018a, A&A, 612, A1
H.E.S.S. Collaboration (Abdalla, H., et al.) 2018b, A&A, 612, A3
Hammell, M. C., & Fesen, R. A. 2008, ApJS, 179, 195
Hughes, J. P. 1987, ApJ, 314, 103
Hwang, U., Petre, R., & Flanagan, K. A. 2008, ApJ, 676, 378
Joye, W. A., & Mandel, E. 2003, in Astronomical Data Analysis Software and Systems XII, 295, 489
Kamitsukasa, F., Koyama, K., Uchida, H., et al. 2015, PASJ, 67, 16
Kamper, K., & van den Bergh, S. 1976, PASP, 88, 587
Kesteven, M. J., & Caswell, J. L. 1987, A&A, 183, 118
Khabibullin, I. I., Churazov, E. M., Chugai, N. N., et al. 2024, A&A, submitted [arXiv:2401.17261]
Koyama, K., Petre, R., Gotthelf, E. V., et al. 1995, Nature, 378, 255
Lallement, R., Babusiaux, C., Vergely, J. L., et al. 2019, A&A, 625, A135
Lallement, R., Vergely, J. L., Babusiaux, C., & Cox, N. L. J. 2022, A&A, 661, A147
Lasker, B. M. 1979, PASP, 91, 153
Leahy, D. A., & Williams, J. E. 2017, AJ, 153, 239
Lucke, P. B. 1978, A&A, 64, 367
Manchester, R. N., Hobbs, G. B., Teoh, A., & Hobbs, M. 2005, AJ, 129, 1993
Mathewson, D. S., Dopita, M. A., Tuohy, I. R., & Ford, V. L. 1980, ApJ, 242, L73
McKee, C. F., & Cowie, L. L. 1975, ApJ, 195, 715
Merloni, A., Predehl, P., Becker, W., et al. 2012, arXiv e-prints [arXiv:1209.3114]
Merloni, A., Lamer, G., Liu, T., et al. 2024, A&A, 682, A34
Michailidis, M., Pühlhofer, G., Becker, W., et al. 2024, arXiv e-prints [arXiv:2401.17312]
Murdin, P., & Clark, D. H. 1979, MNRAS, 189, 501
Park, S., Hughes, J. P., Burrows, D. N., et al. 2003, ApJ, 598, L95
Park, S., Hughes, J. P., Slane, P. O., Mori, K., & Burrows, D. N. 2010, ApJ, 710, 948
Predehl, P., & Schmitt, J. H. M. M. 1995, A&A, 293, 889
Predehl, P., Andritschke, R., Arefiev, V., et al. 2021, A&A, 647, A1
Shan, S.-S., Zhu, H., Tian, W.-W., et al. 2019, Res. Astron. Astrophys., 19, 092
Strüder, L., Briel, U., Dennerl, K., et al. 2001, A&A, 365, L18
Stupar, M., & Parker, Q. A. 2009, MNRAS, 394, 1791
Sunyaev, R., Arefiev, V., Babyshkin, V., et al. 2021, A&A, 656, A132
Thorstensen, J. R., Fesen, R. A., & van den Bergh, S. 2001, AJ, 122, 297
Turner, M. J. L., Abbey, A., Arnaud, M., et al. 2001, A&A, 365, L27
Voges, W., Aschenbach, B., Boller, T., et al. 2000, IAU Circ., 7432, 3
Whiteoak, J. B. Z., & Green, A. J. 1996, A&AS, 118, 329
Wilms, J., Allen, A., & McCray, R. 2000, ApJ, 542, 914
Winkler, P. F., & Kirshner, R. P. 1985, ApJ, 299, 981
Winkler, P. F., Twelker, K., Reith, C. N., & Long, K. S. 2009, ApJ, 692, 1489
Woermann, B., & Jonas, J. L. 1988, MNRAS, 234, 971
Yamaguchi, H., Koyama, K., & Uchida, H. 2011, PASJ, 63, S837
Yang, R.-z., Kafexhiu, E., & Aharonian, F. 2018, A&A, 615, A108
Yao, J. M., Manchester, R. N., & Wang, N. 2017, ApJ, 835, 29
Zeng, H., Xin, Y., Zhang, S., & Liu, S. 2021, ApJ, 910, 78

Appendix A: Specifics of the *XMM-Newton* pointings

The European Photon Imaging Camera (EPIC) is a three-detector system (MOS1, MOS2 (Turner et al. 2001), and PN (Strüder et al. 2001)) mounted on the *XMM-Newton* telescope that operates in the energy range of 0.2-15 keV. EPIC detectors were operating in full frame mode in all three observations, allowing data analysis of diffuse X-ray emission. All detectors and thus all three observations were subjected to an exposure of a few tens of ks, resulting in good statistics for the analysis of images and spectra. In more detail, the profiles of the three observations are described as follows, ID:0823031001 : MOS1 full frame/MOS2 full frame/PN full frame, exposures: 17.7 ks/17.7 ks/15.8 ks, PI: Bettina Posselt, ID:0823030401: MOS1 full frame/MOS2 full frame/PN full frame, exposures: 16.7 ks/16.7 ks/14.8 ks, PI: Bettina Posselt, and ID:0823030301: MOS1 full frame/MOS2 full frame/PN full frame, exposures: 9.0 ks/9.0 ks/7.1 ks, PI: Bettina Posselt. The limited FoV of *XMM-Newton*, of 0.5° size, makes it impossible to derive information about the morphology of a remnant of size 3°, as seen in Fig. 3 and Fig. B.1. However, the improved statistical quality of the data in the respective limited areas, in comparison to ROSAT and/or eROSITA, allows us to examine the consistency of the findings among the three X-ray instruments and perform a detailed spectrum analysis verifying eROSITA best-fit spectral parameters. Data reduction was performed using the eSAS software. In particular, eSAS tasks `emchain` and `epchain` were utilized to reprocess all observation data files. We furthermore employed the `mos-spectra` and `pn-spectra` commands to construct the images and extract the spectrum from the regions of interest. *XMM-Newton* sky maps, from all three observations, were produced by combining data from all three detectors but excluding CCD chips found in anomalous state. Moreover, point sources were filtered out, aiming at enhancing the visibility of the diffuse X-ray emission and avoiding possible contamination of the data. Vignetting corrections were applied, and adaptive smoothing using the default smoothing kernel of 50 counts was performed.

Appendix B: *XMM-Newton* spectral analysis

Spectral extraction and analysis was performed for all three available *XMM-Newton* observations. Apart from the `pn_spectra` and `mos_spectra` eSAS commands, we further made use of `pn_back` and `mos_back` eSAS tasks to estimate the quiescent particle background. *XMM-Newton* observation ID:0823031301 was used as a background control region since it is free of diffuse X-ray emission originating from the remnant. The whole *XMM-Newton* FoV was used for the spectral extraction of the observation ID:0823031001 since it is fully dominated by diffuse X-ray emission emanating from the remnant, as depicted on the upper right panel of Fig. B.1. On the other hand, diffuse X-ray emission from the remnant covers only partially the observation ID:0823031401, and thus one can use approximately half of the *XMM-Newton* FoV as on-source region and half as background region. A simultaneous fitting of the source and background emission was performed in the 0.5-1.7 keV energy range (we restricted the *XMM-Newton* spectral analysis above 0.5 keV since some anomalous fluctuations were detected below 0.5 keV for PN and MOS2 instruments) in a similar manner to the eROSITA spectral analysis. Three distinct models were used to describe the X-ray emission from portions of the remnant as seen with *XMM-Newton*. Those three model components can be discriminated to source emission: `tbabs×vpshock`, X-ray background: `const× const×(apec+tbabs×(apec+apec+pow))`, and soft proton events (instrumental background): `unabsorbed power law+gauss+gauss`. The entire FoV of the *XMM-Newton* ID:0823031001 observation exhibits spectral features which can be well described by either an absorbed CIE model of $kT \sim 0.16$ keV or an absorbed NEI model of $kT \sim 0.8 - 0.9$ keV. The latter finding is in excellent agreement with the eROSITA spectral results from the southwestern parts of the remnant. However, among the selected models for spectral analysis, we show spectral fit results for the `tbabs(vpshock)` model (as shown on the right panel of Fig. B.2). We suggest that the latter model describes this region best since it provides the highest fit quality and absorption column density values that are well aligned with the expected $N_{\rm H}$ values based on optical extinction measurements at the distance of the remnant, as discussed in Sect. 4.3. The latter assertion is also supported by the fact that the corresponding XMM observation does not coincide with regions of enhanced IR emission which is likely related to X-ray absorption (dust clouds), see Sect. 4.3 for a detailed discussion. In addition, aiming at performing a direct spectral consistency check between the two X-ray instruments, we extracted the eROSITA spectrum from a region which is identical to the region of the 0823031001 *XMM-Newton* observation. The obtained spectral fitting results are shown in the two side-by-side panels of Fig. B.2. The main parameters of the spectral fit of ObsID: 0823031001 and eROSITA from the exact same portion of the remnant are summarized in Tab. B.1, and are found to be in excellent agreement. One noticeable difference, still not significant, is that while letting O and Ne vary, on top of Mg, moderately improves the fit for *XMM-Newton* data, it does not improve the one for eRASS:4 data (which can be likely attributed to the lower statistics of the eRASS data compared to *XMM-Newton*). For completeness, we state that, even though we report on Tab. B.1 the best-fit results, if one employs the exact same absorbed CIE model for *XMM-Newton* data as for eRASS:4 (i.e., only Mg elemental abundance is let vary) almost identical fit results are obtained, $kT = 0.17^{+0.01}_{-0.01}$ keV, $N_{\rm H} = 0.52^{+0.02}_{-0.02} \times 10^{22}{\rm cm}^{-2}$, and a Mg abundance of $1.95^{+0.34}_{-0.33}$. A single temperature plasma component appears sufficient to describe the region's spectral features. The latter finding does not come as a surprise since the *XMM-Newton* 0823031001 observation partially overlaps with the C region, as defined in Sec. 4.1, which exhibits similar characteristics. It is noteworthy that when allowing the plasma temperature to vary freely (i.e., no constraints on the acceptable temperature range) both instruments favor a somewhat questionably high plasma temperature when employing NEI models (of the scale of 5-10 keV). However, when forcing the plasma temperature to values below 1 keV and then letting it vary; a best fit of ~0.8 keV temperature is obtained when utilizing eRASS:4 data. On the contrary, when exploiting *XMM-Newton* data, and applying an identical strategy, the same high plasma temperature persists (i.e., the plasma temperature hits the forced high-temperature boundary); thus we fix the latest parameter (i.e., plasma temperature) to the obtained best-fit values from eROSITA (no significant change in the fit quality is found and thus the fit is considered reasonable). Finally, if one tries to use multiple component models (e.g., `tbabs(vapec+vapec)`) no improvement is obtained for eRASS:4 data whereas only an insignificant improvement is obtained for *XMM-Newton* data. The obtained parameters are common for both data sets, $N_{\rm H} \sim 0.44 \times 10^{22}{\rm cm}^{-2}$,

Table B.1: Best-fit parameters of the remnant's X-ray spectrum as derived by both *XMM-Newton* and eRASS:4 data from the exact same portion of the remnant.

Instrument	eROSITA	*XMM-Newton*
Area (10^6 arcs^2)	2.55	2.25
Surf_bri (10^{-3} c/arcs^2)	2.66	212.92
Model	vapec	
kT(keV)	$0.17^{+0.01}_{-0.01}$	$0.16^{+0.01}_{-0.01}$
$N_{\rm H}(10^{22}{\rm cm}^{-2})$	$0.51^{+0.03}_{-0.03}$	$0.63^{+0.02}_{-0.02}$
O	-	$0.78^{+0.17}_{-0.12}$
Ne	-	$0.44^{+0.09}_{-0.07}$
Mg	$2.02^{+0.61}_{-0.56}$	$0.93^{+0.26}_{-0.22}$
χ^2/dof	1.17	-
Model	vnei	
kT(keV)	$0.84^{+0.34}_{-0.21}$	0.84
$N_{\rm H}(10^{22}{\rm cm}^{-2})$	$0.11^{+0.03}_{-0.03}$	0.11
O	$1.48^{+0.22}_{-0.18}$	$1.23^{+0.12}_{-0.11}$
Ne	$2.84^{+0.51}_{-0.45}$	$2.33^{+0.24}_{-0.22}$
Mg	$3.03^{+0.90}_{-0.75}$	$2.86^{+0.36}_{-0.34}$
Ionization time (10^{10}s/cm^3)	$1.83^{+0.76}_{-0.56}$	$1.77^{+0.12}_{-0.12}$
χ^2/dof	1.14	-
Model	vpshock	
kT(keV)	$0.88^{+0.67}_{-0.21}$	0.88
$N_{\rm H}(10^{22}{\rm cm}^{-2})$	$0.14^{+0.04}_{-0.04}$	0.14
O	$1.43^{+0.21}_{-0.18}$	$1.32^{+0.19}_{-0.16}$
Ne	$2.25^{+0.59}_{-0.57}$	$1.94^{+0.25}_{-0.22}$
Mg	$2.32^{+0.92}_{-0.82}$	$2.25^{+0.31}_{-0.29}$
Ionization time (10^{10}s/cm^3)	$4.36^{+3.11}_{-2.13}$	$4.81^{+0.80}_{-0.63}$
χ^2/dof	1.06	-

Notes. The best-fit parameters are given with 1σ errors. The X-ray spectra were extracted from the location of the 0823031001 *XMM-Newton* observation using both X-ray instruments. Where not defined; elemental abundances are set to solar values.

kT~0.54 – 0.64 keV, and kT~0.16 – 0.18 keV. Once again, multiple component models which include NEI models favor questionably high temperatures and the obtained best-fit model is generally unstable.

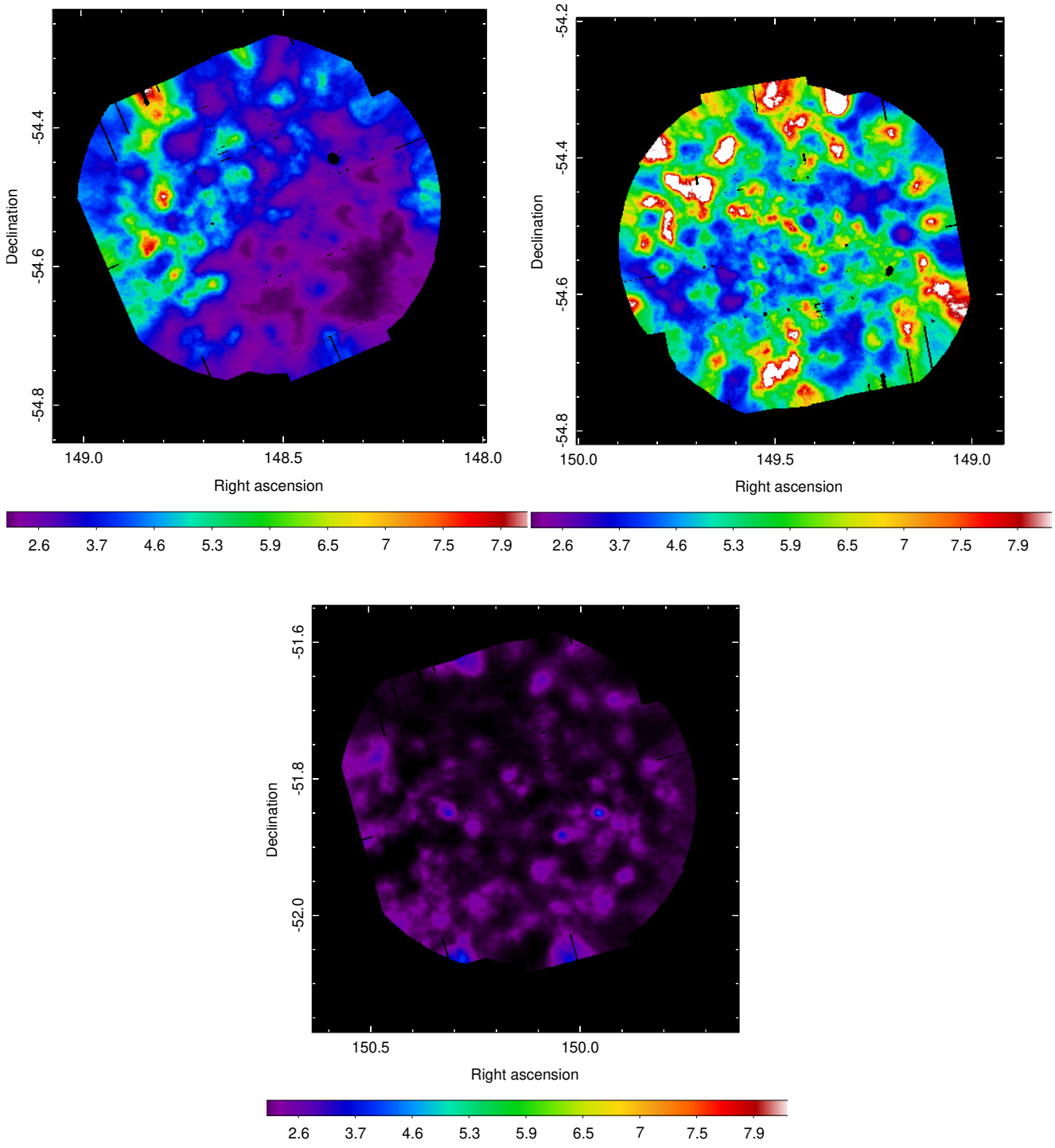

Fig. B.1: *XMM-Newton* surface brightness maps in the 0.3-1.1 keV energy band, in units of counts/s/deg^2. Points sources are filtered out, and the maps, of 5″ pixel size, are adaptively smoothed with a 50 counts kernel and vignetting-corrected. Upper left panel: 0823030401 *XMM-Newton* pointing. Upper right panel: 0823031001 *XMM-Newton* pointing. Lower left panel: 0823030301 *XMM-Newton* pointing. The 0823031001 pointing is fully dominated by X-ray emission originating from the remnant, the 0823030401 pointing is only partially filled with X-ray emission, whereas the 0823030301 pointing is totally free of the remnant's X-ray emission.

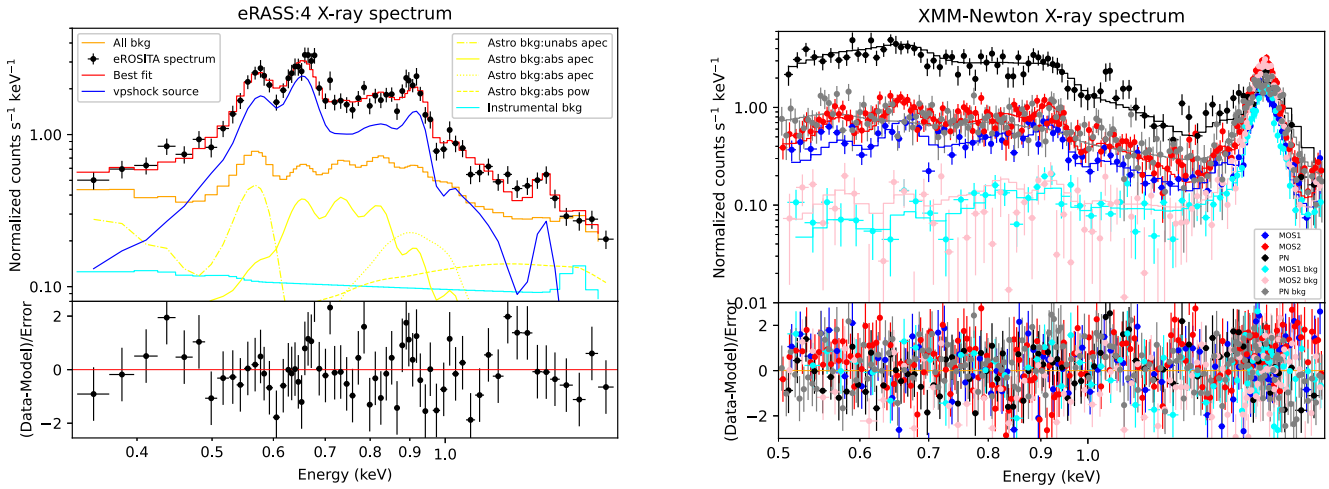

Fig. B.2: X-ray spectra from a portion of the remnant which is spatially coincident with the FoV of the 0823031001 *XMM-Newton* observation. Left panel: eRASS:4 data in the 0.3-1.7 keV energy band. To obtain a representative model for the background emission we made use of the black circlular nearby background control region, defined in Fig. 3, and applied the obtained best-fit model in the simultaneous fitting of the source and background emission of the on-source region. Right panel: pn, mos1, and mos2 data in the 0.5-1.7 keV energy band. The corresponding *XMM-Newton* background spectrum was obtained from the nearby 0823031401 *XMM-Newton* observation, which is free of the remnant emission.

Article II

Appendix C: Single versus multiple component spectral fitting result for the representative regions A, B, C, and the entire remnant

For each individual region, we started the fitting procedure attempting to fit the data with both a single VAPEC model (CIE) and a single VNEI (or VPSHOCK) (NEI) model. In more detail, it appears that a simple absorption model of collisionally ionized diffuse gas, `tbabs(apec)` in Xspec notation, is not sufficient to describe the spectral data, even when O, Ne, and Mg elemental abundances are let to vary (χ^2/dof = 1.78 when fixing the elemental abundances to solar values, and χ^2/dof = 1.69 when letting O, Ne and Mg vary) for region A (northwestern part of the remnant), while it provides relatively good fits, nonetheless not the finest possible, only when the aforementioned elemental abundances are free, for region B (central part of the remnant, χ^2/dof = 1.27) and C (southwestern part of the remnant, χ^2/dof = 1.22). It is noteworthy that when letting Fe vary (on top of the elemental abundances mentioned above) a χ^2/dof = 1.51 value is obtained for region A, however, the elemental abundances for both Mg and Fe are found to be questionably high: around 10 and 30 solar values, respectively, making the derived fit questionable. For regions B and C the improvement is more modest (χ^2/dof = 1.26, 1.19 for regions B and C respectively) and is not characterized by the same extreme elemental abundance values of Ne and Mg as those obtained for region A (i.e., 2.5 and 3.3 solar values were derived for Ne and Mg in the case of region C). A significantly improved fit in all the above cases can also be obtained when letting N free (on top of O, Ne, Mg, and Fe) which results in extremely low N values, and thus one can fix it to zero. In spite of this, the fits obtained are still not ideal (e.g., χ^2/dof = 1.24 for region A), whereas even if it improves significantly the fits for region B and C (χ^2/dof = 1.07 and χ^2/dof = 1.08 respectively) strong residuals $\sim$1.0 − 1.05 keV still persist. When switching to nonequilibrium models (NEI), with free O and Ne elemental abundances (also Mg for region C), a `tbabs(vnei)` model provides significant improvement in the spectral fitting results for region A (χ^2/dof = 1.21), it suggests that a NEI model can provide a fit of equal goodness for region C (χ^2/dof = 1.24, but a 15 keV temperature is derived which is highly questionable), while it results to a somewhat worse fit for region B (χ^2/dof = 1.5). It is noteworthy that the Mg contribution (Mg bump at $\sim$1.3 − 1.4 keV) to the total spectrum is well modeled when employing NEI models by keeping the corresponding elemental abundance fixed to solar value (except for region C which exhibits the strongest Mg peak among all three regions and thus letting the latest elemental abundance varying improves the fit), whereas Fe does not change dramatically the quality of the fit as in the case of the CIE model (the same applies for N elemental abundance). Finally, it is also worth mentioning that NEI models favor elemental abundances values which are in the range of 0.9-2 solar values (i.e., no extreme values are derived). In all of the above cases, a much higher temperature plasma and a significantly lower absorption column density are obtained in comparison to CIE models, as shown in Tab. 2. Therefore, NEI models are considered preferable since the derived absorption column density based on the known distance of the remnant is well-aligned with the spectral fit results of NEI models whereas it falls short of the CIE model (see Sect. 4.3 for a detailed discussion). Similarly, a `tbabs(vpshock)` (NEI) model provides highly consistent results, except for region C, in terms of plasma temperature and absorption column density with a `tbabs(vnei)` model, when applying the same conventions, and the following fitting χ^2/dof values: 1.17 (region A), 1.42 (region B), and 1.16 (region C with a reasonable temperature of 0.99 keV in comparison to 15 keV obtained when employing a `tbabs(vnei)` model).

Multiple component models were also employed, and in particular, two temperature plasmas, aiming at improving the fitting results of the three representative spectra extraction regions, even though a `tbabs(vpshock)` model for regions A and C and a `tbabs(vapec)` model for region B seem to describe the remnant's spectral data relatively well. When using a `tbabs(vapec+vapec)` model we obtained significantly improved fitting results for regions A and B in comparison to single component models, as follows: χ^2/dof = 1.03 for region A,

$\chi^2/dof = 1.01$ for region B (letting O of the cooler component and Ne of the hotter one vary for both regions as shown in Tab. 2, whereas both O and Ne for the cooler component and Ne and Mg for the hotter one can be let vary obtaining almost identical results with only slightly modified elemental abundance values), whereas for region C it becomes clear that a single component model is sufficient for the fitting process, as no improvement and an extremely low normalization value is obtained for the second plasma model component (a result which does not come as a surprise as it was already indicated by the eRASS:4 RGB image of Fig. 2). By using a `tbabs(vnei+vnei)` model a $\chi^2/dof = 0.88$ is obtained for region A with elemental abundances fixed to solar values (one obtains similar results when letting O, Ne, and Mg of the two models vary since they are found to be relatively close to solar values), a $\chi^2/dof = 1.06$ is obtained for region B but letting varying O and Ne elemental abundances for both plasma components, whereas for region C a $\chi^2/dof = 1.06$ can be obtained when letting the O elemental abundance of the cooler component vary but fixing the higher temperature component to 2.0 keV since when letting kT parameter of that hottest component vary, a questionable high temperature of 10 keV scale is obtained, however, it still remains unconstrained. In this case, a $kT = 0.81^{+0.15}_{-0.09}$ keV is obtained for the cooler component with an $N_{\rm H} = 0.29^{+0.03}_{-0.04} \times 10^{22}{\rm cm}^{-2}$. Finally, we considered a `tbabs(vpshock+vpshock)` model, which results to a $\chi^2/dof = 0.87$ for region A with elemental abundances fixed to solar values (once again when letting 0 and Ne free almost identical results are obtained), a $\chi^2/dof = 1.06$ for region B (0 and Ne elemental abundance free for both model components whereas the temperature of the hotter component is fixed to the best fit before running the Xspec error task, since it remains unconstrained when free), whereas for region C it provides a fit of moderately improved quality ($\chi^2/dof = 1.08$ instead of a $\chi^2/dof = 1.16$ of a single `vpshock` model), however, inspecting the corresponding fit and residuals one realizes that the two obtained results (derived from the two distinct models) are almost identical indicating once again that a single component model can sufficiently describe the spectral features of that part of the remnant. In addition, the `tbabs(vpshock+vpshock)` model is highly unstable for that region, since error computation of the individual parameters of the model result to constant refitting. For completeness, we report the obtained best-fit parameters of the `tbabs(vpshock+vpshock)` model for region C as follows: $kT = 3.57$ keV, $\tau = 3.87^{+1.15}_{-0.73} \times 10^9$ s/cm^3, and $kT = 0.78^{+0.07}_{-0.04}$ keV, $\tau = 1.17^{+0.56}_{-0.18} \times 10^{11}$ s/cm^3, and $N_{\rm H} = 0.27^{+0.06}_{-0.05} \times 10^{22}{\rm cm}^{-2}$. In what above, we have fixed the hotter plasma temperature to the best-fit value since it remains unconstrained. We note that for region B when employing a `tbabs(vnei+vnei)` or a `tbabs(vpshock+vpshock)` model since both NEI models contribute to the Mg bump the latest is well modeled by keeping the Mg elemental abundance fixed to solar value. However, one can let Mg elemental abundance of the hotter component vary and obtain a fit of equal goodness which favors a somewhat lower temperature for the cooler component ~ 0.23 keV and higher elemental abundances, twice as high as shown in Tab. 2, of O, Ne for the hotter component. We additionally considered mixed two temperature plasma model components, i.e., one plasma is found in equilibrium while the other one is in nonequilibrium ionization (`tbabs(vapec+vnei)` or `tbabs(vapec+vpshock)`), and we tried to fit the data. When employing the `tbabs(vapec+vnei)` model a $\chi^2/dof = 1.03$ is obtained for region A with abundances fixed to solar, a $\chi^2/dof = 0.99$ is derived for region B by letting vary O and Ne of the cooler component and Ne and Mg of the hotter one, however, the ionization time of the NEI model remains unconstrained - which suggests uncertainty on the nature of the hotter plasma component (NEI or CIE) - thus we fix it to the best-fit value before running the Xspec error task. For region C, the fit is of equal goodness with single component models with one component being substantially weaker (at the level of the astrophysical background components) than the other. Similarly, $\chi^2/dof = 0.96$, $\chi^2/dof = 1.02$, are obtained for regions A and B, respectively, when using a `tbabs(vapec+vpshock)` model, while for region C the single model component remains the preferred option. To sum up, a two-temperature plasma model describes best the spectral features of regions A and B (without a clear preference when it comes to selection between CIE, NEI, or mixed morphology models), whereas region C can be best described by a single plasma in nonequilibrium (`tbabs(vpshock)`). However, for the latter a `tbabs(vpshock+vpshock)` temperature component in equilibrium cannot be excluded. It is noteworthy, that when employing the magenta or blue background regions as control background regions, the obtained χ^2/dof value for all single-component models and for all three regions are worse (significantly higher by a factor of $\sim 1.2 - 1.3$), whereas the two temperature plasma component provide fits of equal goodness regardless of the selected background and of consistent best fit spectral parameters. On the other hand, when fitting the spectrum of the entire remnant, two temperature plasma components provide by far better-fit quality compared to single-temperature models (either CIE or NEI) which can only model the spectrum poorly even when letting N, O, Ne, Mg, and Fe elemental abundances vary. Among all models mentioned above, a two-temperature plasma component in nonequilibrium (`tbabs(vphock+vpshock)`), letting O and Ne to vary, provides a fit of $\chi^2/dof = 1.3$. A best-fit of $\chi^2/dof = 1.19$ quality can be achieved as shown on the last column of Tab. 2. One can try to let Fe of the cooler component vary and obtain a $\chi^2/dof = 1.15$ fit quality, however, the latest action further increases the value of the rest of elemental abundances which are left vary and results in a 7 solar value Fe elemental abundance.

Appendix D: Spectral analysis of the remnant's subregions defined by Voronoi binning analysis

In what below, we consider a `vpshock` model as the representative NEI model for the fitting process, as a `vnei` model results in unconstrained plasma temperatures in many cases. However, we note that in most of the cases, a `vnei` provides fitting results of only marginally worse fit quality but of the same best-fit values as the `vpshock`. In addition, we suggest that where applicable NEI models are favored over a CIE model since the distance of the remnant (either ~2.5 kpc or 0.4 kpc) supports an absorption column density which is well-aligned with nonequilibrium plasma models whereas it falls short of single plasma temperature models in equilibrium. However, in a number of subregions in the remnant's surroundings (i.e., subregions that do not exhibit high diffuse X-ray excess compared to the astrophysical background) CIE models provide an excellent fit to the data. In Fig. D.1 we summarize the spectral best-fit results from all subregions of the remnant. In Tab. D.1 we report on the best-fit spectral parameters of each subregion.

Overall, the detailed spectral analysis of subregions defined by the Voronoi binning algorithm favors an increased absorption column density in the remnant's surroundings, especially to

the south and west of the remnant, supporting previous indications of IRAS data (see Fig. 7) for X-ray absorption in those regions due to the prevalence of dust. In addition, the current analysis concludes that the remnant is of incomplete shell-type (or fragmented annulus) morphology, since its central region, namely region J in this work, is both free of X-ray emission and is not characterized by enhanced absorption column density, and its western part is not observable in X-rays (likely due to X-ray absorption) as resulted from the X-ray spectral fit. The obtained absorption column density map is shown on the left panel of Fig. 8.

Table D.1: Best-fit parameters of the eRASS:4 X-ray spectra from all subregions.

Region	A' region	B' region	C' region	D region	
Model	vpshock	vpshock	vpshock	vpshock	
kT(keV)	$0.61^{+0.38}_{-0.17}$	0.61	2.0	2.0	
$N_{\rm H}(10^{22}{\rm cm}^{-2})$	$0.42^{+0.06}_{-0.06}$	$0.38^{+0.03}_{-0.03}$	$0.23^{+0.03}_{-0.04}$	$0.42^{+0.06}_{-0.07}$	
O	-	-	$0.88^{+0.15}_{-0.11}$	-	
Ne	-	-	$1.12^{+0.30}_{-0.21}$	-	
Mg	-	-	$2.46^{+0.92}_{-0.67}$	-	
Ionization time $(10^9{\rm s/cm}^3)$	$0.90^{+0.12}_{-0.10}$	$8.88^{+1.60}_{-1.47}$	$6.31^{+1.17}_{-0.86}$	$2.13^{+0.67}_{-0.42}$	
χ^2/dof	1.2	1.33	1.02	1.02	
Region	E region	F region	G region	H region	
Model	vpshock+vpshock	vpshock+vpshock	vpshock	vpshock	
kT(keV)	$0.75^{+0.14}_{-0.10}$ $1.68^{+2.24}_{-0.93}$	0.8 $1.37^{+0.86}_{-0.28}$	0.8	$0.43^{+0.33}_{-0.17}$	
$N_{\rm H}(10^{22}{\rm cm}^{-2})$	$0.27^{+0.04}_{-0.04}$	$0.21^{+0.03}_{-0.03}$	$0.40^{+0.03}_{-0.03}$	$0.54^{+0.15}_{-0.11}$	
O	-	-	-	$0.15^{+0.04}_{-0.03}$	
Ne	-	-	-	$0.15^{+0.06}_{-0.06}$	
Mg	-	-	-	-	
Ionization time $(10^9{\rm s/cm}^3)$	167^{+116}_{-75} $1.15^{+0.20}_{-0.18}$	$1.84^{+0.67}_{-0.34}$ $62.0^{+34.3}_{-24.7}$	$9.75^{+1.86}_{-1.46}$	$9.30^{+9.75}_{-3.11}$	
χ^2/dof	1.2	1.01	1.01	1.3	
Region	I region	J region	K region	L region	
Model	vpshock+vpshock	vpshock	vpshock+vpshock	vpshock+vpshock	
kT(keV)	$0.96^{+0.59}_{-0.53}$ $1.15^{+0.82}_{-0.26}$	2.0	$0.88^{+0.23}_{-0.12}$ $1.56^{+2.74}_{-0.67}$	$0.14^{+0.04}_{-0.01}$ $1.26^{+1.50}_{-0.40}$	
$N_{\rm H}(10^{22}{\rm cm}^{-2})$	$0.18^{+0.02}_{-0.02}$	$0.17^{+0.03}_{-0.03}$	$0.28^{+0.05}_{-0.05}$	$0.53^{+0.10}_{-0.13}$	
O	-	-	-	$0.57^{+0.17}_{-0.18}$ -	
Ne	-	-	-	$0.21^{+0.30}_{-0.21}$ $0.82^{+0.67}_{-0.60}$	
Mg	-	-	-	-	
Ionization time $(10^9{\rm s/cm}^3)$	$6.11^{+3.31}_{-1.89}$ $68.5^{+70.2}_{-35.1}$	$6.26^{+0.79}_{-0.63}$	147^{+95}_{-61} $1.02^{+0.19}_{-0.16}$	23400 $35.1^{+16.21}_{-19.7}$	
χ^2/dof	1.33	1.03	0.99	1.08	
Region	M region	N region	O region	P region	Q region
Model	vpshock+vpshock	vpshock	vpshock	vpshock	vpshock
kT(keV)	$0.79^{+0.11}_{-0.08}$ $1.20^{+0.52}_{-0.35}$	$2.43^{+1.22}_{-0.75}$	$0.53^{+0.13}_{-0.11}$	0.8	0.8
$N_{\rm H}(10^{22}{\rm cm}^{-2})$	$0.18^{+0.03}_{-0.02}$	$0.24^{+0.03}_{-0.03}$	$0.24^{+0.05}_{-0.04}$	$0.51^{+0.03}_{-0.04}$	$0.52^{+0.04}_{-0.04}$
O	$0.63^{+0.07}_{-0.07}$ -	$0.78^{+0.08}_{-0.07}$	$0.66^{+0.12}_{-0.10}$	-	$0.27^{+0.08}_{-0.06}$
Ne	$0.56^{+0.13}_{-0.12}$ -	$1.08^{+0.15}_{-0.13}$	$1.07^{+0.19}_{-0.16}$	-	$0.19^{+0.07}_{-0.06}$
Mg	-	-	-	-	$0.76^{+0.29}_{-0.23}$
Fe	-	-	$0.28^{+0.08}_{-0.06}$	-	-
Ionization time $(10^9{\rm s/cm}^3)$	157^{+80}_{-56} $3.50^{+1.18}_{-0.87}$	$8.91^{+1.20}_{-0.91}$	236^{+360}_{-142}	$3.75^{+0.67}_{-0.43}$	$7.6^{+0.35}_{-0.27}$
χ^2/dof	1.1	1.04	1.19	1.25	1.2

Notes. The best-fit parameters are given with 1σ errors. The subregions examined were defined via the Voronoi analysis process. Where not defined, elemental abundances were set to solar values.

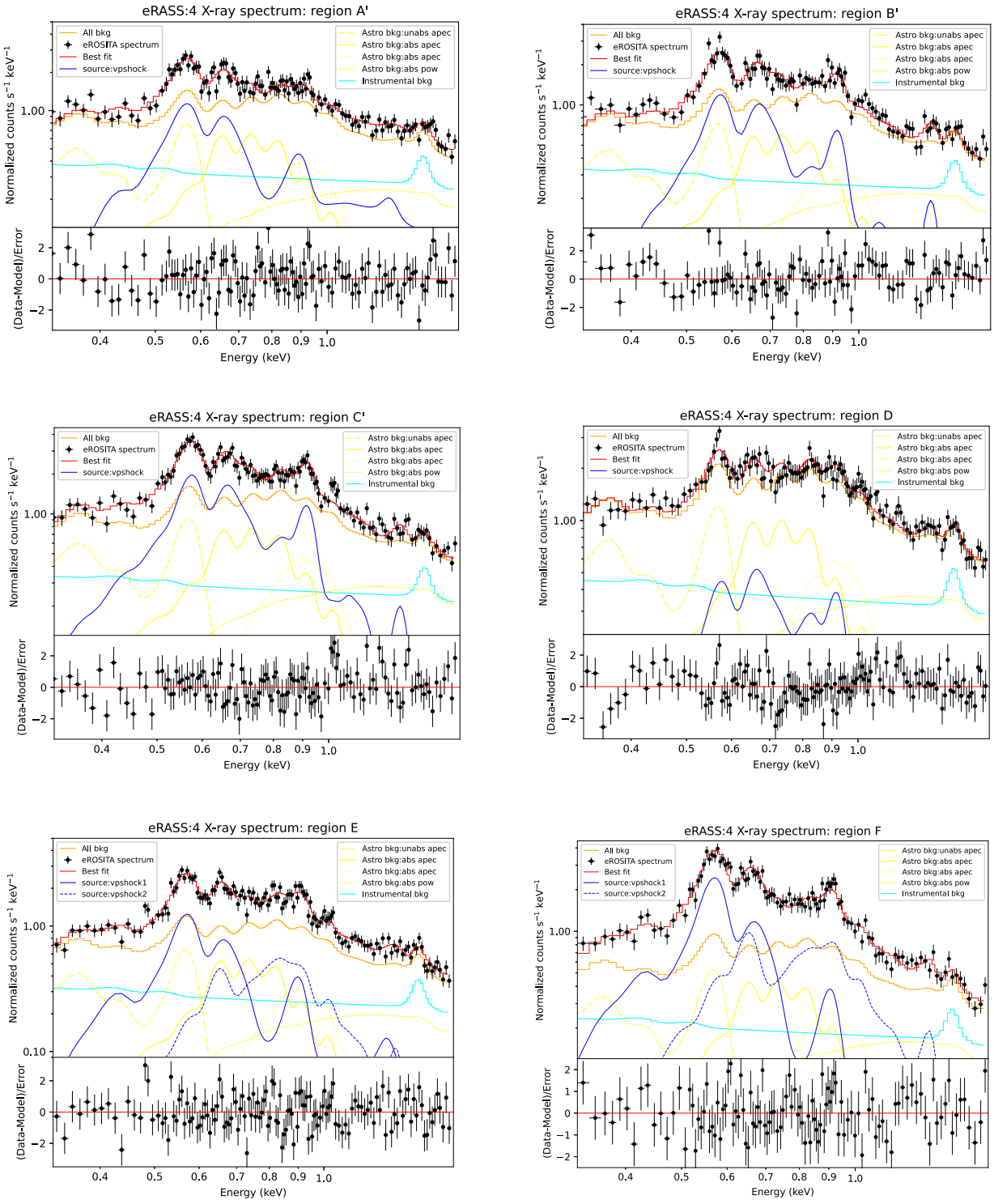

Fig. D.1: eRASS:4 X-ray spectrum in the 0.3-1.7 keV energy band, from the selected subregions of the remnant defined using Voronoi binning analysis, which clearly illustrates the spectral shape change within the remnant.

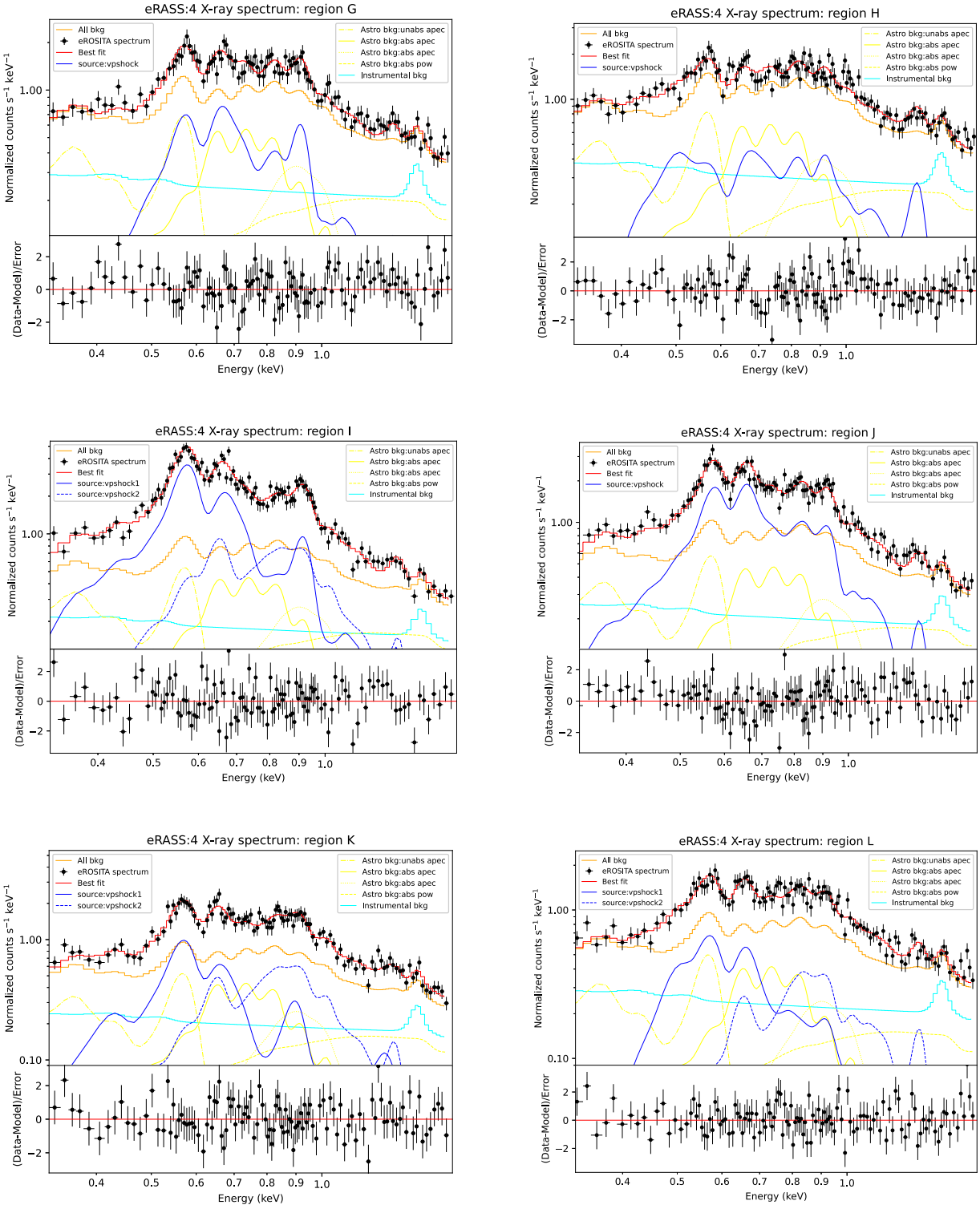

Fig. D.1: continued.

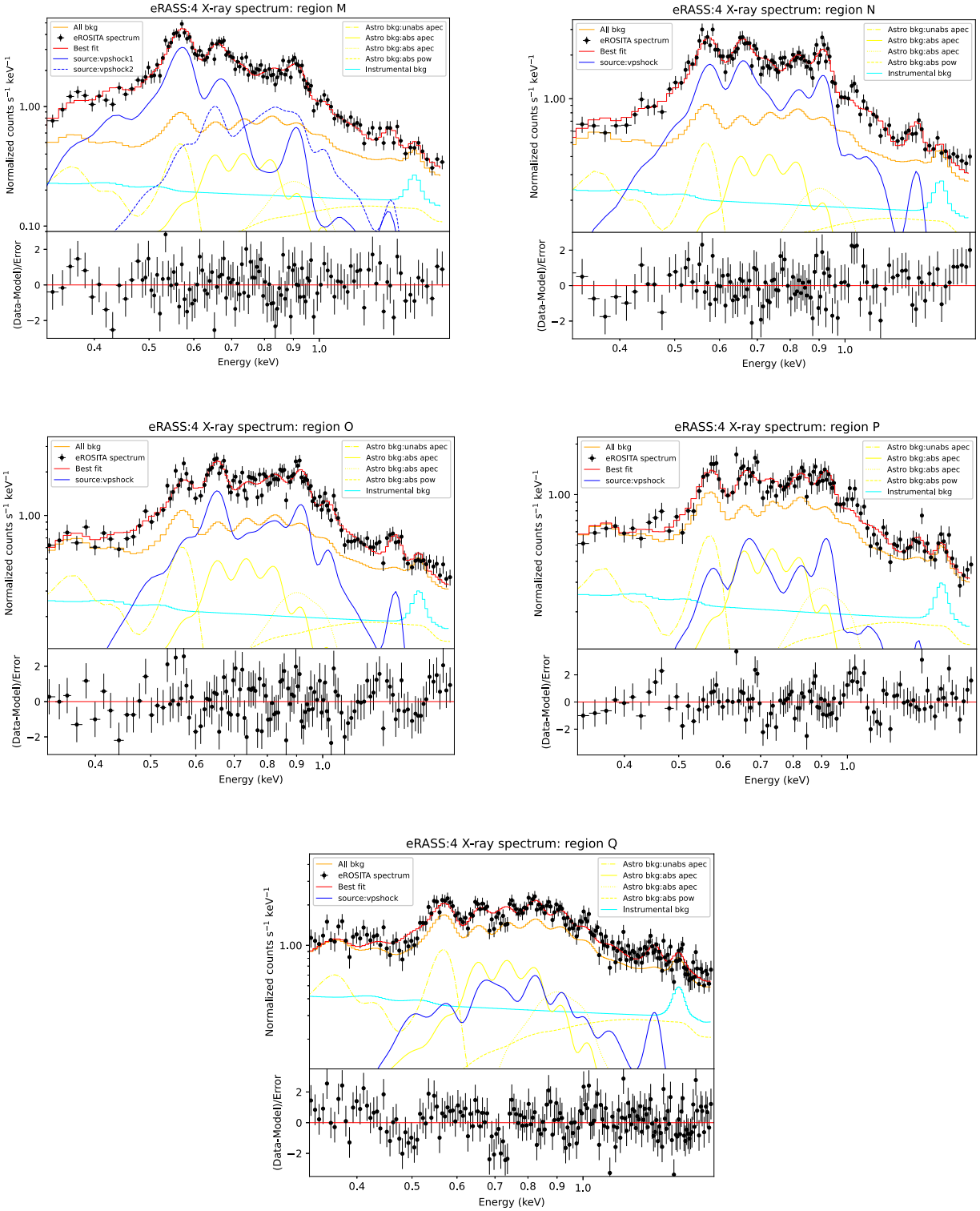

Fig. D.1: continued.

3.2 M. Michailidis, G. Pühlhofer, W. Becker, M. Freyberg, A. Merloni, A. Santangelo, M. Sasaki, A. Bykov, N. Chugai, E. Churazov, I. Khabibullin, R. Sunyaev, V. Utrobin, I. Zinchenko. Study of X-ray emission from the S147 nebula by *SRG*/eROSITA: X-ray imaging, spectral characterization and a multiwavelength picture. In: Astronomy & Astrophysics (A&A), accepted (May 2024)

Astronomy & Astrophysics manuscript no. output
June 10, 2024

Study of X-ray emission from the S147 nebula with SRG/eROSITA: X-ray imaging, spectral characterization and a multiwavelength picture

Miltiadis Michailidis[1], Gerd Pühlhofer[1], Werner Becker[2,3], Michael Freyberg[2], Andrea Merloni[2], Andrea Santangelo[1], Manami Sasaki[4], Andrei Bykov[5], Nikolai Chugai[6], Eugene Churazov[7,8], Ildar Khabibullin[7,9,8], Rashid Sunyaev[7,8,10], Victor Utrobin[6,11], Igor Zinchenko[12]

[1] Institut für Astronomie und Astrophysik Tübingen, Universität Tübingen, Sand 1, D-72076 Tübingen, Germany
[2] Max-Planck Institut für extraterrestrische Physik, Giessenbachstraße, 85748 Garching, Germany
[3] Max-Planck Institut für Radioastronomie, Auf dem Hügel 69, 53121 Bonn, Germany
[4] Dr. Karl Remeis Observatory, Erlangen Centre for Astroparticle Physics, Friedrich-Alexander-Universität Erlangen-Nürnberg, Sternwartstraße 7, 96049 Bamberg, Germany
[5] Ioffe Institute, Politekhnicheskaya st. 26, Saint Petersburg 194021, Russia
[6] Institute of Astronomy, Russian Academy of Sciences, 48 Pyatnitskaya str., Moscow 119017, Russia
[7] Space Research Institute (IKI), Profsoyuznaya 84/32, Moscow 117997, Russia
[8] Max Planck Institute for Astrophysics, Karl-Schwarzschild-Str. 1, D-85741 Garching, Germany
[9] Universitäts-Sternwarte, Fakultät für Physik, Ludwig-Maximilians-Universität München, Scheinerstr.1, 81679 München, Germany
[10] Institute for Advanced Study, Einstein Drive, Princeton, New Jersey 08540, USA
[11] NRC 'Kurchatov Institute', acad. Kurchatov Square 1, Moscow 123182, Russia
[12] Institute of Applied Physics of the Russian Academy of Sciences, 46 Ul'yanov str., Nizhny Novgorod 603950, Russia

Received 30 January 2024 / Accepted 17 May 2024

ABSTRACT

Simeis 147 (S147, G180.0-01.7, "Spaghetti nebula") is a supernova remnant (SNR) extensively studied across the entire electromagnetic spectrum, from radio to GeV γ-rays, except in X-rays. Here, we report the first detection of significant X-ray emission from the entire SNR, using data of the extended ROentgen Survey Imaging Telescope Array (eROSITA) onboard the Russian-German Spektrum Roentgen Gamma (SRG). The object is located at the Galactic anti-center, and its 3° size classifies it among the largest SNRs ever detected in X-rays. By employing ∼14.5 years of *Fermi*-LAT data, our study confirms the association of the remnant with a spatially coincident diffuse GeV excess, namely 4FGL J0540.3+2756e or FGES J0537.6+2751. The X-ray emission is purely thermal, exhibiting strong O, Ne, and Mg lines, whereas it lacks heavier-Z elements. The emission is mainly confined in the 0.5-1.0 keV band, no significant emission is detected above 2.0 keV. Both, a collisional plasma model in equilibrium and a model of non-equilibrium collisional plasma can fit the total spectrum. While the equilibrium model – though statistically disfavoured – cannot be excluded by the X-ray fitting, only the absorption column of the non-equilibrium model is consistent with expectations derived from optical extinction data. Adopting an expansion in a homogeneous medium of typical ISM density, the general SNR properties are broadly consistent with an expansion model that yields an estimated age of $\sim 0.66 - 2 \times 10^5$ yr, i.e. a rather old age. The preference for an X-ray emitting plasma in non-equilibrium, however, adds to the observational evidence which favors a substantially younger age. In a companion paper, we explore a SNR in cavity scenario, resulting in a much younger age that alleviates some of the inconsistencies of the old-age scenario.

Key words. supernova remnants (Individual object: Spaghetti nebula) — multiwavelength study

1. Introduction

Supernovae (SNe) rank among the most intense events in a galaxy in terms of the amount of energy they release. SNe are short timescale events, observable only in a period of months to a few years maximum. On the contrary, their remnants can be observable up to more than 10^5 years until they merge with the Interstellar medium (ISM) and get dissolved. With an average rate of 1-2 SN per century (Keane & Kramer 2008) a total of $\sim$ 1200 supernova remnants are expected to be observable in the Milky Way (MW) at any given moment. Despite the rough estimation of a few thousands SNe, up-to-date findings result in a much lower number of identified SNRs $\sim$ 300 (Green catalog (Green 2019), SNRcat[1] (Ferrand & Safi-Harb 2012)), with the majority of those discovered in radio.

The apparent size of evolved SNRs can vary based on their distance. In close proximity to Earth (hundreds of parsecs), they can reach degree-scale sizes. Current imaging X-ray instruments have a limited field of view (FoV), making them difficult to study in X-rays. In many cases, imaging survey data is the only option. In this respect, eROSITA

[1] http://snrcat.physics.umanitoba.ca/

(extended ROentgen Survey Imaging Telescope Array – a wide-angle grazing-incident X-ray telescope providing all-sky survey data, Predehl et al. (2021)) offers a unique opportunity to study such objects with unprecedented sensitivity. In this category, S147 is a classic example. In this paper, we report the first firm detection of X-rays from the entire S147 SNR using eROSITA all-sky survey (eRASS, Merloni et al. (2024)) data from the first four completed eROSITA all-sky surveys, eRASS:4. We present a thorough examination of the X-ray and multiwavelength properties of the object.

S147, listed in the Atlas of optical nebulosities (Gaze & Shajn 1952), was for the first time discussed, among other nebulosities, as an SNR candidate by Minkowski (1958). A first radio map of the SNR was reported by Dickel & McKinley (1969), revealing the shell-like morphology of the source. More recent radio observations confirm an almost circular shell-type morphology of the source with a diameter of $\sim 200'$ (Reich 2002; Reich et al. 2003; Xiao et al. 2008). The radio emission originates from synchrotron radiation with a rarely observed spectral break at higher frequencies (Xiao et al. 2008). In 1973, the first optical (Hα emission) detailed study of the SNR was reported, showing an SNR with well-defined delicate long filaments (van den Bergh et al. 1973). A good spatial correlation between radio synchrotron and optical emission is observed across the entire remnant. A particular ring-like structure located at the Eastern edge of the SNR, present both in radio synchrotron and Hα data, stands out as a peculiar feature indicating a lopsided morphology that we describe as an "ear-type" morphology due to the presence of an outer shell that appears to be extended further to the East compared to the rest of the multi-shell structures of the remnant. The latter structural feature is significantly present in the optical and of fainter nature in radio observations. This feature is apparent also in the multi-band images of Ren et al. (2018). A void-type structure, towards the East of the center of the SNR, is a common feature in both wavebands.

Depending on the individual method utilized, SNR distance estimates between 0.6 and 1.9 kpc have been computed (Clark & Caswell 1976; Kirshner & Arnold 1979; Sofue et al. 1980; Kundu et al. 1980; Fesen et al. 1985; Kramer et al. 2003; Guseinov et al. 2004; Sallmen & Welsh 2004; Ng et al. 2007; Chatterjee et al. 2009; Dinçel et al. 2015; Chen et al. 2017; Boubert et al. 2017). Earlier estimates that are based on the Σ-D relation and make use of the surface brightness of the SNR and high-velocity gas tend to emerge toward smaller distances < 1.1 kpc (Clark & Caswell 1976; Kirshner & Arnold 1979; Kundu et al. 1980; Guseinov et al. 2004; Sallmen & Welsh 2004), except for Sofue et al. (1980) who report a 1.6 ± 0.3 kpc distance using the Σ-D relation. More recent studies employ the associated runaway star, associated pulsar, and the S147 dust cloud and converge toward a distance of 1.2-1.4 kpc (Ng et al. 2007; Chatterjee et al. 2009; Dinçel et al. 2015; Chen et al. 2017; Boubert et al. 2017). Kochanek et al. (2024) used an alternative strategy to derive the remnant's distance, which yielded a $1.37^{+0.10}_{-0.07}$ kpc distance estimate by examining the appearance of high velocity CaII or NaI absorption lines in hot stars. This result is found to be in excellent agreement with previous estimates. Therefore, a distance of ~ 1.3 kpc is adopted as a central fiducial value for subsequent calculations throughout the rest of this paper, unless otherwise noted.

Falling near the Galactic anti-center, morphologically similar to the Vela SNR, and with an approximate angular size of 3°, S147 is among the largest SNRs ever detected in X-rays. With ROSAT all-sky survey (RASS) (Voges et al. 1999), before eRASS the most sensitive available survey in this energy range, X-ray emission from the location of S147 has already been observed, but neither with a clear shell-type morphology (mostly a patchy appearance) nor with enough X-ray data to exploit and analyze (Sun et al. 1995; Aschenbach 1996). The European X-ray Observatory Satellite (EXOSAT) was the first instrument to attempt to detect X-ray emission from the prominent, bright in radio, Southern rim of the SNR before ROSAT. No X-ray emission at low energies < 2 keV - energy range in which the EXOSAT Low Energy (LE) telescopes operated - was detected. In particular, X-ray flux measurements from the Southern patchy structure of the SNR resulted only in strong constraints on expansion parameters of the remnant (i.e., interstellar density and explosion energy) assuming that the SNR itself is located at a close distance (~ 1.1 kpc) (Sauvageot et al. 1990). Conversely, X-ray emission in the $2 - 6$ keV energy band was detected by the Medium Energy instrument (ME). However, its origin was likely attributed to the transient pulsar A0535+26 mainly due to its relatively hard spectrum (Sauvageot et al. 1990). The latter assertion is confirmed in this work since no emission from the SNR is detected with eROSITA above 2 keV.

A significant number of X-ray sources falls in the sky region where the SNR is located. Among those, the bright high-mass X-ray binary (HMXB) 1A 0535+262 located at the South-Eastern edge of the SNR and the pulsar J0538+2817, located $40'$ to the West of its center, stand out. While 1A 0535+262 is not associated with the SNR, various observations towards the pulsar suggest a plausible association with the remnant. Both the kinematic age (~ 30 kyr) and distance estimates, $1.33^{+0.22}_{-0.16}$ kpc based on parallax (Chatterjee et al. 2009) and 1.2 kpc based on dispersion measurements (DM) (Kramer et al. 2003), are broadly consistent with those of the SNR. The pulsar associated with the remnant was first detected in radio (Anderson et al. 1996) and later in X-ray observations with *XMM-Newton* and *Chandra* (Romani & Ng 2003). The latter X-ray observations revealed extended emission of a faint Pulsar Wind Nebula (PWN G179.72-1.69) accompanying the pulsar. The runaway star HD 37424 with a spectral type B5.0V±0.5 is considered to be the pre-supernova binary companion to the progenitor of the pulsar J0538+2817 (Dinçel et al. 2015; Boubert et al. 2017; Kochanek 2021).

S147 is usually considered to be one of the most evolved Galactic SNRs, with an estimated age of $\gtrsim 10^2$ kyr. Therefore, it has been claimed to be the oldest SNR ever detected in X-rays (Aschenbach 1996). The age estimate is derived from the shock velocity measurements of $\sim 80 - 120$ km/s (Kirshner & Arnold 1979; Phillips et al. 1981). At the same time, S147 is part of the "special group" of the 70 out of the 294 known SNRs that have been reported to be associated or likely associated with Molecular clouds (MC) (Jiang et al. 2010; Chen et al. 2014). Its association with the "S147 dust cloud" is extensively discussed in Chen et al. (2017), establishing the conditions for the presence of spatially extended GeV gamma-ray emission. The GeV emission is found to be in good spatial correlation with the actual extent of the SNR, and interpreted to be of hadronic origin (Katsuta et al. 2012). An updated gamma-ray spec-

Table 1: X-ray instruments used in this work.

Instrument	ObsID	Year	Mode	Exposure (ks)	Pointing
eROSITA	eRASS:4 (088063,085063 084060, 087060, 082063)	2019-2021	survey	14.5[a]	-
MOS1, MOS2, PN	0693270301	2013	Full Frame (x3)	37.5/37.5/33.6	South East
MOS1, MOS2, PN	0693270401	2013	Full Frame (x3)	26.7/26.7/22.7	South
ROSAT	RASS (931214)	1990	survey	17.2[b]	-

[a] Total on-source exposure time
[b] Livetime, on time

Notes. eROSITA, *XMM-Newton* (MOS1, MOS2, PN) and ROSAT observations analyzed in this work. The pointing column describes the position of the *XMM-Newton* observations with respect to the remnant's center.

tral modeling of the source, aiming at constraining the particle acceleration parameters, was conducted in Suzuki et al. (2022). The derived GeV spectrum was found to be in good agreement with the one reported in Katsuta et al. (2012). However, the particle acceleration can be modeled by various parameter sets, and thus its parameters were poorly constrained. The extended GeV source is mainly detected in the 0.2-10 GeV energy band with *Fermi*-LAT and is currently listed in the 12-year *Fermi*-LAT gamma-ray source catalog as 4FGL J0540.3+2756e, as well as in the first catalog of extended sources produced using *Fermi*-LAT data as FGES J0537.6+2751 and in the third catalog of high energy *Fermi*-LAT sources as 3FHL J0537.6+2751e. Morphologically, the GeV emission seems to fit best the Hα filamentary structure rather than regular geometrical shapes. The GeV and Hα flux correlation suggests that the gamma-ray emission could possibly originate from the thin filaments observed in radio continuum and optical data (Katsuta et al. 2012).

The paper is organized as follows: In section 2 we report on the eROSITA observations of the SNR alongside the data analysis of the eROSITA first four all-sky surveys (eRASS:4). Additionally, we compare the eROSITA findings to results obtained from the earlier ROSAT survey and archival *XMM-Newton* observations from small portions of the remnant. We further outline the implications of the presence of dust at and around the remnant's location. A reanalysis of *Fermi*-LAT γ-ray data, from the location of the remnant, is also presented. Section 3 is dedicated to the eROSITA and *XMM-Newton* spectral analysis results and its potential implications (distance and age estimates) adopting a simplified setting of an expansion in homogeneous local medium. In Section 4, we report on the updated γ-ray spectrum of the S147 GeV counterpart and discuss potential scenarios for the origin of the GeV emission on the basis of its GeV Spectral Energy Distribution (SED). Section 5 gives concluding remarks. In a companion paper (Khabibullin et al. 2024, (Paper II) hereafter), we explore the possibility that the SNR expands in a wind-blown cavity, which yields a much younger age estimate for the SNR.

2. X-ray observations and data analysis

The main parameters of all X-ray observations employed in this work are summarized in Tab. 1.

2.1. eROSITA data

The Russian-German Spektrum Roentgen Gamma (SRG) observatory (Sunyaev et al. 2021) consists of two instruments *(i)* eROSITA operating at the softer X-ray band 0.2-8.0 keV with unprecedented sensitivity (Predehl et al. 2021) and *(ii)* the Russian X-ray telescope `MIKHAIL PAVLINSKY` ART-XC, which covers the harder 4.0-30.0 keV X-ray band (Pavlinsky et al. 2021). In this paper, only data from the eROSITA telescopes are used.

eROSITA (Predehl et al. 2021) consists of seven X-ray telescope modules TM1-7 that are aligned in parallel and have identical fields of view of approximately 1° diameter each. Each telescope holds 54 nested mirror shells. Such a system of X-ray mirrors can be roughly described by three numbers: its effective area, its vignetting function, and its point spread function (PSF). A preliminary analysis of the in-flight PSF calibration presented in Merloni et al. (2024) results in an $\sim$ 30" average spatial resolution in survey mode.

Launched on July 13, 2019 towards the L2 Lagrangian point, eROSITA started taking regular survey data on the 13th of December 2019. On January 2022 the fourth eROSITA all-sky survey was completed, and here we report on results obtained with data of eRASS1 to eRASS4, called eRASS:4.

The German and Russian parties involved in the mission are responsible for the analysis of the data of the Eastern and Western Galactic hemisphere, respectively. Since S147 is a large diameter SNR located at the Galactic anti-center, half of its extension falls in the Western and half in the Eastern hemisphere. Therefore, this work is a joint collaboration of the two parties.

We used data of the `c020` processing version. The analysis and data reduction were carried out using `eSASSusers_201009` version (Brunner et al. 2022) of eSASS (eROSITA Standard Analysis Software). All events flagged

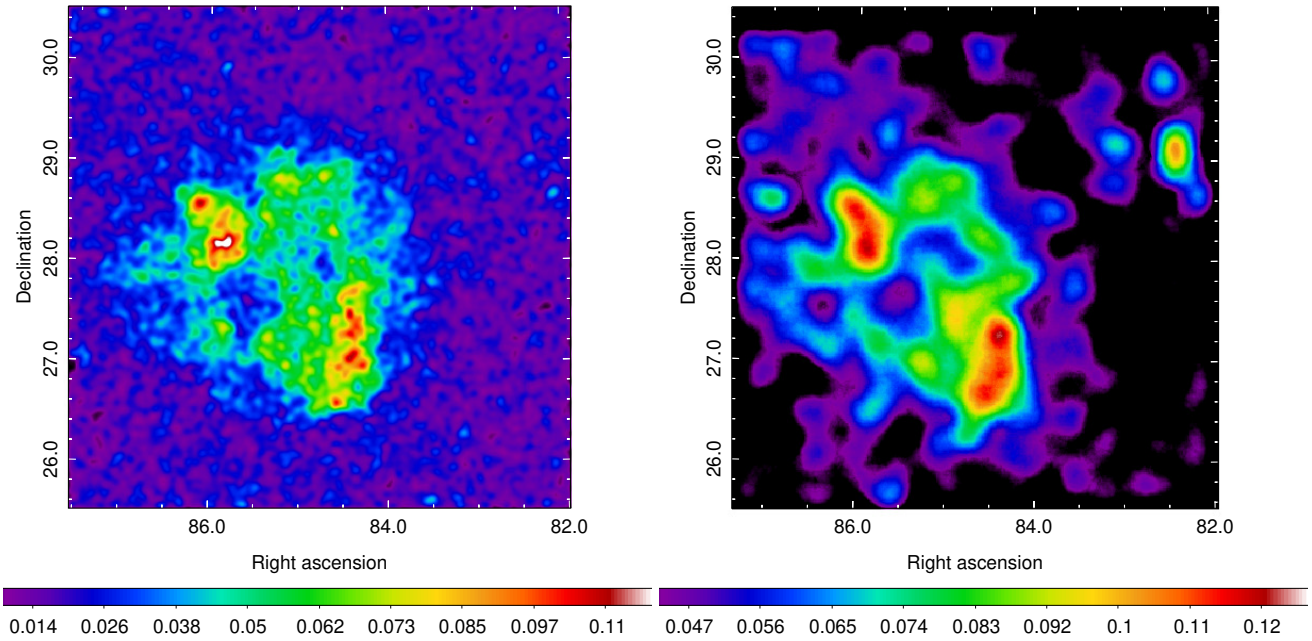

Fig. 1: Left panel: eRASS:4 exposure-corrected intensity sky map in the 0.5-1.0 keV energy band, in units of counts/pixel with a pixel size of 10″. All point sources are filtered out, and the image is convolved with a $\sigma = 100''$ Gaussian aiming at enhancing the visibility of the diffuse X-ray emission. Right panel: ROSAT intensity sky map in the 0.4-2.4 keV energy band (medium RASS band). The ROSAT image is built on a different energy range that maximizes contrast between on-source and background regions, allowing fainter structures to be detected. The image, with a pixel size of 45″, is convolved with a $\sigma = 6.4'$ Gaussian to enhance the visibility of the diffuse emission from the location of the remnant. Except for HMXB 1A 0535+262 and the emission associated to the associated pulsar which were treated independently and effectively masked out from the image, all remaining point sources are not removed. Their proper masking requires a substantially larger extraction radius which heavily affects the faint diffuse emission originating from the remnant.

as corrupt either individually or as part of a corrupt frame were excluded, retaining all four of the recognized legal patterns (`pattern=15`), and identifying and repairing disordered GTIs. Flare inspections, when the survey scans were passing through the S 147 area, were also carried out aiming at avoiding potential contamination of the data sets used for further analysis.

For ease of use, the eROSITA X-ray sky map can be divided into 4700 sky tiles (squares of $\sim 3.6^o \times 3.6^o$ size) which partially overlap. Each sky tile corresponds to a unique six-digit ID (the first three digits express the Right Ascension RA while the last three the Declination Dec of the corresponding center of each particular sky tile). Given that S147 is an $\sim 3^o$ SNR that is not particularly centered at a specific sky tile, its X-ray emission extends into more than one sky tile. Five sky tiles were individually examined for diffuse X-ray emission across the entire SNR in order to achieve complete coverage. In particular, the 088063 sky tile lies at the German half of the sky, while the other four [085063, 084060, 087060, 082063] partially fall in the German and in the Russian halves, respectively.

Fig. 1 illustrates the $5^\circ \times 5^\circ$ mosaic intensity map, in units of counts/pixel, in the energy range of 0.5-1.0 keV. The selection of the energy range was optimized based on the energy spectrum of the source. The image is corrected for uneven exposure by a factor ranging between 0.946 and 1.056. From the image analysis, when exploiting different energy bands (see the corresponding RGB image of Fig. 2), it is evident that the SNR is only detectable at very soft X-rays. The emission is mainly confined in the 0.5-1.0 keV energy band, whereas above 2.0 keV no X-ray emission originating from the SNR can be significantly detected. In more detail, the first step of the mosaic intensity image production is the creation of the individual sky tile count maps. Using a 10″ spatial resolution (i.e., pixel size) and utilizing the `evtool` task of eSASS software, we combine the data for all four surveys and all TMs (all seven TMs were used as any uncertainty in the energy calibration resulting from the light leaks in TM 5 and 7 (Predehl et al. 2021) are not quantitatively impacting our results in the energy band of interest > 0.5 keV) to produce the corresponding count maps. To enhance the visibility of the detected diffuse emission from the source of interest and avoid likely contamination on the signal, we masked out all points sources with detection significance above 3σ using a 110″ extraction radius. Individual brighter sources such as the HMXB 1A 0535+262 and the associated pulsar (accompanied by its faint PWN) were treated independently employing larger extraction regions to be properly masked out. Following `evtool`, `expmap` task was employed to compute the exposure maps at that specific energy range, with an average exposure of ~ 500 s $\cdot$ pixel^{-1}. Finally, Filter Wheel Closed (FWC) data with deep and different exposures for each TM, at a scale of a few hundreds of ks, were used for the creation of the corresponding instrumental background maps. The aforementioned maps were employed to ensure that af-

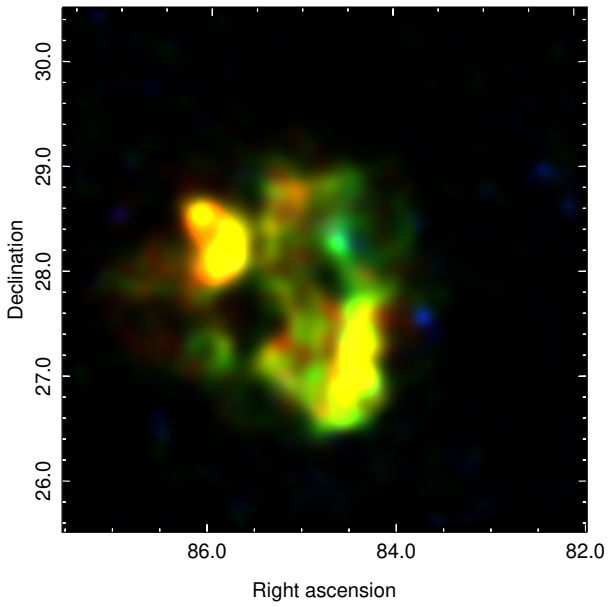

Fig. 2: eRASS:4 RGB exposure-corrected intensity sky map, with energy to color correspondence: R: 0.3-0.6 keV, G: 0.6-1.0 keV, and B: 1.0-1.5 keV, in units of counts/pixel with a pixel size of 10″. Similarly to Fig. 1, all point sources are masked out, and the image is convolved with a $\sigma = 2'$ Gaussian aiming at enhancing the visibility of the diffuse X-ray emission.

ter subtracting the average background level from the mosaic intensity map and correcting for exposure times, which might moderately vary at distinct locations across the remnant, the obtained net mosaic map is a good measure of the surface brightness of the source (i.e., no artifacts from uneven exposure are present in the mosaic intensity maps).

A three-colored image of S147, color-coded as: R:0.3-0.6 keV, G:0.6-1.0 keV, B:1.0-1.5 keV, is shown in Fig. 2. The image reveals that the majority of the SNR's X-ray emission is soft, and well-confined in the 0.5-1.0 keV band. Such a conclusion is additionally confirmed by the spectral analysis process described in section 3.1, where it becomes evident that only some faint X-ray diffuse emission is present above 1.0 keV leaving the remnant totally undetected above 2.0 keV. The diffuse X-ray emission fills almost the entire remnant except for the small void structure East of the center of the remnant, which is also present in radio continuum and Hα data.

The peculiar morphology of S147 complicates an accurate geometrical center estimation. We first compute the geometrical center of the SNR in X-rays, RA: 5h40m53.0647s Dec: 27°49'49.585", by fitting an annulus to the outermost parts of the S147 X-ray diffuse emission. We additionally validate the above result by applying a Minkowski tensor analysis. This analysis is used to parametrize the shape of astrophysical objects, by drawing perpendicular lines to structures of our selection, based on their detection significance, and subsequently deriving those regions of the highest line density (Collischon et al. 2021). The above process was applied to the mosaic intensity sky map (left panel of Fig. 1). In the absence of a strong symmetrical morphology of the remnant, three distinct regions were identified as the most probable candidates of the remnant's X-ray center. Among those, the most probable one is found to be in agreement with the value derived above: R.A. 5h41m152s and Dec: 27°44'59.532". The X-ray center appears to be moderately shifted to the East in comparison to the latest estimate based on radio synchrotron data: RA: 5h39m00s Dec: 27°50'0" (Green 2009). This discrepancy is likely induced by the "ear type" structure detected to the East of the remnant, which is present with a high significance in X-ray and Hα data but appears much fainter in the radio synchrotron data sets. Thus, we speculate that the latter remnant feature might have been excluded from the geometry computation of previous works.

2.2. ROSAT data

S147 was for the first time reported as a potential X-ray emitter based on ROSAT data, although no clear shell-type morphology but rather mostly a patchy appearance was reported. In addition, the statistical quality of the X-ray data did not allow further exploitation and analysis of the remnant (Sun et al. 1995; Aschenbach 1996). Different to eROSITA, ROSAT all-sky survey maps are divided into 1378 sky tiles (squares of $6^o.4 \times 6^o.4$). Therefore, the extended X-ray emission originating from the remnant is confined within a single ROSAT sky tile [ID:931214]. In order to achieve a direct comparison between eROSITA's and ROSAT's view of the remnant, we exploited the publicly available ROSAT all-sky survey data. Data were extracted from the HEASARC archive (High Energy Astrophysics Science Archive Research Center (Smale 2021a)). Data reduction was performed using FTOOLS (Smale 2021b). The right panel of Fig. 1 illustrates the X-ray photon emission, from the location of the remnant, in the medium ROSAT energy band [0.4-2.4 keV], using data from the ROSAT Position Sensitive Proportional Counter detector in survey mode (PSPC) (Voges et al. 2000). Heavy smoothing has been applied, as specified in the caption of Fig. 1, aiming at enhancing the diffuse X-ray emission originating from the remnant. As shown by the side-by-side comparison of the two panels of Fig. 1, significant diffuse X-ray emission of similar morphology to the one obtained in eRASS:4 is also detected with ROSAT. It is noteworthy, that the ROSAT image presented in this study is substantially improved compared to the latest ROSAT view of the remnant reported in Sun et al. (1995); Aschenbach (1996). Considering the same extraction region (i.e., the extraction region used for the spectral analysis of the entire remnant, as defined in the caption of Fig. 9) and the same energy range (i.e., 0.4-2.4 keV) for both ROSAT and eROSITA, the latter performs in ~ 25 times higher survey collection area at the location of the remnant. In particular, with eROSITA we detect a total of 78.652 counts (among which are 30663 source counts) compared to 3356 (among which are 1241 source counts) from ROSAT.

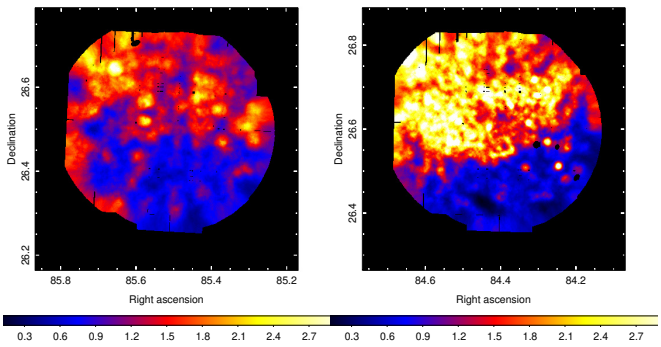

Fig. 3: *XMM-Newton* surface brightness maps in the 0.5-1.0 keV energy band, in units of counts/s/deg^2. All point sources are masked out. The maps, with 5″ pixel size, are adaptively smoothed with a 50 counts kernel and are vignetting-corrected. Left panel: 0693270301 *XMM-Newton* pointing. Right panel: 0693270401 *XMM-Newton* pointing. Both *XMM-Newton* pointings fall at the Southern edge of the remnant and thus its Northern-halves are filled with X-ray emission, whereas its Southern-halves can serve as a background control regions.

2.3. XMM-Newton and Chandra data

Individual smaller parts of S147 have been observed before with *XMM-Newton* (unrelated to the team presenting the work of this paper). In particular, two dedicated *XMM-Newton* pointings towards the remnant have been carried out [ID:0693270301, 0693270401]. Additionally, a third *XMM-Newton* observation [ID:0674180101] towards the HMXB 1A 0535+262 partially contains diffuse X-ray emission from the SNR. However, due to the high contamination of the signal from X-ray emission originating from the binary, we did not further exploit these data. Given the remnant's large size, the two observations mentioned above were performed in discrete parts of the SNR to get a better insight into its nature. The European Photon Imaging Camera (EPIC) consists of three detectors: the `PN` camera (Strüder et al. 2001) and two `MOS` cameras (Turner et al. 2001). Both, yet unpublished, observations (ID: 0693270301: S 147 SE, PN (extended full frame)/MOS1 (full frame)/MOS2 (full frame) exposures: 22.7/26.7/26.7 ks, PI: Jean Ballet - ID: 0693270401: S 147 south, PN (extended full frame)/MOS1 (full frame)/MOS2 (full frame) exposures: 33.6/37.5/37.5 ks, PI: Jean Ballet) exhibit diffuse X-ray emission originating from the SNR. The limited field of view of *XMM-Newton*, of an angular extension of 0.5°, does not allow a thorough analysis of S147's X-ray morphology. Nevertheless, the high sensitivity of the instrument allows us to derive complementary data to eROSITA. In addition, a *Chandra* observation (ID:5770), carried out with the Advanced CCD image spectrometer camera (`ACIS-I`) operating at 0.1-10 keV towards ET Tau, is positioned within the SNR extension. Due to limited statistics, we did not further exploit the available *Chandra* data in the context of this work. Additional *XMM-Newton* [ID:0112200401] and *Chandra* [ID:5538] observations have been directed to explore the X-ray nature of the pulsar J0538+2817 associated to the remnant. The pulsar PSR J0538+2813 and its corresponding Pulsar Wind Nebula (PWN 179.72-1.69), which has an angular size of < 10" (e.g. Romani & Ng (2003); Ng et al. (2007)) and is not resolved in eROSITA data, are effectively excluded by our source masking procedure (using 110" radius). Hence, no influence of their contribution on the spectral properties of the SNR emission presented here is expected. A dedicated analysis of the X-ray emission properties of the region in the vicinity of PSR J0538+2813 will be presented in a separate paper (Bykov et al, in preparation).

eSAS software assembled with the latest calibrations was utilized to perform the X-ray data analysis of the available *XMM-Newton* observations (i.e., data reduction, image production, and spectra extraction). We use the `emchain` and `epchain` eSAS tools to process observation data files. The `mos-spectra` and `pn-spectra` commands were employed to extract images and spectra of the regions of interest. The two panels of Fig. 3 illustrate the two *XMM-Newton* observations towards S 147 for the PN, MOS1, and MOS2 combined data (camera-CCDs found in anomalous state were excluded from the analysis). The two observations reveal a soft, mainly confined in the 0.5-1.0 keV energy band, X-ray diffuse emission component in excellent morphological agreement with the eRASS:4 data. The images are adaptively smoothed, using a smoothing kernel of 50 counts, and vignetting corrected. Point sources have been masked out to enhance the visibility of the diffuse X-ray emission from the remnant. Fig. 9 shows the eRASS:4 5° × 5° intensity sky map (described in detail in section 2.1) overlaid with contours that mark the position (one level contours) of the two *XMM-Newton* observations (white [ID:0693270301] and red [ID:0693270401] contours, respectively).

2.4. A multiwavelength study

2.4.1. X-ray, radio, and optical data correlation

Fig. 4 shows the eRASS:4 mosaic intensity sky map of S 147. Radio synchrotron data obtained from the Canadian Galactic Plane Survey (CGPS) at 1.42 GHz (Taylor et al. 2003) are overlaid on the left panel of Fig. 4 as contours. Optical, Hα data, obtained from the full-sky Hα map (6' FWHM resolution) (Finkbeiner 2003), which is a composite of the Virginia Tech Spectral line Survey (VTSS) in the North and the Southern H-Alpha Sky Survey Atlas (SHASSA) in the South, are overlaid on the right panel of Fig. 4 as contours. The enhanced emission regions and the void-type structure are spatially identical across all three energy bands. The only noticeable difference is detected at the West of the remnant, where both Hα and radio continuum emission seem to extend further to the West in comparison to X-rays. Potential reasons for such a discrepancy are discussed in sec. 2.4.2 and 3.1. For a more detailed study on the nature of this discrepancy refer also to (Paper II). At the same time, the aforementioned image clearly demonstrates that the spatial morphology of the SNR in X-rays is nicely confined within the "ear-type" structure that both Hα/radio continuum data exhibit rather than matched with typical shell-type shapes. It is noteworthy that in a number of different radio synchrotron surveys, operating at different energy bands, i.e., GaLactic and Extragalactic All-sky

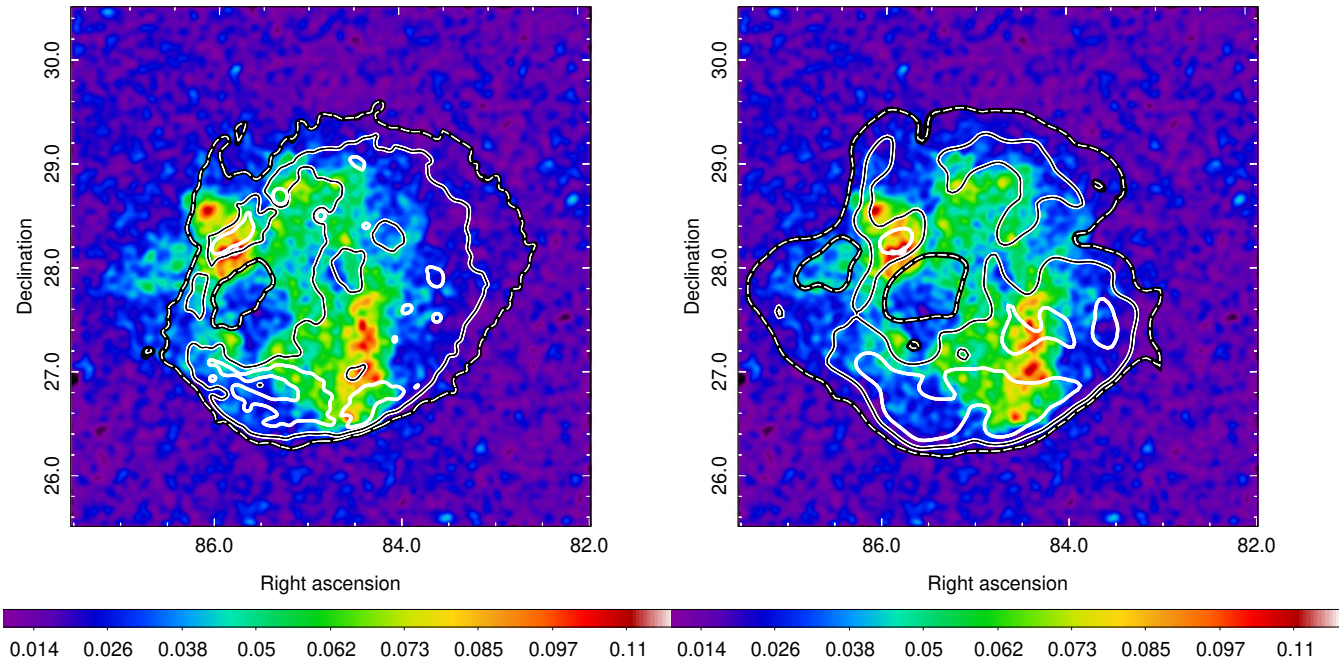

Fig. 4: eRASS:4 exposure-corrected intensity sky map, the same as the one displayed on the left panel of Fig. 1. Left panel: Canadian Galactic Plane Survey (CGPS) data at 1.42 GHz (Taylor et al. 2003) are overlaid as contours. Right panel: Optical Hα data obtained from the full-sky Hα map of 6′ FWHM resolution (Finkbeiner 2003) are overlaid as contours. For both panels, three level contours are used from thin dashed white on thick solid black, to thin solid black on thick solid white, and to solid white to represent fainter to brighter emission regions.

MWA survey (GLEAM)[2] data (Wayth et al. 2015; Hurley-Walker et al. 2017; For et al. 2018; Hurley-Walker et al. 2019) and/or 4850 MHz radio data obtained from PMN (Condon et al. 1993) Southern and tropical surveys, and GB6 (Condon et al. 1991, 1994), the "ear-type" structure at the East of the remnant is hardly discernible, if not absent, likely due to its fainter appearance in comparison to radio continuum emission emanating from the rest of the remnant. However, employing CGPS data an arc structure that nicely encapsulates the diffuse X-ray "ear-type" emission becomes apparent. The latter structure is difficult to be displayed as contours mainly due to the contamination of the radio continuum data from nearby regions. Therefore, it is missing on the left panel of Fig. 4. However, in Figure 3 of (Paper II), we show a composite image of X-ray emission from eROSITA and radio emission from CGPS, where this "ear-type" structure also becomes clearly apparent in the radio data. The SNR's pure thermal nature, as discussed in section 3, could account for such an interconnection between the different energy bands. No universal correlation between Hα and X-rays (i.e., warm and hot gas) in SNR environments exists. Nevertheless, it is not unusual that the remnant's X-ray spatial morphology is tightly correlated with the Hα emission which traces the atomic gas, since the X-ray emission mainly stems from hot thermal plasma. Co-existence of X-rays, Hα, and radio continuum data has been thoroughly investigated before (Cram et al. 1998) and relevant objects have been reported. An example of such a remnant with X-rays, Hα, and radio fine structure is G332.5-5.6 (Stupar et al. 2007).

[2] https://www.mwatelescope.org/science/galactic-science/gleam/

2.4.2. *CO & GeV image correlation*

GeV *Fermi*-LAT data from the location of S147 (Katsuta et al. 2012) and optical and infrared photometry based on the construction of a 3D extinction map (Chen et al. 2017) suggest that S147 has a GeV counterpart, and it might be linked to a dust cloud at a distance of 1 to 1.5 kpc to Earth. According to findings of Chen et al. (2017), the dust cloud, that goes by the name "S147 dust cloud", is most likely associated with the SNR itself, and their interaction may have a significant impact on the generation of gamma-rays.

Compared to the 31 month *Fermi*-LAT data utilized in Katsuta et al. (2012), we employed an additional 12 years of data to verify the association of the extended GeV source 4FGL J0540.3+2756e or FGES J0537.6+2751 with the remnant and provide updated imaging (refining the remnant's morphology in the GeV band) and spectral analysis results. For that, we analyzed Pass 8 LAT data collected from August 4, 2008 to March 28, 2023, using the most recent response function (P8R3), the `fermitools` Ver. 2.0.8 analysis tool, and applying recommended cuts. We analyzed a region of 20° in radius, centered on R.A.: 85.1°, Dec: 27.94° in the 0.1-200 GeV energy range. We used `SOURCE` event data, filtered under the `evclass` = 128 and `evtype` = 3 to employ front and back interactions. Contamination from the Earth's limb is prevented by restricting the zenith angle to a maximum of 90°. We select a spatial binning size of 0.05° per pixel, and we set 30 logarithmic energy bins

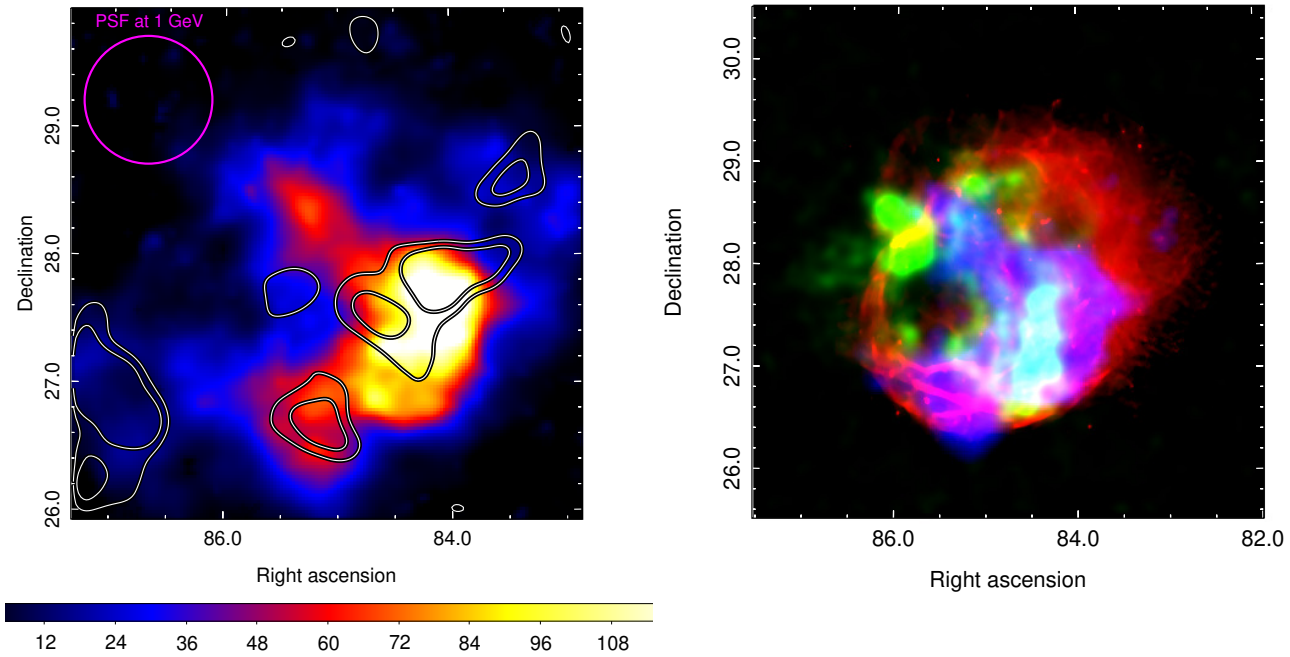

Fig. 5: Left panel: 4° × 4° *Fermi*-LAT TS map >1 GeV. The image, of 90″ pixel size, is convolved with a $\sigma = 1.5'$ Gaussian. The magenta thick circle represents the 68% containment PSF size, derived at the 1 GeV energy threshold used for the construction of the TS map. The black and white contours represent the location of CO clouds (CO Galactic Plane survey data (Dame et al. 2001)) likely interacting with the SNR. Right panel: combined CGPS data at 1.42 GHz, red, 0.5-1.0 keV eRASS:4 data, green, and *Fermi*-LAT data > 1 GeV, blue, from the location of the remnant.

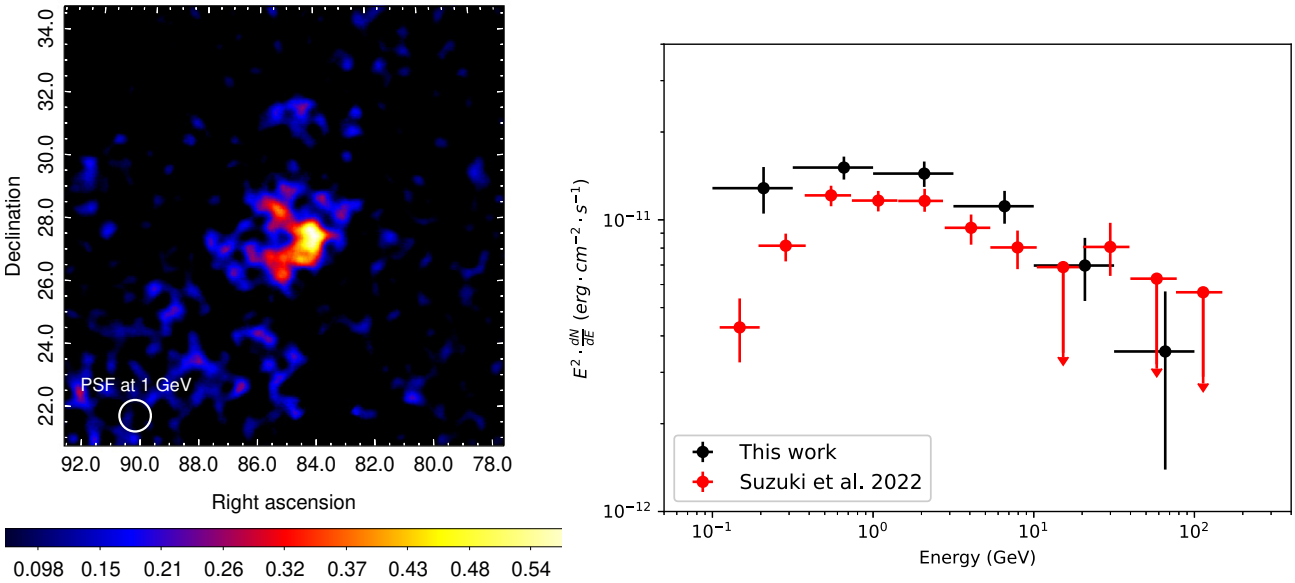

Fig. 6: Left panel: 14° × 14° *Fermi*-LAT residual count map >1 GeV, in units of counts per pixel. The image, with 90″ pixel size, is convolved with a $\sigma = 10.1'$ Gaussian. The white thick circle represents the 68% containment PSF size, derived at the 1 GeV energy threshold used for the construction of the residual count map. Right panel: *Fermi*-LAT GeV SED of S147. Black dots correspond to the *Fermi*-LAT spectrum in the 0.1-100 GeV band, obtained in this work. Red dots correspond to GeV *Fermi*-LAT results reported in Suzuki et al. (2022).

per energy decade for the construction of the exposure map. The likelihood function implemented in Mattox et al. (1996) was exploited to fit the source's spectral data in the most optimal way. Sources were selected from the latest 4FGL catalog alongside with the Galactic diffuse emission component provided in `gll_iem_v07.fits` and the residual background and extragalactic component provided in `iso_P8R3_SOURCE_V3_v1.txt`. Aiming at refining the GeV morphology of S147 we produced both the Test Statistic (TS) map and the residual count map above 1 GeV as shown on the left panels of Fig. 5 and Fig. 6, respectively. Both panels were produced by fitting the event data, letting to vary only the normalization of S 147 and the normalization of all sources within an area of 5° radius from the center of the analysis (center of the source of interest). The extended GeV excess is spatially coincident with the X-ray emission, as illustrated on the right panel of Fig. 5, and with the enhanced optical Hα regions to the Southern part of the remnant as can be concluded by the comparison of the X-ray and Hα data shown in Fig. 4, and is consistent with the remnant's size. A robust GeV detection is confirmed by both a detection significance greater than 10σ and by the absence of significant negative residuals in the corresponding residual count map of Fig. 6.

Exploiting CO Galactic Plane survey data (Dame et al. 2001), we investigated a potential spatial correlation of CO clouds and GeV *Fermi*-LAT data from the location of the remnant. As shown on the left panel of Fig. 5, CO clouds (as plotted with white contours) are spatially coincident with the Southern and Central region of the enhanced gamma-ray emission. However, a similar correlation is missing for the North-Eastern bright GeV blob. Additionally, the three dense clumps, which when combined compose the S147 dust cloud detected in Chen et al. (2017), are in excellent spatial agreement with regions of enhanced CO emission detected in the composite CO survey of the entire Milky Way (MW) (Dame et al. 2001).

It is evident that there is excellent spatial correlation between CO clouds and the Southern+Central rim of S147 that is bright in GeV. Examining whether there is a genuine correlation between the SNR-MC interaction and the origin of the SNR's gamma-ray emission or whether the dust cloud, if positioned in the foreground, is illuminated by CRs originating from the SNR and is therefore emitting in the GeV band, is beyond the scope of this paper. The scenario that gamma-ray emission could originate from thin filaments observed in the optical and radio continuum data, mainly due to the good spatial coincidence of the gamma-ray emission and the thin filament as well as the GeV and Hα flux correlation (Katsuta et al. 2012) cannot be ruled out.

2.4.3. *IR data & dust prevalence*

Having confirmed the detection of the remnant's GeV counterpart and provided the first detailed imaging analysis (with substantially updated results compared to Katsuta et al. (2012)), we furthermore focus on the explanation of the nature of apparent interesting structures that the remnant exhibits. Such prominent features are the two strongest, in terms of surface brightness, diffuse X-ray blobs at the North-East (region B) and South-West (region H) of the remnant, as well as the smaller bright blob at the South-East (region C) of the remnant, and the ear-type structure (region A) and the void structure (region D) as introduced in sec. 3.1. The latter structures, besides in X-rays, are also visible in radio synchrotron and Hα data, as shown in Fig. 4. Fig. 7 demonstrates the presence of enhanced Infrared (IR) emission regions, detected in the infrared band utilizing Infrared Astronomical Satellite (IRAS) data. Examining the two panels of Fig. 7 one easily concludes that the two large X-ray blobs as well as the smaller bright X-ray blob at the South-East of the remnant are spatially coincident with regions where the IR data exhibits the lowest intensity. The same applies to the most Eastern part of the "ear-type" structure, which is also the brightest part of the latter structure in X-rays. At and around the void structure an enhancement of the IR emission in comparison to the aforementioned regions is observed. Overall, in light of the new X-ray data from eROSITA, even though the image analysis indicates strong anti-correlation features (e.g., at the location of the Northern bright X-ray blob) between the X-ray emission and the IRAS data, such an anti-correlation is not seen in the North-West part of the remnant. An X-ray and IR emission anticorrelation was also previously suggested in Chen et al. (2017) by using ROSAT data. The derived absorption spectral parameters obtained from the fit (see section 3.1 for further analysis details) do not strongly support a clear absorption pattern (except for the void-type structure) either, as shown by the reported values of Tab. 2. IR emission is strongest in the South-East and North-West of the remnant. The latter assertion is also confirmed by the hydrogen column density maps of Fig. 8, and could potentially explain the lack of X-ray emission to the Western part of the remnant, assuming that X-ray photons were absorbed due to the prevalence of dust. The strongest absorption column density value, obtained from the spectral analysis of the ten individual sub-regions (see sec. 3.1 for further details) is matching with the location of the void structure of the remnant. Such a finding is also supported by the enhanced IR emission at that particular location of the sky. On the contrary, it is also worth noting that a strong anti-correlation between X-ray and IR data (potential nature is dust destruction by X-rays - refer to McKee et al. (1987); Slavin et al. (2015); Priestley et al. (2021) and references therein, for the efficiency of dust destruction by SNR shockwaves) becomes clearly apparent at the location of the Northern bright X-ray blob of the remnant. This assertion is once again supported by spectral analysis results (that exact region exhibits the lowest absorption column density value across the entire remnant-section 3.1). At that part of the remnant, the IR emission seems to respect the X-ray emission creating a "hole" in the IR data of the same size and shape as the Northern X-ray bright blob of the remnant. Overall, the comparison of IR and X-ray data from the remnant's location provides evidence for the presence of different physical processes underlined by apparent features (i.e., dust destruction by X-rays and X-ray absorption by dust). Those indications are found to be broadly consistent with the conclusions derived by the spectral analysis of individual parts (sub-regions) of the remnant.

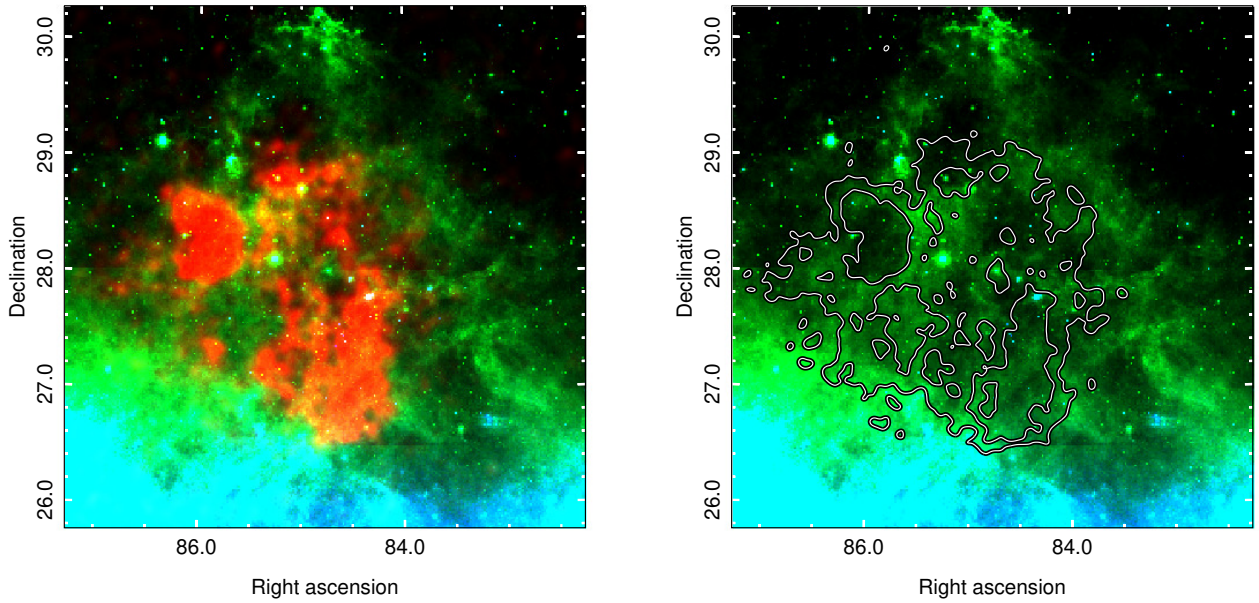

Fig. 7: Left panel: RGB image, energy to colour-coded as follows: eRASS:4 X-ray data in the 0.5-1.0 keV energy band (red), IRAS 25 μm data (green), and IRAS 100 μm data (blue) from the location of S147. Right panel: combined IRAS 25 μm data (green) and IRAS 100 μm data (blue) from the same location as in the left panel. The black and white contours represent two levels of eRASS:4 X-ray data in the 0.5-1.0 keV energy band which we overlaid to the IRAS data, aiming at examining potential anti-correlation features between IR and X-ray emission.

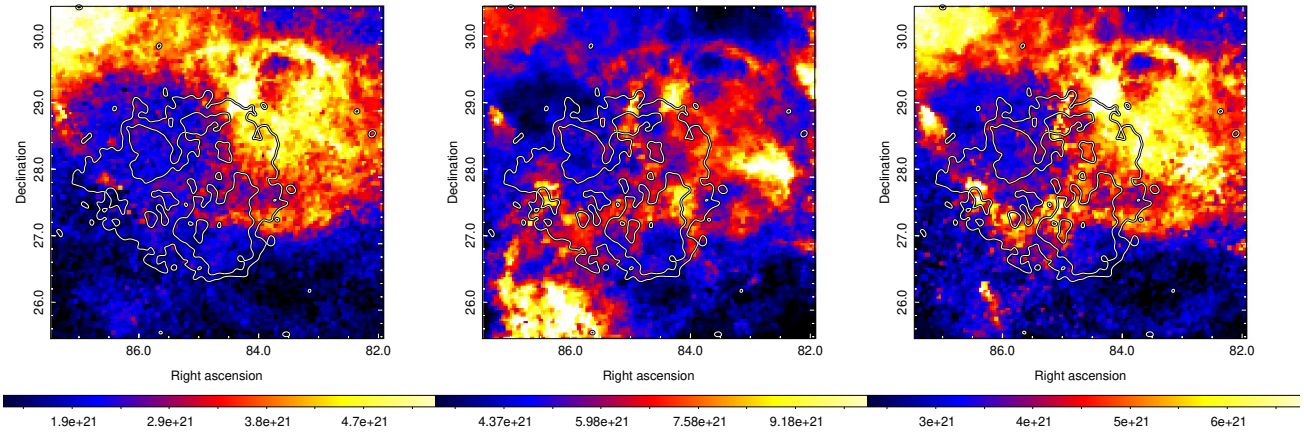

Fig. 8: Hydrogen column density maps ($N_{\rm H}$, in units of cm^{-2}) derived by utilizing the DUSTMAPS python package (Green 2018), employing `bayestar19` data cubes (Green et al. 2019), and converting the obtained extinction to $N_{\rm H}$ according to Eq. 1 (Foight et al. 2016). Left panel: $N_{\rm H}$ map until 0.6 kpc distance. Middle panel: $N_{\rm H}$ map until 1.9 kpc distance. Right panel: $N_{\rm H}$ map until 1.33 kpc distance (preferred distance of the SNR given the distance measurements of the associated pulsar and the runaway star - binary companion to the pulsar's progenitor).

3. *Spectral analysis*

3.1. eROSITA spectra

eRASS:4 event data were selected from ten distinct spectral extraction regions (optimized based on the surface brightness variations detected across the remnant) of polygon shape, as depicted in Fig. 9 in black. The selected regions were defined in `SAOIMAGE DS9` (Joye & Mandel 2003), aiming at inspecting the spectral morphology of the remnant in detail and gaining more insight into interesting individual regions. Among such regions are the ear-type structure, the void region as well as the two brightest X-ray blobs at the South-West and North-East of the remnant. The entire remnant's spectrum was also extracted from the area ob-

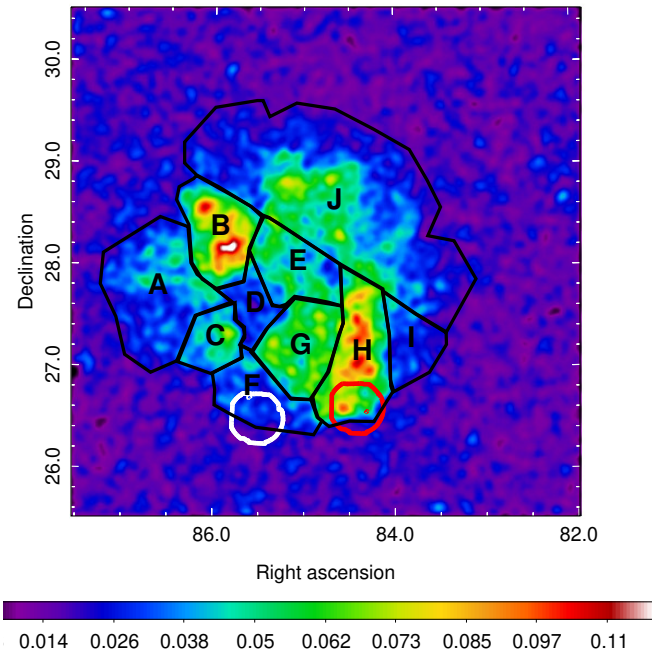

Fig. 9: The same image as in Fig. 1 (with identical features in terms of smoothing and point source removal) depicting the intensity variation across the remnant. The ten distinct sub-regions selected for further spectral analysis are highlighted as black regions. The entire remnant's spectrum was obtained from the large polygonal shape region formed when combining all ten individual sub-regions. White and red contours mark the positions of 0693270301 and 0693270401 *XMM-Newton* pointings (shown in Fig. 3), respectively.

tained when combining all ten aforementioned sub-regions and fitted accordingly as described below. A nearby background control region of circular shape was chosen to the South-East of the remnant which is free of emission from the SNR itself (center: R.A.: 89.08°, Dec: 26.31° radius: 1.58°). Events from TM5 and TM7 were excluded due to their light leak suffering (Predehl et al. 2021). X-ray emitting point sources, detected with a 3σ excess significance or higher, were excluded using an exclusion circular region of $110''$ radius. Individual bright sources, i.e., the HMXB 1A 0535+262 and the associated pulsar (accompanied by its faint PWN), were once again treated independently to avoid likely spectral contamination. The fitting process was conducted in `Xspec Ver. 12.12.1` (Dorman et al. 2003). A minimum of 30 counts per bin has been set for displaying the spectrum before fitting. C-statistics (Cash 1979) was applied for the fitting procedure due to the limited photon statistics. Simultaneous fitting of the source and background emission from the on-source regions was performed by adopting identical spectral models and an identical fitting approach for the background (astrophysical and instrumental) emission, as described in Michailidis et al. (2024) – sec. 4.1.

Even though the majority of the emission from the remnant is confined in the 0.5-1.0 keV energy band, we perform spectral analysis in the broader range of 0.3-2.3 keV since some faint X-ray emission does exist below 0.5 keV and above 1.0 keV. We restrict the spectral analysis to < 2.3 keV since at harder energies the background component becomes dominant. From the spectral analysis of the entire remnant but also the inspection of individual sub-regions we conclude the following. The X-ray emission is found to be solely thermal, with no evidence of a non-thermal component. However, from the fit quality it is not clear whether the hot plasma is in collisional ionization equilibrium (CIE) or not. It is noteworthy that the obtained absorption column density, derived by optical extinction measurements at the distance of the remnant (as shown in Fig. 8), is in good agreement with the corresponding best-fit parameter of non-equilibrium ionization collisional plasma models (NEI). The latter assertion is supported by the lower absorption column density values favored by NEI models compared to CIE model values. Additionally, CIE models require questionably high elemental abundance values (in particular Mg) to explain spectral characteristics at higher energies (i.e., they underpredict the Mg XI line). Among the fitted models, a collisionally ionized diffuse gas `VAPEC`, as CIE model in Xspec notation, and a non-equilibrium collisionally ionized diffuse gas model, either a `VNEI` model or a `VPSHOCK` model (Borkowski et al. 2001) in Xspec notation, provides the best fits to the data. To take into account the interstellar absorption (ISM) at the location of the remnant all three additive models are modified according to the multiplicative `TBABS` absorption model (Wilms et al. 2000) (i.e., we used the following models: `TBABS(VAPEC/VNEI/VPSHOCK)`). All spectral extraction regions exhibit K-shell Oxygen (OVII, OVIII), Neon (NeIX, NeX), and Magnesium (Mg XI, not present in all sub-regions and with statistical significance much lower compared to O, Ne lines) lines. Therefore, in the thermal plasma models described above, elemental abundances were fixed to solar values except for O, Ne, and Mg which were let to vary. It is noteworthy that both models provide poor fits when the aforementioned elemental abundances are fixed to solar values. The rest of the source model parameters were left free when fitting the model to the data.

In Fig 10 we report the results of the simultaneous fit of the on-source and background emission from the two richest bright X-ray blobs in terms of photon statistics as well as from the entire remnant, with an absorbed `VNEI` as the optimal model describing the purely thermal S147 spectrum. We do not see significant X-ray spectral shape changes over the remnant's area. The results of the simultaneous fit of the on-source and background emission (using the same source model) from the remaining 8 selected sub-regions are shown in Fig. A.1 in sec. A in the appendices. The best fit spectral parameters of the `tbabs(vnei)` model, with their 1σ errors, are reported in Tab. 2 for all ten selected sub-regions and the entire remnant. The corresponding areas and surface brightness estimates, for all regions selected for spectral analysis, are summarized in Tab. 3. Significant temperature variations were detected across the remnant (mainly due to the need to better explain the high energy features of the spectrum > 1 keV of some sub-regions selected for spectral analysis as shown in Tab. 2, that "hot NEI solutions" provide). The absorption column density values obtained across the remnant's area neither differ significantly nor exhibit regular patterns. However, particular deviations such as an enhanced absorption column density value at the location of the void structure and a particu-

lar low absorption column density value (the lowest value detected across the whole remnant) at the location of the bright X-ray blob at the North-East of the remnant are clearly apparent, as shown in Tab. 2. Average temperatures of ~ 0.22 keV and of $N_{\rm H} = 0.3\ 10^{22}{\rm cm}^{-2}$ (`VNEI`), and of ~ 0.11 keV and of $N_{\rm H} = 0.51\ 10^{22}{\rm cm}^{-2}$ (`VAPEC`) are obtained, when exploiting data from the entire remnant area, for the two distinct models, respectively. For the best-fit (`VNEI`) model of the entire remnant reported above, a total flux of $F_{\rm total} = 6.93^{+1.98}_{-1.31}{\cdot}10^{-10}$ erg/cm^2/s is obtained in the 0.3-2.3 keV energy range. However, individual sub-regions may exhibit much higher plasma temperature values, as reported in Tab. 2. It is worth noting that the obtained elemental abundance values of O, Ne, and Mg (for both tested models) are inextricably linked to the corresponding normalization value, i.e., the X-ray plasma is characterized by lack of a strong continuum component and solely exhibits X-ray emission lines. In principle, one could restrict their variation range and extract useful conclusions. We describe such an approach in detail in (Paper II). In this work, we choose to let them free and inspect potential variations across the remnant.

Overall, the void structure region (region D), the bright blob at the North-East of the remnant (region B), and the Western region (namely region I) which exhibits only weak X-ray diffuse emission appear to be the coolest. On the other hand, regions C, F, and the bright in X-rays region H appear to be the hottest across the remnant. The nature of the absence of X-ray emission in region D, a feature of the remnant denoted as void structure in this work and detected in radio and optical (Hα) bands as well, could be (at least partially) attributed to X-ray absorption by dust clouds found at the location of the remnant. The latter conclusion is supported by the significant enhancement of the absorption column density found from the spectral fit of that particular region. However, its nature is not entirely clear. No distinct pattern of absorption column density variation was found over the remnant, either. The highest $N_{\rm H}$ value, derived from the best fit among all seven regions, was obtained at the location of the void structure, denoted as region D, which is well correlated with a significant enhancement of the IR emission at that location, as seen in Fig. 7. The lowest $N_{\rm H}$ value was derived at the North-West of the remnant, at the precise location of the enhanced X-ray blob (namely region B). The latter region is characterized by the absence of IR emission (potential dust destruction by X-rays) as shown in Fig. 7.

The above result is also supported by Fig. 8 which depicts absorption column density sky maps towards the location of S147. The above maps were constructed by employing the `DUSTMAPS`[3] python package (Green 2018). In more detail, we analysed `bayestar19` data (Green et al. 2019) in the direction of the remnant making use of the most recently established statistical relation between the mean colour excess/extinction and the absorption column density (Foight et al. 2016), as shown in Eq. 2. We examined the data in the range of the most probable distance measurements of the remnant, 0.6-1.9 kpc, as derived by multiple works in the past (see sec. 1 for more details). Comparing the obtained maps with the derived best-fit absorption column density values of Tab. 2 one concludes that the remnant is placed at a distance greater than 0.6 kpc but moderately smaller than 1.33 kpc (the latter being the distance of both the pulsar associated to the remnant and the runaway star HD 37424 - considered to be the binary companion of its progenitor).

It is noteworthy that in a number of the ten selected sub-regions as well as in the spectrum obtained from the entire remnant, O, Ne, and Mg elemental abundances display sufficiently (for ejecta identification) high values (> 2 solar), as shown in Tab. 2. Regions A and E also appear to be enriched in Si (Silicon), indicating X-ray plasma of ejecta origin despite the evolved state of the remnant (making it perhaps the most evolved SNR that exhibits both, swept-up ISM and ejecta components). However, robust conclusions about the presence of Si cannot be obtained due to the limited statistics of the data. The enhanced elemental abundance values obtained by both the analysis of the X-ray spectrum from the entire remnant and the X-ray spectrum from individual sub-regions suggest that thermal plasma has not yet reached equilibrium, i.e., a NEI model is favored as the optimal way to describe the remnant's spectral characteristics. In fact, in spite of the common belief that ejecta origin abundances in evolved SNRs are unexpected, recent X-ray observations have revealed an increasing number of SNRs with metal-rich ejecta (Yamauchi et al. 1999; Park et al. 2003; Troja et al. 2008; Hwang et al. 2008), regardless of their older age. The latter may partly be attributed to the presence of molecular material in the remnant's surroundings. However, S 147 does not exhibit strong [OIII] lines in its optical spectrum and thus it cannot be classified as O-rich SNR (Dopita et al. 1981; Goss et al. 1979; Lasker 1979; Mathewson et al. 1980), such as the recently discovered X-ray counterpart of G279.0+1.1 SNR that exhibits similar features in its X-ray spectrum (Michailidis et al. 2024).

3.2. XMM-Newton spectra

For both available *XMM-Newton* pointings in the direction of S 147, a spectral analysis using `eSAS` software was carried out. Here, we only show results from ObsId 0693270401 since the statistical quality of its data is significantly higher in comparison to ObsId 0693270301. Fig. 11 delineates the 0693270401 *XMM-Newton* pointing in the soft 0.5-1.0 keV energy band, with the same parameters as the image at the right panel of Fig. 3. The on-source and background regions, of polygon shape, selected for spectral extraction are defined in `SAOIMAGE DS9` and marked with blue and white colours, respectively. `pn_spectra`, `mos_spectra` and `pn_back`, `mos_back` (for an estimate of the quiescent particle background) eSAS tasks were employed for the image construction and spectral extraction. The independently modeled on-source and background emission spectra of MOS1/MOS2/PN are shown on the right panel of Fig. 11. From the spectral analysis, we conclude that both a NEI model, either `VNEI` or `VPSHOCK` model in Xspec notation, and a CIE model, `VAPEC` in Xspec notation, can be used to describe the physical conditions of the S147 plasma. However, on the right panel of Fig 11 we are reporting the best fit `tbabs(vnei)` model, since it provides fitting results that are well aligned with optical extinction measurements at the remnant's distance (i.e., compatible absorption column density values – the same argument applies for the choice of the eRASS models). Similarly to the eROSITA spectral fitting process, the actual

[3] https://dustmaps.readthedocs.io/en/latest/

Table 2: Best-fit spectral parameters of the regions that have been selected to best represent the spectral variation detected across the remnant.

Region	A† region	B region	C* region
Model		vnei	
kT(keV)	$0.41^{+0.09}_{-0.05}$	$0.23^{+0.06}_{-0.04}$	$0.50^{+0.21}_{-0.11}$
$N_H(10^{22}cm^{-2})$	$0.23^{+0.03}_{-0.04}$	$0.18^{+0.04}_{-0.04}$	$0.32^{+0.04}_{-0.04}$
O	$1.30^{+0.40}_{-0.28}$	$1.96^{+0.32}_{-0.25}$	$0.47^{+0.21}_{-0.13}$
Ne	$1.63^{+0.67}_{-0.37}$	$3.48^{+0.96}_{-0.77}$	$1.70^{+0.66}_{-0.54}$
Mg	$5.95^{+3.05}_{-2.07}$	$9.98^{+4.01}_{-2.08}$	-
Ionization time $(10^{10}s \cdot cm^{-3})$	$0.66^{+0.23}_{-0.24}$	$4.59^{+5.74}_{-2.61}$	$0.09^{+0.03}_{-0.02}$
χ^2/dof	1.04	1.09	1.11
Region	D region	E† region	F region
Model		vnei	
kT(keV)	$0.19^{+0.18}_{-0.05}$	$0.42^{+0.14}_{-0.06}$	$2.17^{+1.57}_{-0.83}$
$N_H(10^{22}cm^{-2})$	$0.49^{+0.11}_{-0.12}$	$0.28^{+0.05}_{-0.06}$	$0.33^{+0.03}_{-0.04}$
O	-	$2.41^{+0.62}_{-0.68}$	$0.80^{+0.29}_{-0.23}$
Ne	-	$2.58^{+1.66}_{-0.81}$	$1.19^{+0.43}_{-0.42}$
Mg	-	$7.07^{+4.96}_{-2.72}$	-
Ionization time $(10^{10}s \cdot cm^{-3})$	$2.09^{+6.69}_{-1.21}$	$0.64^{+0.29}_{-0.19}$	$0.065^{+0.03}_{-0.02}$
χ^2/dof	1.34	0.99	1.19
Region	G region	H* region	I region
Model		vnei	
kT(keV)	$0.25^{+0.12}_{-0.04}$	$0.47^{+0.04}_{-0.08}$	$0.21^{+0.06}_{-0.02}$
$N_H(10^{22}cm^{-2})$	$0.29^{+0.05}_{-0.08}$	$0.33^{+0.02}_{-0.01}$	$0.24^{+0.10}_{-0.09}$
O	$2.08^{+0.43}_{-0.35}$	$0.33^{+0.05}_{-0.04}$	$0.57^{+0.12}_{-0.14}$
Ne	$2.62^{+0.88}_{-0.65}$	$0.95^{+0.18}_{-0.16}$	$0.98^{+0.35}_{-0.34}$
Mg	$9.31^{+3.31}_{-2.45}$	-	$11.1^{+0.62}_{-0.43}$
Ionization time $(10^{10}s \cdot cm^{-3})$	$2.32^{+3.06}_{-0.87}$	$0.11^{+0.01}_{-0.01}$	$11.94^{+11.69}_{-7.97}$
χ^2/dof	1.2	1.54	1.22
Region	J* region	Entire remnant	*XMM-Newton*
Model		vnei	
kT(keV)	$0.75^{+0.11}_{-0.17}$	$0.22^{+0.02}_{-0.03}$	Identical to region H
$N_H(10^{22}cm^{-2})$	$0.30^{+0.03}_{-0.01}$	$0.30^{+0.04}_{-0.03}$	
O	$0.46^{+0.06}_{-0.06}$	$2.34^{+0.20}_{-0.18}$	
Ne	$1.00^{+0.18}_{-0.16}$	$3.13^{+0.40}_{-0.34}$	
Mg	-	$9.53^{+1.47}_{-1.31}$	
Ionization time $(10^{10}s \cdot cm^{-3})$	$0.09^{+0.01}_{-0.01}$	$4.27^{+1.87}_{-0.99}$	
χ^2/dof	1.31	1.63	

Notes. The best-fit spectral parameters are provided with 1σ statistical errors. Where not defined, elemental abundances are set to solar values. For regions marked with a *, very small N elemental abundance values (essentially equal to zero) were found. For regions marked with a †, Si appears to be present and the corresponding elemental abundance is highly degenerate, thus we allowed it to vary aiming at improving the fit quality.

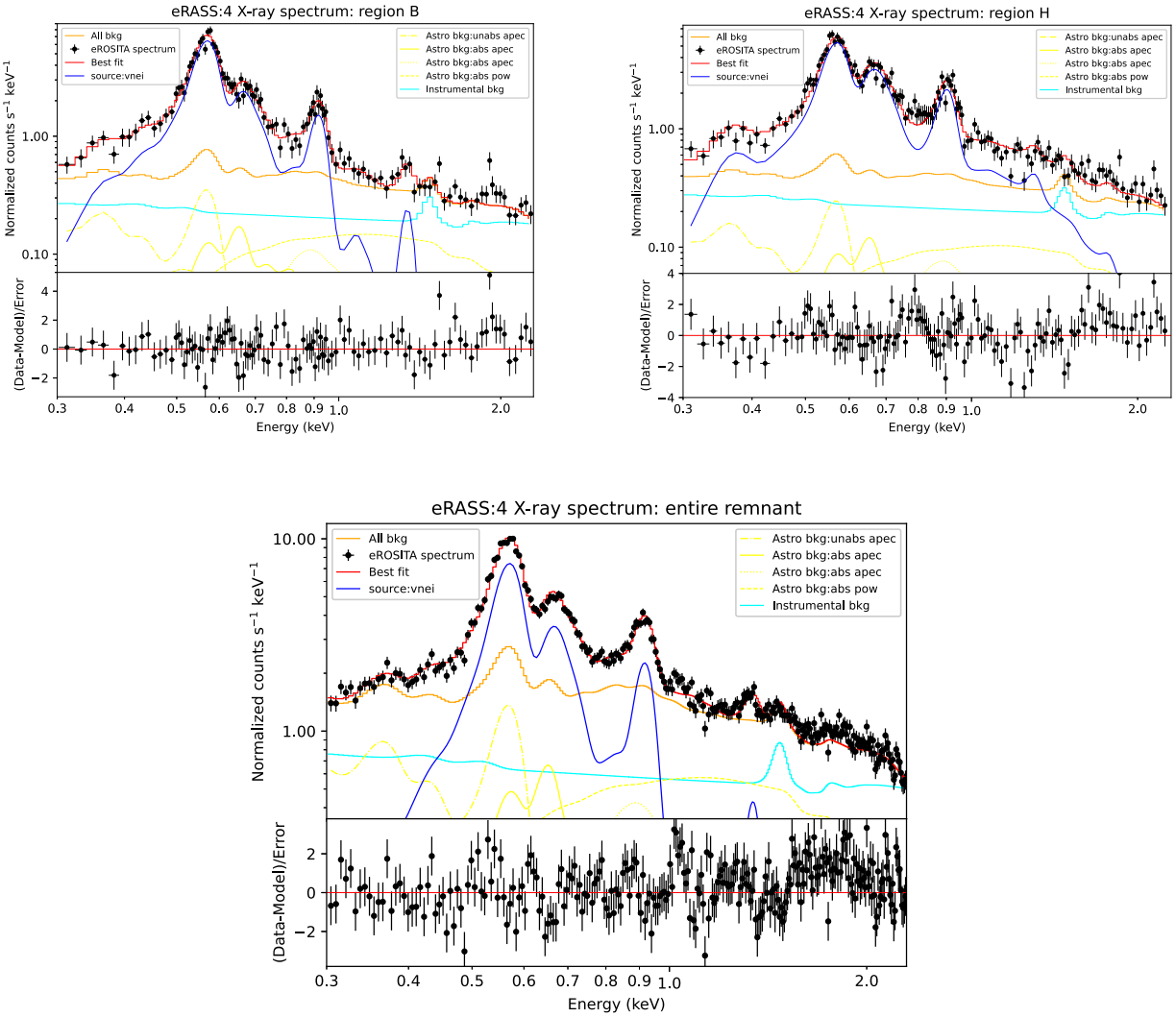

Fig. 10: eRASS:4 X-ray spectra in the 0.3-2.3 keV energy band, from the two significantly enhanced regions of X-ray emission (X-rays blobs: region A and region H) and the entire remnant.

Table 3: Parameters of spectrally analyzed regions

Region	A region	B region	C region	D region	E region	F region
Area (10^6 arcs^2)	14.4	7.17	3.83	2.95	5.62	6.25
Surf_bri (10^{-3} c/arcs^2)	0.68	1.14	0.84	0.64	0.85	0.72
Region	G region	H region	I region	J region	Entire remnant	*XMM-Newton*
Area (10^6 arcs^2)	7.42	7.80	4.40	38.9	105.47	1.2
Surf_bri (10^{-3} c/arcs^2)	0.99	1.12	0.67	0.73	0.81	83.0

Notes. The total area and surface brightness of all regions used for spectral analysis in the 0.3-2.3 keV energy range.

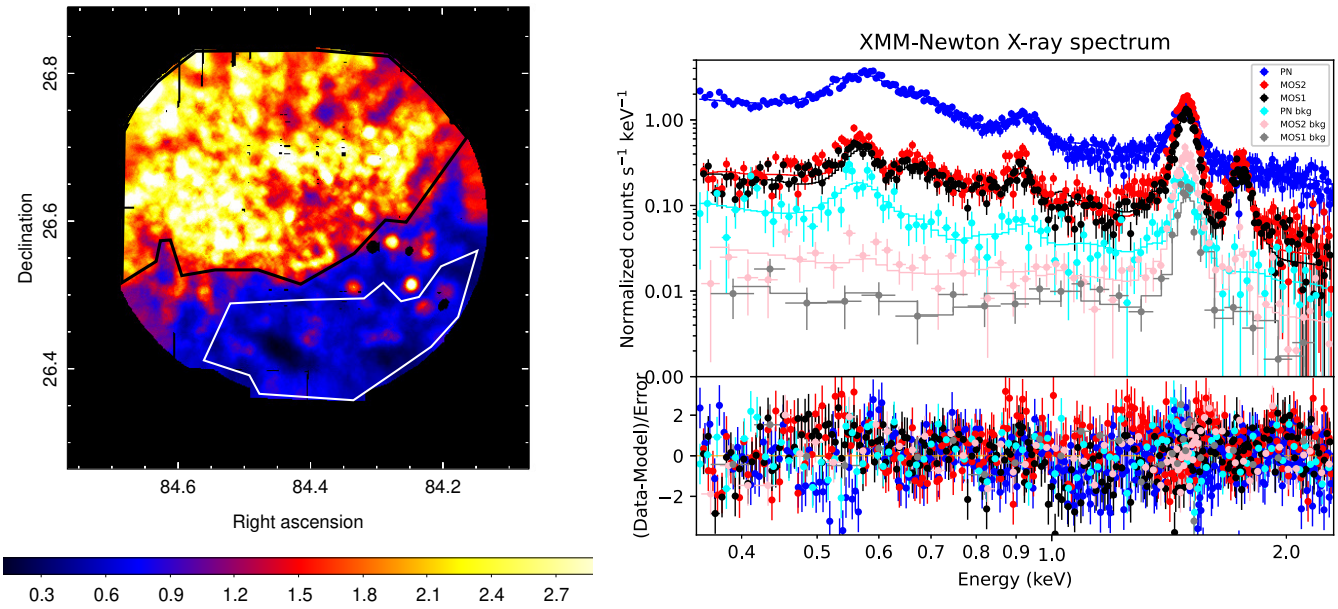

Fig. 11: X-ray spectrum from a portion of the remnant which spatially coincides with the FoV of 0693270401 *XMM-Newton* observation. Left panel: 0693270401 *XMM-Newton* observation, identical to the one of Fig. 3. The black polygonal region illustrates the on-source region whereas the white polygonal region is the representative background region selected to be free of the remnant emission. Right panel: pn, mos1, and mos2 *XMM-Newton* spectrum in the 0.35-2.3 keV energy band.

modeling involved the simultaneous fitting of the on-source and background emission, here in the 0.35-2.3 keV energy band. The *XMM-Newton* spectral analysis is restricted above 0.35 keV since some anomalous fluctuations were observed in the 0.3-0.35 keV energy band. The Xspec package, using C-statistics (Cash 1979), was used for the spectral analysis. Three distinct model components were employed aiming at describing the X-ray emission spectral features from the portions of the remnant as seen with *XMM-Newton*; *i*) source emission: `tbabs`× `vnei`, *ii*) X-ray background: `const`×`const`×`(apec+tbabs`×`(apec+apec+pow))`, and *iii*) soft proton events/instrumental background: `unabsorbed power law+gauss+gauss`. Tab. 2 provides a comprehensive description of the diffuse X-ray emission's spectral parameters of that region. The spectral features that this region exhibits can be well described by adapting the same best-fit model applied to region H (when utilizing eRASS:4 data), which encompasses the emission within the *XMM-Newton* observation 0693270401.

3.3. Distance to the SNR

A distance consistency check based on the absorption column density observed in X-rays (value obtained from spectral fitting and reported in Tab. 2), the distribution of the mean color excess E_{B-V} reported by Lucke (1978), and the extinction estimate obtained from the combination of GAIA and 2MASS photometric data (Lallement et al. 2019, 2022) is applied for the first time in light of the eROSITA X-ray data. In particular, in this work we employ the most recent optical extinction data sets (GAIA-2MASS 3D Galactic Interstellar extinction dust maps (Lallement et al. 2022)) aiming at calculating the expected absorption column density value in the direction of S147. The following statistics relations have been established between the mean color excess/extinction and the X-ray absorption column density (Predehl & Schmitt 1995):

$$\begin{aligned} N_{\rm H}/E_{\rm B-V} &= 5.3\times10^{21}\ {\rm cm}^{-2}\cdot{\rm mag}^{-1} \\ N_{\rm H}[{\rm cm}^{-2}/A_\nu] &= 1.79\times10^{21} \end{aligned} \quad (1)$$

and Foight et al. (2016):

$$\begin{aligned} N_{\rm H}/E_{\rm B-V} &= 8.9\times10^{21}\ {\rm cm}^{-2}\cdot{\rm mag}^{-1} \\ N_{\rm H}[{\rm cm}^{-2}/A_\nu] &= 2.87\pm0.12\times10^{21} \end{aligned} \quad (2)$$

The estimation of the distance was performed with regard to the absorption column densities obtained from the spectral analysis of the entire remnant, ranging between 2.7 and 3.4×10^{21} cm^{-2}. A distance of $0.99^{+0.34}_{-0.26}$ kpc was derived by making use of eq. 2 and employing the Lallement et al. (2022) data sets, as shown in Fig. 12. A larger distance of $1.45^{+0.30}_{-0.17}$ kpc is obtained when employing the older data sets (Lallement et al. 2019). Overall, the derived distance values of the remnant are in good agreement with previous reports and place the remnant at compatible distances with the associated pulsar and progenitor run-away star. We note that one obtains even larger distance values when using eq. 1. However, we argue that since Predehl & Schmitt (1995) employed ROSAT data whereas Foight et al. (2016) utilized higher sensitivity *Chandra* data, a more accurate measurement might be obtained in the latter case (eq. 2).

The interior of the SNR is dominated by thermal hot shocked plasma which radiates through two-body processes

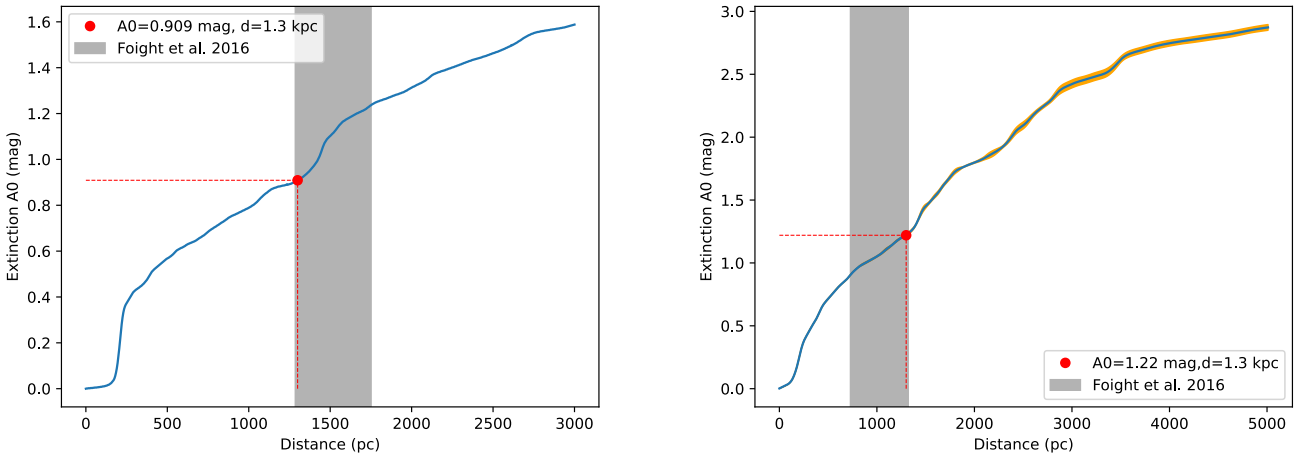

Fig. 12: Left panel: One-dimensional cumulative extinction graph as a function of the distance up to ∼ 3kpc (Lallement et al. (2019) data sets) towards S147, obtained by using the GAIA/2MASS tool for one-dimensional extinction computation https://astro.acri-st.fr/gaia_dev/. Right panel: One-dimensional cumulative extinction graph as a function of the distance up to ∼ 5kpc (updated Lallement et al. (2022) data sets) towards S147, obtained by using the EXPLORE G-Tomo tool for one-dimensional extinction computation https://explore-platform.eu/. In both panels, the black area corresponds to the distance uncertainty estimation when employing Eq. 2 and the obtained best-fit value of the absorption column density derived from the spectral analysis. The red point represents the obtained extinction when assuming that the remnant is located at a distance of 1.3 kpc.

and therefore a proportionality with the electron and ion densities can be obtained (Raymond et al. 1976): $n_e = 1.2 n_H$ (fully ionized plasma). The Emission Measure (EM) can be expressed by the product of the electron and hydrogen number density integrated over the volume:

$$\boldsymbol{EM} = \int n_e \cdot n_H dV \tag{3}$$

Knowing the distance (D) at which the X-ray emitter is positioned and the normalization (norm) parameter obtained from the X-ray fitting process, one can derive the EM (assuming all units in cgs) by:

$$\boldsymbol{norm} = \frac{10^{-14}}{4\pi D^2} EM \tag{4}$$

Once again, we consider as an accurate distance measurement of the remnant the aforementioned distances of the associated pulsar and runaway star. Adopting a remnant distance of 1.33 kpc and a 3° angular size of the object in the X-ray band we compute its real diameter to 70 pc (or 35 pc in radius). Assuming further a spherical distribution of the X-ray emission, a volume of $5.28 \cdot 10^{60}$ cm^{-3} is derived. Using the obtained normalization from the X-ray spectral fit of the entire remnant ($norm = 0.10^{+0.06}_{-0.03}$) and the above-derived value of the volume (assuming the latter to be spherical, the plasma uniformly distributed and a filling factor η=1, i.e., the X-ray emission fills the entire remnant), and combining equations 3 and 4 one obtains a hot plasma density of $n_H = 0.018^{+0.005}_{-0.003}$ cm^{-3} (or $n_e = 0.022^{+0.006}_{-0.004}$ cm^{-3}) using:

$$n_H = \sqrt{\frac{norm \times 4\pi \cdot D^2}{1.2 \cdot \eta \cdot 10^{-14} \cdot V}} \tag{5}$$

3.4. An old-age evolutionary scenario

To set the stage for further, more detailed modeling, we used the Leahy & Williams (2017) SNR evolutionary calculator, assuming that the SNR expands in a homogeneous ISM. In particular, we used as input the derived values for the local Interstellar medium (ISM) n_H (for the obtained absorption column density of the entire remnant: $0.3^{+0.04}_{-0.03}$ 10^{22}cm^{-2} (under the assumption that it is representative along the entire line of sight) and a distance of 1.33 ± 0.1 kpc a local $n_H = 0.73^{+0.16}_{-0.12}$ cm^{-3} is obtained). In addition, we considered an explosion energy of $1 - 3 \times 10^{51}$ erg (Katsuta et al. 2012). Finally, by maintaining the standard values for the remaining parameters of the model, the age of S147 is estimated to $t_{age} = 1.7^{+0.30}_{-0.35} \times 10^5$ years and $t_{age} = 0.76^{+0.13}_{-0.10} \times 10^5$ years for $E_0 = 1 \times 10^{51}$ erg and $E_0 = 3 \times 10^{51}$ erg, respectively. For cross-check purposes, one can compute the age of the remnant utilizing the relation employed in Giacani et al. (2009): $t \sim \frac{\tau}{n_e}$, where τ is the ionization timescale of the emission plasma. Making use of the derived n_e value and the ionization timescale of the hot plasma for the entire remnant, as obtained from the spectral analysis procedure (and reported in Tab. 2), one derives a remnant age of $61.5^{+46.5}_{-24.4}$ kyrs. The latter estimate is consistent with the result obtained from the previous methodology, i.e., the derived age of S147 is of the order of 10^5 years.

Concluding, the above results are not broadly consistent, even within uncertainties, with the pulsar's kinematic age of $3 \pm 0.4 \cdot 10^4$ yrs (Kramer et al. 2003). The above discrepancy can be partially or totally attributed to the lack of knowledge of the actual local density distribution which for the purposes of this work was considered to be homogeneous. The multi-shell appearance of the remnant

in Hα supports a heavily disturbed local medium. In addition, such a scenario of an old SNR contradicts the X-ray properties of the remnant (i.e., an ionization timescale $< 10^{11}$ s $\cdot$ cm^{-3} that supports a young age X-ray plasma in non-equilibrium ionization) and the detection of the GeV emission originating from the SNR. Thus, in (Paper II) we adopt a significantly lower density medium under the assumption that the remnant's progenitor's stellar winds have highly disturbed the local ISM (i.e., a supernova-in-cavity scenario resulting in a young SNR age) trying to address some of the remnant's observational characteristics that appear to contradict the scenario of an old SNR.

4. GeV spectra & multiwavelength SED

We conclude the binned likelihood analysis applied to the extended GeV source 4FGL J0540.3+2756e, which is likely associated with S 147, by evaluating its SED in the 0.1-100 GeV energy band. For the purposes of the spectral analysis we divided the aforementioned energy range into six equally logarithmically-spaced energy bins. The best-fit spatial template implemented in Katsuta et al. (2012) was adopted. The spectral fitting process favors a Log-Parabola (based on the `Signif_Curve` task) as the best model to fit the GeV data instead of a simple power law reported in Katsuta et al. (2012); Suzuki et al. (2022). As shown on the right panel of Fig. 6, the newly derived spectrum deviates from previous results. Spectral points are, however, largely insensitive to the adopted spectral model (best-fit log-parabola or best-fit power-law) used to construct the SED. Our results are found to be in good agreement with the 4FGL-DR3 LogParabola model and updated spectral plot of the remnant [4]. Overall, we conclude that the discrepancy on the final spectral shape can neither originate from the choice of the spectral model nor from the additional years of *Fermi*-LAT data employed in this work for the construction of the remnant's GeV SED. Suzuki et al. (2022) derived broadly consistent spectral results with Katsuta et al. (2012) by using ten additional years. Hence, this inconsistency is rather likely attributed to the updated model used in the 4FGL-DR3 data to model the Galactic diffuse component and the isotropic diffuse component (`gll_iem_v07.fits` and `iso_P8R3_SOURCE_V3_v1.txt` *Fermi*-LAT files respectively). Regarding the specifics of the fit, the normalization of all 4FGL-DR3 sources positioned within 5° from the center of the remnant was left to vary, the same applies to the normalizations of the Galactic diffuse and isotropic backgrounds. Additionally, the normalization of the Log-Parabola model of the S147 counterpart was allowed to vary to obtain the best-fit spectral results.

As part of the remnant's multiwavelength SED study presented in this work, two distinct scenarios can be assumed. $\gamma-$ray emission can be produced by either Inverse Compton (IC) scattering of relativistic electrons interacting with the Cosmic Microwave background (CMB) (leptonic scenario) and/or π_0 decay originating from the interaction of relativistic protons (or heavier nuclei) with gas (hadronic scenario). Based on the detailed study of the GeV counterpart of the remnant performed in Katsuta et al. (2012), a hadronic scenario appears as the most plausible option. In this work, we provide updated spectral results in the GeV band which are moderately different compared to previous works mainly due to the updated models implemented. The obtained shape of the GeV SED and the likely interaction of the remnant with the nearby molecular clouds still supports the aforementioned finding (i.e., a hadronic production of γ-rays). Despite the significant change of the remnant's GeV SED at lower energies, a hadronic scenario is still favored by the obtained SED shape (see the expectations for evolved proton distributions, e.g., Yang et al. (2018)). However, a mixture of hadronic and leptonic contributions to the total SED cannot be excluded. No non-thermal X-ray emission component was detected from the remnant, and thus it does not exist, or it is of sub-dominant nature and cannot be detected with eROSITA. Therefore, no further constraints were provided utilizing the remnant's multiwavelength SED.

5. Discussion

Using eRASS:4 data of the first four completed SRG/eROSITA all-sky surveys, we report the detection of thermal X-ray emission from most of the 3°-sized angular extension of the SNR S 147, as defined in the radio continuum energy range. A comparison with earlier ROSAT Survey data yields good consistency, as does the comparison with archival yet-unpublished *XMM-Newton* pointings towards small portions, to the South and South-East, of the SNR.

The X-ray spatial morphology in the interior of the remnant is in excellent agreement with the morphology of both its optical (Hα) and radio continuum counterparts. The X-ray emission fills almost the entire remnant except for the void structure East of the center of the remnant, where the emission consistently drops in all three wavebands. An arc-like feature detected to the Eastern boundary of the remnant is also present in all three wavebands, giving a unique, ear-type appearance to its shell-type morphology. Thus, we consider it to be a shell-type SNR with some peculiar characteristics. The only noticeable difference between X-rays and lower energy emission is detected at the West of the remnant where both radio continuum and Hα emission are seemingly extended further to the West. A detailed study on the nature of this discrepancy is reported in (Paper II). The purely thermal emission of the SNR in X-rays can be well described by either a non-equilibrium collisional plasma of ~ 0.22 keV temperature with $N_H \sim 0.3\ 10^{22}$cm^{-2}, or a hot plasma in equilibrium of ~ 0.11 keV temperature and with $N_H \sim 0.51\ 10^{22}$cm^{-2}. Its purely thermal nature can also explain the excellent morphological agreement between the X-ray and Hα emission (hot and warm gas) and the general interconnection of the emission in all three wavebands as discussed in sec. 2.4.1. Among the two X-ray models, a NEI model appears as the preferable option mainly due to obtained absorption column density values and the indication for ejecta presence. The absorption column density obtained from NEI models is found to be well-aligned with the expected values derived from optical extinction measurements. On the contrary, CIE models require higher absorption column density values (compared to optical extinction measurements) and unreasonably high elemental abundance values to explain the remnant's spectral characteristics. Significant temperature variation across the remnant was observed, as shown in Tab. 2. The X-ray emis-

[4] https://fermi.gsfc.nasa.gov/ssc/data/access/lat/12yr_catalog/

sion is predominantly soft with a strong detection between 0.5 and 1.0 keV, with no detection above 2.3 keV. In all ten selected spectral extraction sub-regions, the ionization timescale is far from the expected equilibrium values as reported in Tab. 2 (full ionization equilibrium is typically reached at τ values $\geq 10^{12}$ cm$^3 \cdot$ s (Masai 1984)). The high statistical quality of the X-ray spectra obtained from both eROSITA and *XMM-Newton* observations of the remnant strongly supports the presence of ejecta which is noteworthy in such a particularly evolved SNR. The remnant is rich in O (OVII, OVIII), Ne (NeIX+X), and Mg (MgXI), whereas it lacks high-Z elements.

Strongly increased X-ray absorption at the location of the void structure (spectral extraction region D) cannot be excluded. The latter hypothesis is supported by the spectral analysis reported in Tab. 2). Thus, the nature of the SNR's void, found at the central-East of the remnant and consistently appearing in all three wavebands, can be at least partially explained. However, X-ray absorption might not be the primary cause of the lack of X-ray emission from that central-East region of the SNR.

Overall, no particular pattern of absorption column density variation was observed across the remnant, except for the significant decrease of the absorption column density towards region B, observed as a cavity in IR data, which spatially matches with a cavity in the IR data at that location as seen in Fig. 7 and the significant increase of the X-ray absorption column density towards region D, the void structure, which is found to be spatially coincident with regions of enhanced IR emission as seen in images displayed in Fig. 7. An excellent spatial correlation between the Southern bright X-ray blob (region B) and CO emission is obtained, as shown in Fig. 5. The latter could potentially explain the detected GeV emission (i.e., both CO emission and a high EM in X-rays are tracers of high gas densities, which boosts GeV emission of relativistic particles (if present)). However, the bright GeV blob positioned at the North of the remnant lacks the presence of CO clouds that could possibly explain the origin of the gamma-ray emission.

The detection of extended gamma-ray emission from the remnant (Katsuta et al. 2012) is confirmed in this study. In particular, we employed $\sim$ 15 years of *Fermi*-LAT data to successfully identify the nature of the extended diffuse source as the S147 GeV counterpart, which is found to be spatially coincident with the brightest parts of the optical and X-ray emission of the remnant. Additionally, our imaging analysis provides a substantial improvement in the morphology details of the gamma-ray emission. The remnant's GeV SED is best-fitted with a LogParabola, instead of a simple power law as reported in Katsuta et al. (2012); Suzuki et al. (2022). The shape of the GeV SED is still well consistent with a π^o-decay (hadronic) spectrum, which is the most plausible interpretation given the age of the SNR and the association with CO emission tracing molecular gas. In particular, the presence of CO clouds at the Southern rim of the remnant is found to be inextricably linked to the gamma-ray emission, therefore strengthening the hypothesis of hadronic production of γ-rays. Nevertheless, a similar association cannot be confirmed for the Northern GeV blob.

The absorption column ($N_{\rm H}$) analysis, carried out in this work, lends further support to the association of the pulsar/binary companion to the SNR and a distance of the latter around 1.3 kpc. A physical SNR size of 70 pc in X-rays is obtained when using an SNR distance of 1.33 kpc (as obtained from measurements of the distance of the associated runaway star and pulsar). Assuming an evolution of the SNR in undisturbed ISM of ~ 1 cm^{-3}, an $\sim 0.66 - 2 \times 10^5$ yr age estimate for the SNR was obtained using the SNR model calculator reported by Leahy & Williams (2017). This could place it among the oldest Galactic SNRs, if not the oldest. However, we note that the above estimate is highly uncertain due to the assumption on the remnant's explosion energy but most importantly due to the assumption of a homogenous local medium. An alternative scenario of a younger SNR, evolving inside a pre-existing cavity, is considered in (Paper II) which yields more consistent results with some of the remnant's observational characteristics and the associated pulsar's kinematic age ($\sim$ 30 kyrs). However, neither scenario takes into account the possibility of inhomogeneity in the surrounding medium, and further refinements of the models are necessary. Observations of the remnant with future experiments (e.g., XRISM) will shed light on the complexity of its nature.

Acknowledgements This work is based on data from eROSITA, the soft X-ray instrument aboard SRG, a joint Russian-German science mission supported by the Russian Space Agency (Roskosmos), in the interests of the Russian Academy of Sciences represented by its Space Research Institute (IKI), and the Deutsches Zentrum für Luft- und Raumfahrt (DLR). The SRG spacecraft was built by Lavochkin Association (NPOL) and its subcontractors, and is operated by NPOL with support from the Max Planck Institute for Extraterrestrial Physics (MPE).

The development and construction of the eROSITA X-ray instrument was led by MPE, with contributions from the Dr. Karl Remeis Observatory Bamberg & ECAP (FAU Erlangen-Nuernberg), the University of Hamburg Observatory, the Leibniz Institute for Astrophysics Potsdam (AIP), and the Institute for Astronomy and Astrophysics of the University of Tübingen, with the support of DLR and the Max Planck Society. The Argelander Institute for Astronomy of the University of Bonn and the Ludwig Maximilians Universität Munich also participated in the science preparation for eROSITA. The eROSITA data shown here were processed using the eSASS/NRTA software system developed by the German eROSITA consortium.

IK acknowledges support by the COMPLEX project from the European Research Council (ERC) under the European Union's Horizon 2020 research and innovation program grant agreement ERC-2019-AdG 882679. A.M.B. was supported by the RSF grant 21-72-20020. His modeling was performed at the Joint Supercomputer Center JSCC RAS and at the Peter the Great Saint-Petersburg Polytechnic University Supercomputing Center. Rashid Sunyaev acknowledges the support of dvp - N/A pertaining to Member Notification Merge at the Institute for Advanced Study. This research made use of `Montage`[5]. It is funded by the National Science Foundation under Grant Number ACI-1440620, and was previously funded by the National Aeronautics and Space Administration's Earth Science Technology Office, Computation Technologies Project, under Coop-

[5] http://montage.ipac.caltech.edu

erative Agreement Number NCC5-626 between NASA and the California Institute of Technology.

We thank the EXPLORE team for providing us access to the G-TOMO tool of the EXPLORE platform https://explore-platform.eu/ and thus allowing us to exploit updated GAIA/2MASS data which we employed to derive the latest estimates of the remnant age. We thank Denys Malyshev, Victor Doroshenko, and Lorenzo Ducci for fruitful discussions.

References

Anderson, S. B., Cadwell, B. J., Jacoby, B. A., et al. 1996, ApJ, 468, L55
Aschenbach, B. 1996, in Roentgenstrahlung from the Universe, ed. H. U. Zimmermann, J. Trümper, & H. Yorke, 213–220
Aschenbach, B. 1996, ROSAT observations of Supernova Remnants
Borkowski, K. J., Lyerly, W. J., & Reynolds, S. P. 2001, ApJ, 548, 820
Boubert, D., Fraser, M., Evans, N. W., Green, D. A., & Izzard, R. G. 2017, A&A, 606, A14
Brunner, H., Liu, T., Lamer, G., et al. 2022, A&A, 661, A1
Cash, W. 1979, ApJ, 228, 939
Chatterjee, S., Brisken, W. F., Vlemmings, W. H. T., et al. 2009, The Astrophysical Journal, 698, 250
Chen, B. Q., Liu, X. W., Ren, J. J., et al. 2017, MNRAS, 472, 3924
Chen, Y., Jiang, B., Zhou, P., et al. 2014, Supernova Environmental Impacts, ed. A. Ray and R. A. McCray, 170–177
Clark, D. H. & Caswell, J. L. 1976, MNRAS, 174, 267
Collischon, C., Sasaki, M., Mecke, K., Points, S. D., & Klatt, M. A. 2021, A&A, 653, A16
Condon, J. J., Broderick, J. J., & Seielstad, G. A. 1991, AJ, 102, 2041
Condon, J. J., Broderick, J. J., Seielstad, G. A., Douglas, K., & Gregory, P. C. 1994, AJ, 107, 1829
Condon, J. J., Griffith, M. R., & Wright, A. E. 1993, AJ, 106, 1095
Cram, L. E., Green, A. J., & Bock, D. C. J. 1998, PASA, 15, 64
Dame, T. M., Hartmann, D., & Thaddeus, P. 2001, ApJ, 547, 792
Dickel, J. R. & McKinley, R. R. 1969, ApJ, 155, 67
Dinçel, B., Neuhäuser, R., Yerli, S. K., et al. 2015, Monthly Notices of the Royal Astronomical Society, 448, 3196
Dopita, M. A., Tuohy, I. R., & Mathewson, D. S. 1981, ApJ, 248, L105
Dorman, B., Arnaud, K. A., & Gordon, C. A. 2003, in AAS/High Energy Astrophysics Division, Vol. 7, AAS/High Energy Astrophysics Division #7, 22.10
Ferrand, G. & Safi-Harb, S. 2012, Advances in Space Research, 49, 1313
Fesen, R. A., Blair, W. P., & Kirshner, R. P. 1985, ApJ, 292, 29
Finkbeiner, D. P. 2003, ApJS, 146, 407
Foight, D. R., Güver, T., Özel, F., & Slane, P. O. 2016, ApJ, 826, 66
For, B. Q., Staveley-Smith, L., Hurley-Walker, N., et al. 2018, MNRAS, 480, 2743
Gaze, V. F. & Shajn, G. A. 1952, Izvestiya Ordena Trudovogo Krasnogo Znameni Krymskoj Astrofizicheskoj Observatorii, 9, 52
Giacani, E., Smith, M. J. S., Dubner, G., et al. 2009, A&A, 507, 841
Goss, W. M., Shaver, P. A., Zealey, W. J., Murdin, P., & Clark, D. H. 1979, MNRAS, 188, 357
Green, D. A. 2009, VizieR Online Data Catalog, VII/253
Green, D. A. 2019, Journal of Astrophysics and Astronomy, 40, 36
Green, G. 2018, The Journal of Open Source Software, 3, 695
Green, G. M., Schlafly, E., Zucker, C., Speagle, J. S., & Finkbeiner, D. 2019, ApJ, 887, 93
Guseinov, O. H., Ankay, A., & Tagieva, S. O. 2004, Serbian Astronomical Journal, 168, 55
Hurley-Walker, N., Callingham, J. R., Hancock, P. J., et al. 2017, MNRAS, 464, 1146
Hurley-Walker, N., Hancock, P. J., Franzen, T. M. O., et al. 2019, PASA, 36, e047
Hwang, U., Petre, R., & Flanagan, K. A. 2008, The Astrophysical Journal, 676, 378
Jiang, B., Chen, Y., Wang, J., et al. 2010, The Astrophysical Journal, 712, 1147
Joye, W. A. & Mandel, E. 2003, in Astronomical data analysis software and systems XII, Vol. 295, 489
Katsuta, J., Uchiyama, Y., Tanaka, T., et al. 2012, ApJ, 752, 135
Keane, E. F. & Kramer, M. 2008, Monthly Notices of the Royal Astronomical Society, 391, 2009
Khabibullin, I. I., Churazov, E. M., Chugai, N. N., et al. 2024, arXiv e-prints, arXiv:2401.17261
Kirshner, R. P. & Arnold, C. N. 1979, ApJ, 229, 147
Kochanek, C. S. 2021, MNRAS, 507, 5832
Kochanek, C. S., Raymond, J. C., & Caldwell, N. 2024, arXiv e-prints, arXiv:2403.13892
Kramer, M., Lyne, A. G., Hobbs, G., et al. 2003, ApJ, 593, L31
Kundu, M. R., Angerhofer, P. E., Fuerst, E., & Hirth, W. 1980, A&A, 92, 225
Lallement, R., Babusiaux, C., Vergely, J. L., et al. 2019, A&A, 625, A135
Lallement, R., Vergely, J. L., Babusiaux, C., & Cox, N. L. J. 2022, A&A, 661, A147
Lasker, B. M. 1979, Publications of the Astronomical Society of the Pacific, 91, 153
Leahy, D. A. & Williams, J. E. 2017, The Astronomical Journal, 153, 239
Lucke, P. B. 1978, A&A, 64, 367
Masai, K. 1984, Ap&SS, 98, 367
Mathewson, D. S., Dopita, M. A., Tuohy, I. R., & Ford, V. L. 1980, ApJ, 242, L73
Mattox, J. R., Bertsch, D. L., Chiang, J., et al. 1996, ApJ, 461, 396
McKee, C. F., Hollenbach, D. J., Seab, G. C., & Tielens, A. G. G. M. 1987, ApJ, 318, 674
Merloni, A., Lamer, G., Liu, T., et al. 2024, A&A, 682, A34
Michailidis, M., Pühlhofer, G., Santangelo, A., Becker, W., & Sasaki, M. 2024, arXiv e-prints, arXiv:2401.17311
Minkowski, R. 1958, Reviews of Modern Physics, 30, 1048
Ng, C.-Y., Romani, R. W., Brisken, W. F., Chatterjee, S., & Kramer, M. 2007, The Astrophysical Journal, 654, 487
Park, S., Hughes, J. P., Slane, P. O., et al. 2003, The Astrophysical Journal, 592, L41
Pavlinsky, M., Tkachenko, A., Levin, V., et al. 2021, A&A, 650, A42
Phillips, A. P., Gondhalekar, P. M., & Blades, J. C. 1981, Monthly Notices of the Royal Astronomical Society, 195, 485
Predehl, P., Andritschke, R., Arefiev, V., et al. 2021, A&A, 647, A1
Predehl, P. & Schmitt, J. H. M. M. 1995, A&A, 293, 889
Priestley, F. D., Chawner, H., Matsuura, M., et al. 2021, MNRAS, 500, 2543
Raymond, J. C., Cox, D. P., & Smith, B. W. 1976, ApJ, 204, 290
Reich, W. 2002, in Neutron Stars, Pulsars, and Supernova Remnants, ed. W. Becker, H. Lesch, & J. Trümper, 1
Reich, W., Zhang, X., & Fürst, E. 2003, A&A, 408, 961
Ren, J.-J., Liu, X.-W., Chen, B.-Q., et al. 2018, Research in Astronomy and Astrophysics, 18, 111
Romani, R. W. & Ng, C. Y. 2003, ApJ, 585, L41
Sallmen, S. & Welsh, B. Y. 2004, A&A, 426, 555
Sauvageot, J. L., Ballet, J., & Rothenflug, R. 1990, A&A, 227, 183
Slavin, J. D., Dwek, E., & Jones, A. P. 2015, ApJ, 803, 7
Smale, D. A. P. 2021a, http://heasarc.gsfc.nasa.gov/
Smale, D. A. P. 2021b, http://heasarc.gsfc.nasa.gov/docs/software/floods/ftools_menu.html
Sofue, Y., Furst, E., & Hirth, W. 1980, PASJ, 32, 1
Strüder, L., Briel, U., Dennerl, K., et al. 2001, A&A, 365, L18
Stupar, M., Parker, Q. A., Filipović, M. D., et al. 2007, MNRAS, 381, 377
Sun, X., Aschenbach, B., Becker, W., et al. 1995, IAU Circ., 6187, 2
Sunyaev, R., Arefiev, V., Babyshkin, V., et al. 2021, A&A, 656, A132
Suzuki, H., Bamba, A., Yamazaki, R., & Ohira, Y. 2022, ApJ, 924, 45
Taylor, A. R., Gibson, S. J., Peracaula, M., et al. 2003, AJ, 125, 3145
Troja, E., Bocchino, F., Miceli, M., & Reale, F. 2008, A&A, 485, 777
Turner, M. J. L., Abbey, A., Arnaud, M., et al. 2001, A&A, 365, L27
van den Bergh, S., Marscher, A. P., & Terzian, Y. 1973, ApJS, 26, 19
Voges, W., Aschenbach, B., Boller, T., et al. 1999, A&A, 349, 389
Voges, W., Aschenbach, B., Boller, T., et al. 2000, IAU Circ., 7432, 3
Wayth, R. B., Lenc, E., Bell, M. E., et al. 2015, PASA, 32, e025
Wilms, J., Allen, A., & McCray, R. 2000, ApJ, 542, 914
Xiao, L., Fürst, E., Reich, W., & Han, J. 2008, Astronomy & Astrophysics, 482, 783
Yamauchi, S., Koyama, K., Tomida, H., Yokogawa, J., & Tamura, K. 1999, Publications of the Astronomical Society of Japan, 51, 13
Yang, R.-z., Kafexhiu, E., & Aharonian, F. 2018, A&A, 615, A108

Appendix A: eRASS:4 X-ray spectral plots of individual sub-regions

Fig A.1 shows the results of the simultaneous fit of the on-source and background emission from 8 selected sub-regions, with an absorbed `VNEI` as the optimal model describing the purely thermal S147 spectrum. The corresponding best fit spectral parameters are summarized in Tab. 2.

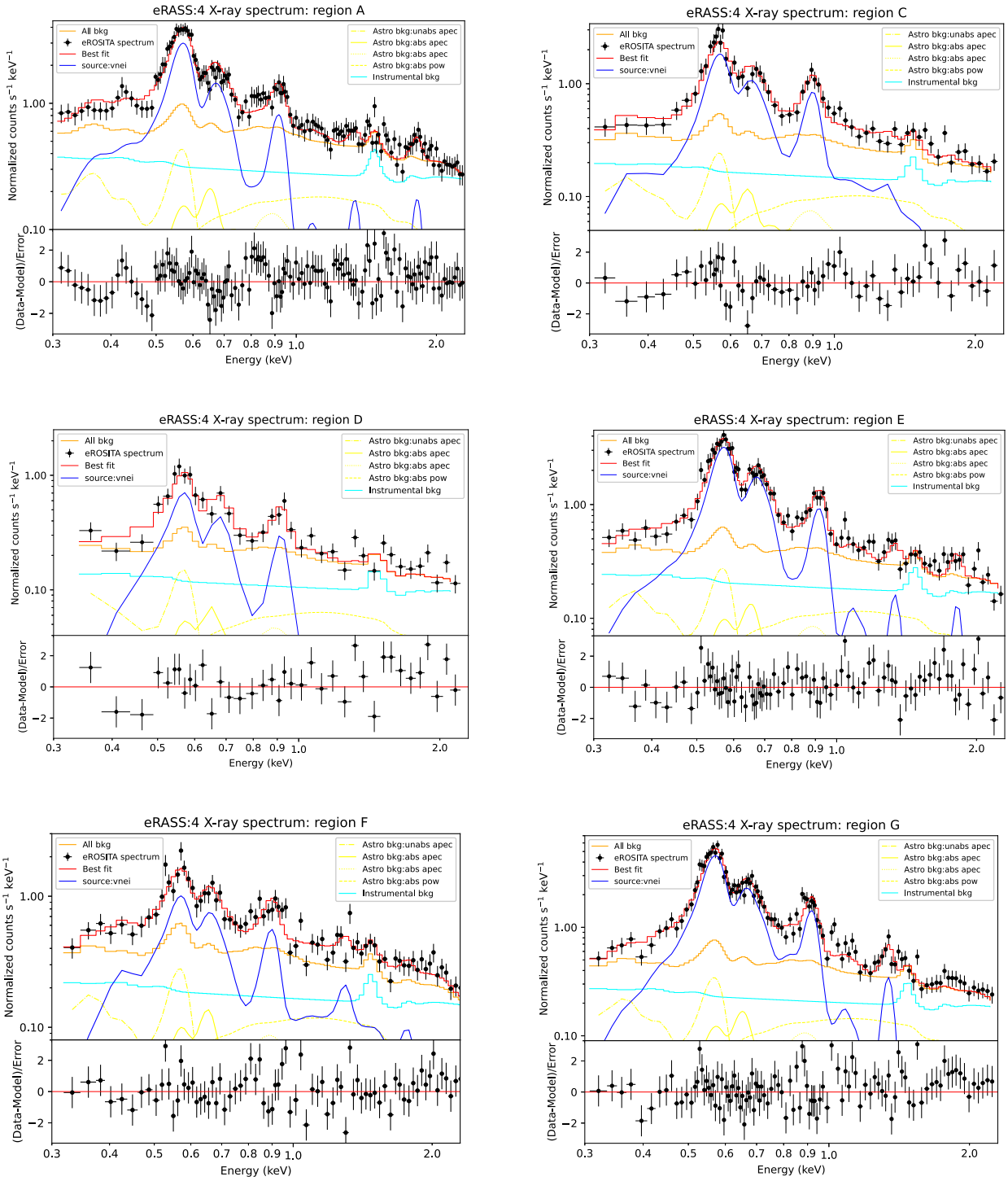

Fig. A.1: eRASS:4 X-ray spectra in the 0.3-2.3 keV energy band, from 8 selected sub-regions of the remnant.

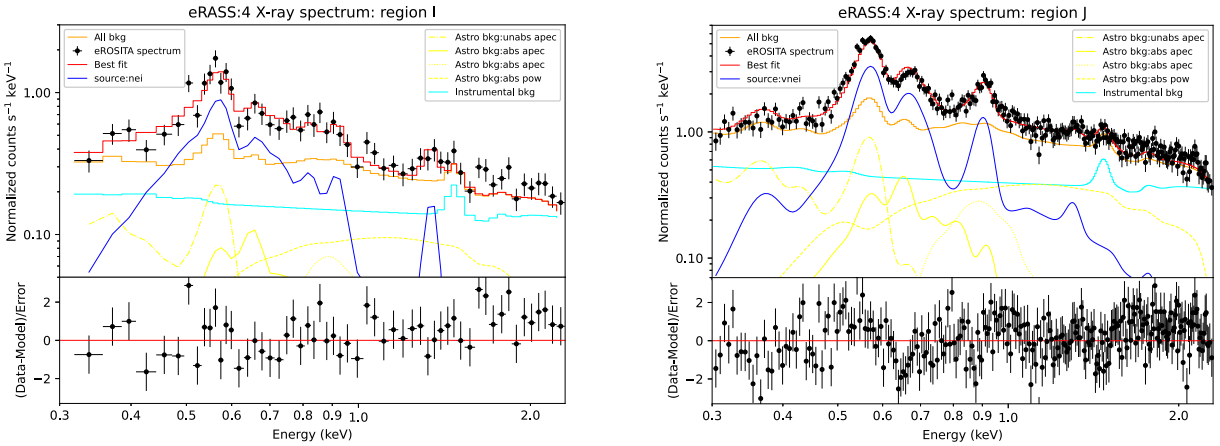

Fig. A.1: Continued.

3.3 I. Khabibullin, E. Churazov, N. Chugai, A. Bykov, R. Sunyaev, V. Utrobin, I. Zinchenko, M. Michailidis, G. Pühlhofer, W. Becker, M. Freyberg, A. Merloni, A. Santangelo, M. Sasaki. Study of X-ray emission from the S147 nebula by *SRG*/eROSITA: supernova-in-the-cavity scenario. In: Astronomy & Astrophysics (A&A), accepted (May 2024)

Astronomy & Astrophysics manuscript no. output
May 16, 2024

Article IV

Study of X-ray emission from the S147 nebula by SRG/eROSITA: supernova-in-the-cavity scenario

Ildar I. Khabibullin[1,2,3], Eugene M. Churazov[2,3], Nikolai N. Chugai[4], Andrei M. Bykov[5], Rashid A. Sunyaev[2,3,6], Victor P. Utrobin[7,4], Igor I. Zinchenko[8], Miltiadis Michailidis[9], Gerd Pühlhofer[9], Werner Becker[10,11], Michael Freyberg[10], Andrea Merloni[10], Andrea Santangelo[9], and Manami Sasaki[12]

[1] Universitäts-Sternwarte, Fakultät für Physik, Ludwig-Maximilians-Universität München, Scheinerstr.1, 81679 München, Germany
[2] Space Research Institute (IKI), Profsoyuznaya 84/32, Moscow 117997, Russia
[3] Max Planck Institute for Astrophysics, Karl-Schwarzschild-Str. 1, D-85741 Garching, Germany
[4] Institute of Astronomy, Russian Academy of Sciences, 48 Pyatnitskaya str., Moscow 119017, Russia
[5] Ioffe Institute, Politekhnicheskaya st. 26, Saint Petersburg 194021, Russia
[6] Institute for Advanced Study, Einstein Drive, Princeton, New Jersey 08540, USA
[7] NRC 'Kurchatov Institute', acad. Kurchatov Square 1, Moscow 123182, Russia
[8] Institute of Applied Physics of the Russian Academy of Sciences, 46 Ul'yanov str., Nizhny Novgorod 603950, Russia
[9] Institut für Astronomie und Astrophysik Tübingen (IAAT), Sand 1, 72076 Tübingen, Germany
[10] Max-Planck Institut für extraterrestrische Physik, Giessenbachstraße, 85748 Garching, Germany
[11] Max-Planck Institut für Radioastronomie, Auf dem Hügel 69, 53121 Bonn, Germany
[12] Dr. Karl Remeis Observatory, Erlangen Centre for Astroparticle Physics, Friedrich-Alexander-Universität Erlangen-Nürnberg, Sternwartstraße 7, 96049 Bamberg, Germany

Received 30 January 2024 / Accepted 10 May 2024

ABSTRACT

The Simeis 147 nebula (S147) is particularly well known for a spectacular net of H_α-emitting filaments. It is often considered one of the largest and oldest ($\sim 10^5$ yr) cataloged supernova remnants in the Milky Way, although the kinematics of the pulsar PSR J0538+2817 suggests that this SNR might be a factor of three younger. The former case is considered in a companion paper, while here we pursue the latter. Both studies are based on the data of SRG/eROSITA All-Sky Survey observations. Here we confront the inferred properties of the X-ray emitting gas data with a scenario of the supernova explosion in a low-density cavity, e.g. a wind-blown-bubble. This scenario assumes that a $\sim 20\,M_\odot$ progenitor star has had small velocity with respect to the ambient interstellar medium, so it stayed close to the center of a dense shell created during its Main Sequence evolution till the moment of the core-collapse explosion. The ejecta first propagate through the low-density cavity until they collide with the dense shell, and only then the reverse shock goes deeper into the ejecta and powers the observed X-ray emission of the nebula. The part of the remnant inside the dense shell remains non-radiative till now and, plausibly, in a state with $T_e < T_i$ and Non-Equilibrium Ionization (NEI). On the contrary, the forward shock becomes radiative immediately after entering the dense shell, and, being subject to instabilities, creates a characteristic "foamy" appearance of the nebula in H_α and radio emission.

Key words. supernova remnants (Individual object: Spaghetti nebula) — multiwavelength study

1. Introduction

Simeis 147 nebula (hereafter S147 for brevity) discovered by G. A. Shajn (Gaze & Shajn 1952) is famous due to its spectacular filamentary appearance in Hα line emission (Lozinskaia 1976). Non-thermal radio (Denoyer 1974; Sofue et al. 1980; Fuerst & Reich 1986; Xiao et al. 2008; Khabibullin et al. 2024) and gamma-ray emission (Katsuta et al. 2012; Suzuki et al. 2022) has been detected from it, indicating that it is most likely a remnant of a supernova explosion (SNR G180.0-01.7), possibly interacting with a molecular cloud at one of its boundaries. A radio and X-ray pulsar was discovered within the extent of the nebula (Anderson et al. 1996; Kramer et al. 2003), for which the measured proper motion directs away from the geometrical center of the nebula (Romani & Ng 2003), indicating that S147 might be indeed powered by a core-collapse supernova explosion $\sim 30,000$ yrs ago (Gvaramadze 2006; Ng et al. 2007).

The size of S147 is however indicative of a much older explosion,$\sim 150,000$ yrs, if canonical values of the explosion energy and the density of the surrounding medium are assumed (e.g. Silk & Wallerstein 1973). This "age dilemma" (Reich et al. 2003; Romani & Ng 2003) can be reconciled if a scenario of an explosion in the wind-blown cavity is invoked, allowing the size of the object to be determined by winds before the explosion (Reich et al. 2003; Gvaramadze 2006). Although such a picture might be relevant for the bulk of the massive stars (e.g. Dwarkadas 2023), relative motion of the star through the surrounding interstellar medium (ISM) apparently makes in-cavity explosions rare.

The evolution of the supernova blast wave inside a wind-blown cavity differs substantially from the self-similar solu-

tion of a point explosion in a uniform medium. It is characterized by a prolonged phase of the free expansion (until ejecta hit the walls of the cavity) and rapid onset of the radiative phase of the forward shock launched into the dense shell (Chevalier & Liang 1989; Tenorio-Tagle et al. 1991).

In the same time, after the passage of the reverse shock through the supernova ejecta, the cavity should be filled with the hot X-ray emitting gas, bearing traces of the enrichment by explosive nucleosynthesis products. Given the large size of S147, this emission is expected to be rather faint and difficult to observe with focusing X-ray telescopes having relatively small Field-of-View, like *Chandra*, *XMM-Newton*, or *Suzaku*. In the course of the all-sky survey (Predehl et al. 2021; Sunyaev et al. 2021), a map of the full extent of the nebula was obtained by SRG/eROSITA, resulting in the first clear detection of soft thermal X-ray emission from S147 with most of the flux coming at energies below ~ 1 keV, as we describe in Michailidis et al. (2024) (hereafter Paper I).

In this paper, we consider key spatial and spectral properties of the newly detected X-ray emission from S147 in relation to the physical scenario of a supernova explosion in an interstellar cavity created by the progenitor star during its main sequence phase. A cannonical SNR in a uniform medium scenario is considered and confronted with the X-ray and multiwavelength data on S147 in (Paper I).

The paper is structured as follows: we give basic information on X-ray observations in Section 2 and outline morphological and spectral properties of the X-ray emission in Section 3. The model of a supernova explosion in a wind-blown bubble, capable of explaining the major properties of the object is presented in Section 4 and discussed in Section 5. Conclusions are summarized in Section 6

2. Observations

The X-ray data used in this paper are identical to those used and described in (Paper I). Namely, they are based on observations of SRG/eROSITA in all four consecutive all-sky surveys (Sunyaev et al. 2021). For imaging analysis, the data of all seven eROSITA telescope modules were used, while the data of two telescope modules (TM) without the on-chip optical blocking filter were excluded from the spectral analysis due to their different spectral response function and susceptibility to optical light leak contamination at low energies (e.g. Predehl et al. 2021).

3. X-ray emission

A comprehensive description of various properties of X-ray emission detected in the direction of the S147 nebula is presented in (Paper I), here we focus on key features that might support the physical scenario we put forward in Section 4.

3.1. Broad-band X-ray morphology

Figure 1 shows surface brightness of the X-ray emission in 0.5-1 keV band from a 3.7°x3.7° patch (in Galactic coordinates) covering the full extent of S147. The image was produced by masking the detected point and mildly extended sources and smooth with a Gaussian kernel with $\sigma = 1'$. The exact procedure is identical to the one used in the previous works on the newly discovered X-ray supernova

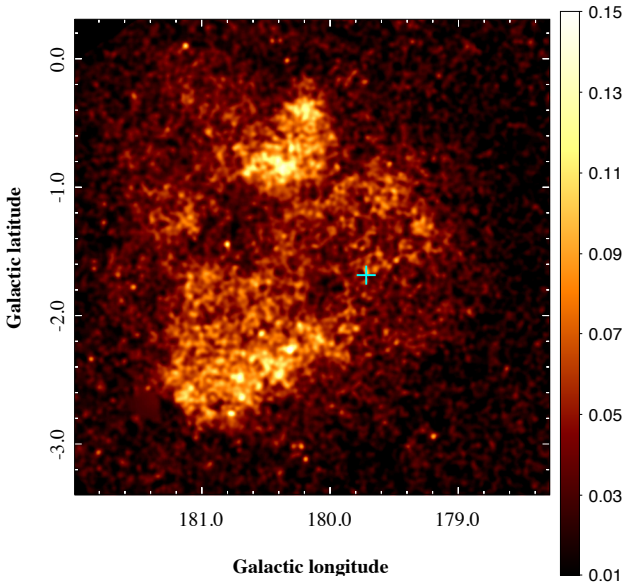

Fig. 1. Broad-band (0.5-1.0 keV) (particle) background-subtracted exposure-corrected X-ray image (linear scale) obtained by SRG/eROSITA in the S147 direction (3.7°×3.7° in Galactic coordinates) after masking of point and mildly extended sources and smoothing with a Gaussian kernel with $\sigma = 1'$. This band maximizes the source-to-background ratio for the SNR emission. The cross marks the position of the pulsar PSR J0538+2817 .

remnants (Churazov et al. 2021; Khabibullin et al. 2023) and is described in (Paper I). The image is centered close to the geometrical center of the Hα and radio emission, at $(l, b) \approx (180.32°, -1.65°)$ (e.g. Kramer et al. 2003), and the position of the pulsar PSR J0538+2817 marked with the cross (the point-like emission of the pulsar itself has been masked). The ratio of the X-ray emission from the SNR to the unrelated background and foreground emission is maximized in this band (the latter is estimated from the adjacent sky regions outside the extent of the nebula). At lower and higher energies, the S147 emission falls below the background level making it barely visible in the 2D image, but still detectable in the background-subtracted source spectrum.

Morphology of the X-ray emission is drastically different from the filamentary and more circular morphology of the Hα and radio emission, as illustrated in Figure 2(top panel), which combines the same SRG/eROSITA X-ray image (blue) with the Hα image (green) from the IGAPS survey (Greimel et al. 2021) and radio image at 1.4 GHz (red) from the CGPS survey (Taylor et al. 2003). Both latter images were convoluted with a median top-hat filter ($r = 40''$) suppressing numerous point sources but leaving diffuse and filamentary emission mostly unaffected.

One can see that X-ray emission is not clearly structured and contains regions of brighter and fainter (by a factor of few compared to the mean one) emission, which are $\sim 1/3 - 1/10$ of the full size of the nebula ($R \sim 100'$) and appear in the form of "blobs" and "depressions" on top of the smooth background emission. No signatures of the global edge-brightening or central peak are visible.

Comparison with the Hα and radio images indicate that some of the bright X-ray regions lie close to the brightest

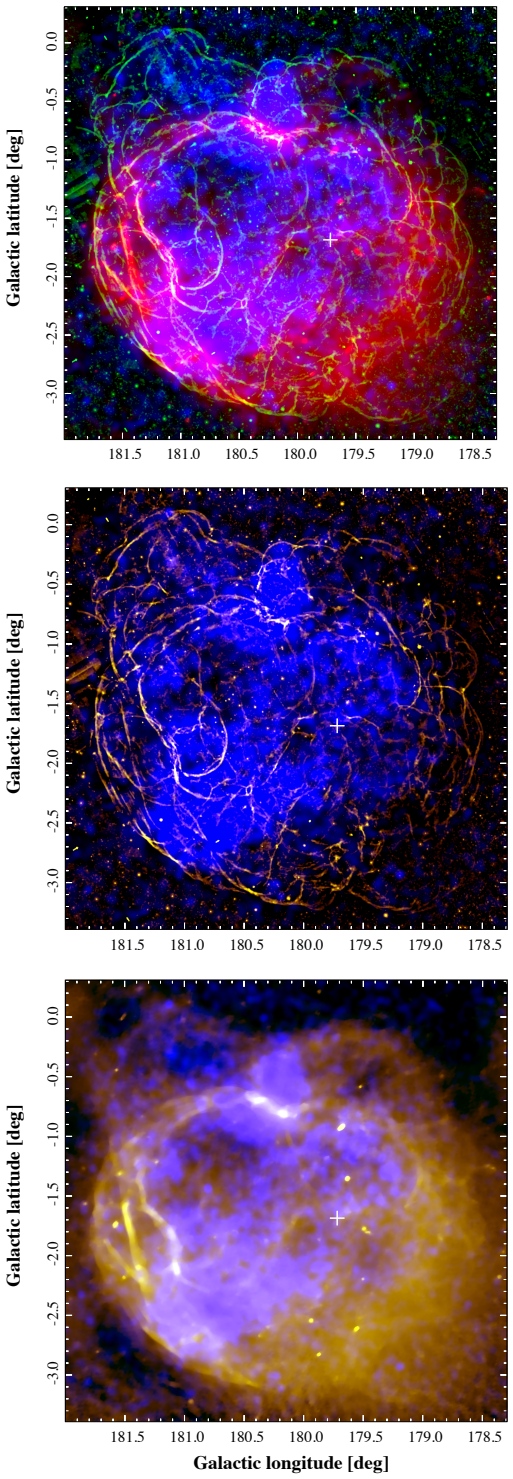

Fig. 2. Multiwavelength view of S147 (in Galactic coordinates). *Top* - combined map of the radio (CGPS data at 1.4GHz, red), wavelet-decomposed (in order to emphasize filamentary structure) Hα (IGAPS data, green) and broad-band X-ray (0.5-1.1 keV, SRG/eROSITA data, blue) emission. The white cross marks the position of PSR J0538+2817. *Middle* - intensity-saturated X-ray image is shown in blue on top of the wavelet-decomposed Hα image, demonstrating that X-ray emission is confined by the Hα-emitting shell. *Bottom* - same as the middle panel but with the 1.4 GHz radio emission as a background.

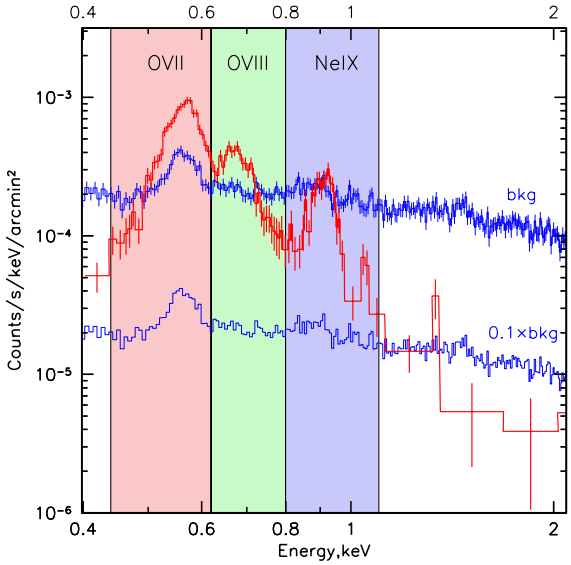

Fig. 3. X-ray spectrum of the whole remnant (red data points) after subtraction of the background signal (blue data points) estimated from an adjacent sky region. Also shown is the level of 10% of the background emission aimed at showing that above 1.5 keV the supernova signal amounts to a few % of the background level, making conclusions regarding its spectral shape at these energies strongly background-sensitive. The three bands containing the brightest emission lines are shown in red (O VII), green (O VII), and blue (Ne IX), and are used for RGB composite images.

optical and radio filaments (as exemplified by the bright region and filaments to Galactic North of the nebula's center at $l, b = 180.25°, -0.75°$), while other X-ray bright regions lack prominent counterparts (as the bright X-ray region to the Galactic South of the center at $l, b = 180.5°, -2.5°$). On the other hand, the largest cavity in X-ray emission, at $l, b = 180.75°, -1.75°$, also coincides with the region of fainter optical and radio emission. No signatures of filamentary X-ray emission are visible.

The X-ray emission appears to be well confined by the optical and radio boundaries. The latter point is even more clearly illustrated by images in the bottom panels of Figure 2, which show intensity-saturated broad-band X-ray image (blue) on top of wavelet decomposed Hα (left panel, highlighting the filamentary optical emission) and radio emission. One can see that X-ray emission reaches the boundaries of the optical and radio emission in the East part of the nebula, while it ends slightly short of it in the West side (appearing more diffuse in the radio and structured on smaller scales in the optical bands). Comparison with the dust and interstellar absorption maps for this region shows no correlations with X-ray morphology on these scales, indicating that the observed variations are intrinsic to the source itself (cf. also a dedicated discussion in Michailidis et al. 2024).

3.2. Narrow-band imaging

Given the inhomogeneous appearance of the X-ray emission from S147 and its complex connection to the emission at other wavelengths, we check for possible correlated spatial variations in its spectral shape by comparing maps accu-

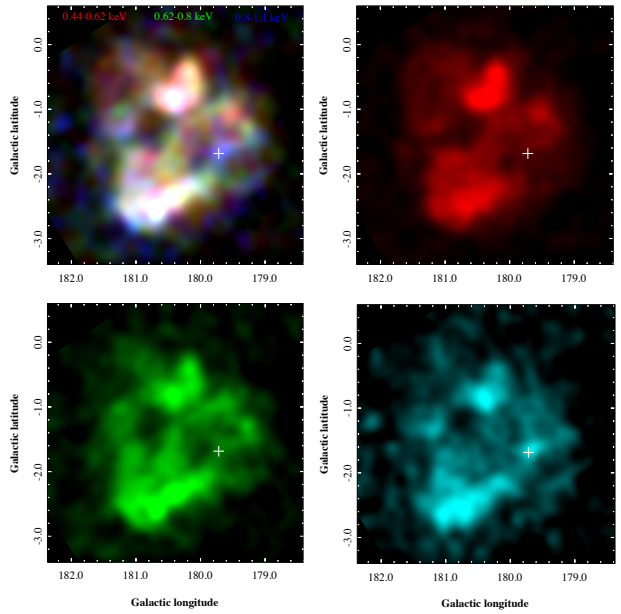

Fig. 4. RGB-composite (top left) and individual narrow-band X-ray images covering the 0.44-1.1 keV band. The red, green and cyan (instead of blue for better visibility) images correspond to 0.44-0.62, 0.62-0.8, and 0.8-1.1 keV bands, respectively. These bands encompass the three brightest X-ray emission lines in the spectrum of S147: O VII, O VIII, and Ne IX.

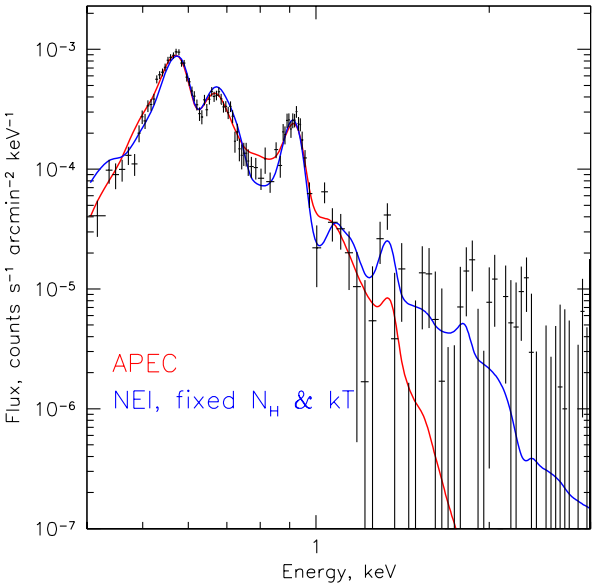

Fig. 5. X-ray spectrum of the entire S147 SNR. The red line shows the best-fitting `APEC` model (single-temperature, collisional ionization equilibrium, solar abundance of metals). This model requires a very large absorbing column density, overpredicts the flux near 0.8 keV (where a significant contribution of Fe XVII line at 826 eV is expected), and underpredicts the Mg XI line flux unless its abundance (relative to oxygen) is very high. For comparison, the blue line shows the NEI model with parameters fixed at physically motivated values. Although formally the value of χ^2 is higher than for the APEC model, the lower value of $N_{\rm H}$ and the ability of the model to better describe regions near Fe XVII and Mg XI lines make this model an appealing interpretation of the S147 spectrum (see text for details).

mulated in narrow energy bands centered on the brightest emission lines in the thermal plasma at $kT = 0.1 - 0.3$ keV: O VII, O VIII, and Ne IX (as shown for entire SNR's spectrum in Figure 3). Namely, Figure 4 shows images in the 0.44-0.62, 0.62-0.8, and 0.8-1.1 keV bands, as well as their RGB combination.

Although moderate "color" variations are clearly visible on the RGB image, all three images share rather similar morphology. Emission in the O VII appears most diffuse, while O VIII appears more filamentary-structured, and Ne IX appears somewhat edge-brightened. These observations justify the consideration of the single spectrum of the full nebula as a proxy for the physical conditions of the X-ray-emitting material. Analysis of the spectra extracted from the individual regions is presented in (Paper I) and confirms the validity of this assumption.

3.3. X-ray spectra

In this section, we consider the most basic characteristics of the entire SNR's X-ray spectrum. The spectrum shown in Fig. 5 features three very prominent lines (O VII, O VIII, Ne IX) below 1 keV and weaker lines at higher energies, among which the line of Mg XI is the most significant.

A starting minimalist's assumption is that for an old SNR, the X-ray emission might be well described by the thermal emission of plasma in collisional ionization equilibrium (CEI). To this end, an absorbed `APEC` model with a fixed (= Solar) abundance of heavy elements can be used. However, this model fails in two aspects: it requires large absorbing column density ($N_{\rm H} \sim 6 \times 10^{22}\,{\rm cm}^{-2}$ that is significantly larger than the expected value $(0.2 - 0.4) \times 10^{22}\,{\rm cm}^{-2}$), overpredicts the flux near ~ 0.8 keV, and underpredicts the flux in the line of Mg XI. This is also reflected in the value of χ^2 (366 for 318 d.o.f., see Table 1). In practice, a large value of χ^2 is anticipated given the complexity of the remnant. The integrated spectrum might include several spectral components with different temperatures and metallicities. We, therefore, will not consider the value of χ^2 as a robust quantitative way of ranking complicated models. Instead, we want to demonstrate that for a set of physically motivated parameters, the model can qualitatively reproduce the observed spectrum. For the S147 model outlined in the Abstract, another spectral model is better motivated. Due to the large size and low density of the gas in the cavity, the ejecta reheated by the reverse shock some 15 kyr ago can remain hot for a long time and may deviate from CIE. This can happen even if ejecta are mixed with a moderate amount of gas that was present in the cavity. However, a single `NEI` model converges to a solution that is not very far from the `APEC` parameters (large N_H and low kT), although with the better χ^2. This is clearly driven by the requirement to describe the O VII/O VIII ratio, where statistics is the highest, and given less weight to other parts of the spectrum. One can further try to push ahead NEI scenario by fixing absorbing column density to the expected value of $N_{\rm H} \sim 2.5 \times 10^{21}\,{\rm cm}^{-2}$ and the electron temperature to sufficiently high value, e.g. $kT = 1$ keV. This model has a higher χ^2 value, but it better describes the spectrum near ~ 0.8 keV and boosts the flux in the

Mg XI line, making this model an appealing interpretation of the S147 spectrum.

The above analysis was done assuming that the abundance of heavy metals is solar. This assumption can be far from reality if X-ray emission is coming from the ejecta. Since at relatively low temperatures, metals' contribution dominates the X-ray emission, the absolute abundance measurements are difficult, while the relative abundances are more robust. Since the lines of oxygen dominate in the observed spectrum, it is convenient to express abundances relative to oxygen rather than hydrogen. In the models described below (§4.4) the ejecta abundances of C, N, and Fe (relative to O) are $\sim 30\%$ of the Solar values, while the abundances of Ne and Mg vary between between 0.6 and 1.7 (relative to O). Letting the abundance of elements free would make the model much more flexible but less constrained. Since the abundance variations relative to oxygen are not very extreme, we freeze the ratios at the solar values but keep in mind that the line ratios might not be accurately predicted by the model. Another important result of the increased abundance is the difference in the derived emission measure that scales approximately linearly with the abundance (as long as metals dominate the spectrum).

4. The model: supernova explosion in a wind-blown bubble

The idea that the supernova might explode in a wind-blown cavity was first proposed for the supernova remnant N132D in LMC (Hughes 1987). In that particular case, the cavity was invoked to resolve the disparity between the large Sedov expansion age and the much smaller age inferred from optical oxygen-rich filaments. In the case of S147, we face a somewhat similar age puzzle.

4.1. S147 age dilemma

The pulsar J0538+2817 and SNR S147 highly likely have a common origin, which is suggested by the pulsar motion directed from the shell center (Romani & Ng 2003). The pulsar distance inferred from VLBI parallax is 1.3 kpc and the proper motion $\mu = 57.9$ mas yr^{-1} (Chatterjee et al. 2009). The most recent absorption-based distance estimates for S147 (e.g., Paper I, Kochanek et al. 2024) are consistent with this value. The pulsar offset of $0^\circ.605$ combined with the proper motion implies the pulsar kinematic age $t_{\rm kin} = 37.6$ kyr. With the SNR angular radius of Hα filamentary shell of $100'$ the physical shell radius is $r = 39$ pc.

The S147 expansion velocity implied by Hα spectroscopic observations is about $100\,{\rm km\,s^{-1}}$ $\rm km\,s^{-1}$(Lozinskaya 1976). This value is consistent with the LAMOST optical spectroscopic survey in the field of S147, which shows a symmetric velocity distribution of the line-emitting gas in the range of ± 100 $\rm km\,s^{-1}$ (Ren et al. 2018). Assuming the SNR expansion in a homogeneous medium with a typical density one can derive the age lower limit by applying the Sedov solution for the point explosion. The inferred SNR age is then $t_{\rm exp} = 0.4r/v = 150$ kyr, which is four times larger than the kinematic age (37.6 kyr). Note, that the radiative expansion regime would produce an even larger age. Alternatively, adopting the expansion age of 37.6 kyr and radius of 39 pc one expects the shell expansion velocity of $v = 0.4r/t = 407\,{\rm km\,s^{-1}}$ that is four times the observed expansion velocity of $100\,{\rm km\,s^{-1}}$.

The disparity between the kinematic and Sedov expansion ages has been recognized by Reich et al. (2003) and Romani & Ng (2003). To resolve the age dilemma Reich et al. (2003) proposed that S147 progenitor exploded in a wind-blown bubble (WBB) with the subsequent SNR deceleration after the collision with a boundary of the massive swept-up shell. We consider this scenario as a likely possibility and explore it in more detail.

4.2. The wind-blown bubble

As an illustration of the WBB conjecture for the S147, we consider the case of a massive SN II progenitor of about $20\,M_\odot$. This case is relevant because it falls in the range of 9-25 $M_\odot$ responsible for neutron stars production (Woosley et al. 2002; Heger et al. 2003); besides, the $20\,M_\odot$ mass is high enough to produce an extended WBB for the typical ISM density.

Commonly, the WBB radius in a homogeneous ISM is estimated using the well-known analytic solution (Weaver et al. 1977). However, to find a more adequate estimate of the expected radius one needs to take into account the ISM pressure that is omitted in the referred analytic solution. We use a thin shell approximation to solve numerically the equations of mass, momentum, and energy conservation of the Weaver et al. (1977) model with the inclusion of the ISM pressure. The latter is composed of the thermal pressure of the Warm Ionized Medium (WIM) component with $nT \approx 3000$ cm^{-3} K (Cox 2005) and relativistic pressure of the interstellar magnetic field $B \approx 3 \times 10^{-6}$ ($B^2/8\pi \approx 3.6 \times 10^{-13}\,{\rm dyn\,cm^{-2}}$) combined with the comparable pressure of cosmic rays. All in all, one expects the total medium pressure of $\approx 10^{-12}\,{\rm dyn\,cm^{-2}}$.

Major properties of the model bubble for the ISM density of $0.3\,{\rm cm^{-3}}$ and three choices of the ISM pressure are illustrated by Figure 6 and Table 2. The Table contains input parameters: stellar mass, main-sequence lifetime (Schaller et al. 1992), mass loss rate, wind velocity, ISM pressure and characteristics at the end of the main sequence: the bubble radius, bubble density, and the shell swept-up mass. The adopted wind parameters correspond to the main sequence O-star star with the mass of 20-25 $M_\odot$ (Howarth & Prinja 1989). The main sequence wind ($0.7\,M_\odot$) is thermalized in the termination shock with the radius $r_t \approx 3\,{\rm pc}$ and uniformly fills throughout the cavity volume.

At the He-burning stage (0.79 Myr) the progenitor becomes red supergiant (RSG) and loses matter via the slow wind ($\sim 15\,{\rm km\,s^{-1}}$) with the mass loss rate of about $10^{-6}\,{\rm Myr}$. Almost all the RSG wind ($\approx 1\,M_\odot$) is expected to be swept up, due to the bubble counter-pressure, into the dense shell with a radius of $\approx 1\,{\rm pc}$, significantly smaller than the bubble radius.

4.3. Effect of cloudy ISM

The model of the almost empty WBB in the homogeneous medium is an idealization. The H I 21 cm data (Dickey & Garwood 1989) imply that the mass spectrum of interstellar clouds, both molecular and diffuse atomic, is $dN/dm \propto m^{-\gamma}$ with $\gamma \sim 2$. Therefore, within $\sim 2 \times 10^3\,M_\odot$ of ISM

Table 1. The simplest spectral model fits to the spectrum of the entire SNR in the 0.4-3 keV band.

Model	kT keV	$N_{\rm H}$ $\rm cm^{-2}$	τ $\rm s\,cm^{-3}$	Normalization $\rm cm^{-6}\,pc$	χ^2 (d.o.f.)
`APEC`	0.12 ± 0.004	$(0.61 \pm 0.03) \times 10^{22}$	-	0.95 ± 0.28	366 (318)
`NEI`	0.14 ± 0.02	$(0.57 \pm 0.07) \times 10^{22}$	$(2.1 \pm 0.1) \times 10^{11}$	0.33 ± 0.28	331 (317)
`NEI`, fixed $kT, N_{\rm H}$	1	0.25×10^{22}	$(2.73 \pm 0.15) \times 10^{9}$	$(0.31 \pm 0.07) \times 10^{-2}$	405 (319)

Notes. The abundance is fixed to solar. Note that for the `NEI` model with free $N_{\rm H}$ and kT, all parameters are highly correlated leading to large uncertainties in their values.

Table 2. Parameters of bubble model.

Physical quantity	Numerical value		
M $(M_\odot)$	20		
t_{ms} (Myr)	8.1		
$\dot{M}$ $(M_\odot\,\rm yr^{-1})$	10^{-7}		
v_w $(\rm km\,s^{-1})$	1500		
p $(10^{-12}\,\rm dyn\,cm^{-2})$	0	1	1.5
r_b (pc)	69	38.5	33.9
ρ_b $(10^{-28}\,\rm g\,cm^{-3})$	0.4	2.3	3.4
M_{ds} $(10^3\,M_\odot)$	14.6	2.5	1.7

Notes. The upper part shows adopted input parameters. Lower part displays bubble radius, density, and swept-up mass for the adopted ISM pressure.

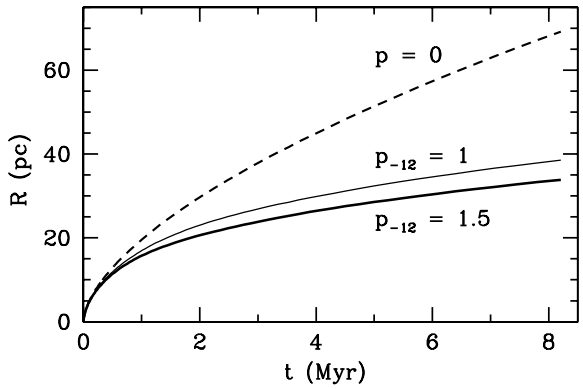

Fig. 6. Radius of the wind-driven bubble formed by the $20\,M_\odot$ star wind at the main sequence. The lines are labeled by the ISM pressure. The model with zero pressure shows the bubble radius based on the analytic solution (Weaver et al. 1977).

swept up by S147, one expects to find a significant number of parsec-size clouds with the density of 10-100 $\rm cm^{-3}$.

The key question is whether some of these clouds avoid disruption by the dense bubble shell and end up inside the bubble. A cloud, in order to cross the shell safely, should have the column density $N_c \approx n_c r_c$ significantly larger than the shell column density $N_s = n r_b/3 \sim 10^{19}\,\rm cm^{-2}$ (for $n = 0.3\,\rm cm^{-3}$ and $r_b = 30\,\rm pc$). A typical cloud that meets this requirement might have the radius of ~ 1 pc and density of $n_c = 30\,\rm cm^{-3}$, in which case $N_c \approx 10^{20}\,\rm cm^{-2}$, by a factor of 10 greater than N_s. Typical column densities of molecular clouds are 1–2 orders of magnitude higher (e.g., Larson 1981; Heyer & Dame 2015). One, therefore, expects to find a significant amount of parsec size interstellar clouds engulfed by the bubble. While these clouds do not affect the bubble dynamics, expanding supernova ejecta will crush clouds, and disperse them into fragments with eventual mixing, thus producing overdensities after their thermalization by the reverse shock.

A cloud with the radius of 1 pc and H density of $30\,\rm cm^{-3}$ has the mass of $\approx 3\,M_\odot$. Whether such clouds can survive a complete stripping due to photoevaporation before the bubble shell crossing depends on the cloud mass m and ionizing flux Q/R^2 as $\dot{m} \propto m^{3/5}(Q/R^2)^{1/5}$ (Bertoldi & McKee 1990). Using the relevant expression from this paper we find that the cloud with the mass $> 1\,M_\odot$ at the distance $r \gtrsim 20\,\rm pc$ survives the photoevaporation during the main sequence lifetime of $20\,M_\odot$ star and thus has a chance to find itself in the bubble.

4.4. Ejecta

To follow the development of the SN explosion within the extended WBB, we explode the pre-SN model based on a $20\,M_\odot$ progenitor evolved by Woosley et al. (2002) from the main sequence up to the onset of core collapse. Unfortunately, Woosley et al. (2002) used so high mass-loss rate that the resultant mass of the corresponding pre-SN was $14.7\,M_\odot$. In turn, we use a moderate mass-loss rate and assume that the $20\,M_\odot$ progenitor lost $\approx 0.7\,M_\odot$ at the main-sequence stage and $\sim 1\,M_\odot$ during the RSG phase. So for our problem, we take the pre-SN model of $18.5\,M_\odot$. To construct the relevant pre-SN model, we modify the original pre-SN model of $14.7\,M_\odot$ by increasing the mass of the hydrogen-rich envelope up to $12.4\,M_\odot$, preserving both the helium core of $6.1\,M_\odot$ and the shape of the profile of density in the hydrogen-rich envelope except for the interface between the helium core and the envelope. The obtained model is exploded with the energy of 10^{51} erg by a piston at the outer edge of the central collapsing core of $1.46\,M_\odot$. The artificial mixing applied to the pre-SN model mimics the intense 3D turbulent mixing at the (C+O)/He and He/H composition interfaces occurring during the explosion (Utrobin et al. 2017). In addition, radioactive ^{56}Ni with mass of $0.07\,M_\odot$, typical for type II SNe, is mixed artificially in velocity space up to nearly $3000\,\rm km\,s^{-1}$. Figure 7 shows the profiles of important chemical elements in the freely expanding ejecta. In light of an analysis of the content of these elements, we investigate the pre-SN models for the progenitor masses in the range from $18\,M_\odot$ to $22\,M_\odot$ (Woosley et al. 2002). In particular, we find that the total

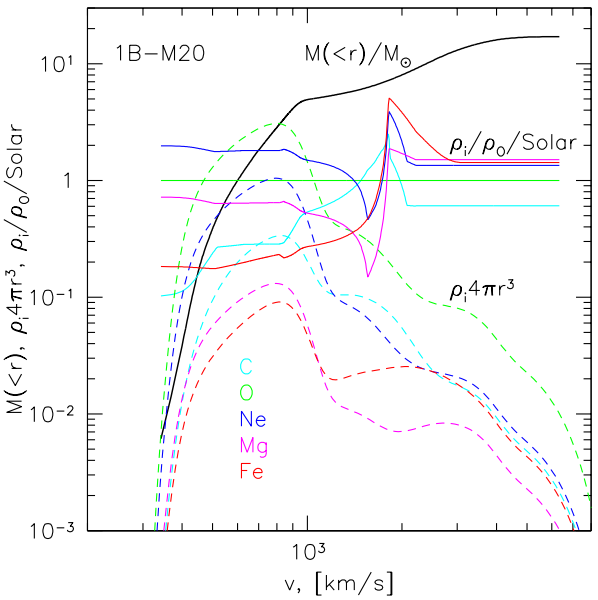

Fig. 7. Ejecta structure for the 1B-M20 model. The black solid line shows the enclosed ejecta mass (for a given velocity). The colored dashed lines show what velocities make the largest contribution to the mass of a given element, namely, the quantity $4\pi r^3 \rho_i$, where ρ_i is the mass density of the i-th element, color-coded as shown in the legend. The colored solid lines show the mass density of the i-th element relative to the mass density of oxygen, normalized by the Solar value.

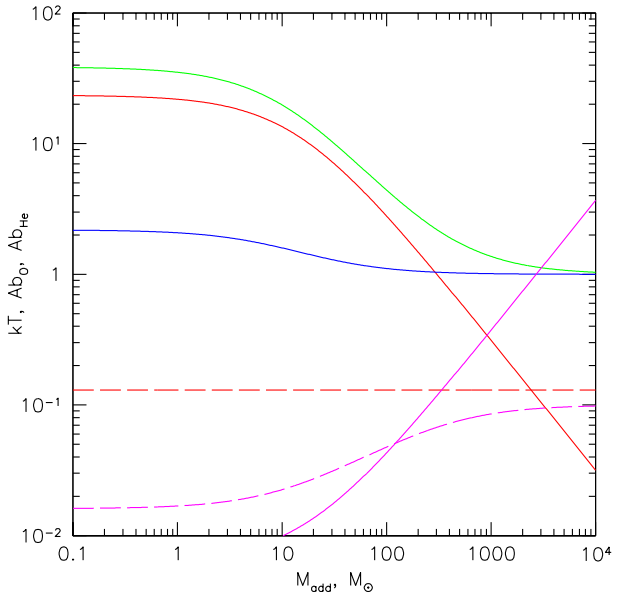

Fig. 8. Dependence of the mean temperature (the solid red line) and He (blue) and O (green) abundances when ejecta are mixed with a given mass ($M_{\rm add}$) of the ISM. For the temperature calculations, we assume that the initial energy $E = 10^{51}$ erg goes entirely into the gas heating, which is fully ionized. For the abundance calculation, we assume solar abundances for the ISM and the 1B-M20 model for the ejecta. For comparison, the horizontal dashed line is the best-fitting temperature for a one-temperature APEC model. The intersection of the red dashed and solid lines suggests a large added mass $\sim 2-3\times10^3\,M_\odot$. Similarly, the dashed magenta line shows the density derived from the normalization of the same model, taking into account the variable abundance of elements (focusing on O). The intersection of the magenta dashed and solid lines suggests a much smaller added mass $\sim 10^2\,M_\odot$. This discrepancy clearly demonstrates that the above set of assumptions (CEI, APEC spectral model, complete mixing of the ejecta and the gas inside the cavity, and $T_e = T_i$) is likely violated.

Mg mass in the ejecta for the $19\,M_\odot$ progenitor is twice as large compared to that of the $20\,M_\odot$ progenitor.

4.5. Morphology of the Hα emission

No doubt that the intricate spaghetti-like structure is a complicated manifestation of the late radiative stage of the SNR liable to different instabilities (Blondin et al. 1998a). The forward shock temperature assuming $T_e = T_i$ is $T = 1.36\times10^5 v_7^2$ K. The cooling time in the postshock gas for the shock with the speed of $100\,{\rm km\,s^{-1}}$ (Lozinskaya 1976) is

$$t_c = \frac{3kT}{4\Lambda n} = 500 v_7^2/n \quad {\rm yr}\,, \qquad (1)$$

where $\Lambda(T) \approx 10^{-21}\,{\rm erg\,s^{-1}\,cm^3}$ (Sutherland & Dopita 1993). With $t_c << t$ the forward shock is indeed radiative.

Pikel'ner (1954) proposed that the Hα filament is a density enhancement at the shock wave intersection that arises in a corrugated shock interacting with an interstellar cloud. Kirshner & Arnold (1979) consider two options for the "filament" — ropelike structure and sheet viewed edge-on — and conclude that filaments are ropelike structures.

We believe that the S147 structure includes both options. The limb brightening is apparent at the shell boundary. However, ropelike filaments seem to be responsible for the majority of spaghetti structures. We share the view of Pikel'ner (1954) that ropelike filaments originate from the intersection of shock waves. The foamy structure of the global radiative shock favors crossing of neighboring protrusions. The shock wave protrusions could originate from either instabilities (Blondin et al. 1998b) or the shock wave propagation in the essentially inhomogeneous ISM. The latter possibility is illustrated by the foamy structure of a model SNR produced by three-dimensional hydrodynamic simulations of a supernova expansion in the inhomogeneous ISM (Martizzi et al. 2015).

The almost circular shape of some filaments suggests that they are produced by the intersection of a convex shock protrusions with a more or less plane shock. In this case, one expects comparable radial and tangential Hα velocity components that should cause an azimuthal dependence of the radial velocity along the circular filament with large impact parameter $p \gtrsim 0.5$ (distance from the shell center in units of the shell radius). The expected behavior of the filament radial velocity could explain the absence of the anti-correlation between the Hα radial velocity and the impact parameter that was established earlier (Lozinskaya 1976; Kirshner & Arnold 1979).

4.6. Spectral model motivated by 1D hydro model

To illustrate specific features of the "shell & cavity" scenario in comparison to the standard Sedov-like situation considered e.g. in Churazov et al. 2021 and Khabibullin

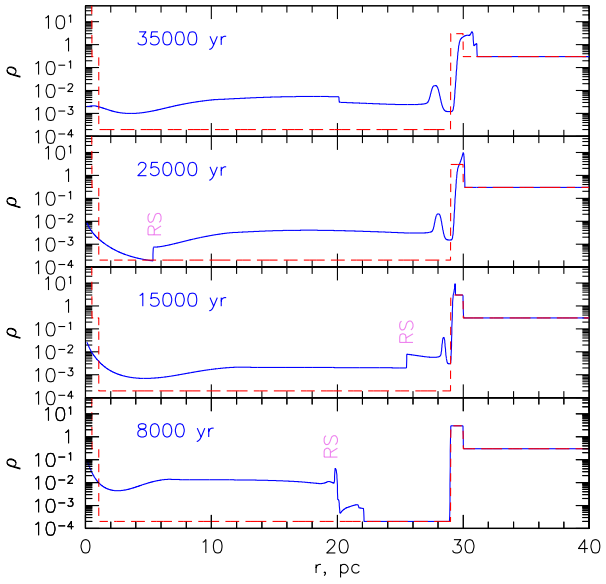

Fig. 9. Propagation of the shock through a low-density cavity bound by a high-density shell.The density is in units of $m_p\,\mathrm{cm}^{-3}$. The dashed line shows the initial density profile, while the blue line shows the density profile evolution. When the forward shock moves through the low-density gas the reverse shock moves outwards. After the collision with the dense shell, the reverse shock propagates deep into the ejecta. These simulations are non-radiative, which is a reasonable approximation for the ejecta and the cavity. The forward shock in the dense gas is radiative, i.e. its structure is not correctly reproduced by these simulations. A jump at 20 pc in the upper panel is the reflected reverse shock that appears in a spherically symmetric 1D model.

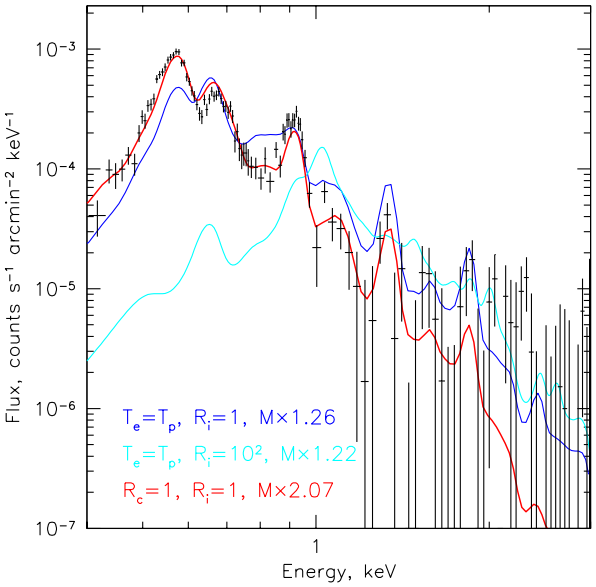

Fig. 10. SNR spectra based on the 1D hydro model shown in Fig. 9 at $t = 3 \times 10^4$ yr. The black crosses are the same data points as in Fig. 5. The models (blue, cyan, and red curves) differ in the level of deviation from the CIE state with $T_e = T_i$. In particular, the blue curve corresponds to instantaneous electron/proton equilibration, i.e. $T_\mathrm{e} = T_\mathrm{p} = T_\mathrm{i}$ and self-consistently calculated evolution of the ionization balance. The cyan curve shows the case when the rate of all collisional processes is artificially increased by a factor of 100 (i.e. this case is close to the CIE state with $T_e = T_i$. The red curve shows the case when most of the energy downstream of the shock goes into protons and the electron/proton equilibration proceeds via pure Coulomb collisions. In all cases, the ionization balance is followed in each shell according to the time evolution of electron temperature. The model spectra were integrated along the line of sight at a projected distance of 0.35 times the radius of the SNR.

et al. 2023, we run a 1D (spherical symmetry) pure hydrodynamic simulation using the `PLUTO` code (Mignone et al. 2007). In this model, homologously expanding ejecta collide with a dense shell. The mass and kinetic energy of the ejecta are set to $15.6\,M_\odot$ and 10^{51} erg, respectively. These parameters broadly agree with the progenitor models discussed above. The density of the ejecta declines with the expansion velocity as v^{-8}. The initial density distribution of the ambient gas is shown in Fig. 9 with the red dashed line. A dense shell, ~ 1 pc thick, has a radius of ~ 30 pc and the mass density $5 \times 10^{-24}\,\mathrm{g\,cm}^{-3}$. It is embedded in a homogeneous ISM with density $5 \times 10^{-25}\,\mathrm{g\,cm}^{-3}$ and the sound speed of $10\,\mathrm{km\,s}^{-1}$. Inside the shell, the density in the cavity is very low $\sim 3 \times 10^{-28}\,\mathrm{g\,cm}^{-3}$. Initially, the pressure is the same in the ISM, the shell, and the cavity.

The time evolution of the gas density over 35 kyr is shown in Fig. 9. Due to the very low density in the cavity, the ejecta almost freely expand over the first ~ 10 kyr. During this period, the reverse shock is not very prominent and the bulk of the ejecta remains cold (see the bottom panel in Fig. 9). Once the ejecta reach the dense shell, a strong reverse shock starts propagating inwards and eventually reaches the center (two middle panels in the same figure). The final stage features a cavity filled with hot and low-density gas (a mixture of the ejecta and the initial gas content of the cavity) and a forward shock slowly propagating through the dense and cold shell. This forward shock can have a complicated structure depending on the properties of the shell. In the scenario considered here, the forward shock powers the H_α filaments of S147, while the hot gas in the cavity produces X-ray emission.

While the parameters used in the model might not match the properties of the S147 progenitor and environment accurately, it is interesting to compare the X-ray spectra expected in this simple model with the data. This can be done in several steps. One needs to calculate the time evolution of the electron temperature in each radial shell, evolve ionization fractions, calculate the energy-dependent emissivity, and integrate it along the line of sight. To this end, we follow the same approach as in Churazov et al. (2021); Khabibullin et al. (2023). Here, for spectra calculations, the `MEKAL` model (Mewe et al. 1985; Liedahl et al. 1995) as implemented in the `XSPEC` package (Arnaud 1996) was used in combination with the evolving ion fractions. For the electron temperature, the following three cases have been considered.

1. $T_e(r,t) = T_h(r,t)$, where r and t are the shell radius and time, respectively, $T_h(r,t)$ is the fluid temperature in the hydro run for a reasonable choice of the mean

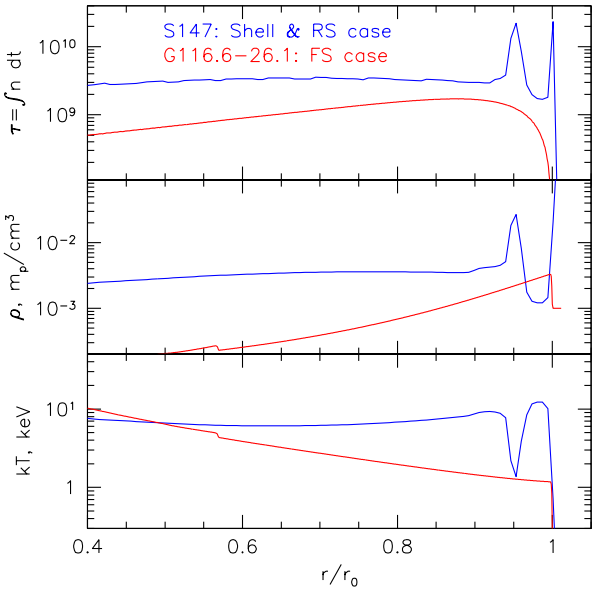

Fig. 11. Radial profile of the ionization parameter $\tau = \int ndt$ (the blue line, top panel) based on 1D model, when most of the X-ray emission is coming from the gas reheated by the reverse shock following the collision of the ejects with the dense shell. The radius is normalized by the characteristic radius r_0, which is approximately equal to the radius of the forward shock. Small amplitude irregularities in the black curve at $r/r_0 \lesssim 0.8$ are the artifact of τ calculations. For comparison, the red curve shows the case when the X-ray emission is mostly due to the gas heated by the forward shock (the parameters for G116-26.1 are used here). Two spikes in τ are clearly visible at large radii. The outmost spike is likely an artifact of our non-radiative run near the inner boundary of the dense shell. The other spike is due to the less dense gas (outer layers of ejecta) that has a relatively high temperature and can contribute to X-ray emission. In this region, oxygen might be completely ionized, but the lines of Si and Fe might be present, as illustrated in Fig. 12. The middle and bottom panels compare the model density and temperature profiles for these two SNRs.

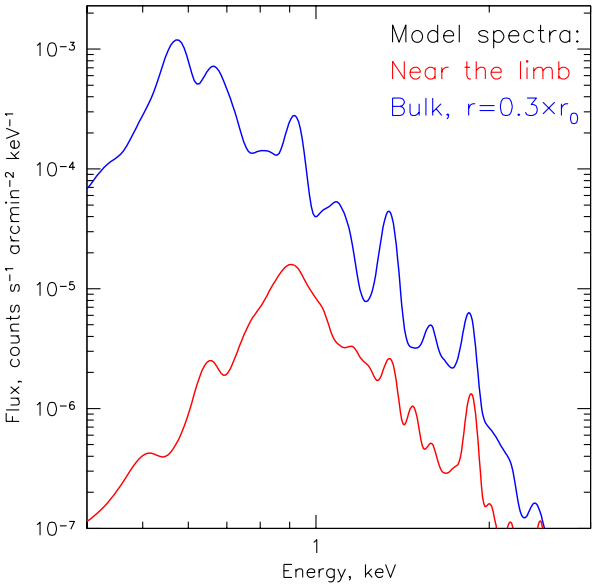

Fig. 12. Projected model spectra for the SN-in-the-WBB scenario near the limb (red) and towards the inner parts of the nebula (blue). The gas near the limb has a larger ionization parameter than the bulk of the volume and, accordingly, lacks oxygen lines, but features the lines of Ne, Fe, and Si. In reality, S147 is far from spherical symmetry and a mixture of components with a range of ionization parameters should be observed.

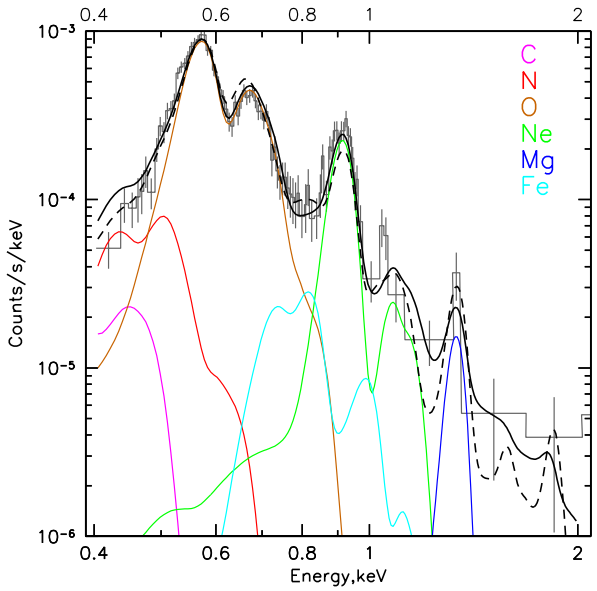

Fig. 13. Contribution of individual elements to the S147 X-ray spectrum in the `NEI` model (black solid line). The dashed line shows the spectrum predicted by the 1D-hydro model.

molecular weight μ. This case corresponds to the equal temperature of all particles (the blue line in Fig.10).

2. In the second case, we assume that most of the energy downstream of the shock goes into protons and electron/proton equilibration proceeds via pure Coulomb collisions (the red line).
3. Finally, the last model also involves Coulomb collisions, but the rate of collisions is artificially increased by a factor of 100 (the cyan line). This model is expected to be close to the first model.
4. For the 2nd version of the model-spectrum plot: Finally, the last model assumes $T_e(r,t) = T_h(r,t)$ similar to the first model, but the rates of ionization/recombination are artificially increased by a factor of 100 (the cyan line). This model is expected to be closer to CIE than other models.

Fig. 10 shows that the second model fits the data surprisingly well, given the simplicity of the model. In this figure, the model spectrum corresponds to the projected distance $r_p = 0.35r_s$ from the center of the SNR, where r_s is the forward shock radius, although the dependence on the value of r_p is rather weak. For solar abundance of heavy elements, the normalization of the predicted surface brightness is a factor of ~ 2 lower than the observed spectrum. Increasing abundance in the model by a factor of 2 brings the model very close to the observed spectrum. Large values of the abundance would overpredict the flux. As follows

from Fig. 8, the full mixing scenario with the small amount of mass (as used in our 1D model) would lead to a larger abundance of Oxygen. This suggests that in S147, most of the X-ray emission is associated with the outer layers of the ejecta. The total energy "problem" apparent in Fig. 8 is easily resolved in the model with $T_i \gg T_e$ with the standard rates of temperature equilibration via Coulomb collisions.

The shell model adopted here has an interesting implication for the temperature and ionization structure of the SNR as seen in X-rays. Indeed, since much of the X-ray emission is expected to come from the gas reheated by the reverse shock, the profile of the ionization parameter $\tau = \int ndt$ can be different from the standard case of a Sedov-like solution, where the forward shock is responsible for X-ray emission. This is illustrated in Fig. 11, which shows the radial profiles of τ for S147 and G116-26.1. The latter is used to illustrate the forward-shock-dominated model, when the ambient medium is uniform. The same `PLUTO` code was used for this problem (see Churazov et al. 2021, for details on the initial conditions). In both cases, the calculation of τ for a given fluid element begins when this fluid element goes through a shock and is heated to temperatures ~ 1 keV.

For S147, the value of τ is almost constant through the entire ejecta, unlike the G116-26.1 case. In addition, S147 might have a spike in τ behind the position of the forward shock, due to the outer layers of ejecta that were reheated by the second reverse shock (see Fig. 9. Depending on the initial gas density in the cavity, such a spike might arise due to this gas. What is needed is a moderately dense gas that can be reheated by reverse shock to high temperatures. This combination of parameters would drive τ up and power X-ray emission. If this model is correct, near the limb of S147 one can expect to find hotter and more highly ionized gas than in the rest of the nebula. This is illustrated in Fig.12.

4.7. Abundances

Most of the above analysis was done assuming solar abundance (or solar mix of abundances) in the X-ray emitting gas. As illustrated by Figs.7 and 8 the abundance of oxygen relative to hydrogen is sensitive to the amount of "cavity gas" added to the ejecta and to the assumption that entire ejecta are mixed with this gas and all this gas contributes to the observed X-ray emission. Given the complexity of S147, this is likely a severe simplification. On the other hand, the variations of abundances relative to oxygen are less extreme, in the range of 0.3-2 for elements from C to Fe, when averaged over the entire ejecta. Fig. 13 shows the contributions of individual elements to the `NEI` model with solar abundances. Clearly, the underabundance of C and N in the adopted ejecta model might affect the absorbing column density derived from the X-ray spectra. For the heavier elements, like Ne, Mg, and Si, a factor of ~ 2 uncertainty (or larger) is feasible. Our conclusion here is that allowing abundance variations, coupled with uncertainties in T_e and non-equilibrium ionization would allow for an even better fit to the observed X-ray spectra, although the degeneracy between parameters would lead to large uncertainties in the derived parameters.

4.8. Non-thermal components in S147

While no signature of non-thermal X-rays was found in the eROSITA data analysis it is still worth discussing the presence of non-thermal components in multiwavelength data since these are needed to justify the SNR model presented above. Indeed, the shocks of velocity $\gtrsim 100$ km s^{-1}at the current stage of S147 evolution are not fast enough to allow particle acceleration above TeV energies with magnetic field amplification which are needed to extend the synchrotron radiation spectra to X-rays as it is likely the case in young SNRs (see e.g. Bykov et al. (2018); Vink (2020)). However, GeV regime electrons and protons can be accelerated and confined in S147 providing the observed radio and gamma-ray emission, and may contain a sizable energy density $\sim$ 10% of the total gas pressure.

The radio image of S147 is composed of "filaments", associated with Hα filaments, and a diffuse component. The appearance of radio filaments has the same origin as the Hα filaments, i.e., the limb brightening. The overall integrated flux density is 34.8 ± 4 Jy at 11 cm (Xiao et al. 2008). The spectrum is flat ($\alpha = -0.30 \pm 0.15, F \propto \nu^{\alpha}$) in the range of $\lesssim 1.5$ GHz and gets steeper at higher frequencies (Xiao et al. 2008). The observed flux at 11 cm can be described based on a simple model of a homogeneous spherical radio-emitting shell filled with cosmic rays and magnetic fields. The outer radius of the SNR is $R_2 = 39$ pc and the inner radius $R_1 = 0.9R_2$ (adopting the SNR distance of 1.3 kpc). For initial estimations, one can assume the equipartition between cosmic rays and magnetic field energy density ($U_{cr} = B^2/8\pi$) with a typical electron-to-proton ratio $\xi_{e,p} = U_e/U_p = 0.01$. The energy spectrum of relativistic electrons responsible for the radio emission is assumed to be $dN/dE = KE^{-p}$ with $p = 2$ in the GeV range consistent with that expected in the diffusive shock acceleration model.

The observed flux at 11 cm then is reproduced for the total energy of relativistic component $E_{rel} = 9{\times}10^{49}$ erg, suggesting the energy density $U_{rel} \approx 4.5 \times 10^{-11}$ erg cm^{-3} and magnetic field of about $24\,\mu G$. Remarkably, the relativistic pressure in this model $p_{rel} \approx 1.5{\times}10^{-11}$ dyn cm^{-2} turns out to be a sizable fraction of the upstream dynamical pressure. Indeed, for $v_s = 100$ km s^{-1} and preshock density $n_0 = 0.3$ cm^{-3} the dynamical pressure is $p_{dyn} = \rho_0 v^2 \approx 7 \times 10^{-11}$ dyn cm^{-2} with the ratio $\xi = p_{rel}/p_{dyn} = 0.2$. The estimates above assumed a homogeneous radio-emitting shell, while the radio images revealed a filamentary structure of the SNR, probably indicating a highly intermittent structure of magnetic fields, which can be probed by combining radio and gamma-ray data.

Non-thermal pressure estimated from radio emission of relativistic electrons in SNR can be compared with that derived from the gamma-ray data. Fermi-LAT observations of S147 by Katsuta et al. (2012) in the energy range 0.2-10 GeV revealed an extended gamma-ray source of luminosity $\sim 1.3 \times 10^{34}$ erg s^{-1} at the assumed distance 1.3 kpc. They pointed out an apparent correlation of the gamma-ray emission with the Hα filaments and found no signal associated with the pulsar PSR J0538+2817. These authors concluded that re-acceleration and further compression of the preexisting cosmic rays can explain the gamma-ray data. Within the hadronic scenario of the S147 gamma-ray origin, the derived gamma-ray luminosity would correspond to the total energy in CR protons $\sim 10^{49}/n_a$ ergs (where

n_a which is measured in cm^{-3} is the average number density of the gas in a single zone homogeneous model). Later on, Suzuki et al. (2022) obtained the 1-100 GeV Fermi-LAT gamma-ray luminosity of S147 $\sim 6 \times 10^{32}$ erg s^{-1} and the spectrum fitted with a broken power law model which has a photon index of about 2.14-2.18 below the break energy ~ 1.4 GeV and a much softer spectrum of a photon index ~ 3.9 above the break which extends down to the cutoff energies > 21 GeV. The radio spectrum discussed above is broadly consistent with that of the low energy gamma-rays having in mind that the momentum distributions of both electrons and protons accelerated by diffusive shock acceleration are expected to have the same power law index (of about 2) in the GeV energy range. The break in the gamma-ray spectrum at 1.4 GeV detected by Fermi-LAT within the hadronic model roughly corresponds to a break in the proton spectrum at about 14 GeV. Then assuming that the electron spectrum has a break at the same energy from the position of the break frequency in the radio spectrum given by Xiao et al. (2008) one can estimate the magnetic field in the diffuse emission to be about μG. If both the filaments and diffuse regions are embedded in a single population of DSA accelerated electrons then the lack of observed break in the radio filaments till 40 GHz implies the magnetic fields there to be above 40 μG.

5. Discussion

Several generic scenarios of "a supernova-in-a-cavity" type have been modeled before (e.g. Tenorio-Tagle et al. 1990) and suggested for S147 (e.g. Reich et al. 2003). Here, to make the formulation of the model more complete, we assume that the cavity is created by the winds of a sufficiently massive star during its Main Sequence (MS) evolutionary phase. The presence of the pulsar and the size of the H_α nebula together suggest the progenitor mass of order 20 $M_\odot$, leading to a well-constrained model. It appears that this model can explain many X-ray properties of S147. In particular, this model naturally predicts X-ray spectra that feature lines of Mg and Si along with the lines of OVII and OVII, and does not require excess low-energy absorption. It also predicts that the X-ray emitting gas extends all the way to the H_α-emitting shell.

We note here, that a qualitatively similar picture is expected if the cavity, needed to reduce the SNR age, is produced by another mechanism rather than MS-driven WBB (e.g Gvaramadze 2006). As long as the mass of the dense shell is large and the cavity is filled with low-density gas, most of the conclusions stay unchanged. From this point of view, the only important parameter for modeling the expected X-ray emission is the observed size of the SNR, which in this model is essentially the original size of the cavity.

A natural implication of this model is that the ions are much hotter in the interior of the dense shell than electrons and that the ionization equilibrium is not achieved. A direct test of these predictions should be possible with forthcoming X-ray bolometers like XRISM (XRISM Science Team 2020), ATHENA (Nandra et al. 2013), and LEM (Kraft et al. 2022). Detection of very broad lines of O, Ne, Mg, and Si ions would be a decisive test of the S147 "hot" scenario. The lack of broadening will instead support the "cold" model. For the time being, S147 can be considered a promising candidate for the list of objects featuring $T_i \gg T_e$ (see, e.g. Raymond et al. 2023). Constraints on weaker lines, e.g. Fe XVII, from forthcoming bolometers would also tighten the constraints on the NEI models.

As a caveat, we mention that it is not entirely clear if the modest abundance enhancement inferred from the observed flux of the NEI plasma represents a serious challenge to the hot model. Potentially, the abundance can be much higher. Yet another simplification used here is the assumption of spherical symmetry, which clearly does not apply to S147.

Another interesting question is how often one could find SN II exploded inside the WBB? The answer depends on the progenitor velocity (v_*) relative to the ISM. The dispersion velocity of OB-stars is $\sim 10\,\mathrm{km\,s^{-1}}$, (Bobylev et al. 2022), although well known RSG Betelgeuse ($M \sim 15\,M_\odot$) shows an even larger velocity wrt ISM, $v_* \approx 30\,\mathrm{km\,s^{-1}}$ (Ueta et al. 2008). The $20\,M_\odot$ star with the velocity of $10\,\mathrm{km\,s^{-1}}$ wrt ISM will run 80 pc to the end of the main sequence lifetime and will reside near the bubble frontal boundary at the distance comparable to the termination shock radius (~ 3 pc). At the subsequent helium burning stage (0.8×10^6 yr) the star will run another 8 pc and escape the bubble. We conclude that most of SNe II explode outside their WBB and S147 should be considered as a rare example of SN II exploded in the WBB presumably owing to the low progenitor velocity with respect to ISM. This might explain a highly unusual Hα appearance of S147, although Vela SNR seems to show a somewhat similar Hα pattern (see Gvaramadze 1999, for a discussion of SNR-in-cavity scenario for the Vela SNR). Yet in Vela, we do not see ring-like structures in the SNR central part unlike in S147, which suggests that Vela and S147 are not identical. Interestingly, a finite progenitor velocity of $\sim 1\,\mathrm{km\,s^{-1}}$ could result in the supernova offset with respect to the bubble center (Mackey et al. 2015), which in turn could also bring about the observed deviations from sphericity of S147.

In the model discussed here, the age estimate based on the kinematics of the pulsar J0538+2817 broadly agrees with the observed characteristics of S147. This strengthens the association of the pulsar with the supernova. This implies that the pulsar is plausibly inside the SNR and might affect its properties. Some tantalizing hints might be spotted in Fig.4. This will be the subject of a separate study.

6. Conclusions

We argue that new X-ray data of SRG/eROSITA lends support for S147 being a type II SN exploded in a low-density cavity. The main features of this scenario can be summarized as follows.

- The supernova went off in a cavity that was formed during MS stage of a $\sim 20\,M_\odot$ star is a plausible scenario that leads to the formation of the cavity.
- This star had a relatively small velocity relative to the ambient ISM. As a result, a dense shell around the cavity is approximately spherical and the SN explosion was not far from its center.
- The age is consistent with that derived from the kinematics of the pulsar PSR J0538+2817 (~ 35 kyr).
- The X-ray emission comes predominantly from the gas inside the cavity. The gas there has $T_e \ll T_i$ and is not in the collisional ionization equilibrium. This gas was reheated by reverse shock following the collision of the ejecta with the dense shell. A large fraction of ejecta

kinetic energy is "reflected" by the shell back into the cavity.
- The H_α and narrow radio filaments are associated with the radiative forward shock that propagates through the dense shell.
- Diffuse radio is due to the particles accelerated at the radiative shocks, but now living in an environment with a much weaker magnetic field.
- Eventual fate of an SNR in the cavity: hot and low-density gas bubble (no oxygen lines) until it dissolves in the ISM.
- Other scenarios for the cavity formation might be consistent with X-ray data, as long as the mass of the dense shell is large.

Finally, we note that S147 has a very complicated morphology and spectra from radio to gamma-rays and the above model is not intended to reproduce all this complexity. However, we believe that it captures some of the essential features of this remarkable SNR.

Acknowledgments

This work is partly based on observations with the eROSITA telescope onboard SRG space observatory. The SRG observatory was built by Roskosmos in the interests of the Russian Academy of Sciences represented by its Space Research Institute (IKI) in the framework of the Russian Federal Space Program, with the participation of the Deutsches Zentrum für Luft- und Raumfahrt (DLR). The eROSITA X-ray telescope was built by a consortium of German Institutes led by MPE, and supported by DLR. The SRG spacecraft was designed, built, launched, and is operated by the Lavochkin Association and its subcontractors. The science data are downlinked via the Deep Space Network Antennae in Bear Lakes, Ussurijsk, and Baikonur, funded by Roskosmos.

The development and construction of the eROSITA X-ray instrument was led by MPE, with contributions from the Dr. Karl Remeis Observatory Bamberg & ECAP (FAU Erlangen-Nuernberg), the University of Hamburg Observatory, the Leibniz Institute for Astrophysics Potsdam (AIP), and the Institute for Astronomy and Astrophysics of the University of Tübingen, with the support of DLR and the Max Planck Society. The Argelander Institute for Astronomy of the University of Bonn and the Ludwig Maximilians Universität Munich also participated in the science preparation for eROSITA. The eROSITA data were processed using the eSASS/NRTA software system developed by the German eROSITA consortium and analysed using proprietary data reduction software developed by the Russian eROSITA Consortium.

IK acknowledges support by the COMPLEX project from the European Research Council (ERC) under the European Union's Horizon 2020 research and innovation program grant agreement ERC-2019-AdG 882679. A.M.B. was supported by the RSF grant 21-72-20020. His modeling was performed at the Joint Supercomputer Center JSCC RAS and at the Peter the Great Saint-Petersburg Polytechnic University Supercomputing Center. Rashid Sunyaev acknowledges the support of dvp - N/A pertaining to Member Notification Merge at the Institute for Advanced Study.

This research made use of `Montage`[1]. It is funded by the National Science Foundation under Grant Number ACI-1440620, and was previously funded by the National Aeronautics and Space Administration's Earth Science Technology Office, Computation Technologies Project, under Cooperative Agreement Number NCC5-626 between NASA and the California Institute of Technology.

References

Anderson, S. B., Cadwell, B. J., Jacoby, B. A., et al. 1996, ApJ, 468, L55
Arnaud, K. A. 1996, in Astronomical Society of the Pacific Conference Series, Vol. 101, Astronomical Data Analysis Software and Systems V, ed. G. H. Jacoby & J. Barnes, 17
Bertoldi, F. & McKee, C. F. 1990, ApJ, 354, 529
Blondin, J. M., Wright, E. B., Borkowski, K. J., & Reynolds, S. P. 1998a, ApJ, 500, 342
Blondin, J. M., Wright, E. B., Borkowski, K. J., & Reynolds, S. P. 1998b, ApJ, 500, 342
Bobylev, V. V., Bajkova, A. T., & Karelin, G. M. 2022, Astronomy Letters, 48, 243
Bykov, A. M., Ellison, D. C., Marcowith, A., & Osipov, S. M. 2018, Space Sci. Rev., 214, 41
Chatterjee, S., Brisken, W. F., Vlemmings, W. H. T., et al. 2009, ApJ, 698, 250
Chevalier, R. A. & Liang, E. P. 1989, ApJ, 344, 332
Churazov, E. M., Khabibullin, I. I., Bykov, A. M., et al. 2021, MNRAS, 507, 971
Cox, D. P. 2005, ARA&A, 43, 337
Denoyer, L. K. 1974, AJ, 79, 1253
Dickey, J. M. & Garwood, R. W. 1989, ApJ, 341, 201
Dwarkadas, V. V. 2023, Galaxies, 11, 78
Fuerst, E. & Reich, W. 1986, A&A, 163, 185
Gaze, V. F. & Shajn, G. A. 1952, Izvestiya Krymskoj Astrofizicheskoj Observatorii, 9, 52
Greimel, R., Drew, J. E., Monguió, M., et al. 2021, A&A, 655, A49
Gvaramadze, V. 1999, A&A, 352, 712
Gvaramadze, V. V. 2006, A&A, 454, 239
Heger, A., Fryer, C. L., Woosley, S. E., Langer, N., & Hartmann, D. H. 2003, ApJ, 591, 288
Heyer, M. & Dame, T. M. 2015, ARA&A, 53, 583
Howarth, I. D. & Prinja, R. K. 1989, ApJS, 69, 527
Hughes, J. P. 1987, ApJ, 314, 103
Katsuta, J., Uchiyama, Y., Tanaka, T., et al. 2012, ApJ, 752, 135
Khabibullin, I. I., Churazov, E. M., Bykov, A. M., Chugai, N. N., & Sunyaev, R. A. 2023, MNRAS, 521, 5536
Khabibullin, I. I., Churazov, E. M., Bykov, A. M., Chugai, N. N., & Zinchenko, I. I. 2024, MNRAS, 527, 5683
Kirshner, R. P. & Arnold, C. N. 1979, ApJ, 229, 147
Kochanek, C. S., Raymond, J. C., & Caldwell, N. 2024, arXiv e-prints, arXiv:2403.13892
Kraft, R., Markevitch, M., Kilbourne, C., et al. 2022, arXiv e-prints, arXiv:2211.09827
Kramer, M., Lyne, A. G., Hobbs, G., et al. 2003, ApJ, 593, L31
Larson, R. B. 1981, MNRAS, 194, 809
Liedahl, D. A., Osterheld, A. L., & Goldstein, W. H. 1995, ApJ, 438, L115
Lozinskaia, T. A. 1976, AZh, 53, 38
Lozinskaya, T. A. 1976, Soviet Ast., 20, 19
Mackey, J., Gvaramadze, V. V., Mohamed, S., & Langer, N. 2015, A&A, 573, A10
Martizzi, D., Faucher-Giguère, C.-A., & Quataert, E. 2015, MNRAS, 450, 504
Mewe, R., Gronenschild, E. H. B. M., & van den Oord, G. H. J. 1985, A&AS, 62, 197
Michailidis, M., Pühlhofer, G., Becker, W., et al. 2024, arXiv e-prints, arXiv:2401.17312
Mignone, A., Bodo, G., Massaglia, S., et al. 2007, ApJS, 170, 228
Nandra, K., Barret, D., Barcons, X., et al. 2013, arXiv e-prints, arXiv:1306.2307
Ng, C. Y., Romani, R. W., Brisken, W. F., Chatterjee, S., & Kramer, M. 2007, ApJ, 654, 487
Pikel'ner, S. 1954, Izvestiya Ordena Trudovogo Krasnogo Znameni Krymskoj Astrofizicheskoj Observatorii, 12, 93

[1] `http://montage.ipac.caltech.edu`

Predehl, P., Andritschke, R., Arefiev, V., et al. 2021, A&A, 647, A1
Raymond, J. C., Ghavamian, P., Bohdan, A., et al. 2023, ApJ, 949, 50
Reich, W., Zhang, X., & Fürst, E. 2003, A&A, 408, 961
Ren, J.-J., Liu, X.-W., Chen, B.-Q., et al. 2018, Research in Astronomy and Astrophysics, 18, 111
Romani, R. W. & Ng, C. Y. 2003, ApJ, 585, L41
Schaller, G., Schaerer, D., Meynet, G., & Maeder, A. 1992, A&AS, 96, 269
Silk, J. & Wallerstein, G. 1973, ApJ, 181, 799
Sofue, Y., Furst, E., & Hirth, W. 1980, PASJ, 32, 1
Sunyaev, R., Arefiev, V., Babyshkin, V., et al. 2021, A&A, 656, A132
Sutherland, R. S. & Dopita, M. A. 1993, ApJS, 88, 253
Suzuki, H., Bamba, A., Yamazaki, R., & Ohira, Y. 2022, ApJ, 924, 45
Taylor, A. R., Gibson, S. J., Peracaula, M., et al. 2003, AJ, 125, 3145
Tenorio-Tagle, G., Bodenheimer, P., Franco, J., & Rozyczka, M. 1990, MNRAS, 244, 563
Tenorio-Tagle, G., Rozyczka, M., Franco, J., & Bodenheimer, P. 1991, MNRAS, 251, 318
Ueta, T., Izumiura, H., Yamamura, I., et al. 2008, PASJ, 60, S407
Utrobin, V. P., Wongwathanarat, A., Janka, H.-T., & Müller, E. 2017, ApJ, 846, 37
Vink, J. 2020, Physics and Evolution of Supernova Remnants (Springer Nature)
Weaver, R., McCray, R., Castor, J., Shapiro, P., & Moore, R. 1977, ApJ, 218, 377
Woosley, S. E., Heger, A., & Weaver, T. A. 2002, Reviews of Modern Physics, 74, 1015
Xiao, L., Fürst, E., Reich, W., & Han, J. L. 2008, A&A, 482, 783
XRISM Science Team. 2020, arXiv e-prints, arXiv:2003.04962

3.4 M. Michailidis, G. Pühlhofer, A. Santangelo, W. Becker, M. Sasaki. A look at the high energy aspects of the supernova remnant G309.8+00.0 with eROSITA and *Fermi*-LAT. In: Astronomy & Astrophysics (A&A), accepted (June 2024)

Astronomy & Astrophysics manuscript no. output
June 10, 2024

Article V

A look at the high energy aspects of the supernova remnant G309.8+00.0 with eROSITA and *Fermi*-LAT

M. Michailidis[1], G. Pühlhofer[1], A. Santangelo[1], M. Sasaki[2], W. Becker[3,4]

[1] Institut für Astronomie und Astrophysik Tübingen (IAAT), Sand 1, 72076 Tübingen, Germany
e-mail: michailidis@astro.uni-tuebingen.de
[2] Dr. Karl Remeis Observatory, Erlangen Centre for Astroparticle Physics, Friedrich-Alexander-Universität Erlangen-Nürnberg, Sternwartstraße 7, 96049 Bamberg, Germany
[3] Max-Planck-Institut für extraterrestritche Physik, Giessenbachstrasse, 85748 Garching, Germany
[4] Max-Planck Institut für Radioastronomie, Auf dem Hügel 69, 53121 Bonn, Germany

Received 17 April 2024 / Accepted 05 June 2024

ABSTRACT

Supernova remnant (SNR) detection along the Galactic plane poses a number of challenges. A diffuse X-ray emission component emanating from unidentified sources on the Galactic plane further complicates such detection in X-rays. Due to the presence of dense dust clouds along the Galactic plane, X-ray photons are also subject to high absorption. Similarly, diffuse signals from the Galactic plane cause γ-ray contamination from the signal of individual objects. The SNR G309.8+00.0 lies exactly on the Galactic plane, with its center coinciding with galactic latitude (b)=0°. In this paper we report the first detection of the SNR G309.8+00.0 in X-rays and γ-rays, using stacked data from the first four consecutive eROSITA (extended ROentgen Survey Imaging Telescope Array onboard the Russian-German Spektrum Roentgen Gamma (SRG)) all-sky surveys (eRASS:4) and $\sim$ 15.5 yr of Pass 8 data recorded from *Fermi*-LAT, respectively. The SNR appears to have an elliptical shape of $0^\circ.43 \times 0^\circ.32$ size in both radio synchrotron and X-ray data. The SNR's emission exhibits a shell-like morphology and good spatial correlation in both energy bands. The X-ray emission is solely detected in the 1-2 keV energy band (subject to strong absorption at soft X-rays) and the spectral analysis results of eRASS:4 data present a purely thermal SNR with a high absorption column density $3.1^{+0.7}_{-0.5} \cdot 10^{22}$ cm^{-2} and a temperature of 0.34 ± 0.1 keV. Although the thermal plasma appears to be in equilibrium, the limited statistics do not allow us to exclude non-equilibrium models. The X-ray spectral analysis of the remnant resulted in the detection of relatively (given the limited statistics) prominent Mg triplet lines at 1.33-1.47 keV and silicon (Si XIII) at 1.74-1.9 keV energies. In combination with optical extinction data, the absorption column density values derived from the remnant's spectral analysis support a remnant's distance greater than 6 kpc, rather than a 3.12 kpc distance as reported in the literature, and yield an age of $1 - 3.5 \cdot 10^5$ yr. Employing $\sim$ 15.5 yr of *Fermi*-LAT γ-ray data at and around the remnant's vicinity we confirm the detection of the to-date unidentified 4FGL J1349.5-6206c source that can either be modeled as a single source or a conglomerate of multiple distinct source components. In the latter case, the detailed inspection of the *Fermi*-LAT γ-ray data in the direction of the remnant allows us to decompose the 4FGL J1349.5-6206c source into four point-like components, among which one is spatially coincident with the SNR G309.8+00.0 shell. We detect the component that spatially coincides with the SNR with a significance of 5.8σ above 1 GeV with *Fermi*-LAT and thus argue that the SNR G309.8+00.0 likely represents at least a significant portion (if not all) of the emission from the 4FGL J1349.5-6206c γ-ray source, detected with 9.8σ significance $>$ 1 GeV with *Fermi*-LAT.

Key words. supernova remnants (Individual object: SNR G309.8+00.0) — multiwavelength study — cosmic rays: acceleration

1. Introduction

Since the last two decades, Galactic supernova remnants (SNRs) have been confirmed to accelerate particles (electrons and nuclei) up to the highest energies. The first detection of X-ray synchrotron emission from SNRs was reported by Koyama et al. (1995), and since then, several tens of Galactic SNRs have been detected to be purely non-thermal in X-rays or to exhibit at least a non-thermal component in their X-ray spectrum. In the last decade, a few tens of Galactic SNRs have been detected at even higher energies, i.e., GeV/TeV energies (Acero et al. 2016; H. E. S. S. Collaboration et al. 2018b,a). Accelerated TeV electrons may emit X-rays through synchrotron (Koyama et al. 1995), but may also emit γ-rays through Inverse Compton (IC). In addition, in a number of γ-ray SNRs the characteristic pion-decay signature has been detected providing evidence for proton (nuclei) acceleration from SNRs (Ackermann et al. 2013). Lately, there is ample evidence, for example Michailidis et al. (2024a,b), Khabibullin et al. (2024) and Guo & Liu, in prep., that an increasing number of relatively old SNRs observed in γ-rays, of hadronic origin, are characterized by a purely thermal emission component in X-rays and the absence of a non-thermal X-ray component. Since the same population of relativistic TeV electrons is responsible for both X-ray synchrotron emission and γ-ray emission of leptonic origin, it is not surprising that the latter assertion holds, e.g., refer to HESS J1614-518 (Pühlhofer et al., in prep.), a newly identified SNR with a non-thermal X-ray spectrum accompanied by γ-ray emission of leptonic origin. However, no such Universal correlation has been confirmed across all γ-ray SNRs. Although only a small fraction, of the total number of detected Galactic SNRs, $\sim$ 300 – Green catalog (Green 2019), SNRcat[1] (Ferrand & Safi-Harb 2012), of

[1] http://snrcat.physics.umanitoba.ca/

the order of $\sim 10\%$ of Galactic SNRs are observable in γ-rays to date, the study of those objects in the highest energies and the detection and identification of new SNRs emitting in γ-rays is of great importance on gaining further insight into the particle acceleration in our Galaxy and the fraction of the energy budget of the cosmic-ray (CR) spectrum that is attributed to those objects.

X-ray and γ-ray emission from Galactic SNRs is difficult to detect when the latter objects lie along the Galactic plane. The reason for this is that X-ray photons are strongly absorbed due to the prevalence of dust clouds on the Galactic plane. At the same time, the X-ray and γ-ray signals from the Galactic plane are strongly contaminated by diffuse emission, in both energy bands, potentially originating from dozens of nearby unidentified objects. Additionally, X-ray and γ-ray emission is only observed at specific stages of the SNR evolution posing an extra difficulty in detecting SNRs in the latter energies from the entire population of observed Galactic SNRs.

On the contrary, the fact that radio synchrotron emission, which is not subjected to strong absorption, stems from a population of GeV electrons that lose energy slower compared to higher energy particles (i.e., TeV electrons responsible for X-ray synchrotron emission) makes it an ideal energy range to search for Galactic SNR. In fact, the large majority of Galactic SNRs are observed in radio given that the life time of the responsible particles for the emission is greater than the age of the SNRs. Consequently, the main criterion for the classification of an object as a SNR is the detection of a shell-type morphology and a non-thermal spectral index in radio synchrotron data. However, an increasing number of Galactic SNRs has been detected at higher energies – X-rays and γ-rays – in recent years with the latest X-ray all-sky surveys: now eROSITA and previously ROSAT (detection of several tens of Galactic SNRs emitting in X-rays), the *Fermi*-LAT γ-ray all-sky survey (Acero et al. 2016), and also with HESS at TeV energies (H. E. S. S. Collaboration et al. 2018a; H.E.S.S. Collaboration et al. 2018). By investigating those objects in X-rays and γ-rays, we are able to gain valuable information about their nature, including the physics of shocks, magnetic field strength, heating and acceleration mechanisms, as well as individual properties such as their distance and age estimates.

In this work, we report the first detection of the SNR G309.8+00.0 in X-rays and the identification of at least a significant fraction of the emission from the to-date named 4FGL J1349.5-6206c *Fermi*-LAT source as the remnant's GeV counterpart by utilizing stacked data from the first four consecutive eROSITA (extended ROentgen Survey Imaging Telescope Array) all-sky surveys (eRASS:4) and ~ 15.5 yr of Pass 8 data recorded from *Fermi*-LAT, respectively. With its center lying on the Galactic plane, G309.8+00.0 belongs to the class of SNRs that are subjected to strong absorption features at softer X-rays (< 1 keV) mainly due to its location. The remnant was detected for the first time in the radio wavelengths as an elliptical shell and identified as a SNR due to its non-thermal spectral index with the high resolution surface brightness contour maps at 480 MHz and 5000 MHz obtained by the Molonglo cross telescope and the Parkes 64-m radio telescope, respectively (Clark et al. 1975). A strong radio point source was also detected nearly at the center of the shell, just 4' to the North of the remnant's geometrical center. However, due to its steep spectrum (according to the Molonglo Observatory Synthesis Telescope (MOST) data, an -1.0 spectral index was derived for the central point source (Whiteoak & Green 1996), a value which is consistent with background extragalactic sources) and lack of pulsations, it is considered to be quite likely of extragalactic origin. The latter point-like object appears to have an optical counterpart, currently named 2MASS J13503303-6159245/Gaia DR3 5865571591306465280, however, due to its low galactic latitude (b) the spatial coincidence might occur by chance. Spatial and spectral consistent results, compared to the above studies, were obtained with higher resolution maps obtained from the Fleurs synthesis telescope at 1415 MHz (Caswell et al. 1980). However, the first detailed grey-scale map, rather than contours, was reported by Whiteoak & Green (1996) by exploiting MOST radio data at 843 MHz. In the latter maps, the remnant appears as a well-defined shell of elliptical shape and $25' \times 19'$ size. Finally, no masser (OH) detection from the satellite line of the hydroxyl radical (OH) at 1720.5 MHz with Parkes telescope was found, as reported in Green et al. (1997).

A recent study by Wang et al. (2020) on the SNRs distances in the inner disk utilizing red clump stars (RCS) as tracers resulted in a 3.12 ± 0.22 kpc primary distance estimate with the highest reliability. However, the authors note that this SNR, as several others in their study, exhibits two distance gradients. The secondary distance measurement is estimated to be 5.61 ± 0.42 kpc. Finally, Pavlović et al. (2013) reported a 4 kpc remnant's distance based on the radio surface-brightness-to-diameter distance estimate method.

Except for an unidentified *Fermi*-LAT GeV source, 4FGL J1349.5-6206c, that could potentially be associated with the SNR mainly due to its location; the SNR G309.8+00.0 has not been detected in any other wavelengths. We note that the latter γ-ray source has not been studied individually and has been modeled as a point-like object in the latest *Fermi*-LAT catalogs (4FGL-DR4, 4FGL-DR3 (Ballet et al. 2023; Abdollahi et al. 2022)). It is noteworthy that even though the latter source was initially included in the 1FGL catalog (Abdo et al. 2010), it was then removed from the 2FGL (Nolan et al. 2012) and 3FGL catalogs (Acero et al. 2015), and it was not included in the first *Fermi*-LAT catalog of SNRs (Acero et al. 2016). A weak signal of 1.3σ significance was reported from the remnant's location as part of a population study of Galactic SNRs at very high energies (TeVs) with HESS (H. E. S. S. Collaboration et al. 2018a).

This paper is outlined as follows. Section 2 is dedicated to the X-ray imaging and spectral analysis of the SNR G309.8+00.0 using eRASS:4 data. In section 3 we report on the distance and age estimates of the remnant based on the absorption column density values derived from the X-ray spectral fitting. In addition, we examine potential pulsar associations with the remnant. Section 4 describes the detailed inspection of the spatial morphology of the γ-ray emission detected at and around the remnant with *Fermi*-LAT (4FGL J1349.5-6206c). The GeV spectral energy distribution (SED) for the 4FGL J1349.5-6206c and its component which is spatially coincident with the SNR G309.8+00.0 is also presented by putting the measured fluxes into context. Section 5 gives concluding remarks.

2. X-ray data analysis

In this work, we report on the analysis results of X-ray data taken during the first four eROSITA all-sky surveys (eRASS:4), in the c020 processing version. eROSITA is the primary instrument aboard the Russian-German Spektrum Roentgen Gamma (SRG) observatory (Sunyaev et al. 2021). It consists of seven parallel aligned telescopes of 1° field of view (FoV) each (TM1-7) operating in the 0.2-10.0 keV energy range (Merloni et al. 2012; Predehl et al. 2021). It achieves a $\sim 30''$ average spatial resolution in survey mode (Merloni et al. 2024). In contrast to the rest of the telescopes, modules TM5 and TM7 are not equipped with an alu-

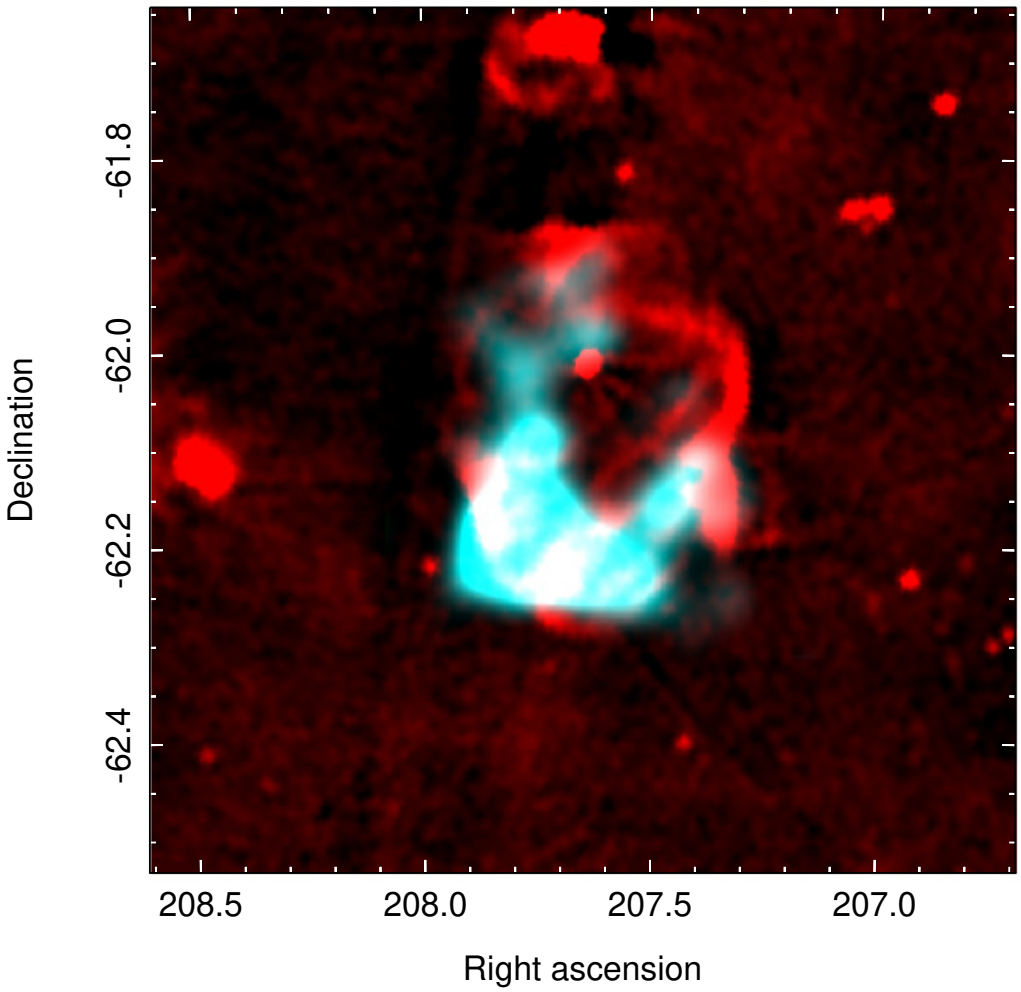

Fig. 1. Combined SUMSS 843 MHz: Sydney University Molonglo Sky Survey (red) and 1-2 keV eRASS:4 (cyan) image at and around the SNR G309.8+00.0 location. The X-ray emission component is restricted to the 1.0-2.0 keV energy band in which the X-ray emission from the remnant is concentrated. A linear color distribution is used for both image components. The image components are plotted in units of Janskys/beam and counts/pixel with a pixel size of $11''$ and $4''$ for the radio and X-ray components, respectively. The radio component is convolved with a 1σ Gaussian kernel and the X-ray component has been adaptively smoothed with a Gaussian kernel of 5σ to enhance the visibility of the diffuse emission. Point sources above 3σ significance are filtered out from the X-ray image using a $60''$ radius kernel.

minum on-chip filter, and thus to avoid signal contamination that could distort further estimates carried out below, mainly due to potential light leak suffering (Predehl et al. 2021), data collected from TM5 and TM7 were used for imaging analysis purposes but were excluded in the spectral analysis process. `evtool` and `srctool` tasks of eSASS (eROSITA Standard Analysis Software) version `eSASSusers_201009` (Brunner et al. 2022) were employed for data reduction and data processing purposes. From the 4700 partially overlapping sky tiles (of $3^\circ.6 \times 3^\circ.6$ size each) of eSASS pipeline, the SNR G309.8+00.0 lies entirely on the 205153 tile. Each tile is named after its center coordinates. The first three digits correspond to the RA whereas the last three to the Dec of the tile's center. Only data from the sky tile mentioned above were used in this work.

The combined SUMSS 843 MHz: Sydney University Molonglo Sky Survey (red) and 1-2 keV eRASS:4 (cyan) image of the SNR G309.8+00.0 is shown in Fig. 1. The X-ray image component (intensity sky map) was optimized aiming at emphasizing the diffuse X-ray emission originating from the SNR and avoiding likely contamination of the signal from unrelated nearby sources. All X-ray point-like sources with at least a 3σ detection significance were masked out using a kernel radius of $60''$. The X-ray image, of $4''$ pixel size, has been adaptively smoothed according to the smoothing algorithm of Ebeling et al. (2006) with a Gaussian kernel of 5σ to enhance the diffuse X-ray emis-

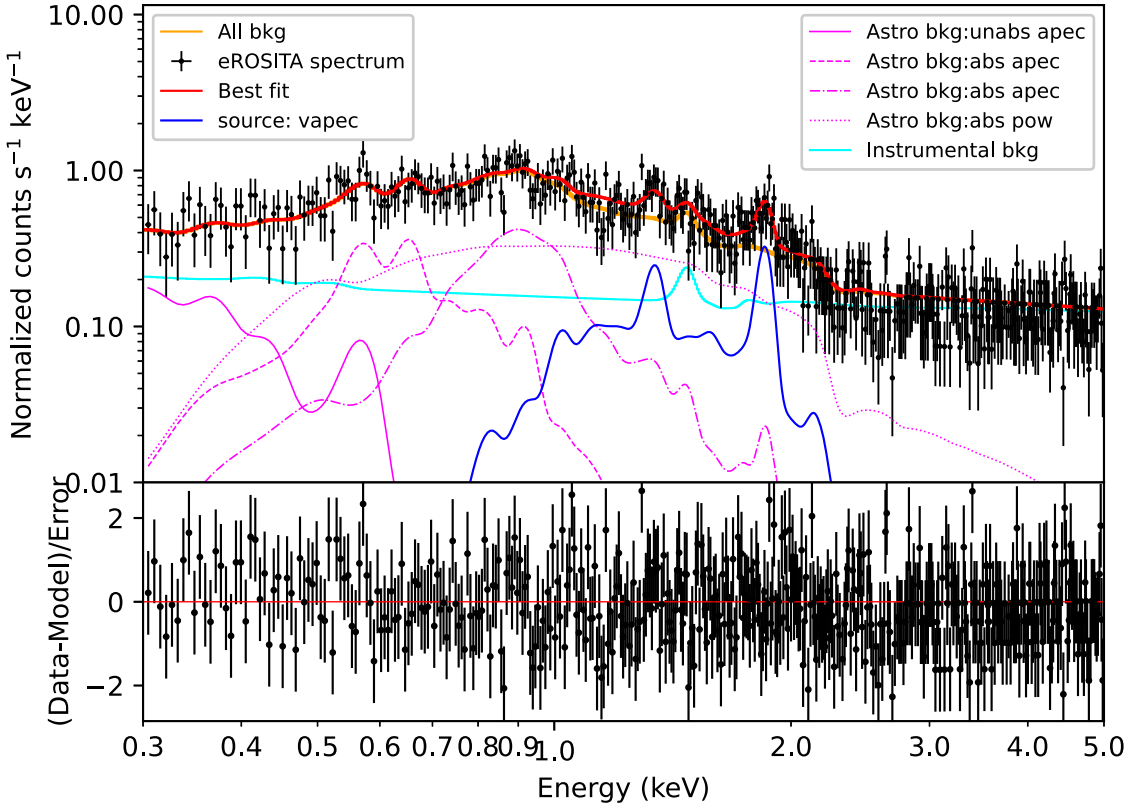

Fig. 2. Energy spectrum in the 0.3-5.0 keV energy band obtained from the selected on-source region as defined in the text (section 3), using eRASS:4 data obtained from TM1,2,3,4, and 6. Following the fitting procedure, a rebinning process that combines two spectral bins into one was used solely for visual purposes. The G309.8+00.0 X-ray energy spectrum is best described by a thermal plasma component in equilibrium (tbabs×vapec) indicated with the blue solid line. All components contributing to the total emission are displayed in detail. The orange line stands for the sum of all background components i.e., instrumental (cyan color), and astrophysical (magenta color), detected at and around G309.8+00.0, revealing the overall contribution of the source to the total spectrum.

sion visibility. The majority of the X-ray emission emanating from the SNR is confined in the 1-2 keV energy band. The latter energy range was optimized after detailed inspection of the remnant's X-ray spectrum. The emission in both radio synchrotron and X-rays appears to be in good morphological correlation and confined within a well-defined shell of elliptical shape. However, significant X-ray emission is only detected in the lower half of the shell. As shown by the X-ray imaging analysis, the northern half and in particular the northern edge of the remnant's shell are only marginally detected above the background level, $< 3\sigma$ detection significance in X-rays. Additionally, G309.8+00.0 can be classified as a limb-brightened SNR, similar to, for example, the Cygnus loop SNR. We observe a somewhat incomplete ring-like structure in X-rays since there is more hot gas in our line of sight at the edges compared to when looking through the central parts of the remnant. However, the limited statistics of the data forbid the construction of a high-quality image that demonstrates such a comparison between the brightness of the remnant at the central regions compared to the edges since the central regions brightness is only marginally above the background level. A size of $0^\circ.43 \times 0^\circ.32$ is obtained in X-rays, by fitting an ellipse to the outermost regions of emission, in excellent agreement with the remnant's radio size reported in the literature.

2.1. X-ray spectral analysis

The `srctool` task of the eSASS pipeline was used to extract the corresponding spectral files for spectral fitting purposes. The collected data from TM5 and TM7 were excluded to avoid contamination issues, as mentioned in section 2. The X-ray spectral analysis was carried out using the to-date version of the Xspec code (Borkowski et al. 2006; Yamaguchi et al. 2011). Given the faint appearance of the SNR in X-rays (300^{+210}_{-120} source counts in 1-2 keV energy range, depending on the selected background control region) Cash statistics (Cash 1979) was preferred over Chi-Square (Pearson 1900) for the evaluation of the goodness of the fit and no rebinning of the X-ray photons was applied prior to the fitting process. No significant X-ray point sources were detected within the remnant's extension. However, an identical strategy to section 2 was adopted to avoid potential signal contribution to the remnant's X-ray spectrum by unrelated point sources. Points sources above 3σ significance were masked carefully with a kernel radius of $60''$ since a larger masking radius

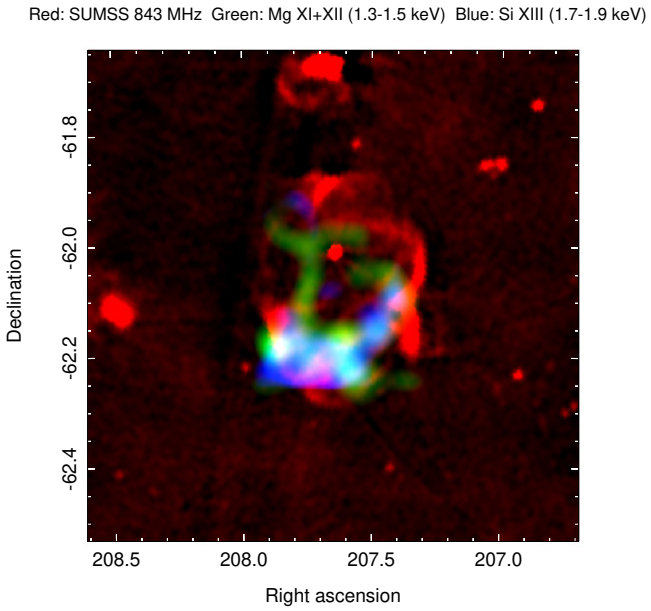

Fig. 3. Combined SUMSS 843 MHz: Sydney University Molonglo Sky Survey (red), 1.3-1.5 keV eRASS:4 (green), and 1.7-1.9 keV eRASS:4 (blue) image at and around the SNR G309.8+00.0 location. A spectrally motivated selection of X-ray narrow energy ranges was made to demonstrate the spatial distribution of Mg XI+XII and Si XIII emission lines across the remnant's area. A linear color distribution is used for all three image components. The radio and X-ray components of this sky map were constructed using an identical approach in terms of pixel size, smoothing, and point source removal as described in the caption of Figure 1.

would remove a significant fraction from the faint diffuse X-ray emission of the remnant.

Table 1 summarizes the spectral parameters and 1σ error results of the best-fit model to the X-ray spectrum of the SNR G309.8+00.0 (shown in Fig. 2). The latter results were obtained by performing a simultaneous fitting of the source and background emission from the selected on-source region (a circular region centered at (l)=309.785°, (b)=−0.025° with a radius of 0.27°). The parameters of the background model, used to describe the background emission from the on-source region, were fixed to the best-fit values obtained from the spectral analysis of a surrounding background control region located to the South-East of the remnant that is free of source emission (a circular region centered at (l)=310.11°, (b)=−0.4° with a radius of 0.27°). No re-scaling was required since the on-source and background control regions were selected to be of the same area. The latter background control region was selected to represent best the background emission of the on-source region after carefully inspecting the surrounding regions for potential contamination from foreground and/or background sources. The background emission was found to be best described by the following model in Xspec notation: `apec+tbabs(apec+apec+pow) + gaussian + expfac(bkn2pow + powerlaw + powerlaw) + powerlaw + gaussian + gaussian + gaussian+ gaussian + gaussian + gaussian + gaussian + gaussian + gaussian`. The latter model is a convolution of the i) astrophysical background (`apec+tbabs(apec+apec+pow)`) which represents the Local Hot Bubble (LHB) low temperature plasma, the Galactic Halo (GH) plasma, and the Cosmic X-ray Background (CXB) – the product of the combined emission from unresolved Active Galactic Nuclei (AGN), and ii) of the instrumental background which can be expressed as a combination of power law and Gaussian model components in the selected energy range for spectral fitting: `gaussian + expfac(bkn2pow + powerlaw + powerlaw) + powerlaw + gaussian + gaussian + gaussian+ gaussian + gaussian + gaussian`.

Table 1. Best-fit parameters of the SNR G309.8+00.0 X-ray spectrum.

Model	tbabs×vapec
kT(keV)	$0.34^{+0.1}_{-0.1}$
$N_H(10^{22}$ cm$^{-2})$	$3.1^{+0.7}_{-0.5}$
$Si/Si_\odot$	$3.6^{+2.3}_{-1.2}$
norm	$0.08^{+0.18}_{-0.04}$
CSTAT/d.o.f	0.96

Notes. The best-fit parameters are shown along with 1σ errors. Where not defined otherwise, elemental abundances are set to nearly solar values according to Wilms et al. (2000).

The X-ray emission originating from the SNR appears to be purely thermal. A simple absorbed thermal plasma in equilibrium appears to describe its spectrum well (tbabs × vapec as described in Tab. 1). Non-equilibrium thermal components were tested and provide fits of equal goodness with similar best-fit spectral parameters (e.g., for a tbabs × vnei model (almost identical parameters were obtained for a tbabs × vpshock model), kT= $0.34^{+0.13}_{-0.13}$ keV, $N_{\rm H} = 3.4^{+1.0}_{-0.8}$ 10^{22} cm^{-2}, $Si/Si_\odot = 2.6^{+4.5}_{-0.8}$, and $\tau = 1.42^{+unconstrained}_{-1.07} \cdot 10^{11}$ cm^{-3} s – unconstrained, with 1σ errors). The derived ionization timescales ($\tau > 10^{11}$ cm^{-3} s – full ionization equilibrium is typically reached at τ values $\geq 10^{12}$ cm^{3}s (Masai 1984)) support the hypothesis for a plasma that broadly speaking is found in equilibrium. We note, however, that the limited statistics of the data do not allow us to reject non-equilibrium models (i.e., tbabs × vpshock and tbabs × vnei (Borkowski et al. 2001; Wilms et al. 2000)). In addition, the limited photon statistics pose a significant challenge in assessing in detail the remnant's X-ray spectrum. They do not permit us to examine the X-ray emission from individual sub-regions such as the most prominent arc at the southeast of the SNR which also spatially coincides with the brightest arc of its radio synchrotron emission. Thus, given the size of the SNR we plan to request a deep follow-up pointed observation to provide a more robust spectral classification of the remnant. It should be noted that an *XMM-Newton* observation, ObsId: 0742110101, which was conducted to study X-ray emission from the nearby radio quiet SNR G309.4-0.1, is marginally covering the remnant, although the extremely small overlap region, which does not exhibit enhanced X-ray emission, prohibits further investigation. Despite the faint appearance of the remnant, a relatively (given the limited statistics of the X-ray data) prominent Mg triplet line at 1.33-1.47 keV and Si emission (XIII Heα lines) at 1.7-1.9 keV were identified. Driven by the physics conclusions obtained from the X-ray spectral analysis of the remnant we construct an RGB image with spectrally motivated energy to color correspondence (Red: SUMSS 843 MHz, Green: eRASS:4 1.3-1.5 keV, Blue: eRASS:4 1.7-1.9 keV), as shown in Figure 3. The latter figure describes how the two most prominent elemental abundances distribute across the remnant's area. The Si emission appears to be con-

centrated mainly in the southeastern part of the shell, whereas the Mg emission appears to be homogeneously distributed on a ring-like morphology that follows the edges of the remnant's elliptical shape.

With a surface brightness of $7.32 \cdot 10^{-4}$ photons arcsec^{-2}, estimated from an area of $2.93 \cdot 10^{6}$ arcsec^{2} – on-source region, and a total flux of $F_{\rm total} = 1.42^{+0.87}_{-0.51} \cdot 10^{-11}$ erg cm^{-2} s^{-1} (1σ errors) in the 1-2 keV energy range, the SNR G309.8+00.0 is classified among the faintest Galactic SNR ever detected in X-rays.

3. Distance and age estimates

Three distance estimates have been proposed to date for the SNR G309.8+00.0, which indicate that the SNR is probably located at a distance < 4 kpc, as discussed in detail in section 1. In this

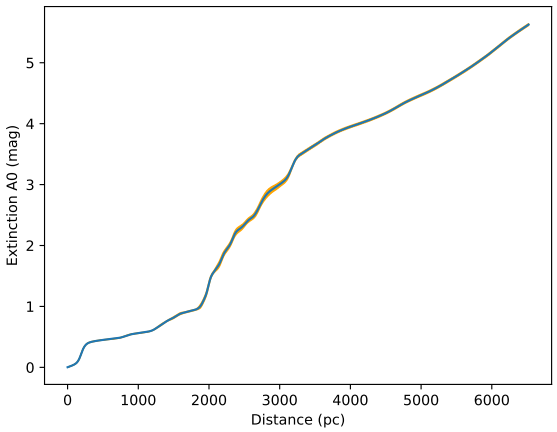

Fig. 4. One-dimensional cumulative extinction as a function of the distance in the direction of the SNR G309.8+00.0. The graph was created by using the EXPLORE G-Tomo app https://explore-platform.eu/ which provides updated extinction data sets extended up to ~ 6 kpc by using GAIA eDR3 and 2MASS data (Lallement et al. 2022). The orange range indicates the area of uncertainty where significant uncertainty exists.

work, we use eRASS:4 data aiming to provide the first distance estimate based on the properties of the remnant itself. Making use of the absorption column density values obtained from the X-ray spectral fit and adopting the most recent statistical relation between X-ray absorption and mean color excess (Foight et al. 2016) based on *Chandra* observations of SNRs

$$\begin{array}{lcl} N_{\rm H}/E_{\rm B-V} & = & 8.9 \times 10^{21}\ {\rm cm}^{-2} \cdot {\rm mag}^{-1} \\ N_{\rm H}[{\rm cm}^{-2}/A_{\nu}] & = & 2.87(\pm 0.12) \times 10^{21} \end{array} , \quad (1)$$

an optical extinction of $A_{\nu} \equiv A_0 \equiv A(550\ {\rm nm}) = 10.7^{+2.7}_{-2.1}$ is derived (errors were estimated by taking into account errors in the absorption column density and errors defined from the empirical relation used). Employing the latest optical extinction data sets by Lallement et al. (2022), a distance well above 6 kpc (of the order of 10 kpc) is derived, as shown in Fig. 4. These distance values are inconsistent with earlier estimations of the remnant's distance reported in the literature. However, all distance method estimates for this remnant are subject to large scattering and uncertainty. Therefore we discuss below the linear size and age estimates of the remnant adopting two distinct distances suggested as best from this work and the literature.

By adopting a distance to the remnant of 3.12 kpc and 10 kpc and taking into account the remnant's angular size of $0^{\circ}.43 \times 0^{\circ}.32$, one derives a 23.3×17.3 pc and 75×56 pc size, respectively. Using the absorption column density obtained from the X-ray spectral fit one derives a local density of $3.2^{+0.9}_{-0.7}$ cm^{-3} and $1.0^{+0.2}_{-0.2}$ cm^{-3}, respectively (errors were estimated by taking into account errors in the absorption column density). Employing the SNR evolutionary model calculator developed by Leahy & Williams (2017) one obtains a $0.9 - 2.0 \cdot 10^{4}$ yr and a $1.0 - 3.5 \cdot 10^{5}$ yr remnant's age (errors were estimated by taking into account errors in the computed local density) for the two distinct cases. We note that such age estimates are only rough approximations especially due to the limited statistics of the collected X-ray photons. It is, however, not possible to obtain a more accurate distance measurement since the SNR does not have a firm association with nearby pulsars (in fact, if future studies probe a type Ia progenitor origin; the remnant is not considered to be associated with a pulsar), and as discussed in section 4, there are no apparent molecular clouds associated with the remnant.

To this end, we also checked for potential pulsars in the near vicinity of the SNR that could be possibly associated with the remnant if the latter is not of type Ia progenitor origin. There are 16 nearby pulsars within 2° from the remnant's center, as shown in Tab. 2. Among those, nine are highly unlikely to be associated with the SNR due to their old age, which exceeds 10^{6} yr. Among the rest, two pulsars do not have computed ages and thus cannot be examined in detail (J1349-63, J1357-62). However, assuming the remnant's age of the order of $10^{4} - 10^{5}$ yr (within uncertainties from the two different approaches employed above) the extremely high pulsars' transverse velocities required to reach their present location do not permit a remnant's association with those two pulsars. Among the five remaining pulsars with compatible age with the SNR, only two have acceptable transverse velocities. Since for those two pulsars there is no distance estimate we exploit both possible distance estimates of the remnant adopted in this work. The J1350-6225 (4FGL J1350.6-6224) pulsar, which is located just 0.35° away from the remnant's center (still outside the remnant's extension), has an age of $2.5 \cdot 10^{5}$ yr and a $\upsilon_{\rm trans} \sim 240$ km s^{-1} (assuming a 10 kpc distance) or a $\upsilon_{\rm trans} \sim 75$ km s^{-1} (assuming a 3.12 kpc distance). The J1358-6025 (4FGL J1358.3-6026) pulsar, which is located well outside of the remnant's extension (1.88° from the remnant's center), has an age of $3.2 \cdot 10^{5}$ yr and a $\upsilon_{\rm trans} \sim 313$ km s^{-1} (assuming a 3.12 kpc distance). However, assuming a 10 kpc distance we derive a $\upsilon_{\rm trans} \sim 1000$ km s^{-1} for the latter pulsar, and thus a potential association with the remnant is forbidden if the latter lies at a 10 kpc distance, and in general at distances above 5 kpc. The latter two pulsars appear as the most prominent candidates to be associated with the SNR G309.8+00.0, only if the remnant is not of SN type Ia progenitor origin. Based on the ages of the nearby pulsars, a distance of 10 kpc appears reasonable for this SNR.

4. γ-ray *Fermi*-LAT data analysis

4.1. γ-ray observation and data reduction

We select ~ 15.5 yr from 239557417 to 731081752 mission elapsed time at the start and end of the observation – 2008 August 4 (15:43:36.0) to 2024 March 2 (14:15:46.0), start and end coordinated universal time (UTC) of the observation – of

Table 2. Pulsars within 2° of the remnant's center.

Pulsar	Ang. sep. (°)	DM $pc \cdot cm^{-3}$	D_1 kpc	D_2 kpc	Age Myr	v_{transv} $km \cdot s^{-1}$
J1337-6306	1.84	777.7	12.9(14.1)	-	9.3	43.6
J1338-6204	1.46	640.3	12.4(9.9)	-	1.4	220.7
J1341-6220 (4FGL J1341.7-6216)	1.07	719.7	12.6(11.2)	-	0.01	$2.3 \cdot 10^4$
J1344-6059	1.3	435	7.4(7.6)	-	200	0.8
J1345-6115	1.01	278	5.6(5.0)	-	6.1	15.8
J1348-6307	1.06	597	10.6(10.3)	-	3.9	49.2
J1349-6130	0.59	283.9	5.5(5.0)	-	0.8	69.2
J1349-63	1.86	478	9.3(9.5)	-	–	$2.95 \cdot 10^4/2.95 \cdot 10^3$(*)
J1350-6225 (4FGL J1350.6-6224)	0.35	–	–	-	0.25	74.5/239(†)
J1354-6249	0.87	254	5.2(4.6)	-	3.2	24.1
J1355-6206	0.55	547	7.5(8.3)	-	1410	0.05
J1357-62	0.88	416.7	6.5(6.7)	-	–	$9.8 \cdot 10^3/980$(*)
J1358-6025 (4FGL J1358.3-6026)	1.88	–	–	-	0.32	312.8/1003(†)
J1359-6038	1.83	293.7	5.5(5.2)	-	0.32	536.7
J1400-6325	1.78	563	9.2(11.3)	7.0	0.01	$2.8 \cdot 10^4$
J1403-6310	1.82	305	5.7(5.5)	-	70.3	2.52

Notes. The first and second columns provide the pulsar's name and angular separation from the remnant's center. The third column gives the dispersion measure (DM). The fourth and fifth columns present the pulsar's distance from Earth based on DM measurements and potential associations, respectively. The values within parentheses correspond to older distance estimates based on the NE2001 electron density model (Cordes & Lazio 2003). Since 2017, the electron density model for DM-based distance calculations has been substantially updated to the current version YMW16 (Yao et al. 2017). The sixth column gives the pulsar's spin-down age. The seventh column displays the transverse velocity required for each pulsar to move from the remnant's center to its present location. No proper motion estimates are provided for all the above pulsars. (*)v_{transv} estimate based on the SNR age $10^4/10^5$ yr. (†) v_{transv} estimate based on the two distinct SNR distance approaches considered in this work $3.12/10$ kpc.

Pass 8 (P8R3) 'SOURCE' class data, front and back interactions included (evclass=128, evtype=3), collected with *Fermi*-LAT to inspect the emission at and around the SNR G309.8+00.0 and examine a potential association with the unidentified 4FGL J1349.5-6206c γ-ray source. The Fermitools[2] version 2.0.8 was employed for data reduction and analysis purposes. A region of interest (ROI) of $20^\circ \times 20^\circ$ centered at the coordinates of the 4FGL J1349.5-6206c γ-ray source (RA: 207.4°, Dec: -62.1°) was selected. The latter ROI was selected since it encompassed both the extension of the unidentified 4FGL J1349.5-6206c source and the SNR G309.8+00.0. For the imaging analysis, we restrict ourselves above 1 GeV due to the limited spatial resolution of the instrument at lower energies, given the small angular size of the SNR. This way we make sure that the γ-ray emission from the SNR G309.8+00.0, of $0^\circ.43 \times 0^\circ.32$ size, can be resolved given the improved point spread function (PSF) of the instrument at higher energies. A broader 100 MeV-100 GeV energy range is adopted for the spectral analysis. To remove Earth limb emission which contaminates our signal we set an upper cut and exclude events with zenith angles above 90°. The standard binned likelihood analysis of Fermitools was used with an 0.025° bin size to secure a good sampling of the *Fermi*-LAT PSF. The background modeling is achieved by using the Galactic diffuse component `(gll_iem_v07.fits)` and the isotropic diffuse component `(iso_P8R3_SOURCE_V3_v1.txt)` as background sources in our model. In addition, all sources included in the recently released incremental 4FGL-DR4 (Ballet et al. 2023; Abdollahi et al. 2022) *Fermi*-LAT 14-year source catalog and contained within our ROI were included in the model. Spectral parameters of sources within 5° from the ROI's center were let vary along with the normalizations of the Galactic and isotropic diffuse components. The remaining parameters were fixed to the catalog values. For imaging analysis purposes above 5 GeV and 10 GeV, only the normalization of the sources and the normalizations of the two background components within a 2° region from the ROI's center were allowed to vary due to the improved PSF performance[3].

4.2. γ-ray spatial morphology and SED

Aiming at examining the γ-ray emission from the 4FGL J1349.5-6206c – designation c stands for a source found in a region with bright and/or possibly incorrectly modeled diffuse emission – and any other sources in our ROI that were missed and were not cataloged in 4FGL-DR4 we create both residuals and Test Statistic (TS) maps at three distinct energy ranges: 1 GeV-1 TeV, 5 GeV-1 TeV, and 10 GeV-1 TeV. Both the residual count maps and the TS maps in the latter energy ranges were produced by modeling the emission from all 4FGL-DR4 sources and the two background components within our ROI. The residual count maps were inspected to ensure that our source(s) of interest, which is located at the center of our ROI, appears to be the brightest and there are no strong negative residuals from the subtracted sources. In Fig. 5 we present the obtained TS maps in the three different energy ranges. On each panel, the PSF size at the lower energy cut is provided to demonstrate the resolution capacity of the instrument in each sky map. We cut each obtained TS map to a $1^\circ.33 \times 1^\circ.33$ size to focus on the emission at and around the small angular size SNR G309.8+00.0.

We started examining the spatial morphology of the γ-ray emission by inspecting the "richest" data sets > 1 GeV. As shown

[2] https://fermi.gsfc.nasa.gov/ssc/data/analysis/scitools/references.html

[3] refer to the SLAC page https://www.slac.stanford.edu/exp/glast/groups/canda/lat_Performance.htm for further details on the analysis performance of the instrument

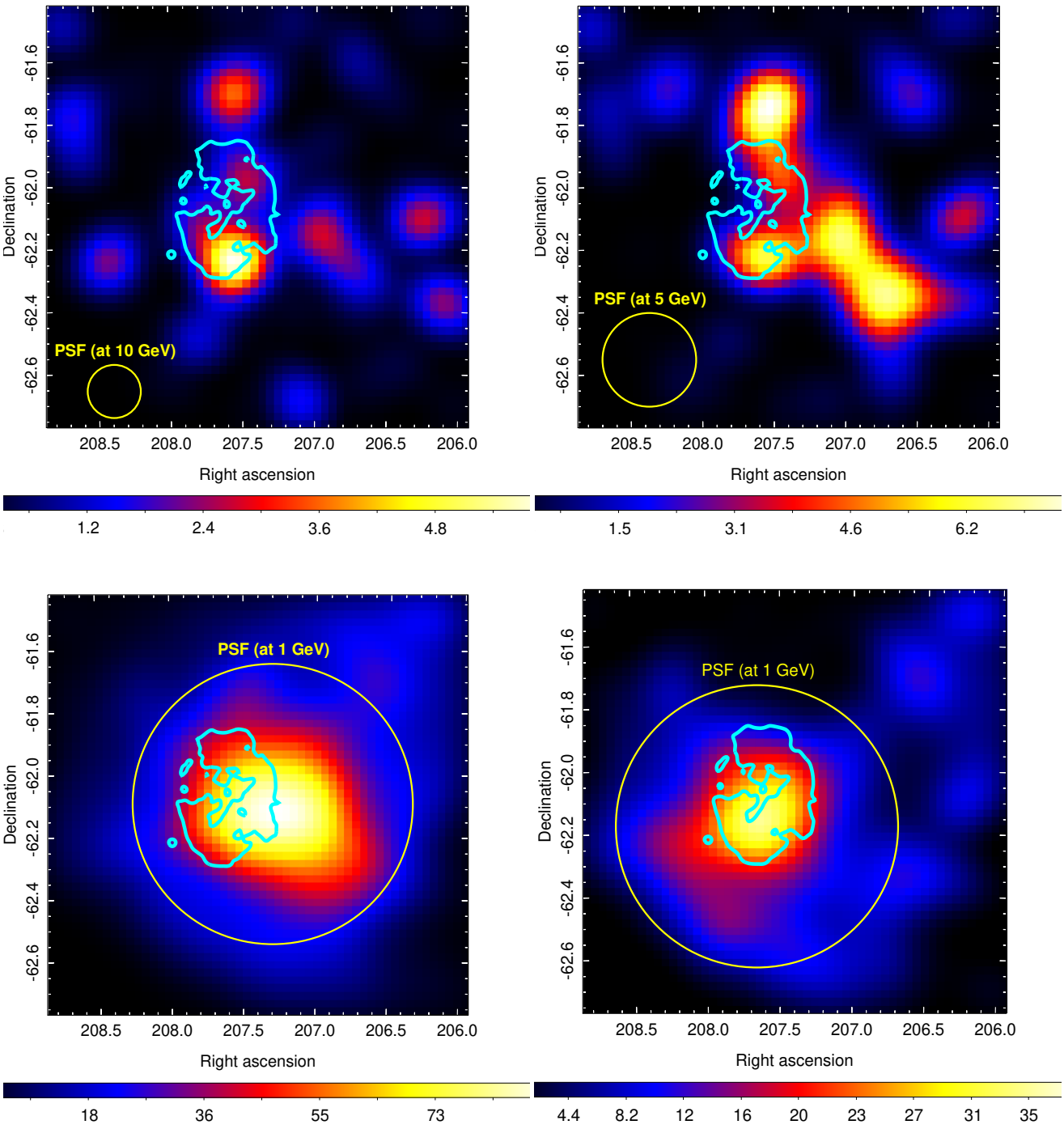

Fig. 5. $1^\circ.33 \times 1^\circ.33$ *Fermi*-LAT TS maps from the location of the SNR G309.8+00.0 at different energy ranges. All sky maps, of $90''$ pixel size, centered at the best-fit coordinates of the 4FGL J1349.5-6206c source have been smoothed with a 2.5σ Gaussian kernel. Upper left panel: *Fermi*-LAT TS map above 10 GeV. Upper right panel: *Fermi*-LAT TS map above 5 GeV. Lower left panel: *Fermi*-LAT TS map above 1 GeV. Lower right panel: *Fermi*-LAT TS map above 1 GeV when modeling the src-north, src-west, and src-northwest components of the 4FGL J1349.5-6206c source. The cyan contour marks the SNR G309.8+00.0 extension as seen in SUMSS 843 MHz radio data. The yellow circle represents the 68% containment size of the PSF at the energy threshold of each sky map, with no smoothing applied.

in Fig. 5, there is a single centroid, detected with a 9.8σ significance, spatially coincident with the SNR's location. However, due to the size of the PSF at those energies, we cannot conclude if the latter GeV source, named 4FGL J1349.5-6206c, is a single source or if the γ-ray emission is a conglomerate of several sub-sources. Since there is no strong observational evidence that supports the presence of dense material at the western side of the SNR (as seen in the lower panel of Fig. 6 and dis-

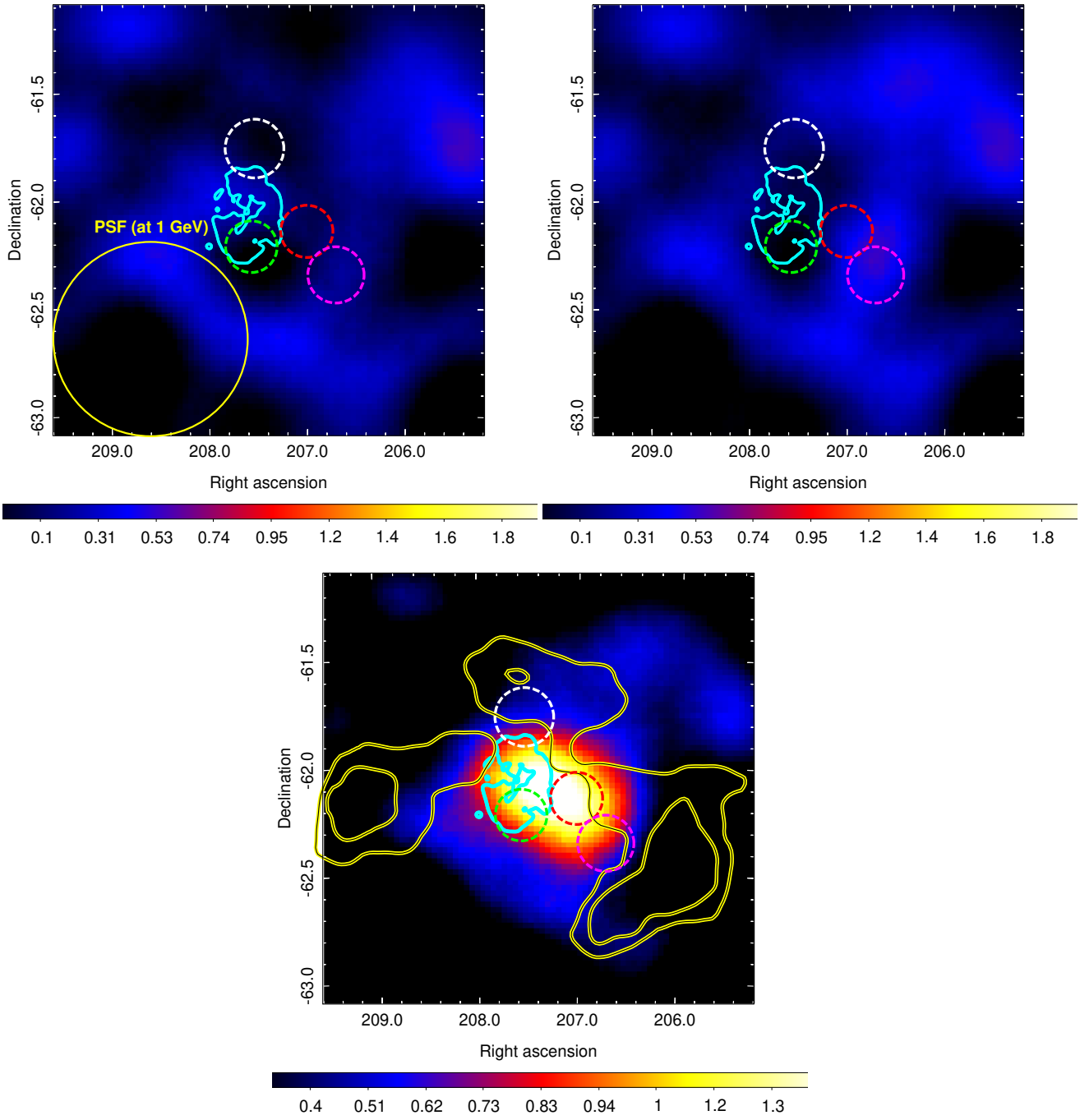

Fig. 6. $2^\circ.0 \times 2^\circ.0$ *Fermi*-LAT residual count maps above 1 GeV (in units of counts/pixel), from the location of the SNR G309.8+00.0, applying different modeling to the γ-ray emission from the 4FGL J1349.5-6206c source. All sky maps, of $90''$ pixel size, centered at the best-fit coordinates of the 4FGL J1349.5-6206c source have been smoothed with a 6.5σ Gaussian kernel. Upper left panel: residual map obtained by modeling the 4FGL J1349.5-6206c as four point-like sources. Upper right panel: residual map obtained by modeling the 4FGL J1349.5-6206c as a single source according to the 4FGL-DR4 catalog model. Lower panel: residual map obtained by excluding from the model the 4FGL J1349.5-6206c source. The yellow and black contours mark the position of nearby CO clouds as obtained from the CO Galactic plane map (Dame et al. 2001). In all panels, the cyan contour marks the SNR G309.8+00.0 extension as seen in SUMSS 843 MHz radio data. The green, white, red, and magenta dashed circles (centered on the maximum TS values and with radius obtained setting a lower TS cut of 2σ, > 5 GeV) provide the locations of the 4 components (src, src-north, src-west, and src-southwest, respectively) that the 4FGL J1349.5-6206c source can be decomposed to. The yellow circle represents the 68% containment size of the PSF at the energy threshold of each sky map, with no smoothing applied. The latter PSF size applies to all three panels, however, since it appears that the instrument's PSF cannot resolve individual components of the 4FGL J1349.5-6206c source at ~ 1 GeV, we only present it on the upper left-hand panel to avoid overcrowding.

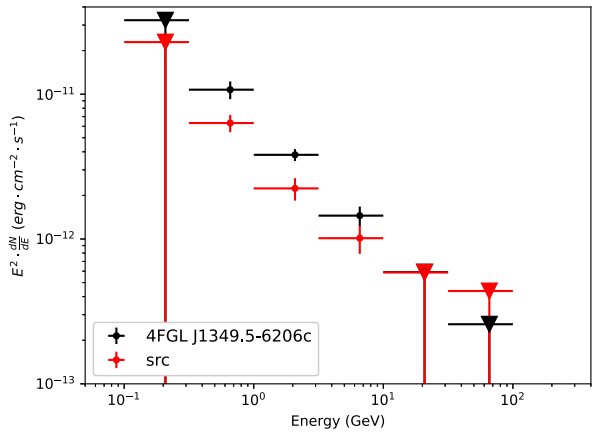

Fig. 7. 4FGL J1349.5-6206c and src *Fermi*-LAT SED in the 0.1-100 GeV energy range. Black dots correspond to the *Fermi*-LAT spectrum of the 4FGL J1349.5-6206c γ-ray source. Red dots represent the *Fermi*-LAT spectrum of the src (spatially coincident source to the SNR G309.8+00.0) γ-ray source. As expected from the obtained TS maps of Figure 5 the γ-ray emission of the 4FGL J1349.5-6206c γ-ray source is dominated by the src component at higher energies.

cussed at the end of this section) that could subsequently support a hadronically induced gamma-ray scenario, where accelerated nuclei interact with atomic nuclei originating from the dense material giving birth to gamma-ray emission through π^0-decay, and due to the puzzling nature of gamma-ray emission from such an evolved SNR; in this work, we also exploit the alternative scenario that the 4FGL J1349.5-6206c source consists of distinct source components. Therefore, as a next step, we inspect the emission above 5 GeV. The improved PSF size at those energies allows us to identify at least three distinct source components from this region since there are three centroids whose angular separation exceeds the instrument's PSF size. In particular, we detect the src-north component (RA: 207.53°, Dec:$-$61.75°) with 3σ significance, the src-southwest component (RA: 207.75°, Dec: $-$62.35°) with a 2.7σ significance, and the src component (RA: 207.56°, Dec: $-$62.23°) with a 2.5σ significance. Additionally, a potential fourth component, the src-west (RA: 207.04°, Dec: $-$62.16°) is detected with a 2.7σ significance. With src we denote the component that spatially coincides with the SNR G309.8+00.0. Despite the reduced photon statistics we also inspected γ-ray emission from the location of interest above 10 GeV which confirms the presence of four distinct sources. The src-west component is now clearly resolved as a separate centroid due to the improved PSF. The src-southwest component is no longer detectable above 10 GeV. Among the latter components, the only significant one $>$ 10 GeV is the src detected with a 2.5σ significance. We note that the location of the src component coincides with the brightest part of the remnant's X-ray emitting shell.

For each sub-component of the 4FGL J1349.5-6206c source, a point-like source spatial template yields a likelihood quality fit of the same goodness as when modeled as extended sources. Thus, we replace the 4FGL J1349.5-6206c source in our model with four distinct point-like sources and re-run the likelihood fit. This way we obtain the residual count map above 1 GeV which perfectly models the emission of 4FGL J1349.5-6206c, as shown in Fig. 6 and also the TS map above 1 GeV having modeled the 4FGL J1349.5-6206c sub-components that are not spatially coincident with the SNR G309.8+00.0, as shown on the lower right panel of Fig. 5. The src component is detected $>$ 1 GeV with a 5.8 σ significance. When treating the src as extended and the rest three as point-like sources no significant improvement in the fit quality is obtained.

The spectral energy distribution of the src object adopting a LogParabola spectral model is presented in Fig. 7 along with the spectral energy distribution of the 4FGL J1349.5-6206c γ-ray source (when treated as a single source) adopting the spatial and spectral model provided in the 4FGL-DR4 catalog (spectral parameters: α=3.0, β=0.2). A powerlaw model describes well the GeV SED of both sources, however, a LogParabola model is preferred over a simple powerlaw based on the *Signif_Curve* Fermitools task. The shapes and the narrow energy range of the GeV SED of both sources do not allow us to discriminate between a hadronic and a leptonic mechanism for the production of gamma-rays. However, the remnant's evolved stage favors a hadronic interpretation. If future studies confirm an age as large as 10^5 yr, the nature of the gamma-ray emission becomes even more puzzling, placing this remnant among the oldest gamma-ray loud SNRs ever detected, along with e.g., the G279.0+01.1 (Michailidis et al. 2024b) and the S147 (Michailidis et al. 2024a). Particle acceleration at such large ages is questionable due to the rapid decrease of the shock speed at the latter stages of the SNRs evolution. However, recent theoretical works, e.g. Yasuda & Lee (2019), demonstrate that under specific conditions, usually low-density environments (e.g., SNR-in-cavity scenario, see Khabibullin et al. (2024) for a showcase example), even leptonically induced gamma-ray emission could be observed from old SNRs. Since there is still uncertainty in terms of which parts of the emission of the 4FGL J1349.5-6206c source are associated with the SNR G309.8+00.0 in combination with the absence of X-ray emission of non-thermal nature (X-ray synchrotron emission) we do not provide a multiwavelength SED of the latter source. This is a task for the future.

We also examined our ROI for CO clouds that could potentially interact with accelerated nuclei originating from the SNR G309.8+00.0 and thus yielding γ-ray emission. No CO clouds were found to be spatially coincident with the 4FGL J1349.5-6206c γ-ray source as shown on the lower panel of Fig. 6. In addition, the inspection of AKARI and WISE (Wide-field Infrared Survey Explorer) infrared (IR) data from the location of the remnant did not yield the detection of enhanced IR emission regions to the western part of the SNR and thus there is no evidence that would make us believe that the γ-ray emission stems from the interaction of the shocks with material.

5. Discussion and conclusions

We present the first study of the well-established, from radio observations, SNR G309.8+00.0 at higher energies. We report the detection of its X-ray counterpart using data from the first four eROSITA all-sky surveys (eRASS:4) and investigate the nature of the unidentified 4FGL J1349.5-6206c γ-ray source using 15.5 yr of *Fermi*-LAT data. We conclude that the SNR is most likely to account for at least a significant portion (if not all) of the emission from the latter γ-ray source. This work is evident of the importance of the multiwavelength study of supernova remnants in determining key properties of their nature.

Utilizing eRASS:4 data we provide the first X-ray view of the SNR 309.8+00.0. The X-ray emission is mainly confined to the 1-2 keV energy range. The spatial morphology of the X-ray emission is best fitted by an ellipse of 0°.43 $\times$ 0°.32 size and its

shell-type appearance is in good spatial correlation with the radio synchrotron emission from the SNR. The X-ray emission mainly fills the southern half of the remnant's shell. The SNR exhibits limb-brightening features since it appears brighter at the edges of the shell compared to when looking through its central parts. Moving to the physical processes and the physics interpretation behind the above imaging results, we conclude that the nature of the X-ray emission originating from the SNR is purely thermal and likely in equilibrium. However, non-equilibrium models provide spectral fits of equal goodness and thus cannot be excluded due to the limited statistics of the X-ray data. Either there is an absence of a continuum non-thermal component or the faint emission of the SNR does not allow its detection with an all-sky survey of limited exposure such as eROSITA. The remnant's X-ray spectrum is well-fitted by the tbabs×vapec thermal plasma model in equilibrium with a kT=0.34 ± 0.1 keV and a $N_{\rm H} = 3.1^{+0.7}_{-0.5}$ 10^{22} cm^{-2}. Despite the limited statistics we detect relatively prominent Mg XI+XII (1.3-1.5 keV) and Si XIII (1.7-1.9 keV) emission lines across the remnant's area. The silicon emission is mainly confined to the southeastern portion of the remnant whereas the magnesium emission is more uniformly distributed on the ring-like structure of the X-ray shell.

Due to the strong absorption at soft X-rays (< 1 keV) no detailed comparison of the elemental abundance fractions can be made and thus we cannot disentangle between a thermonuclear and a core-collapse progenitor origin. Even though the shell-type morphology of typical Ia progenitor origin SNRs is usually highly symmetrical mainly due to the lack of a massive progenitor star, that exhibits strong stellar winds that disturb the surrounding medium, this does not come as a requirement (e.g., refer to the Kepler SNR (Chiotellis et al. 2012) and the SNR G321.3-3.9 (Mantovanini et al. 2024)). In contrast to the SNR G309.8+00.0, typical type Ia SNRs have been mainly found in less dense medium away from the Galactic plane which would explain their symmetrical shape mainly due to the lower density medium within which they expand. However, there have been reports of type Ia SNRs with disturbed shapes that are located close to the Galactic plane. The SNR G321.3-3.9 is a showcase example of an elliptical-shaped SNR that lies close to the Galactic plane and is believed to be of type Ia progenitor origin, as reported by Mantovanini et al. (2024). Therefore, the location of the SNR G309.8+00.0 would explain its elliptical, and thus less symmetrical, shape. A deep X-ray observation of the remnant is necessary to investigate in detail its X-ray spectrum and consequently its progenitor nature. In addition, optical studies of the remnant would be essential to examine the presence of radiative shocks in dense knots that would be evident of circumstellar material (CSM) shed by the progenitor. Toward this end, we also investigated the full-sky Hα map with 6' (FWHM) resolution (Finkbeiner 2003) from the remnant's location, but no optical counterpart was found.

We also provide a distance and age estimate of the SNR using the absorption column density values derived from its X-ray spectral fit. The distance value of the order of 10 kpc that we derived, by exploiting the latest optical extinction data sets by Lallement et al. (2022) and the derived $N_{\rm H}$ values, appears to be inconsistent with previous distance measurements of the remnant (3.12 kpc (Wang et al. 2020)). The large uncertainties in the methods employed, both in this work and in the literature, for the distance computation force us to discuss age estimates when considering both a 3.12 kpc and a 10 kpc distance. We obtain an age of the order of 10^4 yr and an age of the order of 10^5 yr in the two distinct cases.

In the case of a core-collapse (CC)-type SN progenitor, we also examined potential associations with nearby pulsars. The J1350-6225 (4FGL J1350.6-6224) pulsar, which is located just 0.35° away from the remnant's center, and the J1358-6025 (4FGL J1358.3-6026) pulsar located 1.88° away from the remnant's center (both outside the remnant's extension) appear to be the most probable candidates based on their age and transverse velocity estimates that would be required to reach their present location assuming that they started traveling from the center of the remnant.

Employing 15.5 years of *Fermi*-LAT data and carrying a detailed spatial data analysis of the γ-ray emission at and around the SNR G309.8+00.0, we show that the emission from the unidentified 4FGL J1349.5-6206c source can either be modeled as a single source that is likely associated with the SNR or be decomposed to four point-like components. In the latter case, the src component which is spatially coincident with the southern part of the SNR G309.8+00.0 (which is also the brightest – enhanced X-ray emission – part of the remnant's X-ray emitting shell) is detected with a 5.8σ significance above 1 GeV. Thus we conclude that at least a significant part of the γ-ray emission (if not all), named after 4FGL J1349.5-6206c, is likely associated with the SNR G309.8+00.0. The spectral shape of both the src component and the entire 4FGL J1349.5-6206c source appears to be best-fitted with a LogParabola. However, a powerlaw model cannot be ruled out. The spatial component of the src component can be well-fitted with both a point-like and an extended morphology. An improved PSF size is required to inspect in detail the emission spatial components < 5 GeV aiming at addressing the bias of the limited photon statistics at higher energies and consequently disentangle between a single source or multiple distinct source components. The shape and narrow energy range to which both the src component and the 4FGL J1349.5-6206c source GeV SED extends prevent us from providing a more complete description of the nature of the gamma-ray emission and distinguishing between hadronic and leptonic origin of the gamma-ray photons. However, the relatively old remnant's age of $10^4 - 10^5$ yr supports a hadronic gamma-ray interpretation.

This analysis demonstrates the importance of multiwavelength studies in determining the key properties of Galactic SNRs. An in-depth examination of the SNR G309.8+00.0 is, however, prohibited due to its location. To fully understand the true physical processes behind the emission mechanics of this SNR, future studies utilizing longer exposure times in X-rays and an improved instrument PSF at $\sim$ GeV energies will be required.

Acknowledgements

M.M. and G.P. acknowledge support from the Deutsche Forschungsgemeinschaft through grant PU 308/2-1.

This work is based on data from eROSITA, the soft X-ray instrument aboard SRG, a joint Russian-German science mission supported by the Russian Space Agency (Roskosmos), in the interests of the Russian Academy of Sciences represented by its Space Research Institute (IKI), and the Deutsches Zentrum für Luft- und Raumfahrt (DLR). The SRG spacecraft was built by Lavochkin Association (NPOL) and its subcontractors, and is operated by NPOL with support from the Max Planck Institute for Extraterrestrial Physics (MPE).

The development and construction of the eROSITA X-ray instrument was led by MPE, with contributions from the Dr. Karl Remeis Observatory Bamberg & ECAP (FAU Erlangen-Nuernberg), the University of Hamburg Observatory, the Leibniz Institute for Astrophysics Potsdam (AIP), and the Institute

for Astronomy and Astrophysics of the University of Tübingen, with the support of DLR and the Max Planck Society. The Argelander Institute for Astronomy of the University of Bonn and the Ludwig Maximilians Universität Munich also participated in the science preparation for eROSITA. The eROSITA data shown here were processed using the eSASS/NRTA software system developed by the German eROSITA consortium.

We thank the EXPLORE team which provided us access to the G-TOMO tool of the EXPLORE platform https://explore-platform.eu/ allowing us to exploit updated GAIA-2MASS data.

References

Abdo, A. A., Ackermann, M., Ajello, M., et al. 2010, ApJS, 188, 405
Abdollahi, S., Acero, F., Baldini, L., et al. 2022, ApJS, 260, 53
Acero, F., Ackermann, M., Ajello, M., et al. 2015, ApJS, 218, 23
Acero, F., Ackermann, M., Ajello, M., et al. 2016, ApJS, 224, 8
Ackermann, M., Ajello, M., Allafort, A., et al. 2013, Science, 339, 807
Ballet, J., Bruel, P., Burnett, T. H., Lott, B., & The Fermi-LAT collaboration. 2023, arXiv e-prints, arXiv:2307.12546
Borkowski, K. J., Hendrick, S. P., & Reynolds, S. P. 2006, The Astrophysical Journal, 652, 1259
Borkowski, K. J., Lyerly, W. J., & Reynolds, S. P. 2001, ApJ, 548, 820
Brunner, H., Liu, T., Lamer, G., et al. 2022, A&A, 661, A1
Cash, W. 1979, ApJ, 228, 939
Caswell, J. L., Haynes, R. F., Milne, D. K., & Wellington, K. J. 1980, MNRAS, 190, 881
Chiotellis, A., Schure, K. M., & Vink, J. 2012, A&A, 537, A139
Clark, D. H., Caswell, J. L., & Green, A. J. 1975, Australian Journal of Physics Astrophysical Supplement, 37, 1
Cordes, J. M. & Lazio, T. J. W. 2003, NE2001.I. A New Model for the Galactic Distribution of Free Electrons and its Fluctuations
Dame, T. M., Hartmann, D., & Thaddeus, P. 2001, ApJ, 547, 792
Ebeling, H., White, D. A., & Rangarajan, F. V. N. 2006, Monthly Notices of the Royal Astronomical Society, 368, 65
Ferrand, G. & Safi-Harb, S. 2012, Advances in Space Research, 49, 1313
Finkbeiner, D. P. 2003, ApJS, 146, 407
Foight, D. R., Güver, T., Özel, F., & Slane, P. O. 2016, ApJ, 826, 66
Green, A. J., Frail, D. A., Goss, W. M., & Otrupcek, R. 1997, AJ, 114, 2058
Green, D. A. 2019, Journal of Astrophysics and Astronomy, 40, 36
H. E. S. S. Collaboration, Abdalla, H., Abramowski, A., et al. 2018a, A&A, 612, A3
H. E. S. S. Collaboration, Abdalla, H., Abramowski, A., et al. 2018b, A&A, 612, A1
H.E.S.S. Collaboration, Abdalla, H., Abramowski, A., et al. 2018, A&A, 612, A8
Khabibullin, I. I., Churazov, E. M., Chugai, N. N., et al. 2024, arXiv e-prints, arXiv:2401.17261
Koyama, K., Petre, R., Gotthelf, E. V., et al. 1995, Nature, 378, 255
Lallement, R., Vergely, J. L., Babusiaux, C., & Cox, N. L. J. 2022, A&A, 661, A147
Leahy, D. A. & Williams, J. E. 2017, The Astronomical Journal, 153, 239
Mantovanini, S., Becker, W., Khokhriakova, A., et al. 2024, arXiv e-prints, arXiv:2401.17294
Masai, K. 1984, Ap&SS, 98, 367
Merloni, A., Lamer, G., Liu, T., et al. 2024, A&A, 682, A34
Merloni, A., Predehl, P., Becker, W., et al. 2012, arXiv e-prints, arXiv:1209.3114
Michailidis, M., Pühlhofer, G., Becker, W., et al. 2024a, arXiv e-prints, arXiv:2401.17312
Michailidis, M., Pühlhofer, G., Santangelo, A., Becker, W., & Sasaki, M. 2024b, A&A, 685, A23
Nolan, P. L., Abdo, A. A., Ackermann, M., et al. 2012, ApJS, 199, 31
Pavlović, M. Z., Urošević, D., Vukotić, B., Arbutina, B., & Göker, Ü. D. 2013, ApJS, 204, 4
Pearson, K. 1900, The London, Edinburgh, and Dublin Philosophical Magazine and Journal of Science, 50, 157
Predehl, P., Andritschke, R., Arefiev, V., et al. 2021, A&A, 647, A1
Sunyaev, R., Arefiev, V., Babyshkin, V., et al. 2021, A&A, 656, A132
Wang, S., Zhang, C., Jiang, B., et al. 2020, A&A, 639, A72
Whiteoak, J. B. Z. & Green, A. J. 1996, A&AS, 118, 329
Wilms, J., Allen, A., & McCray, R. 2000, ApJ, 542, 914
Yamaguchi, H., Koyama, K., & Uchida, H. 2011, Publications of the Astronomical Society of Japan, 63, S837
Yao, J. M., Manchester, R. N., & Wang, N. 2017, ApJ, 835, 29
Yasuda, H. & Lee, S.-H. 2019, ApJ, 876, 27

3.5 G. Pühlhofer, M. Michailidis, N. Nguyen, A. Santangelo, W. Becker, M. Sasaki, G. Ponti. Identification of HESS J1614-518 as Supernova remnant using GLEAM, eROSITA and *Fermi*-LAT survey data. In: Astronomy & Astrophysics (A&A), to be submitted

Astronomy & Astrophysics manuscript no. output
June 10, 2024

Identification of HESS J1614-518 as Supernova remnant using GLEAM and eROSITA survey data

G. Pühlhofer[1], M. Michailidis[1⋆], N. T. Nguyen-Dang[1], A. Santangelo[1], M. Sasaki[2], W. Becker[3], G. Ponti[3]

[1] Institut für Astronomie und Astrophysik Tübingen (IAAT), Sand 1, 72076 Tübingen, Germany
e-mail: gerd.puehlhofer@uni-tuebingen.de
[2] Universität Erlangen/Nürnberg, Dr.-Remeis-Sternwarte, Sternwartstraße 7, D-96049, Bamberg, Germany or ECAP Erlangen
[3] Max-Planck-Institut für extraterrestritche Physik, Giessenbachstrasse, 85748 Garching, Germany

To be submitted

ABSTRACT

We report new soft X-ray and radio continuum observations of the TeV-emitting supernova remnant (SNR) candidate HESS J1614-518, using eROSITA and MWA data. Radio continuum data were retrieved from the GLEAM survey, X-ray data from the first four completed full-sky eRASS surveys. An object displaying a shell-type morphology is discovered in GLEAM data, matching the TeV source position and morphology. An X-ray counterpart is discovered in eRASS data above ~ 1.3 keV, in good agreement with the radio and TeV sources, above a softer and more extended X-ray component which is likely unrelated to the object. The findings confirm the SNR nature of HESS J1614-518. A combined GeV-TeV γ-ray spectrum, using updated data from Fermi-LAT, displays a peak structure that is compatible with Inverse Compton emission from relativistic electrons in a standard one-zone emission scenario.

Key words. supernova remnants (Individual object: HESS J1614-518) — multiwavelength study — cosmic rays: acceleration

1. Introduction

Galactic supernova remnants are predominantly discovered in the radio continuum band, and to a smaller extent in the X-ray domain. A discovery of an SNR in the gamma-ray domain might be interpreted as an indication of a strong hadronic component of the relativistic particles responsible for the gamma-ray emission, given that relativistic hadrons only radiate at gamma-ray energies, above the energy threshold for π^0-production. In recent years, several TeV sources along the Galactic plane have been discovered, the nature of which could not be immediately clarified. In particular, the H.E.S.S. Galactic plane survey (HGPS) has yielded a considerable number of unidentified sources. From statistical considerations and also from the center-filled morphology of these sources, it is likely that many of those objects are pulsar wind nebulae (PWNe). Only a small number of HGPS sources was suggested to be SNR candidates, based on the shell-type appearance of the TeV sources (H.E.S.S. Collaboration et al. 2018). Amongst those sources, HESS J1614-518 stood out at the time of discovery because of a comparatively luminous counterpart in the Fermi-LAT band showing a hard spectrum below 1 TeV with a differential photon index of $\sim$2 (H.E.S.S. Collaboration et al. 2018). Such a spectral shape was indicative of a standard hadronic emission spectrum from a relativistic hadronic particle population currently being accelerated by diffusive shock acceleration.

Convincing counterparts to HESS J1614-518 with matching morphology in energy bands below the gamma-ray regime have not been reported yet in the literature. The source has a diameter of $\sim 0.8^\circ$ and is located in the Galactic Plane, which both complicates the identification of counterparts. A tentative detection of extended X-ray emission in the 3-7 keV band with XMM-Newton from a North-Eastern portion of the object was reported in H.E.S.S. Collaboration et al. (2018). We report here the discovery of a radio-continuum emitting shell in morphological agreement with the TeV shell, as well as extended X-ray emission from the object that is consistent with the TeV morphology. While a spectral index of the radio emission cannot be determined because of the sparseness of the radio data, the combination of the gamma-ray, radio and X-ray information firmly classifies the source as a SNR. We also readdress the GeV-TeV spectrum in view of the fact that more Fermi-LAT data and updated analysis methods have become available (de Palma et al. 2019; Guo & Xin 2021).

The paper is organized as follows: In section 2, the observations and the reduction of the X-ray data from the eROSITA survey is described. We also present updated GeV results using the full Fermi-LAT data set available to date. To obtain a clear identification of the different counterparts, in section 3 we perform a quantitative comparison of the TeV, radio, and X-ray morphologies of the sources. In section 4 we put the measured fluxes into context of broadband spectral models describing the emission from assumed nonthermal particle populations. In section 5, we discuss the distance to HESS J1614-465 in view of the obtained results. All results are further discussed in section 6 and are put into context of data from other SNRs. We conclude with a summary in section 7.

2. Observations and data reduction

The TeV data (sky map and energy spectrum of the entire source) used in this paper have been obtained with the H.E.S.S. telescopes and are retrieved from H.E.S.S. Collaboration et al. (2018), with an energy threshold of 1 TeV for the sky maps and a 0.3 TeV spectral energy threshold. The radio continuum sky

⋆ Corresponding author, e-mail: michailidis@astro.uni-tuebingen.de

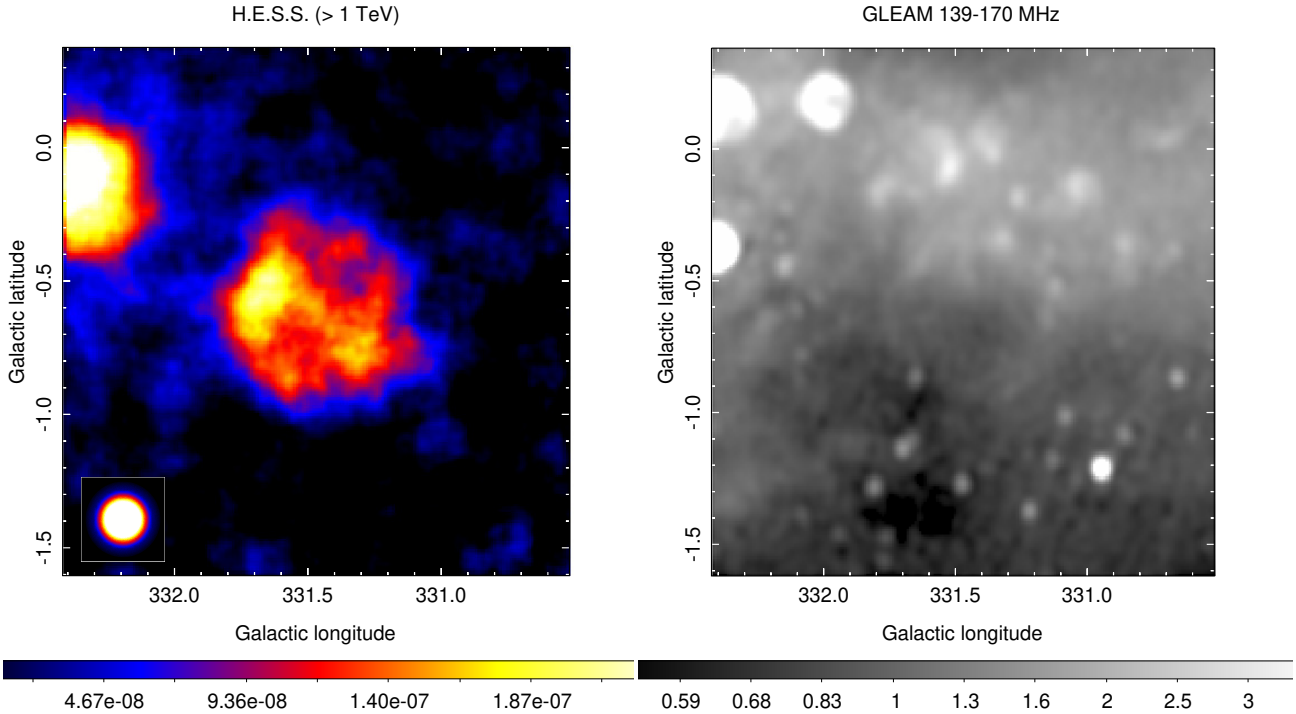

Fig. 1. Left panel: TeV surface brightness map of HESS J1614-518, expressed in units of counts/[$m^2 \cdot s \cdot deg^2$] above 1 TeV (H.E.S.S. Collaboration et al. 2018). The image (pixel size $\sim 36''$) is correlated with a circle with a radius of 0.1 deg, and was additionally convolved with a Gaussian with $\sigma = 36''$ to remove statistically not significant features, similar to what was done in (H.E.S.S. Collaboration et al. 2018). Right panel: GLEAM radio continuum intensity map at the 139-170 MHz frequency range, in units of Jy beam^{-1}. The beam size is $3.299' \times 3.018'$, no further smoothing was applied to the image (whose pixel size is $\sim 34''$).

map (139-170 MHz) is taken from the publicly available GaLactic and Extragalactic All-sky MWA survey (GLEAM)[1], a survey of the entire radio sky south of declination 30° at the frequency range between 72 and 231 MHz (Wayth et al. 2015; Hurley-Walker et al. 2017; For et al. 2018; Hurley-Walker et al. 2019b). The remnant is visible on all five discrete GLEAM radio continuum maps, 72-103 MHz, 103-139 MHz, 139-170 MHz, 170-201 MHz, and 200-230 MHz that provide nearly contiguous coverage. For display purposes and further morphology analysis, we selected the frequency band 139-170 MHz where the remnant is best visible and appears to have a well-defined shell structure. A GLEAM RGB cube, formed as R:72-103 MHz, G:103-134 MHz, B:139-170 MHz, was also employed aiming at discriminating the shell-type morphology of the remnant from nearby HII regions and extracting the remnant's flux density. The TeV and radio sky maps are shown in Fig. 1, left and right panel, respectively.

X-ray sky maps and spectrum are derived from the first four surveys of the eROSITA all-sky survey, making use of a single sky tile of square shape and a size of $3.6^\circ \times 3.6^\circ$ (ObsID 242141, named after a unique six-digit configuration: the first three digits correspond to Right Ascension (RA) and the last three to Declination (Dec) of the tile center). The X-ray analysis is described in section 2.1. GeV γ-ray sky maps, above 10 GeV, and the spectrum of the source in the 1-800 GeV energy band are derived from publicly available Fermi-LAT data; the analysis is described in section 2.2.

[1] `https://www.mwatelescope.org/science/galactic-science/gleam/`

2.1. eROSITA data analysis

eROSITA is a wide-field X-ray instrument consisting of seven co-aligned individual telescopes, which is hosted on the spacecraft Spectrum-X-Gamma (Merloni et al. 2012; Sunyaev et al. 2021; Predehl et al. 2021). The instrument covers an energy range of 0.2-10 keV. In the initial survey phase, which started in 2019, the satellite is steered to cover the entire sky every six months. For the presented results, data from four surveys, eRASS:4, have been analyzed. Pipeline version c020 was adopted and data processing was carried out using the `evtool` and `srctool` tasks of version `eSASSusers_201009` of (Brunner et al. 2022) of eSASS (eROSITA Standard Analysis Software).

2.1.1. Image analysis

Data analysis was performed using a single sky tile, with ObsID: 242141. The data reduction process involves deleting all events flagged as corrupt either individually or as part of a corrupt frame, retaining all four of the recognized legal patterns (`pattern=15`), and identifying and repairing disordered GTIs. For the image production, events from all 7 telescopes, TM1-7, were used. The left panel of Fig. 2 shows a $4.2^\circ \times 4.2^\circ$ sky area around HESS J1614-518, using a broad energy range from 0.2-5.0 keV. A $60'$ extraction radius was used to filter out all point sources above 3σ detection significance. Additionally, the bright sources RCW 103 (an SNR) and 4U 1608-52 (a Low Mass X-ray Binary, LMXB) as well as the SNR Kes 32 are masked for clarity. The binary is visible in eRASS2 and eRASS4, while it was found in off-state during eRASS1 and eRASS3.

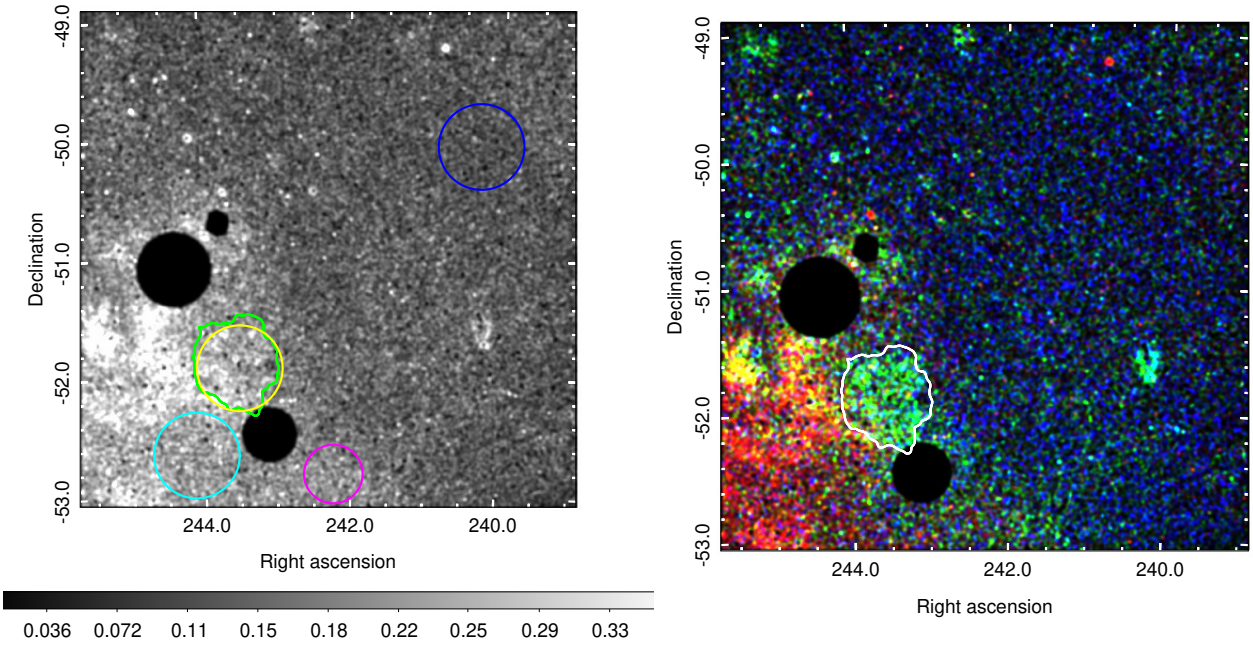

Fig. 2. eRASS:4 intensity sky maps of the area around HESS J1614-518. At the left panel, the full energy band 0.2-5.0 keV is shown with a linear grey-scale. At the right panel, an RGB representation (R: 0.2-1.3 keV, G: 1.3-2.5 keV, B: 2.5-5.0 keV) with a squared color palette is used, to enhance the visibility of distinct structures. The images are plotted in units of counts/pixel with a pixel size of $10''$, and are convolved with a $\sigma = 45''$ Gaussian. The green (left panel) and white (right panel) contours mark the 5 σ significance TeV extent of HESS J1614-518 as measured with H.E.S.S. (H.E.S.S. Collaboration et al. 2018). Point sources are filtered out, and the LMXB 4U 1608-52 as well as the SNRs RCW 103 and Kes 32 are masked. At the left panel, additionally, the four spectral extraction regions used for the analysis are shown. The yellow circle denotes the on-source region with position and extension corresponding to the radio GLEAM centroid as defined in Tab. 2. Blue and cyan circles represent the selected background control regions, while the magenta circle represents a region adjacent to the cyan-schemed region which was used to validate the quality of the background model.

This sky map is overall dominated by diffuse extended emission, which is mainly confined to below 1.3 keV. The emission from HESS J1614-518 only becomes apparent when filtering out this soft emission. The right panel of Fig. 2 shows an RGB representation of the map (R: 0.2-1.3 keV, G: 1.3-2.5 keV, and B: 2.5-5.0 keV), where the X-ray emission coincident with the TeV source becomes clearly apparent. The range of the medium energy band was optimized using the energy spectrum extracted from the HESS J1614-518 region as discussed below. At the left panel of Fig. 3, the same sky field is shown after restriction to the energy range 1.3-2.5 keV, clearly demonstrating that the emission is confined inside the outer 5σ TeV emission significance contour detected with H.E.S.S. (H.E.S.S. Collaboration et al. 2018). There is also no extension of this diffuse emission region into the LMXB area. To illustrate this, at the right panel of Fig. 3 the shown data set was restricted to the first eRASS survey, during which the LMXB was in an off state, and the mask is omitted.

2.1.2. Spectral analysis

To derive an energy spectrum from the TeV source region, events were selected from a circular region with radius 0.4° around the position RA=243.510°, Dec=-51.919°. Position and extension correspond to the TeV centroid as reported in H.E.S.S. Collaboration et al. (2018) and to a radius that encompasses both the TeV emission and the radio shell (see section 3), respectively. A systematic uncertainty check was also performed by extracting the spectrum from the radio and X-ray best fit regions. No significant variation was found in the parameters of the spectral fits. Events from five telescopes, TM1, TM2, TM3, TM4, and TM6 were used for the spectrum extraction, while TM5 and TM7 event data were omitted since the latter telescopes suffer from light leaks discovered at early stages during the commissioning phase of eROSITA, specifically due to sun-light reaching the CCD by-passing the filter wheel as the consequence of the lack of Aluminium (Al) on-chip optical filters on those telescopes. As a precaution against possible contamination of our signal, and thus of the derived spectrum, by point sources that fall within the region of interest, we applied a similar filter to the one used in Fig. 2, setting a $60'$ extraction radius in order to exclude all point sources detected with a 3σ significance or higher. One of the point sources stands out because it is located just $1'$ away from the geometrical center of both the TeV and radio shell-type emission, called XMMU J161406.0-515225. As of now, this source has not been considered as a CCO (central compact object) candidate, because it has been classified as an X-ray emitting star (Lin et al. 2012) after the detection of an optical counterpart reported in Landi et al. (2006). However, the possibility of an unresolved binary (cf., e.g., the CCO and its stellar binary companion in the SNR HESS J1731-347, Doroshenko et al. 2016) cannot be excluded.

An estimate of the astrophysical background which is representative for the source region is hampered by the diffuse, uneven emission in the surrounding area, which is considered to stem from diffuse emission from the Galactic Plane along

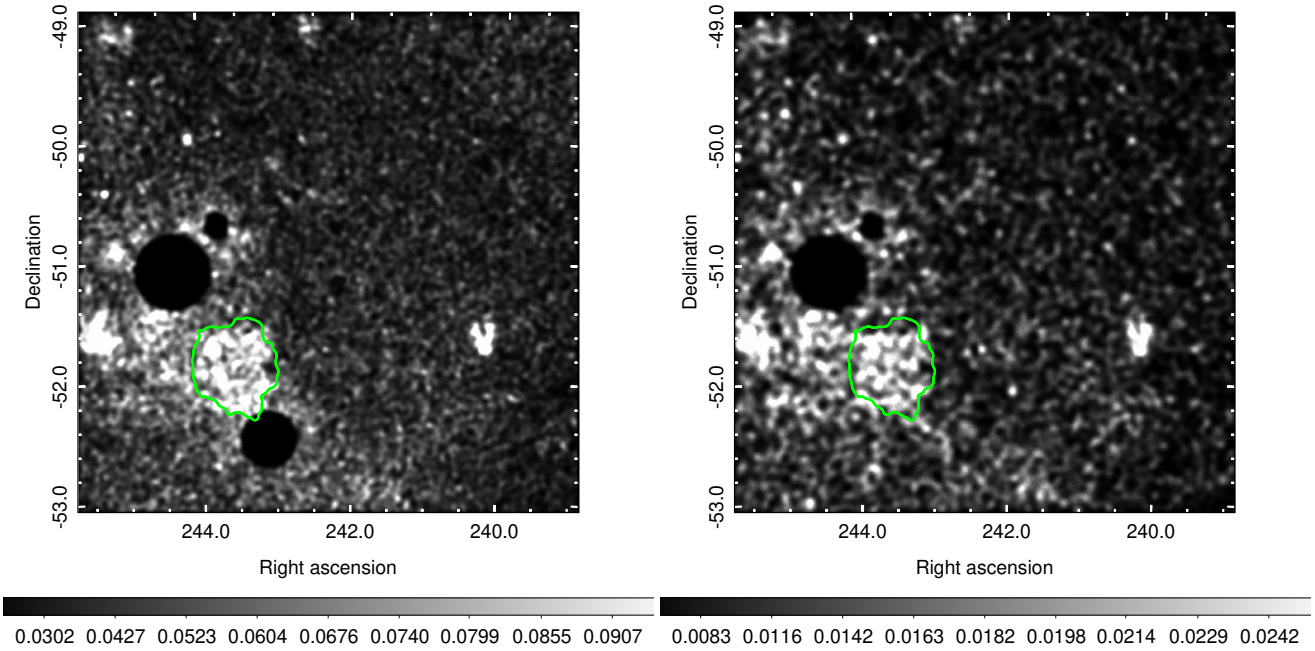

Fig. 3. eRASS intensity sky maps of the area around HESS J1614-518, restricted to the 1.3-2.5 keV energy band in which the emission from HESS J1614-518 is concentrated. A squared color distribution is used on both panels. The images are plotted in units of counts/pixel with a pixel size of $10''$, and are convolved with a $\sigma = 75''$ and $\sigma = 100''$ Gaussian for the left and right panels, respectively. Point sources are filtered out, and the LMXB 4U 1608-52 (only left panel) as well as the SNRs RCW 103 and Kes 32 are masked. The green contour marks the 5 σ significance TeV extent of HESS J1614-518 as measured with H.E.S.S. (H.E.S.S. Collaboration et al. 2018). At the left panel, the entire eRASS:4 data set is shown. To illustrate that the emission from HESS J1614-518 is fully confined inside the TeV contour also towards the LMXB position, at the right panel the data set is restricted to eRASS:1 during which the LMXB was in a low state and is not masked in the image.

with emission from unresolved sources. Two nearby circular regions, which are of same size as the source extraction region and are free of apparent strong sources, were chosen to estimate the background at the source position (see left panel of Fig. 2). The blue-schemed region has been chosen to be free of diffuse foreground and/or background emissions except for the astrophysical background, whose components are described below. Contrary to that, the cyan-schemed region has been chosen such that it is likely fully dominated by the diffuse foreground and/or background of the softer extended X-ray emission detected at and around HESS J1614-518, in the energy range below ~ 1.3 keV, but free of what we believe are unrelated X-ray excesses detected in the surrounding area of HESS J1614-518. These two control regions, when appropriately combined (details see below), yeald a spectrum that matches the source region's spectrum in the energy range < 1.3 keV, i.e. outside of the energy range where emission from HESS J1614-518 appears visible.

The contribution of the soft diffuse foreground and/or background emission component that the cyan region displays at energies > 1.3 keV is very relevant to correctly model the X-ray excess emission originating from the region of interest, since it exhibits strong emission lines in the 1.3-2.5 keV energy range, even though those appear less significant compared to the emission at softer X-rays. We validated the quality of the background model by additionally extracting the spectrum from an adjacent region as shown on the left panel of Fig. 2 with a magenta circle. This region was chosen as the best available additional control region with visually similar background properties, i.e. free of X-ray sources but dominated by the apparent diffuse foreground and/or background emission. Indeed, the same strong emission lines in the 1.3-2.5 keV energy band are present as in the cyan-circled background, so the features are not specific to the cyan-circled control region (i.e., the same background model, as introduced below, has been successfully applied to the magenta-colored background control region).

The background emission is modeled with the following components: the instrumental or particle background arising

Table 1. Best-fit parameters of the HESS J1614-518 X-ray spectrum.

Region	Background (Cyan)		On source (Yellow)		
Model	vapec+vapec		pow	vapec	vapec
$kT_{(keV)}$	$0.25^{+0.01}_{-0.01}$	$0.63^{+0.05}_{-0.05}$		$1.13^{+0.12}_{-0.07}$	$0.96^{+0.06}_{-0.06}$
Γ			$1.79^{+0.38}_{-0.32}$		
$N_{H(10^{22}cm^{-2})}$	$0.09^{+0.03}_{-0.03}$	$0.98^{+0.12}_{-0.11}$	$0.82^{+0.32}_{-0.22}$	$2.47^{+0.14}_{-0.15}$	$3.00^{+0.19}_{-0.17}$
Ne	$3.21^{+0.86}_{-0.82}$	$1.78^{+0.46}_{-0.41}$	N.A		
Mg			N.A		$0.27^{+0.26}_{-0.24}$
Al		$4.52^{+1.83}_{-1.64}$	N.A		
Si			N.A		$0.20^{+0.12}_{-0.10}$
S		$4.56^{+1.99}_{-1.68}$	N.A		$0.04^{+0.26}_{-0.04}$
χ^2/dof	1.01		1.11	1.28	1.15

Notes. Best-fit parameters are reported along with 1σ errors. Where not defined otherwise, elemental abundances are set to Wilms (Wilms et al. 2000).

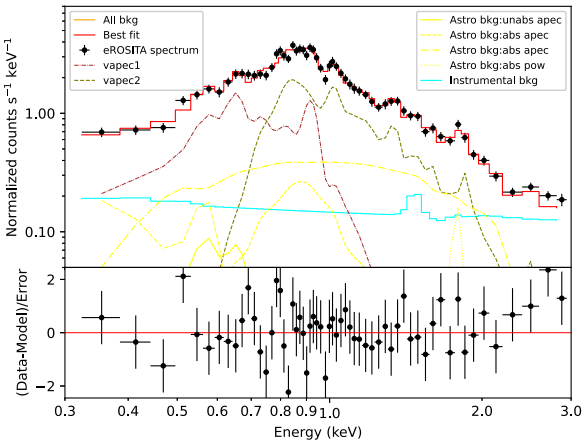

Fig. 4. Energy spectrum in the 0.3-3.0 keV energy band extracted from the cyan background control region (see Fig. 2), using eRASS:4 data obtained from TM1-4 and TM6. For visual purposes, adjacent bins are combined until they have a significant detection above 10σ, and a minimum number of 30 counts per bin was applied. The spectrum is modeled with a two-temperature plasma model representing the diffuse foreground and/or background emission component (represented in brown and olive colors). Yellow spectra represent the instrumental background.

from the production of particle secondaries when cosmic-rays interact with the spacecraft and the detector shield (in xspec notation `gaussian + expfac(bkn2pow + powerlaw + powerlaw) + powerlaw + gaussian + gaussian + gaussian+ gaussian + gaussian + gaussian`), the Local Hot Bubble (LHB) originating from the low-temperature plasma which encircles the Galactic neighborhood (expressed in terms of a non-absorbed `apec`), the Galactic Halo (GH) (well-modeled by a two-temperature absorbed plasma `apec+apec`), and the Cosmic X-ray Background (CXB) accounting for the combined emission of unresolved AGN (described by a single absorbed `powerlaw` component). The diffuse foreground and/or background emission component described above is well modeled by a two-temperature plasma model with temperatures of 0.25 keV and 0.63 keV, respectively (`vapec+vapec`), as shown in Fig. 4. Whether that diffuse X-ray emission component should be attributed to foreground and/or background emission is not clear, as indicated by the spectral analysis results (see Tab. 1). The cooler plasma is certainly located in front of HESS J1614-518, given its low absorption column density obtained from the best fit of the source spectrum. The location of the hotter plasma (whether in the foreground, in the background, or coincident with the source) cannot be constrained from the absorption. A similar discussion of that soft X-ray emission component dominating the complex region at and around Kes 32, which is located just 1° to the North of HESS J1614-518, is reported in Vink (2004).

For the on-source fit, given the limited effective area of eROSITA above ∼3 keV, no statistically significant excess counts are detected above that energy from the source region, therefore the fit was a priori restricted to < 3.0 keV. We note that there are hints of diffuse X-ray emission in the eRASS:4 spectrum above 3.0 keV, primarily in the 3.0-6.0 keV energy range weak emission from a population of non-thermal particles could be present. But above 3.0 keV the background becomes dominant (as shown on the right-hand panel of Fig. 5), and we lack a sufficient amount of data (low statistics) to exploit and conduct a detailed spectral analysis in those harder energy ranges. Nevertheless, these hints are consistent to what was reported in H.E.S.S. Collaboration et al. (2018) (i.e., a hard diffuse emission component in the 3.0-7.0 keV energy band) when exploiting XMM-Newton data from the location of HESS J1614-518.

The lower energy threshold was set to 0.3 keV, given that the background model fits the data in the blue and cyan background control regions in the 0.3-3.0 keV energy band with high precision ($\chi^2/d.o.f = 1.01$, see Tab. 1 and Fig. 4). In fact, restricting the fit range to > 1.3 keV would impact the results reported below (e.g. the fitted power-law index would change from ~ 1.8 to ~ 0.9), because of the narrow fit energy range. Since we are confident in the background model below 1.3 keV, we decided to include that energy range in the fits.

The source spectrum is derived with a simultaneous (xspec Ver. 12.12.1 (Dorman et al. 2003)) fit of on-source and background region, using both reference background regions (cyan and blue circles, see above) to determine the background in the on-source region. As introduced above, the blue-colored circular region is well modeled when employing all four aforementioned background components (of astrophysical and instrumental origin), whereas the cyan background control region requires two additional vapec components We determine the thermal plasma temperatures and the photon indices of the astrophysical and instrumental background components from the blue background control region. Those values are then frozen when fitting the cyan background control region. Finally, the on-source (yellow) and cyan (for background) regions are simultaneously fitted, keeping fixed the plasma temperature, elemental abundances, and photon indices (i.e., all spectral components of the cyan background control region except the normalizations). As additional source component, either a non-thermal or a thermal component is then used. C-statistics (Cash 1979) were applied in the fitting procedure to take the low-number statistics into account. To model the Galactic absorption $N_{\rm H}$ towards the source, the `TBABS` absorption model with Wilms abundances (Wilms et al. 2000) was used.

The source was modeled either with a power-law representing synchrotron emission from relativistic electrons, or with an apec model representing hot plasma composed of collisionally ionized diffuse gas (Foster et al. 2012). The power-law fit ($\chi^2/dof = 1.11$) yields a photon index of $\Gamma = 1.79^{+0.38}_{-0.32}$ and an absorption column density of $N_{\rm H} = 0.82^{+0.32}_{-0.22} \times 10^{22}{\rm cm}^{-3}$, and is shown in Fig. 5. The apec fit ($\chi^2/dof = 1.28$) yields a temperature $kT = 1.13^{+0.12}_{-0.07}$ keV with $N_{\rm H} = 2.47^{+0.14}_{-0.15} \times 10^{22}{\rm cm}^{-3}$, as shown on the left panel of Fig. 6. The hot plasma model goodness of fit can be significantly improved to an only marginally worse fit ($\chi^2/dof = 1.15$) compared to the power-law model, when permitting extremely low plasma emission lines. In particular, Magnesium (Mg), Sulfur (S), and Silicon (Si) then need to be strongly sub-solar, as shown in Tab. 1. The obtained temperature and absorption column density in this case are $kT = 0.96^{+0.06}_{-0.06}$ keV and $N_{\rm H} = 3.0^{+0.19}_{-0.17} \times 10^{22}{\rm cm}^{-3}$, respectively, the fit is shown on the right panel of Fig. 6.

Given the limited statistics (excess of ~ 1200 counts in the 1.3-2.5 keV energy range, depending on the selected background control region), the narrow energy band, and the contamination from the larger-scale diffuse emission, from purely statistical arguments neither of the two physical models can be clearly favoured. However, three arguments strongly favour the power-law interpretation. Firstly, the low elemental abundances

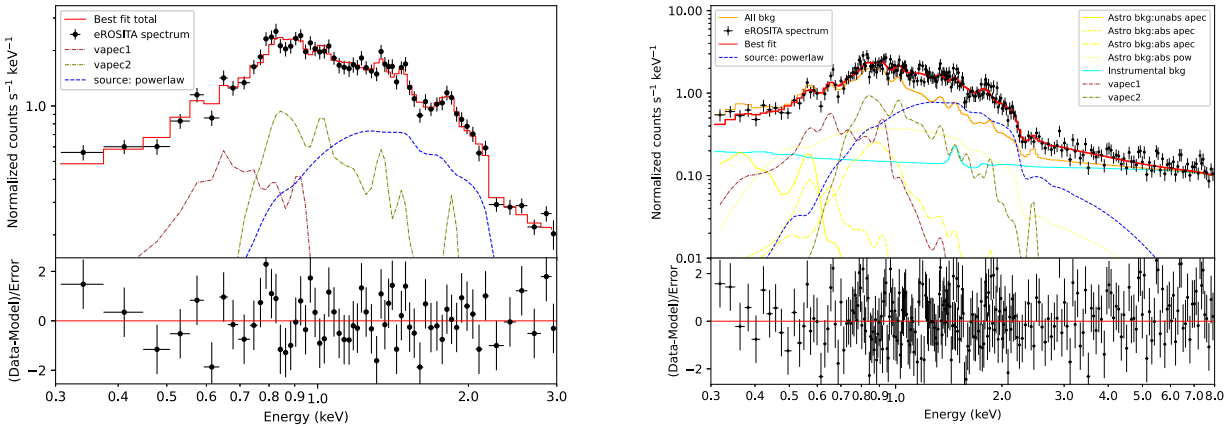

Fig. 5. Left panel: Energy spectrum in the 0.3-3.0 keV energy band obtained from the on-source region (yellow circle in Fig. 2), using eRASS:4 data obtained from TM1-4 and TM6. For visual purposes only, adjacent bins are combined until they have a significant detection at least as large as 10σ, a minimum number of 30 counts per bin was set. HESS J1614-518 energy spectrum is best described by a simple power law indicated with the blue dashed line. The brown and olive dash-dotted lines represent the two plasma temperature model of the diffuse foreground and/or background emission component that dominates at softer X-rays as shown in Fig. 4. Right panel: The same energy spectrum is shown, but raw (no further re-binning than the initial 30 counts per bin has been applied) in the broader 0.3-8.0 keV energy band and with all components contributing to the total emission displayed in detail. The orange line stands for the sum of all background components i.e., instrumental (cyan color), astrophysical (yellow color), and diffuse foreground and/or background (brown and olive colors) detected at and around HESS J1614-518, revealing the overall contribution of the source to the total spectrum.

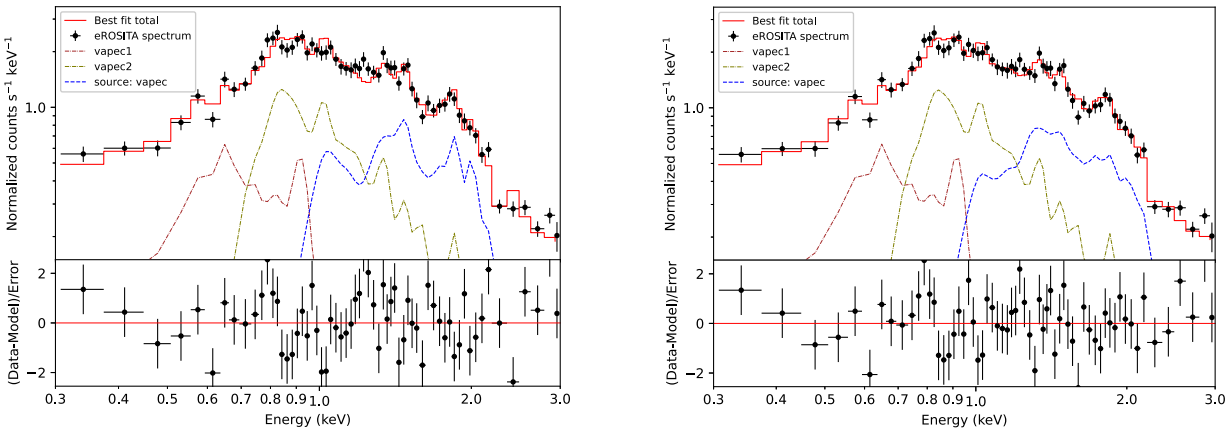

Fig. 6. Left panel: The same energy spectrum as Fig. 5 is shown. A single temperature plasma (vapec) model with abundances set to Wilms (Wilms et al. 2000) is used, instead of a power law, to model the emission from HESS J1614-518. Right panel: The same energy spectrum as Fig. 5 is shown. A single temperature plasma (vapec) model with strongly suppressed Mg, S, and Si emission lines is shown. The rest of the elemental abundances are set to Wilms (Wilms et al. 2000) values.

required for a good thermal fit are untypical for SNR plasmas (adopting the identification of the source as SNR as argued in this paper). Secondly, when attempting to fit the spectrum up to 8 keV (i.e., include that faint diffuse emission above 3.0 keV as mentioned above) an unreasonably high plasma temperature of the scale of 10 keV would be required to describe the spectrum. Keeping the plasma temperature fixed to what is obtained from the spectral fit in the 0.3-3.0 keV energy range ($kT \sim 1.0$ keV, as shown in Tab. 1), positive residuals become apparent in the 3.0-7.0 keV energy band indicating the existence of a weak population of non-thermal particles which cannot be well-modeled by thermal plasma models. And thirdly, when extrapolating the spectrum – after restriction to the extraction region used to derive the XMM-Newton result mentioned in the introduction – into the 3-7 keV range, the power-law is consistent (within the uncertainties of the power-law index) with the flux derived with XMM-Newton in that energy range, while the apec model falls short of it (by a factor of 0.78 [0.67-0.89]). Therefore, we claim that the power-law interpretation is favoured, and conclude that the flux derived with eROSITA from the entire source is likely a measure of its synchrotron emission.

2.2. Fermi-LAT data analysis

Based on four years of Fermi-LAT data (3FGL, LAT Collaboration 2015), Acero et al. (2015) have derived a GeV spectrum from HESS J1614-518. This result was used in H.E.S.S. Collaboration et al. (2018) to produce a GeV-TeV spectrum of the source, which showed a rather hard ($\Gamma \sim 2$) spectrum below 1 TeV indicative of a hadronic emission spectrum, and a softening at higher energies. To improve the LAT spectrum, we have used data until January 2023 (in total ~ 14.5 years) and have derived an updated sky map above 10 GeV and an updated spectrum above 1 GeV.

To this end, we analyzed Pass 8 Fermi-LAT data (P8R3) using the `fermitools` Ver. 2.0.8 standard analysis software, selecting a region of 40° size centered on the remnant's TeV coordinates (see Tab. 2), Source event class and type were selected so that front and back interactions (evclass=128, evtype=3) are included in the data sets. A maximum zenith angle of 90° was used for the data selection. To secure a good sampling of the Fermi-LAT Point Spread Functions (PSF), we set an angular bin size of 0.05°. The Fermi-LAT background was modeled by including the Galactic diffuse component (`gll_iem_v07.fits`), the isotropic diffuse component (`iso_P8R3_SOURCE_V3_v1.txt`), and all sources present in the Fermi-LAT 12 year point source catalog (4FGL-DR3). We chose to let the normalization of all sources within 5° of the center of the region of interest (ROI) free, and fixed the remaining parameters to default catalog values. A maximum likelihood analysis, described in Mattox et al. (1996), was employed to maximize the probability of the model fitting the data. The 4FGL-DR3 extended GeV source 4FGL J1615.3-5146e that is associated with the remnant appears with different spectral parameters than the 3FGL source in Acero et al. (2015), with a Log-Parabola spectrum being favoured over a simple power law. Therefore we tested both models in the following.

We perform a series of binned analysis procedures for extended Fermi-LAT sources. Both residual count map and Test Statistic (TS) maps were constructed to assess the morphology of the gamma-ray emission. The detection significance calculation is based on the maximum likelihood Test Statistic (TS). The process of TS map creation is contingent on a simulated point source which is moved through the grid obtaining the maximum likelihood fit at each position of the grid $2\Delta\ln(\text{likelihood})$. On the left panel of Fig. 7, the Fermi-LAT Test Statistic (TS) skymap above 10 GeV is shown. The right panel of the same figure illustrates the residual count map above 10 GeV, from the exact same position of the sky.

Four distinct approaches were employed for the production of the GeV SED of the source of interest. Initially, we adopted the default 4FG-DR3 spatial disk model of the remnant, Ra=243.83°, Dec=-51.78°, and Radius=0.42°, which favors a reconstructed source position that is somewhat shifted to the North-East (by $\sim 0.3°$) in comparison to the radio and TeV best-fit position of the remnant. This discrepancy is also visible in the obtained GeV skymaps of Fig. 7. We then moderately modified the parameters of this default spatial disk model by changing its center and size according to the best-fit TeV (H.E.S.S. Collaboration et al. 2018) and radio centroids as obtained from this work, respectively, and re-ran the spectral analysis. The two models derived when moderately modifying the spatial disk parameter to match those of the TeV and radio centroids are consistent with the default spatial disk Fermi/LAT model, while the resulting difference in flux and spectrum is negligible. Finally, for consistency purposes between the GeV and TeV data, a shell-type structure as defined in H.E.S.S. Collaboration et al. (2018) was also adopted as a spatial template, to evaluate whether the GeV emission is also consistent with a shell-type emisssion pattern as observed in the TeV range. As expected by the obtained morphology of the source at GeV energies, the TS value for a shell-like spatial template is slightly lower than that for a disk template (~ 280 vs ~ 320), however it is statistically similarly acceptable, and motivated by the TeV result it is a viable physics model of the source also in the GeV band. The GeV flux derived with a shell model is only $\sim 7\%$ lower than that derived with a disk-like template. Thus, the GeV spectrum derived with the disk model can also be used to estimate the spectrum under a shell hypothesis, for example when describing the γ-ray SED with a one-zone model.

For the spectral fitting procedure, the normalizations of all 4FGL-DR3 sources included in the model within 5° distance from the analysis (source of interest) center, as well as the normalizations of the Galactic diffuse and isotropic background were let to vary. A Log-Parabola describes the GeV spectrum of HESS J1614-518 better than a power-law (a result which is also supported by the derived spectral plots of all 4FGL-DR3 sources[2]). To derive spectral data points, the data are divided into five equally-spaced (in log-space) bins. The resulting SED in the 1-800 GeV energy band is shown in the right panel of Fig. 8, together with the H.E.S.S. data, revealing a substantially steeper spectrum than what was previously reported when using 4 years of Fermi-LAT data (3FGL).

The result is largely insensitive to the adopted spectral model (best-fit log-parabola or best-fit power-law) used to construct the SED. In particular, as explicitly stated in the 12 year Fermi/LAT source catalog[2] sources are modeled as a Log-Parabola if statistically significant curvature is detected (according to `Signif_Curve task`), or as a simple powerlaw otherwise. Overall, we conclude that this discrepancy between published and updated results arises as a combination of the additional years of Fermi/LAT data employed in this work and the updated model used in the 4FGL-DR3 data to model the Galactic diffuse component and the isotropic diffuse component (`gll_iem_v07.fits` and `iso_P8R3_SOURCE_V3_v1.txt` Fermi/LAT files respectively).

Fermi-LAT analysis results reported in this work are consistent with those obtained by Guo & Xin (2021) who analyzed ~ 12 years of Fermi-LAT data in a similar effort to refine the morphology of the GeV emission, and broadly consistent in terms of spectral shape with the obtained spectral plots (and corresponding spectral models) of 4FGL-DR3 sources[2].

2.3. GLEAM data analysis

For this work, we used publicly available GLEAM radio continuum data, which were extracted using the GLEAM's team cutout server into 3° raw cutouts. However, the first release of GLEAM radio data (Wayth et al. 2015) covers the extragalactic sky minus the Galactic Plane (for the most part) and since HESS J1614-518 is located on the Galactic plane, although raw intensity maps from the location of our source of interest are available, no further analysis products have been publicly released. This prevents us from cleaning the images and/or performing a detailed radio spectral analysis of the remnant. However, since the publicly available image products have pixels in units of Jy/beam, they can be used for rough flux estimates.

[2] `https://fermi.gsfc.nasa.gov/ssc/data/access/lat/12yr_catalog/`

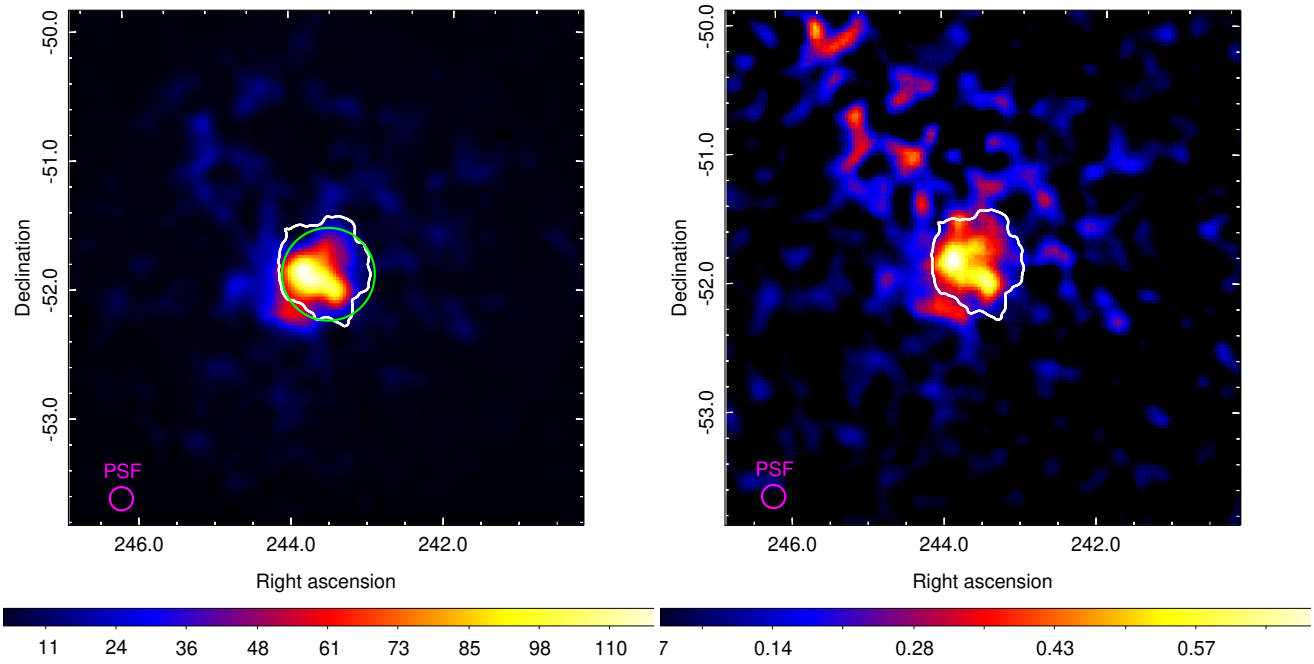

Fig. 7. Left panel: $4^\circ \times 4^\circ$ Fermi-LAT TS map above 10 GeV, centered at the best fit coordinates of the TeV emission according to Tab. 2. The best fit position and size of the counterpart from the GLEAM survey data is illustrated as green circle. The image, which has a $90''$ pixel size, is convolved with a $\sigma = 2.25'$ Gaussian. Right panel: Fermi-LAT residual count map above 10 GeV from the same portion of the sky. The image, which has a $90''$ pixel size, is convolved with a $\sigma = 3.75'$ Gaussian. The white contour marks the 5 σ significance extent of the TeV source as detected with H.E.S.S. (H.E.S.S. Collaboration et al. 2018). The magenta circle represents the 68% containment size of the PSF at the energy threshold of the sky maps (10 GeV), no smoothing applied. *To be checked: Ideally, the PSF representation would be an inset with the same color scale as the actual source.*

As a zero-order attempt, a flux can be derived from the entire on-source region. Taking into account the central frequency (155 MHz) of the 139-170 MHz wide-frequency band used for the construction of the right-hand panel radio continuum image of Fig. 1, the exact size and shape of the beam at that particular declination of the remnant's position, and considering as an extraction region the best radio fit as obtained in sec. 3 and reported in Tab. 2 and a nearby background extraction region of the same size and shape, a source flux can be obtained by simply subtracting the derived background flux from the on-source flux making use of the following mathematical formula for the total flux calculation:

$$\text{Total flux}[\text{erg/cm}^2/\text{s}] = 10^{-23} \times \text{Total flux}[\text{Jy/beam}] \times (\text{pixelarea}[(^\circ)^2] \times \text{central frequency}[\text{Hz}]/\text{beamvolume}[(^\circ)^2]) \quad (1)$$

Beamvolume is defined as:

$$\text{beamvolume} = \frac{\pi \times \phi \times \theta}{4 \times ln2} \quad (2)$$

where ϕ and θ represent the Full Width Half Maximum (FWHM) of the semi-major and semi-minor axis of the beam in deg (an elliptical beam of $\sim 0.055^\circ \times 0.05^\circ$ size is obtained at the remnant's location, as mentioned in the caption of Fig. 1). However, the such-derived result is unstable and not trustworthy (negative flux values, obtained results depend heavily on the selection of the background region), given that the source is located in a highly contaminated region.

A more sophisticated approach in terms of selection of the proper on-source and background regions is therefore necessary. We adopted a similar approach as the one used in the Hurley-Walker et al. (2019a). Here, the `POLYGON_FLUX`[3] software was employed, providing an interactive view of either a single band GLEAM radio continuum image or of the GLEAM RGB cube. In Fig. 9 we show the obtained RGB cube that we inspected in this work for the optimal selection of the on-source and background control regions. The aforementioned image provides a wide frequency coverage of the region of interest, allowing us to distinguish candidate remnants from HII regions, since the latter appear as optically thick structures in dark blue color in the images, due to radio synchrotron absorption. Those dark blue HII regions mainly positioned at the North-Western side of the remnant prevent the detection of the radio synchrotron shell of the remnant when looking at higher frequencies (e.g., at 1.4 GHZ, 873 MHz with the Australian Telescope Compact Array (ATCA) as discussed in H.E.S.S. Collaboration et al. (2018)) where most of the emission seems to be associated with the surrounding HII regions rather than being attributed to the remnant. The proper selection of the flux extraction regions is achieved by inspecting the GLEAM RGB cube and drawing a polygon region that contains the area that the SNR extends over (without including those parts where the remnant overlaps with nearby HII regions - an identical cut to the North-Western parts of the remnant as in sec. 3, where we study the morphology of the remnant, was applied), and additionally disentangling which parts of the annulus surrounding the polygon are representative of the background by excluding polygonal regions which are likely contaminated with HII regions or emission originating from unre-

[3] `https://github.com/nhurleywalker/polygon-flux`

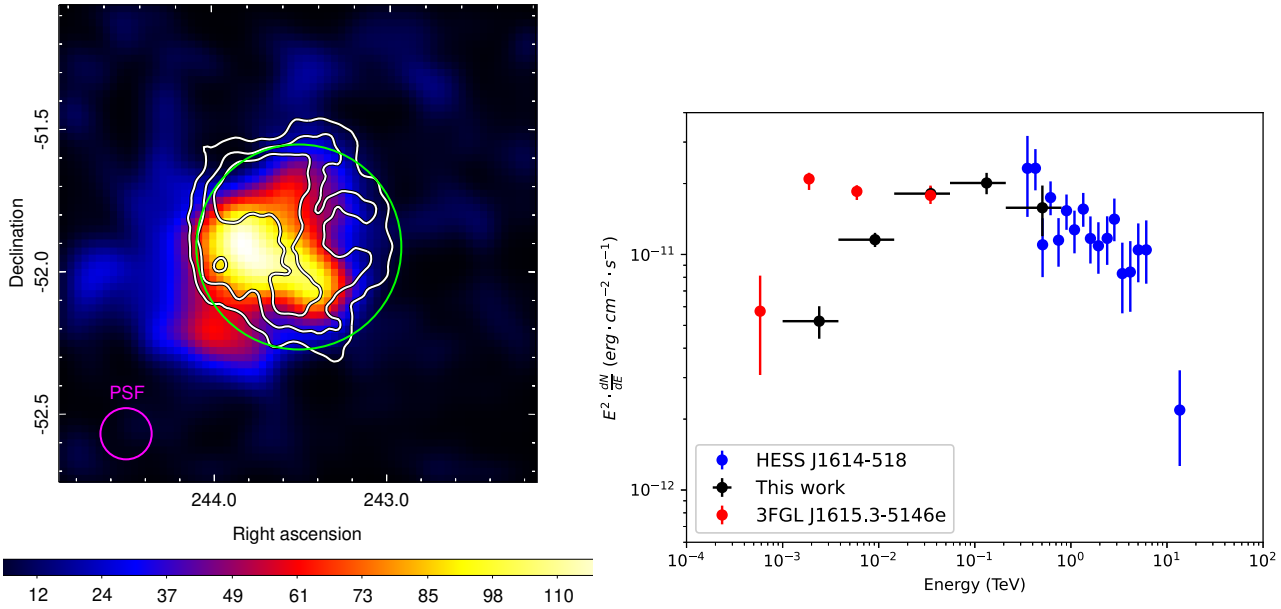

Fig. 8. Left panel: $1.7^\circ \times 1.7^\circ$ Fermi-LAT TS map >10 GeV centered at the best fit coordinates of the TeV emission according to Tab. 2. The white contours mark the 5, 7, 9, 11 σ significance of the source as detected with H.E.S.S. (H.E.S.S. Collaboration et al. 2018). The best fit position of the radio GLEAM survey data is illustrated in green. The image, of 90″ pixel size, is convolved with a $\sigma = 2.25'$ Gaussian. The magenta thick circle represents the 68% containment PSF size, applied at the 10 GeV energy threshold used for the construction of the TS map. Right panel: HESS J1614-518 γ-ray SED. Black dots correspond to the Fermi-LAT spectrum in the 1-800 GeV band. Red and blue dots correspond to the 3FGL GeV spectrum from Acero et al. (2015) and to the H.E.S.S. TeV spectrum from H.E.S.S. Collaboration et al. (2018), respectively.

lated objects. On the right panel of Fig. 9, the selected polygons are displayed. Further explanation of the individual polygons can be found in the caption of the corresponding figure. We calculated the total flux inside the white polygon (on-source region) and the yellow polygonal region (background control region). We then extrapolated these values to the total area of the SNR as computed from the best radio fit in sec. 3 and subtracted the background flux from the on-source value to derive the source flux. The derived flux is $0.31^{+0.19}_{-0.14} \times 10^{-13}$erg/cm^2/s at 155 MHz. $0.13^{+0.08}_{-0.06} \times 10^{-13}$erg/cm^2/s at 88 MHz, $0.23^{+0.15}_{-0.10} \times 10^{-13}$erg/cm^2/s at 118 MHz, and $0.29^{+0.18}_{-0.12} \times 10^{-13}$erg/cm^2/s at 200 MHz. Flux errors were estimated by taking into account errors in the beam size at each individual frequency, errors in the surface brightness calculation when inspecting the reconstructed GLEAM maps by `SAOIMAGE DS9` (i.e., adding up the surface brightness values of each pixel), and errors from the radio morphology study when extrapolating the selected on-source and background regions to the obtained best-fit size and shape of the remnant. The latter error dominates the total error values by a wide margin.

Table 2. Best-fit parameters of HESS J1614-518 observation to a 2D shell model, using H.E.S.S., GLEAM, and eROSITA images.

Data	Parameter (degree)	Best-fit value	Lower bound	Upper bound
TeV	R.A.	243.54	-0.01	+0.01
	Dec.	-51.87	-0.01	+0.01
	R_{in}	0.18	-0.02	+0.02
	R_{out}	0.42	-0.01	+0.01
Radio	R.A.	243.51	-0.02	+0.10
	Dec.	-51.92	-0.04	+0.04
	R_{in}	0.25	-0.03	+0.05
	R_{out}	0.36	-0.09	+0.10
X-rays	R.A.	243.61	-0.01	+0.01
	Dec.	-51.94	-0.02	+0.01
	R_{in}	0.18	-0.01	+0.01
	R_{out}	0.45	-0.01	+0.02

Notes. The values for the TeV data were taken from H.E.S.S. Collaboration et al. (2018). In this work, we treat the parameters derived in the latter work as representative for our analysis, i.e., the position of the centroids is fixed to the TeV centroid.

3. Morphological results

The TeV morphology has been identified in H.E.S.S. Collaboration et al. (2018) as shell-type. The morphology can satisfactorily be described by a thick spherical shell, with homogeneous emission inside the thick shell, which is projected onto the sky (see Tab. 2 for the fit parameters). From the image (Fig. 1) and the radial profile (see Fig. A.1 in H.E.S.S. Collaboration et al. (2018)), respectively, it seems in addition that – even if statistics is limited – there is no full azimuthal symmetry, and some emission might emerge from inside the shell.

The GLEAM (radio continuum emission at 0.139-0.17 GHz) survey data towards the area in which HESS J1614-518 is located exhibit extended diffuse emission likely associated with the Galactic plane as well as nearby HII regions. Nevertheless, a shell-type emission structure co-located with HESS J1614-518 is clearly visible. Given the position and sizes of the TeV and radio sources, it is likely that the emissions stem from the same

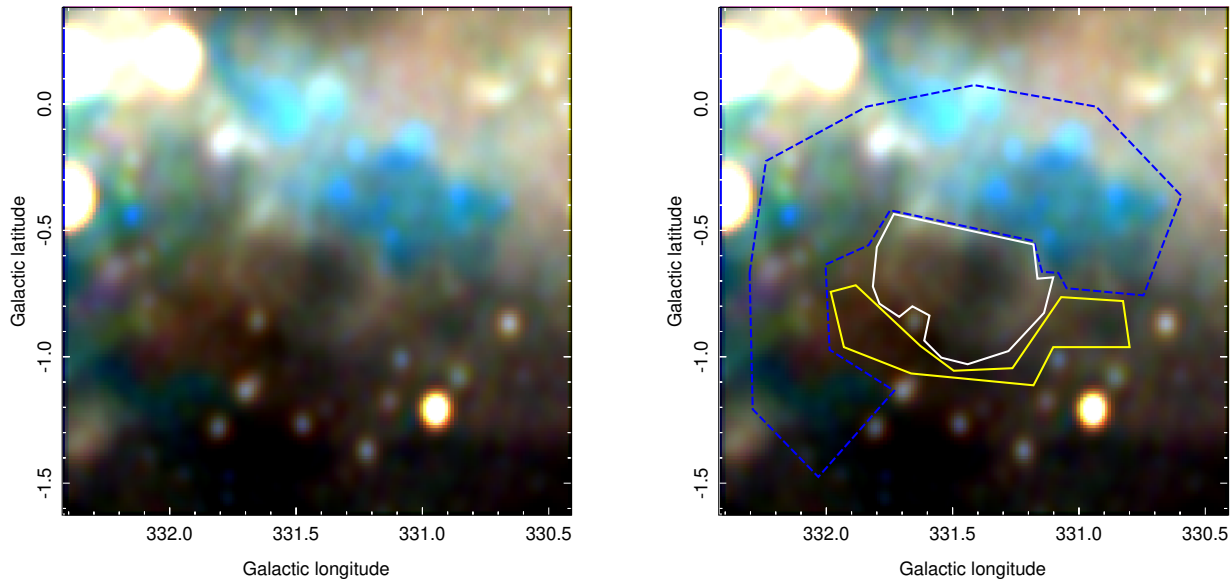

Fig. 9. The two panels show the GLEAM RGB cube with color-to-energy correspondence as follows: R:72-103 MHz, G:103-134 MHz, and B:139-170 MHz. Although the images depict a complex background region, HESS J1614-518 is clearly discernible as an elliptical shape in white color at the center of the image. The remnant is surrounded by HII regions which become apparent in dark blue colors since they become optically thick absorbing radio synchrotron emission at lower frequency bands. The right panel indicates the flux computation method used in this work. The white polygon encapsulates the region that the SNR extends over, the blue-dashed line corresponds to contaminated regions that are not representative of the background, whereas the yellow region indicates the background control region.

astrophysical object, despite the high source density towards the Galactic plane. To quantify the agreement, we applied the same source model to the GLEAM data as was used for the TeV shell. Since there is no available template for the diffuse extended emission, we excluded the strongest contaminated area from the fitting procedure (see Fig. 10). The fit model is a homogeneous spherical 3D shell projected onto a 2D plane and is described by the following equation:

$$\varepsilon = \mathrm{A} \times \frac{2}{3}\pi(R_{\mathrm{out}}^3 - R_{\mathrm{in}}^3) \begin{cases} \sqrt{R_{out}^2 - r^2} - \sqrt{R_{in}^2 - R^2},\ R < R_{in} \\ \sqrt{R_{out}^2 - R^2},\ R_{in} < R < R_{out} \\ 0,\ \text{otherwise} \end{cases} \tag{3}$$

Here, R_{in} and R_{out} are the inner and outer radius of the shell, respectively. R denotes the distance from the point of interest to the center of the shell. The amplitude A indicates the relative strength of emission from the shell compare to the background. Fitting is performed using the *Sherpa*[4] environment. First, a model of a flat background is fit to the data. Once the background level is obtained, we add the main component that describes the emission from the SNR candidate. The above shell model is folded with the point spread function (PSF) of the corresponding instrument and multiplied with the exposure map before being fit to the data. We assume a Gaussian PSF with the FWHM interpreted from the primary beam size of the MWA of 2.4 arcmin (Wayth et al. 2015). This PSF assumption is also consistent with the average PSF calculated by Hurley-Walker et al. (2019b). Fit parameters are the center of the homogeneous shell, inner radius and the thickness of the shell. For the center coordinates of the emitting shell, we first fix them to the best-fit values of the TeV shell morphology, and later allow them to vary. The resulting fit parameters are given in Tab. 2. The source centroids of the radio and the TeV sources are within errors identical, confirming the cross-identification of the two sources. As also expected from the image, the shell width of the radio source is smaller with an outer radius of 0.36°, see also the comparison of the radial profiles in Fig. 11. Given the available data, we nevertheless conclude that there is strong evidence that the radio shell seen in GLEAM data and the TeV shell-type source HESS J1614-518 are from the same astrophysical object.

The X-ray emission seen from the direction of HESS J1614-518 is apparently more center-filled than the radio shell (Fig. 3). We fit the same 2D shell model to the eRASS:4 image in the energy range 1.31-3.10 keV, where the X-ray emission is most visible. Similar to the radio image fitting, a single Gaussian profile is also used as the PSF of eROSITA survey, where the FWHM is the half energy width (HEW) at 15 arcsec (Predehl et al. 2021). Here, we mask the data coming from the bright point source toward the southern part of the SNR candidate. We also restricted the fitting area as a circular region closely surrounding HESS J1614-518, which does not include the source HESS J1616-508 (Fig. 10). Best-fit results for the X-ray morphology investigation are shown in Tab. 2.

As can be seen from the residual image (Fig. 10), the shell model does not model the entire X-ray emission from the source. To quantify whether a shell description is warranted by the data, we adopted the procedure introduced in H.E.S.S. Collaboration et al. (2018) and compared the shell fit result to a result from a

[4] https://cxc.cfa.harvard.edu/sherpa/

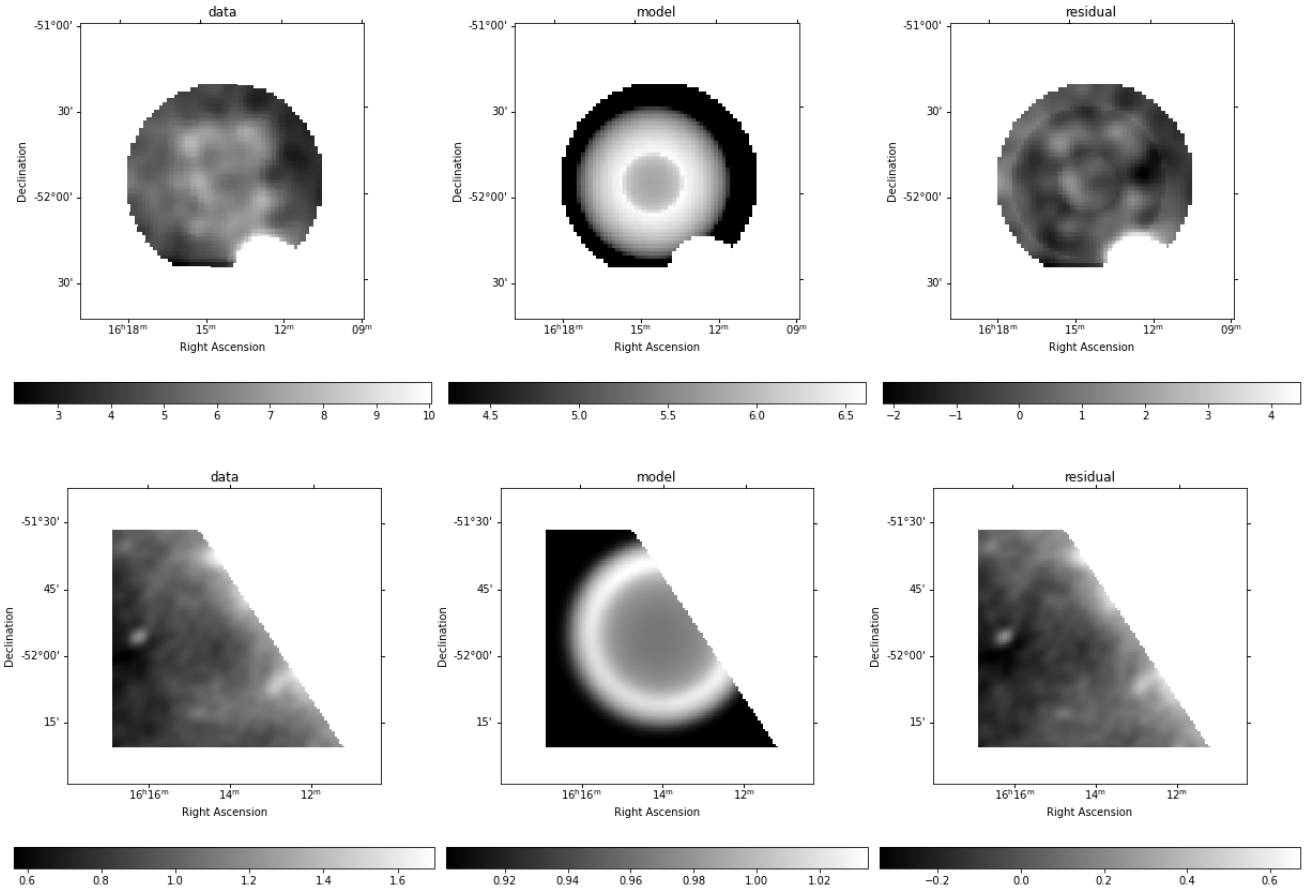

Fig. 10. Upper panel, left to right: Data, best-fit model, and residual images when fitting the eROSITA image of HESS J1614-518 to a 2D shell model. The image used for the morphology study is in the energy range 1.31-3.10 keV, binned with 8 × 8 pixels (1 pixel corresponds to 10") and smoothed with a Gaussian kernel of σ = 2 bins. The bright source towards the southwest direction is excluded from the fitting procedure. Lower panel: Similarly, the best-fit results for morphology study of the radio shell based on GLEAM data are shown. Note that the maxima and minima of the color scales differ between the images for the purpose of visual inspection. This approach however exaggerates the significance of the residuals.

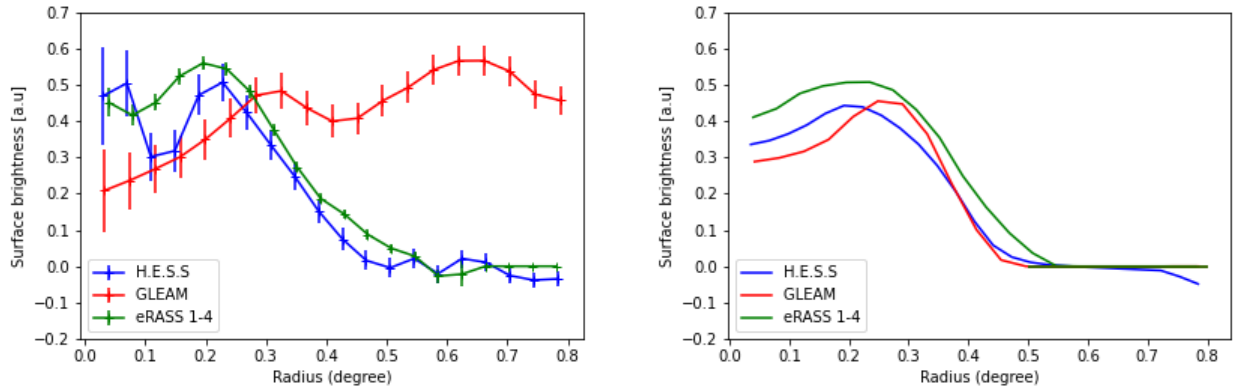

Fig. 11. Left panel: Radial emission profile of HESS J1614-518. Data from the H.E.S.S Galactic survey, GLEAM and eRASS:4 are plotted in blue, red and green points, respectively. All surface brightnesses are extracted from concentric annuli around the TeV best-fit shell center (H.E.S.S. Collaboration et al. 2018). All profiles were normalized to an arbitrary unit for better visualization of the shell structure. The increase of the surface brightness of the radio data beyond $\sim 0.4^\circ$ is attributed to the contamination towards the northwest direction. Right panel: Radial profiles are computed from 2D shell models fitted to H.E.S.S, GLEAM, and eRASS:4 data depicted in the left panel. Similar to the left panel, these profiles originate from annular extraction areas centered at the TeV emission center. Only the 2D shell models are plotted here, disregarding the central peak in the TeV image and the contamination in the radio image.

Gaussian as null hypothesis description. The *Akaike Information Criterion* (AIC) is used to quantify the improvement of the fit with the shell model H_1 to the Gaussian hypothesis H_0, since the two models are non-nested meaning they can not be cross-transformed continuously. First we calculate the AIC value for each best fit model:

$$\mathrm{AIC} = 2k - 2\ln \mathscr{L}_{ML} \tag{4}$$

where $\mathscr{L}_{ML}$ is the log likelihood of the best-fit model, and k are the degrees of freedom. Then we estimate the likelihood of the improvement of H_1 to the best-fit null hypothesis H_0:

$$\mathscr{L}_{\mathrm{AIC,H_0}} = C\dot{\exp}(-\frac{\mathrm{AIC,H_0} - \mathrm{AIC,H_1}}{2}) \tag{5}$$

where C is set to unity. The computed $\mathscr{L}_{\mathrm{AIC,H_0}}$ of the shell model for the X-ray data is 1.67×10^{-5}. We argue that the setting is similar to the one used in (H.E.S.S. Collaboration et al. 2018), where the interpretation of $\mathscr{L}_{\mathrm{AIC,H_0}}$ as a null-hypothesis probability (with $C = 1$) was verified with simulations. The derived value therefore confirms that the shell-hypothesis is warranted by the X-ray data with sufficient degree of certainty. For the radio data, the shell interpretation is much clearer already by eye, which is confirmed by an extremely low $\mathscr{L}_{\mathrm{AIC,H_0}}$ when the same test is applied to the radio data. *To be checked: The null hypothesis* $\mathrm{H_0}$ *is the Gaussian (the best-fit Gaussian, in fact), whereas the shell model is the tested hypothesis* $\mathrm{H_1}$. *Make sure this is clear.*

From the best-fit model depicted in Fig. 10, it is evident that the 2D shell effectively represents the data. While the best-fit centers agree within the margin of errors, the X-ray shell appears to be more diffuse and wider compared to the radio shell (see Table. 2). On the other hand, from the Fermi-LAT analysis, the residual count map above 10 GeV appears as a spatial disk with some extended wings toward the south-west and south-east directions of the SNR (see Fig. 7, section 2.2). This is also the case for other TeV-selected SNRs such as HESS J1534-571 (Araya 2017), HESS J1731-347 and SN 1006 (Condon et al. 2017). It is worth mentioning that the GeV disks of the above TeV SNRs reside relatively well within the TeV shell and show the most detection significance near the TeV peak, whilst the GeV disk of HESS J1614-518 presents a anti-correlation to the TeV profile.

4. Broadband spectral results

Table 3. The required energy budget for protons in different scenarios.

Target density ($\mathrm{cm^{-3}}$)	1		10	
Distance (kpc)	3.5	5.5	3.5	5.5
$W_\mathrm{p}^\mathrm{tot}$ ($\times 10^{51}$ erg)	0.63	1.13	0.06	0.11

To construct a broadband spectral energy distribution from HESS J1614-518, we used archival TeV data H.E.S.S. Collaboration et al. (2018) as well as the GeV, X-ray, and radio continuum GLEAM spectra derived in this work. For the GLEAM data, as mentioned in sec. 2.3, we must treat the obtained flux results with caution, mainly due to high contamination at and around the remnant's location.

The SED is plotted in Fig. 12. To construct expected model SEDs in a leptonic scenario (GeV-TeV emission from Inverse Compton scattering of relativistic electrons) and in a hadronic scenario (GeV-TeV emission from π^0-decay following interactions of relativistic protons with gas), the *naima*[5] (Zabalza 2015) package is employed.

A pure leptonic emission model is also plotted in Fig. 12. The emission modeling package *naima* was used to calculate the flux coming from different processes, assuming a simple one-zone model with a exponential cutoff power-law particle distribution. The particle cutoff energy is at 5 TeV and the spectral index is 1.8. Constrained by the radio and X-ray flux, the magnetic field is estimated to be 25 μG. The IC scattering of high energy CR electrons are considered from three target photon fields, namely the FIR photon fields from heated dust, the NIR photon fields from stellar emission and the cosmic microwave background (CMB). The temperature and energy density of the FIR and NIR fields are calculated based on the relation in Shibata et al. (2011) assuming a distance of 5.5 kpc. The values are 2500 K and 1.42 eV $\mathrm{cm^{-3}}$ for the FIR and 30 K and 0.74 eV $\mathrm{cm^{-3}}$ for the NIR photon fields, respectively. These values are consistent with the estimation of the absorption of the very high energy gamma rays in the Milky Way (Vernetto & Lipari 2016). The required total energy in the CR electrons for the distance 5.5 kpc is 5.29 x 10^{48} erg, approximately 0.5% of the typical kinetic energy released in a supernova explosion. At a distance of 3.5 kpc, the electron energy is roughly half of the above value. This leptonic energy is of the same order as other SNRs such as RCW 86 (H. E. S. S. Collaboration et al. 2018).

To be able to compare with the hadronic dominant gamma rays production at VHE range, we also constructed a combination leptonic + hadronic model as following. The protons particle distribution follows a powerlaw of index 1.7 with cut-off energy at 30 TeV. The gamma rays at GeV-TeV are assumed to be the products of π^0-decay following the interaction between CR protons and nearby gas with typical average target density of 1 $\mathrm{cm^{-3}}$. In order to reproduce the data points from Fermi - LAT (this work) and H.E.S.S. (H.E.S.S. Collaboration et al. 2018), the required total energy of protons is 1.13×10^{51}erg, which exceeds the typical total kinetic energy of supernovae. For the π^0-decay to take over the gamma rays production at GeV-TeV range, the energy injected in electrons has to be lower, in this example 1.27×10^{48}erg. Consequently, the magnetic field strength needs to have higher value at 50 μG. In addition to the typical value of target gas density, a denser environment, e.g. a molecular cloud, at 10 $\mathrm{cm^{-3}}$ is also considered. Table 3 summarizes the total energy content of protons for different target densities and distance to the SNR.

The contamination towards the North-West direction of the source (Fig. 9) in the radio image could indicate the presence of molecular clouds nearby the source. However, the fact that the GeV emission comes from the opposite part of the SNR implies that the GeV gamma rays is not likely to stem from hadronic interaction of CRs and nearby cold gas. Furthermore, the total energy of protons required to reproduce the gamma ray spectrum at the GeV-TeV range is unrealistic because it is of order of the SNR's total kinetic energy. Analysis of other TeV emitting SNRs, e.g. RX J1713.7-3946 (Aharonian et al. 2006b; Fukui et al. 2012), RX J0852.0-4622 (Fukui et al. 2017) and HESS J1731-347 (Fukuda et al. 2014) predict that the total CR protons energy for a hadronic scenario of gamma rays is around $\sim 10^{49}$ erg. Therefore, the observed gamma rays are not likely to originate from hadronic induced processes.

[5] https://naima.readthedocs.io/en/latest/

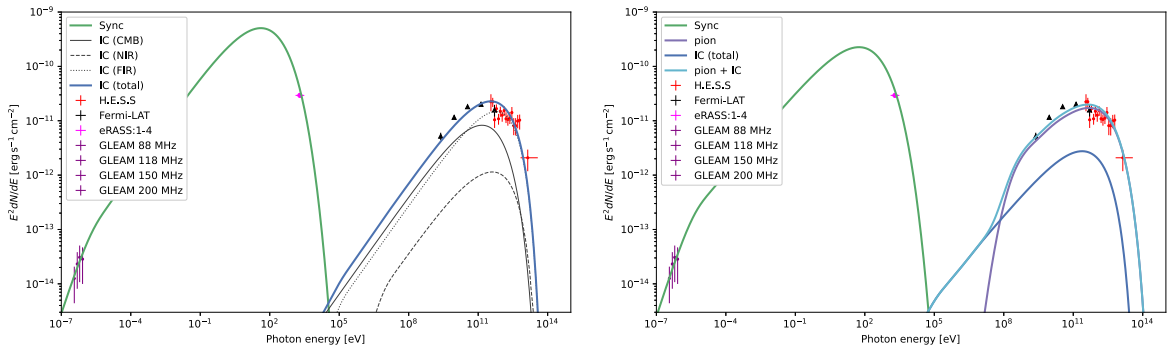

Fig. 12. Broadband SED of HESS J1614-518. Left: A pure leptonic origin of cosmic rays interaction is plotted. The IC emission at very high energy is fitted to the data points from *Fermi*-LAT and H.E.S.S. The synchrotron flux is constrained with eRASS:1-4 data (this work) and radio (GLEAM survey). Right: A leptonic + hadronic model of gamma rays production is also presented.

5. Distance to HESS J1614-465, age, and pulsar association

In the last two decades, distance measurements have been attempted on the remnant. When assumed that the remnant's progenitor star was part of the Pismis open cluster, which is positioned in the remnant's center vicinity, a 1.0 ± 0.4 kpc distance can be derived (Piatti et al. 2000). A similar distance is also obtained from HI void line velocity measurements (Sagittarius-Carina spiral arm) (H.E.S.S. Collaboration et al. 2018). On the other hand, considering a potential association of the remnant with the XMMU J161406.0-515225 point source (Sakai et al. 2011) and the diffuse Suzaku Src A (Matsumoto et al. 2008), both located close to the center of the remnant, a rough distance scale of 10 kpc is derived based on the derived absorption column values. It is noteworthy that Matsumoto et al. (2008) spectral analysis of Src A extended source gave acceptable results for both an absorbed powerlaw (of $\Gamma = 1.73$ and $N_H = 1.21 \times 10^{22}$cm^{-2} - results highly consistent with what we obtained in this work in terms of power law index and consistent within uncertainties in terms of absorption column density) and an apec model, however, the apec model provided an uncomfortably large temperature of ~ 10 keV and thus they adopted the non-thermal powerlaw model for the rest of their analysis. Finally, a distance of 5.5 kpc - compatible with the Norma-Cygnus spiral arm has been considered (H.E.S.S. Collaboration et al. 2018).

In this work, we made use of the remnant's derived best-fit absorption column density to provide more insight into its distance estimation, since all distance measurements reported to date come from potential remnant's associations and not from the object itself. In more detail, a $N_h = 0.82^{+0.32}_{-0.22} \times 10^{22}$cm^{-2} arises as the best fit from the X-ray spectral fitting process. Taking into consideration the latest statistical relation between the observed absorption in X-rays with extinction/mean color excess (Foight et al. 2016):

$$\begin{aligned} N_H/\mathrm{E_{B-V}} &= 8.9 \times 10^{21}\ \mathrm{cm^{-2} \cdot mag^{-1}} \\ N_H[cm^{-2}/A_v] &= 2.87(\pm 0.12) \times 10^{21} \end{aligned} \quad (6)$$

one obtains an extinction range as follows: $A_v = 2.86^{+1.23}_{-0.88}$mag. Comparing the derived extinction to GAIA/2MASS data sets (Lallement et al. 2019) one places the remnant well above 3.5 kpc, as shown on the left panel of Fig. 13. However, when employing the latest data sets (Lallement et al. 2022) as provided by G-Tomo app-EXPLORE[6] significantly lower distances are favored towards the direction of the remnant, as shown on the right panel of Fig. 13. In particular, comparing the obtained extinction values to Lallement et al. (2022) data sets a distance range of $3.51^{+1.76}_{-0.88}$ kpc is derived as shown on the right panel of Fig. 13 in black, with the best-fit absorption column density value corresponding to a 3.51 kpc distance and thus likely placing the remnant at the Scutum-Crux spiral arm. The above results suggest that a potential association of the remnant with the Pismis open cluster and HI void (1.2-1.5 kpc), which would place the remnant at the Sagittarius-Carina spiral arm is highly unlikely. Similarly, a potential association of the remnant with the XMMU J161406.0-515225 point source and the diffuse Suzaku Src A which would place the remnant at a distance of the scale of 10 kpc is also highly unlikely. However, such an association with the aforementioned X-ray sources cannot be excluded given that the distance measurements of the latest were performed based on the absorption column density obtained from the X-ray spectral fitting and thus carrying large uncertainties. Finally, an association of the remnant with the Norma-Cygnus spiral arm (at ~ 5.5kpc distance) cannot be excluded. If one uses the derived best-fit absorption column density considering that the X-ray emission is of thermal nature, then an extinction lower threshold of 8.0 mag is derived; potentially placing the remnant at a distance well above 6 kpc which is highly unlikely.

A potential association with Pismis 22 could provide constraints on the remnant's age, given that the open cluster age is estimated to be $\sim 40 \pm 15$ Myrs (Piatti et al. 2000). However, the distance computation that we performed in this work disfavors such an association. In light of the new X-ray data, one can now employ the evolutionary models of SNR as provided in Leahy & Williams (2017) to derive an age estimate. Assuming a distance of 3.51 kpc one derives a 44 pc linear diameter for the remnant (using the 0.36° remnant's angular radius, as estimated from the GLEAM radio data). Adopting the default inputs, except for the local ISM number density which is computed to be $n_H = 0.76^{+0.65}_{-0.39}$ cm^{-3} (for $N_H = 0.82^{+0.32}_{-0.22}$ 10^{22}cm^{-2} and a distance of $3.51^{+1.76}_{-0.88}$ kpc as derived above), and assuming an explosion energy of 10^{51} erg, one obtains a remnant's age of $3.9^{+2.35}_{-1.4}$ 10^4 yrs.

All the estimates reported above are provided for an adopted distance of ~ 3.5 kpc. Nevertheless, the later estimates are based on empirical relations. Such empirical relations carry substan-

[6] https://explore-platform.eu/

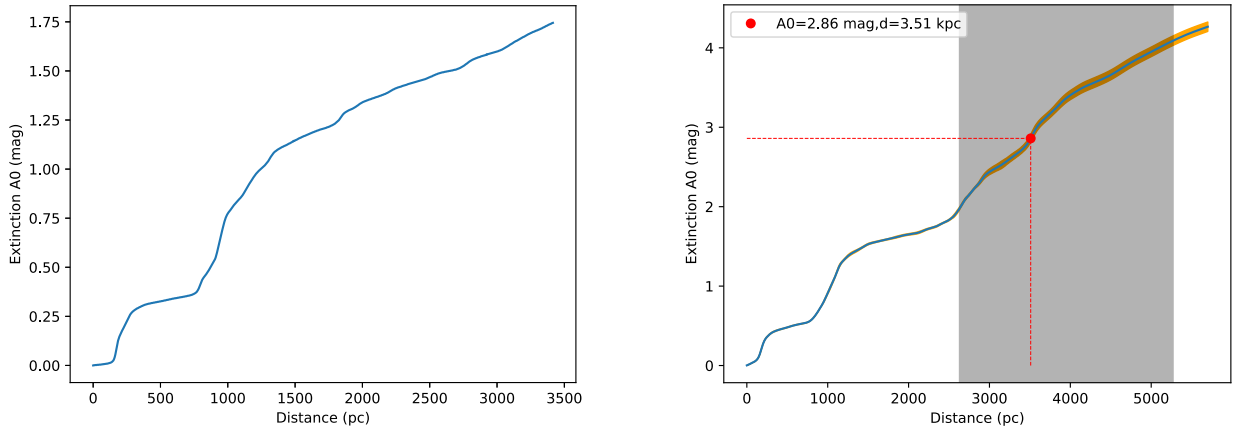

Fig. 13. One-dimensional cumulative extinction as a function of the distance. Left panel: The GAIA/2MASS tool: `https://astro.acri-st.fr/gaia_dev/` is employed, which provides extinction data sets up to 3.5 kpc (Lallement et al. 2019). Right panel: The G-Tomo app created by EXPLORE based on GAIA eDR3 and 2MASS data: `https://explore-platform.eu/` is employed, which provides updated extinction data sets extended up to 5.5 kpc (Lallement et al. 2022).

Table 4. Pulsars within 2° the remnant's center.

Pulsar	Ang. sep. (°)	DM $\mathrm{pc\cdot cm^{-3}}$	D_1 kpc	D_2 kpc	Age kyr	Power ($\dot{E}$) 10^{34} erg $\cdot$ s^{-1}	v_{transv} km $\cdot$ s^{-1}
J1613-5211	0.27	360.1	4.72(6.42)	-	377	0.79	57.68
J1615-5137 (4FGL_J1615.3-5136)	0.36	–	(< 4.10)[a]	-	267	7.3	< 95 ($80.8^{+39.3}_{-20.3}$)[b]
J1614-5048 (4FGL_J1614.5-5047)	1.12	582.4	5.15(7.94)	–	7.42	160	13265
J1617-5055	1.14	467.0	4.74(6.82)	-	8.13	1600	11342
J1616-5017	1.68	194.0	3.48(4.67)	-	167	1.6	597.4

Notes. The table is splitted in two halves: the upper half contains the first three pulsars which lie within the remnant's extension. The rest of the pulsars that lie well outside the remnant's structure are displayed in the lower half of the table. The first and second columns give the pulsar's name and angular separation from the remnant's center (as defined in this work using on the radio GLEAM data). The third column gives the Dispersion Measure. The fourth and fifth columns give the pulsar's distance from Earth based on DM measurements and potential associations, respectively. The values within parenthesis correspond to older distance estimates based on the NE2001 electron density model (Cordes & Lazio 2002). Since 2017, YMW16 is considered the default model for DM-based distance calculations (Yao et al. 2017). The sixth column corresponds to the pulsar's spin-down age. The seventh column presents the pulsar's spin down power. The eighth column displays the transverse velocity required for each pulsar to move from the remnant's center to its present location.

[a] Upper limit distance reported in de Palma et al. (2019)
[b] Computed transverse velocity assuming the remnant's distance of $3.51^{+1.76}_{-0.88}$ kpc

tial scatter. Thus, an alternative scenario with a somewhat larger distance proposed in the literature is examined. Assuming a 5.5 kpc distance (consistent with the derived distance in this work within uncertainties), as reported in H.E.S.S. Collaboration et al. (2018), one computes a 69 pc linear diameter for the remnant by adopting the 0.36° remnant's angular radius, as estimated from the GLEAM radio data. Following a series of identical calculations, as for the case of a 3.5 kpc distance, one derives a local ISM number density of $n_{\mathrm{H}} = 0.48^{+0.19}_{-0.13}$ cm^{-3}, which yields a $1.11^{+0.34}_{-0.24}$ 10^5 yrs age for the remnant according to Leahy & Williams (2017) SNR evolutionary models. However, H.E.S.S. Collaboration et al. (2018) derived local density values of the order of $n_{\mathrm{H}} = 17 - 110$ cm^{-3} from atomic (HI) and molecular (H2) gas distribution data at a distance of 5.5 kpc. Such high values are reasonable if the SNR is indeed located within a spiral arm. Adopting a $n_{\mathrm{H}} = 10$ cm^{-3} as a possible value for a homogeneous density at a distance of 3.5 kpc we obtain a ~ 3.2 10^5 yrs upper limit age for the remnant. It is noteworthy that a 69 pc SNR size (as derived by assuming a distance of 5.5 kpc) cannot line up with the evolutionary SNR solutions when such high local density values $n_{\mathrm{H}} = 17 - 110$ cm^{-3} are considered unless one assumes a higher explosion energy. Assuming the broadly adopted explosion energy of 10^{51} erg, the remnant is expected to have a linear size < 41 pc for $n_{\mathrm{H}} = 17$ cm^{-3} and < 22 pc for $n_{\mathrm{H}} = 110$ cm^{-3} since it expands at a much denser medium. This means that a significantly smaller distance than 5.5 kpc would be required to explain such high local density values given its angular size. In the latter case, the corresponding ages cannot exceed $< 4.4 \times 10^5$ yrs and $< 2.2 \times 10^5$ yrs, respectively. For a remnant of 0.36° angular radius to be located at a distance of 5.5 kpc, a moderately increased explosion energy, $> 4 \times 10^{51}$ erg for $n_{\mathrm{H}} = 17$ cm^{-3}, and a significantly increased explosion energy, $> 4 \times 10^{52}$ erg for $n_{\mathrm{H}} = 110$ cm^{-3}, would be required.

Twenty-one pulsars fall within 2° angular extension from the remnant's radio centroid. Among the twenty-one nearby pulsars, only five have ages that could be compatible with the remnant's young age. The rest are considerably older, $> 5 \times 10^5$ yrs (the majority of which have ages well above 10^6 yrs). The main prop-

erties of the latter five candidates, from the ATNF pulsar catalog[7] (Manchester et al. 2005) together with their computed transverse velocities (using the remnant's center as a starting point and taking into account each pulsar's spin-down age), are summarized in Tab. 4. Among the latter five pulsars, we singled out three, J1613-5211, J1615-5137 (4FGL J1615.3-5136) and J1616-5017, as the most probable candidates since for J1614-5048 and J1617-5055 (which is considered to be associated with HESS J1616-508) the estimated transverse velocity that would be required to reach theirs present location, assuming the remnant's center as a starting point, forbids an association with the remnant. A newly discovered gamma-ray pulsar (it was not included in the 3FGL catalog (Acero et al. 2015), however, it is as of recently part of the 4FGL point source Fermi-LAT catalog under the name 4FGL J1615.3-5136 and its detection and main properties are discussed in more detail in de Palma et al. (2019)), which is considered to be associated with the J1615-5137 radio pulsar, stands out mainly due to its energetics (it exhibits the highest spin down power (7.3×10^{34} erg $\cdot$ s^{-1}, as shown in Tab. 4) among the three candidates), distance from the remnant's center, and computed transverse velocity. We note that since there is no distance estimate for the latter gamma-ray emitting pulsar (except for an upper limit estimate of 4.1 kpc reported in de Palma et al. (2019) which results to a $v_{\rm transv} = 94.3$ km/s), assuming a $3.51^{+1.76}_{-0.88}$ kpc distance (derived remnant's distance), one obtains a $80.8^{+39.3}_{-20.3}$ km/s transverse velocity. It is noteworthy that a potential association with any of the aforementioned pulsars disfavors the extreme close (1.5 kpc distance, related to Pismis 22) and extreme distant (10 kpc) distance estimates/scenarios reported in the literature and is well aligned with the $3.51^{+1.76}_{-0.88}$ kpc remnant's distance reported in this work.

6. Discussion

To be revised: The counterparts of HESS J1614-518 found in the radio continuum and in the X-ray band clearly classify HESS J1614-518 as an SNR. We find that the X-ray emission does not stem from hot gas, but rather from accelerated electrons to TeV energies (synchrotron). This result is compatible with the earlier indication for a non-thermal X-ray component reported in H.E.S.S. Collaboration et al. (2018) by using XMM-Newton data, even though the XMM-Newton results are subject to large systematic uncertainties. The good spatial coincidence of the X-ray, GeV, and TeV emission further supports the results obtained from the modeling of the multiwavelength SED of the SNR, so to say a preference on the leptonic scenario for the origin of gamma ray emission mainly due to the unrealistic total energy of protons required to reconstruct the GeV-TeV spectrum of the remnant, since the same population of accelerated TeV electrons is expected to emit in X-rays through synchrotron and in gamma-rays through inverse Compton. Such a result is also in line with the latest tendency, even if not universally confirmed, that the absence of a non-thermal component in the X-ray spectrum of Galactic SNRs is accompanied by the detection of gamma-ray emission of hadronic origin, while non-thermal X-rays are usually accompanied by leptonically induced gamma-rays (Michailidis et al. 2024a,b; Khabibullin et al. 2024; Guo & Liu 2024). On the other hand, because the electron particle energies emitting radio synchrotron and TeV inverse Compton emission are very different, different morphologies are viable even in a leptonic TeV scenario. Different outcomes are equally feasible in a hadronic setting. Overall, a good spatial correlation of the emission from this SNR is observed across the entire EM spectrum.

In light of the new X-ray data, the distance estimate provided in this work favors a distance of 3.5 kpc for this remnant waning extremely small and large distances of 1 kpc and 10 kpc, respectively, as discussed in the literature by uncertain associations of the remnant with objects that appear spatially coincident with the SNR by chance (refer to sec. 5 for a detailed discussion concerning potential associations). Nevertheless, a 5.5 kpc distance, suggested by H.E.S.S. Collaboration et al. (2018), cannot be ruled out since it is consistent with the derived distance in this study within uncertainties. Despite the fact that we are not able to distinguish between a thermonuclear and a core-collapse origin for a remnant with the information that the present data provide, based on reasonable section criteria, we identified J1613-5211, J1615-5137 (4FGL J1615.3-5136) and J1616-5017 pulsars as the most likely candidates for being associated with the remnant, if the latter is not of type Ia progenitor origin. The association of the remnant with any of these pulsars would also support the idea that the remnant is located at 3.5 kpc. This work emphasizes the importance of multiwavelength studies of Galactic SNR to determine their nature and key properties.

7. Conclusion

To be revised: HESS J1614-518 was originally discovered by H.E.S.S. and reported in Aharonian et al. (2006a). Rowell et al. (2008) reported on a closer look at the HESS J1614-518 source, which has so far been unidentified, suggesting a potential X-ray counterpart as well as a possible link with Pismis 22 open cluster, which happens to lie at the same location. HESS J1614-518 was eventually classified as a supernova remnant candidate purely based on morphological criteria, namely its shell-like appearance in the TeV energy band, only after a comprehensive study of H.E.S.S. Galactic Plane Survey (HGPS) carried out by H.E.S.S. Collaboration et al. (2018). HESS J1614-518 has likely not been discovered in earlier X-ray surveys like the ROSAT all-sky survey because of its extension, mild surface brightness, and contamination with large-scale diffuse emission. A putative detection of X-rays from a small portion of the source without permitting retrieval of any conclusive results was reported using XMM-Newton data (H.E.S.S. Collaboration et al. 2018) largely due to large systematic errors caused by significant stray light impact caused by adjacent strong X-ray emitters (e.g., RCW 103 SNR and 4U 1608-52 LMXB). The detection of significant X-ray emission from HESS J1614-518 using eRASS data demonstrates the potential of exploiting eROSITA's sensitivity even in survey phase to detect X-ray emission from non-thermal SNRs in the Galactic Plane when guided by information from higher and lower energy bands. The X-ray emission has a shell-type appearance, it conforms to the TeV morphology at all 4 sides of the remnant and is strictly contained within the outermost 5σ significance contour detected by H.E.S.S. as depicted in all eRASS images. On top of the detection of HESS J1614-518 X-ray counterpart we report on the additional detection of its radio counterpart utilizing one-year of GLEAM radio data from the source location, thus confirming the SNR nature of the source. A well-defined shell spatially coincident with both the TeV and X-ray extension of the source becomes clearly apparent in the 139-170 MHz radio band, though the sparseness of the data does not allow us to further inspect the radio emission aside from the total flux calculation of the radio synchrotron emission originating from the remnant, which is based on a detail inspection of the radio emission and its nature at and around the remnant of

[7] https://www.atnf.csiro.au/research/pulsar/psrcat/

interest. In particular, we inspected the GLEAM RGB cube that permits us to discriminate between thermal radio (HII regions) and radio synchrotron emission (remnant candidates) thus allowing us to properly select the on-source and background control regions for the calculation of the remnant's flux density, which found to be of the order of 0.31×10^{-13}erg/cm^2/s.

The spectral analysis performed at and around HESS J1614-518 confirms the presence of a soft diffuse foreground and/or background emission component mainly confined below 1.3 keV, which plays a key role though on determining the source spectrum due to the strong emission lines that exhibits in the 1.3-2.5 keV energy range. That soft diffuse component, which has also been reported to be present in Vink (2004) when analyzing the adjacent Kes 32 SNR with Chandra data, can be well described by a two-temperature plasma which we believe to stem from a combination of the diffuse Galactic Plane emission and emission from unresolved sources from the region of interest. The emission from the source itself can be best described by a simple absorbed power law of $\Gamma = 1.79^{+0.67}_{-0.51}$, confirming the non-thermal nature of the remnant indicated by XMM-Newton spectral analysis > 3.0 keV in H.E.S.S. Collaboration et al. (2018) and been broadly consistent with the best-fit spectral parameters of the diffuse Suzaku Src A (Matsumoto et al. 2008) which is likely associated with the remnant. However, a single temperature plasma with strongly suppressed Mg, S, and Si emission lines cannot be excluded due to the limited statistical quality of data.

Exploiting 10.5 additional years of Fermi-LAT data we managed to refine the morphology of the GeV emission from the location of HESS J1614-518 and successfully confirm it as HESS J1614-518 counterpart providing both an updated TS sky map and a residual count map from the location of the source of interest. The updated spectrum in the 1-800 GeV energy band reveals a much steeper spectrum, described best by a LogParabola, in comparison to the relatively hard spectrum below 1 TeV as reported in Acero et al. (2015); H.E.S.S. Collaboration et al. (2018), and thus waning strong indications for hadronic origin production of gamma-rays from the source.

Despite not being at the prime focus of this paper we report on the detection of diffuse X-ray emission from the location of the adjacent, hitherto unidentified, HESS J1616-508 TeV emitter. The diffuse emission is partially overlapping with both RCW103 and Kes 32 but of different origin as its spatial morphology indicates. However, the poor statistic does not allow us to distinguish between a PWN or SNR scenario for the origin of the emission.

The obtained N_H values from the X-ray spectral analysis of the remnant result in a remnant's distance of $3.51^{+1.76}_{-0.88}$ kpc by means of optical extinction data. A physical SNR size of 44 pc in X-rays is then derived under the assumption of the above distance estimate. A $3.9^{+2.35}_{-1.4} \times 10^4$ yrs age estimate is obtained using the SNR model calculator reported by Leahy & Williams (2017). Among the twenty-one pulsars positioned at and in the near vicinity of the remnant's extension (within 2° from its radio center), we singled out three as the most compelling candidates based on age and transverse velocity measurements. Among the latter three, J1615-5137 (which as of recently been identified as a gamma-ray pulsar 4FGL J1615.3-5136) stands out due to its angular separation from the remnant's center and its high energetics.

Acknowledgements

MM and GP acknowledge support from the Deutsche Forschungsgemeinschaft through grant PU 308/2-1.

This work is based on data from eROSITA, the soft X-ray instrument aboard SRG, a joint Russian-German science mission supported by the Russian Space Agency (Roskosmos), in the interests of the Russian Academy of Sciences represented by its Space Research Institute (IKI), and the Deutsches Zentrum für Luft- und Raumfahrt (DLR). The SRG spacecraft was built by Lavochkin Association (NPOL) and its subcontractors, and is operated by NPOL with support from the Max Planck Institute for Extraterrestrial Physics (MPE).

The development and construction of the eROSITA X-ray instrument was led by MPE, with contributions from the Dr. Karl Remeis Observatory Bamberg & ECAP (FAU Erlangen-Nuernberg), the University of Hamburg Observatory, the Leibniz Institute for Astrophysics Potsdam (AIP), and the Institute for Astronomy and Astrophysics of the University of Tübingen, with the support of DLR and the Max Planck Society. The Argelander Institute for Astronomy of the University of Bonn and the Ludwig Maximilians Universität Munich also participated in the science preparation for eROSITA. The eROSITA data shown here were processed using the eSASS/NRTA software system developed by the German eROSITA consortium.

We thank the EXPLORE team which provided us access to the G-TOMO tool of the EXPLORE platform `https://explore-platform.eu/` allowing us to exploit updated GAIA/2MASS data. We thank Denys Malyshev, Victor Doroshenko and Lorenzo Ducci for fruitful discussions as well as the anonymous referee for his significant comments that help improving this manuscript to its current finalized version...

References

Acero, F., Ackermann, M., Ajello, M., et al. 2015, ApJS, 218, 23
Aharonian, F., Akhperjanian, A. G., Bazer-Bachi, A. R., et al. 2006a, ApJ, 636, 777
Aharonian, F., Akhperjanian, A. G., Bazer-Bachi, A. R., et al. 2006b, A&A, 449, 223
Araya, M. 2017, ApJ, 843, 12
Brunner, H., Liu, T., Lamer, G., et al. 2022, A&A, 661, A1
Cash, W. 1979, ApJ, 228, 939
Condon, B., Lemoine-Goumard, M., Acero, F., & Katagiri, H. 2017, ApJ, 851, 100
Cordes, J. M. & Lazio, T. J. W. 2002, arXiv e-prints, astro
de Palma, F., Clark, C., & Di Venere, L. 2019, in International Cosmic Ray Conference, Vol. 36, 36th International Cosmic Ray Conference (ICRC2019), 560
Dorman, B., Arnaud, K. A., & Gordon, C. A. 2003, in AAS/High Energy Astrophysics Division, Vol. 7, AAS/High Energy Astrophysics Division #7, 22.10
Foight, D. R., Güver, T., Özel, F., & Slane, P. O. 2016, ApJ, 826, 66
For, B. Q., Staveley-Smith, L., Hurley-Walker, N., et al. 2018, MNRAS, 480, 2743
Foster, A. R., Ji, L., Smith, R. K., & Brickhouse, N. S. 2012, ApJ, 756, 128
Fukuda, T., Yoshiike, S., Sano, H., et al. 2014, ApJ, 788, 94
Fukui, Y., Sano, H., Sato, J., et al. 2017, ApJ, 850, 71
Fukui, Y., Sano, H., Sato, J., et al. 2012, ApJ, 746, 82
Guo, X. & Liu, X. 2024, A&A
Guo, X.-L. & Xin, Y.-L. 2021, in Proc. 37th International Cosmic Ray Conference (ICRC 2021), Vol. PoS(ICRC2021)629 (PoS-SISSA), 6
H. E. S. S. Collaboration, Abramowski, A., Aharonian, F., et al. 2018, A&A, 612, A4
H.E.S.S. Collaboration, Abdalla, H., Abramowski, A., et al. 2018, A&A, 612, A8
Hurley-Walker, N., Callingham, J. R., Hancock, P. J., et al. 2017, MNRAS, 464, 1146
Hurley-Walker, N., Gaensler, B. M., Leahy, D. A., et al. 2019a, PASA, 36, e048
Hurley-Walker, N., Hancock, P. J., Franzen, T. M. O., et al. 2019b, PASA, 36, e047
Khabibullin, I. I., Churazov, E. M., Chugai, N. N., et al. 2024, arXiv e-prints, arXiv:2401.17261
Lallement, R., Babusiaux, C., Vergely, J. L., et al. 2019, A&A, 625, A135
Lallement, R., Vergely, J. L., Babusiaux, C., & Cox, N. L. J. 2022, A&A, 661, A147
Landi, R., Bassani, L., Malizia, A., et al. 2006, The Astrophysical Journal, 651, 190
LAT Collaboration. 2015, Fermi Large Area Telescope Third Source Catalog
Leahy, D. A. & Williams, J. E. 2017, The Astronomical Journal, 153, 239
Lin, D., Webb, N. A., & Barret, D. 2012, The Astrophysical Journal, 756, 27
Manchester, R. N., Hobbs, G. B., Teoh, A., & Hobbs, M. 2005, AJ, 129, 1993
Matsumoto, H., Uchiyama, H., Sawada, M., et al. 2008, Publications of the Astronomical Society of Japan, 60, S163
Mattox, J. R., Bertsch, D. L., Chiang, J., et al. 1996, ApJ, 461, 396
Merloni, A., Predehl, P., Becker, W., et al. 2012, arXiv e-prints, arXiv:1209.3114
Michailidis, M., Pühlhofer, G., Becker, W., et al. 2024a, arXiv e-prints, arXiv:2401.17312
Michailidis, M., Pühlhofer, G., Santangelo, A., Becker, W., & Sasaki, M. 2024b, arXiv e-prints, arXiv:2401.17311
Piatti, A. E., Clariá, J. J., & Bica, E. 2000, A&A, 360, 529
Predehl, P., Andritschke, R., Arefiev, V., et al. 2021, A&A, 647, A1
Rowell, G., Horns, D., Fukui, Y., & Moriguchi, Y. 2008, in American Institute of Physics Conference Series, Vol. 1085, American Institute of Physics Conference Series, ed. F. A. Aharonian, W. Hofmann, & F. Rieger, 241–244
Sakai, M., Yajima, Y., & Matsumoto, H. 2011, PASJ, 63, S879
Shibata, T., Ishikawa, T., & Sekiguchi, S. 2011, ApJ, 727, 38
Sunyaev, R., Arefiev, V., Babyshkin, V., et al. 2021, A&A, 656, A132
Vernetto, S. & Lipari, P. 2016, Phys. Rev. D, 94, 063009
Vink, J. 2004, ApJ, 604, 693
Wayth, R. B., Lenc, E., Bell, M. E., et al. 2015, PASA, 32, e025
Wilms, J., Allen, A., & McCray, R. 2000, ApJ, 542, 914
Yao, J. M., Manchester, R. N., & Wang, N. 2017, ApJ, 835, 29
Zabalza, V. 2015, in International Cosmic Ray Conference, Vol. 34, 34th International Cosmic Ray Conference (ICRC2015), 922

Chapter 4

Indirect DM studies

Published works are presented here as originally published, with the permission of the publishers. Publications that are either submitted or in a "to be submitted" stage are reprinted with permission from the co-authors. Copyright holders with the corresponding copyright notices are listed below.

Article I

4.1 M. Michailidis, L. Marafatto, D. Malyshev, F. Iocco, G. Zaharijas, O. Sergijenko, M.I. Bernardos, C. Eckner, A. Boyarsky, A. Sokolenko, A. Santangelo. Prospects for annihilating dark matter from M31 and M33 observations with the Cherenkov Telescope Array. In: Journal of Cosmology and Astroparticle Physics (JCAP) 2023.8, 073 (Aug. 2023)

Journal of Cosmology and Astroparticle Physics
An IOP and SISSA journal

Prospects for annihilating dark matter from M31 and M33 observations with the Cherenkov Telescope Array

Miltiadis Michailidis,[a] **Lorenzo Marafatto,**[b] **Denys Malyshev,**[a] **Fabio Iocco,**[c,d] **Gabrijela Zaharijas,**[b] **Olga Sergijenko,**[e,l,m] **Maria Isabel Bernardos,**[f] **Christopher Eckner,**[b,g] **Alexey Boyarsky,**[h] **Anastasia Sokolenko**[i,j,k] **and Andrea Santangelo**[a]

[a]Institut für Astronomie und Astrophysik Tübingen, Universität Tübingen, Sand 1, Tübingen D-72076, Germany
[b]Center for Astrophysics and Cosmology, University of Nova Gorica, Vipavska 13, Nova Gorica SI-5000, Slovenia
[c]Dipartimento di Fisica "Ettore Pancini", Università degli Studi di Napoli "Federico II", Complesso Universitario Monte S. Angelo, Napoli I-80126, Italy
[d]INFN, Sezione di Napoli, Complesso Universitario Monte S. Angelo, Napoli I-80126, Italy
[e]Astronomical Observatory, Taras Shevchenko National University of Kyiv, Kyiv, Ukraine
[f]Dipartimento di Fisica e Astronomia dell'Università degli Studi di Padova, and INFN, Sezione di Padova, Padova, Italy
[g]LAPTh, CNRS, USMB, Annecy F-74940, France
[h]Lorentz Institute, Leiden University, Niels Bohrweg 2, Leiden NL-2333 CA, The Netherlands
[i]University of Chicago, Kavli Institute for Cosmological Physics, Chicago, IL 60637, U.S.A.
[j]Fermi National Accelerator Laboratory, Theoretical Astrophysics Group, Batavia, IL 60510, U.S.A.
[k]Institute of High Energy Physics, Austrian Academy of Sciences, Nikolsdorfergasse 18, Vienna 1050, Austria
[l]Main Astronomical Observatory of the National Academy of Sciences of Ukraine, Zabolotnoho str. 27, Kyiv 03143, Ukraine
[m]Space Technology Centre, AGH University of Science and Technology, Aleja Mickiewicza 30, Kraków 30-059, Poland

JCAP08(2023)073

Article I

https://doi.org/10.1088/1475-7516/2023/08/073

E-mail: michailidis@astro.uni-tuebingen.de, lmaraf@yahoo.com,
denys.malyshev@astro.uni-tuebingen.de, fabio.iocco@unina.it,
gabrijela.zaharijas@ung.si, muszka.na.rowerku@gmail.com,
mariaisabel.bernardos@pd.infn.it, eckner@lapth.cnrs.fr, boyarsky@mail.cern.ch,
sokolenko@kicp.uchicago.edu, andrea.santangelo@uni-tuebingen.de

Received April 20, 2023
Revised July 3, 2023
Accepted July 10, 2023
Published August 29, 2023

Abstract. M31 and M33 are the closest spiral galaxies and the largest members (together with the Milky Way) of the Local group, which makes them interesting targets for indirect dark matter searches. In this paper we present studies of the expected sensitivity of the Cherenkov Telescope Array (CTA) to an annihilation signal from weakly interacting massive particles from M31 and M33. We show that a 100 h long observation campaign will allow CTA to probe annihilation cross-sections up to $\langle\sigma v\rangle \approx 5 \cdot 10^{-25}\,\mathrm{cm}^3\,\mathrm{s}^{-1}$ for the $\tau^+\tau^-$ annihilation channel (for M31, at a DM mass of 0.3 TeV), improving the current limits derived by HAWC by up to an order of magnitude. We present an estimate of the expected CTA sensitivity, by also taking into account the contributions of the astrophysical background and other possible sources of systematic uncertainty. We also show that CTA might be able to detect the extended emission from the bulge of M31, detected at lower energies by the *Fermi*/LAT.

Keywords: dark matter experiments, dark matter theory, gamma ray experiments

ArXiv ePrint: 2304.08202

JCAP08(2023)073

Contents

1 Introduction

Cosmological and astrophysical observations of diverse nature suggest that the majority of the matter in the Universe consists of a non-electromagnetically interacting component, often referred to as Dark Matter (DM), see e.g. Bertone et al. [1], Zyla et al. [2]. Despite the DM density having been measured with a great accuracy to be $\Omega_{\rm DM}h^2 = 0.11933 \pm 0.00091$ (Akrami et al. [3]), little is known about its very nature.

Whereas different scenarios with regards to the nature and origin of DM that have been proposed by physicists throughout the years — such as for instance Primordial Black Holes — have not been entirely ruled out at the moment (see e.g. Villanueva-Domingo et al. [4]), yet ample data evidence keep holding around the fact that it is more likely that the DM nature is non-baryonic, thus requiring physics beyond the Standard Model (SM) Bertone et al. [1], Zyla et al. [2]. Indeed, many SM extensions proposed to date naturally include a DM candidate, namely a particle complying with all astrophysical and cosmological requirements,

JCAP08(2023)073

Article I

and produced in the right abundance in the early Universe, see e.g. Zyla et al. [2] for a recent review of such candidates.

Within the broadly considered SM extensions providing DM candidates, the Weakly Interacting Massive Particles (WIMPs) are one of the most widely explored in particle and astroparticle physics. MeV–TeV mass scale self-annihilating WIMPs with a weak-scale cross-section (DM-particles velocities averaged annihilation cross-section $\langle\sigma v\rangle_{\rm th} = 3{\cdot}10^{-26}\,{\rm cm}^3\,{\rm s}^{-1}$) can naturally produce the observed abundance of the DM as a result of thermal freeze-out in the early Universe, see Lee and Weinberg [5], Feng and Kumar [6], and Profumo [7], Baer et al. [8].

If WIMPs constitute the entirety of the DM, their annihilation into the SM particles with the consequent production of photons (see e.g. Cirelli et al. [9], for a review) makes WIMPs good candidates for indirect searches of the annihilation signal from certain DM-dominated objects. The produced photons are expected to have a hard spectrum which continues up to WIMP's mass. While the exact shape of the spectrum depends on the type of SM particles into which WIMPs primarily annihilate ("annihilation channel"), the maximum of the spectral energy density is located in the TeV band for a TeV-scale WIMP. This makes the very high energy (VHE) band an important window for indirect WIMP-DM searches.

The TeV band is currently being explored by several Imaging Atmospheric Cherenkov Telescopes (IACTs). These facilities utilise Cherenkov radiation from the secondary particles produced in interactions of primary cosmic rays with the atmosphere to detect and characterise the properties of the incident primary particle. Currently, major operational IACTs are H.E.S.S. (located in Southern Hemisphere), MAGIC, and VERITAS (both — Northern Hemisphere).

During the last decade these telescopes performed a number of dedicated WIMP DM search campaigns in the TeV band. These include a dedicated multi-year campaign for the search of the annihilation of WIMPs close to the Galactic Center (GC) region with H.E.S.S. (Abdalla et al. [10], Rinchiuso and Moulin [11], Rinchiuso et al. [12], Rinchiuso [13]); individual and joint multi-facility campaigns on nearby dwarf spheroidal galaxies (dSphs) (Aliu et al. [14], Acciari et al. [15], Ahnen et al. [16], Zitzer and VERITAS collaboration [17], Yapici and Smith [18], H.E.S.S. collaboration et al. [19], Oakes [20]), DM annihilation searches in nearby galaxy clusters (Abramowski et al. [21]) and searches for clumps of DM in our galaxy (Glawion et al. [22], Abdalla et al. [23]). For a complete report of all observations performed by current IACTs see Doro et al. [24].

At somewhat higher energies ($\gtrsim 10\,{\rm TeV}$) DM searches are extensively performed by high-altitude broad field of view instruments such as e.g. ARGO-YBJ (Bernardini and ARGO-YBJ collaboration [25]) (currently decommissioned), HAWC (Mostafá [26]) and most recently the LHAASO (Bai et al. [27]) observatory. The tightest constraints on the parameters of annihilating DM provided by these facilities arise from the non-detection of a DM annihilation signal in the MW halo (Abeysekara et al. [28]), dSphs (Albert et al. [29]), DM sub-halos (Coronado-Blázquez and Sánchez-Conde [30]) and nearby galaxies (Albert et al. [31]).

In the GeV-TeV band, the WIMPs' properties are constrained dominantly by the space-based missions, e.g., *Fermi*/LAT (Atwood et al. [32]). The primary targets for the searches in this band were dwarf spheroidals (Hoof et al. [33], Drlica-Wagner et al. [34], Baring et al. [35]), galaxy clusters (Aleksić et al. [36], Arlen et al. [37], Ackermann et al. [38], Huang et al. [39], Thorpe-Morgan et al. [40]), Galactic Center observations (see e.g. Ackermann et al. [41], Abazajian et al. [42], and references therein), nearby galaxies (Li et al. [43], Di Mauro

JCAP08(2023)073

et al. [44]) and DM sub-halos (Nieto et al. [45], Nieto [46], Coronado-Blázquez et al. [47], Coronado-Blázquez et al. [48]).

Despite enormous dedicated efforts, the state-of-the-art WIMP DM searches only marginally approach the thermal annihilation cross-section scale. The best limits are obtained for WIMP masses $\lesssim 0.1$ TeV, which are based on the joint-analysis of the observational data from 27 dSphs by *Fermi*/LAT (Hoof et al. [33]). For $b\bar{b}$ and $\tau^+\tau^-$ annihilation channels in this mass range, the derived limits are by an order of magnitude better than the thermal cross-section (see however Linden [49]). For higher DM masses, the tightest constraints resulted from a dedicated multi-year 254 h long H.E.S.S. observational campaign on the GC. For a preferable DM profile, Abdallah et al. [50] have shown that the obtained H.E.S.S. limits can reach the thermal cross-section for the $\tau^+\tau^-$ annihilation channel and WIMP masses of the order of ~ 1 TeV, while at higher masses the derived limits are quickly degrading.

The gap between the sensitivity of current-generation instruments and the required sensitivity to probe the thermal annihilation cross-section in a broad portion of the WIMP parameter space offers ample opportunities for next-generation facilities to push forward the frontiers in indirect DM searches. Some of these facilities (e.g., LHAASO) already produced first results and are performing DM-dedicated campaigns (see e.g. He et al. [51], Neronov and Semikoz [52]), while others (e.g., Cherenkov Telescope Array (CTA)) are still in the construction phase.

The CTA will be composed of two sites, one in the Northern (La Palma, Canary Islands, Spain) and one in the Southern Hemisphere (Paranal Observatory, Chile), which will enable observations to cover the entire Galactic plane and a large fraction of the extra-galactic sky (see e.g. CTA Consortium [53]). The arrays will include three different telescope sizes to maximize the energy range of the instrument (from 20 GeV to more than 300 TeV). With more than 100 telescopes in the Northern and Southern Hemispheres combined, in the next decade, the CTA will be the largest ground-based IACT γ-ray observatory in the world. The CTA will have an order of magnitude higher effective area and broader field of view than the current generation of IACTs (Cherenkov Telescope Array Consortium [54]). This makes CTA one of the best instruments for indirect DM searches at TeV energies.

Present-day indirect DM searches are focused on several classes of objects, which include such DM-dominated objects as dwarf spheroidal galaxies; clusters of galaxies, or the MW's Galactic Center. As a viable alternative to these commonly considered objects, we consider studies of the annihilation DM signal from nearby spiral galaxies (i.e., M31 and M33). The DM search in such galaxies (M33) had been previously performed in 2008 with the Whipple 10 m γ-ray telescope (Wood et al. [55]) and recently by HAWC (Albert et al. [31]), towards M31 resulting in competitive to other targets constraints. In what follows, we perform detailed studies to address the CTA potential to constrain the parameters of annihilating WIMP DM using observations of M31 and M33. We note also that M31 is the subject of a ~ 150 h long key science program. The proposed indirect DM search can additionally strengthen the scientific goals of that program.

The paper is organized as follows. In section 2, we describe the motivation for selecting M31 and M33 from all nearby spiral galaxies for this study. In this section we also quantitatively describe the expected signal from annihilating WIMPs as well as summarize details of astrophysics back/fore-ground emission relevant to the analysis. CTA data simulation and analysis are described in section 3. In section 4, we report on the CTA's sensitivity to an annihilating WIMP signal for several considered annihilation channels. Special attention is

JCAP08(2023)073

devoted to an accurate treatment of uncertainties related to the astrophysical background, the lack of knowledge of the actual DM density distribution in the considered objects as well as the impact of instrumental systematic uncertainties. Finally, in section 5, we shortly summarize the derived conclusions.

2 Expected signal and target selection

2.1 DM annihilation signal

WIMP annihilation with its antiparticle (that in many scenarios is the WIMP itself, a Majorana particle) leads to the production of SM particles. Depending on the type of the produced SM particles several annihilation channels (e.g. quark $b\bar{b}$, $t\bar{t}$, leptonic $\tau^+\tau^-$, $\mu^+\mu^-$ or bosonic W^+W^-, ZZ annihilation channels) can be contemplated. Annihilation/decay of the produced SM particles results in the emission of secondary photons, which can be detected with ground or space-based observatories.

The same DM annihilation process taking place in the early Universe is to be expected in all environments, and it will depend on the local DM density. In astrophysical objects with a given DM density distribution $\rho(r)$, the observed signal is therefore characterised by a spatial and spectral components (see for more details a review by Bergström et al. [56])

$$\frac{d\Phi}{dE_\gamma d\Omega} = \frac{1}{8\pi} \cdot \frac{\langle\sigma\upsilon\rangle}{m_\chi^2} \cdot \left.\frac{dN_\gamma}{dE_\gamma}\right|_i \cdot \int\limits_{\text{l.o.s.}} \rho^2_{\text{DM}}(r(\ell), \Omega) d\ell \tag{2.1}$$

where m_χ is WIMP's mass and i presents WIMPs primary annihilation channel.

The differential term $\frac{d\Phi}{dE_\gamma d\Omega}$ on the left side of this equation corresponds to the observed photon flux. The right-hand side can be thought of as a product of two factors: *(i)* astrophysical, determined by DM density content in the object (J-factor)

$$dJ/d\Omega = \int\limits_{\text{l.o.s.}} \rho^2_{\text{DM}}(r(\ell), \Omega) d\ell \tag{2.2}$$

and expressed as the line of sight (l.o.s.) integral of the DM density squared within the solid angle $d\Omega$ of the observation. Where ℓ is the variable that parametrizes the l.o.s., and r is the radial distance from the center of the selected target. *(ii)* Particle physics term $\left.\frac{dN_\gamma}{dE_\gamma}\right|_i$ presenting the final-state photon spectrum of one annihilation of DM particles annihilating via annihilation channel i. The remaining coefficients serve to account for the frequency of annihilation events (DM-particles velocity-averaged annihilation cross-section $\langle\sigma\upsilon\rangle$) and relate to the number of annihilation events (term m_x^{-2}).

Among all possible annihilation channels, we focus here only on $b\bar{b}$ ("benchmark channel" in what below), $\tau^+\tau^-$ and W^+W^- channels as widely discussed representatives of the annihilation channels.

The typical spectral shape of the signal expected from the annihilation of DM with the mass $m_x = 1\,\text{TeV}$ is shown in figure 1 which is based on Cirelli et al. [9] tables. We note that the spectrum of W^+W^- annihilation channel can be substantially different at energies close to the m_x with/without accounting for electroweak (EW) corrections (Ciafaloni et al. [57]). For this channel, we explicitly present results corresponding to the spectrum obtained without EW corrections and to the spectrum which is based on the model-independent

JCAP08(2023)073

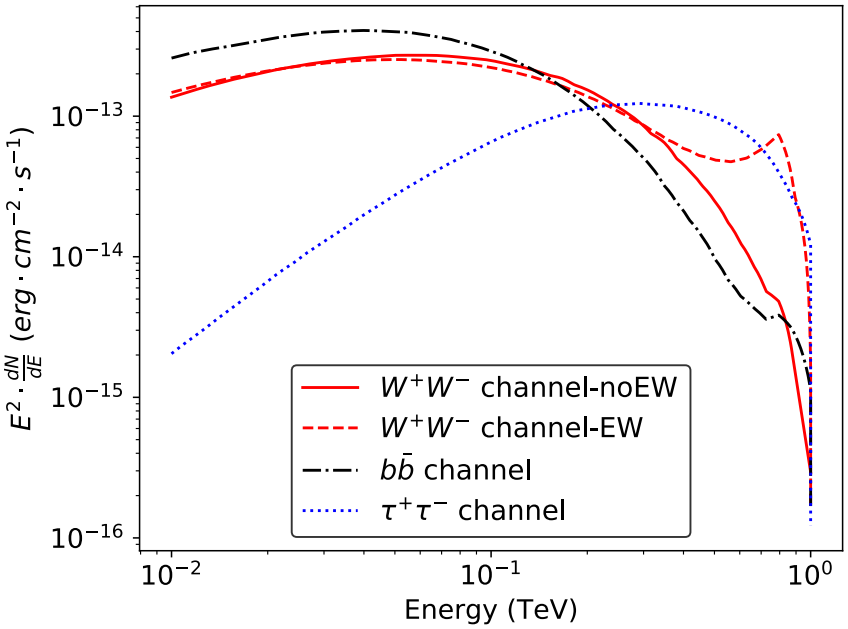

Figure 1. Expected 1 TeV mass WIMP DM annihilation spectrum in the M31 assuming the benchmark density model. The red, blue, and black lines show the annihilation spectra in W^+W^-, $b\bar{b}$, and $\tau^+\tau^-$ channels.

treatment of EW corrections. Similarly, one could employ the HDMSpectra[1] code introduced in Bauer et al. [58] which performs similar calculations to Cirelli et al. [9] code aiming at constructing the obtained spectral shape from DM annihilation signal. This code computes DM annihilation spectra for DM masses above the EW symmetry breaking and all the way to the Planck scales, thus it is considered to considerably improve computed results for the W^+W^- annihilation channel by accounting for all relevant EW corrections. However, to be conservative, we explicitly derive all the results for the W^+W^- annihilation channel without accounting for EW corrections. Namely, we did not include EW corrections for the W^+W^- annihilation channel, since such corrections are model-dependent and account for a strong modification in the energy spectrum of DM particles with masses greater than the electroweak scale (Ciafaloni et al. [57], Cirelli et al. [9], Cirelli et al. [59]). In more detail, EW corrections are responsible for a slight enhancement of the lower energy regime of the spectrum due to the conversion of a small portion of high-energy particles to a substantial amount of lower-energy particles. In addition, forbidden final states are enabled, resulting in the presence of the whole population of stable particles in the final spectrum, regardless of the primary channel of annihilation. Finally, they are responsible for the perception of a model-dependent strong peak, with an energy value associated with the DM mass, in the DM annihilation spectrum through the W^+W^- annihilation channel which determines all the constraints prevailing over the entire spectrum (Viana et al. [60]). The impact of EW correction to the DM annihilation spectrum, through the W^+W^- channel, is illustrated in figure 1 with the red-dashed line.

[1] https://github.com/nickrodd/HDMSpectra.

JCAP08(2023)073

2.2 Selected targets

M31 (Andromeda Galaxy) and M33 (Triangulum Galaxy) are the DM-dominated spiral galaxies closest to the Milky Way, which makes them potentially interesting targets for indirect searches of decaying or annihilating DM. Located at distances of 778 kpc (M31, see e.g. Karachentsev et al. [61]) and 840 kpc (M33; Freedman et al. [62]) these galaxies are among the best-studied objects in terms of DM density distribution.

The relative proximity of M31 and M33 galaxies allowed several dedicated studies of the DM profiles in these objects. The comprehensive list of DM profiles presented in the literature for these objects is given in table 2 and table 3. The tables summarise the basic information on the galaxies (coordinates, distance, visibility from Southern or Northern CTA site) as well as parameters of DM density profiles. The last ones include density profile adopted in the corresponding study (isothermal (ISO; King [63]), Navarro-Frank-White (NFW; Navarro et al. [64]), Einasto (Einasto [65]), Burkert (Burkert [66]), see also see appendix C), parameters of the profiles (characteristic radius r_s and density ρ_s) and the bibliographic reference for the work reporting the corresponding profile.

2.3 Benchmark DM density profiles

Demonstrating a good agreement at large distances from M31 and M33 centers, dark matter density profiles are still rather uncertain closer to the centers of these objects. In what follows, we select Einasto (for M31) and NFW (for M33) profiles with the parameters considered by Di Mauro et al. [44] as benchmark, while using the rest to estimate the uncertainty connected to the poor knowledge of DM density distribution in M31 and M33. The benchmark profiles are marked with a dagger (†) symbol in table 2 and 3.

All considered density profiles and J-factors as functions of distance from the object's center are shown with thin lines in top and bottom panels of figure 2 correspondingly. The benchmark profiles correspond to the thick black line. In order to avoid any underestimation of the actual DM density uncertainty, we calculated the fractional uncertainty $\delta\rho_s/\rho_s = 0.04$ of the Einasto profile of M31, which stands for the uncertainty in the determination of the benchmark model itself and appears to be is negligible compared to the green uncertainty region, as shown in the top left panel of figure 3, which correspond to the actual uncertainty of DM density distribution within the object of interest. The two-dimensional representation of M31 J-factor for the reference density profile is presented in the left panel of figure 3.

2.4 Gamma-ray emission of conventional astrophysical origin

In addition to a suggested signal from annihilating DM the emission from M31 and M33 directions is complemented by several types of conventional astrophysics fore- and background (point-like and/or diffuse) emissions. These backgrounds include MW galactic diffuse emission, as well as contributions from galactic and extra-galactic sources.

In the particular case of M31, we note also the possible presence of a diffuse GeV/TeV signal originating from the nucleus/bulge/disk of this galaxy. Such a signal was reported in M31 observations in the GeV band with *Fermi*/LAT (Ackermann et al. [67], Eckner et al. [68], Karwin et al. [69], Armand and Calore [70]). The signal is moderately extended (radial disk with a radius of 0.4° (Ackermann et al. [67], Karwin et al. [69])) and characterised by a relatively soft best-fit spectrum (2.8 ± 0.3, Karwin et al. [69]). The observed emission can be interpreted within several models, including millisecond pulsar population (Eckner et al. [68]) or annihilating/decaying DM particles (Karwin et al. [69]).

JCAP08(2023)073

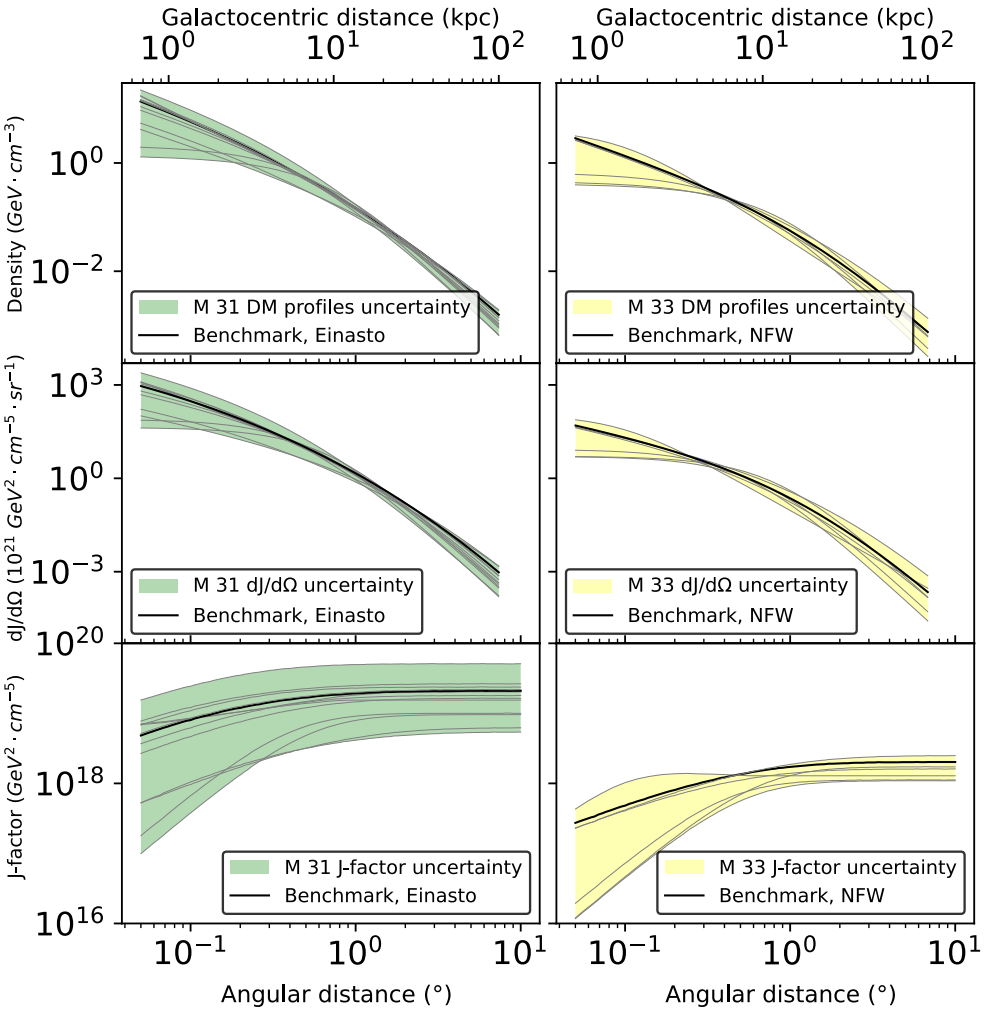

Figure 2. DM density profiles, see table 2 and 3 for the relevant profiles, and corresponding J-factors as a function of the angular distance from the center of the objects of interest (left panels: M31, right panels: M33). Upper panels: DM density distribution profiles. Central panels: differential J-factor values dJ/dΩ of the corresponding DM profiles. Lower panels: integrated J-factor values over solid angle for the corresponding profiles. The benchmark DM models (Einasto for M31 and NFW for M33, see section 2.3) used in the analysis are highlighted with the bold black solid line in all panels.

In the case of M33, no extended signal was clearly observed despite several dedicated searches (Abdo et al. [71], Ackermann et al. [67], Karwin et al. [69], Di Mauro et al. [44], Xi et al. [72]). At the same time, a presence of a relatively weak (6–7σ significance) source was reported at the position of M33 (Ajello et al. [73]). However, we did not include the above source in this analysis since it is not included in either the 3FHL or 4FGL catalogs.

To estimate the contribution from the galactic and extragalactic sources we consider nearby known GeV sources with the spectrum potentially continuing to the TeV band. The searches within 3FHL (Ajello et al. [74]) (7 yr *Fermi*/LAT catalogue of sources detected

JCAP08(2023)073

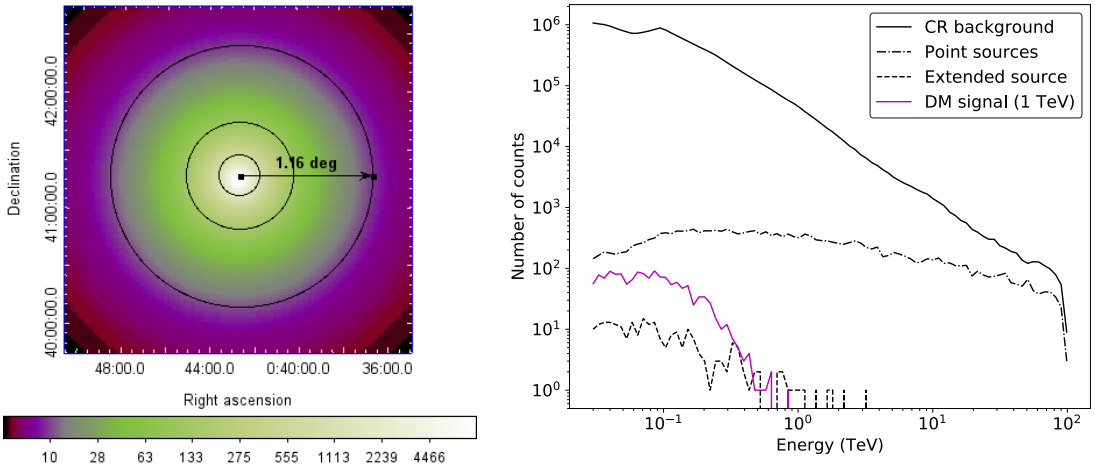

Figure 3. Left: DM source template for the Einasto profile that was presented in Di Mauro et al. [44] (benchmark model). The image is centered on M31. The color illustrates J-factor in units of $10^{20}\,\mathrm{GeV}^2\cdot\mathrm{cm}^{-5}$. Black contours present the distances at which J-factor decreases by a factor of 10, 100, 1000 in comparison to its maximum. Right plot: expected number of photons predicted by CTA simulations towards M31 direction as a function of energy from the sources contributing to the observed signal for a single realization of the data. An extended source that represents the contribution from M31 bulge with the parameters reported in Karwin et al. [69]. The stacked contribution from 6 point sources present in the FoV of CTA, as shown in the left panel of figure 4. The DM signal corresponds to the benchmark density model of M31, 1 TeV DM mass, $b\bar{b}$ annihilation channel and $\langle\sigma v\rangle = 2.05\cdot10^{-24}\,\mathrm{cm}^3\cdot\mathrm{s}^{-1}$, corresponding to the value the CTA will be capable of excluding at 95% c.l. level, see section 4.1.

above 10 GeV), 4FGL-DR2 (Abdollahi et al. [75]) (12 years catalogue of *Fermi*/LAT sources detected above 0.1 GeV) and TeVCAT[2] resulted in six and four point sources within the CTA FoV (5° radius) around M31's and M33's positions respectively, as shown in figure 4.

The basic parameters of the considered sources (coordinates, shape, spectral parameters — normalisation and spectral index, possible type, and multiwavelength identification) are summarised in table 4.

3 Data simulation and analysis

3.1 Data simulation

The simulation of the data was performed with `ctools` v.1.7.3[3] simulation and analysis package, in energy band 0.03 TeV–100 TeV. For both M31 and M33, we consider 100 hours long observation centered at the corresponding objects. As discussed in section 1 the current strategy for the forthcoming CTA DM observations includes 150 hours observation towards M31, while for M33 there is no planning to this point (Cherenkov Telescope Array Consortium [54]). In this work, for simplicity, we consider 100 hours simulation time for both considered targets.

[2] http://tevcat2.uchicago.edu/.
[3] http://cta.irap.omp.eu/ctools/.

JCAP08(2023)073

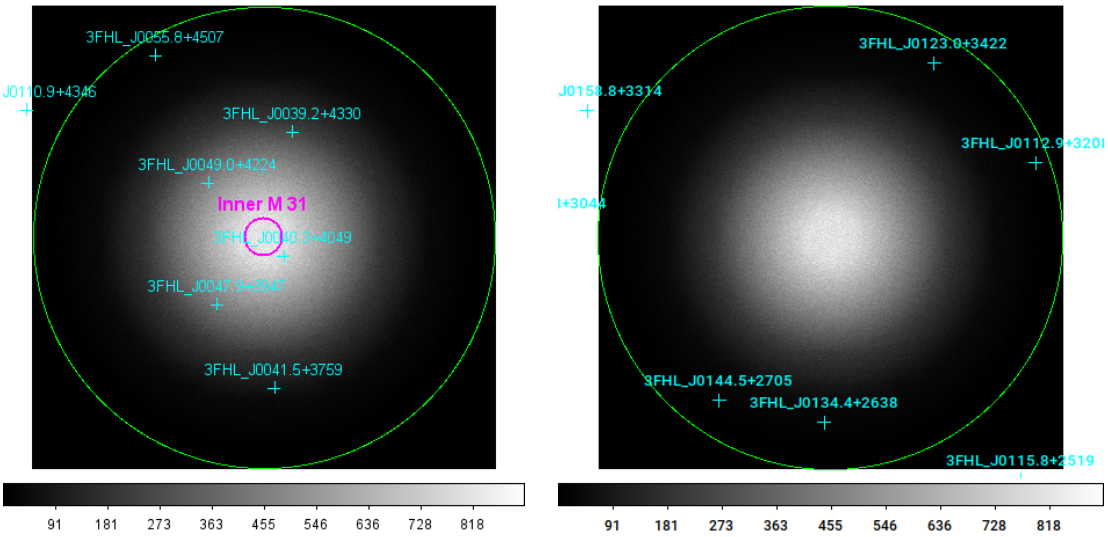

Figure 4. The simulated CTA maps of gamma-like events to the direction of M31 (left) and M33 (right) galaxies (background not subtracted). The positions of known *Fermi*/LAT sources detected above 10 GeV from 3FHL catalogue are shown with cyan crosses. The green circle illustrates the FoV of CTA with a 5° radius. The magenta ellipse at the left panel presents the extended Inner M31 source — a radial disk with 0.4° radius (Karwin et al. [69]).

Galaxy	**Exposure** h	**Culmination** (North/South)	**prod3b-v2 IRF**	**E_{min}** TeV
M31	100	12°/66°	`North_z20_50h`/—	0.06/—
M33	100	2°/56°	`North_z20_50h`/`South_z60_50h`	0.06/0.13

Table 1. The basic parameters of M31 and M33 used for the CTA data simulation. The first column corresponds to the name of the galaxy/target, while the second one expresses the minimal zenith angle by which each target can be observed by each CTA array. The instrument response functions, based on the minimal zenith angle estimation, used for each target and each array, are reported in the third column. The last column represents the minimum energy, based on the latest CTA suggestions, that one should consider when performing simulation using different IRFs.

For the simulation and subsequent data analysis, we utilised `prod3b-v2` instrument response functions (IRF).[4] These IRFs are available for North (La Palma) and South (Paranal) CTA sites and a set of zenith angles which additionally determine the proper low-energy threshold $E_{\rm min}$ for the analysis.

The minimal zenith angle under which a source with declination δ is visible from an observational site with latitude lat is given by $\mathrm{mza} = |\delta - \mathrm{lat}|$. For reasonable quality observations, we additionally demand $\mathrm{mza} < 60°$. The basic parameters used for the data simulation of M31 and M33 galaxies are summarized in table 1.

[4]When the analysis was at its latest stages `prod5.v0.1` IRF were released. We argue that the new IRFs do not affect significantly the derived results, see e.g. left panel of figure 5 for the comparison of `prod3b-v2` vs. `prod5.v0.1` results.

JCAP08(2023)073 Article I

For the simulations of the data, we explicitly consider that the following sources in the FoV of the CTA are contributing to the observed emission:

- Residual Cosmic ray background (implemented as "CTAIrfBackground" within `ctools`).
- Astrophysical sources in the near vicinity of the target. These include fore/background point-like sources from 3FHL catalogue (Ajello et al. [74]) of sources detected by *Fermi*/LAT above 10 GeV as well as extended source presenting the extended emission from inner parts of M31 reported by Karwin et al. [69]. The basic information about all included sources is summarized in table 4.

Given the high galactic latitudes of both galaxies selected for the analysis, we neglected the contribution from the galactic diffuse emission. Aiming in constraining the parameters of WIMP DM (potentially not present in the real data) we did not include any contribution from the annihilating DM to the simulated data.

We simulated the data according to the model described above using `ctobssim` (50 random realizations of the data, defined by initial random seed) and `ctmodel` (one, non-randomized realization of the model) `ctools` routines. The data simulated with `ctmodel` was used as Asimov dataset for the analysis described in detail below.

3.2 Data analysis

We analysed the simulated data within the frame of standard binned CTA data analysis[5] implemented in `ctools`. We additionally cross-checked the results with an alternative implementation of the analysis used by Acharyya et al. [76].

The analysis relies on the fitting of the 3D (spatial and spectral) model of the region to the data.[6] The model used for the analysis of simulated data included all components used for data simulation (residual CR background as well as astrophysical sources in the FoV of the CTA). Aiming to constrain the parameters of annihilating WIMP DM we additionally included in the model the template (DM source) presenting such a contribution. DM source template for a set of considered annihilation channels and WIMP masses was composed of spectral and spatial parts as described in section 2.1. The spectral part is based on approximations of WIMP annihilation spectra by Ciafaloni et al. [57], Cirelli et al. [9], Cirelli et al. [59]. For the spatial part of the model, we considered several DM profiles for each of the considered objects, see table 2 and table 3. J-factors for each of the considered models were calculated with the publicly available `CLUMPY` v.3.0.0 code (Charbonnier et al. [77], Hütten et al. [78]). The results presented below were obtained with `ctulimit` task and correspond to 95% confidence level upper limits on $\langle\sigma v\rangle$.

To determine the mean expected CTA sensitivity for annihilating DM signal in the considered objects, we utilised the Asimov dataset described in section 3.1 with benchmark DM profiles for each of the considered annihilation channels ($b\bar{b}, W^+W^-$ and $\tau\bar{\tau}$). We also used 50 simulated randomized datasets to estimate the uncertainties connected to the random realizations of the simulated/observed datasets.

We additionally identify several sources of systematic uncertainties which can significantly affect the derived limits. These sources include effects of: *(i)* poor knowledge of

[5] See e.g. binned analysis tutorial at http://cta.irap.omp.eu/ctools/users/tutorials/quickstart/index.html.

[6] See details of the implementation of the fitting procedure at ctools website http://cta.irap.omp.eu/ctools/users/user_manual/likelihood.html.

JCAP08(2023)073

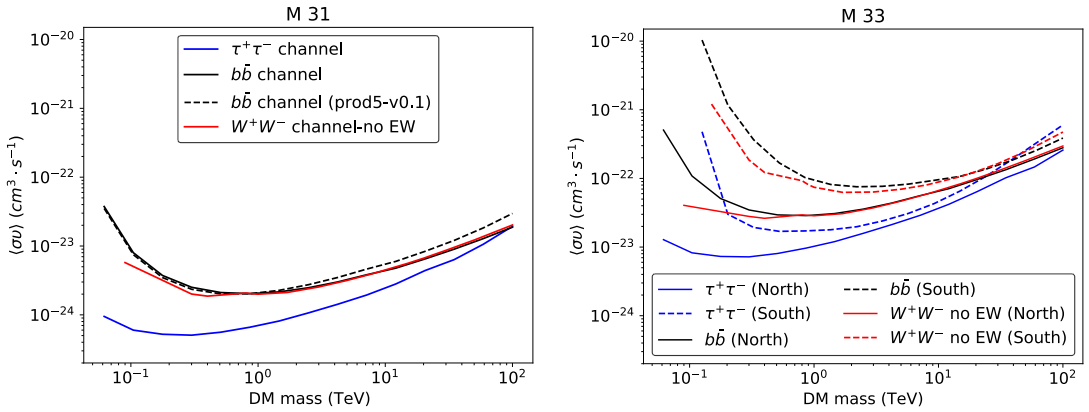

Figure 5. 95% confidence level expected CTA upper limits on velocity-averaged WIMPs annihilation cross-section from 100 h long observations of M31 (left panel) and M33 (right panel) with CTA-North. The benchmark density profiles are assumed in both cases. Blue, black, and red curves correspond to $\tau^+\tau^-$, $b\bar{b}$ and W^+W^- annihilation channels. The black dashed line at the left panel illustrates upper limits results for the $b\bar{b}$ annihilation channel when utilizing `prod5-v0.1` IRFs. Dashed curves at the right panel correspond to the limits which could be obtained with 100 h observations of the same objects with CTA-South array.

DM profiles in selected objects; *(ii)* poor modeling of nearby fore/background astrophysical sources; *(iii)* poor knowledge of CTA response functions (including effective area, PSF and residual CR background mismodeling). We study the contributions from each of these effects in detail and summarize the used approaches and derived results in what below.

4 Results

4.1 Expected CTA sensitivity

In this section we present the main results of our analysis, CTA sensitivity to DM signal from M31 and M33, using Asimov data set and considering the benchmark DM-source models described in section 2.2. Under "CTA limits" we mean the limits which CTA could provide for the case of no signal observation, i.e. CTA sensitivity for a detection of annihilating DM signal.

Figure 5 presents 95% confidence level expected upper limits for the weighted velocity annihilation cross-section for $b\bar{b}$, $\tau^+\tau^-$ and W^+W^- annihilation channels for 100 h long observations of M31 and M33. We note, however, that more constraining results can be obtained when one considers the contribution of DM subhalos, since the presence of such DM substructures can moderately and/or significantly boost the DM annihilation signal, depending on the modeling approach employed. A detailed modeling of such DM substructures in M31 field halo and how the presence of the latest can provide constraints tightening on the corresponding cross-sections is discussed in appendix D. In what below, we additionally discuss the impact of several considered sources of systematic uncertainties on the derived limits.

4.2 Effects of uncertainties on the DM density distribution

To assess the uncertainties arising from the incomplete knowledge of the DM density distribution in the selected objects, we identified several M31/M33 DM profiles reported in the

JCAP08(2023)073

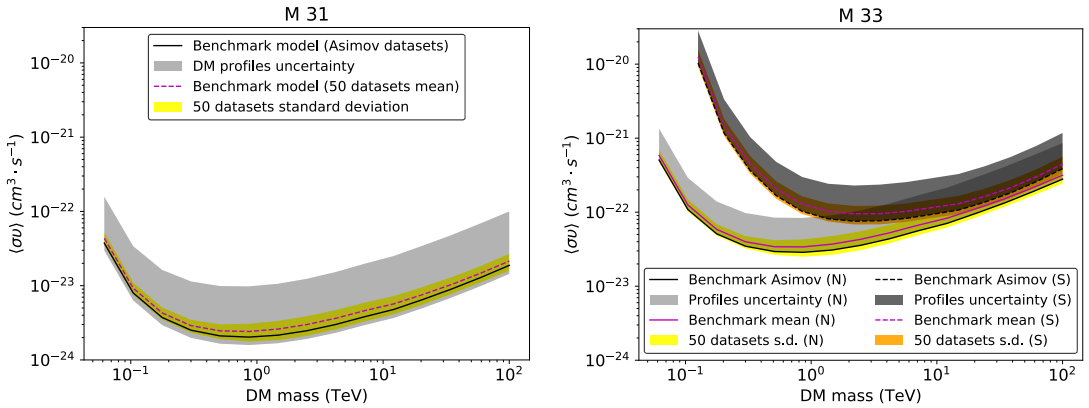

Figure 6. Left: the grey shaded region resent the range of limits on velocity-averaged annihilation cross-section ($b\bar{b}$ annihilation channel) for 100 h long M31 (left panel) observations with CTA-North for the set of DM density profiles summarized in table 2 and 3. The black solid lines correspond to expected limits for the benchmark models of DM density profiles, based on the simulated Asimov data set. The magenta line and yellow shaded regions correspond to the mean values and standard deviations of the expected limits from 50 random statistically independent realizations of the data. Right panel: same for M33. Results for the CTA-North and CTA-South arrays are indicated with (N) and (S) correspondingly.

literature and repeated the analysis described in section 3.2 for each DM profile. The complete list of the considered profiles is given in table 2 and table 3. Corresponding J-factor profiles as functions of the distance to the center of the corresponding galaxy are shown in figure 2. As demonstrated by this figure, the difference in J-factors' profiles at some distances can reach an order of magnitude, resulting in about the same potential worsening of the derived limits on the WIMP annihilation cross-section.

We conclude that the current measurements of the DM density distribution in M31 and M33 carry sizable uncertainties, especially so in the central regions of these galaxies. These DM-density uncertainties are one of the dominant systematic ones which can substantially worsen any derived results. An additional source of J-factor uncertainty is the contribution from the DM annihilating in the MW halo. Our estimations show that this contribution at positions of M31 and M33 galaxies is sub-dominant in comparison to the DM-annihilation signal in M 31 and M 33, see appendix A. Correspondingly, in what below, we neglect the contribution from DM annihilating in the MW halo.

The results of our analysis are shown in figure 6 for the benchmark $b\bar{b}$ channel and in figure 11 and 12 for $\tau^+\tau^-$, and W^+W^- channels correspondingly. The shaded regions correspond to the envelope of the upper limits obtained for all considered profiles. For the illustration in figure 6 we additionally present the uncertainty region connected to random data realizations. These regions are shown with yellow and orange colors for the Northern and Southern CTA site respectively.

4.3 Effects of uncertainties on the astrophysical backgrounds

Additional uncertainty during the analysis can arise from the presence of poorly modelled point-like or diffuse sources in the CTA's FoV. In the case of M31, we note the presence of

JCAP08(2023)073

a central diffuse astrophysical source, (see e.g. Karwin et al. [69]) which potentially could mimic DM annihilation signal and spoil CTA sensitivity for DM studies in this object.

To assess the impact of the presence of the discussed point-like/diffuse sources, we performed simulations/analysis of the data similar to section 3.2 with and without explicit modelling of the sources (see table 4). The obtained in both cases upper limits coincide with a discrepancy of 10%. This allows us to conclude on the relative unimportance of the contribution of nearby sources for the presented results.

4.4 GeV emission from the Inner M31 bulge

The GeV *Fermi*/LAT spectrum energy distribution of the central astrophysical source in M31 is shown in figure 7 with light-grey (reported by Ackermann et al. [67]) and orange points (reported in the recent study Armand and Calore [70]). The red line and shaded region show the best-fit power law parameters of Karwin et al. [69] above 1 GeV. Assuming that the M31 spectrum continues to the TeV band as a power law, our modelling shows that the CTA will not be able to detect this source. Blue upper limits present 95% c.l. flux upper limits that CTA could reach with a 100 h long observation of the region. For the illustration with a green line, we show the spectrum of 12.1 TeV DM annihilating to $b\bar{b}$ channel. The strength of the signal corresponds to the 95% upper limit reported in figure 6 for annihilation cross-section at this mass.

We additionally explore the possibility of a break/hardening of M31 spectral index at ~ 5 GeV energies, as marginally indicated by *Fermi*/LAT spectral points. Figure 7, right panel, shows the TS of the detection of M31 central source as a function of the assumed spectral index. We conclude that the CTA will be able to detect M31 with $TS \gtrsim 9$ only if its spectrum is harder than ~ 2.4, while high significance detection ($TS \gtrsim 25$) is achieved only if its spectrum is harder than ~ 2.3. The corresponding power law for high-significance detection is shown in the left panel with a black solid line.

4.5 Impact of systematic uncertainty

In this section, we discuss the impact of the systematic uncertainties of the instrumental origin and/or related to miss-identified CR on the derived results. Aiming this, we adopt two different approaches to describe systematic uncertainties in the modeling of the data. In general, systematic uncertainties arise from imperfectly known or poorly controlled instrument characteristics. E.g., the energy-dependent under(over)-estimation of the effective area uncontrollably changing with time can induce artificial spectral features and consequently lead to the false-positive detection of annihilating-DM signal.

In both methodologies, briefly summarized below, we assume 0.1 (10%) energy scale and 0.1° spatial scale systematic uncertainties of CTA. These values are close to the characteristic ones for currently operating facilities, such as H.E.S.S. (Aharonian et al. [79]). We however explore also lower levels of systematics — 1% and 3% to illustrate the gain of the decreased level of systematics which can be achieved with the next-generation instruments.

Systematics via likelihood function modification. The contribution of the systematic uncertainties can be accounted for by multiplying the predicted signal by scale parameters and profiling their likelihood over the value of the selected parameters. We select scale parameter $\boldsymbol{\alpha} = \alpha_{ij}$ for which we assume Gaussian nuisance likelihood with an i, j-independent variance σ_α^2. In principle, the distributions are considered log-normal fainting to zero as a α goes

JCAP08(2023)073

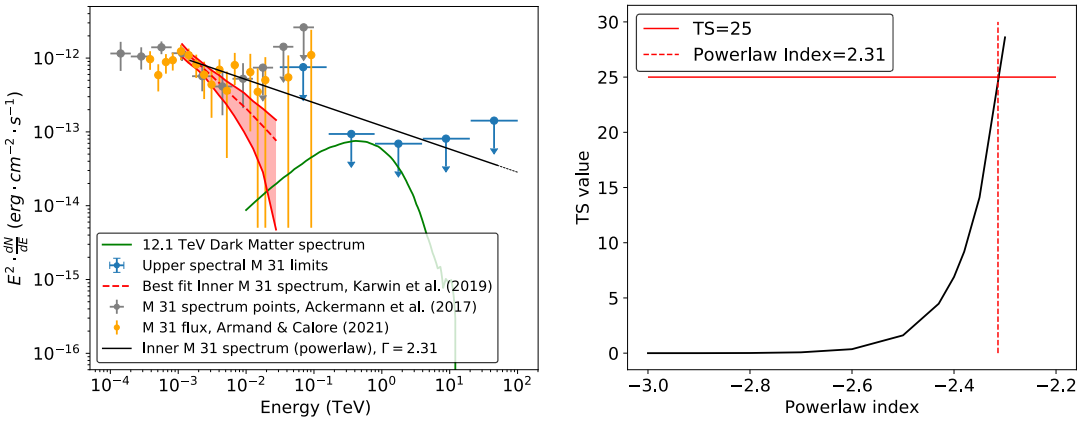

Figure 7. Left: *Fermi*/LAT spectrum and CTA sensitivity to the inner M31 source. The red dashed line inside the red butterfly diagram corresponds to the best-fit powerlaw model for an analysis in the energy range of 10^{-3} to 10^{-2} TeV of the Inner M31 component of M31 galaxy (spectrum: powerlaw, spatial model: radial disk of 0.4° radius) reported in Karwin et al. [69]. Grey points show the results of Eckner et al. [68], Ackermann et al. [67]. The orange points correspond to M31 spectrum with disk-like M31 model (Armand and Calore [70]). The blue upper limits present the upper spectral limits on Inner M31 emission (M31 bulge) that CTA could provide with a 100 h-long observation of M31 region. The green solid curve present the annihilation spectrum of 12.1 TeV WIMP DM (benchmark M31 density profile, $b\bar{b}$ channel, $\langle\sigma v\rangle = 4.78 \cdot 10^{-24}\,\mathrm{cm}^3 \cdot \mathrm{s}^{-1}$). The black solid line highlights the case in which M31 could be detected at 5σ significance level. Normalization of the line matches one reported by Karwin et al. [69] at 1.5 GeV and continues to higher energies as a powerlaw with the slope 2.31.

Right: detection test-statistics value for M31 assuming that its spectrum matches one reported by Karwin et al. [69] at 1.5 GeV and continues to higher energies as a powerlaw with the given slope.

to zero. Based on that scale parameter, we utilize for our analysis the following modified likelihood function (see e.g., Silverwood et al. [80])

$$\boldsymbol{L}(\boldsymbol{\mu}, \boldsymbol{\alpha} \mid \boldsymbol{n}) = \prod_{i,j} \frac{(\mu_{ij}\alpha_{ij})^{n_{ij}}}{\sqrt{2\pi}\sigma_\alpha n_{ij}!} e^{-\mu_{ij}\alpha_{ij}} e^{-\frac{(1-\alpha_{ij})^2}{2\sigma_a^2}} \,. \tag{4.1}$$

Such a modification of the likelihood provides the opportunity for upper limit derivations when systematic uncertainties (e.g., effective area) enter linearly the calculation of the total signal. The obtained upper limits are presented with the red dashed and dash-dotted line in figure 9, for 10% and 3% systematic uncertainty respectively.

Systematics via exposure constraining. Alternatively, one can address the impact of systematic uncertainties by modeling them via limiting the statistic of the data. The observations of the same constant in time phenomena for a time period t result in relative statistical errors scaling $\propto t^{-1/2}$. E.g., for a source with a constant with time count rate r cts/s the observed after time t number of photons would be $N = rt$ with corresponding relative statistical uncertainty $dN_{\rm stat}/N = N^{-1/2} \propto t^{-1/2}$ decreasing with increasing of observational time. We define the relative systematic uncertainty α as $dN_{\rm syst}/N = \alpha$ which remains constant and does not decrease with the increase of observational exposure. This type of uncertainty can reflect poorly controllable behavior of the instrument, e.g. energy dependent quasi-random variations of the effective area during the observation.

JCAP08(2023)073

To treat the systematic uncertainty we propose to limit the observational time to the characteristic value for which $dN_{\rm syst} = dN_{\rm stat}$, i.e., to stop the observation as soon as expected systematic uncertainty becomes equal to the statistical one. Longer observation will lead only to the decrease of statistical uncertainty, which will become sub-dominant in comparison to systematical one.

The requirement $dN_{\rm stat} = dN_{\rm syst}$ can be reformulated in terms of the maximal number of observed photons as $N_{\rm max} = \alpha^{-2}$. We note that $N_{\rm max}$ should not be treated as the total number of photons received during the observation, but rather as a number of photons in the smallest possible statistically independent energy/spatial bins. We note also that generally speaking, the level of systematic $\alpha = \alpha(E)$ can be a function of energy.

The spatial $\delta\theta$ and energy δE resolutions of the instrument naturally define statistically independent energy and spatial bins. To properly identify the time for which at a given energy $dN_{\rm stat} = dN_{\rm syst}$ we propose that the observation at energies $[E; E + \delta E]$ should be stopped as soon as the number of photons in any spatial bin of size $\delta\theta$ reached $\alpha^{-2}(E)$. This allows to have in each of the statistically independent spatial/energy bins the number of photons dominated by statistics uncertainty and thus neglect the presence of systematics.

The characteristic values of CTA energy and spatial resolutions are $\sim 10\%$ and $\sim 0.1^\circ$ correspondingly. Accordingly, we split 0.03 TeV to 100 TeV simulation energy range over a number of energy and spatial bins. We explicitly limit the observing time when systematic uncertainty becomes equal to the statistical one. I.e. at energies $[E; 1.1 \cdot E]$ we stop the observation as soon as any spatial bin of 0.1°-radius accommodates more than $N = 100$ photons for $\alpha = 0.1$ and $N = 1111$ photons for $\alpha = 0.03$. We note, that for most observational cases, the highest number of photons in spatial bins at any energy is reached in the spatial bin centered at the center of FoV of the CTA. Due to off-axis decrease of CTA effective area, this position is characterised by the strongest level of the residual cosmic-ray background. In the absence of bright astrophysical sources in the FoV, this background is obviously dominating the observed emission.

We show the number of photons as a function of energy, for a region of 0.1° spatial scale centered at the center of CTA FoV in figure 8, left panel. The red horizontal line illustrates 100 photons — the characteristic number of photons at which the observation should be stopped for the systematic level $\alpha = 0.1$. The right panel of the figure presents the exposure required to reach 100 photons in the considered bin as a function of energy. This illustrates that the considered level of systematic affects only the low-energy part of the CTA data. Namely, any energy/spatial bin (10% energy width and 0.1° spatial scale) at above $\gtrsim 0.5$ TeV for 100 h long observation does not accommodate more than 100 photons. Correspondingly, at these energies, we performed standard binned analysis (assuming bin size $\sim 10\%$ energy width and $\sim 0.1^\circ$ spatial scale) for 100 h Asimov dataset.

At lower energies, we performed dedicated, time-limited simulations of Asimov datasets for each of the considered 10% energy width bins in a way similar to the simulations described above. For each of the considered bins, including the above-threshold bin at $E > 0.5$ TeV we performed the standard binned analysis and build log-likelihood profiles as a function of DM template normalization (proportional to $\langle\sigma v\rangle$). Adding log-likelihood profiles for all energy bins, we built a joint log-likelihood profile which allowed us to constrain DM annihilation cross-section as a function of DM mass for such energy-dependent exposure observation.

The results of this approach are summarised in figure 9, for 10% and 3% systematics respectively (blue dashed and dot-dashed lines correspondingly). The red lines present the results of the systematic treatment based on the modification of the log-likelihood function

JCAP08(2023)073

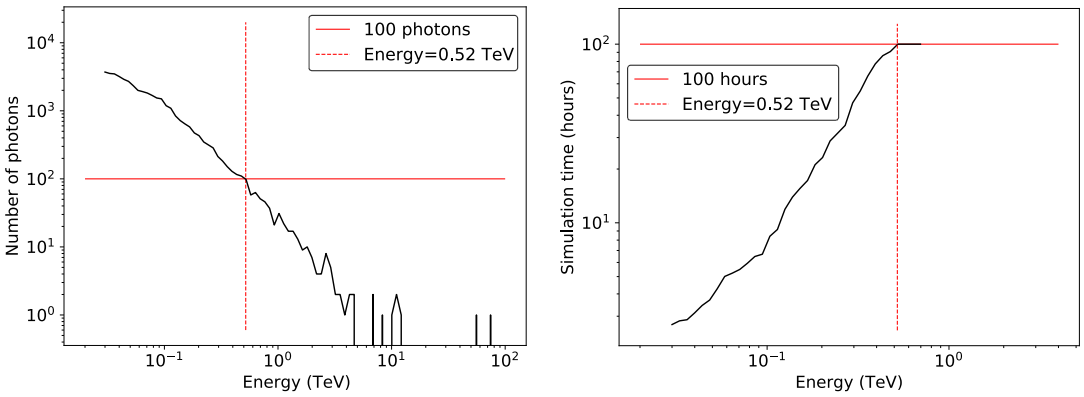

Figure 8. Left: number of detected photons in the 10% energy width bins in 0.03–100 TeV energy band. The solid red line shows 100 photons, the characteristic value for which systematic and statistical uncertainties are equal for 10% systematic uncertainty ($\alpha = 0.1$). The energies > 0.52 TeV (red dashed vertical line) are dominated by statistical uncertainties.

Right: simulation time in the considered energy bins required for systematic uncertainty to be equal or smaller than the statistical one. The solid red line corresponds to 100 hours of simulation time.

described above for similar values of systematic uncertainties. Despite the entirely different approaches considered and generally different treatment of the systematics, we found the results to be broadly consistent with each other at lower levels of systematics (1% or 3%). We note, that the results are not totally identical since the two distinct strategies suggest different origin of the systematic uncertainty and treat it differently. E.g. the first discussed strategy is based on the modification of the log-likelihood function which applies to the whole energy range of the analysis whereas the second one has its basis on the exposure time constraining which only affects the lower energy regimes where the systematic uncertainty dominates over the statistical uncertainty. We note that the Night Sky Brightness maps (NSB) indicate a higher level of emission in the direction of M31, and thus the enhanced background at the location of the Galaxy indicates an even higher level of systematic uncertainty.

We would like to note also that the considered "systematics via exposure constraining" approach allows us to identify the scale of systematics which does not affect the observations at 100 h timescale. Namely, the maximum number of the photons in 0.1°, 10% energy-width bins seen in simulation is $\lesssim 10^4$, which translates to the systematic level of $\sim 1\%$. We argue that for the lower values of systematic, the 100 h observations will not be affected by considered systematics.

The discussed approach to the systematic treatment allows also to identify the most effective sharing of the observational time between different instruments of the CTA array. Consisting of large (LST), medium (MST), and small (SST) size telescopes CTA observatory can perform observations by its different sub-arrays sensitive to low (LST), intermediate (MST), and high (SST) energies. The exposure time required to reach a given number of photons per energy/spatial bin is typically an increasing function of energy, see e.g. figure 8, right panel. For a given level of systematics, this allows to vary the observational time, making it the shortest for the LST and longest for SST telescopes without loss of the scientific outcome of observation. The freed telescopes' time can be used for observations of other targets.

JCAP08(2023)073

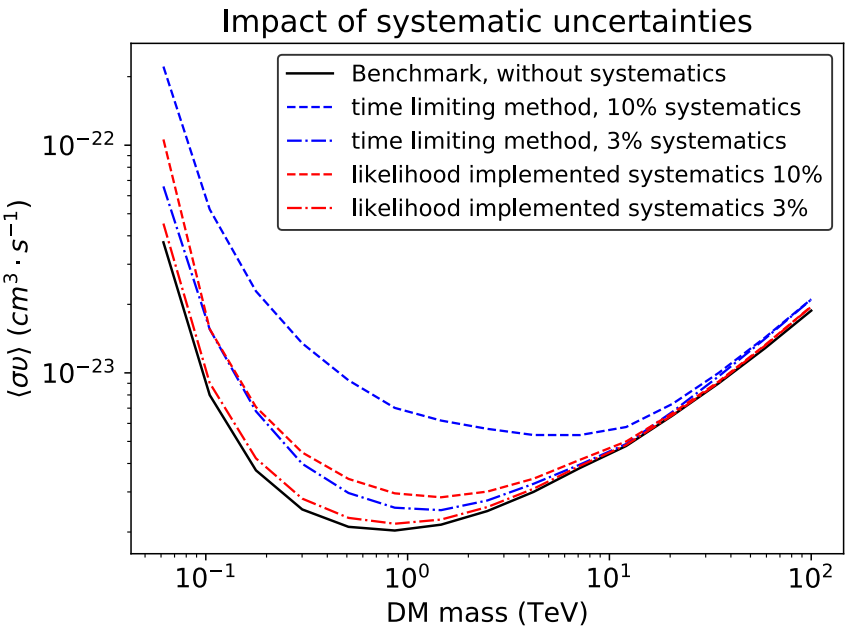

Figure 9. M31 upper limits comparison for the benchmark model with and without the presence of systematic uncertainties ($b\bar{b}$ channel). The black solid line corresponds to the upper limits without the presence of systematic uncertainties. The blue/red dashed lines correspond to the upper limits in the presence of systematics (10% energy scale, 0.1° spatial scale) following the time-constraining methodology and the likelihood implemented systematics method respectively. The blue/red dash-dotted lines have the same representation but for 3% energy scale.

5 Conclusions and discussion

Along with the MW, M31, and M33 are the two largest spiral galaxies in the Local group. The proximity of these two galaxies permits detailed studies of DM distribution, showing the DM dominated nature of these objects and making them interesting targets for annihilating WIMPs searches with current and upcoming observational facilities.

In this work, we performed 100-hour long simulation of these galaxies with the next-generation TeV observatory CTA aiming to study the prospects of detecting annihilating DM within these objects. Where applicable under "CTA limits/constraints" we meant the limits which CTA could provide for the case of no signal observation, i.e. CTA sensitivity for a detection of annihilating DM signal. We report the expected prospects of detection for DM velocity-averaged annihilation cross-section for a set of annihilation channels ($b\bar{b}$, $\tau^+\tau^-$ and W^+W^-). We have paid special attention to the factors that can affect the CTA sensitivity to the expected signal. In particular, we analysed uncertainties connected to *(i)*: the possible astrophysical background emission in the FoV of CTA; *(ii)* the uncertainties of DM density distribution; *(iii)*: imperfect or poor knowledge of the instrument itself, i.e. systematic uncertainties.

We found that the uncertainties on the DM profiles result in the highest uncertainty in the derived prospects. Namely, for the density profiles summarized in table 2 the corresponding uncertainty can reach an order of magnitude for certain annihilation channels, see figure 6, 11, and 12. We, therefore, argue that the detailed studies of DM distribution in

JCAP08(2023)073
Article I

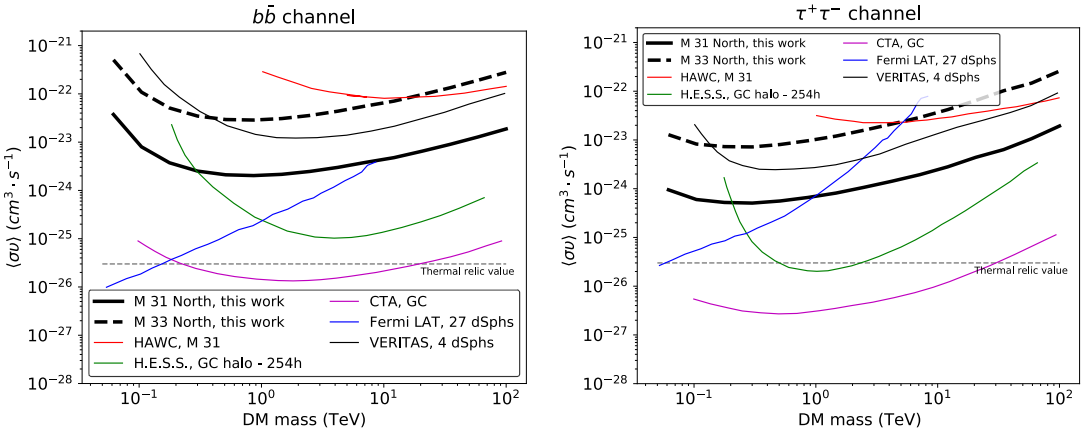

Figure 10. Comparison of constraints on the $b\bar{b}$ (left panel) and $\tau^+\tau^-$ (right panel) channel of the upper limits of this work — M31 (solid black line-benchmark model) and M33 (dashed black line-benchmark model) — with the previous published HAWC limits (red solid line for the same Einasto model that we consider as benchmark model for M31 (Albert et al. [31])), H.E.S.S. limits of observations of the GC (green solid line (Abdallah et al. [50])), the limits of the observations of 27 dSphs of the MW by Fermi satellite (blue solid line (Hoof et al. [33])), the limits from the GC by CTA (magenta solid line (Di Mauro et al. [44])), and the combined analysis of observations of 4 dSphs by VERITAS (cyan solid line (Archambault et al. [81])).

M31 and M33 are essential for the accurate estimate of WIMP annihilation detection within these objects.

Figure 5 summarizes the 95% constraints derived for the benchmark density profiles for all considered channels for both discussed galaxies. The figure illustrates that the observation of M31 from the Northern (La Palma) CTA site generally provides better constraints in comparison to M33 observations. The best limits are derived for $\tau^+\tau^-$ annihilation channel and reached the level of $5 \cdot 10^{-25}\,\mathrm{cm}^3\,\mathrm{s}^{-1}$ at energies $\sim 0.3\,\mathrm{TeV}$.

The 100 h long CTA observations of M31/M33 could improve — by an order of magnitude — the limits derived by modern facilities from non-observation of the annihilation signal from M31 by HAWC (Albert et al. [31]) or from 4 dSphs by VERITAS (Archambault et al. [81]), see figure 10. At the same time, the observations of the Galactic Center with modern observatories (see e.g. Abdallah et al. [50]) or with CTA (Di Mauro et al. [44]) could be able to provide better constraints. At below 10 TeV energies, the expected limits are also substantially worse than the limits derived from *Fermi*/LAT observations of 27 dSphs (Hoof et al. [33]). We argue, however, that taking into account the possible effects of highly uncertain astrophysical background and DM density distribution, the observations of the proposed in this work targets could provide important constraints on WIMP DM parameter space.

The possible astrophysical emitting sources that are reported in the literature for both M31 and M33 do not appear bright enough to strongly affect the derived results. A particular set of simulations and fitting was dedicated to ascertaining whether or not the extended Inner M31 astrophysical source is detectable by CTA. The simple powerlaw fit that we performed resulted in a power index value of 2.3 or harder, for such detection to be possible (see figure 7).

Finally, the last cause of sensitivity loss, studied in this work, is the systematic uncertainties case. For the characteristic values of the systematic uncertainty of 3–10% expected for CTA, we compare the results of two approaches of the systematics treatment. One of the

JCAP08(2023)073

approaches is based on the modification of log-likelihood function used for the fitting of the model to the data while the second is based on the constraint of the observational time so the statistical uncertainty becomes comparable to the systematics level, see 4.5. Although the results of the two different approaches are not identical, this is understandable due to the distinctive nature of the strategies employed. Both methods result in a somewhat comparable sensitivity loss (mainly for lower levels of systematics i.e., 1% and 3%) in comparison to no systematic case, see figure 9. The loss affects mostly low DM masses, the limits for which are strongly dominated by low-energy data, where the systematics plays the most significant role. In the case of 10% systematics the expected loss of sensitivity can reach a factor of 3 indicating potential substantial worsening of CTA limits at low DM masses.

The exposure limiting approach to systematic treatment allows also to identify the systematics level $\alpha_{\rm min} \sim 1\%$ at which 100 h long CTA observations will not be sensitive to the systematic effects. Finally, we propose the energy-dependent observational strategy, which allows efficient use of different telescopes from the CTA array in the presence of systematics. Namely, we argue that in this case, the observational time can be selected to be shortest for LST telescopes and the longest for SST ones without compromising the scientific outcome of the observation. The freed telescopes' time can be used for the observation of other targets.

Acknowledgments

We would like to thank Torsten Bringmann for helpful discussions. This work was conducted in the context of the CTA Dark Matter Exotic Physics Working Group. This paper has gone through internal review by the CTA Consortium. This work has been supported by the Fermi Research Alliance, LLC under Contract No. DE-AC02-07CH11359 with the U.S. Department of Energy, Office of High Energy Physics. The work of CE is further supported by the "Agence Nationale de la Recherche" through grant ANR-19-CE31-0005-01 (PI: F. Calore). AS is supported by the Kavli Institute for Cosmological Physics at the University of Chicago through an endowment from the Kavli Foundation and its founder Fred Kavli. AB is supported by the European Research Council (ERC) Advanced Grant "NuBSM" (694896). DM is supported by DFG through the grant MA 7807/2-1 and DLR through the grant 50OR2104. The authors acknowledge support by the state of Baden-Württemberg through bwHPC.

We gratefully acknowledge financial support from the following agencies and organizations: State Committee of Science of Armenia, Armenia; The Australian Research Council, Astronomy Australia Ltd, The University of Adelaide, Australian National University, Monash University, The University of New South Wales, The University of Sydney, Western Sydney University, Australia; Federal Ministry of Education, Science and Research, and Innsbruck University, Austria; Conselho Nacional de Desenvolvimento Científico e Tecnológico (CNPq), Fundação de Amparo à Pesquisa do Estado do Rio de Janeiro (FAPERJ), Fundação de Amparo à Pesquisa do Estado de São Paulo (FAPESP), Fundação de Apoio à Ciência, Tecnologia e Inovação do Paraná — Fundação Araucária, Ministry of Science, Technology, Innovations and Communications (MCTIC), Brasil; Ministry of Education and Science, National RI Roadmap Project DO1-153/28.08.2018, Bulgaria; The Natural Sciences and Engineering Research Council of Canada and the Canadian Space Agency, Canada; CONICYT-Chile grants CATA AFB 170002, ANID PIA/APOYO AFB 180002, ACT 1406, FONDECYT-Chile grants, 1161463, 1170171, 1190886, 1171421, 1170345, 1201582, Gemini-ANID 32180007, Chile, W.M. gratefully acknowledges support by the ANID BASAL projects ACE210002 and FB210003, and FONDECYT 11190853; Croatian Science Foundation, Rudjer Boskovic Institute, University of Osijek, University of Rijeka,

JCAP08(2023)073

University of Split, Faculty of Electrical Engineering, Mechanical Engineering and Naval Architecture, University of Zagreb, Faculty of Electrical Engineering and Computing, Croatia; Ministry of Education, Youth and Sports, MEYS LM2015046, LM2018105, LTT17006, EU/MEYS CZ.02.1.01/0.0/0.0/16_013/0001403, CZ.02.1.01/0.0/0.0/18_046/0016007 and CZ.02.1.01/0.0/0.0/16_019/0000754, Czech Republic; Academy of Finland (grant nr.317636 and 320045), Finland; Ministry of Higher Education and Research, CNRS-INSU and CNRS-IN2P3, CEA-Irfu, ANR, Regional Council Ile de France, Labex ENIGMASS, OCEVU, OSUG2020 and P2IO, France; The German Ministry for Education and Research (BMBF), the Max Planck Society, the German Research Foundation (DFG, with Collaborative Research Centres 876 & 1491), and the Helmholtz Association, Germany; Department of Atomic Energy, Department of Science and Technology, India; Istituto Nazionale di Astrofisica (INAF), Istituto Nazionale di Fisica Nucleare (INFN), MIUR, Istituto Nazionale di Astrofisica (INAF-OABRERA) Grant Fondazione Cariplo/Regione Lombardia ID 2014-1980/RST_ERC, Italy; ICRR, University of Tokyo, JSPS, MEXT, Japan; The Netherlands Research School for Astronomy (NOVA), Netherlands Organization for Scientific Research (NWO), The Netherlands; University of Oslo, Norway; Ministry of Science and Higher Education, DIR/WK/2017/12, the National Centre for Research and Development and the National Science Centre, UMO-2016/22/M/ST9/00583, Poland; Slovenian Research Agency, grants P1-0031, P1-0385, I0-0033, J1-9146, J1-1700, N1-0111, and the Young Researcher program, Slovenia; South African Department of Science and Technology and National Research Foundation through the South African Gamma-Ray Astronomy Programme, South Africa; The Spanish groups acknowledge the Spanish Ministry of Science and Innovation and the Spanish Research State Agency (AEI) through the government budget lines PGE2021/28.06.000X.411.01, PGE2022/28.06.000X.411.01 and PGE2022/28.06.000X.711.04, and grants PID2022-139117NB-C44, PID2019-104114RB-C31, PID2019-107847RB-C44, PID2019-104114RB-C32, PID2019-105510GB-C31, PID2019-104114RB-C33, PID2019-107847RB-C41, PID2019-107847RB-C43, PID2019-107847RB-C42, PID2019-107988GB-C22, PID2021-124581OB-I00, PID2021-125331NB-I00; the "Centro de Excelencia Severo Ochoa" program through grants No. CEX2019-000920-S, CEX2020-001007-S, CEX2021-001131-S; the "Unidad de Excelencia María de Maeztu" program through grants No. CEX2019-000918-M, CEX2020-001058-M; the ''Ramón y Cajal" program through grants RYC2021-032552-I, RYC2021-032991-I, RYC2020-028639-I and RYC-2017-22665; the "Juan de la Cierva-Incorporación" program through grants No. IJC2018-037195-I, IJC2019-040315-I. They also acknowledge the "Atracción de Talento" program of Comunidad de Madrid through grant No. 2019-T2/TIC-12900; the project "Tecnologiás avanzadas para la exploracioń del universo y sus componentes" (PR47/21 TAU), funded by Comunidad de Madrid, by the Recovery, Transformation and Resilience Plan from the Spanish State, and by NextGenerationEU from the European Union through the Recovery and Resilience Facility; the La Caixa Banking Foundation, grant No. LCF/BQ/PI21/11830030; the "Programa Operativo" FEDER 2014-2020, Consejería de Economía y Conocimiento de la Junta de Andalucía (ref. 1257737), PAIDI 2020 (ref. P18-FR-1580) and Universidad de Jaén; "Programa Operativo de Crecimiento Inteligente" FEDER 2014-2020 (ref. ESFRI-2017-IAC-12), Ministerio de Ciencia e Innovación, 15% co-financed by Consejería de Economía, Industria, Comercio y Conocimiento del Gobierno de Canarias; the "CERCA" program and the grant 2021SGR00426, both funded by the Generalitat de Catalunya; and the European Union's Horizon 2020 GA:824064 and NextGenerationEU (PRTR-C17.I1); Swedish Research Council, Royal Physiographic Society of Lund, Royal Swedish Academy of Sciences, The Swedish Na-

JCAP08(2023)073

tional Infrastructure for Computing (SNIC) at Lunarc (Lund), Sweden; State Secretariat for Education, Research and Innovation (SERI) and Swiss National Science Foundation (SNSF), Switzerland; Durham University, Leverhulme Trust, Liverpool University, University of Leicester, University of Oxford, Royal Society, Science and Technology Facilities Council, U.K.; U.S. National Science Foundation, U.S. Department of Energy, Argonne National Laboratory, Barnard College, University of California, University of Chicago, Columbia University, Georgia Institute of Technology, Institute for Nuclear and Particle Astrophysics (INPAC-MRPI program), Iowa State University, the Smithsonian Institution, V.V.D. is funded by NSF grant AST-1911061, Washington University McDonnell Center for the Space Sciences, The University of Wisconsin and the Wisconsin Alumni Research Foundation, U.S.A.

The research leading to these results has received funding from the European Union's Seventh Framework Programme (FP7/2007-2013) under grant agreements No. 262053 and No. 317446. This project is receiving funding from the European Union's Horizon 2020 research and innovation programs under agreement No. 676134.

A previous version of this article is also available as report FERMILAB-PUB-23-163-V.

A Summary of DM profiles and upper limit results for $\tau^+\tau^-$ and W^+W^- annihilation channels

In this section, we summarize a large sample of DM density profiles reported in the literature for M31 and M33 galaxies. In table 2 and 3 we present the basic information on these objects (coordinates, distance, possible CTA observational site) as well as parameters of DM density profiles (scale density and radius) used in this work to estimate the uncertainties connected to density uncertainties in these objects.

Using the profiles reported in table 2 and 3 we derived, additionally to figure 6 — representing upper limits towards the benchmark annihilation channel — the 95% confidence level upper limits for DM annihilation in the direction of both M31 and M33 for the rest two ($\tau^+\tau^-$ and W^+W^-) representative channels for DM searches. The obtained results are presented in figure 11 and 12.

B Astrophysical emitting gamma-ray sources

The astrophysical sources within 5° from the positions of M31 and M33 detected in the GeV band are summarized in table 4. The point sources are adapted from 3FHL catalogue (Ajello et al. [74]) of *Fermi*/LAT sources detected above 10 GeV, the parameters of diffuse source ("Inner M31") are adapted from Karwin et al. [69]. The table summarizes basic information about the sources (catalogue/reference, coordinates, suggested in 3FHL type and redshift) as well as spectral parameters of sources in the GeV band (spectral shape, slope, and flux).

C Contribution of the galactic diffuse halo

The expected flux from DM self-annihilation is proportional to the square of the DM density integrated along the line of sight (see J-factor eq. (2.2)). Calculating the expected flux from DM annihilation, one should take into account the contribution from DM annihilation signal originating from the MW DM halo. The J-factor of the MW halo is given by:

$$J(\psi) = \int_0^{\ell_{\rm max}} \rho^2 \left(\sqrt{R_{\rm sc}^2 - 2\ell R_{\rm sc} \cos\psi + \ell^2} \right) d\ell$$

Galaxy	l, b (°)	Distance kpc	CTA site	Profile	r_s kpc	ρ_s GeV/cm^3	$\log_{10}[J(0.5°)]$ GeV/cm^5	references
M31	121.17, −21.57	778	North	NFW	8.18	$1.43423 \cdot 10^{0}$	19.33	[82]
				NFW	12.5	$6.60504 \cdot 10^{-1}$	19.16	[83]
				NFW	34.6 ± 2	$8.46 \cdot 10^{-2}$	18.52	[84]
				NFW	16.5 ± 1.5	$4.18 \cdot 10^{-1}$	19.09	[85]
				NFW	$30.2^{12.1}_{-8.8}$	—	—	[86]
				NFW (M31a)	12.94	—	—	[87]
				NFW (M31b)	14.03	—	—	[87]
				NFW (M31d)	17.46	—	—	[87]
				NFW	7.63	$2.342132 \cdot 10^{0}$	19.67	[88]
				Burkert	9.06 ± 0.53	$1.4 \cdot 10^{0}$	18.71	[85]
				Burkert	6.86	$2.171312 \cdot 10^{0}$	18.83	[83]
				Einasto†	178 ± 18	$3.08 \cdot 10^{-4}$	19.24	[85]/ [44]
				Einasto	387 ± 44	$5.32 \cdot 10^{-5}$	18.51	[85]
				Einasto	135.0	$5.1246 \cdot 10^{-4}$	19.36	[83]
				Moore	31.0 ± 3	$5.54 \cdot 10^{-2}$	19.19	[85]
				Moore	25.0	$7.7818 \cdot 10^{-2}$	19.15	[83]
				SIS	> 8.1	—	—	[86]
				HYB	> 117.5	—	—	[86]

Table 2. A summary of basic parameters of M31. The table summarizes Galactic coordinates of M31 (l, b), the distance to the object, visibility from Northern (La Palma) or Southern (Chile) CTA site as well as parameters of DM density distribution (profile type, characteristic densities ρ_s and radii r_s, and the J-factor log-posterior assuming integration over a circular region with angular radius of 0.5°). The benchmark profile is highlighted with a dagger (†) symbol, see text for the details.

Galaxy	l, b (°)	Distance kpc	CTA site	Profile	r_s kpc	ρ_s GeV/cm^3	$\log_{10}[J(0.5°)]$ GeV/cm^5	references
M33	133.61, −31.33	840	North/South	NFW	35	$5.74 \cdot 10^{-2}$	18.14	[89]
				NFW†	22.41	$0.1 \cdot 10^{0}$	18.13	[44]
				NFW	20.78	$0.1 \cdot 10^{0}$	18.05	[90]
				Burkert	12	$4.2 \cdot 10^{-1}$	17.86	[89]
				Burkert	7.5	$6.83 \cdot 10^{-1}$	17.87	[90]
				Burkert	9.6	$4.669 \cdot 10^{-1}$	17.17	[44]
				Pseudo-Iso	1.39	$4.04 \cdot 10^{0}$	18.11	[91]

Table 3. A summary of basic parameters of M33. The table summarizes Galactic coordinates of M31 (l, b), the distance to the object, visibility from Northern (La Palma) or Southern (Chile) CTA site as well as parameters of DM density distribution (profile type, characteristic densities ρ_s and radii r_s, and the J-factor log-posterior assuming integration over a circular region with angular radius of 0.5°). The benchmark profile is highlighted with a dagger (†) symbol, see text for the details.

where ψ is the angular distance from the GC, $R_{\rm sc} = 8.5\,{\rm kpc}$ is the Sun-Galactic Center distance and $l_{\rm max}$ is defined as

$$\ell_{\rm max} = \sqrt{R_{\rm MW}^2 + R_{\rm sc}^2 \sin^2\psi} + R_{\rm sc}\cos\psi$$

JCAP08(2023)073

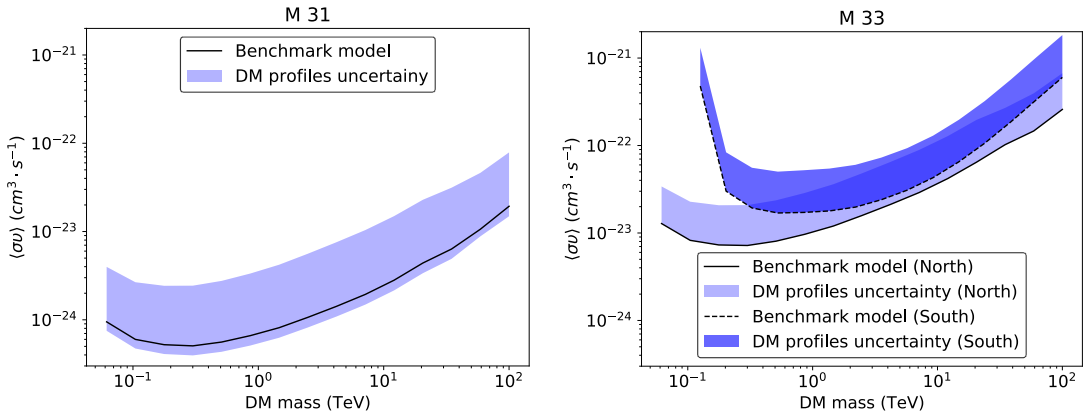

Figure 11. Left: M31 upper limits uncertainty region for all different DM profiles — $\tau^+\tau^-$ annihilation channel. With the black solid line, we highlight the upper limits for the benchmark model. Right: M33 upper limits uncertainty region for all different DM profiles — $\tau^+\tau^-$ annihilation channel. With the black solid/dashed line, we highlight the upper limits for the benchmark model for the Northern/Southern CTA site respectively.

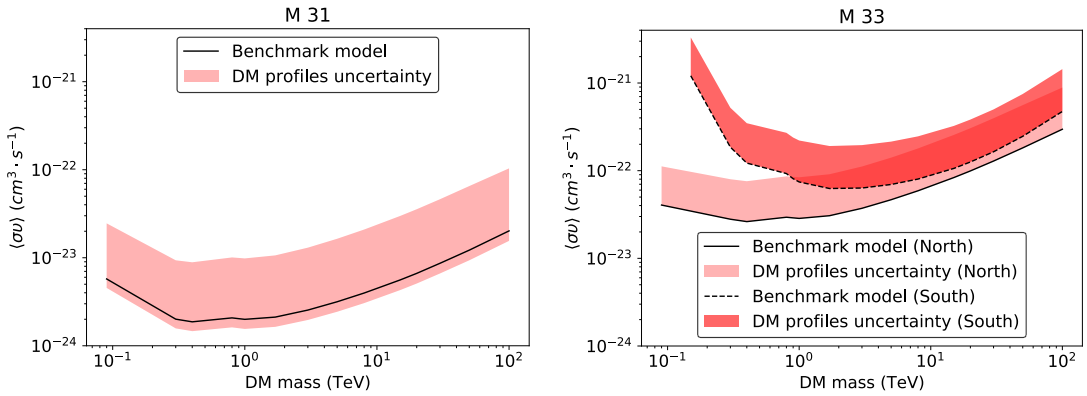

Figure 12. Left: M31 upper limits uncertainty region for all different DM profiles — W^+W^- annihilation channel. With the black solid line, we highlight the upper limits for the benchmark model. Right: M33 upper limits uncertainty region for all different DM profiles — W^+W^- annihilation channel. With the black solid/dashed line, we highlight the upper limits for the benchmark model for the Northern/Southern CTA site respectively.

where $R_{\rm MW}$ corresponds to the radius of MW DM halo. In this analysis, we consider $R_{\rm MW} = \infty$, which results in $\ell_{\rm max} = \infty$, since the contribution of the signal at large radii is negligible in comparison to the signal closer to the center.

The list of DM density profiles in the MW existing in the literature is given in table 5 (see Pieri et al. [92], Abdallah et al. [93], and references therein). In what below, we briefly summarise the profiles present in the table and which are characterised by four parameters $(\alpha, \beta, \gamma, \delta)$: a generalized profile proposed by Hernquist [94], Dehnen [95] and Zhao [96]. Different combinations of the four parameter values lead to different DM distribution, i.e., $(1, 3, 1, 0)$ corresponds to the widely used NFW profile (Navarro et al. [64]), $(2, 3, 1, 1)$ cor-

JCAP08(2023)073

Point sources								
Catalog	Source name	RA °	Dec °	Class	z	spectral shape	Index	Integrated Flux 10^{-11} ph cm^{-2} s^{-1}
M31								
3FHL	J0055.8+4507	13.95	45.13	—	—	PowerLaw	−3.47	2.11
3FHL	J0039.2+4330	9.81	43.51	bcu	—	Powerlaw	−4.11	2.38
3FHL	J0049.0+4224	12.27	42.40	—	—	Powerlaw	−2.33	2.65
3FHL	J0040.3+4049	10.09	40.83	bcu	—	Powerlaw	−1.56	2.48
3FHL	J0047.9+3947	11.98	39.79	bll	0.25	Powerlaw	−2.33	8.37
3FHL	J0041.5+3759	10.38	37.99	bcu	0.38	Powerlaw	−1.86	2.82
M33								
3FHL	J0123.0+3422	20.77	34.37	bll	0.27	PowerLaw	−2.03	6.24
3FHL	J0112.9+3208	18.24	32.15	fsrq	0.60	Powerlaw	−2.69	3.57
3FHL	J0134.4+2638	23.61	26.65	bcu	—	Powerlaw	−2.17	7.79
3FHL	J0144.5+2705	26.14	27.09	bll	—	Powerlaw	−2.88	25.19
Extended source								
Reference	Source name	RA °	Dec °	spatial shape	Size	spectral shape	Index	Integrated Flux 10^{-9} ph cm^{-2} s^{-1}
(Karwin et al. [69])	Inner M31	10.68	41.26	Radial disk	0.4°	Powerlaw	-2.8 ± 0.3	0.5

Table 4. GeV/TeV sources, within 5° radius (CTA FoV) from M31 and M33 detected by Fermi/LAT above 30 GeV. The first four columns stand for the reference/catalogue, sources' names, and coordinates. The fifth column stands for the class (as indicated in 3FHL catalogue) of the point sources or the spatial shape of the Inner M31, where bll corresponds to Bl Lac blazars, bcu – blazars of uncertain type, and the frsq — flat spectrum radio quasars. The sixth column indicates the redshift of the point sources and the spatial size of the Inner M31. The next two columns stand for the spectrum (spectral shape and index) for all sources. Finally, the last columns report the total integrated flux in 10–1000 GeV range for the point sources and in 1–100 GeV range for the Inner M31.

responds to a Burkert profile (Burkert [66]), $(1.5, 3, 1.5, 0)$ corresponds to a Moore profile and $(2, 2, 0, 0)$ to an Isothermal profile (King [63]). Einasto profile (Einasto [65]) follows a different parametrization based on a single parameter α. A different parametrization of a DM density profile based on five different parameters $(r_o, a, \alpha, \beta, \gamma)$ is also found in Pullen et al. [97]; following the equations:

$$\begin{aligned}
\text{Hernquist}: \quad & \rho_{\rm Her}(r) = \rho_s \cdot \left(\delta + \frac{r}{r_s}\right)^{-\gamma} \cdot \left(1 + \left(\frac{r}{r_s}\right)^{\alpha}\right)^{\frac{\gamma-\beta}{a}} \\
\text{Einasto}: \quad & \rho_{\rm Ein}(r) = \rho_s \cdot \exp\left\{-\frac{2}{\alpha} \cdot \left[\left(\frac{r}{r_s}\right)^{\alpha} - 1\right]\right\} \\
\text{Pullen}: \quad & \rho_{\rm Pul}(r) = \rho_s \cdot \left(\frac{r_o}{r}\right)^{\gamma} \cdot \frac{\left[1 + \left(\frac{r_o}{r_s}\right)^{\alpha}\right]^{\frac{\beta-\gamma}{\alpha}}}{\left[1 + \left(\frac{r}{r_s}\right)^{\alpha}\right]^{\frac{\beta-\gamma}{\alpha}}}
\end{aligned} \tag{C.1}$$

where r_s is the scale radius and ρ_s is the scale density of the profile. For the DM profile presented in Pullen et al. [97], $r_o = 8.5$ kpc is the distance from the Sun to the GC.

Some other profiles can be obtained as the combination of two or more of the profiles above. A characteristic example is the HYB profile, which is a combination of SIS and NFW (hereafter hybrid profile).

JCAP08(2023)073

Profile	α	β	γ	δ	r_s kpc	ρ_s GeV/cm^3	Reference
NFW (VLII)	1	3	1	0	21	$0.307 \cdot 10^0$	Pieri et al. [92]
NFW	1	3	1	0	21	$0.307 \cdot 10^0$	Abdallah et al. [93]
NFW	1	3	1	0	$16.1^{17}_{-7.8}$	$0.531 \cdot 10^0$	Nesti and Salucci [98], Aartsen et al. [99]
NFW	1	3	1	0	20	$0.259 \cdot 10^0$	Abbasi et al. [100]
NFW	1	3	1	—	25	$0.3 \cdot 10^0$	Pullen et al. [97]
NFW	1	3	1	0	21.7	$0.303 \cdot 10^0$	ANTARES collaboration [101]
NFW-c	—	—	1.2	—	21.7	$0.207 \cdot 10^0$	ANTARES collaboration [101]
NFW-c	—	—	1.3	—	20	$0.271 \cdot 10^0$	Agrawal et al. [102]
NFW	1	3	1	0	20	$0.345 \cdot 10^0$	Karwin et al. [103]
NFW-c	—	—	1.2	—	20	$0.271 \cdot 10^0$	Karwin et al. [103]
NFW	1	3	1	0	20	$0.345 \cdot 10^0$	Daylan et al. [104]
NFW-c	—	—	1.2	—	20	$0.271 \cdot 10^0$	Daylan et al. [104]
NFW-c	—	—	1.4	0	20	$0.213 \cdot 10^0$	Daylan et al. [104]
NFW	1	3	1	0	23.8	$0.14 \cdot 10^0$	Gómez-Vargas et al. [105]
NFW-c	0.76	3.3	1.37	0	18.5	$0.23 \cdot 10^0$	Gómez-Vargas et al. [105]
Einasto (Aq)	0.17	—	—	—	20	$0.106 \cdot 10^0$	Pieri et al. [92]
Einasto	0.17	—	—	—	20	$0.079 \cdot 10^0$	Abdallah et al. [93]
Einasto	0.17	—	—	—	28.4	$0.033 \cdot 10^0$	Abdallah et al. [93]
Einasto	0.16	—	—	—	20	$0.0606 \cdot 10^0$	Abbasi et al. [100]
Einasto	0.17	—	—	—	21.7	$0.0707 \cdot 10^0$	ANTARES collaboration [101]
Einasto	0.17	—	—	—	20	$0.081 \cdot 10^0$	Daylan et al. [104]
Einasto*	0.22	—	—	—	19.7	$0.08 \cdot 10^0$	Gómez-Vargas et al. [105]
Burkert	2	3	1	1	$9.26^{5.6}_{-4.2}$	$1.568 \cdot 10^0$	Nesti and Salucci [98], Aartsen et al. [99]
Burkert	2	3	1	1	2	$37.76 \cdot 10^0$	Gómez-Vargas et al. [105]
Moore	1.5	3	1.5	0	28	$0.0527 \cdot 10^0$	Abbasi et al. [100]
Kravtsov	2	3	0.4	0	10	$0.703 \cdot 10^0$	Abbasi et al. [100]
Isothermal	2	2	0	—	4	$0.3 \cdot 10^0$	Pullen et al. [97]
Isothermal	2	2	0	0	4	$2.206 \cdot 10^0$	ANTARES collaboration [101]
Ka	2	3	0.2	—	11	$0.4 \cdot 10^0$	Pullen et al. [97]
Kb	2	3	0.4	—	12	$0.4 \cdot 10^0$	Pullen et al. [97]

Table 5. Distribution profiles in GC.

In table 5 all Einasto profiles use $\alpha = 0.17$ except for Einasto* which uses $\alpha = 0.22$. The majority of the remaining profiles are described by the generalized profile proposed by Hernquist [94], Dehnen [95] and Zhao [96] or the Pullen parametrization profiles (see eq. (C.1)).

In the case of the Burkert profile in Gómez-Vargas et al. [105], we choose $r_s = 2\,\mathrm{kpc}$ based on Hooper et al. [106], Guedes et al. [107], Ackermann et al. [108] and using, for the normalization, the local density suggested in Catena and Ullio [109]. This value appears to be compatible with the observational constraints from Iocco et al. [110]. However, a more recent work favors a much larger scale radius and a slightly different normalization for Burkert profiles (see Nesti and Salucci [98] and Aartsen et al. [99]).

In figure 13 we present the obtained profiles of the DM density distribution reported in table 5 and the corresponding J-factors. Figure 14 shows the relative contribution of the MW

JCAP08(2023)073

JCAP08(2023)073

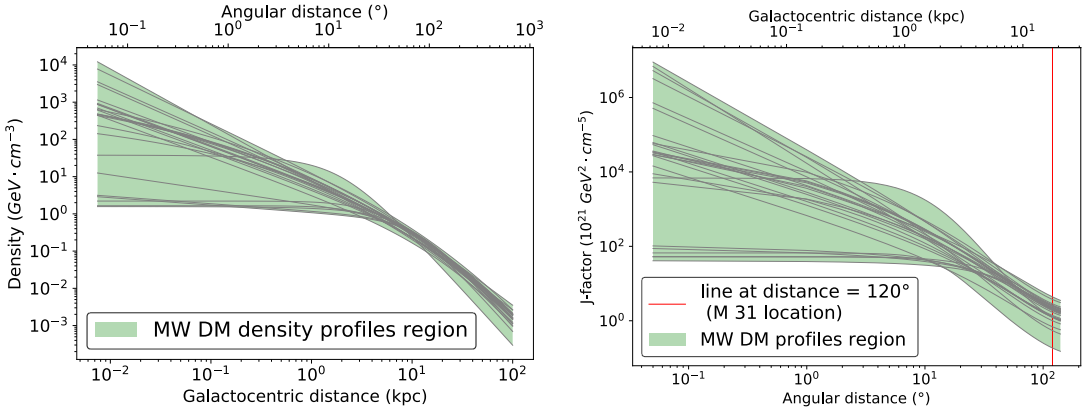

Figure 13. Left panel: DM density profiles (see table 5) in our galaxy as a function of distance from the GC, in kpc. Right panel: J-factor plotted as a function of angular distance in degrees from the GC, for all the different profiles (see table 5). In the plot there is a vertical line, in red, which corresponds to the angular distance of M31 from the GC.

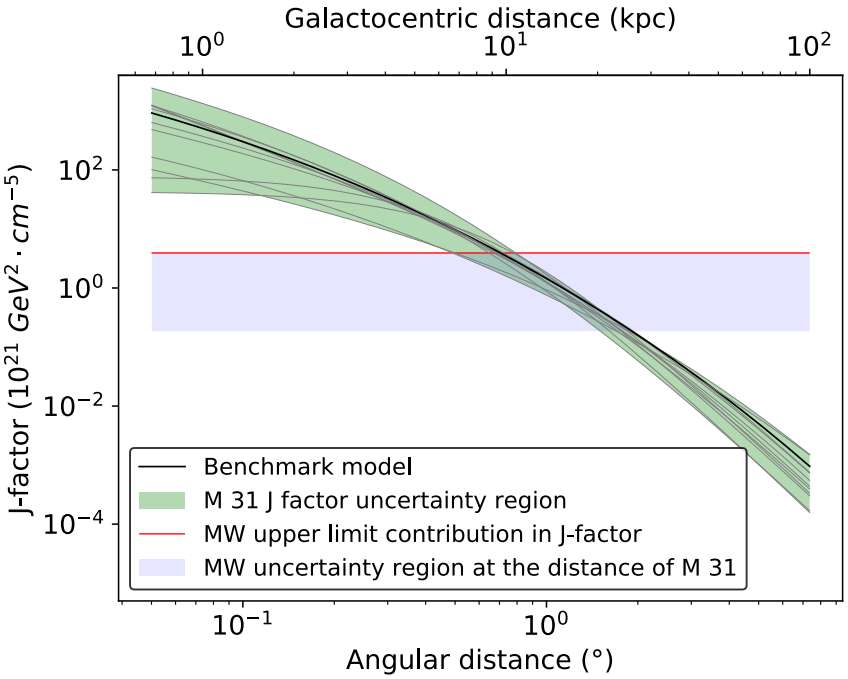

Figure 14. J-factors for M31 and the GC. The green band is the J-factor uncertainty for M31 from this work. The solid black lines correspond to the twelve different DM profiles that we collected from the literature. The benchmark model is highlighted with the bold black solid line. The blue band is the J-factor uncertainty region as seen from the GC at the distance of M31 galaxy. The red solid line stands for the upper limits contribution of the MW to the J-factor values of M31.

DM halo in comparison to the signal from M31. The signal from the M31 center can be at least two orders of magnitude exceeding the MW DM halo contribution. The M31 and MW DM halo signals become equal only at about 1° away from M31 center. Being sub-dominant, the contribution from MW DM halo was neglected in this paper.

D Effect of the DM substructures to the upper limits results

As an additional step, we cross-checked the used DM signal templates with ones produced by `CLUMPY` software.[7] The utilisation of this software allowed us also to estimate the contribution from the DM substructures present in M31/M33 DM halo.

Given that the total DM density distribution is the sum of a smooth contribution and a distribution of sub-halos, the latter must be interpreted as scaled-down versions of the host halo. The presence of such substructures can significantly enhance the expected signal, and therefore their implementation should be properly treated.

For the modeling of the substructures, we selected a substructure spatial distribution $dN_{\rm sub}/dV$ that follows the smooth parent halo profile. A mass density distribution described by the function $dN_{\rm sub}/dM \propto M^{-\alpha_M}$, with $\alpha_M = 1.9$ and 10% mass fraction in substructures, was considered as suggested by numerical simulations of Milky-like halos (Springel et al. [111], Madau et al. [112]). The threshold mass for the smallest and the most massive subhalos are fixed to $10^{-6}\,{\rm M}\odot$ and $10^{-2}\,{\rm M_{tot}}$ respectively, when $\rm M_{tot}$ is the total mass of the corresponding galaxy, utilizing the subclumps mass-concentration relationship reported in Sánchez-Conde and Prada [113]. However, there are several works that suggest that the concentration of subhalos is greater in comparison to that of field halos of the same mass, which indicates a larger substructure boosting factor (Ghigna et al. [114], Bullock et al. [115], Diemand et al. [116], Diemand et al. [117], Bartels and Ando [118], Zavala and Afshordi [119]). It is noteworthy, that Moliné et al. [120] attempted to refine the substructure boost model provided by Sánchez-Conde and Prada [113] by utilizing data of N-body `Via Lactea` and `Elvis` Milky Way size-simulations. They obtained boost values of a factor of 2–3 greater in comparison to previous reports. However, one has also to consider the suppression level on the boosting factor when considering unavoidable tidal stripping effects — which appears to suppress significantly the boost factor in cases of dSphs subhalos (only a few tens of percent gain on the total boost factor is obtained in such cases) whereas it introduces an intermediate suppressing of the total boost factor for field halos such as M31 (of the level of 20–30%). In this case, we would expect moderately more constraining upper limits results in comparison to those obtained in this work by adopting the more conservative benchmark boost factor introduced in Sánchez-Conde and Prada [113]. A more complete overview of the impact of the substructure boosting on the upper limit results on the DM annihilation cross-section from extragalactic halo observations is given in Ando et al. [121] where the authors acknowledge that numerical simulations provide the most accurate assessment in resolved regimes, however, they pinpoint the dangers of the unavoidable extrapolation of the substructure properties which introduces large uncertainties to the heavily enhanced obtained boost factor, and thus such results should be treated with caution. Such a high uncertainty on the obtained boosting factor becomes evident when nearly every single individual work reports on a different derived boosting factor, ranging from 2 to values greater than 100 for galaxy-size halos. As a complementary approach, they provide great insight into semi-analytic modelings, such as Press-Schechter formalism and tidal-stripping modeling, which in

[7] https://clumpy.gitlab.io/CLUMPY/.

JCAP08(2023)073

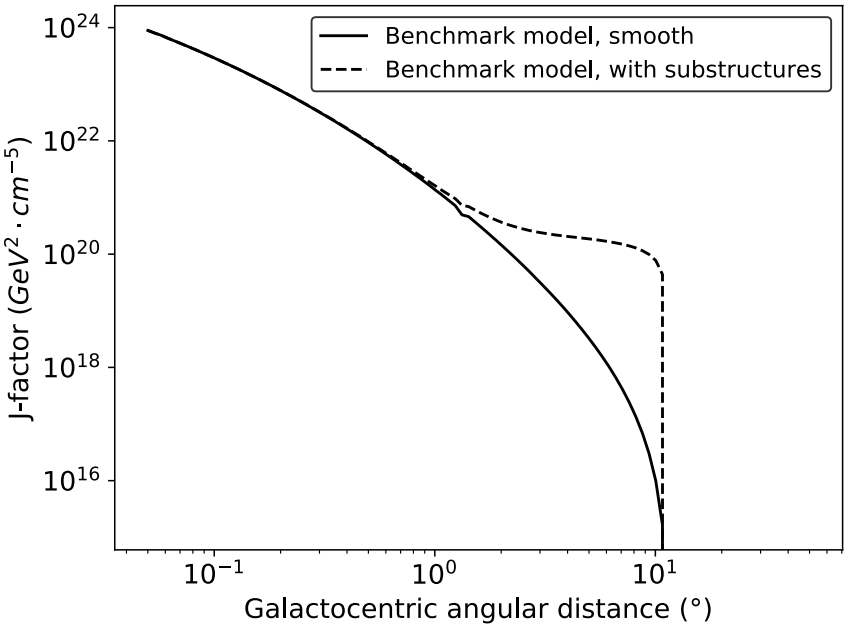

Figure 15. J-factor as a function of the angular distance for the benchmark profile of M31 galaxy. The black solid line corresponds to the J-factor values without including substructures. The black dashed line corresponds to the J-factor values when including substructures.

contrast to N-body simulations appear to be more modest resulting in an order of unity for galaxy-size halos. One could even consider a much greater enhancement on the substructure boosting when considering that prompt DM cusps survived tidal stripping and thus are present today, as introduced in Delos and White [122]. To summarize, computing the exact boost factor that DM subhalos introduce; comes as a great challenge, and it is still remaining highly uncertain; thus in this work, we adopt the most conservative approach introduced in Sánchez-Conde and Prada [113] aiming at not overestimating our upper limits result.

Figure 15 shows the radial dependency of the J-factor, as obtained using `CLUMPY` v3.0.1 code (Charbonnier et al. [77], Bonnivard et al. [123], Hütten et al. [78]), for the benchmark profile of M31 that was considered in this work, verifying the significant contribution of the sub-halos at the outskirts of the parent halo. The above behavior has been analytically discussed in Han et al. [124], and it is attributed to the decreasement of the fraction of the mass bound of the substructures towards the center of the galaxy due to tidal stripping.

In figure 16 we present the more constraining results that we obtain in the presence of DM substructures in comparison to the smooth profile that we considered as benchmark profile for M31 in this work. In addition, this figure shows that when considering a larger DM source template, where the subhalos contribution is stronger, the upper limits results become even more constraining in comparison to a smaller DM source template.

The upper limit results when including substructures should not be considered final certain results in any case, since the nature of the DM sub-halos is still unrevealed. When more information and details for the actual nature of those substructures (i.e. mass, spatial distribution as well as the description of the DM distribution within each halo; changing each of those parameters results in different J-factor values) will be available, then more accurate analysis will be conducted.

JCAP08(2023)073

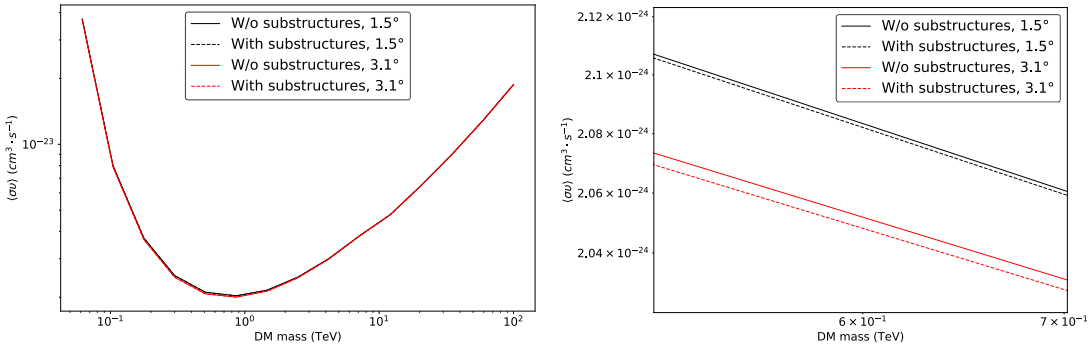

Figure 16. M31 upper limits (2σ) comparison for the benchmark model, with and without substructures. Left plot: the solid lines (both black and red) correspond to the benchmark DM profile without the presence of substructures, when considering 1.5° and 3.1° spatial size of the DM source template respectively. The dashed lines (both the black and the red one) correspond to the benchmark DM profile in the presence of substructures, when considering 1.5° and 3.1° spatial size of the DM source template respectively. Right plot: left plot zoomed in for higher accuracy.

References

[1] G. Bertone, D. Hooper and J. Silk, *Particle dark matter: Evidence, candidates and constraints*, *Phys. Rept.* **405** (2005) 279 [hep-ph/0404175] [INSPIRE].

[2] Particle Data collaboration, *Review of Particle Physics*, *Prog. Theor. Exp. Phys.* **2020** (2020) 083C01 [INSPIRE].

[3] Planck collaboration, *Planck 2018 results. Part VII. Isotropy and Statistics of the CMB*, *Astron. Astrophys.* **641** (2020) A7 [arXiv:1906.02552] [INSPIRE].

[4] P. Villanueva-Domingo, O. Mena and S. Palomares-Ruiz, *A brief review on primordial black holes as dark matter*, *Front. Astron. Space Sci.* **8** (2021) 87 [arXiv:2103.12087] [INSPIRE].

[5] B.W. Lee and S. Weinberg, *Cosmological Lower Bound on Heavy Neutrino Masses*, *Phys. Rev. Lett.* **39** (1977) 165 [INSPIRE].

[6] J.L. Feng and J. Kumar, *The WIMPless Miracle: Dark-Matter Particles without Weak-Scale Masses or Weak Interactions*, *Phys. Rev. Lett.* **101** (2008) 231301 [arXiv:0803.4196] [INSPIRE].

[7] S. Profumo, *Astrophysical Probes of Dark Matter*, in proceedings of the *Theoretical Advanced Study Institute in Elementary Particle Physics: Searching for New Physics at Small and Large Scales*, Boulder, CO, U.S.A., 4–29 June 2012, pp. 143–189 [DOI:10.1142/9789814525220_0004] [arXiv:1301.0952] [INSPIRE].

[8] H. Baer, K.-Y. Choi, J.E. Kim and L. Roszkowski, *Dark matter production in the early Universe: beyond the thermal WIMP paradigm*, *Phys. Rept.* **555** (2015) 1 [arXiv:1407.0017] [INSPIRE].

[9] M. Cirelli et al., *PPPC 4 DM ID: A Poor Particle Physicist Cookbook for Dark Matter Indirect Detection*, *JCAP* **03** (2011) 051 [arXiv:1012.4515] [INSPIRE].

[10] H.E.S.S. collaboration, *H.E.S.S. Limits on Linelike Dark Matter Signatures in the* 100 *GeV to* 2 *TeV Energy Range Close to the Galactic Center*, *Phys. Rev. Lett.* **117** (2016) 151302 [arXiv:1609.08091] [INSPIRE].

[11] L. Rinchiuso and E. Moulin, *Dark matter searches toward the Galactic Centre halo with H.E.S.S.*, in proceedings of the *52nd Rencontres de Moriond on Very High Energy Phenomena in the Universe*, La Thuile, Italy, 18–25 March 2017, pp. 255–262 [arXiv:1711.08634] [INSPIRE].

JCAP08(2023)073

[12] L. Rinchiuso, E. Moulin, A. Viana, C. Van Eldik and J. Veh, *Dark matter gamma-ray line searches toward the Galactic Center halo with H.E.S.S. Part I*, *PoS* **ICRC2017** (2018) 893 [arXiv:1708.08358] [INSPIRE].

[13] L. Rinchiuso, *Latest results on dark matter searches with H.E.S.S.*, in proceedings of the *7th Roma International Conference on Astroparticle Physics (RICAP18)*, Rome, Italy, 4–7 September 2018, *EPJ Web Conf.* **209** (2019) 01023 [arXiv:1901.05299] [INSPIRE].

[14] E. Aliu et al., *Upper limits on the VHE gamma-ray emission from the Willman 1 satellite galaxy with the MAGIC Telescope*, *Astrophys. J.* **697** (2009) 1299 [arXiv:0810.3561] [INSPIRE].

[15] V.A. Acciari et al., *VERITAS Search for VHE Gamma-ray Emission from Dwarf Spheroidal Galaxies*, *Astrophys. J.* **720** (2010) 1174 [arXiv:1006.5955] [INSPIRE].

[16] MAGIC collaboration, *Limits to Dark Matter Annihilation Cross-Section from a Combined Analysis of MAGIC and Fermi-LAT Observations of Dwarf Satellite Galaxies*, *JCAP* **02** (2016) 039 [arXiv:1601.06590] [INSPIRE].

[17] B. Zitzer, *The VERITAS Dark Matter Program*, in proceedings of the *35th International Cosmic Ray Conference (ICRC 2017)*, Busan, Republic of Korea, 12–20 July 2017, *PoS* **ICRC2017** (2018) 904 [arXiv:1708.07447] [INSPIRE].

[18] T. Yapici and A.J. Smith, *Dark Matter Searches with HAWC*, *PoS* **ICRC2017** (2018) 891 [arXiv:1708.07461] [INSPIRE].

[19] H.E.S.S. collaboration, *Search for dark matter annihilation in the Wolf-Lundmark-Melotte dwarf irregular galaxy with H.E.S.S.*, *Phys. Rev. D* **103** (2021) 102002 [arXiv:2105.04325] [INSPIRE].

[20] L. Oakes, *Combined Dark Matter searches towards dwarf spheroidal galaxies with Fermi-LAT, HAWC, H.E.S.S., MAGIC and VERITAS*, in proceedings of the *36th International Cosmic Ray Conference (ICRC 2019)*, Madison, WI, U.S.A., 24 July-1 August 2019, *PoS* **ICRC2019** (2021) 012 [arXiv:1909.06310] [INSPIRE].

[21] A. Abramowski et al., *Search for Dark Matter Annihilation Signals from the Fornax Galaxy Cluster with H.E.S.S.*, *Astrophys. J.* **750** (2012) 123 [*Erratum ibid.* **783** (2014) 63] [arXiv:1202.5494] [INSPIRE].

[22] D. Glawion et al., *Unidentified Fermi Objects in the view of H.E.S.S. — Possible Dark Matter Clumps*, *PoS* **ICRC2019** (2021) 518 [arXiv:1909.01072] [INSPIRE].

[23] H.E.S.S. collaboration, *Search for dark matter annihilation signals from unidentified Fermi-LAT objects with H.E.S.S.*, *Astrophys. J.* **918** (2021) 17 [arXiv:2106.00551] [INSPIRE].

[24] M. Doro, M.A. Sánchez-Conde and M. Hütten, *Fundamental Physics Searches with IACTs*, arXiv:2111.01198 [INSPIRE].

[25] P. Bernardini, *ARGO-YBJ experiment in Tibet*, *J. Phys. Conf. Ser.* **120** (2008) 062022 [INSPIRE].

[26] M.A. Mostafá, *The High-Altitude Water Cherenkov Observatory*, *Braz. J. Phys.* **44** (2014) 571 [arXiv:1310.7237] [INSPIRE].

[27] LHAASO collaboration, *The Large High Altitude Air Shower Observatory (LHAASO) Science Book (2021 Edition)*, *Chin. Phys. C* **46** (2022) 035001 [arXiv:1905.02773] [INSPIRE].

[28] A.U. Abeysekara et al., *A Search for Dark Matter in the Galactic Halo with HAWC*, *JCAP* **02** (2018) 049 [arXiv:1710.10288] [INSPIRE].

[29] A. Albert et al., *Dark Matter Limits From Dwarf Spheroidal Galaxies with The HAWC Gamma-Ray Observatory*, *Astrophys. J.* **853** (2018) 154 [arXiv:1706.01277] [INSPIRE].

[30] J. Coronado-Blázquez and M.A. Sánchez-Conde, *Constraints to dark matter annihilation from high-latitude HAWC unidentified sources*, *Galaxies* **8** (2020) 5 [arXiv:2001.02536] [INSPIRE].

JCAP08(2023)073

[31] A. Albert et al., *Search for Dark Matter Gamma-ray Emission from the Andromeda Galaxy with the High-Altitude Water Cherenkov Observatory*, *JCAP* **06** (2018) 043 [*Erratum ibid.* **04** (2019) E01] [arXiv:1804.00628] [INSPIRE].

[32] W.B. Atwood et al., *The Large Area Telescope on the Fermi Gamma-ray Space Telescope Mission*, *Astrophys. J.* **697** (2009) 1071 [arXiv:0902.1089] [INSPIRE].

[33] S. Hoof, A. Geringer-Sameth and R. Trotta, *A Global Analysis of Dark Matter Signals from 27 Dwarf Spheroidal Galaxies using 11 Years of Fermi-LAT Observations*, *JCAP* **02** (2020) 012 [arXiv:1812.06986] [INSPIRE].

[34] A. Drlica-Wagner et al., *Search for Gamma-Ray Emission from DES Dwarf Spheroidal Galaxy Candidates with Fermi-LAT Data*, *Astrophys. J. Lett.* **809** (2015) L4 [arXiv:1503.02632] [INSPIRE].

[35] M.G. Baring, T. Ghosh, F.S. Queiroz and K. Sinha, *New Limits on the Dark Matter Lifetime from Dwarf Spheroidal Galaxies using Fermi-LAT*, *Phys. Rev. D* **93** (2016) 103009 [arXiv:1510.00389] [INSPIRE].

[36] J. Aleksić et al., *MAGIC Gamma-Ray Telescope Observation of the Perseus Cluster of Galaxies: Implications for Cosmic Rays, Dark Matter and NGC 1275*, *Astrophys. J.* **710** (2010) 634 [arXiv:0909.3267] [INSPIRE].

[37] T. Arlen et al., *Constraints on Cosmic Rays, Magnetic Fields, and Dark Matter from Gamma-Ray Observations of the Coma Cluster of Galaxies with VERITAS and Fermi*, *Astrophys. J.* **757** (2012) 123 [arXiv:1208.0676] [INSPIRE].

[38] M. Ackermann et al., *Constraints on Dark Matter Annihilation in Clusters of Galaxies with the Fermi Large Area Telescope*, *JCAP* **05** (2010) 025 [arXiv:1002.2239] [INSPIRE].

[39] X. Huang, G. Vertongen and C. Weniger, *Probing Dark Matter Decay and Annihilation with Fermi LAT Observations of Nearby Galaxy Clusters*, *JCAP* **01** (2012) 042 [arXiv:1110.1529] [INSPIRE].

[40] C. Thorpe-Morgan, D. Malyshev, C.-A. Stegen, A. Santangelo and J. Jochum, *Annihilating dark matter search with* 12 *yr of Fermi LAT data in nearby galaxy clusters*, *Mon. Not. Roy. Astron. Soc.* **502** (2021) 4039 [arXiv:2010.11006] [INSPIRE].

[41] M. Ackermann et al., *The Fermi Galactic Center GeV Excess and Implications for Dark Matter*, *Astrophys. J.* **840** (2017) 43 [arXiv:1704.03910] [INSPIRE].

[42] K.N. Abazajian, S. Horiuchi, M. Kaplinghat, R.E. Keeley and O. Macias, *Strong constraints on thermal relic dark matter from Fermi-LAT observations of the Galactic Center*, *Phys. Rev. D* **102** (2020) 043012 [arXiv:2003.10416] [INSPIRE].

[43] Z. Li, X. Huang, Q. Yuan and Y. Xu, *Constraints on the dark matter annihilation from Fermi-LAT observation of M31*, *JCAP* **12** (2016) 028 [arXiv:1312.7609] [INSPIRE].

[44] M. Di Mauro, X. Hou, C. Eckner, G. Zaharijas and E. Charles, *Search for γ-ray emission from dark matter particle interactions from Andromeda and Triangulum Galaxies with the Fermi Large Area Telescope*, *Phys. Rev. D* **99** (2019) 123027 [arXiv:1904.10977] [INSPIRE].

[45] D. Nieto et al., *The search for galactic dark matter clump candidates with Fermi and MAGIC*, arXiv:1109.5935 [INSPIRE].

[46] D. Nieto, *Hunting for dark matter subhalos among the Fermi-LAT sources with VERITAS*, *PoS* **ICRC2015** (2016) 1216 [arXiv:1509.00085] [INSPIRE].

[47] J. Coronado-Blázquez et al., *Unidentified Gamma-ray Sources as Targets for Indirect Dark Matter Detection with the Fermi-Large Area Telescope*, *JCAP* **07** (2019) 020 [arXiv:1906.11896] [INSPIRE].

[48] J. Coronado-Blázquez et al., *Spectral and spatial analysis of the dark matter subhalo candidates among Fermi Large Area Telescope unidentified sources*, *JCAP* **11** (2019) 045 [arXiv:1910.14429] [INSPIRE].

[49] T. Linden, *Robust method for treating astrophysical mismodeling in dark matter annihilation searches of dwarf spheroidal galaxies*, *Phys. Rev. D* **101** (2020) 043017 [arXiv:1905.11992] [INSPIRE].

[50] H.E.S.S. collaboration, *Search for dark matter annihilations towards the inner Galactic halo from 10 years of observations with H.E.S.S.*, *Phys. Rev. Lett.* **117** (2016) 111301 [arXiv:1607.08142] [INSPIRE].

[51] D.-Z. He, X.-J. Bi, S.-J. Lin, P.-F. Yin and X. Zhang, *Prospect for dark matter annihilation signatures from gamma-ray observation of dwarf galaxies by LHAASO*, *Phys. Rev. D* **100** (2019) 083003 [arXiv:1903.11910] [INSPIRE].

[52] A. Neronov and D. Semikoz, *LHAASO telescope sensitivity to diffuse gamma-ray signals from the Galaxy*, *Phys. Rev. D* **102** (2020) 043025 [arXiv:2001.11881] [INSPIRE].

[53] CTA collaboration, *Cherenkov Telescope Array: The Next Generation Gamma-ray Observatory*, *PoS* **ICRC2017** (2018) 1071 [arXiv:1709.05434] [INSPIRE].

[54] CTA Consortium, *Science with the Cherenkov Telescope Array*, World Scientific (2018) [arXiv:1709.07997] [DOI:10.1142/10986] [INSPIRE].

[55] M. Wood et al., *A Search for Dark Matter Annihilation with the Whipple* 10 *m Telescope*, *Astrophys. J.* **678** (2008) 594 [arXiv:0801.1708] [INSPIRE].

[56] L. Bergström, P. Ullio and J.H. Buckley, *Observability of gamma-rays from dark matter neutralino annihilations in the Milky Way halo*, *Astropart. Phys.* **9** (1998) 137 [astro-ph/9712318] [INSPIRE].

[57] P. Ciafaloni, M. Cirelli, D. Comelli, A. De Simone, A. Riotto and A. Urbano, *On the Importance of Electroweak Corrections for Majorana Dark Matter Indirect Detection*, *JCAP* **06** (2011) 018 [arXiv:1104.2996] [INSPIRE].

[58] C.W. Bauer, N.L. Rodd and B.R. Webber, *Dark matter spectra from the electroweak to the Planck scale*, *JHEP* **06** (2021) 121 [arXiv:2007.15001] [INSPIRE].

[59] M. Cirelli et al., *Erratum: PPPC 4 DM ID: A Poor Particle Physicist Cookbook for Dark Matter Indirect Detection*, *JCAP* **10** (2012) E01 [INSPIRE].

[60] A. Viana, H. Schoorlemmer, A. Albert, V. de Souza, J.P. Harding and J. Hinton, *Searching for Dark Matter in the Galactic Halo with a Wide Field of View TeV Gamma-ray Observatory in the Southern Hemisphere*, *JCAP* **12** (2019) 061 [arXiv:1906.03353] [INSPIRE].

[61] I.D. Karachentsev, V.E. Karachentseva, W.K. Huchtmeier and D.I. Makarov, *A Catalog of Neighboring Galaxies*, *Astron. J.* **127** (2004) 2031 [INSPIRE].

[62] W.L. Freedman, C.D. Wilson and B.F. Madore, *New Cepheid distances to nearby galaxies based on BVRI CCD photometry. Part II. The local group galaxy M33*, *Astrophys. J.* **372** (1991) 455.

[63] I.R. King, *The Structure of star clusters. Part 3. Some simple dynamical models*, *Astron. J.* **71** (1966) 64 [INSPIRE].

[64] J.F. Navarro, C.S. Frenk and S.D.M. White, *A Universal density profile from hierarchical clustering*, *Astrophys. J.* **490** (1997) 493 [astro-ph/9611107] [INSPIRE].

[65] J. Einasto, *On the Construction of a Composite Model for the Galaxy and on the Determination of the System of Galactic Parameters*, *Trudy Astrofiz. Inst. Alma-Ata* **5** (1965) 87.

[66] A. Burkert, *The Structure of dark matter halos in dwarf galaxies*, *Astrophys. J. Lett.* **447** (1995) L25 [astro-ph/9504041] [INSPIRE].

[67] M. Ackermann et al., *Observations of M31 and M33 with the Fermi Large Area Telescope: A Galactic Center Excess in Andromeda?*, *Astrophys. J.* **836** (2017) 208 [arXiv:1702.08602] [INSPIRE].

JCAP08(2023)073

[68] C. Eckner et al., *Millisecond pulsar origin of the Galactic center excess and extended gamma-ray emission from Andromeda — a closer look*, *Astrophys. J.* **862** (2018) 79 [arXiv:1711.05127] [INSPIRE].

[69] C. Karwin, S. Murgia, S. Campbell and I. Moskalenko, *Fermi-LAT Observations of γ-Ray Emission Towards the Outer Halo of M31*, in proceedings of the *36th International Cosmic Ray Conference (ICRC 2019)*, Madison, WI, U.S.A., 24 July-1 August 2019, *PoS* **ICRC2019** (2021) 570 [arXiv:1903.10533] [INSPIRE].

[70] C. Armand and F. Calore, *Gamma-ray image reconstruction of the Andromeda galaxy*, *Phys. Rev. D* **103** (2021) 083023 [arXiv:2102.06447] [INSPIRE].

[71] A.A. Abdo et al., *Constraints on Cosmological Dark Matter Annihilation from the Fermi-LAT Isotropic Diffuse Gamma-Ray Measurement*, *JCAP* **04** (2010) 014 [arXiv:1002.4415] [INSPIRE].

[72] S.-Q. Xi, H.-M. Zhang, R.-Y. Liu and X.-Y. Wang, *GeV γ-Ray Emission from M33 and Arp 299*, *Astrophys. J.* **901** (2020) 158 [arXiv:2003.07830] [INSPIRE].

[73] M. Ajello, M. Di Mauro, V.S. Paliya and S. Garrappa, *The γ-Ray Emission of Star-forming Galaxies*, *Astrophys. J.* **894** (2020) 88 [arXiv:2003.05493] [INSPIRE].

[74] M. Ajello et al., *3FHL: The Third Catalog of Hard Fermi-LAT Sources*, *Astrophys. J. Suppl.* **232** (2017) 18 [arXiv:1702.00664] [INSPIRE].

[75] S. Abdollahi et al., *Fermi Large Area Telescope Fourth Source Catalog*, *Astrophys. J. Suppl.* **247** (2020) 33 [arXiv:1902.10045] [INSPIRE].

[76] A. Acharyya et al., *Sensitivity of the Cherenkov Telescope Array to a dark matter signal from the Galactic centre*, *JCAP* **01** (2021) 057 [arXiv:2007.16129] [INSPIRE].

[77] A. Charbonnier, C. Combet and D. Maurin, *CLUMPY: a code for gamma-ray signals from dark matter structures*, *Comput. Phys. Commun.* **183** (2012) 656 [arXiv:1201.4728] [INSPIRE].

[78] M. Hütten, C. Combet and D. Maurin, *CLUMPY v3: γ-ray and ν signals from dark matter at all scales*, *Comput. Phys. Commun.* **235** (2019) 336 [arXiv:1806.08639] [INSPIRE].

[79] F. Aharonian et al., *Observations of the Crab Nebula with H.E.S.S.*, *Astron. Astrophys.* **457** (2006) 899 [astro-ph/0607333] [INSPIRE].

[80] H. Silverwood, C. Weniger, P. Scott and G. Bertone, *A realistic assessment of the CTA sensitivity to dark matter annihilation*, *JCAP* **03** (2015) 055 [arXiv:1408.4131] [INSPIRE].

[81] VERITAS collaboration, *Dark Matter Constraints from a Joint Analysis of Dwarf Spheroidal Galaxy Observations with VERITAS*, *Phys. Rev. D* **95** (2017) 082001 [arXiv:1703.04937] [INSPIRE].

[82] J.J. Geehan, M.A. Fardal, A. Babul and P. Guhathakurta, *Investigating the Andromeda Stream. Part 1. Simple analytic bulge-disk-halo model for M31*, *Mon. Not. Roy. Astron. Soc.* **366** (2006) 996 [astro-ph/0501240] [INSPIRE].

[83] E. Tempel, A. Tamm and P. Tenjes, *Visible and dark matter in M31. Part 2. A dynamical model and dark matter density distribution*, arXiv:0707.4374 [INSPIRE].

[84] Y. Sofue, *Dark halos of M31 and the Milky Way*, *Publ. Astron. Soc. Jap.* **67** (2015) 75 [arXiv:1504.05368] [INSPIRE].

[85] A. Tamm, E. Tempel, P. Tenjes, O. Tihhonova and T. Tuvikene, *Stellar mass map and dark matter distribution in M31*, *Astron. Astrophys.* **546** (2012) A4 [arXiv:1208.5712] [INSPIRE].

[86] K. Hayashi and M. Chiba, *The prolate dark matter halo of the Andromeda galaxy*, *Astrophys. J.* **789** (2014) 62 [arXiv:1405.4606] [INSPIRE].

[87] L.M. Widrow and J. Dubinski, *Equilibrium disk-bulge-halo models for the Milky Way and Andromeda galaxies*, *Astrophys. J.* **631** (2005) 838 [astro-ph/0506177] [INSPIRE].

[88] T. Kirihara, Y. Miki and M. Mori, *Puzzling Outer-Density Profile of the Dark Matter Halo in the Andromeda Galaxy*, *Publ. Astron. Soc. Jap.* **66** (2014) L10 [arXiv:1408.4920] [INSPIRE].

[89] E. Borriello et al., *Searching for Dark Matter in Messier 33*, *Astrophys. J. Lett.* **709** (2010) L32 [arXiv:0906.2013] [INSPIRE].

[90] E. López Fune, P. Salucci and E. Corbelli, *Radial dependence of the dark matter distribution in M33*, *Mon. Not. Roy. Astron. Soc.* **468** (2017) 147 [arXiv:1611.01409] [INSPIRE].

[91] M.S. Seigar, *The dark matter halo density profile, spiral arm morphology and black hole mass of M33*, *ISRN Astron. Astrophys.* **2011** (2011) 725697 [arXiv:1103.3200] [INSPIRE].

[92] L. Pieri, J. Lavalle, G. Bertone and E. Branchini, *Implications of High-Resolution Simulations on Indirect Dark Matter Searches*, *Phys. Rev. D* **83** (2011) 023518 [arXiv:0908.0195] [INSPIRE].

[93] H.E.S.S. collaboration, *Search for γ-Ray Line Signals from Dark Matter Annihilations in the Inner Galactic Halo from 10 Years of Observations with H.E.S.S.*, *Phys. Rev. Lett.* **120** (2018) 201101 [arXiv:1805.05741] [INSPIRE].

[94] L. Hernquist, *An Analytical Model for Spherical Galaxies and Bulges*, *Astrophys. J.* **356** (1990) 359 [INSPIRE].

[95] W. Dehnen, *A Family of Potential-Density Pairs for Spherical Galaxies and Bulges*, *Mon. Not. Roy. Astron. Soc.* **265** (1993) 250 [INSPIRE].

[96] H.S. Zhao, *Analytical models for galactic nuclei*, *Mon. Not. Roy. Astron. Soc.* **278** (1996) 488 [astro-ph/9509122] [INSPIRE].

[97] A.R. Pullen, R.-R. Chary and M. Kamionkowski, *Search with EGRET for a Gamma Ray Line from the Galactic Center*, *Phys. Rev. D* **76** (2007) 063006 [*Erratum ibid.* **83** (2011) 029904] [astro-ph/0610295] [INSPIRE].

[98] F. Nesti and P. Salucci, *The Dark Matter halo of the Milky Way, AD 2013*, *JCAP* **07** (2013) 016 [arXiv:1304.5127] [INSPIRE].

[99] IceCube collaboration, *Search for Dark Matter Annihilation in the Galactic Center with IceCube-79*, *Eur. Phys. J. C* **75** (2015) 492 [arXiv:1505.07259] [INSPIRE].

[100] IceCube collaboration, *Search for dark matter from the Galactic halo with the IceCube Neutrino Telescope*, *Phys. Rev. D* **84** (2011) 022004 [arXiv:1101.3349] [INSPIRE].

[101] ANTARES collaboration, *Search of Dark Matter Annihilation in the Galactic Centre using the ANTARES Neutrino Telescope*, *JCAP* **10** (2015) 068 [arXiv:1505.04866] [INSPIRE].

[102] P. Agrawal, B. Batell, P.J. Fox and R. Harnik, *WIMPs at the Galactic Center*, *JCAP* **05** (2015) 011 [arXiv:1411.2592] [INSPIRE].

[103] C. Karwin, S. Murgia, T.M.P. Tait, T.A. Porter and P. Tanedo, *Dark Matter Interpretation of the Fermi-LAT Observation Toward the Galactic Center*, *Phys. Rev. D* **95** (2017) 103005 [arXiv:1612.05687] [INSPIRE].

[104] T. Daylan et al., *The characterization of the gamma-ray signal from the central Milky Way: A case for annihilating dark matter*, *Phys. Dark Univ.* **12** (2016) 1 [arXiv:1402.6703] [INSPIRE].

[105] G.A. Gómez-Vargas et al., *Constraints on WIMP annihilation for contracted dark matterin the inner Galaxy with the Fermi-LAT*, *JCAP* **10** (2013) 029 [arXiv:1308.3515] [INSPIRE].

[106] D. Hooper, C. Kelso and F.S. Queiroz, *Stringent and Robust Constraints on the Dark Matter Annihilation Cross Section From the Region of the Galactic Center*, *Astropart. Phys.* **46** (2013) 55 [arXiv:1209.3015] [INSPIRE].

[107] J. Guedes, S. Callegari, P. Madau and L. Mayer, *Forming Realistic Late-Type Spirals in a LCDM Universe: The Eris Simulation*, *Astrophys. J.* **742** (2011) 76 [arXiv:1103.6030] [INSPIRE].

[108] M. Ackermann et al., *Constraints on the Galactic Halo Dark Matter from Fermi-LAT Diffuse Measurements*, *Astrophys. J.* **761** (2012) 91 [arXiv:1205.6474] [INSPIRE].

JCAP08(2023)073

[109] R. Catena and P. Ullio, *A novel determination of the local dark matter density*, *JCAP* **08** (2010) 004 [arXiv:0907.0018] [INSPIRE].

[110] F. Iocco, M. Pato, G. Bertone and P. Jetzer, *Dark Matter distribution in the Milky Way: microlensing and dynamical constraints*, *JCAP* **11** (2011) 029 [arXiv:1107.5810] [INSPIRE].

[111] V. Springel et al., *The Aquarius Project: the subhalos of galactic halos*, *Mon. Not. Roy. Astron. Soc.* **391** (2008) 1685 [arXiv:0809.0898] [INSPIRE].

[112] P. Madau, J. Diemand and M. Kuhlen, *Dark matter subhalos and the dwarf satellites of the Milky Way*, *Astrophys. J.* **679** (2008) 1260 [arXiv:0802.2265] [INSPIRE].

[113] M.A. Sánchez-Conde and F. Prada, *The flattening of the concentration-mass relation towards low halo masses and its implications for the annihilation signal boost*, *Mon. Not. Roy. Astron. Soc.* **442** (2014) 2271 [arXiv:1312.1729] [INSPIRE].

[114] S. Ghigna, B. Moore, F. Governato, G. Lake, T. Quinn and J. Stadel, *Density profiles and substructure of dark matter halos. Converging results at ultra-high numerical resolution*, *Astrophys. J.* **544** (2000) 616 [astro-ph/9910166] [INSPIRE].

[115] J.S. Bullock et al., *Profiles of dark haloes. Evolution, scatter, and environment*, *Mon. Not. Roy. Astron. Soc.* **321** (2001) 559 [astro-ph/9908159] [INSPIRE].

[116] J. Diemand, M. Kuhlen and P. Madau, *Formation and evolution of galaxy dark matter halos and their substructure*, *Astrophys. J.* **667** (2007) 859 [astro-ph/0703337] [INSPIRE].

[117] J. Diemand et al., *Clumps and streams in the local dark matter distribution*, *Nature* **454** (2008) 735 [arXiv:0805.1244] [INSPIRE].

[118] R. Bartels and S. Ando, *Boosting the annihilation boost: Tidal effects on dark matter subhalos and consistent luminosity modeling*, *Phys. Rev. D* **92** (2015) 123508 [arXiv:1507.08656] [INSPIRE].

[119] J. Zavala and N. Afshordi, *Universal clustering of dark matter in phase space*, *Mon. Not. Roy. Astron. Soc.* **457** (2016) 986 [arXiv:1508.02713] [INSPIRE].

[120] Á. Moliné, M.A. Sánchez-Conde, S. Palomares-Ruiz and F. Prada, *Characterization of subhalo structural properties and implications for dark matter annihilation signals*, *Mon. Not. Roy. Astron. Soc.* **466** (2017) 4974 [arXiv:1603.04057] [INSPIRE].

[121] S. Ando, T. Ishiyama and N. Hiroshima, *Halo Substructure Boosts to the Signatures of Dark Matter Annihilation*, *Galaxies* **7** (2019) 68 [arXiv:1903.11427] [INSPIRE].

[122] M.S. Delos and S.D.M. White, *Prompt cusps and the dark matter annihilation signal*, arXiv:2209.11237 [INSPIRE].

[123] V. Bonnivard, M. Hütten, E. Nezri, A. Charbonnier, C. Combet and D. Maurin, *CLUMPY: Jeans analysis, γ-ray and ν fluxes from dark matter (sub-)structures*, *Comput. Phys. Commun.* **200** (2016) 336 [arXiv:1506.07628] [INSPIRE].

[124] J. Han, S. Cole, C.S. Frenk and Y. Jing, *A unified model for the spatial and mass distribution of subhaloes*, *Mon. Not. Roy. Astron. Soc.* **457** (2016) 1208 [arXiv:1509.02175] [INSPIRE].

4.2 M. Michailidis, C. Thorpe-Morgan, D. Malyshev, A. Santangelo, J. Jochum. Dark Matter Density Profiles (DM_ρcat): A Review. In: Astronomy & Astrophysics (A&A), to be submitted

Astronomy & Astrophysics manuscript no. output
June 10, 2024

Dark Matter Density Profiles (DM_ρcat): A Review

Miltiadis Michailidis [1⋆ ⋆⋆], Charles Thorpe-Morgan[1], Denys Malyshev [1], Andrea Santangelo[1], Josef Jochum[1]

[1] Institut für Astronomie und Astrophysik Tübingen, Universität Tübingen, Sand 1, D-72076 Tübingen, Germany

To be submitted

ABSTRACT

We present the most comprehensive catalog of Dark Matter (DM) density profiles to date, which we refer to as the Dark Matter Density (ρ) profiles catalog (DM_ρcat). The widespread evidence for dark matter, an all pervading unseen mass in the universe, is by now abundant and presents one of the greatest challenges to our understanding of cosmology. From measurements of the properties of dark matter dominated objects one is able to determine the distribution of dark matter in objects, an integral part of calculating the J/D-factor, for annihilating and decaying dark matter respectively, and in searching for indirect signals. In this paper, we collate and summarise the vast number of dark matter profiles for different categories of objects in literature. We summarise profiles for Dwarf Spheroidals (dSphs), Dwarf galaxies, Spiral galaxies, Lenticular galaxies, Elliptical galaxies, Galaxy Clusters, as well as display differing profiles for the Galactic center. In total we present differing profiles for a total of 1095 objects. In a companion paper, we will report on the results obtained by examining this vast pool of profiles and showcase the implications of the uncertainty of the actual DM density distribution in astrophysical objects. We will investigate the J/D-factors of these profiles as well as outline the correlation between several fitting parameters such as the Virial mass ($M_{\rm Virial}$), the concentration parameter (c), and the DM column density (S).

Key words. Dark Matter, Indirect detection, Annihilation, Decay (Individual object: dSphs, dwarf galaxies, spiral galaxies, lenticular galaxies, elliptical galaxies, galaxy groups, galaxy clusters, Galactic center) — review

Article VII

1. Introduction

Observations of numerous phenomena have, and continue to, confirm the presence of a universally pervading unseen mass within our universe (Zwicky 1933; Rubin 1983; Walsh et al. 1979; Smoot et al. 1992; Clowe et al. 2006; Bradač et al. 2008a; Ragozzine et al. 2012; Jee et al. 2016). This unseen mass that does not interact with particles of the standard model (therefore coined as dark matter (DM)) presents one of the biggest shortcomings in our understanding of cosmology and the ΛCDM model (Komatsu et al. 2009). With evidence for dark matter visible across a host of different objects spanning a wide range of size and mass, dark matter appears to be present almost universally in the objects we observe.

The gamma-ray flux produced by DM annihilation/decay is a function of the integral of the DM density (squared or linearly related to the latter, for DM annihilation and decay respectively, refer to sec. 2 for more details). Therefore, the detectability of the DM signal depends strongly on the DM density distribution. Sources that have both a large J/D-factor and relatively low astrophysical gamma-ray backgrounds are ideal targets for DM annihilation and/or decay searches. Those requirements have resulted in a number of galactic and extragalactic targets which appear to be the most promising regions for DM searches. From sub-galactic to galactic, and up to galaxy clusters, we can identify promising targets for indirect DM searches. The GC (Aharonian et al. 2004, 2006; Aharonian et al. 2009, 2006; H. E. S. S. Collaboration et al. 2018; Cholis et al. 2009; Di Mauro et al. 2019; Wood et al. 2013; Pierre et al. 2014; Acharyya et al. 2021), the Galactic diffuse halo (Ackermann et al. 2012; Zaharijas et al. 2013; Viana et al. 2019) , dSphs (Aharonian et al. 2008; H. E. S. S. Collaboration et al. 2011; Abramowski et al. 2014; Abdo et al. 2010; Albert et al. 2017; Acciari et al. 2010; Zitzer & Collaboration 2017; Albert et al. 2008; Aliu et al. 2009; MAGIC Collaboration et al. 2016; Zitzer & Collaboration 2017; Yapici & Smith 2017; H. E. S. S. Collaboration et al. 2021; Oakes et al. 2019) and galaxy clusters (Wood et al. 2008; Ackermann et al. 2010; Thorpe-Morgan et al. 2021; Aleksić et al. 2010; Abramowski et al. 2012a) are among the most popular regions for Indirect DM searches. However, it is important to carefully inspect the DM detectability from various celestial objects (e.g., elliptical, lenticular, and spiral galaxies) aiming at confirming the universal presence of DM. How clean or contaminated with foreground emission the signal of a DM target appears does not only depend on its features (i.e., size, astrophysical background, distance), but also on the energy band in which it is observed (e.g., galaxy clusters which are characterized by high X-ray emission due to presence of hot gas appear contaminated in the X-ray band; while at GeV and TeV energies they are considered uncontaminated). New promising targets keep being discovered as the extragalactic field is broadened. However, one can focus on sources that are targets of the numerous

⋆ A web version of the DM_ρcat is available at: http://astro.uni-tuebingen.de/~morgan/Home.html
⋆⋆ E-mail: michailidis@astro.uni-tuebingen.de

observational campaigns operating almost across the entire electromagnetic spectrum, as reported above.

With such mounting evidence, the abundance of which is supported by the latest measurements of Planck, suggesting that dark matter comprises approximately 26.4% of the energy density of the Universe (Planck Collaboration et al. 2018); naturally, this has spawned innumerable different searches in attempts to detect the annihilation or decay of dark matter, the detection of such secondary products being called "Indirect detection".

Indirect searches, as stated, focus on the detection of standard model particles that are the product of dark matter decay/ annihilation events, with the search focus being on dark matter dominated objects. Such objects are chosen for study due to the maximisation of the potential dark matter signal they can produce. Thus, astrophysical targets with properties that maximise this signal, such as those with high dark matter densities, large angular sizes and low astrophysical foreground emissions are preferential targets for study. Of these properties, the dark matter density profile is perhaps simultaneously the most complex to derive, and important parameter in determining the viability of an astrophysical target for study. Given that DM does not interact with standard model particles, the dark matter density profile of any object cannot be measured directly, constituting another source of error and complexity in its derivation. Therefore, DM profiles must be derived from the observations of the physical properties of an object, or by numerical simulations (Evrard et al. 1996; Buote 2004; Refregier 2003; Burkert 1995; Gilmore et al. 2007; Gentile et al. 2007b). For example, a common method for deriving the DM density profile of Dwarf Spheroidal galaxies (dSphs) is to measure the velocity dispersion of the constituent stars, allowing one to build up a picture of the radial velocity of the system and thus determine the DM profile, e.g., Chang & Necib (2021). Furthermore, many profiles for larger objects e.g., clusters are determined through the derivation of parameters from X-ray surveys, e.g., Ettori et al. (2017). Information on the emission of the intracluster-medium and other physical properties of the cluster allow a similar profile to be derived as in the case of the dSphs.

Following this introduction the article will be laid out as follows. In section 2 we discuss the form of the signal from annihilating and decaying DM, and its implication on dark matter density profiles. We furthermore outline the objects we have compiled profiles for and state the general forms of the profiles themselves. Section 3 is dedicated to the methodology and contains details of the process we undertook to compile the profiles as well as our selection criteria. Finally, section 4 discusses the main features of the compiled sample and showcases the importance of the existence of such a catalog for future DM studies.

2. Signal and Object Sample

The predicted flux of gamma rays from DM annihilation (i.e., pair annihilation of DM-particles into standard model (SM)-particles) is given by (refer to Bergström et al. 1998, for an excellent review):

$$\frac{d\Phi}{dE_\gamma} = \frac{1}{8\cdot\pi}\cdot\frac{\langle\sigma\cdot\upsilon\rangle}{M_\chi^2}\cdot\frac{dN_\gamma}{dE_\gamma}\cdot\int_{\Delta\Omega}\int_{l.o.s.}\rho_\chi^2(l,\Omega)dld\Omega. \quad (1)$$

The differential term $\frac{d\Phi}{dE_\gamma}$ on the left side of the equation represents the observed photon flux. On the right side, the equation is divided into two distinct parts. The expected DM annihilation signal from a DM-dominated region depends mainly on those two factors: the so-called particle physics and the astrophysical J-factors.

The particle physics factor (P) is a function of the velocity-weighted annihilation cross-section $\langle\sigma\cdot\upsilon\rangle$, the mass of the DM particle M_χ and the differential yield of gamma rays that are produced in an annihilation event set by the corresponding channels. The photon spectrum per annihilation $\frac{dN_\gamma}{dE_\gamma}$ is derived (A stands for annihilation):

$$P_A = \frac{1}{8\cdot\pi}\cdot\frac{\langle\sigma\cdot\upsilon\rangle}{M_\chi^2}\cdot\frac{dN_\gamma}{dE_\gamma}. \quad (2)$$

The astrophysical J-factor depends on the chosen DM density profile and, in a nutshell, represents the number of annihilations. The astrophysical terms are combined in the J-factor as an integral of the squared DM density distribution (ρ_χ) over the line of sight (l.o.s.), and inside the observed solid angle $\Delta\Omega$:

$$J = \int_{\Delta\Omega}\int_{l.o.s.}\rho_\chi^2(l,\Omega)dld\Omega. \quad (3)$$

Similarly, the subsequent photon spectrum from the decay of massive DM particles is given by:

$$\frac{d\Phi}{dE_\gamma} = \frac{1}{4\cdot\pi}\cdot\frac{1}{M_\chi\cdot\tau_\chi}\cdot\frac{dN_\gamma}{dE_\gamma}\cdot\int_{\Delta\Omega}\int_{l.o.s.}\rho_\chi(l,\Omega)dld\Omega, \quad (4)$$

τ_χ is the DM particle lifetime.

Similarly to the annihilation signal, the decay signal is written as the product of a term depending on the particle properties (D stands for decay):

$$P_D = \frac{1}{4\cdot\pi}\cdot\frac{1}{M_\chi\cdot\tau_\chi}\cdot\frac{dN_\gamma}{dE_\gamma}, \quad (5)$$

and a term depending on the DM density distribution in the object of interest, namely D-factor:

$$D = \int_{\Delta\Omega}\int_{l.o.s.}\rho_\chi(l,\Omega)dld\Omega. \quad (6)$$

Since it is complicated to measure a "model-independent" DM profile for different objects (imperfect knowledge of the object's actual DM density distribution), a variety of analytic approximations based on theoretical estimations (ISO), N-body simulations (NFW, Einasto) and/or empirical fits to the data (Burkert) have been proposed. In general, mainly two classes of profiles are employed, independently of the DM target of interest: *i*) profiles that favor a steep rising of the DM density towards the center of the DM-dominated object (cusp behavior), e.g., NFW and Einasto, and *ii*) profiles that exhibit central constant density (cored-behavior), e.g., Burkert and Isothermal. In particular, the NFW profile (Navarro et al. 1997), evolving as r^{-1} close to the center of the object of interest (steeply

rising DM density towards the center and thus "cuspy" halo), is a traditional benchmark choice motivated by N-body simulations. Additionally, a generalized NFW profile was also proposed by Zhao (Zhao (1996)). In more recent numerical simulations, a profile that does not converge to a power law towards the center of the object, but is moderately shallower at kpc scales, is emerging as a better fit. The aforementioned profile, namely the Einasto (Einasto 1965), is characterised by a shape parameter α which can vary. A value of 0.17 is considered the central, fiducial value most commonly adopted. More recently, it has been discovered that simulated DM halos match better with an Einasto DM density distribution over a wider range of radii in comparison with the NFW (Merritt et al. (2006), Navarro et al. (2010) and Chemin et al. (2011)). Cored or Isothermal profiles, such as the Burkert (Burkert 1995) and/or Isothermal and Pseudo-Isothermal (PIS) (Gunn & Gott (1972), King (1966), Bahcall & Soneira (1980), Carignan & Freeman (1985)) profiles may be instead more motivated by the observations of galactic rotation curves. On the other hand, there are also profiles steeper than NFW like those proposed by Moore and collaborators (Moore et al. 1999).

In this study, several types of profiles have been included. Therefore, for consistency and direct comparison purposes, we have adopted the generalised density distribution, which is based on four parameters (α, β, γ, δ), proposed by Hernquist (1990), Dehnen (1993) and Zhao (1996) as our benchmark profile. It is noteworthy that a similar parametrisation of DM density profiles based on five different parameters (r_o, a, α, β, γ) has also been introduced in Pullen et al. (2007). However, there are also individual profiles that can not be embedded into the generalized format of profiles that we broadly adopt in this work. In the latter cases a different parametrisation is adopted as shown in eq. 7.

Aside from the profiles mentioned above, profiles that account for peculiar characteristics of the density distribution have also been utilized before, and consequently are included in this study. coreNFW/Reads (Read et al. 2016) DM density profiles, which is a modification of the NFW profile by inserting the f^n function which inserts a shallower profile below a core radius r_c, is also used. A core-Modified profile is also included, which attempts to avoid the singularity of the NFW profile at the Galactic Center (Brownstein 2009). A new semi-empirical profile (Li et al. 2020) is also part of this work. DM profiles that take into account baryonic feedback are also considered (Di Cintio et al. 2014). A Bound DM profile (BDM) which behaves as a NFW profile away from the galactic center but the density has a core inner radius is also used (de la Macorra 2010a). An alternative to CDM that has recently gained much attention is the Bose-Einstein Condensate Scalar Field Dark Matter model (BEC/SFDM) (Sin 1994) which we also consider in this work. A soliton core embedded in a NFW halo which is dominant at large radius is also used (FDM: soliton+NFW) (Marsh & Pop 2015; Schive et al. 2014). The mathematical expression of all those distinct profiles are presented in eq. 7.

In the latter equation, r_s/r_o stands for the typical scale radius and ρ_s/ρ_o is the typical scale density. Especially for the DM profile presented in Pullen et al. (2007) we note that r_o is the distance of our Sun (Solar System) from the GC, which is equal to 8.5 kpc. ρ_s is the local density of the halo at the Solar System. a is the core radius, and α, β, γ are the parameters that determine the halo model. Similarly, for the ISO/PIS profile r_c stands for the core radius and $\rho_o = \frac{V_c^2(\infty)}{4\pi r_c^2}$, with $V(\infty) = 105.4$ km s^{-1}.

More recently, a modified Einasto profile has been proposed, reflecting the baryonic feedback effects. This profile is denoted as EinastoB (Cirelli et al. 2011) and it displays a profile steeper in the center with respect to DM-only simulations. EinastoB follows the above mathematical expression of Einasto profile, with $\alpha = 0.11$.

Finally, hybrid profiles that can be obtained from the combination of two or more of the above profiles have been reported in the literature before. A characteristic example is the HYB profile which is a combination of a SIS and a NFW profile (hereafter denoted as "hybrid" profile (Hayashi & Chiba 2014)).

Overall, the different DM density profiles differ mostly in their innermost regions, close to the centers of the targeted objects, whereas they appear similar at distances above a few kpc from the center of the object of interest. Consequently, DM signals from the innermost regions will be more sensitive to the choice of DM profile.

Driven by the conclusion, obtained in Michailidis et al. (2023), that the imperfect knowledge of the DM density distribution provides the most significant cause of uncertainty (among broadly considered causes of uncertainty, i.e., the DM signal contamination by the astrophysical background, the impact of DM sub-structures, and the systematic uncertainties) on the derived sensitivity limits of modern instruments (i.e., the upcoming Cherenkov Telescope Array (CTA)), we provide a comprehensive catalog of all DM density profiles (to the best of our knowledge) from a variety of different objects. We aim to report a complete catalog of all DM density distribution profiles known for all objects considered as prominent DM targets. In this work we summarise 5658 profiles from 1095 distinct objects collected from the literature. These are as summarised in Tab. 1 and displayed in Tab. 4-10 (sorted by number of objects). Each table consists of 9 main columns listing the object and the various parameters and references of each profile as displayed in Tab. 2. For profiles that cannot be described by the parameters r_s and ρ_s (e.g., SIS and CIS), or when r_s and/or ρ_s are not given and insufficient data are provided to compute them, an additional column is provided. The latter column contains the values of the parameters that provide information for the dark halo of the corresponding object (e.g., halo masses and dispersion velocities). In this way, we extend both the number of objects and the collection of the corresponding DM density profiles reported in Boyarsky et al. (2009) by a factor of greater than 3 and 5, respectively (refer to Tab. 1). In those tables, the profiles are displayed in the generalised form of Hernquist (1990), Dehnen (1993) and Zhao (1996) except when such a form is not applicable (e.g., Einasto profile). While we provide the name of the DM density profile used in the literature in the second column of each table, some of the profiles in eq. 7 can be obtained from the generalized Hernequist form with unique four parameters. These profiles are outlined together with their unique four parameters from the Hernequist formula in Tab. 3. Whereas all profiles reported in the literature are presented in the aforementioned tables, data sets used for further analysis purposes in our upcoming work (Michailidis et al. 2024) were selected after applying a number of recommended cuts.

$NFW:$	$\rho_{NFW}(r)$	$=$	$\rho_s \cdot \frac{r_s}{r} \cdot (1+\frac{r}{r_s})^{-2}$	Navarro et al. (1997)
$gNFW:$	$\rho_{gNFW}(r)$	$=$	$\rho_s \cdot (\frac{r_s}{r})^{\gamma} \cdot (1+\frac{r}{r_s})^{\gamma-3}$	Zhao (1996), Klypin et al. (2001)
$Einasto:$	$\rho_{Ein}(r)$	$=$	$\rho_s \cdot exp\{-\frac{2}{\alpha} \cdot [(\frac{r}{r_s})^{\alpha}-1]\}$	Einasto (1965)
$Isothermal/PIS:$	$\rho_{Iso}(r)$	$=$	$\frac{\rho_s}{1+(\frac{r}{r_s})^2}$	Gunn & Gott (1972), Jimenez et al. (2003)
$King:$	$\rho_{King}(r)$	$=$	$\frac{\rho_s}{(1+(\frac{r}{r_s})^2)^{3/2}}$	King (1962), Binney & Tremaine (1987)
$Burkert:$	$\rho_{Bur}(r)$	$=$	$\frac{\rho_s}{(1+\frac{r}{r_s})\cdot(1+(\frac{r}{r_s})^2)}$	Burkert (1995)
$Moore:$	$\rho_{Moo}(r)$	$=$	$\rho_s(\frac{r_s}{r})^{1.5} \cdot (1+(\frac{r}{r_s})^{1.5})^{-1}$	Moore et al. (1999)
$Hernquist:$	$\rho_{Her}(r)$	$=$	$\rho_s \cdot (\delta+\frac{r}{r_s})^{-\gamma} \cdot (1+(\frac{r}{r_s})^{\alpha})^{\frac{\gamma-\beta}{\alpha}}$	Hernquist (1990)
$Zhao:$	$\rho_{Zhao}(r)$	$=$	$\rho_s \cdot (\frac{r}{r_s})^{-\gamma} \cdot (1+(\frac{r}{r_s})^{\alpha})^{\frac{\gamma-\beta}{\alpha}}$	Zhao (1996)
$DPL:$	$Hernquist$	$(\delta=0,$	$\alpha=1)$	Bernal et al. (2018)
$DC14:$	$Hernquist$	$(\delta=0,$	$baryonic feedback)$	Di Cintio et al. (2014)
$coreNFW(Reads):$	$M_{cNFW}=$	$M_{NFW}f^n$	$f=tanh(r/r_c), 0<n\leq 1$	Read et al. (2016)
$Pullen:$	$\rho_{Pul}(r)$	$=$	$\rho_s \cdot (\frac{r_o}{r})^{\gamma} \cdot \frac{[1+(\frac{r_o}{a})^{\alpha}]^{\frac{\beta-\gamma}{\alpha}}}{[1+(\frac{r}{a})^{\alpha}]^{\frac{\beta-\gamma}{\alpha}}}$	Pullen et al. (2007)
$Dehnen:$	$\rho_{Deh}(r)$	$=$	$\frac{M_0\cdot(3-\gamma)}{4\pi r_0^3}(\frac{r}{r_0})^{-\gamma}(1+\frac{r}{r_0})^{\gamma-4}$	Dehnen (1993)
$Kazantzidis:$	$\rho_{Kaz}(r)$	$=$	$Cr^{-a}exp(-\frac{r}{r_b})$	Kazantzidis et al. (2004)
$coreModified:$	$\rho_{com}(r)$	$=$	$\frac{\rho_s}{1+(\frac{r}{r_s})^3}$	Brownstein (2009)
$Lucky13:$	$\rho_{130}(r)$	$=$	$\frac{\rho_s}{(1+\frac{r}{r_s})^3}$	Li et al. (2020)
$BDM:$	$\rho_{BDM}(r)$	$=$	$\rho_o \cdot (\frac{r}{r_s}+\frac{r_c}{r_s})^{-1} \cdot (1+\frac{r}{r_s})^{-2}$	de la Macorra (2010b)
$soliton+DM:$	$\rho_{FDM}(r)$	$=$	$\Theta(r_\eta-r)\rho_{sol}+\Theta(r-r_\eta)\rho_{NFW}$	Marsh & Pop (2015), Schive et al. (2014)
$BEC:$	$\rho_s(r)$	$=$	$\frac{1.9(10m_{22})^{-2}r_c^{-4}}{(1+9.1\times10^{-2}(r/r_c)^2)^8}10^9 M_\odot kpc^{-3}$	Sin (1994)
$SIS:$	$\rho_{SIS}(r)$	$=$	$\frac{\sigma^2}{2\pi G r^2}$	Hayashi & Chiba (2014)
$N04:$	$\rho_{N04}(r)$	$=$	$\rho_s exp(\frac{2}{\alpha}) \cdot exp\{-\frac{2}{\alpha}(\frac{r}{r_s})^{\alpha}\}$	Navarro et al. (2004)
$TF:$	$\rho_{TF}(r)$	$=$	$\frac{M\alpha^2}{4\pi r^2(r^2+\alpha^2)^{3/2}}$	Wilkinson & Evans (1999)
$LOG:$	$\rho_{LOG}(r)$	$=$	$\frac{v_o^2(3r_o^2+r^2)}{4\pi G(r^2+r_o^2)^2}$	Binney & Tremaine (1987)
$Power\ Law:$	$\rho_{POW}(r)$	$\propto$	$r^{a_{DM}}$	

(7)

As well as providing density profiles for Dark Matter mass, we also provide density profiles for the total mass (and/or DM+stars mass) of the targeted objects when DM-only mass is not available. The latter profiles are highlighted with a dagger (and/or *) symbol and primarily concern galaxy clusters.

3. Method summary

From reviewing the literature, and in particular from the articles that report DM density profiles for all objects considered prominent DM targets, we have compiled 5658 DM density profiles for 1095 objects. There is a direct correlation between the DM density parameters of each profile and the Hubble constant. Hence, for the purposes of this

Table 1. Summary of target types, target number, and DM density profiles number for each target type in DM_ρcat.

Type of object	Number of Objects	Number of profiles	List of objects
Galactic center	1	33	Tab. 4
dSphs	36	186	Tab. 7
Late type galaxies	569 (+32K)	3935 (+74K)	Tab. 10
Lenticular galaxies	10	32	Tab. 5
Early type galaxies	33	168	Tab. 6
Galaxy groups	54	101	Tab. 8
Galaxy clusters	392	1204	Tab. 9
total	1095 (+32K)	5659 (+74K)	

Table 2. Structure and information of the catalog presented in this work.

№	Column name	Units	Description
1	"Object"	-	The object's name
2	"Profile"	-	The DM density profile name: NFW, generalized NFW (gNFW), N04, Isothermal/ Pseudo-Isothermal (ISO), Singular Isothermal (SIS), Non-singular Isothermal (NIE), cored Isothermal (CIS), Burkert (BUR), Moore (MOO), core (coreNFW), coreMOD, Hernequist (HER), Logarithmic (LOG), Power Law (POW), DC14, Lucky13, Reads, DPL, King, Dehnen, BDM, Kazantzidis, Zhao, Soliton+NFW as defined in eq. 7
3	α	-	DM density profile shape parameter (Hernequist/Einasto/POW)
4	β	-	DM density profile shape parameter (Hernequist)
5	γ	-	DM density profile shape parameter (Hernequist/gNFW)
6	δ	-	DM density profile shape parameter (Hernequist)
7	r_s	kpc (Mpc for GCs)	Scale radius (or scale length)
8	ρ_s	$10^{-3} M_\odot \cdot pc^{-3}$	Scale density
9	"Additional info"	-	An additional column is provided for the cases of profiles that cannot be described by r_s and ρ_s (e.g., SIS and CIS) or where r_s and/or ρ_s are not given and not enough data are provided to compute them. This column contains the values of the parameters that provide information for the dark halo of the corresponding object (e.g., halo mass, velocity dispersion).
10	"References"	-	Reference to the article which provides the profile parameters

Notes. This shows the information provided in the respective column, along with a description of the quantity. The 9^{th} column is optional.

Table 3. DM density profiles definition according to the four unique parameters of the Hernequist formula.

HER	NFW	gNFW	BUR	MOO	ISO	King	coreModified	DPL	Lucky13	DC14	core
$\boldsymbol{\alpha}$	1	1	2	1.5	2	2	3	1	1	α	1 (or 2)
$\boldsymbol{\beta}$	3	3	3	3	2	3	3	β	3	β	3
$\boldsymbol{\gamma}$	1	γ	1	1.5	0	0	0	γ	0	γ	0
$\boldsymbol{\delta}$	0	0	1	0	0	0	0	0	0	0	0

Notes. DC14 profile follows a unique parametrization which is dependent to M_*/M_{halo}, as defined in Di Cintio et al. (2014).

study, we have maintained the values of the DM density parameters normalized to the H_o value of their time (Tully 2023). The values of the profile parameters that are given as a function of the Hubble constant were normalized to the current best H_o value of 73.8 km/s/Mpc. In its current form, the catalog includes a comprehensive sample of objects, including possible outliers (i.e., profiles whose parameters appear to differ significantly from the majority of profile parameters reported for a specific object, profiles whose scale length values are extrapolated outside of the observational data, profiles whose parameters are largely uncertain (errors)). A renormalisation of all parameter values has been carried out in the companion paper (Michailidis et al. 2024) to meet the current best value of H_o at 73.8 (73-75) km/s/Mpc (refer to Tully (2023) and references therein for a historical review of H_o). Our objective is to obtain robust conclusions from the analysis of the data, and apply uniform selection criteria to eliminate any outliers that may contaminate our analysis.

4. Conclusions

Arguably the greatest unknown in contemporary astrophysics is dark matter. There is ample evidence that dark

matter is prevalent across a wide range of mass scales and types of objects, including dwarf spheroidal galaxies (dSphs), galaxies, clusters of galaxies, and features of the early universe. To attempt to explain how DM is distributed across astrophysical objects, many differing DM density distribution profiles have been reported in the literature.

In this work, we present the most comprehensive DM catalog, DM_ρcat, by collating and summarizing 5658 DM density profiles from 1095 prominent DM targets. As such, we expand upon the most recent DM density profile catalogue (Boyarsky et al. 2009) by a factor greater than 5. The vast majority of the profiles are of NFW (or gNFW), Isothermal, Einasto, and Burkert nature. Correlations between different DM density profiles and objects of different classes are shown in the Bubble chart of Fig. 1. Fig. 2 illustrates how many profiles display cuspy and cored behaviors for each class of objects examined in this work. On average, more than five different DM density profiles (either of a different nature or of the same nature, but with differences in parameters) have been reported for each object, highlighting the difficulty of determining the exact DM distribution for objects of all mass scales. It is noteworthy that Galaxy Clusters and Late-type galaxies (spiral galaxies and Dwarfs) account for 88% of the sample of objects for which DM density profiles have been reported. From the Bubble chart, we can also conclude that NFW/gNFW profiles represent the majority of profiles for all observed masses. In contrast, while NFW profiles account for nearly 80% of all reported profiles for galaxy clusters, ISO, EIN, HER and BUR profiles account for a comparable number of profiles for late-type spirals and dwarfs and dSphs. A cusped-NFW profile is strongly preferred for all types of objects (and especially for galaxy clusters) with the exception of late-type spirals and dwarfs and dSphs for which there is no clear preference between a cored and a cusped profiles as shown in Fig. 2. Various types of profiles require detailed solidity testing to determine whether this is a characteristic of the objects (related to the actual DM density distribution in the objects) or whether such a conclusion is motivated (biased) by the "popularity" of certain profiles.

It is noteworthy that Zhu et al. (2023) and Yasin et al. (2023) have recently carried out an extensive analysis of the DM properties of $\sim$ 10K and $\sim$ 22K nearby galaxies based on integral-field stellar kinematics from the MaNGA survey (in the final Sloan Digital Sky Survey (SDSS) Data Release 17 (DR17)) and the galaxies observations in HI (ALFALFA survey) and optical light (SDSS survey), respectively. NFW, gNFW, and BUR profiles have been mainly employed to describe the distribution of DM in the latter objects. These studies result in a 31-fold increase in the number of DM-studied objects and a 13-fold increase in the number of DM density profiles collected to date from more than 300 individual works. Such combined studies of numerous objects that recent optical catalogs permit will significantly increase the number of objects studied for DM shortly.

The imperfect knowledge of the actual DM density distribution across the objects can hugely affect our sensitivity limits as reported in Michailidis et al. (2023). Thus we believe that this large database will serve as a useful tool for future DM studies, allowing the derivation of DM constraints and sensitivity limits from all observed objects within uncertainty ranges. Special attention should be paid to the various sources of uncertainties that impact the DM sensitivity of current Imaging Air Cherenkov Telescopes – IACTs (i.e., HESS, MAGIC, VERITAS) and the upcoming CTA. The extent to which upper limit results are affected, depends on whether the DM density distribution appears to continue to rise or platuea in the central regions when compared to a standard profile used as a benchmark for a specific object in a study. This can significantly alter the derived results and DM constraints. A large flat core in the DM distribution (e.g, Burkert profile) can severely worsen the instrument sensitivity by an order of magnitude (Michailidis et al. 2023) compared to a cuspy profile (e.g., NFW, Moore, Einasto) for the same object. We conclude that a thorough testing of the reliability of the profiles is necessary.

On-going studies of prominent DM objects result in the derivation of new DM density profiles from both objects included in this catalog and others that have never been studied in DM before. Thus we plan to frequently update the web version of the catalog[1] to the best of our ability.

Acknowledgements The authors acknowledge support by the state of Baden-Württemberg through bwHPC. This work was supported by DFG through the grant MA 7807/2-1

[1] http://astro.uni-tuebingen.de/~morgan/Home.html

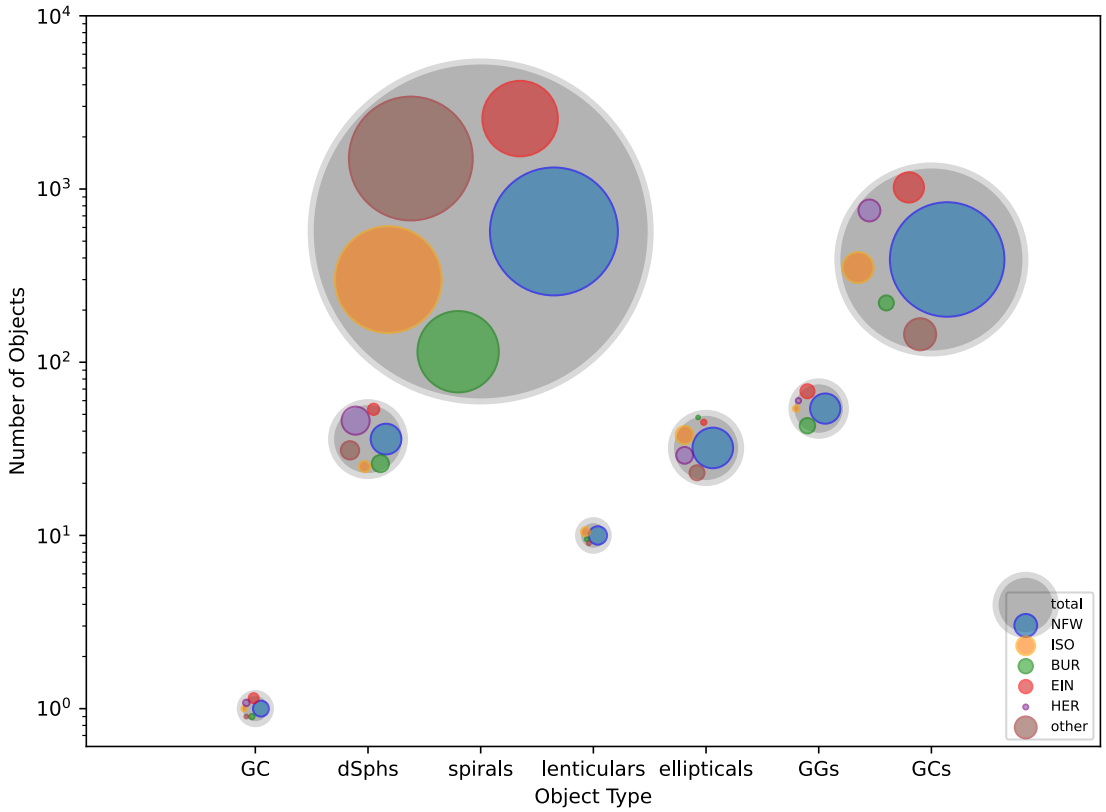

Fig. 1. Bubble graph. The size of the bubbles represents the number of different density profiles reported for each class of objects (GC: Galactic center, dSphs: Dwarf Spheroidals, spirals: spiral galaxies, lenticulars: lenticular galaxies, ellipticals: elliptical galaxies, GGs: galaxy groups, GCs: galaxy clusters).

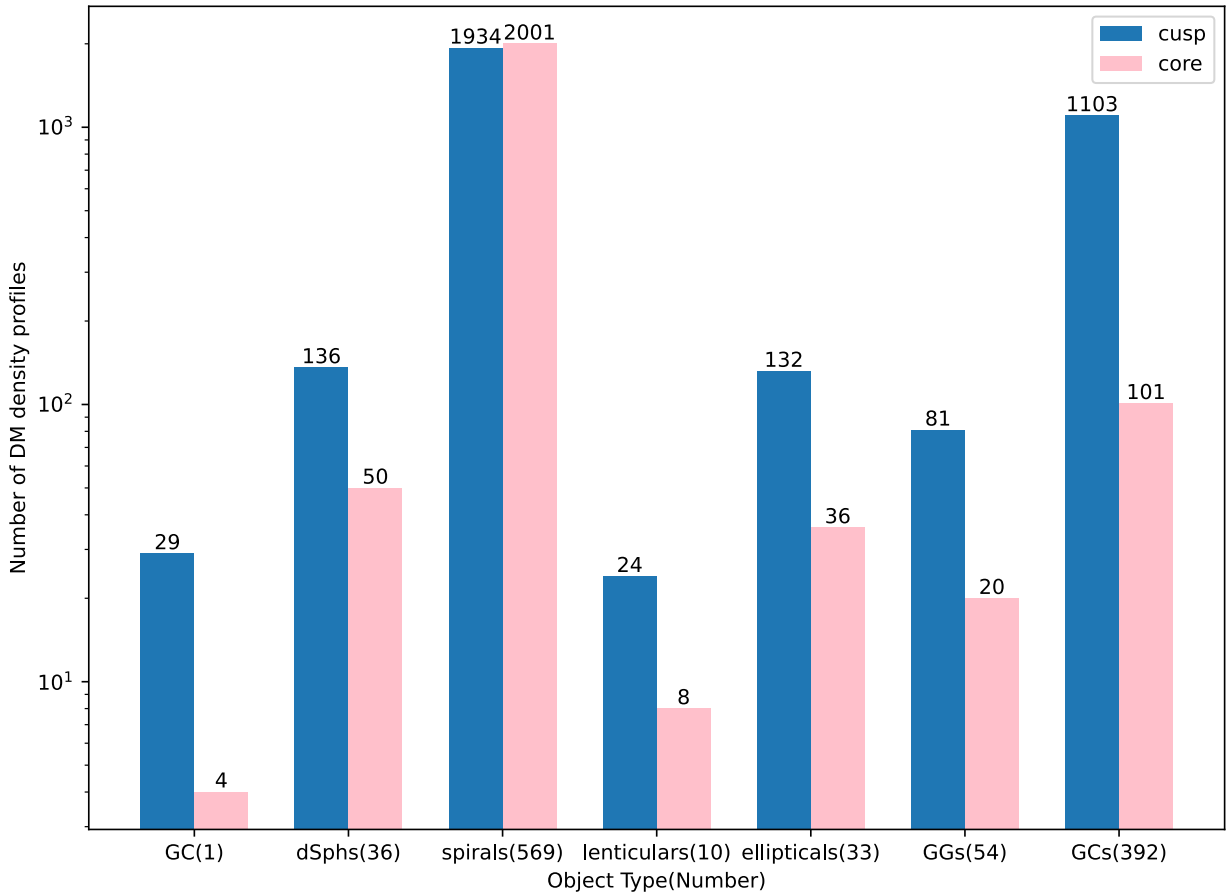

Fig. 2. Histogram. A comparison of the number of cusp and core profiles for each object class.

Table 4. DM density distribution profiles for the Galactic center.

	Profile	α	β	γ	δ	r_s **kpc**	ρ_s $10^{-3}M_\odot \cdot pc^{-3}$	**Reference**
	NFW	1	3	1	0	21	8.1	Pieri et al. (2011)
	NFW	1	3	1	0	21	8.07	Abdallah et al. (2018); Abramowski et al. (2011)
	NFW	1	3	1	0	$16.1^{+17}_{-7.8}$	$14.0^{+29.0}_{-9.3}$	Nesti & Salucci (2013); Aartsen et al. (2015)
	NFW	1	3	1	0	20	7.89	Abbasi et al. (2011)
	NFW	1	3	1	0	25	7.89	Pullen et al. (2007)
	NFW	1	3	1	0	21.7	7.97	ANTARES Collaboration (2015)
	NFW	1	3	1	0	10.7 ± 2.9	18.2 ± 7.4	Sofue (2015)
	NFW	1	3	1	0	8.82	12.16	Widrow & Dubinski (2005)
	NFW	1	3	1	0	12.96	2.95	Widrow & Dubinski (2005)
	gNFW	-	-	1.3	-	21.7	5.44	ANTARES Collaboration (2015)
	gNFW	-	-	1.2	-	20	7.13	Agrawal et al. (2015)
	NFW	1	3	1	0	20	8.94	Karwin et al. (2017)
	gNFW	-	-	1.2	-	20	7.13	Karwin et al. (2017)
	NFW	1	3	1	0	20	9.01	Daylan et al. (2016)
	gNFW	-	-	1.2	-	20	7.13	Daylan et al. (2016)
	gNFW	-	-	1.4	–	20	5.6	Daylan et al. (2016)
GC	NFW	1	3	1	0	23.8	3.68	Gómez-Vargas et al. (2013)
	HER(NFW_c)	0.76	3.3	1.37	0	18.5	6.05	Gómez-Vargas et al. (2013)
	EIN	0.17	-	-	-	20	2.8	Pieri et al. (2011)
	EIN	0.17	-	-	-	20	2.08	Abdallah et al. (2018); Abramowski et al. (2011)
	EIN	0.17	-	-	-	28.4	0.87	Abdallah et al. (2018); Cirelli et al. (2011)
	EIN	0.16	-	-	-	20	7.89	Abbasi et al. (2011)
	EIN	0.17	-	-	-	21.7	1.86	ANTARES Collaboration (2015)
	EIN	0.17	-	-	-	20	2.1	Daylan et al. (2016)
	EIN*	0.22	-	-	-	19.7	2.1	Gómez-Vargas et al. (2013)
	BUR	2	3	1	1	$9.26^{+5.6}_{-4.2}$	41.3^{+62}_{-16}	Nesti & Salucci (2013); Aartsen et al. (2015)
	BUR	2	3	1	1	2	993.1	Gómez-Vargas et al. (2013)
	MOO	1.5	3	1.5	0	28	7.1	Abbasi et al. (2011)
	HER(Kravtsov)	2	3	0.4	0	10	9.7	Abbasi et al. (2011)
	ISO	2	2	0	0	4	7.89	Pullen et al. (2007)
	ISO	2	2	0	0	4	58.02	ANTARES Collaboration (2015)
	Ka	2	3	0.2	0	11	10.5	Pullen et al. (2007)
	Kb	2	3	0.4	0	12	10.5	Pullen et al. (2007)

Table 5. DM density distribution profiles in lenticular galaxies. Where a reference is not provided, it follows the reference of the first row of the corresponding table cell.

Galaxy	**Profile**	α	β	γ	δ	r_s kpc	ρ_s $10^{-3}M_\odot \cdot pc^{-3}$	**Additional info**	**Reference**
NGC 1023	NFW	1	3	1	0	21.53	15.00		Samurović (2017)
	NFW	1	3	1	0	10.77	20.00		
NGC 4526	NFW	1	3	1	0	47.72	9.00		Samurović (2017)
	NFW	1	3	1	0	63.63	70.00		
NGC 2768	NFW	1	3	1	0	42.29 ± 10.57	5.00 ± 2.00		Samurović (2014)
NGC 3115	NFW	1	3	1	0	15.96 ± 2.28	90.00 ± 20.00		Samurović (2014)
	NFW	1	3	1	0	15.96 ± 2.28	80.00 ± 20.00		
	NFW	1	3	1	0	15.96 ± 2.28	100.00 ± 20.00		
NGC 5102	NFW	1	3	1	0	-		$f_{DM} = 0.37 \pm 0.04$	Mitzkus et al. (2017)
	gNFW	-	-	-1.4 ± 0.3	-	20.00		$f_{DM} = 0.58 \pm 0.16$	
NGC 3998	NFW	1	3	1	0	36.65	3.17		Boardman et al. (2016)
NGC 4262	NFW(I)	1	3	1	0	14.8 ± 2.7		$M_h = 1.5 \pm 0.15 \cdot 10^{11} M_\odot$	Khoperskov et al. (2014)
	NFW(II)	1	3	1	0	13 ± 2.1		$M_h = 1.8 \pm 0.3 \cdot 10^{11} M_\odot$	
	NFW(III)	1	3	1	0	11 ± 2		$M_h = 1.9 \pm 0.4 \cdot 10^{11} M_\odot$, $\alpha, r_a, \gamma = 0.93 \pm 0.30, 0.95 \pm 0.1, 1.1 \pm 0.20$	
	ISO(I)	2	2	0	0	1.7 ± 0.48		$M_h = 1.25 \pm 0.16 \cdot 10^{11} M_\odot$	
	ISO(II)	2	2	0	0	2 ± 0.3		$M_h = 1.2 \pm 0.2 \cdot 10^{11} M_\odot$	
	ISO(III)	2	2	0	0	2.4 ± 0.46		$M_h = 1.6 \pm 0.2 \cdot 10^{11} M_\odot$, $\alpha, r_a, \gamma = 0.90 \pm 0.30, 1.33 \pm 0.2, 0.68 \pm 0.09$	
SPRC 7	NFW(I)	1	3	1	0	17.4 ± 1.77		$M_h = 1.83 \pm 0.11 \cdot 10^{11} M_\odot$	Khoperskov et al. (2014)
	NFW(II)	1	3	1	0	14.6 ± 1.64		$M_h = 1.9 \pm 0.11 \cdot 10^{11} M_\odot$	
	ISO(I)	2	2	0	0	1.82 ± 0.5		$M_h = 1.81 \pm 0.52 \cdot 10^{11} M_\odot$	
	ISO(II)	2	2	0	0	1.56 ± 0.23		$M_h = 1.2 \pm 0.2 \cdot 10^{11} M_\odot$	
NGC 1012	gNFW	-	-	$1.09^{+0.62}_{-0.62}$ (≤ 1.76)	-			$c_{-2} \leq 29.8$, $M_{200} = -$(not given)	Relatores et al. (2019)
NGC 5128	NFW	1	3	1	0	14.40	20.00		Samurović (2010)
	BUR	2	3	1	1	10.00	20.00		
	NFW	1	3	1	0	72.66	0.89		Dumont et al. (2023)
	core	2	3	0	0	123.06	0.29		Dumont et al. (2023)
	NFW	1	3	1	0	52.20	4.00		Pearson et al. (2022)
	NFW	1	3	1	0	14.40	10.00		Peng et al. (2004)
	ISO	2	2	0	0	4.5	24.30		
	NFW	1	3	1	0	22.34	35.00		Samurović (2016b)
	NFW	1	3	1	0	22.34	30.00		
	NFW	1	3	1	0	22.34	45.00		

Table 6. DM density distribution profiles in elliptical galaxies. Profiles marked with a † symbol represent total mass (luminous+dark matter). Profiles marked with * represent DM+stars (NFW+stars) mass. Where a reference is not provided, it follows the reference of the first row of the corresponding table cell.

Galaxy	**Profile**	α	β	γ	δ	r_s **kpc**	ρ_s $10^{-3}M_\odot \cdot pc^{-3}$	**Additional info**	**Reference**
NGC 720	NFW*	1	3	1	0	26.67	13.60		Humphrey et al. (2006)
	NFW*	1	3	1	0	25.57	15.18		Humphrey et al. (2012)
	NFW	1	3	1	0	9.49/3.68	-		McDaniel et al. (2021)
	HER	1	4	1	0	15.2/7.2	-		
	ISO	2	2	0	0	1.58/0.55	-		
	NFW	1	3	1	0	5.62/5.46	-		
	HER	1	4	1	0	11.3/10.66	-		
	ISO	2	2	0	0	0.71/0.67	-		
	ISO	2	2	0	0	0.23/0.25	-		Buote et al. (2002)
	NFW	1	3	1	0	3.19/3.52	-		
	HER	1	4	1	0	6.96/7.61	-		
NGC 1407	NFW*	1	3	1	0	36.11	13.27		Humphrey et al. (2006)
	NFW†(> 7.65kpc)	1	3	1	0	30.75	28.79		Zhang et al. (2007)
	NFW(> 7.65kpc)	1	3	1	0	83.7	–		Zhang et al. (2007)
	gNFW(> 7.65kpc)	-	-	0	-	50.4	–		Zhang et al. (2007)
	NFW(> 9kpc)	1	3	1	0	31.5	28.79		Zhang et al. (2007)
	gNFW(> 9kpc)	-	-	0	-	11.7	28.79		Zhang et al. (2007)
	gNFW	-	-	1.03	-	56.30	5.19		Wasserman et al. (2018)
	NFW	1	3	1	0	71.49 ± 13.00	8.0 ± 2.0		Samurović (2014)
	NFW	1	3	1	0	71.49 ± 13.00	7.0 ± 2.0		Samurović (2014)
	NFW	1	3	1	0	84.49 ± 13.00	7.0 ± 2.0		Samurović (2014)
NGC 4261	NFW*	1	3	1	0	281.08	0.31		Humphrey et al. (2006)
NGC 4472	NFW*	1	3	1	0	63.08	6.00		Humphrey et al. (2006)
	NFW	1	3	1	0	$11.7^{+0.4}_{-0.4}$	$130.00^{+20.00}_{-20.00}$		Samurović (2012)
NGC 4649	NFW*	1	3	1	0	40.00	19.97		Humphrey et al. (2006)
NGC 2974	NFW	1	3	1	0	2.10	$11.00 \cdot 10^2$		Weijmans et al. (2008)
	NFW	1	3	1	0	130.00	1.10		
	NFW	1	3	1	0	38.00	6.70		
	ISO	2	2	0	0	0.23	$19.00 \cdot 10^3$		
	ISO	2	2	0	0	5.40	60.00		
	gNFW	-	-	0.6	0	51.72	7.41		Yang et al. (2020)
NGC 4494	NFW	1	3	1	0	38.30	1.27		Napolitano et al. (2009)
	NFW	1	3	1	0	45.30	1.10		
	NFW	1	3	1	0	31.57	2.09		
	LOG(core)	-	-	-	-	18.69		$v_o = 147$km/s	
	LOG(core)	-	-	-	-	15.70		$v_o = 172$km/s	
	LOG(core)	-	-	-	-	14.55		$v_o = 146$km/s	
	NFW	1	3	1	0	52.33 ± 16.10	3.50 ± 2.00		Samurović (2014)
NGC 821	NFW	1	3	1	0	700^{+500}_{-300}	$0.128^{+0.08}_{-0.05}$		Forestell & Gebhardt (2010)
	POW	n=0.1	-	-	-	0.034	$25.00^{+25.00}_{-9.00}$		Forestell & Gebhardt (2010)
	NFW	1	3	1	0	17.25	6.77		Weijmans et al. (2009)

Table 6 Continued.

Galaxy	Profile	α	β	γ	δ	r_s kpc	ρ_s $10^{-3} M_\odot \cdot pc^{-3}$	Additional info	Reference
NGC 3379	NFW	1	3	1	0	19.91	6.77		Weijmans et al. (2009)
NGC 5846	NFW	1	3	1	0	1149^{+6000}_{-600}	$0.025^{+0.17}_{-0.022}$		Zhu et al. (2016a)
	core	2	3	0	0	$50.00^{+30.00}_{-20.00}$	$4.00^{+2.3}_{-1.5}$		Zhu et al. (2016a)
	constrainedNFW	1	3	1	0	$74.00^{+37.00}_{-23.00}$	$1.60^{+0.9}_{-0.6}$		Zhu et al. (2016a)
	NFW	1	3	1	0	35.21 ± 17.61	45.00 ± 20.00		Samurović (2014)
	NFW	1	3	1	0	29.34 ± 17.61	60.00 ± 20.00		Samurović (2014)
	NFW	1	3	1	0	35.21 ± 11.74	60.00 ± 20.00		Samurović (2014)
NGC 4374	NFW	1	3	1	0	81.5	2.61		Napolitano et al. (2011)
	NFW	1	3	1	0	56.7	5.30		
	NFW	1	3	1	0	42.34	6.47		
	NFW	1	3	1	0	41.69	7.79		
	LOG(core)	-	-	-	-	20.48		$v_o = 456$km/s	
	LOG(core)	-	-	-	-	15.50		$v_o = 425$km/s	
	LOG(core)	-	-	-	-	14.12		$v_o = 412$km/s	
NGC 5128	NFW	1	3	1	0	14.40	20.00		Samurović (2010)
	BUR	2	3	1	1	10.00	20.00		Samurović (2010)
	NFW	1	3	1	0	72.66	0.89		Dumont et al. (2023)
	core	2	3	0	0	123.06	0.29		Dumont et al. (2023)
	NFW	1	3	1	0	52.20	4.00		Pearson et al. (2022)
	NFW	1	3	1	0	14.40	10.00		Peng et al. (2004)
	ISO	2	2	0	0	4.5	24.30		Peng et al. (2004)
	NFW	1	3	1	0	22.34	35.00		Samurović (2016b)
	NFW	1	3	1	0	22.34	40.00		Samurović (2016b)
	NFW	1	3	1	0	22.34	45.00		Samurović (2016b)
NGC 4636	NFW	1	3	1	0	5.00	120.00		
	NFW	1	3	1	0	10.00	33.00		
	NFW	1	3	1	0	40.00	3.00		Schuberth et al. (2006)
	NFW	1	3	1	0	120.00	0.75		
	NFW	1	3	1	0	240.00	0.50		
	NFW	1	3	1	0	5.00	195.00		
	NFW	1	3	1	0	5.00	230.00		
	NFW	1	3	1	0	20.00	13.50		
	NFW	1	3	1	0	120.00	1.00		
	NFW	1	3	1	0	120.00	1.45		
	NFW	1	3	1	0	120.00	1.20		
	NFW	1	3	1	0	80.00	1.90		
	NFW	1	3	1	0	120.00	1.10		
	NFW	1	3	1	0	120.00	1.20		
	NFW	1	3	1	0	80.00	2.30		
	NFW	1	3	1	0	120.00	1.10		
	NFW	1	3	1	0	120.00	1.35		
	NFW	1	3	1	0	120.00	1.40		
	NFW	1	3	1	0	79.38	3.14		Mathews (2021)

Table 6 Continued.

Galaxy	Profile	α	β	γ	δ	r_s kpc	ρ_s $10^{-3}M_\odot \cdot pc^{-3}$	Additional info	Reference
NGC 7507	NFW	1	3	1	0	30	1.191		
	NFW	1	3	1	0	25	1.191		
	NFW	1	3	1	0	1	1.191		
	NFW	1	3	1	0	9	6.135		Salinas et al. (2012)
	NFW	1	3	1	0	8	6.135		
	NFW	1	3	1	0	1	6.135		
	LOG(core)	-	-	-	-	0.025		$v_o = 60$km/s	
	LOG(core)	-	-	-	-	7		$v_o = 100$km/s	
	LOG(core)	-	-	-	-	74		$v_o = 210$km/s	
	NFW	1	3	1	0	23.5	1.18		Lane et al. (2015)
	NFW	1	3	1	0	9	6.09		
	NFW	1	3	1	0	34.8	1.18		
	NFW	1	3	1	0	13.3	6.09		
	NFW	1	3	1	0	42.8	1.18		
	NFW	1	3	1	0	16.0	6.09		
NGC 1399	core	1	3	0	0	$11.6^{+0.7}_{-0.7}$	$140.00^{+1.00}_{-1.00}$		Richtler et al. (2004)
	NFW	1	3	1	0	$33.5^{+1.00}_{-1.00}$	$10.00^{+0.6}_{-0.6}$		Richtler et al. (2004)
	LOG(core)	-	-	-	-	10.5		$v_o = 370$km/s	Richtler et al. (2004)
	NFW	1	3	1	0	39.56	35.00		Samurović (2016a)
	NFW	1	3	1	0	39.56	30.00		
	NFW	1	3	1	0	39.56	48.00		
NGC 3377	NFW	1	3	1	0	$21.4^{+2.50}_{-2.50}$	$5.53^{+1.32}_{-1.16}$		Caso (2022)
	EIN	0.125	-	-	-	$19.8^{+2.80}_{-2.80}$	$1.30^{+0.2}_{-0.2}$		Caso (2022)
	NFW	1	3	1	0	21.15 ± 7.93	7.0 ± 4.0		Samurović (2014)
	NFW	1	3	1	0	21.15 ± 7.93	3.0 ± 1.5		
	NFW	1	3	1	0	23.77 ± 7.93	3.5 ± 2.0		
NGC 4486 (M87)	NFW(Fig.10)	1	3	1	0	unconstrained	unconstrained		Murphy et al. (2011)
	LOG(core)					$36.00^{+7.00}_{-3.00}$		$v_o = 800.0^{+75.0}_{-25.0}$km/s	Murphy et al. (2011)
	NFW	1	3	1	0	25.03 ± 4.17	70.00 ± 10.00		Samurović (2014)
	NFW	1	3	1	0	29.20 ± 4.17	75.00 ± 10.00		
Mrk 1216	NFW	1	3	1	0	$12.1^{+7.1}_{-4.4}$	114.25		Buote & Barth (2019)
	EIN	0.17	-	-	-	14	85.42		Buote & Barth (2019)
NGC 6166	NFW	1	3	1	0	400.00	0.82		Kelson et al. (2002)
NGC 2434	NFW	1	3	1	0	80.8	3.50		Rix et al. (1997)
	LOG	-	-	-	-	-		$v_o = 300 \pm 15$km/s	Rix et al. (1997)
NGC 1400	NFW	1	3	1	0	51.99 ± 13.00	3.5 ± 1.0		Samurović (2014)
NGC 4278	NFW	1	3	1	0	11.35 ± 2.27	75.00 ± 30.00		Samurović (2014)
NGC 4365	NFW	1	3	1	0	28.25 ± 11.30	50.00 ± 20.00		Samurović (2014)
	NFW	1	3	1	0	28.50 ± 11.30	40.00 ± 20.00		Samurović (2014)
	NFW	1	3	1	0	28.50 ± 11.30	55.00 ± 20.00		Samurović (2014)
IC4451	NFW	1	3	1	0	16.47/6.62	-		McDaniel et al. (2021)
	HER	1	4	1	0	34.1/12.37	-		

Table 6 Continued.

Galaxy	Profile	α	β	γ	δ	r_s kpc	ρ_s $10^{-3} M_\odot \cdot pc^{-3}$	Additional info	Reference
	ISO	2	2	0	0	2.75/1.3	-		
	NFW	1	3	1	0	3.35/3.19	-		
	HER	1	4	1	0	7.29/6.78	-		
	ISO	2	2	0	0	0.22/0.24	-		
IC4956	NFW	1	3	1	0	13.84/5.37	-		McDaniel et al. (2021)
	HER	1	4	1	0	28.9/11.63	-		
	ISO	2	2	0	0	2.07/0.82	-		
NGC 1521	NFW	1	3	1	0	19.35/7.38	-		McDaniel et al. (2021)
	HER	1	4	1	0	35.56/13.87	-		
	ISO	2	2	0	0	2.96/0.92	-		
	NFW	1	3	1	0	4.69/4.49	-		
	HER	1	4	1	0	8.98/9.18	-		
	ISO	2	2	0	0	0.37/0.48	-		
	NFW	1	3	1	0	31.10	8.44		Humphrey et al. (2012)
NGC 4125	NFW	1	3	1	0	9.24/3.48	-		McDaniel et al. (2021)
	HER	1	4	1	0	14.87/5.95	-		
	ISO	2	2	0	0	1.34/0.5	-		
	NFW	1	3	1	0	5.21/3.89	-		
	HER	1	4	1	0	19.96/8.16	-		
	ISO	2	2	0	0	1.19/0.54	-		
	NFW*	1	3	1	0	47.0	3.13		Humphrey et al. (2006)
NGC 4555	NFW	1	3	1	0	12.83/4.24	-		McDaniel et al. (2021)
	HER	1	4	1	0	30.85/10.34	-		
	ISO	2	2	0	0	0.95/0.32	-		
	NFW	1	3	1	0	3.82/3.82	-		
	HER	1	4	1	0	8.53/9.65	-		
	ISO	2	2	0	0	0.42/0.27	-		
NGC 6482	NFW	1	3	1	0	13.43/4.81	-		McDaniel et al. (2021)
	HER	1	4	1	0	29.84/11.6	-		
	ISO	2	2	0	0	1.62/0.64	-		
	NFW	1	3	1	0	6.9/6.76	-		
	HER	1	4	1	0	15.02/13.63	-		
	ISO	2	2	0	0	0.75/0.64	-		
	NFW*	1	3	1	0	27.78	12.94		Humphrey et al. (2006)
NGC 7785	NFW	1	3	1	0	11.96/4.74	-		McDaniel et al. (2021)
	HER	1	4	1	0	44.71/11.02	-		
	ISO	2	2	0	0	6.85/1.68	-		
NGC 7796	NFW	1	3	1	0	11.98/5.73	-		McDaniel et al. (2021)
	HER	1	4	1	0	26.85/10.23	-		
	ISO	2	2	0	0	1.2/1.48	-		
	NFW	1	3	1	0	2.25/2.08	-		
	HER	1	4	1	0	4.5/4.88	-		
	ISO	2	2	0	0	0.13/0.1	-		

Table 6 Continued.

Galaxy	Profile	α	β	γ	δ	r_s **kpc**	ρ_s $10^{-3}M_\odot \cdot pc^{-3}$	Additional info	Reference
NGC 953	NFW	1	3	1	0	11.78/3.62	-		McDaniel et al. (2021)
	HER	1	4	1	0	23.49/8.96	-		
	ISO	2	2	0	0	1.22/0.45	-		
	NFW	1	3	1	0	1.95/1.98	-		
	HER	1	4	1	0	4.32/4.26	-		
	ISO	2	2	0	0	0.16/0.22	-		
NGC 57	NFW	1	3	1	0	4.35/2.96	-		McDaniel et al. (2021)
	HER	1	4	1	0	6.02/5.27	-		
	ISO	2	2	0	0	0.51/0.44	-		

Table 7. DM density profiles in dSphs (classical and Ultra faint (UF) dwarfs).

dSphs	Profile	α	β	γ	δ	r_s kpc	ρ_s $10^{-3}M_\odot \cdot pc^{-3}$	Additional info	References
Carina	HER	1.47	5.6	0.95	0	2.042	10.96		Geringer-Sameth et al. (2015)
	NFW	1	3	1	0	0.795		$V_{max} = 13^{+1}_{-1}$ km/s	Walker et al. (2009)
	core	1	3	0	0	0.150		$V_{max} = 11^{+2}_{-1}$ km/s	Walker et al. (2009)
	HER	$1.83^{+0.77}_{-0.81}$	$6.31^{+2.23}_{-2.07}$	$0.77^{+0.23}_{-0.27}$	0	$13.49^{+37.78}_{-10.47}$	$3.31^{+16.19}_{-2.6}$		Hayashi et al. (2020), Hayashi et al. (2016)
	BUR	2	3	1	1	–		$log(\rho_o \cdot r_o M_\odot^{-1} \cdot pc^2) = 1.2^{+1.2}_{-0.1}$	Wolf & Bullock (2012)
	NFW	1	3	1	0	0.2065	304.0		Klop et al. (2017)
	ISO	2	2	0	0	0.22	136.0		H. E. S. S. Collaboration et al. (2011)
	NFW	1	3	1	0	0.54	44.63		H. E. S. S. Collaboration et al. (2011)
	NFW	1	3	1	0	1.372 ± 0.058	6.8 ± 4		Hayashi & Chiba (2012)
	core	2	3	0	0	0.453 ± 0.021	65 ± 3		Hayashi & Chiba (2012)
	BUR	2	3	1	0	0.32 ± 0.02	210 ± 30		Frigerio Martins (2009)
	NFW	1	3	1	0	0.17		$log_{10}(J\text{GeV}^2\text{cm}^{-5}) = 18.1 \pm 0.23$	MAGIC Collaboration et al. (2016)
Draco	HER	2.01	6.34	0.71	0	3.697	18.41		Geringer-Sameth et al. (2015)
	BUR	2	3	1	1	0.35	360		Bringmann et al. (2009)
	NFW	1	3	1	0	0.5	130		Bringmann et al. (2009)
	BUR	2	3	1	1	0.178	2.58		Mashchenko et al. (2006)
	NFW	1	3	1	0	2.81	1.55		Mashchenko et al. (2006)
	NFW	1	3	1	0	0.795		$V_{max} = 20^{+3}_{-2}$ km/s	Walker et al. (2009)
	core	1	3	0	0	0.150		$V_{max} = 17^{+3}_{-2}$ km/s	Walker et al. (2009)
	HER	$2.04^{+0.64}_{-0.79}$	$6.19^{+2.31}_{-2.03}$	$1.03^{+0.14}_{-0.15}$	0	$19.95^{+37.59}_{-14.20}$	$1.70^{+5.71}_{-1.31}$		Hayashi et al. (2020), Hayashi et al. (2016)
	BUR	2	3	1	1	–		$log(\rho_o \cdot r_o M_\odot^{-1} \cdot pc^2) = 2.0^{+0.4}_{-0.3}$	Wolf & Bullock (2012)
	NFW	1	3	1	0	0.3507	230.0		Klop et al. (2017)
	EIN	$0.41^{+0.23}_{-0.21}$	-	-	-	$0.28^{+0.33}_{-0.20}$	$85.0^{+68.0}_{-29.0}$		Bonnivard et al. (2015), Saturni et al. (2019)
	Kazantzidis	1(cusp)	–	–	-	1.189	31.0		Sánchez-Conde et al. (2007)
	Kazantzidis	0(core)	–	–	-	0.232	360.00		Sánchez-Conde et al. (2007)
	NFW	1	3	1	0	$0.901^{+0.06}_{-0.07}$	29.0 ± 3.0		Hayashi & Chiba (2012)
	core	2	3	0	0	0.359 ± 0.03	210.0 ± 20.0		Hayashi & Chiba (2012)
	BUR	2	3	1	1	0.24 ± 0.01	690 ± 120		Frigerio Martins (2009)
	NFW	1	3	1	0	0.35		$log_{10}(J\text{GeV}^2\text{cm}^{-5}) = 18.8 \pm 0.16$	MAGIC Collaboration et al. (2016)
Fornax	HER	2.13	6.97	0.61	0	1.241	32.52		Geringer-Sameth et al. (2015)
	NFW	1	3	1	0	0.795		$V_{max} = 18^{+1}_{-1}$ km/s	Walker et al. (2009)
	core	1	3	0	0	0.150		$V_{max} = 16^{+2}_{-0}$ km/s	Walker et al. (2009)
	HER	$1.98^{+0.64}_{-0.74}$	$6.63^{+2.11}_{-2.15}$	$0.44^{+0.40}_{-0.29}$	0	$1.86^{+2.93}_{-0.71}$	$28.84^{+30.04}_{-19.07}$		Hayashi et al. (2020, 2016)
	BUR	2	3	1	1	$0.79^{+0.13}_{-0.11}$	$15.94^{+4.36}_{-3.17}$		Wolf & Bullock (2012)
	NFW	1	3	1	0	0.4731	133.0		Klop et al. (2017)
	BUR	2	3	1	1	$1.0^{+0.8}_{-0.4}$	–		Amorisco et al. (2013)
	NFW	1	3	1	0	3	–		Amorisco et al. (2013)
	NFW	1	3	1	0	98.00	5.80		Abramowski et al. (2012b)

Table 7 Continued.

dSphs	Profile	α	β	γ	δ	r_s kpc	ρ_s $10^{-3} M_\odot \cdot pc^{-3}$	Additional info	References
	NFW	1	3	1	0	220.00	0.50		Abramowski et al. (2012b)
	NFW	1	3	1	0	50.00	6.50		Abramowski et al. (2012b)
	NFW	1	3	1	0	34.00	8.80		Abramowski et al. (2012b)
	NFW	1	3	1	0	200.00	0.61		Abramowski et al. (2012b)
	BUR	2	3	1	1	12.00	72.8		Abramowski et al. (2012b)
	BUR	2	3	1	1	94.00	3.10		Abramowski et al. (2012b)
	NFW	1	3	1	0	7.28	3.56		Brownsberger & Randall (2021)
	NFW	1	3	1	0	3.92	4.26		Brownsberger & Randall (2021)
	core	1	3	0	0	1.92 ± 0.41	50.33		Brownsberger & Randall (2021)
	core	1	3	0	0	1.0 ± 0.39	67.62		Brownsberger & Randall (2021)
	BUR	2	3	1	1	1.45 ± 0.16	12.26		Brownsberger & Randall (2021)
	BUR	2	3	1	1	0.81 ± 0.09	15.95		Brownsberger & Randall (2021)
	NFW-like	0.5-1.5	3	0.5-1.5	0	2.4	5.8		Goerdt et al. (2006)
	core (small)	0.5-1.5	3	0	0	0.91	100.0		Goerdt et al. (2006)
	core (large)	0.5-1.5	3	0	0	2.2	100.0		Goerdt et al. (2006)
	NFW	1	3	1	0	1.823 ± 0.051	7.20 ± 0.30		Hayashi & Chiba (2012)
	core	2	3	0	0	1.323 ± 0.053	25.0 ± 1.0		Hayashi & Chiba (2012)
	NFW	1	3	1	0	0.44		$log_{10}(J\text{GeV}^2\text{cm}^{-5}) = 18.2 \pm 0.21$	MAGIC Collaboration et al. (2016)
Leo I	HER	1.93	6.15	0.84	0	6.271	6.57		Geringer-Sameth et al. (2015)
	NFW	1	3	1	0	0.795		$V_{max} = 20^{+2}_{-2}$ km/s	Walker et al. (2009)
	core	1	3	0	0	0.150		$V_{max} = 18^{+2}_{-2}$ km/s	Walker et al. (2009)
	HER	$1.68^{+0.85}_{-0.80}$	$6.17^{+2.31}_{-2.05}$	$1.35^{+0.32}_{-0.61}$	0	$3.16^{+15.90}_{-2.40}$	$4.47^{+133.57}_{-4.31}$		Hayashi et al. (2020, 2016)
	Log(core)	-	-	-	-	1.5 ± 0.6	> 29.37		Bustamante-Rosell et al. (2021)
	NFW	1	3	1	0	> 5.6	2.87		Bustamante-Rosell et al. (2021)
	BUR	2	3	1	1	–		$log(\rho_o \cdot r_o M_\odot^{-1} \cdot pc^2) = 2.3^{+0.5}_{-0.6}$	Wolf & Bullock (2012)
	NFW	1	3	1	0	0.4027	159.0		Klop et al. (2017)
	NFW	1	3	1	0	0.34 ± 0.02	110.0 ± 10.0		Hayashi & Chiba (2012)
	core	2	3	0	0	$0.256^{+16.0}_{-14.0}$	350.0 ± 40.0		Hayashi & Chiba (2012)
	BUR	2	3	1	1	0.27 ± 0.02	530 ± 130		Frigerio Martins (2009)
Leo II	HER	1.76	5.95	0.82	0	0.781	120.23		Geringer-Sameth et al. (2015)
	NFW	1	3	1	0	0.795		$V_{max} = 18^{+3}_{-3}$ km/s	Walker et al. (2009)
	core	1	3	0	0	0.150		$V_{max} = 15^{+2}_{-3}$ km/s	Walker et al. (2009)
	HER	$1.77^{+0.81}_{-0.81}$	$6.27^{+2.26}_{-2.08}$	$0.99^{+0.38}_{-0.48}$	0	$7.24^{+31.66}_{-5.95}$	$4.90^{+55.36}_{-4.57}$		Hayashi et al. (2020, 2016)
	BUR	2	3	1	1	–		$log(\rho_o \cdot r_o M_\odot^{-1} \cdot pc^2) = 1.4^{+1.7}_{-0.1}$	Wolf & Bullock (2012)
	NFW	1	3	1	0	0.3055	183.0		Klop et al. (2017)
	BUR	2	3	1	1	0.18 ± 0.02	610 ± 180		Frigerio Martins (2009)
	NFW	1	3	1	0	0.29		$log_{10}(J\text{GeV}^2\text{cm}^{-5}) = 17.6 \pm 0.18$	MAGIC Collaboration et al. (2016)
Sculptor	HER	1.68	5.8	0.81	0	1.066	46.45		Geringer-Sameth et al. (2015)
	NFW	1	3	1	0	0.795		$V_{max} = 19^{+1}_{-1}$ km/s	Walker et al. (2009)
	core	1	3	0	0	0.150		$V_{max} = 16^{+1}_{-1}$ km/s	Walker et al. (2009)
	HER	$1.79^{+0.77}_{-0.82}$	$6.51^{+2.19}_{-2.18}$	$0.45^{+0.41}_{-0.31}$	0	$1.29^{+1.87}_{-0.50}$	$85.11^{+133.66}_{-65.62}$		Hayashi et al. (2020, 2016)
	NFW	1	3	1	0	1.00	64.0		Richardson & Fairbairn (2014)

Table 7 Continued.

dSphs	Profile	α	β	γ	δ	r_s kpc	ρ_s $10^{-3}M_\odot \cdot pc^{-3}$	Additional info	References
	core	1	3	0	0	1.00	400.0		Richardson & Fairbairn (2014)
	gNFW	–	–	0.5 ± 0.3	-	$0.35^{+0.30}_{-0.10}$	300.0 ± 200.0		Zhu et al. (2016b)
	gNFW	–	–	0	-	$0.37^{+0.10}_{-0.07}$	500.0 ± 200.0		Zhu et al. (2016b)
	gNFW	–	–	1	-	$0.57^{+0.7}_{-0.15}$	80.0 ± 70.0		Zhu et al. (2016b)
	BUR	2	3	1	1	$0.41^{+0.08}_{-0.07}$	$9.94^{+12.37}_{-2.36}$		Wolf & Bullock (2012)
	NFW	1	3	1	0	0.3935	167.00		Klop et al. (2017)
	ISO	2	2	0	0	0.05	2210.0		H. E. S. S. Collaboration et al. (2011)
	ISO	2	2	0	0	0.5	91.3		H. E. S. S. Collaboration et al. (2011)
	ISO	2	2	0	0	0.05	2400.0		H. E. S. S. Collaboration et al. (2011)
	ISO	2	2	0	0	0.5	94.0		H. E. S. S. Collaboration et al. (2011)
	NFW	1	3	1	0	1.26	34.92		H. E. S. S. Collaboration et al. (2011)
	NFW	1	3	1	0	0.48	149.96		H. E. S. S. Collaboration et al. (2011)
	NFW	1	3	1	0	1.32	34.92		H. E. S. S. Collaboration et al. (2011)
	NFW	1	3	1	0	0.51	149.96		H. E. S. S. Collaboration et al. (2011)
	ISO	2	2	0	0	0.5		$M(< 1.8kpc) = 3.4 \pm 0.710^8 M_\odot$	Battaglia et al. (2008)
	NFW	1	3	1	0	1.34	34.92		Battaglia et al. (2008)
	NFW	1	3	1	0	$0.687^{+0.020}_{-0.017}$	31.0 ± 1.0		Hayashi & Chiba (2012)
	core	2	3	0	0	$0.405^{+0.016}_{-0.016}$	130.00 ± 5.00		Hayashi & Chiba (2012)
	NFW	1	3	1	0	0.38		$log_{10}(J\text{GeV}^2\text{cm}^{-5}) = 18.6 \pm 0.18$	MAGIC Collaboration et al. (2016)
Sextans	HER	1.98	6.06	0.63	0	6.203	4.09		Geringer-Sameth et al. (2015)
	NFW	1	3	1	0	0.795		$V_{max} = 11^{+2}_{-2}$ km/s	Walker et al. (2009)
	core	1	3	0	0	0.150		$V_{max} = 10^{+1}_{-2}$ km/s	Walker et al. (2009)
	HER	$1.77^{+0.79}_{-0.79}$	$6.31^{+2.25}_{-2.09}$	$0.73^{+0.44}_{-0.45}$	0	$2.51^{+15.27}_{-1.58}$	$14.13^{+47.53}_{-13.32}$		Hayashi et al. (2020, 2016)
	ISO	2	2	0	0	3.00	9.82		Battaglia et al. (2011)
	ISO	2	2	0	0	1.50	13.27		Battaglia et al. (2011)
	NFW	1	3	1	0	3.45	3.39		Battaglia et al. (2011)
	BUR	2	3	1	1	$0.66^{+0.28}_{-0.20}$	$6.17^{+10.32}_{-3.10}$		Wolf & Bullock (2012)
	NFW	1	3	1	0	0.2018	382.0		Klop et al. (2017)
	NFW	1	3	1	0	$3.51^{+0.207}_{-0.242}$	1.00 ± 0.10		Hayashi & Chiba (2012)
	core	2	3	0	0	$2.88^{+0.58}_{-0.43}$	5.0 ± 0.4		Hayashi & Chiba (2012)
	BUR	2	3	1	1	0.65 ± 0.06	350 ± 150		Frigerio Martins (2009)
	NFW	1	3	1	0	0.2		$log_{10}(J\text{GeV}^2\text{cm}^{-5}) = 18.4 \pm 0.27$	MAGIC Collaboration et al. (2016)
Ursa Minor	HER	1.64	5.29	0.78	0	0.394	318.64		Geringer-Sameth et al. (2015)
	NFW	1	3	1	0	0.795		$V_{max} = 19^{+2}_{-2}$ km/s	Walker et al. (2009)
	core	1	3	0	0	0.15		$V_{max} = 15^{+2}_{-2}$ km/s	Walker et al. (2009)
	HER	$1.65^{+0.87}_{-0.77}$	$6.41^{+2.17}_{-2.12}$	$1.16^{+0.44}_{-0.66}$	0	$1.55^{+6.58}_{-0.89}$	$12.59^{+99.61}_{-12.13}$		Hayashi et al. (2020), Hayashi et al. (2016)
	BUR	2	3	1	1	–		$log(\rho_o \cdot r_o M_\odot^{-1} \cdot pc^2) = 1.5^{+0.7}_{-0.1}$	Wolf & Bullock (2012)
	BUR	2	3	1	1	0.28 ± 0.02	660 ± 160		Frigerio Martins (2009)
	NFW	1	3	1	0	0.63	100.0		Strigari et al. (2007), Sánchez-Conde et al. (2011)

Table 7 Continued.

dSphs	Profile	α	β	γ	δ	r_s kpc	ρ_s $10^{-3}M_\odot \cdot pc^{-3}$	Additional info	References
	NFW	1	3	1	0	3.1	10.0		Strigari et al. (2007), Sánchez-Conde et al. (2011)
	NFW	1	3	1	0	0.46		$log_{10}(J\text{GeV}^2\text{cm}^{-5}) = 18.8 \pm 0.19$	MAGIC Collaboration et al. (2016)
Crater II	NFW	1	3	1	0	2.04	14.49		Borukhovetskaya et al. (2022)
	HER	$1.6^{+0.8}_{-0.9}$	$6.1^{+2.1}_{-2.4}$	$0.9^{+0.5}_{-0.5}$	0	3.98	0.25		Hayashi et al. (2023), Hayashi et al. (2016)
Bootes I	HER	1.96	5.91	0.53	0	6.286	18.4		Geringer-Sameth et al. (2015)
	HER	$1.8^{+0.8}_{-0.8}$	$6.3^{+2.1}_{-2.2}$	$0.7^{+0.5}_{-0.6}$	0	5.01	15.85		Hayashi et al. (2023), Hayashi et al. (2016)
	NFW	1	3	1	0	0.27		$log_{10}(J\text{GeV}^2\text{cm}^{-5}) = 18.8 \pm 0.22$	MAGIC Collaboration et al. (2016)
Coma Berenices	HER	1.99	6.44	0.43	0	5.133	102.71		Geringer-Sameth et al. (2015)
	HER	$1.9^{+0.8}_{-0.7}$	$6.3^{+2.1}_{-2.2}$	$0.5^{+0.4}_{-0.4}$	0	3.98	79.43		Hayashi et al. (2023), Hayashi et al. (2016)
	EIN	$0.64^{+0.25}_{-0.29}$	-	-	-	$1.00^{+4.60}_{-0.70}$	$37.0^{+54.0}_{-28.0}$		Bonnivard et al. (2015), Saturni et al. (2019)
	NFW	1	3	1	0	0.18		$log_{10}(J\text{GeV}^2\text{cm}^{-5}) = 19.0 \pm 0.25$	MAGIC Collaboration et al. (2016)
Canes Venatici I	HER	1.86	6.0	0.67	0	2.265	13.66		Geringer-Sameth et al. (2015)
	HER	$1.9^{+0.8}_{-0.7}$	$6.3^{+2.1}_{-2.2}$	$0.7^{+0.4}_{-0.5}$	0	10.0	6.31		Hayashi et al. (2023), Hayashi et al. (2016)
	EIN	$0.32^{+0.32}_{-0.45}$	-	-	-	$1.90^{+2.80}_{-1.10}$	$2.5^{+6.7}_{-1.4}$		Bonnivard et al. (2015), Saturni et al. (2019)
Canes Venatici II	HER	1.92	6.09	0.43	0	8.043	35.07		Geringer-Sameth et al. (2015)
	HER	$1.8^{+0.8}_{-0.8}$	$6.3^{+2.1}_{-2.2}$	$0.8^{+0.5}_{-0.5}$	0	5.01	15.85		Hayashi et al. (2023), Hayashi et al. (2016)
	NFW	1	3	1	0	0.2		$log_{10}(J\text{GeV}^2\text{cm}^{-5}) = 17.9 \pm 0.25$	MAGIC Collaboration et al. (2016)
Hercules	HER	1.81	6.39	0.55	0	0.851	23.99		Geringer-Sameth et al. (2015)
	HER	$1.8^{+0.8}_{-0.8}$	$6.3^{+2.1}_{-2.3}$	$1.0^{+0.7}_{-0.6}$	0	1.00	39.81		Hayashi et al. (2023), Hayashi et al. (2016)
	NFW	1	3	1	0	0.19		$log_{10}(J\text{GeV}^2\text{cm}^{-5}) = 18.1 \pm 0.25$	MAGIC Collaboration et al. (2016)
Leo IV	HER	1.93	6.32	0.55	0	0.878	16.01		Geringer-Sameth et al. (2015)
	HER	$1.8^{+0.8}_{-0.8}$	$6.2^{+2.1}_{-2.3}$	$0.9^{+0.6}_{-0.7}$	0	1.96	5.01		Hayashi et al. (2023), Hayashi et al. (2016)
	NFW	1	3	1	0	0.19		$log_{10}(J\text{GeV}^2\text{cm}^{-5}) = 17.9 \pm 0.28$	MAGIC Collaboration et al. (2016)
Leo V	HER	1.91	5.89	0.51	0	2.483	22.2		Geringer-Sameth et al. (2015)
	HER	$1.9^{+0.8}_{-0.7}$	$6.3^{+2.1}_{-2.2}$	$0.6^{+0.4}_{-0.6}$	0	6.31	5.01		Hayashi et al. (2023), Hayashi et al. (2016)
Leo T	HER	1.88	6.71	0.65	0	4.439	28.75		Geringer-Sameth et al. (2015)
	HER	$1.8^{+0.8}_{-0.8}$	$6.2^{+2.1}_{-2.3}$	$1.0^{+0.7}_{-0.6}$	0	1.58	39.81		Hayashi et al. (2023), Hayashi et al. (2016)
Segue 1	HER	1.91	6.39	0.76	0	1.81	87.88		Geringer-Sameth et al. (2015)
	HER	$1.6^{+0.8}_{-0.9}$	$6.2^{+2.1}_{-2.3}$	$1.6^{+0.6}_{-0.3}$	0	0.316	125.89		Hayashi et al. (2023), Hayashi et al. (2016)

Table 7 Continued.

dSphs	Profile	α	β	γ	δ	r_s kpc	ρ_s $10^{-3}M_\odot \cdot pc^{-3}$	Additional info	References
	EIN	$0.53^{+0.33}_{-0.26}$	-	-	-	$0.32^{+4.02}_{-0.25}$	$1.6^{+22.7}_{-1.3}$		Bonnivard et al. (2015), Saturni et al. (2019)
	EIN	$0.1<\frac{1}{n}<0.5$	-	-	-	0.07	100.0		Martinez et al. (2009), Sánchez-Conde et al. (2011)
	EIN	n=3.3	-	-	-	0.15	110.0		Paiano et al. (2011)
	NFW	1	3	1	0	0.15		$log_{10}(J\text{GeV}^2\text{cm}^{-5}) = 19.5 \pm 0.29$	MAGIC Collaboration et al. (2016)
Segue 2	HER	1.84	5.59	0.79	0	0.481	5.54		Geringer-Sameth et al. (2015)
	HER	$1.8^{+0.8}_{-0.8}$	$6.4^{+2.1}_{-2.2}$	$0.7^{+0.5}_{-0.7}$	0	1.26	39.81		Hayashi et al. (2023), Hayashi et al. (2016)
Ursa Major I	HER	1.87	6.25	0.71	0	3.198	14.42		Geringer-Sameth et al. (2015)
	HER	$1.7^{+0.8}_{-0.8}$	$6.2^{+2.1}_{-2.3}$	$1.1^{+0.7}_{-0.6}$	0	1.96	25.12		Hayashi et al. (2023), Hayashi et al. (2016)
Ursa Major II	HER	1.86	6.37	0.58	0	4.283	73.6		Geringer-Sameth et al. (2015)
	HER	$1.8^{+0.8}_{-0.8}$	$6.3^{+2.1}_{-2.2}$	$0.8^{+0.5}_{-0.6}$	0	3.98	50.12		Hayashi et al. (2023), Hayashi et al. (2016)
	NFW	1	3	1	0	0.18		$log_{10}(J\text{GeV}^2\text{cm}^{-5}) = 19.3 \pm 0.28$	MAGIC Collaboration et al. (2016)
Antlia 2	HER	$2.00^{+0.7}_{-0.7}$	$6.20^{+2.0}_{-2.2}$	$0.40^{+0.2}_{-0.3}$	0	$31.62^{+47.81}_{-15.77}$	$0.40^{+0.86}_{-0.24}$		Hayashi et al. (2023), Hayashi et al. (2016)
Draco 2	HER	$1.7^{+0.8}_{-0.8}$	$6.4^{+2.1}_{-2.2}$	$0.9^{+0.6}_{-0.7}$	0	$0.126^{+3.04}_{-0.124}$	$12.59^{+1246}_{-12.55}$		Hayashi et al. (2023), Hayashi et al. (2016)
	Soliton+NFW	–	–	–	-	0.105		$m_{22} = 5.6$	Calabrese & Spergel (2016)
Eridanus II	HER	$1.9^{+0.9}_{-0.8}$	$6.3^{+2.1}_{-2.3}$	$1.2^{+0.6}_{-0.4}$	0	$6.31^{+33.50}_{-5.05}$	$2.51^{+37.30}_{-2.39}$		Hayashi et al. (2023), Hayashi et al. (2016)
	Dehnen	–	–	0(core)	-	0.877		$M_o = 4.79\ 10^8 M_\odot$	Contenta et al. (2018)
	Dehnen	–	–	1(cusp)	-	1.078		$M_o = 2.94\ 10^8 M_\odot$	Contenta et al. (2018)
Grus 1	HER	$1.8^{+0.8}_{-0.8}$	$6.3^{+2.1}_{-2.2}$	$0.6^{+0.4}_{-0.6}$	0	$3.98^{+27.64}_{-3.48}$	$10.0^{+148.0}_{-9.0}$		Hayashi et al. (2023), Hayashi et al. (2016)
Grus 2	HER	$1.7^{+0.8}_{-0.8}$	$6.5^{+2.1}_{-2.2}$	$1.0^{+0.6}_{-0.7}$	0	$0.063^{+0.73}_{-0.062}$	$19.95^{+1975}_{-19.94}$		Hayashi et al. (2023), Hayashi et al. (2016)
Horologium I	HER	$1.7^{+0.8}_{-0.8}$	$6.4^{+2.1}_{-2.2}$	$1.1^{+0.7}_{-0.6}$	0	0.158	1585		Hayashi et al. (2023), Hayashi et al. (2016)
Triangulum II	HER	$1.7^{+0.8}_{-0.9}$	$6.5^{+2.2}_{-2.1}$	$0.8^{+0.6}_{-0.7}$	0	0.063	3.98		Hayashi et al. (2023), Hayashi et al. (2016)
	EIN	$0.52^{+0.32}_{-0.27}$	-	-	-	$0.64^{+1.76}_{-0.55}$	$800.0^{+2070.0}_{-660.0}$		Bonnivard et al. (2015), Saturni et al. (2019)
	Soliton+NFW	–	–	–	-	0.16		$m_{22} = 3.8$	Calabrese & Spergel (2016)
Hydra II	HER	$1.7^{+0.8}_{-0.9}$	$6.6^{+2.2}_{-2.1}$	$0.8^{+0.6}_{-0.7}$	0	0.025	3.16		Hayashi et al. (2023), Hayashi et al. (2016)
Pisces II	HER	$1.7^{+0.8}_{-0.8}$	$6.4^{+2.1}_{-2.2}$	$1.1^{+0.7}_{-0.6}$	0	0.1	630.96		Hayashi et al. (2023), Hayashi et al. (2016)
Tucana 2	HER	$1.7^{+0.8}_{-0.9}$	$6.3^{+2.1}_{-2.3}$	$1.0^{+0.7}_{-0.6}$	0	0.50	50.12		Hayashi et al. (2023), Hayashi et al. (2016)

Table 7 Continued.

dSphs	Profile	α	β	γ	δ	r_s kpc	ρ_s $10^{-3}M_\odot \cdot pc^{-3}$	Additional info	References
Tucana 3	HER	$1.7^{+0.8}_{-0.8}$	$6.5^{+2.2}_{-2.1}$	$0.9^{+0.6}_{-0.7}$	0	0.063	3.98		Hayashi et al. (2023), Hayashi et al. (2016)
Tucana 4	HER	$1.7^{+0.8}_{-0.8}$	$6.3^{+2.1}_{-2.3}$	$1.1^{+0.7}_{-0.6}$	0	0.32	100.0		Hayashi et al. (2023), Hayashi et al. (2016)
Reticulum II	HER	$1.8^{+0.8}_{-0.8}$	$6.3^{+2.1}_{-2.2}$	$0.8^{+0.5}_{-0.6}$	0	1.96	39.81		Hayashi et al. (2023), Hayashi et al. (2016)
	EIN	$0.56^{+0.29}_{-0.27}$	-	-	-	$0.41^{+2.36}_{-0.34}$	$65.0^{+220.0}_{-50.0}$		Bonnivard et al. (2015), Saturni et al. (2019)
	EIN	0.4	-	-	-	0.2	70.0		Regis et al. (2017)
Sagittarius	truncatedISO	1.156	-	-	-	0.34		$m_h = 2.4 \cdot 10^9\ M_\odot, r_{cut} = 4.08kpc$	Viana et al. (2012)
	NFW	1	3	1	0	1.30	11.0		Viana et al. (2012)
Willman I	HER	$1.8^{+0.9}_{-0.8}$	$6.4^{+2.1}_{-2.2}$	$1.2^{+0.6}_{-0.5}$	0	1.58	31.62		Hayashi et al. (2023), Hayashi et al. (2016)
	NFW	1	3	1	0	0.18	400		Bringmann et al. (2009)
	NFW	1	3	1	0	0.173	400.0		Simon & Geha (2007), Sánchez-Conde et al. (2011)
	NFW	1	3	1	0	0.17		$log_{10}(J\text{GeV}^2\text{cm}^{-5}) = 19.1 \pm 0.31$	MAGIC Collaboration et al. (2016)

Table 8. DM density distribution profiles in galaxy groups. Profiles marked with a † symbol represent total mass (luminous+dark matter). Where a reference is not provided, it follows the reference of the first row of the corresponding table cell.

Galaxy group	Profile	α	β	γ	δ	r_s kpc	ρ_s $10^{-3} M_\odot \cdot pc^{-3}$	References
NGC 5044	NFW	1	3	1	0	77.00 ± 2.00	4.02	Gastaldello et al. (2007)
	BUR	2	3	1	1	16.97 ± 2.36	87.32 ± 27.73	Gopika & Desai (2021)
	EIN	$\alpha = 0.24 \pm 0.003$	-	-	-	84.42 ± 0.18	0.862 ± 0.010	Gopika & Desai (2023)
NGC 1550	NFW	1	3	1	0	48.00 ± 4.00	11.73	Gastaldello et al. (2007)
	NFW†	1	3	1	0	94.96	3.12	Sun et al. (2009)
	BUR	2	3	1	1	21.86 ± 2.78	45.72 ± 13.10	Gopika & Desai (2021)
NGC 2563	NFW	1	3	1	0	76.00 ± 22.00	3.06	Gastaldello et al. (2007)
	BUR	2	3	1	1	38.11 ± 6.88	11.49 ± 5.07	Gopika & Desai (2021)
	EIN	$\alpha = 0.19 \pm 0.06$	-	-	-	61.47 ± 7.71	1.11 ± 0.305	Gopika & Desai (2023)
NGC 533	NFW	1	3	1	0	43.00 ± 4.0	11.73	Gastaldello et al. (2007)
	NFW†	1	3	1	0	100.66	2.64	Sun et al. (2009)
	BUR	2	3	1	1	39.61 ± 4.29	12.37 ± 3.5	Gopika & Desai (2021)
NGC 5129	NFW	1	3	1	0	43.00 ± 10.00	8.10	Gastaldello et al. (2007)
	NFW†	1	3	1	0	111.95	1.39	Sun et al. (2009)
	BUR	2	3	1	1	42.63 ± 4.71	8.13 ± 0.99	Gopika & Desai (2021)
	EIN	$\alpha = 0.49 \pm 0.12$	-	-	-	71.86 ± 5.38	0.775 ± 0.115	Gopika & Desai (2023)
NGC 4325	NFW	1	3	1	0	75.00 ± 18.00	4.25	Gastaldello et al. (2007)
	NFW†	1	3	1	0	86.32	3.5	Sun et al. (2009)
	BUR	2	3	1	1	35.15 ± 3.36	17.76 ± 2.54	Gopika & Desai (2021)
NGC 6338	NFW†	1	3	1	0	120.68	3.63	Sun et al. (2009)
NGC 741	NFW†	1	3	1	0	167.21	1.08	Sun et al. (2009)
NGC 383	NFW†	1	3	1	0	191.91	1.11	Sun et al. (2009)
NGC 1132	NFW†	1	3	1	0	249.72	0.36	Sun et al. (2009)
NGC 4104	NFW†	1	3	1	0	125.61	2.28	Sun et al. (2009)
NGC 6269	NFW†	1	3	1	0	36.65	3.17	Sun et al. (2009)
NGC 5098	NFW†	1	3	1	0	93.49	2.28	Sun et al. (2009)
NGC 1407	NFW	1	3	1	0	$170.00^{+200.00}_{-80.00}$	$1.20^{+1.70}_{-0.80}$	Romanowsky et al. (2009)
	NFW	1	3	1	0	$140.00^{+160.00}_{-70.00}$	$1.50^{+2.10}_{-1.00}$	
	NFW	1	3	1	0	230^{+290}_{-110}	$0.83^{+1.23}_{-0.50}$	
	NFW	1	3	1	0	120^{+40}_{-40}	$2.4^{+1.8}_{-0.9}$	
NGC 6842	EIN	$a = 0.17$	-	-	-	12.26	87.43	Buote (2017)
	NFW	1	3	1	0	10.55	120.40	
	ISO	2	2	0	0	1.3	$1.15 \cdot 10^3$	
	NFW	1	3	1	0	5.1	659.54	Khosroshahi et al. (2004)
NGC 1600	NFW	1	3	1	0	4.71	985.86	Runge et al. (2022)
	EIN	$\alpha = 0.16$	-	-	-	10.01	259.93	
	NFW	1	3	1	0	21.24	95.68	
	EIN	$\alpha = 0.16$	-	-	-	34.90	39.11	
UGC 5088	NFW†	1	3	1	0	87.42	2.12	Sun et al. (2009)
UGC 842	NFW†	1	3	1	0	93.29	5.01	Sun et al. (2009)
Abell 262	NFW	1	3	1	0	141 ± 16	2.35	Gastaldello et al. (2007)
	NFW†	1	3	1	0	185.06	1.44	Sun et al. (2009)
	BUR	2	3	1	1	53.38 ± 2.19	15.49 ± 1.30	Gopika & Desai (2021)
	EIN	$\alpha = 0.25 \pm 0.02$	-	-	-	161.16 ± 17.16	0.439 ± 0.075	Gopika & Desai (2023)
Abell 2717	NFW	1	3	1	0	233.0 ± 18	0.99	Gastaldello et al. (2007)
	NFW†	1	3	1	0	347.26	0.53	Sun et al. (2009)
	BUR	2	3	1	1	115.92 ± 5.02	4.36 ± 0.24	Gopika & Desai (2021)
	EIN	$\alpha = 0.29 \pm 0.03$	-	-	-	253.23 ± 13.38	0.222 ± 0.025	Gopika & Desai (2023)
Abell 3581	NFW†	1	3	1	0	79.81	8.09	Sun et al. (2009)
Abell 1177	NFW†	1	3	1	0	105.39	3.61	Sun et al. (2009)
Abell 160	NFW†	1	3	1	0	232.24	0.86	Sun et al. (2009)
Abell 3880	NFW†	1	3	1	0	194.38	1.98	Sun et al. (2009)
Abell 1991	NFW†	1	3	1	0	161.22	2.78	Sun et al. (2009)
Abell 1275	NFW†	1	3	1	0	147.82	2.06	Sun et al. (2009)
Abell 2092	NFW†	1	3	1	0	22.34	45.00	Sun et al. (2009)

Table 8 Continued.

Galaxy group	Profile	α	β	γ	δ	r_s **kpc**	ρ_s $10^{-3} M_\odot \cdot pc^{-3}$	References
Abell 744	NFW†	1	3	1	0	204.50	1.31	Sun et al. (2009)
Abell 2462	NFW†	1	3	1	0	192.74	1.38	Sun et al. (2009)
Abell 1692	NFW†	1	3	1	0	124.34	3.93	Sun et al. (2009)
Abell 2550	NFW†	1	3	1	0	138.74	2.62	Sun et al. (2009)
Abell 2589	BUR	2	3	1	1	83.11 ± 1.15	6.29 ± 0.15	Gopika & Desai (2021)
	EIN	$\alpha = 0.29 \pm 0.02$	-	-	-	130.74 ± 3.94	0.666 ± 0.035	Gopika & Desai (2023)
MKW 4	NFW	1	3	1	0	81.00 ± 7.00	5.28	Gastaldello et al. (2007)
	NFW†	1	3	1	0	137.11	1.86	Sun et al. (2009)
	BUR	2	3	1	1	41.73 ± 2.70	21.76 ± 3.49	Gopika & Desai (2021)
	EIN	$\alpha = 0.18 \pm 0.02$	-	-	-	68.24 ± 3.78	1.77 ± 0.202	Gopika & Desai (2023)
AWM 4	NFW	1	3	1	0	154.00 ± 17.00	2.43	Gastaldello et al. (2007)
	BUR	2	3	1	1	76.96 ± 6.16	9.19 ± 1.01	Gopika & Desai (2021)
	EIN	$\alpha = 0.31 \pm 0.05$	-	-	-	204.42 ± 29.99	0.388 ± 0.098	Gopika & Desai (2023)
RGH 80	NFW	1	3	1	0	78.00 ± 8.00	3.16	Gastaldello et al. (2007)
	BUR	2	3	1	1	28.24 ± 1.94	21.68 ± 3.57	Gopika & Desai (2021)
	EIN	$\alpha = 0.23 \pm 0.01$	-	-	-	70.24 ± 1.22	0.876 ± 0.030	Gopika & Desai (2023)
HCG 51	NFW†	1	3	1	0	218.01	0.51	Sun et al. (2009)
RBS 461	NFW†	1	3	1	0	116.88	3.92	Sun et al. (2009)
IC 1860	NFW	1	3	1	0	101.10 ± 12.00	2.78	Gastaldello et al. (2007)
	BUR	2	3	1	1	53.34 ± 1.65	9.33 ± 0.49	Gopika & Desai (2021)
	EIN	$\alpha = 0.40 \pm 0.04$	-	-	-	117.53 ± 9.07	0.560 ± 0.075	Gopika & Desai (2023)
ESO 5520200	NFW	1	3	1	0	171.00 ± 27.00	1.68	Gastaldello et al. (2007)
	BUR	2	3	1	1	120.87 ± 12.54	3.21 ± 0.52	Gopika & Desai (2021)
	EIN	$\alpha = 0.21 \pm 0.04$	-	-	-	208.57 ± 12.32	0.288 ± 0.031	Gopika & Desai (2023)
ESO 3060170	NFW	1	3	1	0	162.00 ± 54.00	2.35	Gastaldello et al. (2007)
	BUR	2	3	1	1	56.10 ± 2.22	17.70 ± 0.56	Gopika & Desai (2021)
ESO 552-020	NFW†	1	3	1	0	140.05	2.25	Sun et al. (2009)
ESO 306-017	NFW†	1	3	1	0	22.34	45.00	Sun et al. (2009)
ESO 351-021	NFW†	1	3	1	0	194.25	0.67	Sun et al. (2009)
RXJ 1159.8+5531	NFW	1	3	1	0	104.00 ± 77.00	3.90	Gastaldello et al. (2007)
	BUR	2	3	1	1	47.03 ± 4.07	18.75 ± 3.01	Gopika & Desai (2021)
RXJ 1022+3830	NFW†	1	3	1	0	157.19	1.98	Sun et al. (2009)
RXJ 1159	NFW†	1	3	1	0	218.49	1.01	Sun et al. (2009)
RXC J2315.7-0222	NFW†	1	3	1	0	62.38	8.96	Démoclès et al. (2010)
RXC J0216.7-4749	NFW†	1	3	1	0	346.85	0.52	Démoclès et al. (2010)
SLS2 J143000	NFW	1	3	1	0	179.50	3.11	Thanjavur et al. (2010)
	HER	1	4	1	0	391.40	1.29	
	ISO	2	2	0	0	6323.23	0.031	
SLS2 J143139	NFW	1	3	1	0	118.84	5.27	Thanjavur et al. (2010)
	HER	1	4	1	0	292.74	1.75	
	ISO	2	2	0	0	2864.35	0.032	
MS 0116.3-0115	NFW	1	3	1	0	202.00 ± 115.00	1.09	Gastaldello et al. (2007)
	BUR	2	3	1	1	71.09 ± 6.29	7.09 ± 0.93	Gopika & Desai (2021)
3C 449	NFW†	1	3	1	0	147.14	1.02	Sun et al. (2009)
3C 442A	NFW†	1	3	1	0	22.34	45.00	Sun et al. (2009)
AS 1101	NFW†	1	3	1	0	152.29	3.29	Sun et al. (2009)

Table 9. DM density distribution profiles in Galaxy Clusters. Profiles marked with a † symbol represent total mass (luminous+dark matter). Where a reference is not provided, it follows the reference of the first row of the corresponding table cell.

Cluster	**Profile**	α	β	γ	δ	r_s **Mpc**	ρ_s $10^{-3} M_\odot \cdot pc^{-3}$	**Additional info**	**References**
Perseus	NFW	1	3	1	0	0.477	0.725		Sánchez-Conde et al. (2011)
	NFW	1	3	1	0	0.384	1.06		Aleksić et al. (2010)
	NFW†	1	3	1	0	0.36	1.18		Simionescu et al. (2011)
	NFW	1	3	1	0	0.390	0.97		Ettori et al. (2002)
	King(ISO)	2	3	0	0	0.1	6.14		Ettori et al. (2002)
	NFW†	1	3	1	0	0.47	0.92		Darragh-Ford et al. (2023)
Coma	NFW	1	3	1	0	0.609	0.644		Sánchez-Conde et al. (2011)
	NFW	1	3	1	0	0.36	1.183		Gavazzi et al. (2009)
	NFW	1	3	1	0	0.7	0.73		Kubo et al. (2007)
	NFW	1	3	1	0	0.46	0.82		Ettori et al. (2002)
	King(ISO)	2	3	0	0	0.18	2.63		Ettori et al. (2002)
	NFW	1	3	1	0	0.61	0.48		Ando & Nagai (2012)
	NFW†	1	3	1	0	0.20	6.09		Rines et al. (2004), Rines et al. (2003)
	NFW†	1	3	1	0	0.47	0.84		
	HER†	1	4	1	0	0.68	0.39		
	HER†	1	4	1	0	1.9	0.05		
	SIS†	2	2	2	0	0.68	0.39		
	NFW†	1	3	1	0	0.81	0.26		Okabe et al. (2010a)
	SIS†	2	2	2	0	-		$\sigma_v = 673.0^{+73.7}_{-69.7}$ km/s	
	NFW†	1	3	1	0	0.78	0.27		Okabe et al. (2014)
	NFW†	1	3	1	0	0.86	0.22		
Ophiuchus	NFW	1	3	1	0	0.760	0.581		Sánchez-Conde et al. (2011)
Virgo	HER	1	4	1	0	$1.07^{-0.20}_{+0.36}$	0.16 ± 0.07		McLaughlin (1999)
	NFW	1	3	1	0	$0.560^{-0.15}_{+0.20}$	$0.32^{0.26}_{-0.13}$		McLaughlin (1999)
	NFW	1	3	1	0	0.433	0.681		Sánchez-Conde et al. (2011)
Fornax	NFW	1	3	1	0	0.098	5.8		Abramowski et al. (2012b)
	NFW	1	3	1	0	0.220	0.5		
	NFW	1	3	1	0	0.050	6.5		
	NFW	1	3	1	0	0.034	8.8		
	NFW	1	3	1	0	0.200	0.61		
	BUR	2	3	1	1	0.012	72.8		
	BUR	2	3	1	1	0.094	3.1		
	NFW	1	3	1	0	0.201	1.10		Sánchez-Conde et al. (2011)
	NFW	1	3	1	0	0.26	0.72		Ando & Nagai (2012)
NGC 5813	NFW	1	3	1	0	0.115	1.45		Sánchez-Conde et al. (2011)
	NFW	1	3	1	0	0.16	0.89		Ando & Nagai (2012)
NGC 5846	NFW	1	3	1	0	0.132	1.35		Sánchez-Conde et al. (2011)
	NFW	1	3	1	0	0.11	1.06		Ando & Nagai (2012)
SPT 0517-5430	NFW†	1	3	1	0	0.28	1.88		McInnes et al. (2009)
SPT 0509-5342	NFW†	1	3	1	0	0.24	1.79		McInnes et al. (2009)
SPT 0528-5300	NFW†	1	3	1	0	0.28	1.12		McInnes et al. (2009)
SCSO J232540.2-544430.9	NFW†	1	3	1	0	0.06	5.78		McInnes et al. (2009)
SCSO J232230.9-541608.3	NFW†	1	3	1	0	0.11	4.0		McInnes et al. (2009)
31 more SCS...	NFW†	1	3	1	0				McInnes et al. (2009)
Abell 1795	NFW	1	3	1	0	$0.41^{0.13}_{-0.09}$	0.91		Schmidt & Allen (2007)

Table 9 Continued.

Cluster	Profile	α	β	γ	δ	r_s Mpc	ρ_s $10^{-3} M_\odot \cdot pc^{-3}$	Additional info	References
	NFW	1	3	1	0	0.56	0.49		Ando & Nagai (2012)
	NFW	1	3	1	0	1.02	0.22		Ettori et al. (2002)
	King(ISO)	2	3	0	0	0.31	1.05		
	NFW	1	3	1	0	0.39	0.96		Ettori et al. (2019)
	EIN	$\alpha = 5$	-	-	-	0.48		$c = 1.92$	
	ISO	2	2	0	0	0.14	3.93		
	BUR	2	3	1	1	0.15	0.40		
	HER	1	4	1	0	0.72	0.24		
	NFW	1	3	1	0	0.411 ± 0.007	1.05 ± 0.03		Bernal et al. (2017)
	NFW	1	3	1	0	$0.45^{+1.59}_{-0.23}$	0.83		Voigt & Fabian (2006)
	POW	$1.24^{+0.15}_{-0.16}$	-	-	-	-	-		
Abell 2029	NFW	1	3	1	0	$0.28^{0.03}_{-0.02}$	2.27		Schmidt & Allen (2007)
	NFW	1	3	1	0	0.68	0.44		Ando & Nagai (2012)
	NFW	1	3	1	0	1.39	0.18		Ettori et al. (2002)
	King(ISO)	2	3	0	0	0.43	0.86		
	NFW	1	3	1	0	0.51	0.83		Ettori et al. (2019)
	EIN	$\alpha = 5$	-	-	-	0.57		$c = 1.95$	
	ISO	2	2	0	0	0.20	3.30		
	BUR	2	3	1	1	0.19	0.38		
	HER	1	4	1	0	0.93	0.22		
	NFW†	1	3	1	0	0.35	1.93		Darragh-Ford et al. (2023)
	NFW	1	3	1	0	0.77	0.89		Lewis et al. (2003)
	POW	-1.19 ± 0.04	-	-	-	-	–		
	NFW	1	3	1	0	0.351 ± 0.007	1.84 ± 0.05		Bernal et al. (2017)
	NFW	1	3	1	0	$0.58^{+0.94}_{-0.25}$	0.88		Voigt & Fabian (2006)
	POW	$1.13^{+0.09}_{-0.09}$	-	-	-	-	-		
Abell 478	NFW	1	3	1	0	$0.56^{0.09}_{-0.08}$	0.68		Schmidt & Allen (2007)
	NFW	1	3	1	0	0.66	0.45		Ando & Nagai (2012)
	NFW	1	3	1	0	0.51	0.80		Babyk et al. (2014)
	NFW†	1	3	1	0	0.48	1.07		Darragh-Ford et al. (2023)
	NFW†	1	3	1	0	0.80	0.44		Okabe et al. (2016)
	SIS†	2	2	2	0	-		$\sigma_v = 958.67^{+58.11}_{-62.96}$km/s	
	NFW	1	3	1	0	0.505 ± 0.015	0.93 ± 0.04		Bernal et al. (2017)
	NFW	1	3	1	0	$1.03^{+inf}_{-0.63}$	0.35		Voigt & Fabian (2006)
	POW	$0.94^{+0.10}_{-0.10}$	-	-	-	-	-		
Abell 1413	NFW	1	3	1	0	$0.43^{0.14}_{-0.09}$	0.90		Schmidt & Allen (2007)
	NFW	1	3	1	0	0.408 ± 0.011	1.19 ± 0.05		Bernal et al. (2017)
Abell 2204	NFW	1	3	1	0	$0.18^{0.08}_{-0.05}$	5.73		Schmidt & Allen (2007)
	NFW†	1	3	1	0	0.28	2.25		Corless et al. (2009)
	NFW†	1	3	1	0	0.41	0.93		
	NFW†	1	3	1	0	0.4	1.08		Dahle (2006)
	NFW(CS02)†	1	3	1	0	0.3	2.02		Clowe & Schneider (2002a)
	SIS(CS02)†	2	2	2	0	-		$\sigma_v = 1040$km/s	Clowe & Schneider (2002a)
	NFW	1	3	1	0	0.30	2.02		Clowe & Schneider (2002b)
	SIS	2	2	2	0	-		$\sigma_v = 1035^{+65}_{-71}$ km/s	
Abell 383	NFW	1	3	1	0	$0.45^{0.16}_{-0.08}$	0.63		Schmidt & Allen (2007)
	NFW†	1	3	1	0	0.72	0.29		Bardeau et al. (2007)

Table 9 Continued.

Cluster	Profile	α	β	γ	δ	r_s Mpc	ρ_s $10^{-3} M_\odot \cdot pc^{-3}$	Additional info	References
	SIS†	2	2	2	0			$\theta_E = 7.4$", $\sigma = 619$km/s	
	NFW	1	3	1	0	0.43	0.52		Babyk et al. (2014)
	NFW	1	3	1	0	0.25	2.33		Chiu et al. (2018)
	NFW†	1	3	1	0	0.26	2.18		Newman et al. (2013a), Newman et al. (2013b)
(prolate)	NFW†	1	3	1	0	0.37	0.93		
	gNFW	-	-	$0.55^{+0.2}_{-0.05}$	-	0.10	16.42		Sand et al. (2008)
	gNFW	-	-	$0.45^{+0.2}_{-0.25}$	-	0.10	18.30		
	NFW	1	3	1	0	0.43	0.76		Huang et al. (2011)
	NFW	1	3	1	0	0.271 ± 0.009	1.71 ± 0.10		Bernal et al. (2017)
	SIS	2	2	2	0	-		$\sigma_v = 875.19^{34.37}_{-41.47}$km/s	Okabe et al. (2010b), Oguri et al. (2010)
	CIS	-	-	-	-			$\theta_E = 0.27$", $\theta_C < 0.04$"	
	NFW	1	3	1	0	0.22	2.65		
Abell 963	NFW	1	3	1	0	$0.40^{0.16}_{-0.10}$	0.88		Schmidt & Allen (2007)
	NFW†	1	3	1	0	0.23	3.93		Bardeau et al. (2007)
	SIS†	2	2	2	0			$\theta_E = 12.3$", $\sigma = 812$km/s	
	NFW†	1	3	1	0	0.20	2.77		Newman et al. (2013a), Newman et al. (2013b)
	SIS	2	2	2	0	-		$\sigma_v = 816.53^{37.85}_{-42.83}$km/s	Okabe et al. (2010b), Oguri et al. (2010)
	CIS	-	-	-	-			$\theta_E = 0.4$", $\theta_C = 0.46$"	
	NFW	1	3	1	0	0.95	0.16		
RXJ0439.0+0521	NFW	1	3	1	0	$0.21^{0.08}_{-0.06}$	2.29		Schmidt & Allen (2007)
RXJ1504.1-0248	NFW	1	3	1	0	$0.62^{0.43}_{-0.19}$	0.63		Schmidt & Allen (2007)
RXJ2129.6+0005	NFW	1	3	1	0	$0.41^{0.72}_{-0.20}$	0.74		Schmidt & Allen (2007)
	SIS	2	2	2	0	-		$\sigma_v = 879.92^{62.12}_{-52.16}$km/s	Okabe et al. (2010b), Oguri et al. (2010)
	CIS	-	-	-	-			$\theta_E = 0.33$", $\theta_C = 0.15$"	
	NFW	1	3	1	0	0.73	0.28		
	NFW	1	3	1	0	0.37	1.13		Chiu et al. (2018)
Abell 1835	NFW	1	3	1	0	$0.71^{0.12}_{-0.14}$	0.51		Schmidt & Allen (2007)
	NFW†	1	3	1	0	1.32	0.28		Bardeau et al. (2007)
	SIS†	2	2	2	0			$\theta_E = 26.6$", $\sigma = 1240$km/s	
	NFW	1	3	1	0	0.55	0.80		Allen et al. (2001)
	NFW†	1	3	1	0	0.30	2.41		Corless et al. (2009)
	NFW†	1	3	1	0	0.59	0.57		
	NFW†	1	3	1	0	1.01	0.28		Bardeau et al. (2007)
	NFW†	1	3	1	0	0.43	0.9		Dahle (2006)
	NFW(CS02)†	1	3	1	0	0.74	0.37		Clowe & Schneider (2002a)
	SIS(CS02)†	2	2	2	0	-		$\sigma_v = 1180$km/s	Clowe & Schneider (2002a)
	NFW†	1	3	1	0	0.64	0.68		Schmidt et al. (2001)
	NFW	1	3	1	0	0.75	0.37		Clowe & Schneider (2002b)
	SIS	2	2	2	0	-		$\sigma_v = 1233^{+66}_{-70}$ km/s	
	SIS	2	2	2	0	-		$\sigma_v = 1050.55^{56.49}_{-41.65}$km/s	Okabe et al. (2010b), Oguri et al. (2010)
	CIS	-	-	-	-			$\theta_E = 0.61$", $\theta_C = 0.46$"	

Table 9 Continued.

Cluster	Profile	α	β	γ	δ	r_s **Mpc**	ρ_s $10^{-3} M_\odot \cdot pc^{-3}$	Additional info	References
	NFW	1	3	1	0	0.91	0.28		
	NFW	1	3	1	0	$0.80^{+1.59}_{-0.38}$	0.42		Voigt & Fabian (2006)
	POW	$1.14^{+0.11}_{-0.11}$	-	-	-	-	-		
14 new objects...									Dahle (2006)
Abell 611	NFW	1	3	1	0	$0.32^{0.24}_{-0.11}$	1.23		Schmidt & Allen (2007)
	NFW	1	3	1	0	0.51	0.87		Chiu et al. (2018)
	NFW†	1	3	1	0	0.32	1.51		Newman et al. (2013a), Newman et al. (2013b)
	constrainedNFW	1	3	1	0	0.34	0.94		Romano et al. (2010)
	NFW	1	3	1	0	0.40	0.68		
	SIS	2	2	2	0	-		$\sigma_v = 778^{+26}_{-27}$ km/s	
	NFW	1	3	1	0	0.30	1.03		Newman et al. (2009)
	SIS	2	2	2	0	-		$\sigma_v = 929.34^{57.70}_{-45.26}$km/s	Okabe et al. (2010b), Oguri et al. (2010)
	CIS	-	-	-	-			$\theta_E = 0.33$", $\theta_C = 0.11$"	
	NFW	1	3	1	0	0.57	0.47		
Zwicky 3146	NFW	1	3	1	0	$1.14^{>5.0}_{-0.71}$	0.22		Schmidt & Allen (2007)
Abell 2537	NFW	1	3	1	0	$0.35^{0.28}_{-0.15}$	1.09		Schmidt & Allen (2007)
	NFW†	1	3	1	0	0.44	0.99		Newman et al. (2013a), Newman et al. (2013b)
MS2137.3-2353	NFW	1	3	1	0	$0.20^{0.03}_{-0.02}$	2.77		Schmidt & Allen (2007)
	NFW†	1	3	1	0	0.12	7.75		Newman et al. (2013a), Newman et al. (2013b)
	gNFW	1	3	$0.95^{+0.05}_{-0.30}$	-	0.20	3.45		Sand et al. (2008)
	gNFW	-	-	$0.60^{+0.15}_{-0.02}$	-	0.20	5.23		
	NFW	1	3	1	0	0.11	11.65		Comerford & Natarajan (2007), Comerford et al. (2006)
	NFW†	1	3	1	0	0.15	5.37		(Donnarumma et al. 2009)
	NFW(X-rays)	1	3	1	0	0.16	4.32		(Donnarumma et al. 2009)
	NFW(X-rays)	1	3	1	0	0.15	5.37		(Donnarumma et al. 2009)
	NFW(X-rays)	1	3	1	0	0.16	4.35		(Allen et al. 2001)
	NFW(X-rays)	1	3	1	0	0.18	3.75		(Schmidt & Allen 2007)
	NFW(X-rays)	1	3	1	0	0.16	9.39		Gavazzi (2005)
	NFW(X-rays)	1	3	1	0	0.09	11.65		Comerford et al. (2006)
	NFW	1	3	1	0	1.14	0.31		Umetsu et al. (2016), Umetsu et al. (2014)
	NFW	1	3	1	0	0.42	0.93		Chiu et al. (2018)
	NFW	1	3	1	0	$0.34^{+0.74}_{-0.16}$	1.34		Voigt & Fabian (2006)
	POW	$1.25^{+0.14}_{-0.15}$	-	-	-	-	-		
MACSJ0242.6-2132	NFW	1	3	1	0	$0.22^{0.06}_{-0.05}$	2.31		Schmidt & Allen (2007)
	dPIE(ISO)	2	2	0	0			$r_{cut} = 1.5, r_c = 0.06, 918.5^{+29.0}_{-36.1}$ km/s	Allingham et al. (2023)
	NFW†	1	3	1	0	0.21	5.05		
MACSJ1427.6-2521	NFW	1	3	1	0	$0.17^{0.12}_{-0.06}$	2.71		Schmidt & Allen (2007)
MACSJ2229.8-2756	NFW	1	3	1	0	$0.16^{0.13}_{-0.07}$	3.24		Schmidt & Allen (2007)
MACSJ0947.2+7623	NFW	1	3	1	0	$0.35^{0.24}_{-0.13}$	1.41		Schmidt & Allen (2007)
MACSJ1931.8-2635	NFW	1	3	1	0	$0.69^{2.46}_{-0.36}$	0.42		Schmidt & Allen (2007)

Table 9 Continued.

Cluster	Profile	α	β	γ	δ	r_s Mpc	ρ_s $10^{-3} M_\odot \cdot pc^{-3}$	Additional info	References
	NFW	1	3	1	0	0.27	2.85		Chiu et al. (2018)
MACSJ1115.8+0129	NFW	1	3	1	0	$1.61^{>5.0}_{-1.14}$	0.14		Schmidt & Allen (2007)
	NFW	1	3	1	0	0.87	0.36		Chiu et al. (2018)
MACSJ1532.9+3021	NFW	1	3	1	0	$0.37^{0.23}_{-0.12}$	1.03		Schmidt & Allen (2007)
MACSJ0011.7-1523	NFW	1	3	1	0	$0.59^{0.25}_{-0.19}$	0.42		Schmidt & Allen (2007)
MACSJ1720.3+3536	NFW	1	3	1	0	$0.40^{0.18}_{-0.13}$	0.87		Schmidt & Allen (2007)
	NFW	1	3	1	0	0.44	1.12		Chiu et al. (2018)
MACSJ0429.6-0253	NFW	1	3	1	0	$0.17^{0.05}_{-0.04}$	3.18		Schmidt & Allen (2007)
	NFW	1	3	1	0	0.57	0.98		Umetsu et al. (2016), Umetsu et al. (2014)
	NFW	1	3	1	0	0.35	1.53		Chiu et al. (2018)
MACSJ0159.8-0849	NFW	1	3	1	0	$0.38^{0.18}_{-0.10}$	1.15		Schmidt & Allen (2007)
	NFW	1	3	1	0	0.58	0.84		Amodeo et al. (2016)
MACSJ0329.7-0212	NFW	1	3	1	0	$0.32^{0.11}_{-0.07}$	1.05		Schmidt & Allen (2007)
	NFW	1	3	1	0	0.36	1.60		Chiu et al. (2018)
RXJ1347.5-1144	NFW	1	3	1	0	$0.54^{0.08}_{-0.11}$	1.07		Schmidt & Allen (2007)
	NFW	1	3	1	0	0.30	4.23		Broadhurst et al. (2008)
	NFW	1	3	1	0	0.37	2.05		Allen et al. (2001)
	NFW	1	3	1	0	0.74	0.75		Chiu et al. (2018)
	NFW†	1	3	1	0	0.23	8.51		Kling et al. (2005)
	SIS†	2	2	2	0	-		$\sigma_v = 1400^{+130}_{-140}$	
	gNFW	-	-	0	-	0.16	16.68		Bradač et al. (2008b)
	NFW	1	3	1	0	0.35	1.80		Bradač et al. (2008b)
	NFW	1	3	1	0	$0.60^{+0.46}_{-0.22}$	0.87		Voigt & Fabian (2006)
	POW	$1.3^{+0.1}_{-0.1}$	-	-	-	-	-		
3C295	NFW	1	3	1	0	$0.16^{0.03}_{-0.03}$	3.32		Schmidt & Allen (2007)
	NFW	1	3	1	0	0.16	3.44		Allen et al. (2001)
MACSJ1621.6+3810	NFW	1	3	1	0	$0.26^{0.21}_{-0.11}$	1.78		Schmidt & Allen (2007)
	NFW	1	3	1	0	0.70	0.54		Martinet et al. (2016)
	NFW	1	3	1	0	0.56	0.54		Martinet et al. (2016)
MS1621.5+2640	NFW†	1	3	1	0	0.94	0.24		Amodeo et al. (2016)
MACSJ1311.0-0311	NFW	1	3	1	0	$0.33^{0.18}_{-0.11}$	0.90		Schmidt & Allen (2007)
MACSJ1423.8+2404	NFW	1	3	1	0	$0.18^{0.03}_{-0.02}$	3.22		Schmidt & Allen (2007)
	NFW	1	3	1	0	0.65	0.54		Martinet et al. (2016)
	NFW	1	3	1	0	1.66	0.17		Sereno & Zitrin (2012)
MACSJ0744.9+3927	NFW	1	3	1	0	$0.36^{0.19}_{-0.13}$	0.85		Schmidt & Allen (2007)
	NFW	1	3	1	0	1.02	0.30		Chiu et al. (2018)
	NFW	1	3	1	0	1.50	0.41		Sereno & Zitrin (2012)
A2142	NFW	1	3	1	0	0.78	0.42		Ando & Nagai (2012)
	NFW	1	3	1	0	1.65	0.13		Ettori et al. (2002)
	King(ISO)	2	3	0	0	0.48	0.65		
	NFW	1	3	1	0	0.71	0.42		Ettori et al. (2019)
	EIN	$\alpha = 5$	-	-	-	0.87		$c = 1.27$	
	ISO	2	2	0	0	0.24	2.12		
	BUR	2	3	1	1	0.24	0.23		
	HER	1	4	1	0	1.26	0.10		

Table 9 Continued.

Cluster	Profile	α	β	γ	δ	r_s **Mpc**	ρ_s $10^{-3} M_\odot \cdot pc^{-3}$	Additional info	References
	NFW†	1	3	1	0	0.54	0.72		Munari et al. (2014)
A3266	NFW	1	3	1	0	0.69	0.45		Ando & Nagai (2012)
	NFW	1	3	1	0	1.58	0.12		Ettori et al. (2002)
	King(ISO)	2	3	0	0	0.36	0.87		
	NFW	1	3	1	0	1.14	0.18		Ettori et al. (2019)
	EIN	$\alpha = 5$	-	-	-	0.77		$c = 1.34$	
	ISO	2	2	0	0	0.31	1.11		
	BUR	2	3	1	1	0.31	0.13		
	HER	1	4	1	0	1.95	0.04		
A401	NFW	1	3	1	0	0.68	0.45		Ando & Nagai (2012)
	NFW	1	3	1	0	0.84	0.42		Babyk et al. (2014)
A754	NFW	1	3	1	0	0.67	0.45		Ando & Nagai (2012)
	NFW	1	3	1	0	0.71	0.44		Ando & Nagai (2012)
	NFW	1	3	1	0	1.62	0.11		Ettori et al. (2002)
	King(ISO)	2	3	0	0	0.47	0.62		
A2256	NFW	1	3	1	0	0.65	0.46		Ando & Nagai (2012)
	NFW	1	3	1	0	1.42	0.12		Ettori et al. (2002)
	King(ISO)	2	3	0	0	0.57	0.42		
A3667	NFW	1	3	1	0	0.63	0.47		Ando & Nagai (2012)
A399	NFW	1	3	1	0	0.59	0.48		Ando & Nagai (2012)
	NFW	1	3	1	0	1.22	0.19		Babyk et al. (2014)
A85	NFW	1	3	1	0	0.58	0.48		Ando & Nagai (2012)
	NFW	1	3	1	0	1.28	0.16		Ettori et al. (2002)
	King(ISO)	2	3	0	0	0.32	1.01		
	NFW	1	3	1	0	0.69	0.46		Babyk et al. (2014)
	NFW	1	3	1	0	0.58	0.48		Ettori et al. (2019)
	EIN	$\alpha = 5$	-	-	-	0.64		$c = 1.49$	
	ISO	2	2	0	0	0.19	2.38		
	BUR	2	3	1	1	0.19	0.26		
	HER	1	4	1	0	0.91	0.15		
A3571	NFW	1	3	1	0	0.57	0.49		Ando & Nagai (2012)
	NFW	1	3	1	0	1.12	0.24		Ettori et al. (2002)
	King(ISO)	2	3	0	0	0.28	1.56		
ZwCl1215	NFW	1	3	1	0	0.57	0.48		Ando & Nagai (2012)
	NFW	1	3	1	0	1.04	0.19		Ettori et al. (2019)
	EIN	$\alpha = 5$	-	-	-	1.34		$c = 0.75$	
	ISO	2	2	0	0	0.31	0.95		
	BUR	2	3	1	1	0.30	0.12		
	HER	1	4	1	0	1.33	0.07		
A2065	NFW	1	3	1	0	0.53	0.50		Ando & Nagai (2012)
A3558	NFW	1	3	1	0	0.52	0.51		Ando & Nagai (2012)
A119	NFW	1	3	1	0	0.51	0.51		Ando & Nagai (2012)
	NFW	1	3	1	0	1.10	0.18		Ettori et al. (2002)
	ISO	2	2	0	0	0.58	0.42		
	NFW†	1	3	1	0	0.23	2.01		Rines et al. (2004), Rines et al. (2003)
	NFW†	1	3	1	0	0.45	0.45		

Table 9 Continued.

Cluster	Profile	α	β	γ	δ	r_s Mpc	ρ_s $10^{-3} M_\odot \cdot pc^{-3}$	Additional info	References
	HER†	1	4	1	0	0.79	0.14		
	HER†	1	4	1	0	1.68	0.04		
	SIS†	2	2	2	0	0.68	0.19		
	NFW	1	3	1	0	0.54	0.71		Babyk et al. (2014)
A1644	NFW	1	3	1	0	0.50	0.52		Ando & Nagai (2012)
	NFW	1	3	1	0	1.22	0.09		Ettori et al. (2019)
	EIN	$\alpha = 5$	-	-	-	1.12		$c = 0.66$	
	ISO	2	2	0	0	0.30	0.67		
	BUR	2	3	1	1	0.30	0.08		
	HER	1	4	1	0	2.03	0.02		
A3158	NFW	1	3	1	0	0.49	0.52		Ando & Nagai (2012)
	NFW	1	3	1	0	0.61	0.35		Ettori et al. (2019)
	EIN	$\alpha = 5$	-	-	-	0.53		$c = 1.57$	
	ISO	2	2	0	0	0.22	1.40		
	BUR	2	3	1	1	0.22	0.16		
	HER	1	4	1	0	1.20	0.07		
A3391	NFW	1	3	1	0	0.49	0.52		Ando & Nagai (2012)
A3562	NFW	1	3	1	0	0.45	0.54		Ando & Nagai (2012)
	NFW	1	3	1	0	0.34	0.97		Ettori et al. (2002)
	King(ISO)	2	3	0	0	0.20	1.66		
A2147	NFW	1	3	1	0	0.43	0.56		Ando & Nagai (2012)
A3376	NFW	1	3	1	0	0.43	0.56		Ando & Nagai (2012)
	NFW	1	3	1	0	0.18	1.41		Ettori et al. (2002)
	King(ISO)	2	3	0	0	0.11	2.20		
A496	NFW	1	3	1	0	0.43	0.56		Ando & Nagai (2012)
	NFW	1	3	1	0	0.74	0.28		Ettori et al. (2002)
	King(ISO)	2	3	0	0	0.20	1.61		
	NFW†	1	3	1	0	0.095	14.02		Rines et al. (2004), Rines et al. (2003)
	NFW†	1	3	1	0	0.30	0.91		
	HER†	1	4	1	0	0.42	0.43		
	HER†	1	4	1	0	1.1	0.07		
	SIS†	2	2	2	0	0.68	0.16		
	NFW	1	3	1	0	0.36	0.92		Markevitch et al. (1999)
HydraA	NFW	1	3	1	0	0.42	0.56		Ando & Nagai (2012)
	NFW	1	3	1	0	0.25	1.48		Ettori et al. (2019)
	EIN	$\alpha = 5$	-	-	-	0.30		$c = 2.45$	
	ISO	2	2	0	0	0.22	1.42		
	BUR	2	3	1	1	0.01	0.60		
	HER	1	4	1	0	0.47	0.39		
	NFW†	1	3	1	0	0.46	0.57		
	SIS†	2	2	2	0	-		$\sigma_v = 631.93^{+43.71}_{-47.77}$km/s	
Hydra	NFW	1	3	1	0	0.34	0.63		Ando & Nagai (2012)
A4059	NFW	1	3	1	0	0.42	0.56		Ando & Nagai (2012)
A2199	NFW	1	3	1	0	0.42	0.57		Ando & Nagai (2012)
	NFW	1	3	1	0	0.56	0.48		Ettori et al. (2002)
	King(ISO)	2	3	0	0	0.18	2.27		

Table 9 Continued.

Cluster	Profile	α	β	γ	δ	r_s Mpc	ρ_s $10^{-3} M_\odot \cdot pc^{-3}$	Additional info	References
	NFW†	1	3	1	0	0.20	3.01		Rines et al. (2004), Rines et al. (2003)
	NFW†	1	3	1	0	1.02	0.10		
	HER†	1	4	1	0	0.64	0.24		
	HER†	1	4	1	0	2.89	0.02		
	SIS†	2	2	2	0	0.68	0.21		
	NFW	1	3	1	0	0.18	3.11		Markevitch et al. (1999)
A133	NFW	1	3	1	0	0.40	0.57		Ando & Nagai (2012)
	NFW	1	3	1	0	0.24	3.67		Babyk et al. (2014)
	NFW	1	3	1	0	0.221 ± 0.008	2.08 ± 0.15		Bernal et al. (2017)
A576	NFW	1	3	1	0	0.39	0.58		Ando & Nagai (2012)
	NFW†	1	3	1	0	0.18	7.56		Rines et al. (2004), Rines et al. (2003)
	NFW†	1	3	1	0	0.47	0.74		
	HER†	1	4	1	0	0.58	0.47		
	HER†	1	4	1	0	1.65	0.06		
	SIS†	2	2	2	0	0.68	0.34		
2A0335	NFW	1	3	1	0	0.38	0.59		Ando & Nagai (2012)
	NFW	1	3	1	0	0.63	0.33		Ettori et al. (2002)
	King(ISO)	2	3	0	0	0.19	1.63		
2A 0335+096	NFW	1	3	1	0	$0.13^{+5.38}_{-0.10}$	3.74		Voigt & Fabian (2006)
	POW	$0.55^{+0.09}_{-0.09}$	-	-	-	-	-		
A2657	NFW	1	3	1	0	0.38	0.59		Ando & Nagai (2012)
A2063	NFW	1	3	1	0	0.38	0.59		Ando & Nagai (2012)
A1736	NFW	1	3	1	0	0.37	0.59		Ando & Nagai (2012)
MKW3s	NFW	1	3	1	0	0.37	0.60		Ando & Nagai (2012)
MKW 4	NFW	1	3	1	0	0.154 ± 0.007	1.71 ± 0.13		Bernal et al. (2017)
A2589	NFW	1	3	1	0	0.36	0.61		Ando & Nagai (2012)
	NFW	1	3	1	0	0.21	1.13		Buote & Lewis (2004)
	POW	1.65 ± 0.21	-	-	-	-	–		
	NFW†	1	3	1	0	0.26	1.06		Zappacosta et al. (2006)
	N04†	0.41 ± 0.07	-	-	-	0.19		$c = 7.1 \pm 0.3$	Zappacosta et al. (2006)
	POW†	1.82 ± 0.18	-	-	-	-	–		Zappacosta et al. (2006)
A2052	NFW	1	3	1	0	0.35	0.61		Ando & Nagai (2012)
A2634	NFW	1	3	1	0	0.34	0.62		Ando & Nagai (2012)
A4038	NFW	1	3	1	0	0.33	0.63		Ando & Nagai (2012)
EXO0422	NFW	1	3	1	0	0.32	0.64		Ando & Nagai (2012)
A1367	NFW	1	3	1	0	0.54	0.51		Ando & Nagai (2012)
	NFW	1	3	1	0	0.72	0.17		Ettori et al. (2002)
	King(ISO)	2	3	0	0	0.72	0.25		
	NFW†	1	3	1	0	0.095	22.41		Rines et al. (2004), Rines et al. (2003)
	NFW†	1	3	1	0	0.37	0.87		
	HER†	1	4	1	0	0.39	0.75		
	HER†	1	4	1	0	1.6	0.05		
	SIS†	2	2	2	0	0.68	0.23		
Centaurus	NFW	1	3	1	0	0.39	0.58		Ando & Nagai (2012)

Table 9 Continued.

Cluster	Profile	α	β	γ	δ	r_s **Mpc**	ρ_s $10^{-3} M_\odot \cdot pc^{-3}$	Additional info	References
	NFW	1	3	1	0	0.35	0.88		Ettori et al. (2002)
	King(ISO)	2	3	0	0	0.08	7.20		
M49	NFW	1	3	1	0	0.19	0.82		Ando & Nagai (2012)
NGC463	NFW	1	3	1	0	0.11	1.05		Ando & Nagai (2012)
NGC504	NFW	1	3	1	0	0.17	0.87		Ando & Nagai (2012)
common	EIN	$\eta = 3.87$	-	-	-	1.247	-		Ando & Nagai (2012)
A68	NFW†	1	3	1	0	0.55	0.66		Bardeau et al. (2007)
	SIS†	2	2	2	0			$\theta_E = 12.9$", $\sigma = 880$km/s	
	SIS	2	2	2	0	-		$\sigma_v = 869.03^{70.82}_{-75.14}$km/s	Okabe et al. (2010b), Oguri et al. (2010)
	CIS	-	-	-	-			$\theta_E = 0.3$", $\theta_C = 0.11$"	
	NFW	1	3	1	0	0.56	0.42		
A209	NFW†	1	3	1	0	0.75	0.39		Bardeau et al. (2007)
	SIS†	2	2	2	0			$\theta_E = 12.4$", $\sigma = 883$km/s	
	NFW	1	3	1	0	0.58	0.38		Babyk et al. (2014)
	NFW	1	3	1	0	0.90	0.32		Chiu et al. (2018)
	SIS	2	2	2	0	-		$\sigma_v = 918.76^{34.06}_{-40.37}$km/s	Okabe et al. (2010b), Oguri et al. (2010)
	CIS	-	-	-	-			$\theta_E = 0.7$", $\theta_C = 0.65$"	
	NFW	1	3	1	0	1.14	0.18		
A267	NFW†	1	3	1	0	0.36	0.95		Bardeau et al. (2007)
	SIS†	2	2	2	0			$\theta_E = 6.7$", $\sigma = 634$km/s	
	SIS	2	2	2	0	-		$\sigma_v = 778.05^{45.65}_{-37.28}$km/s	Okabe et al. (2010b), Oguri et al. (2010)
	CIS	-	-	-	-			$\theta_E = 0.26$", $\theta_C = 0.07$"	
	NFW	1	3	1	0	0.33	1.05		
A1689	NFW†	1	3	1	0	0.75	0.83		Bardeau et al. (2007)
	SIS†	2	2	2	0			$\theta_E = 31.8$", $\sigma = 1277$km/s	
	NFW†	1	3	1	0	0.81	0.54		Bardeau et al. (2005)
	SIS†	2	2	2	0			$\theta_E = 22.4$", $\sigma = 998$km/s	Bardeau et al. (2005)
	POW†	$q = 0.75$	-	-	-			$\theta_E = 14.60$"	Bardeau et al. (2005)
	SIS†	2	2	2	0			$\theta_E = 23.8$", $\sigma = 1028$km/s	Clowe & Schneider (2001a)
	NFW†	1	3	1	0	0.44	1.80		Clowe & Schneider (2001a)
	POW†	$q = 0.88$	-	-	-			$\theta_E = 18.0$"	King et al. (2002a)
	NFW†	1	3	1	0	0.55	1.08		King et al. (2002a)
	NFW	1	3	1	0	0.21	9.98		Broadhurst et al. (2008)
	NFW	1	3	1	0	0.21	9.98		Broadhurst et al. (2008)
	NFW†	1	3	1	0	0.17	12.33		Corless et al. (2009)
	NFW†	1	3	1	0	0.23	6.09		
	NFW(CS01)†	1	3	1	0	0.31	1.8		Clowe & Schneider (2001b)
	SIS†	2	2	2	0	-		$\sigma_v = 1028 \pm 35$km/s	Clowe & Schneider (2001b)
	NFW†	1	3	1	0	0.23	6.71		Umetsu & Broadhurst (2008)
	NFW†	1	3	1	0	0.56	0.83		Bardeau et al. (2007)
	NFW†	1	3	1	0	0.41	3.14		Limousin et al. (2007)
	NFW†	1	3	1	0	0.60	0.54		Bardeau et al. (2005)
	NFW(C03)†	1	3	1	0	0.27	3.44		
	NFW†	1	3	1	0	0.37	1.60		King et al. (2002a)
	NFW†	1	3	1	0	0.41	1.08		King et al. (2002b)

Table 9 Continued.

Cluster	Profile	α	β	γ	δ	r_s **Mpc**	ρ_s $10^{-3} M_\odot \cdot pc^{-3}$	Additional info	References
	NFW(SL+WL)†	1	3	1	0	0.25	6.24		Umetsu & Broadhurst (2008)
	NFW(WL)†	1	3	1	0	0.23	7.19		Umetsu & Broadhurst (2008)
	NFW†	1	3	1	0	0.36	3.14		Halkola et al. (2006)
	SIS†	2	2	2	0	0.11	1450		Halkola et al. (2006)
	NFW†	1	3	1	0	0.23	7.53		Broadhurst et al. (2005a)
	NFW†	1	3	1	0	0.50	1.80		Halkola et al. (2006)
	NFW†	1	3	1	0	0.47	2.17		Broadhurst et al. (2005b)
	NFW†	1	3	1	0	0.26	3.24		Andersson & Madejski (2004)
	NFW†	1	3	1	0	0.27	3.44		Clowe (2003)
	NFW†	1	3	1	0	0.27	5.65		Lemze et al. (2008)
	NFW†	1	3	1	0	–		$c = 22.1$	Medezinski et al. (2007)
	NFW†	1	3	1	0	–		$c = 6.0$	Bardeau et al. (2007)
	NFW	1	3	1	0	0.30	3.99		Umetsu et al. (2015), and references therein
	NFW	1	3	1	0	0.21	3.67		Clowe & Schneider (2001a)
	SIS	2	2	2	0	-		$\sigma_v = 1028 \pm 35$ km/s	Clowe & Schneider (2001a)
	NFW	1	3	1	0	0.87	1.03		Halkola et al. (2006)
	NFW†	1	3	1	0	0.67	1.80		
	SIS (DM)	2	2	2	0	$r_c = 0.11$		$\sigma_v = 1450^{+39}_{-31}$ km/s	
	SIS†	2	2	2	0	$r_c = 0.1$		$\sigma_v = 1514^{+18}_{-17}$ km/s	
A1763	NFW†	1	3	1	0	1.05	0.29		Bardeau et al. (2007)
	SIS†	2	2	2	0			$\theta_E = 15$", $\sigma = 932$km/s	
A2218	NFW†	1	3	1	0	0.38	2.46		Bardeau et al. (2007)
	SIS†	2	2	2	0			$\theta_E = 21.2$", $\sigma = 1040$km/s	
A2219	NFW†	1	3	1	0	0.84	0.66		Bardeau et al. (2007)
	SIS†	2	2	2	0			$\theta_E = 23.4$", $\sigma = 1175$km/s	
	NFW	1	3	1	0	1.05	0.61		Hoekstra et al. (2002)
	SIS	2	2	2	0	-		$\sigma_v = 1132.87^{43.65}_{-58.12}$km/s	Okabe et al. (2010b), Oguri et al. (2010)
	CIS	-	-	-	-			$\theta_E = 0.47$", $\theta_C = 0.07$"	
	NFW	1	3	1	0	0.39	1.44		
A2390	NFW†	1	3	1	0	0.47	1.33		Bardeau et al. (2007)
	SIS†	2	2	2	0			$\theta_E = 18.1$", $\sigma = 1015$km/s	
	NFW	1	3	1	0	0.76	0.44		Allen et al. (2001)
	NFW†	1	3	1	0	0.76	0.45		Newman et al. (2013a), Newman et al. (2013b)
	NFW	1	3	1	0	0.650 ± 0.020	0.56 ± 0.03		Bernal et al. (2017)
	SIS	2	2	2	0	-		$\sigma_v = 951.38^{55.34}_{-31.23}$km/s	Okabe et al. (2010b), Oguri et al. (2010)
	CIS	-	-	-	-			$\theta_E = 0.49$", $\theta_C = 0.13$"	
	NFW	1	3	1	0	0.42	1.13		
A1703	NFW	1	3	1	0	0.31	3.36		Broadhurst et al. (2008)
	NFW†	1	3	1	0	0.42	1.55		Zitrin et al. (2010)
A370	NFW	1	3	1	0	0.51	1.99		Broadhurst et al. (2008)
	NFW(G1)	1	3	1	0	0.42	1.08		Comerford & Natarajan (2007), Comerford et al. (2006)
	NFW(G2)	1	3	1	0	0.35	1.29		

Table 9 Continued.

Cluster	Profile	α	β	γ	δ	r_s Mpc	ρ_s $10^{-3} M_\odot \cdot pc^{-3}$	Additional info	References
CIG 2244-02	NFW	1	3	1	0	0.37	0.84		Comerford & Natarajan (2007), Comerford et al. (2006)
3C 220.1	NFW	1	3	1	0	0.33	0.84		Comerford & Natarajan (2007), Comerford et al. (2006)
MS 0451.6-0305	NFW	1	3	1	0	0.46	1.47		Comerford & Natarajan (2007), Comerford et al. (2006)
MS 1137.5-6625	NFW	1	3	1	0	0.54	0.47		Comerford & Natarajan (2007), Comerford et al. (2006)
CIG 0054-27	NFW(G1)	1	3	1	0	0.60	0.065		Comerford & Natarajan (2007), Comerford et al. (2006)
	NFW(G2)	1	3	1	0	0.45	0.19		
CI 0016+1609	NFW(DG256)	1	3	1	0	0.47	0.19		Comerford & Natarajan (2007), Comerford et al. (2006)
	NFW(DG251)	1	3	1	0	0.33	0.22		
	NFW(DG254)	1	3	1	0	0.45	0.41		
CI 0939+4713	NFW(G1)	1	3	1	0	0.19	0.93		Comerford & Natarajan (2007), Comerford et al. (2006)
	NFW(G2)	1	3	1	0	0.27	0.60		
	NFW(G3)	1	3	1	0	0.24	0.93		
ZwCI 0024+1652	NFW(#362)	1	3	1	0	0.30	0.98		Comerford & Natarajan (2007), Comerford et al. (2006)
	NFW(#374)	1	3	1	0	0.34	0.84		
	NFW(#380)	1	3	1	0	0.39	0.50		
CL0024+1654 (clump 1)	NFW†	1	3	1	0	0.083	49.26		Kneib et al. (2003)
(clump 2)	NFW†	1	3	1	0	0.34	0.80		Kneib et al. (2003)
	NFW	1	3	1	0	0.32	3.03		Umetsu et al. (2010)
100 more old references... 23 new object									Comerford & Natarajan (2007), Comerford et al. (2006)
AC 114	NFW	1	3	1	0			$r_{sP} = 190 \pm 30$(") 0.69, $k_{NFW} = 0.19 \pm 0.019$ 0.6	Sereno et al. (2010)
	NIE(ISO)	-	-	-	-			$b = 23.3 \pm 1.3$("), $r_{sP} = 11.1 \pm 1.2$(")	Sereno et al. (2010)
A2319	NFW	1	3	1	0	1.30	0.17		Ettori et al. (2002)
	King(ISO)	2	3	0	0	0.27	1.41		
	NFW	1	3	1	0	0.42	1.11		Ettori et al. (2019)
	EIN	$\alpha = 5$	-	-	-	0.40		$c = 2.64$	
	ISO	2	2	0	0	0.24	2.03		
	BUR	2	3	1	1	0.23	0.24		
	HER	1	4	1	0	0.67	0.43		
A3627	NFW	1	3	1	0	0.52	0.46		Ettori et al. (2002)
	King(ISO)	2	3	0	0	0.19	1.74		
PKS0745	NFW	1	3	1	0	1.15	0.24		Ettori et al. (2002)
	King(ISO)	2	3	0	0	0.40	0.90		
	NFW†	1	3	1	0	0.46	1.21		Darragh-Ford et al. (2023)
	NFW	1	3	1	0	$0.36^{0.13}_{-0.11}$	1.70		Schmidt & Allen (2007)
	NFW	1	3	1	0	0.64	0.65		Allen et al. (2001)

Table 9 Continued.

Cluster	Profile	α	β	γ	δ	r_s **Mpc**	ρ_s $10^{-3} M_\odot \cdot pc^{-3}$	Additional info	References
	NFW	1	3	1	0	$0.36^{+0.98}_{-0.20}$	1.45		Voigt & Fabian (2006)
	POW	$0.91^{+0.15}_{-0.16}$	-	-	-	-	-		
TRIANG	NFW	1	3	1	0	0.67	0.55		Ettori et al. (2002)
	King(ISO)	2	3	0	0	0.26	1.86		
Abell 168	NFW†	1	3	1	0	0.29	1.29		Rines et al. (2004), Rines et al. (2003)
	NFW†	1	3	1	0	0.85	0.13		
	HER†	1	4	1	0	0.88	0.12		
	HER†	1	4	1	0	2.94	0.02		
	SIS†	2	2	2	0	0.68	0.20		
	NFW	1	3	1	0	0.18	2.84		Babyk et al. (2014)
Abell 539	NFW†	1	3	1	0	0.095	15.89		Rines et al. (2004), Rines et al. (2003)
	NFW†	1	3	1	0	0.11	11.37		
	HER†	1	4	1	0	0.234	0.77		
	HER†	1	4	1	0	0.66	0.19		
	SIS†	2	2	2	0	0.68	0.18		
A 194	NFW†	1	3	1	0	0.15	2.00		Rines et al. (2004), Rines et al. (2003)
	NFW†	1	3	1	0	0.27	0.52		
	HER†	1	4	1	0	0.47	0.16		
	HER†	1	4	1	0	1.26	0.03		
	SIS†	2	2	2	0	0.68	0.08		
A262	NFW	1	3	1	0	0.159 ± 0.006	1.64 ± 0.10		Bernal et al. (2017)
A 262	NFW	1	3	1	0	0.11	6.23		Babyk et al. (2014)
42 new objects...									Babyk et al. (2014)
Abell 2261	NFW	1	3	1	0	0.7	0.67		Chiu et al. (2018)
	SIS	2	2	2	0	-		$\sigma_v = 1078.32^{54.66}_{-29.73}$km/s	Okabe et al. (2010b), Oguri et al. (2010)
	CIS	-	-	-	-			$\theta_E = 0.5$", $\theta_C = 0.08$"	
	NFW	1	3	1	0	0.45	1.06		
RXJ 2248.7-4431	NFW	1	3	1	0	0.57	0.77		Chiu et al. (2018)
	NFW†	1	3	1	0	0.86	0.36		Gruen et al. (2013), Umetsu et al. (2014), Merten et al. (2015), Melchior et al. (2015)
	NFW†	1	3	1	0	0.75	0.58		Gruen et al. (2013)
	SIS†	2	2	2	0	-		$\sigma_v = 1216 \pm 76$ km/s	
cluster2	NFW†	1	3	1	0	0.33	0.75		
RXJ1532.9-+3021	NFW	1	3	1	0	0.27	2.34		Chiu et al. (2018)
	NFW	1	3	1	0	$0.81^{+13.07}_{-0.53}$	0.33		Voigt & Fabian (2006)
	POW	$1.18^{+0.20}_{-0.19}$	-	-	-	-	-		
MACSJ1206.2-0847	NFW	1	3	1	0	0.48	1.30		Chiu et al. (2018)
	NFW†	1	3	1	0	1.29	0.26		Amodeo et al. (2016)
	NFW†	1	3	1	0	0.79	0.33		Biviano et al. (2023)
	gNFW	-	-	0.73	-	0.87	0.22		
	NFW†	1	3	1	0	0.68	0.64		Eichner et al. (2013)

Table 9 Continued.

Cluster	Profile	α	β	γ	δ	r_s **Mpc**	ρ_s $10^{-3} M_\odot \cdot pc^{-3}$	Additional info	References
	gNFW	-	-	0.91 ± 0.04	-	0.3 ± 0.003	1.9 ± 0.3		Caminha et al. (2017)
	NFW†	1	3	1	0	0.38	1.80		Biviano et al. (2013)
	NFW	1	3	1	0	0.40	1.65		Umetsu et al. (2012)
MACSJ0416.1-2403	NFW	1	3	1	0	0.82	0.31		Chiu et al. (2018)
	NFW†	1	3	1	0	0.63	0.35		Balestra et al. (2016)
	EIN†	m=5	-	-	-	0.68		$M_{200} = 1.01 \cdot 10^{15} M_\odot$	
	SIS†	2	2	2	0	0.02	1390.6		
	HER†	1	4	1	0	1.50	0.06		
	BUR†	2	3	1	1	0.36	0.29		
MACSJ1149.5+2223	NFW	1	3	1	0	1.47	0.16		Chiu et al. (2018)
	NFW	1	3	1	0	4.44	0.04		Sereno & Zitrin (2012)
MACSJ0717.5+3745	NFW	1	3	1	0	2.30	0.08		Chiu et al. (2018)
	NFW	1	3	1	0	0.91	0.54		Martinet et al. (2016)
	NFW	1	3	1	0	2.56	0.10		Sereno & Zitrin (2012)
	NFW†	1	3	1	0	1.26	0.2		Medezinski et al. (2013)
MACSJ0647.7+7015	NFW	1	3	1	0	0.67	0.53		Chiu et al. (2018)
	NFW	1	3	1	0	4.40	0.05		Sereno & Zitrin (2012)
	x2 TriaxialNFW								Chiu et al. (2018)
A 644	NFW	1	3	1	0	0.33	1.52		Ettori et al. (2019)
	EIN	$\alpha = 5$	-	-	-	0.33		$c = 2.99$	
	ISO	2	2	0	0	0.17	3.51		
	BUR	2	3	1	1	0.17	0.36		
	HER	1	4	1	0	0.48	0.76		
	NFW†	1	3	1	0	0.48	0.94		Buote et al. (2005)
A 2255	NFW	1	3	1	0	1.48	0.08		Ettori et al. (2019)
	EIN	$\alpha = 5$	-	-	-	0.96		$c = 0.88$	
	ISO	2	2	0	0	0.44	0.42		
	BUR	2	3	1	1	0.41	0.06		
	HER	1	4	1	0	2.24	0.02		
RXC1825	NFW	1	3	1	0	0.51	0.49		Ettori et al. (2019)
	EIN	$\alpha = 5$	-	-	-	0.50		$c = 1.71$	
	ISO	2	2	0	0	0.23	1.29		
	BUR	2	3	1	1	0.22	0.16		
	HER	1	4	1	0	0.91	0.12		
MACSJ2228.5+2037	NFW†	1	3	1	0	0.89	0.31		Amodeo et al. (2016)
MACSJ2243.3-0935	NFW†	1	3	1	0	0.87	0.31		Amodeo et al. (2016)
17 new objects...									Amodeo et al. (2016)
RXJ1524.2-3154	NFW†	1	3	1	0	0.21	3.14		Darragh-Ford et al. (2023)
15 new objects...									Darragh-Ford et al. (2023)
RXC J0003.8+0203	NFW	1	3	1	0	0.14	3.61		Ettori et al. (2010)
Abell 3911	NFW	1	3	1	0	0.26	1.53		Ettori et al. (2010)
Abell 3827	NFW	1	3	1	0	0.39	0.92		Ettori et al. (2010)
RXC J0049.4-2931	NFW	1	3	1	0	0.07	11.14		Ettori et al. (2010)
Abell 2034	NFW	1	3	1	0	0.98	0.26		Ettori et al. (2010)
13 new objects...									Ettori et al. (2010)
A2667	NFW†	1	3	1	0	0.73	0.38		Newman et al. (2013a), Newman et al. (2013b)

Table 9 Continued.

Cluster	Profile	α	β	γ	δ	r_s **Mpc**	ρ_s $10^{-3} M_\odot \cdot pc^{-3}$	Additional info	References
CI 1358+62	NFW	1	3	1	0	0.46	0.87		Hoekstra et al. (2002)
EMSS 1358+6245	NFW†	1	3	1	0	0.15	2.04		Arabadjis et al. (2002)
MS 2053-04	NFW	1	3	1	0	0.44	0.74		Hoekstra et al. (2002)
	NFW (S)	1	3	1	0	0.099	11.74		Gavazzi et al. (2003)
	NFW (W)	1	3	1	0	0.10	10.61		Gavazzi et al. (2003)
	ISO (S)	2	2	0	0			$r_c/r_s = 14.1$, $\sigma_v = 1022^{+40}_{-30}$ km/s	
	ISO (W)	2	2	0	0			$r_c/r_s < 61$, $\sigma_v = 900 \pm 150$ km/s	
	NFW	1	3	1	0	0.66	0.54		Martinet et al. (2016)
MS 1054-03	NFW	1	3	1	0	0.82	0.47		Hoekstra et al. (2002)
ACT-CL J0102-4915 (NW)	NFW†	1	3	1	0	0.59	0.29		
(NW)	SIS†	2	2	2	0	–		$\sigma_v = 1061$km/s	
(SE)	NFW†	1	3	1	0	0.41	0.30		Jee et al. (2014), Kim et al. (2021)
(SE)	SIS†	2	2	2	0	–		$\sigma_v = 1017$km/s	
(global)	NFW†	1	3	1	0	0.94	0.26		
IDCS J1426.5+3508	NFW†	1	3	1	0	0.28	0.25		Mo et al. (2016)
	NFW†	1	3	1	0	0.38	0.46		
A2163	NFW†	1	3	1	0	1.25	0.22		Okabe et al. (2011)
	NFW†	1	3	1	0	0.58	0.75		Radovich et al. (2008)
	SIS†	2	2	2	0			$\theta_e = 22''$, $\sigma = 1139^{+53}_{-56}$ km/s	Radovich et al. (2008)
SDSSJ0851+3331	NFW† (W)	1	3	1	0	0.44	0.93		Oguri et al. (2012)
	NFW† (S+W)	1	3	1	0	0.25	3.18		
SDSSJ0915+3826	NFW†	1	3	1	0	0.03	127.83		Oguri et al. (2012)
	NFW† (S+W)	1	3	1	0	0.04	45.68		
SDSSJ0957+0509	NFW†	1	3	1	0	0.03	131.29		Oguri et al. (2012)
	NFW† (S+W)	1	3	1	0	0.15	2.97		
SDSSJ1004+4112	NFW†	1	3	1	0	0.39	0.62		Oguri et al. (2012)
	NFW† (S+W)	1	3	1	0	0.19	2.70		
SDSSJ1029+2623	NFW†	1	3	1	0	0.13	5.71		Oguri et al. (2012)
	NFW† (S+W)	1	3	1	0	0.14	5.24		
	NFW†	1	3	1	0	0.06	44.23		Oguri et al. (2013)
22 new objects...									Oguri et al. (2012)
EAGLE 1	NFW	1	3	1	0	0.20	1.69		Schaller et al. (2015)
EAGLE 2	NFW	1	3	1	0	0.35	0.79		Schaller et al. (2015)
EAGLE 3	NFW	1	3	1	0	0.45	0.39		Schaller et al. (2015)
EAGLE 4	NFW	1	3	1	0	0.31	0.96		Schaller et al. (2015)
EAGLE 5	NFW	1	3	1	0	0.33	0.57		Schaller et al. (2015)
EAGLE 6	NFW	1	3	1	0	0.26	1.11		Schaller et al. (2015)
Abell 0851	NFW	1	3	1	0	0.63	0.54		Martinet et al. (2016)
LCDCS0829	NFW	1	3	1	0	0.67	0.54		Martinet et al. (2016)
OC02	NFW	1	3	1	0	0.49	0.54		Martinet et al. (2016)
NEP200	NFW	1	3	1	0	0.79	0.54		Martinet et al. (2016)
RXJ2328	NFW	1	3	1	0	0.57	0.54		Martinet et al. (2016)
CLJ0152	NFW	1	3	1	0	0.68	0.54		Martinet et al. (2016)
	NFW†	1	3	1	0	0.31	0.62		Jee et al. (2005)
RXJ1716	NFW	1	3	1	0	0.69	0.54		Martinet et al. (2016)

Table 9 Continued.

Cluster	Profile	α	β	γ	δ	r_s Mpc	ρ_s $10^{-3} M_\odot \cdot pc^{-3}$	Additional info	References
1E 0657-56	NFW†	1	3	1	0	0.75	0.39		Clowe et al. (2004), Barrena et al. (2002), Melchior et al. (2015)
	NFW†	1	3	1	0	0.75	0.39		Clowe et al. (2004)
	King(ISO)†	2	3	0	0	0.21	3.85		Clowe et al. (2004)
SCSO J233227-535827	NFW†	1	3	1	0	0.68	0.39		Melchior et al. (2015), High et al. (2010), Gruen et al. (2014)
Abell 3261	NFW†	1	3	1	0	0.54	0.47		Melchior et al. (2015)
MACSJ0018	NFW	1	3	1	0	1.96	0.15		Sereno & Zitrin (2012)
MACSJ0025	NFW	1	3	1	0	2.36	0.11		Sereno & Zitrin (2012)
MACSJ0257	NFW	1	3	1	0	1.20	0.31		Sereno & Zitrin (2012)
MACSJ0451	NFW	1	3	1	0	2.45	0.11		Sereno & Zitrin (2012)
MACSJ0911	NFW	1	3	1	0	0.78	0.57		Sereno & Zitrin (2012)
MACSJ2129	NFW	1	3	1	0	2.07	0.12		Sereno & Zitrin (2012)
MACSJ2214	NFW	1	3	1	0	1.49	0.22		Sereno & Zitrin (2012)
Abell S1063	gNFW	-	-	0.99	0	0.78	0.44		Sartoris et al. (2020)
A115	NFW	1	3	1	0	0.42	0.78		Kim et al. (2019)
	SIS	2	2	2	0	-		$\sigma_v = 922^{+72}_{-67}$ km/s	
	SIS	2	2	2	0	-		$\sigma_v = 818.02^{86.85}_{-86.08}$km/s	Okabe et al. (2010b), Oguri et al. (2010)
	CIS	-	-	-	-			$\theta_E = 0.27$", $\theta_C = 0.06$"	
	NFW	1	3	1	0	0.61	0.35		
MS 0440.5+0204	NFW†	1	3	1	0	0.22	5.10		Carrasco et al. (2021)
	SIS†	2	2	2	0	-		$\sigma_v = 894^{+52}_{-61}$ km/s	Carrasco et al. (2021)
SL2S J02140-0535	NFW	1	3	1	0	0.08	6.09		Verdugo et al. (2016)
RCS 0224-0002	NFW	1	3	1	0	0.12	0.53		Rzepecki et al. (2007)
	NIE(ISO)	-	-	-	-	0.01		925 km/s	
XMMU J1230.3+1339	NFW†	1	3	1	0	0.35	0.76		Lerchster et al. (2011)
	SIS†	2	2	2	0	-		$\sigma_v = 1308 \pm 284$ km/s	
XMMU J2235.3-2557	NFW†	1	3	1	0	0.54	0.72		Jee et al. (2009)
	SIS†	2	2	2	0			$\sigma_v = 1145 \pm 70$ km/s	
CL J1226+3332	NFW†	1	3	1	0	0.60	0.31		Jee & Tyson (2009)
MACS J0949.8+1708	dPIE(ISO)	2	2	0	0			$r_{cut} = 1.5, r_c = 0.12$, $1236.1^{+59.3}_{-310.6}$ km/s	Allingham et al. (2023)
	NFW†	1	3	1	0	0.41	1.82		
A1201	gNFW	-	-	1.0 ± 0.1	-	0.30	1.11		Smith et al. (2017), Rines et al. (2013)
RCS2 J232727.7-020437	NFW†	1	3	1	0	0.52	1.24		Schrabback et al. (2018)
SPT-CL J2040–4451	NFW†	1	3	1	0	0.64	0.41		Jee et al. (2017)
	NFW†	1	3	1	0	0.82	0.38		Zohren et al. (2022)
A209	NFW	1	3	1	0	0.50	0.50		Paulin-Henriksson et al. (2007)
	SIS	2	2	2	0	-		$\sigma_v = 924 \pm 84$ km/s	Paulin-Henriksson et al. (2007)
ACT-CL J0022.2-0036	NFW†	1	3	1	0	< 0.21	> 5.98		Miyatake et al. (2013)
	constrainedNFW†	1	3	1	0	0.54	0.76		
A3128	NFW†	1	3	1	0	0.52	0.75		McCleary et al. (2015)
A2744	NFW†	1	3	1	0	0.67	0.54		Medezinski et al. (2016)
CIZA J0107.7+5408	NFW†	1	3	1	0	0.44	0.80		Finner et al. (2023)

Table 9 Continued.

Cluster	Profile	α	β	γ	δ	r_s **Mpc**	ρ_s $10^{-3} M_\odot \cdot pc^{-3}$	Additional info	References
NE sub	NFW†	1	3	1	0	0.29	0.99		
SW sub	NFW†	1	3	1	0	0.31	0.97		
SPT-CL J0156-5541	NFW†	1	3	1	0	0.48	0.47		Zohren et al. (2022)
SPT-CL J0205-5829	NFW†	1	3	1	0	0.11	0.81		Zohren et al. (2022)
SPT-CL J0313-5334	NFW†	1	3	1	0	0.41	0.48		Zohren et al. (2022)
SPT-CL J0459-4947	NFW†	1	3	1	0	0.50	0.43		Zohren et al. (2022)
SPT-CL J0607-4448	NFW†	1	3	1	0	0.22	0.60		Zohren et al. (2022)
SPT-CL J0640-5113	NFW†	1	3	1	0	0.56	0.44		Zohren et al. (2022)
SPT-CL J2341-5724	NFW†	1	3	1	0	0.53	0.46		Zohren et al. (2022)
USGC S152	NFW	1	3	1	0	0.046 ± 0.001	7.83 ± 0.42		Bernal et al. (2017)
RX J1159+5531	NFW	1	3	1	0	0.217 ± 0.004	1.00 ± 0.03		Bernal et al. (2017)
A1991	NFW	1	3	1	0	0.174 ± 0.005	2.12 ± 0.10		Bernal et al. (2017)
A907	NFW	1	3	1	0	0.309 ± 0.010	1.58 ± 0.09		Bernal et al. (2017)
ZwCl0104	SIS	2	2	2	0	-		$\sigma_v = 665.85^{42.71}_{-57.95}$km/s	Okabe et al. (2010b), Oguri et al. (2010)
	CIS	-	-	-	-			$\theta_E = 0.14$", $\theta_C = 0.0$"	
	NFW	1	3	1	0	0.19	2.12		
RXJ0142	SIS	2	2	2	0	-		$\sigma_v = 886.80^{43.55}_{-46.56}$km/s	Okabe et al. (2010b), Oguri et al. (2010)
	CIS	-	-	-	-			$\theta_E = 0.27$", $\theta_C = 0.03$"	
	NFW	1	3	1	0	0.30	1.56		
A291	SIS	2	2	2	0	-		$\sigma_v = 801.74^{53.89}_{-51.28}$km/s	Okabe et al. (2010b), Oguri et al. (2010)
	CIS	-	-	-	-			$\theta_E = 0.42$", $\theta_C = 0.5$"	
	NFW	1	3	1	0	1.04	0.14		
A521	SIS	2	2	2	0	-		$\sigma_v = 789.23^{43.63}_{-43.87}$km/s	Okabe et al. (2010b), Oguri et al. (2010)
	CIS	-	-	-	-			$\theta_E = 0.33$", $\theta_C = 0.28$"	
	NFW	1	3	1	0	0.75	0.23		
A586	SIS	2	2	2	0	-		$\sigma_v = 1035.32^{40.04}_{-67.58}$km/s	Okabe et al. (2010b), Oguri et al. (2010)
	CIS	-	-	-	-			$\theta_E = 0.46$", $\theta_C = 0.07$"	
	NFW	1	3	1	0	0.30	2.31		
ZwCl0740	SIS	2	2	2	0	-		$\sigma_v = 726.93^{66.62}_{-58.09}$km/s	Okabe et al. (2010b), Oguri et al. (2010)
	CIS	-	-	-	-			$\theta_E = 0.47$", $\theta_C = 0.94$"	
	NFW	1	3	1	0	0.81	0.20		
ZwCl0839	SIS	2	2	2	0	-		$\sigma_v = 766.05^{57.14}_{-47.89}$km/s	Okabe et al. (2010b), Oguri et al. (2010)
	CIS	-	-	-	-			$\theta_E = 0.20$", $\theta_C < 0.12$"	
	NFW	1	3	1	0	0.25	1.63		
A697	SIS	2	2	2	0	-		$\sigma_v = 1021.91^{41.13}_{-45.14}$km/s	Okabe et al. (2010b), Oguri et al. (2010)
	CIS	-	-	-	-			$\theta_E = 0.56$", $\theta_C = 0.38$"	
	NFW	1	3	1	0	1.0	0.22		
ZwCl1454	SIS	2	2	2	0	-		$\sigma_v = 702.37^{69.49}_{-67.89}$km/s	Okabe et al. (2010b), Oguri et al. (2010)

Table 9 Continued.

Cluster	Profile	α	β	γ	δ	r_s **Mpc**	ρ_s $10^{-3} M_\odot \cdot pc^{-3}$	Additional info	References
	CIS	-	-	-	-			$\theta_E = 0.2$", $\theta_C = 0.09$"	
	NFW	1	3	1	0	0.48	0.42		
A2009	SIS	2	2	2	0	-		$\sigma_v = 800.80^{40.11}_{-49.15}$km/s	Okabe et al. (2010b), Oguri et al. (2010)
	CIS	-	-	-	-			$\theta_E = 0.31$", $\theta_C = 0.13$"	
	NFW	1	3	1	0	0.31	1.30		
ZwCl1459.4	SIS	2	2	2	0	-		$\sigma_v = 864.90^{53.43}_{-71.78}$km/s	Okabe et al. (2010b), Oguri et al. (2010)
	CIS	-	-	-	-			$\theta_E = 0.28$", $\theta_C = 0.04$"	
	NFW	1	3	1	0	0.32	1.29		
RXJ1720	SIS	2	2	2	0	-		$\sigma_v = 879.13^{61.09}_{-54.04}$km/s	Okabe et al. (2010b), Oguri et al. (2010)
	CIS	-	-	-	-			$\theta_E = 0.28$", $\theta_C < 0.14$"	
	NFW	1	3	1	0	0.23	2.55		
A2485	SIS	2	2	2	0	-		$\sigma_v = 777.49^{60.07}_{-64.03}$km/s	Okabe et al. (2010b), Oguri et al. (2010)
	CIS	-	-	-	-			$\theta_E = 0.28$", $\theta_C = 0.17$"	
	NFW	1	3	1	0	0.60	0.32		
A2631	SIS	2	2	2	0	-		$\sigma_v = 959.71^{50.90}_{-35.71}$km/s	Okabe et al. (2010b), Oguri et al. (2010)
	CIS	-	-	-	-			$\theta_E = 0.3$", $\theta_C < 0.04$"	
	NFW	1	3	1	0	0.28	1.97		
A689	NFW	1	3	1	0	6.69	0.007		Oguri et al. (2010)
Abell 3112	NFW	1	3	1	0	$0.19^{+0.39}_{-0.09}$	2.64		Voigt & Fabian (2006)
	POW	$1.31^{+0.15}_{-0.16}$	-	-	-	-	-		
Abell 3581	NFW	1	3	1	0	$0.07^{+0.23}_{-0.04}$	5.81		Voigt & Fabian (2006)
	POW	$1.34^{+0.22}_{-0.24}$	-	-	-	-	-		
Sersic 159-03	NFW	1	3	1	0	$0.20^{+0.37}_{-0.10}$	1.91		Voigt & Fabian (2006)
	POW	$1.09^{+0.14}_{-0.15}$	-	-	-	-	-		

Table 10. DM density distribution profiles in spirals and late-type galaxies. Profiles marked with a † symbol represent total mass (luminous+dark matter). Where a reference is not provided, it follows the reference of the first row of the corresponding table cell.

Galaxy	**Profile**	α	β	γ	δ	r_s **kpc**	ρ_s $10^{-3}M_\odot \cdot pc^{-3}$	**Additional info**	**References**
MW	ISO	2	2	0	0	1.6	349.89		Battaglia et al. (2005)
	NFW	1	3	1	0	14.17	14.72		
	NFW	1	3	1	0	17.33	14.72		
	TF	-	-	-	-			$\alpha = 105.00$kpc, $M = 1.2^{+1.8}_{-0.5} \cdot 10^{12} M_\odot$	
	NFW	1	3	1	0	20.2	5.97		Borukhovetskaya et al. (2022)
	BUR	2	3	1	1	9.11	23.66		Macciò et al. (2012)
	NFW	1	3	1	0	0.34	2.00		
112 MW globular clusters	total mass	-	-	-	-	r_{core}	ρ_{core}		Baumgardt & Hilker (2018)
NGC 300	NFW	1	3	1	0	4.0 ± 1.53	26.77		Westmeier et al. (2011)
	BUR	2	3	1	1	4.04 ± 1.1	25 ± 18		
	ISO	2	2	0	0	0.74 ± 0.35	135 ± 119		
	ISO	2	2	0	0	1.4	109.0		de Blok & McGaugh (1997)
	ISO	2	2	0	0	1.5	73.85		Kent (1987)
	ISO	2	2	0	0	1.5	78.99		Lake & Feinswog (1989)
	ISO	2	2	0	0	12.4	6.0		Puche & Carignan (1991), Puche et al. (1990)
	BUR	2	3	1	1	4.13	38.09		Wang & Chen (2021)
	NFW	1	3	1	0	48.38	0.48		
NGC 0300A	ISO	2	2	0	0	7.10	9.90		Athanassoula et al. (1987a)
NGC 0300B	ISO	2	2	0	0	9.00	6.60		Athanassoula et al. (1987a)
M31	NFW	1	3	1	0	25.65	44.4		Di Mauro et al. (2019)
	BUR	2	3	1	1	9.06	36.8		
	EIN	a=0.17	-	-	-	178	0.00812		
	ISO	2	2	0	0	0.98	739.7		Rodríguez-Meza (2012)
	NFW	1	3	1	0	8.18	37.8		Geehan et al. (2006)
	NFW	1	3	1	0	12.5	17.4		Tempel et al. (2007)
	NFW	1	3	1	0	34.6 ± 2	2.23 ± 0.24		Sofue (2015)
	NFW	1	3	1	0	16.5 ± 1.5	11.0 ± 1.8		Tamm et al. (2012)
	NFW	1	3	1	0	$30.2^{12.1}_{-8.8}$		$M = 1.82 \cdot 10^{12} M_\odot$	Hayashi & Chiba (2014)
	NFW(M31a)	1	3	1	0	12.94	5.4		Widrow & Dubinski (2005)
	NFW(M31b)	1	3	1	0	14.03	4.2		
	NFW(M31d)	1	3	1	0	17.46	2.8		
	NFW	1	3	1	0	7.63	61.7		Kirihara et al. (2014), Fardal et al. (2007)
	NFW	1	3	1	0	28.5 ± 1.0	3.3		Frigerio Martins (2009)
	BUR	2	3	1	1	9.06 ± 0.53	36.8 ± 4		Tamm et al. (2012)
	BUR	2	3	1	1	6.86	57.2		Tempel et al. (2007)
	EIN[a]	0.17	-	-	-	178 ± 18	0.0081 ± 0.0002		Tamm et al. (2012)
	EIN[b]	0.17	-	-	-	387 ± 44	0.0014 ± 0.0003		
	EIN[c]	0.17	-	-	-	135.0	0.014		Tempel et al. (2007)

Table 10 Continued.

Galaxy	Profile	α	β	γ	δ	r_s kpc	ρ_s $10^{-3}M_\odot \cdot pc^{-3}$	Additional info	References
	MOO	1.5	3	1.5	0	31.0 ± 3	1.46 ± 0.26		Tamm et al. (2012)
	MOO	1.5	3	1.5	0	25.0	2.05		Tempel et al. (2007)
	SIS	2	2	2	0	> 8.1		$M = 1.39 \cdot 10^{12} M_\odot$	Hayashi & Chiba (2014)
	HYB	2	3	2	0	> 117.5		$M = 1.08 \cdot 10^{12} M_\odot$	Hayashi & Chiba (2014)
M33	NFW	1	3	1	0	35	1.51		Borriello et al. (2010), Corbelli (2003)
	NFW	1	3	1	0	22.41	2.64		Di Mauro et al. (2019)
	NFW	1	3	1	0	21.09	2.52		López Fune et al. (2017), Corbelli (2003)
	NFW	1	3	1	0	37.46	0.41		Seigar (2011)
	BUR	2	3	1	1	12	11.05		Borriello et al. (2010), Corbelli (2003)
	BUR	2	3	1	1	7.5	18		López Fune et al. (2017)
	BUR	2	3	1	1	9.6	12.3		Di Mauro et al. (2019)
	ISO	2	2	0	0	1.39	106.41		Seigar (2011)
ESO 116-G12	NFW	1	3	1	0	7.295	16.81		Gentile et al. (2004)
	MOO	1.5	3	1.5	0	12.13	2.63		
	BUR	2	3	1	1	4.27	45.79		
	ISO	2	2	0	0	2.16	53.18		
	ISO	2	2	0	0	2.983	27.74		Rodríguez-Meza (2012)
	BUR	2	3	1	1	4.39	46.5		Rodrigues et al. (2017)
	NFW	1	3	1	0	14.5 ± 14.0	5.91		Frigerio Martins (2009)
ESO 287-G13	NFW	1	3	1	0	14.481	10.28		Gentile et al. (2004)
	Moore	1.5	3	1.5	0	25.938	1.51		
	BUR	2	3	1	1	24.045	5.32		
	ISO	2	2	0	0	15.75	4.43		
	BUR	2	3	1	1	27.59	4.54		Rodrigues et al. (2017)
ESO 79-G14	NFW	1	3	1	0	14.84	10.1		Gentile et al. (2004)
	MOO	1.5	3	1.5	0	23.75	1.61		
	BUR	2	3	1	1	8.31	32.5		
	ISO	2	2	0	0	5.21	23.63		
	BUR	2	3	1	1	7.81	36.03		Wang & Chen (2021)
	NFW	1	3	1	0	268.5	0.10		
	BUR	2	3	1	1	7.96	34.5		Rodrigues et al. (2017)
	NFW	1	3	1	0	330.0 ± 1400.0	0.15		Frigerio Martins (2009)
NGC 1090	NFW	1	3	1	0	11.939	11.80		Gentile et al. (2004)
	MOO	1.5	3	1.5	0	21.132	1.75		
	BUR	2	3	1	1	8.829	19.2		
	ISO	2	2	0	0	4.03	25.11		
	BUR	2	3	1	1	8.97	18.5		Rodrigues et al. (2017)
	BUR	2	3	1	1	5.07	68.68		Wang & Chen (2021)
	NFW	1	3	1	0	32.82	1.46		
NGC 7393	NFW	1	3	1	0	14.835	10.1		Gentile et al. (2004)

Table 10 Continued.

Galaxy	Profile	α	β	γ	δ	r_s kpc	ρ_s $10^{-3}M_\odot \cdot pc^{-3}$	Additional info	References
	BUR	2	3	1	1	5.54	54.2		Rodrigues et al. (2017)
	MOO	1.5	3	1.5	0	26.704	1.48		Gentile et al. (2004)
	BUR	2	3	1	1	7.84	41.36		
	ISO	2	2	0	0	5.39	33.97		Gentile et al. (2004)
	ISO	2	2	0	0	2.98	4.82		Rodríguez-Meza (2012)
I 467	ISO	2	2	0	0	31.90	0.40		Kent (1986)
IC 10	BUR	2	3	1	1	$2.0^{+0}_{-1.5}$	$158.49^{+239.62}_{-58.49}$		Gammaldi et al. (2021)
	NFW	1	3	1	0	6.8	6.31		
	NFW	1	3	1	0	2.68	32.01		Oh et al. (2015)
	ISO	2	2	0	0	0.27 ± 0.12	190.4 ± 76.4		
IC 1613	BUR	2	3	1	1	$7.0^{+0}_{-1.2}$	$2.0^{+0.24}_{-0.22}$		Gammaldi et al. (2021)
	NFW	1	3	1	0	4.0	7.94		Gammaldi et al. (2021)
	NFW	1	3	1	0	1.51	8.49		Oh et al. (2015)
	ISO	2	2	0	0	0.20 ± 0.04	19.25 ± 3.45		Oh et al. (2015)
IC 0342	ISO	2	2	0	0	27.30	2.8		Athanassoula et al. (1987b)*
	POW	-1.02	-	-	-	-	-		
IC 2233	ISO	2	2	0	0	3.7	23.00		de Blok & Bosma (2002)*
	NFW	1	3	1	0	15133	0.0024		
IC 2574	ISO	2	2	0	0	4.99 ± 0.34	6.70 ± 0.7		de Blok et al. (2008)
	NFW	1	3	1	0	> 6775.1	< 0.0024		de Blok et al. (2008)
	ISO	2	2	0	0	6.3 ± 0.3	4.9 ± 0.2		Chemin et al. (2011)
	NFW	1	3	1	0	58.26	0.23		Chemin et al. (2011)
	EIN	n=1.1 ± 0.3	-	-	-	15.1 ± 5.0	0.7 ± 0.3		Chemin et al. (2011)
	ISO	2	2	0	0	5.77 ± 0.16	7.8 ± 0.2		Oh et al. (2008)
	NFW	1	3	1	0	> 9140.65	< 0.0023		Oh et al. (2008)
	NFW	1	3	1	0	10000	0.0008		de La Macorra et al. (2011)
	BDM					17.2	10.0	$r_c = 18.3$kpc	de La Macorra et al. (2011)
	ISO	2	2	0	0	11.08 ± 5.43	2.40		Li et al. (2020), Li et al. (2019)
	BUR	2	3	1	1	15.69 ± 8.17	3.02		
	NFW	1	3	1	0	143.87 ± 7.74	0.051		
	NFW	1	3	1	0	107.59 ± 4.36	0.051		
	EIN	$\alpha = 0.33 \pm 0.10$	-	-	-	230.07 ± 140.20	0.032		
	EIN	$\alpha = 0.76 \pm 0.06$	-	-	-	18.39 ± 1.42	0.47		
	DC14					22.03 ± 3.05	1.48		
	DC14					9.72 ± 0.75	2.09		
	coreNFW	1	3	0	0	58.11 ± 6.54	9.77		
	coreNFW	1	3	0	0	5.12 ± 0.53	16.98		
	Lucky13					20.49 ± 6.54	4.27		
	Lucky13					12.70 ± 0.92	5.50		
174 more SPARC	ISO								Li et al. (2020)
	BUR								Li et al. (2020)
	NFW								Li et al. (2020)

Table 10 Continued.

Galaxy	Profile	α	β	γ	δ	r_s kpc	ρ_s $10^{-3} M_\odot \cdot pc^{-3}$	Additional info	References
	NFW								Li et al. (2020)
	EIN								Li et al. (2020)
	EIN								Li et al. (2020)
	DC14								Li et al. (2020)
	DC14								Li et al. (2020)
	coreNFW								Li et al. (2020)
	coreNFW								Li et al. (2020)
	Lucky13								Li et al. (2020)
	Lucky13								Li et al. (2020)
153 SPARC	NFW								Rodrigues et al. (2023)
	BUR								Rodrigues et al. (2023)
IC 5152	ISO	2	2	0	0	0.37	378.79 ± 40.76		van Eymeren et al. (2009)
	NFW	1	3	1	0	3.43	6.77		
NGC 0224	ISO	2	2	0	0	25.00	4.2		Athanassoula et al. (1987a)
NGC 0247A	ISO	2	2	0	0	12.10	6.50		Athanassoula et al. (1987a)
NGC 0247B	ISO	2	2	0	0	8.10	10.00		
N 247	ISO	2	2	0	0	1.4	114.0		de Blok & McGaugh (1997)
	ISO	2	2	0	0	11.2	6.65		Kent (1987)
	ISO	2	2	0	0	24.2	5.0		Puche & Carignan (1991)
NGC 0253	ISO	2	2	0	0	23.30	4.30		Athanassoula et al. (1987a)
	ISO	2	2	0	0	26.9	15.0		Puche & Carignan (1991)
NGC 0488A	ISO	2	2	0	0	20.00	5.30		Athanassoula et al. (1987a)
NGC 0488B	ISO	2	2	0	0	15.00	8.50		Athanassoula et al. (1987a)
NGC 0598	ISO	2	2	0	0	8.0	10.70		Athanassoula et al. (1987a)
NGC 1087	ISO	2	2	0	0	3.70	38.50		Athanassoula et al. (1987a)
NGC 2336	ISO	2	2	0	0	36.70	1.30		Athanassoula et al. (1987a)
NGC 2403	ISO	2	2	0	0	9.00	13.10		Athanassoula et al. (1987a)
	BUR	2	3	1	1	7.24	25.5		Rodrigues et al. (2017)
	BUR	2	3	1	1	6.82	28.7		Rodrigues et al. (2017)
	ISO	2	2	0	0	4.66	17.48		Begeman et al. (1991)
(1)	ISO	2	2	0	0	3.76 ± 0.15	28.6 ± 1.9		de Blok et al. (2008)
(1)	NFW	1	3	1	0	14.16	7.34		de Blok et al. (2008)
(2)	ISO	2	2	0	0	2.51 ± 0.32	59.1 ± 14.3		de Blok et al. (2008)
(2)	NFW	1	3	1	0	12.98	8.64		de Blok et al. (2008)
	ISO	2	2	0	0	0.8	470.0		de Blok & McGaugh (1997)
	ISO	2	2	0	0	8.7	11.0		Puche & Carignan (1991), Begeman (1987), Begeman (1989)
	ISO	2	2	0	0	3.3	35.9		Kent (1987)
	ISO	2	2	0	0	3.5	32.20		Lake & Feinswog (1989)
	ISO	2	2	0	0	2.1 ± 0.1	78.4 ± 4.7		Chemin et al. (2011)
	NFW	1	3	1	0	11.15	11.51		Chemin et al. (2011)
	EIN	n=5.3 ± 0.5	-	-	-	14.6 ± 1.8	1.7 ± 0.4		Chemin et al. (2011)

Table 10 Continued.

Galaxy	Profile	α	β	γ	δ	r_s kpc	ρ_s $10^{-3}M_\odot \cdot pc^{-3}$	Additional info	References
	BUR	2	3	1	1	5.83	32.28		Wang & Chen (2021)
	NFW	1	3	1	0	14.5	5.70		
NGC 2403d	ISO	2	2	0	0	2.1 ± 0.1	81.8 ± 5.2		Chemin et al. (2011)
	NFW	1	3	1	0	10.88	11.98		Chemin et al. (2011)
	EIN	n=5.6 ± 0.5	-	-	-	15.6 ± 2.0	1.5 ± 0.4		Chemin et al. (2011)
NGC 2639	ISO	2	2	0	0	0.0	0.0		Athanassoula et al. (1987b)
NGC 2775	ISO	2	2	0	0	0.0	0.0		Athanassoula et al. (1987b)
NGC 2841A	ISO	2	2	0	0	30.00	5.00		Athanassoula et al. (1987b)
NGC 2841B	ISO	2	2	0	0	32.60	4.10		Athanassoula et al. (1987b)
NGC 2841	ISO	2	2	0	0	8.24	23.12		Begeman et al. (1991)
	BUR	2	3	1	1	13.91	25.3		Rodrigues et al. (2017)
	ISO	2	2	0	0	1.36 ± 0.75	674.8 ± 736.4		de Blok et al. (2008)
	NFW	1	3	1	0	18.58	15.24		de Blok et al. (2008)
	ISO	2	2	0	0	21.6	9.0		Puche & Carignan (1991), Begeman (1987), Begeman (1989)
	ISO	2	2	0	0	11.6	14.81		Kent (1987)
	ISO	2	2	0	0	0.6 ± 0.1	> 1000		Chemin et al. (2011)
	NFW	1	3	1	0	10	70		Chemin et al. (2011)
	EIN	n=12.4 ± 1.5	-	-	-	11.2 ± 0.6	10.7 ± 1.2		Chemin et al. (2011)
	NFW	1	3	1	0	50.0 ± 15.0	31.0 ± 10.0		Samurović et al. (2015)
	ISO	2	2	0	0	11.0 ± 4.0	12.0 ± 5.0		Samurović et al. (2015)
	NFW	1	3	1	0	4.7	398.11		de La Macorra et al. (2011)
	BDM					4.6	398.11	$r_c = 0.001$kpc	de La Macorra et al. (2011)
NGC 3109	ISO	2	2	0	0	6.30	5.10		Athanassoula et al. (1987b)
	ISO	2	2	0	0	3.5	12.6		de Blok & McGaugh (1997)
	ISO	2	2	0	0	6.0	9.4		Jobin & Carignan (1990)
	NFW	1	3	1	0	14.9	0.75		Carignan et al. (2013)
	NFW	1	3	1	0	36.86	0.21		Carignan et al. (2013)
	ISO	2	2	0	0	3.2	18		Carignan et al. (2013)
	ISO	2	2	0	0	2.1	28		Carignan et al. (2013)
	ISO	2	2	0	0	2.98	14.81		Rodríguez-Meza (2012)
NGC 3198	ISO	2	2	0	0	23.40	2.40		Athanassoula et al. (1987b)
	ISO	2	2	0	0	5.37	14.05		Begeman et al. (1991)
	ISO	2	2	0	0	17.2 ± 1.0	4.00		Blais-Ouellette et al. (1999)
	ISO	2	2	0	0	11.7 ± 1.0	8.0		Blais-Ouellette et al. (1999)
	ISO	2	2	0	0	3.9 ± 0.1	76.0		Blais-Ouellette et al. (1999)
(1)	ISO	2	2	0	0	2.72 ± 0.13	46.9 ± 4.0		de Blok et al. (2008)
	NFW	1	3	1	0	14.21	7.16		de Blok et al. (2008)
(2)	ISO	2	2	0	0	1.86 ± 0.12	97.1 ± 12.2		de Blok et al. (2008)
	NFW	1	3	1	0	8.94	13.7		de Blok et al. (2008)

Table 10 Continued.

Galaxy	Profile	α	β	γ	δ	r_s kpc	ρ_s $10^{-3}M_\odot \cdot pc^{-3}$	Additional info	References
	ISO	2	2	0	0	10.9	9.00		Puche & Carignan (1991), Begeman (1987), Begeman (1989)
	ISO	2	2	0	0	1.3	240.92		Kent (1987)
	ISO	2	2	0	0	1.5	180.16		Lake & Feinswog (1989)
	ISO	2	3	0	0	9.25	12.80		Lake & Feinswog (1989)
	ISO	2	4	0	0	14.0	8.97		Lake & Feinswog (1989)
	ISO	2	2	0	0	2.8 ± 0.3	44.3 ± 7.4		Chemin et al. (2011)
	NFW	1	3	1	0	17.12	4.83		Chemin et al. (2011)
	EIN	n=2.0 ± 0.3	-	-	-	13.0 ± 0.7	2.2 ± 0.3		Chemin et al. (2011)
	NFW	1	3	1	0	9.0	25.12		de La Macorra et al. (2011)
	BDM					3.7	251.19	$r_c = 3.7$kpc	de La Macorra et al. (2011)
	NFW	1	3	1	0	18	1.8		
	BUR	2	3	1	1	17.7 ± 2	4.7		
	BUR	2	3	1	1	4.34	97.4		Rodrigues et al. (2017)
	BUR	2	3	1	1	4.21	106		Rodrigues et al. (2017)
	BUR	2	3	1	1	9.42	15.89		Wang & Chen (2021)
	NFW	1	3	1	0	28.01	1.97		
NGC 3198d	ISO	2	2	0	0	2.7 ± 0.2	47.1 ± 5.9		Chemin et al. (2011)
	NFW	1	3	1	0	16.64	5.10		Chemin et al. (2011)
	EIN	n=2.1 ± 0.3	-	-	-	13.1 ± 0.6	2.2 ± 0.2		Chemin et al. (2011)
NGC 3741	NFW	1	3	1	0	22.8	0.93		Gentile et al. (2007a)
	BUR	2	3	1	1	$2.97^{0.57}_{-0.43}$	1.65 ± 0.33		
	soliton+NFW	-	-	-	-	$15.7^{2.5}_{-4.4}$	1.77		Bernal et al. (2018)
UGC 7321	NFW	1	3	1	0	18	1.8		Gentile et al. (2007a)
	BUR	2	3	1	1	17.7 ± 2	4.7		
NGC 3359	ISO	2	2	0	0	25.00	1.80		Athanassoula et al. (1987b)
NGC 3898A	ISO	2	2	0	0	8.70	39.30		Athanassoula et al. (1987b)
NGC 3898B	ISO	2	2	0	0	16.70	9.50		Athanassoula et al. (1987b)
NGC 3992	ISO	2	2	0	0	30.00	2.90		Athanassoula et al. (1987b)
	BUR	2	3	1	1	6.29	107.71		Wang & Chen (2021)
	NFW	1	3	1	0	22.72	7.27		
NGC 4258	ISO	2	2	0	0	16.70	5.30		Athanassoula et al. (1987b)
	ISO	2	2	0	0	10.6	8.57		Kent (1987)
	ISO	2	2	0	0	8.5	11.73		Lake & Feinswog (1989)
NGC 4321	ISO	2	2	0	0	13.30	6.80		Athanassoula et al. (1987b)
	ISO	2	2	0	0	2.55 ± 0.24	198.0 ± 123.0		Tan et al. (2022)
	BUR	2	3	1	1	5.72 ± 14.61	16.2 ± 79.3		Tan et al. (2022)
	NFW	1	3	1	0	66.77 ± 21.88	1.48 ± 0.53		Tan et al. (2022)
	MOO	1.5	3	1.5	0	43.88 ± 251.20	1.20 ± 10.11		Tan et al. (2022)
	EIN	0.17	-	-	-	8.44 ± 1.84	38.7 ± 13.8		Tan et al. (2022)
	coreMOD	3	3	0	0	4.10 ± 0.25	55.70 ± 20.00		Tan et al. (2022)
	DC14					0.037 ± 0.0049	747.0 ± 0.61		Tan et al. (2022)

Table 10 Continued.

Galaxy	Profile	α	β	γ	δ	r_s kpc	ρ_s $10^{-3}M_\odot \cdot pc^{-3}$	Additional info	References
	coreNFW	1	3	0	0	5.23 ± 0.36	64.30 ± 41.70		Tan et al. (2022)
	Lucky13					5.08 ± 32.96	4.20 ± 54.8		Tan et al. (2022)
NGC 4378	ISO	2	2	0	0	0.0	0.0		Athanassoula et al. (1987b)
NGC 4395	ISO	2	2	0	0	18.70	1.80		Athanassoula et al. (1987b)
	ISO	2	2	0	0	0.90	175.60		de Blok & Bosma (2002)
	NFW	1	3	1	0	7.68	11.18		de Blok & Bosma (2002)
	ISO	2	2	0	0	0.7 ± 0.1	258.0 ± 9.0		Kuzio de Naray et al. (2006)
	NFW	1	3	1	0	10.33	6.94		Kuzio de Naray et al. (2006)
	constrainedNFW	1	3	1	0	13.71	4.69		Kuzio de Naray et al. (2006)
	ISO	2	2	0	0	0.7 ± 0.1	258.0 ± 9.0		Kuzio de Naray et al. (2008)
	ISO	2	2	0	0	0.57 ± 0.05	318.0 ± 42.0		Kuzio de Naray et al. (2008)
	NFW	1	3	1	0	10.33	6.94		Kuzio de Naray et al. (2008)
	NFW	1	3	1	0	7.42	9.55		Kuzio de Naray et al. (2008)
NGC 4698A	ISO	2	2	0	0	6.70	38.00		Athanassoula et al. (1987b)
NGC 4698B	ISO	2	2	0	0	6.30	41.90		Athanassoula et al. (1987b)
NGC 4736	ISO	2	2	0	0	4.90	85.70		Athanassoula et al. (1987b)
	BUR	2	3	1	1	0.84	983		Rodrigues et al. (2017)
	ISO	2	2	0	0	1.44 ± 1.57	22.4 ± 41.5		de Blok et al. (2008)
	NFW	1	3	1	0	0.89	837.36		de Blok et al. (2008)
	ISO	2	2	0	0	1.1	292.91		Kent (1987)
	ISO	2	2	0	0	1.8 ± 1.9	17.0 ± 28.4		Chemin et al. (2011)
	NFW	1	3	1	0	1.36	299.87		Chemin et al. (2011)
	EIN	n=$10^{-3} \pm 0.7$	-	-	-	5.4 ± 16.8	5.5 ± 7.4		Chemin et al. (2011)
	NFW	1	3	1	0	0.3	31622.78		de La Macorra et al. (2011)
	BDM					0.2	50118.72	$r_c = 0.05$kpc	de La Macorra et al. (2011)
NGC 5033	ISO	2	2	0	0	30.00	2.80		Athanassoula et al. (1987b)
	ISO	2	2	0	0	6.5	13.21		Puche & Carignan (1991), Begeman (1987), Begeman (1989)
	ISO	2	2	0	0	7.5	13.44		Kent (1987)
NGC 5055	ISO	2	2	0	0	26.70	2.20		Athanassoula et al. (1987b)
	BUR	2	3	1	1	13.71	10.4		Rodrigues et al. (2017)
	ISO	2	2	0	0	7.15 ± 1.12	11.1 ± 3.1		de Blok et al. (2008)
	NFW	1	3	1	0	4.87	149.86		de Blok et al. (2008)
	ISO	2	2	0	0	8.2	8.6		Kent (1987)
	ISO	2	2	0	0	20.90	3.00		Bosma (1981)
	ISO	2	2	0	0	11.7 ± 0.9	4.8 ± 0.5		Chemin et al. (2011)
	NFW	1	3	1	0	167.16	0.17		Chemin et al. (2011)
	EIN	n=0.5 ± 0.1	-	-	-	22.6 ± 0.6	1.3 ± 0.1		Chemin et al. (2011)
	ISO	2	2	0	0	9.8 ± 2.7	4.8 ± 2.2		Jovanović (2017)
	NFW	1	3	1	0	$36.43^{+24.12}_{-11.43}$	$0.37^{+0.34}_{-0.22}$		Jovanović (2017)
	BUR	2	3	1	1	10.59	18.43		Wang & Chen (2021)
	NFW	1	3	1	0	24.65	3.74		

Table 10 Continued.

Galaxy	Profile	α	β	γ	δ	r_s kpc	ρ_s $10^{-3}M_\odot \cdot pc^{-3}$	Additional info	References
NGC 5194	ISO	2	2	0	0	1.90	393.40		Athanassoula et al. (1987b)
NGC 5236	ISO	2	2	0	0	20.00	4.00		Athanassoula et al. (1987b)
NGC 5383	ISO	2	2	0	0	23.70	3.50		Athanassoula et al. (1987b)
NGC 5408	ISO	2	2	0	0	3.36	9.22 ± 2.11		van Eymeren et al. (2009)
	NFW	1	3	1	0	18.84	6.29		van Eymeren et al. (2009)
NGC 5457	ISO	2	2	0	0	20.00	3.20		Athanassoula et al. (1987b)
NGC 5963	ISO	2	2	0	0	5.10	37.70		Athanassoula et al. (1987b)
NGC 6503	ISO	2	2	0	0	7.40	14.70		Athanassoula et al. (1987b)
	ISO	2	2	0	0	2.00	59.90		Begeman et al. (1991)
	ISO	2	2	0	0	2.5	39.32		Puche & Carignan (1991), Begeman (1987), Begeman (1989)
	gNFW	-	-	< 0.19	-	< 1.70	> 532.47		Relatores et al. (2019)
	BUR	2	3	1	1	5.01	36.41		Wang & Chen (2021)
	NFW	1	3	1	0	14.67	4.47		
	soliton+NFW	-	-	-	-	$9.73^{0.93}_{-1.0}$	9.35		Bernal et al. (2018)
NGC 6946	ISO	2	2	0	0	18.70	7.20		Athanassoula et al. (1987b)
	BUR	2	3	1	1	16.91	10.2		Rodrigues et al. (2017)
	ISO	2	2	0	0	3.32 ± 1.23	55.6 ± 42.3		de Blok et al. (2008)
	NFW	1	3	1	0	117.27	0.51		de Blok et al. (2008)
	ISO	2	2	0	0	3.7 ± 0.2	44.2 ± 4.1		Chemin et al. (2011)
	NFW	1	3	1	0	41.74	2.08		Chemin et al. (2011)
	EIN	n=2.6 ± 0.9	-	-	-	18.7 ± 7.4	1.8 ± 1.2		Chemin et al. (2011)
	NFW	1	3	1	0	6.6	79.43		de La Macorra et al. (2011)
	BDM					5.9	100.0	$r_c = 0.12$kpc	de La Macorra et al. (2011)
	soliton+NFW	-	-	-	-	$5.7^{1.2}_{-1.5}$	79.06		Bernal et al. (2018)
NGC 7217	ISO	2	2	0	0	2.70	158.60		Athanassoula et al. (1987b)
	ISO	2	2	0	0	13.0	63.0		Spano et al. (2008)
	NFW	1	3	1	0	16.0	32.0		Spano et al. (2008)
NGC 7331	ISO	2	2	0	0	15	5.53		Puche & Carignan (1991), Begeman (1987), Begeman (1989)
	BUR	2	3	1	1	18.20	8.75		Rodrigues et al. (2017)
	ISO	2	2	0	0	91.20	1.76		Begeman et al. (1991)
	ISO	2	2	0	0	3.88 ± 0.98	58.0 ± 27.8		de Blok et al. (2008)
	NFW	1	3	1	0	103.98	0.54		de Blok et al. (2008)
	ISO	2	2	0	0	9.35 ± 1.43	10.1 ± 2.4		de Blok et al. (2008)
	NFW	1	3	1	0	24.55	5.86		de Blok et al. (2008)
	ISO	2	2	0	0	103.0	1.7		Broeils (1992), Begeman (1987), Begeman (1989)
	ISO	2	2	0	0	27.2	4.7		Kent (1987)
	ISO	2	2	0	0	5.2 ± 0.5	26.1 ± 3.6		Chemin et al. (2011)

Table 10 Continued.

Galaxy	Profile	α	β	γ	δ	r_s kpc	ρ_s $10^{-3}M_\odot \cdot pc^{-3}$	Additional info	References
	NFW	1	3	1	0	50.97	1.44		Chemin et al. (2011)
	EIN	n=13.1 ± 19.7	-	-	-	> 1000	0.0 ± 0.0		Chemin et al. (2011)
NGC 7793	ISO	2	2	0	0	1.50	123.00		Athanassoula et al. (1987b)
	BUR	2	3	1	1	INF	25.0		Rodrigues et al. (2017)
	BUR	2	3	1	1	INF	25.4		Rodrigues et al. (2017)
	ISO	2	2	0	0	2.40 ± 0.48	53.3 ± 15.7		de Blok et al. (2008)
	NFW	1	3	1	0	7.80	20.12		de Blok et al. (2008)
	ISO	2	2	0	0	INF	25.7 ± 1.0		de Blok et al. (2008)
	NFW	1	3	1	0	> 6667.7	< 0.0024		de Blok et al. (2008)
	ISO	2	2	0	0	2.5	39.0		Puche & Carignan (1991)
	ISO	2	2	0	0	1.9 ± 0.2	78.2 ± 11.2		Chemin et al. (2011)
	NFW	1	3	1	0	16.85	5.53		Chemin et al. (2011)
	EIN	n=0.3 ± 0.1	-	-	-	3.7 ± 0.1	22.7 ± 1.9		Chemin et al. (2011)
	NFW	1	3	1	0	8.7	19.95		de La Macorra et al. (2011)
	BDM					7.2	25.12	$r_c = 0.06$kpc	de La Macorra et al. (2011)
	BUR	2	3	1	1	3.26	44.29		Wang & Chen (2021)
	NFW	1	3	1	0	31.28	0.83		
NGC 7793s	ISO	2	2	0	0	3.5 ± 0.7	51.8 ± 6.8		Chemin et al. (2011)
	NFW	1	3	1	0	42.63	2.08		Chemin et al. (2011)
	EIN	n=9.3 ± 42.3	-	-	-	> 1000	$< 10^{-3}$		Chemin et al. (2011)
NGC 0891	ISO	2	2	0	0	20.00	3.20		Athanassoula et al. (1987b)
NGC 4244	ISO	2	2	0	0	13.30	3.00		Athanassoula et al. (1987b)
NGC 5907	ISO	2	2	0	0	26.90	3.20		Athanassoula et al. (1987b)
	BUR	2	3	1	1	5.41	117.28		Wang & Chen (2021)
	NFW	1	3	1	0	16.53	12.01		
NGC 701	ISO	2	2	0	0	4.30	35.41		Kent (1986)
	NFW	1	3	1	0	70.00	63.63		Samurović (2017)
NGC 753	ISO	2	2	0	0	10.90	6.82		Kent (1986)
NGC1085	ISO	2	2	0	0	7.00	362.3		Kent (1986)*
	NFW	1	3	1	0	80.00 ± 20.00	15.96 ± 2.28		Kent (1986)
	NFW	1	3	1	0	100.00 ± 20.00	15.96 ± 2.28		Samurović (2014)
NGC 1325	ISO	2	2	0	0	–	0.13		Kent (1986)
NGC 1353	ISO	2	2	0	0	3.50	70.7		Kent (1986)
NGC 1417	ISO	2	2	0	0	19.8	3.97		Kent (1986)
NGC 1421	ISO	2	2	0	0	8.00	11.5		Kent (1986)
NGC 2590	ISO	2	2	0	0	10.90	10.09		Kent (1986)
NGC 2608	ISO	2	2	0	0	3.00	33.31		Kent (1986)
NGC 2708	ISO	2	2	0	0	2.80	172.23		Kent (1986)
NGC 2715	ISO	2	2	0	0	36.70	0.32		Kent (1986)
NGC 2815	ISO	2	2	0	0	13.50	7.8		Kent (1986)
NGC 2998	ISO	2	2	0	0	29.00	1		Kent (1986)
	ISO	2	2	0	0	24.8	1.8		Broeils (1992)
	BUR	2	3	1	1	17.96	7.02		Wang & Chen (2021)

Table 10 Continued.

Galaxy	Profile	α	β	γ	δ	r_s kpc	ρ_s $10^{-3} M_\odot \cdot pc^{-3}$	Additional info	References
	NFW	1	3	1	0	24.05	4.76		
NGC 3054	ISO	2	2	0	0	17.60	4.59		Kent (1986)
NGC 3067	ISO	2	2	0	0	6.40	11.13		Kent (1986)
NGC 3200	ISO	2	2	0	0	3.50	112.6		Kent (1986)
NGC 3495	ISO	2	2	0	0	3.30	72.45		Kent (1986)
NGC 4062	ISO	2	2	0	0	13.10	3.05		Kent (1986)
	ISO	2	2	0	0	12.0	10.0		Spano et al. (2008)
	NFW	1	3	1	0	5.2	75.0		Spano et al. (2008)
NGC 4605	ISO	2	2	0	0	1.00	236.88		Kent (1986)
	ISO	2	2	0	0	4.20	63.00		Athanassoula et al. (1987b)
NGC 4800	ISO	2	2	0	0	1.00	569.11		Kent (1986)
NGC 4861	ISO	2	2	0	0	2.22	13.98 ± 1.58		van Eymeren et al. (2009)
	NFW	1	3	1	0	13.24	5.97		van Eymeren et al. (2009)
NGC 7537	ISO	2	2	0	0	15.10	1.82		Kent (1986)
NGC 7541	ISO	2	2	0	0	6.90	23.81		Kent (1986)
	ISO	2	2	0	0	11.7	18.40		Athanassoula et al. (1987b)
NGC 7664	ISO	2	2	0	0	5.80	21.26		Kent (1986)
	ISO	2	2	0	0	15.00	8.5		Athanassoula et al. (1987b)
NGC 853	gNFW	-	-	< 1.29	0	< 4.83	> 23.30		Relatores et al. (2019)
NGC 959	gNFW	-		0.68	-	< 4.41	> 16.35		Relatores et al. (2019)
	ISO	2	2	0	0	0.4 ± 0.1	1117.0 ± 29.0		Kuzio de Naray et al. (2008)
	NFW	1	3	1	0	4.48	55.25		Kuzio de Naray et al. (2008)
NGC 1035	gNFW	-	-	< 0.61	-	< 5.05	> 82.61		Relatores et al. (2019)
	gNFW	-	-	0.7	-	2.93	83.78		Cooke et al. (2022)
NGC 4376	gNFW	-	-	< 0.7	-	< 3.70	> 68.48		Relatores et al. (2019)
NGC 4396	gNFW	-	-	0.66	-	6.38	30.46		Relatores et al. (2019)
NGC 4632	gNFW	-	-	1.18	-	> 5.26	< 10.56		Relatores et al. (2019)
NGC 5949	gNFW	-	-	< 0.76	-	< 2.98	> 120.26		Relatores et al. (2019)
	ISO	2	2	0	0	1.0	426.0		Spano et al. (2008)
	NFW	1	3	1	0	12.0	10.0		Spano et al. (2008)
NGC 6106	gNFW	-	-	< 0.71	-	< 5.18	> 51.88		Relatores et al. (2019)
	gNFW	-	-	0.7	-	1.45	361.84		Cooke et al. (2022)
NGC 6207	gNFW	-	-	< 0.83	-	< 5.51	> 54.11		Relatores et al. (2019)
NGC 7320	gNFW	-	-	< 0.76	-	< 1.93	> 206.65		Relatores et al. (2019)
UGC 3371	gNFW	-	-	< 0.59	-	< 5.21	> 15.87		Relatores et al. (2019)
	ISO	2	2	0	0	3.70	18.00		de Blok & Bosma (2002)
	BUR	2	3	1	1	5.55	20.8		Rodrigues et al. (2017)
	BUR	2	3	1	1	10.76	3.87		Rodrigues et al. (2017)
	NFW	1	3	1	0	11676.50	0.0024		de Blok & Bosma (2002)
	NFW	1	3	1	0	9.63	6.17		van den Bosch & Swaters (2001)
	NFW	1	3	1	0	11.64	4.07		van den Bosch & Swaters (2001)
UGC 4169	gNFW	-	-	< 0.78	-	< 5.20	> 34.60		Relatores et al. (2019)

Table 10 Continued.

Galaxy	Profile	α	β	γ	δ	r_s kpc	ρ_s $10^{-3}M_\odot \cdot pc^{-3}$	Additional info	References
UGC 11891	gNFW	-	-	< 1.44	-	< 11.42	> 4.88		Relatores et al. (2019)
NGC 7339	BUR	2	3	1	1	7.84	41.36		Gentile et al. (2004)
	ISO	2	2	0	0	5.39	33.97		Gentile et al. (2004)
	NFW	1	3	1	0	14.84	10.10		Gentile et al. (2004)
	MOO	1.5	3	1.5	0	26.7	1.48		Gentile et al. (2004)
NGC 2903	ISO	2	2	0	0	7.78	11.78		Begeman et al. (1991)
	BUR	2	3	1	1	6.80	47.8		Rodrigues et al. (2017)
	ISO	2	2	0	0	1.01 ± 0.45	541.1 ± 480.5		de Blok et al. (2008)
	NFW	1	3	1	0	8.51	33.50		de Blok et al. (2008)
	ISO	2	2	0	0	4	35.7		Begeman (1987), Begeman (1989)
	ISO	2	2	0	0	2.9	80.21		Kent (1987)
	ISO	2	2	0	0	3.5	56.86		Lake & Feinswog (1989)
	ISO	2	2	0	0	0.0 ± 0.1	> 1000		Chemin et al. (2011)
	NFW	1	3	1	0	4.16	180.91		Chemin et al. (2011)
	EIN	n=9.6 ± 2.1	-	-	-	3.2 ± 0.4	72.4 ± 19.4		Chemin et al. (2011)
	NFW	1	3	1	0	3.9	251.19		de La Macorra et al. (2011)
	BDM					1.9	1584.89	$r_c = 1.9$kpc	de La Macorra et al. (2011)
	BUR	2	3	1	1	4.12	133.61		Wang & Chen (2021)
	NFW	1	3	1	0	12.95	14.26		
NGC 1566	ISO	2	2	0	0	1.9 ± 0.6	92 ± 50		Elagali et al. (2019)
	BUR	2	3	1	1	4.3 ± 0.8	82 ± 37		Elagali et al. (2019)
	NFW	1	3	1	0	9.52 ± 1.78	4.5		Elagali et al. (2019)
NGC 1705	ISO	2	2	0	0	0.13 ± 0.03	3600 ± 1800		Elson et al. (2013)
	NFW	1	3	1	0	1.02	254.85		Elson et al. (2013)
NGC 1560	ISO	2	2	0	0	10.69	5.51		Begeman et al. (1991)
	ISO	2	2	0	0	1.60	57.10		de Blok & Bosma (2002)
	NFW	1	3	1	0	26.70	1.55		de Blok & Bosma (2002)
	ISO	2	2	0	0	1.8	40.60		de Blok & McGaugh (1997)
	NFW	1	3	1	0	6.03	9.88		Gentile et al. (2010)
	soliton+NFW	-	-	-	-	$12.7^{1.3}_{-1.7}$	2640.1		Bernal et al. (2018)
N55	IS0	2	2	0	0	8.7	7		Puche & Carignan (1991), Côté et al. (2000)
	ISO	2	2	0	0	2.4	36.2		de Blok & McGaugh (1997)
	ISO	2	2	0	0	8.7	7.0		Puche et al. (1991)
N801	IS0	2	2	0	0	74	0.3		Puche & Carignan (1991), Côté et al. (2000), Broeils (1992)
	BUR	2	3	1	1	21.10	4.43		Wang & Chen (2021)
	NFW	1	3	1	0	313.5	0.04		
NGC 1569	ISO	2	2	0	0	2.71 ± 0.81	15.23 ± 2.45		Oh et al. (2015)
	NFW	1	3	1	0	5.66	6.44		
NGC 5585	ISO	2	2	0	0	2.8 ± 0.3	60.00		Blais-Ouellette et al. (1999), Cote et al. (1991)

Table 10 Continued.

Galaxy	Profile	α	β	γ	δ	r_s kpc	ρ_s $10^{-3}M_\odot \cdot pc^{-3}$	Additional info	References
	ISO	2	2	0	0	4.1 ± 0.4	23.00		Blais-Ouellette et al. (1999)
	ISO	2	2	0	0	4.3 ± 0.4	24.00		Blais-Ouellette et al. (1999)
	ISO	2	2	0	0	1.3	104		de Blok & McGaugh (1997)
	ISO	2	2	0	0	3.0 ± 0.2	54.0 ± 6.0		Cote et al. (1991)
	ISO	2	2	0	0	2.80	69.0		Spano et al. (2008)
	NFW	1	3	1	0	16.0	5.0		Spano et al. (2008)
NGC 925	ISO	2	2	0	0	> 6667.7	< 0.0024		de Blok et al. (2008)
	BUR	2	3	1	1	8.46	16.1		Rodrigues et al. (2017)
	NFW	1	3	1	0	16.82	4.45		de Blok et al. (2008)
	ISO	2	2	0	0	9.6 ± 1.8	6.0 ± 0.8		Chemin et al. (2011)
	NFW	1	3	1	0	105.57	0.23		Chemin et al. (2011)
	EIN	n=0.1 ± 0.1	-	-	-	8.9 ± 0.6	4.5 ± 0.5		Chemin et al. (2011)
	NFW	1	3	1	0	10000	0.0002		de La Macorra et al. (2011)
	BDM					10.3	31.62	$r_c = 12.0$kpc	de La Macorra et al. (2011)
NGC 2976	ISO	2	2	0	0	5.09 ± 2.54	35.5 ± 3.1		de Blok et al. (2008)
	BUR	2	3	1	1	2.38	110		Rodrigues et al. (2017)
	NFW	1	3	1	0	> 6667.7	< 0.0024		de Blok et al. (2008)
	ISO	2	2	0	0	4.5 ± 2.8	36.6 ± 4.7		Chemin et al. (2011)
	NFW	1	3	1	0	32.70	1.04		Chemin et al. (2011)
	EIN	n=4.9 ± 77.8	-	-	-	> 1000	0.0 ± 0.6		Chemin et al. (2011)
	NFW	1	3	1	0	10000	0.002		de La Macorra et al. (2011)
	BDM					2.5	316.23	$r_c = 2.5$kpc	de La Macorra et al. (2011)
	BUR	2	3	1	1	2.06	118.78		Wang & Chen (2021)
	NFW	1	3	1	0	112.8	0.07		
NGC 3031	ISO	2	2	0	0	4.13 ± 23.4	12.2 ± 124.6		de Blok et al. (2008)
	BUR	2	3	1	1	5.03	28.3		Rodrigues et al. (2017)
	NFW	1	3	1	0	11.06	5.86		de Blok et al. (2008)
	ISO	2	2	0	0	2.0	68.44		Kent (1987)
	ISO	2	2	0	0	0.8 ± 0.3	740.0 ± 434.0		Chemin et al. (2011)
	NFW	1	3	1	0	4.77	82.18		Chemin et al. (2011)
	EIN	n=0.1 ± 0.2	-	-	-	7.7 ± 0.9	7.0 ± 1.7		Chemin et al. (2011)
	NFW	1	3	1	0	1.9	1584.89		de La Macorra et al. (2011)
	BDM					9.5	2511.89	$r_c = 0.19$kpc	de La Macorra et al. (2011)
NGC 4236	ISO	2	2	0	0	3.6	15.22		Kent (1987)
	ISO	2	2	0	0	3.0	22.67		Lake & Feinswog (1989)
NGC 3521	ISO	2	2	0	0	1.32 ± 0.76	370.2 ± 451.1		de Blok et al. (2008)
	BUR	2	3	1	1	2.14	1010		Rodrigues et al. (2017)
	NFW	1	3	1	0	11.67	16.09		de Blok et al. (2008)
	ISO	2	2	0	0	2.5 ± 0.9	75.6 ± 45.8		Chemin et al. (2011)
	NFW	1	3	1	0	17.00	6.29		Chemin et al. (2011)
	EIN	n=1.2 ± 0.9	-	-	-	9.4 ± 1.6	6.1 ± 2.5		Chemin et al. (2011)
	NFW	1	3	1	0	5.3	158.49		de La Macorra et al. (2011)
	BDM					2.0	1995.26	$r_c = 2.0$kpc	de La Macorra et al. (2011)

Table 10 Continued.

Galaxy	Profile	α	β	γ	δ	r_s kpc	ρ_s $10^{-3}M_\odot \cdot pc^{-3}$	Additional info	References
	BUR	2	3	1	1	14.24	17.43		Wang & Chen (2021)
	NFW	1	3	1	0	229.36	0.17		
NGC 3621	ISO	2	2	0	0	5.88 ± 0.32	13.0 ± 1.1		de Blok et al. (2008)
	BUR	2	3	1	1	12.04	10.5		Rodrigues et al. (2017)
	NFW	1	3	1	0	26.26	2.49		de Blok et al. (2008)
	ISO	2	2	0	0	5.6 ± 0.2	14.4 ± 0.9		Chemin et al. (2011)
	NFW	1	3	1	0	20.55	3.83		Chemin et al. (2011)
	EIN	n=6.4 ± 1.0	-	-	-	39.9 ± 12.3	0.3 ± 0.2		Chemin et al. (2011)
	NFW	1	3	1	0	7.9	31.62		de La Macorra et al. (2011)
	BDM					7.7	31.62	$r_c = 0.01$kpc	de La Macorra et al. (2011)
N 5023	ISO	2	2	0	0	0.90	200.70		de Blok & Bosma (2002)
	NFW	1	3	1	0	9.90	9.65		de Blok & Bosma (2002)
N 2366	ISO	2	2	0	0	0.70	147.30		de Blok & Bosma (2002)
	NFW	1	3	1	0	6.05	9.23		de Blok & Bosma (2002)
	ISO	2	2	0	0	1.32 ± 0.07	37.3 ± 2.4		de Blok et al. (2008)
	NFW	1	3	1	0	> 6667.7	< 0.0024		de Blok et al. (2008)
	ISO	2	2	0	0	1.3 ± 0.1	40.1 ± 4.2		Chemin et al. (2011)
	NFW	1	3	1	0	24.33	0.89		Chemin et al. (2011)
	EIN	n=1.1 ± 0.2	-	-	-	3.2 ± 0.3	5.7 ± 1.1		Chemin et al. (2011)
	ISO	2	2	0	0	0.94	56.66 ± 10.42		van Eymeren et al. (2009)
	NFW	1	3	1	0	12.50	5.82		van Eymeren et al. (2009)
	ISO	2	2	0	0	1.47 ± 0.06	44.6 ± 2.2		Oh et al. (2008)
	NFW	1	3	1	0	> 12215.08	< 0.0023		Oh et al. (2008)
	NFW	1	3	1	0	18.6	1.59		de La Macorra et al. (2011)
	BDM					2.2	79.43	$r_c = 2.2$kpc	de La Macorra et al. (2011)
	NFW	1	3	1	0	17.20	1.44		Oh et al. (2015)
	ISO	2	2	0	0	1.21 ± 0.04	43.89 ± 2.51		Oh et al. (2015)
N 3274	ISO	2	2	0	0	0.30	1259.40		de Blok & Bosma (2002)
	NFW	1	3	1	0	2.18	117.96		de Blok & Bosma (2002)
N 5533	ISO	2	2	0	0	34.6	1.0		Broeils (1992)
N 4455	ISO	2	2	0	0	1.30	63.20		de Blok & Bosma (2002)
	NFW	1	3	1	0	25.58	1.48		de Blok & Bosma (2002)
N 100	ISO	2	2	0	0	1.40	105.30		de Blok & Bosma (2002)
	NFW	1	3	1	0	16.82	4.45		de Blok & Bosma (2002)
NGC 3738	NFW	1	3	1	0	33.92	11.51		Oh et al. (2015)
	ISO	2	2	0	0	0.45 ± 0.04	2132.36 ± 277.75		Oh et al. (2015)
NGC 24	ISO	2	2	0	0	5.6	22.0		Chemin et al. (2006)
	BUR	2	3	1	1	1.53	403.45		Wang & Chen (2021)
	NFW	1	3	1	0	9.41	9.37		
NGC 45	ISO	2	2	0	0	6.2	13.0		Chemin et al. (2006)
	ISO	2	2	0	0	4.2	32.0		Chemin et al. (2006)
N 6674	ISO	2	2	0	0	119.5	0.6		Broeils (1992)
NGC 7137	ISO	2	2	0	0	0.6 ± 0.1	274.0 ± 17.0		Kuzio de Naray et al. (2008)

Table 10 Continued.

Galaxy	Profile	α	β	γ	δ	r_s kpc	ρ_s $10^{-3} M_\odot \cdot pc^{-3}$	Additional info	References
	NFW	1	3	1	0	5.06	18.54		Kuzio de Naray et al. (2008)
NGC5846-UDG1	NFW	1	3	1	0		1.8	$c = 6, M_h = 10^{8.89}\ M_\odot$	Liang et al. (2023)
	BUR	2	3	1	1		10.27	$c = 22, M_h = 10^{9.82}\ M_\odot$	Liang et al. (2023)
NGC 5204	ISO	2	2	0	0	2.7 ± 0.1	41.00		Sicotte & Carignan (1997)
NGC 6822	ISO	2	2	0	0	1.63	42.40		Weldrake et al. (2003)
	NFW	1	3	1	0	47.68	0.67		Weldrake et al. (2003)
	ISO	2	2	0	0	1.40	47.90		Weldrake et al. (2003)
	NFW	1	3	1	0	140.60	0.21		Weldrake et al. (2003)
	ISO	2	2	0	0	1.51	44.60		Weldrake et al. (2003)
	NFW	1	3	1	0	11916.99	0.0023		Weldrake et al. (2003)
	ISO	2	2	0	0	1.24	53.20		Weldrake et al. (2003)
	NFW	1	3	1	0	113.76	0.25		Weldrake et al. (2003)
	ISO	2	2	0	0	1.29	52.40		Weldrake et al. (2003)
	NFW	1	3	1	0	11914.28	0.0023		Weldrake et al. (2003)
	NFW	1	3	1	0	87.00 ± 49.0	0.28		Frigerio Martins (2009)
	BUR	2	3	1	1	$3.3^{+0.8}_{-0.7}$	$31.62^{+8.19}_{-6.5}$		Gammaldi et al. (2021)
	NFW	1	3	1	0	5.9	7.94		Gammaldi et al. (2021)
	ISO	2	2	0	0	1.87	29.22		Namumba et al. (2017)
	NFW	1	3	1	0	49.52	0.54		Namumba et al. (2017)
	ISO	2	2	0	0	1.46	64.76		Rodríguez-Meza (2012)
UGCA 442	ISO	2	2	0	0	1.7	71.0		Côté et al. (2000)
UGC 8017	NFW	1	3	1	0	379.0 ± 3600.0	221.55		Frigerio Martins (2009)
	ISO	2	2	0	0	2.48	480.7		Rodríguez-Meza (2012)
UGC 11455	NFW	1	3	1	0	121.0 ± 13.0	1.33		Frigerio Martins (2009)
	ISO	2	2	0	0	6.30	73.98		Rodríguez-Meza (2012)
	BUR	2	3	1	1	8.83	59.86		Wang & Chen (2021)
	NFW	1	3	1	0	522.5	0.05		
U 2885	ISO	2	2	0	0	13.20	8.5		Kent (1986)
	ISO	2	2	0	0	1.0	1656.0		de Blok & McGaugh (1997)
	ISO	2	2	0	0	44.9	1.3		Roelfsema & Allen (1985)
U 11810	ISO	2	2	0	0	30.1	0.77		Kent (1986)
U 12810	ISO	2	2	0	0	3.90	71.99		Kent (1986)
UGC 2259	ISO	2	2	0	0	41.84	5.28		Begeman et al. (1991)
	ISO	2	2	0	0	0.4	948		de Blok & McGaugh (1997)
	ISO	2	2	0	0	5.5	17.0		Carignan et al. (1988)
	ISO	2	2	0	0	9.1	7.91		Kent (1987)
	ISO	2	2	0	0	0.45	751.0		Swaters et al. (2003)
	NFW	1	3	1	0	3.18	63.00		Swaters et al. (2003)
UGC 4115	ISO	2	2	0	0	0.94 ± 0.03	148.2 ± 2.4		de Blok et al. (2001)
	NFW	1	3	1	0	35.57	1.36		de Blok et al. (2001)
	soliton+NFW	-	-	-	-	1.53	280		Bernal et al. (2018)
UGC 11454	ISO	2	2	0	0	1.95 ± 0.10	146.9 ± 11.8		de Blok et al. (2001)
	NFW	1	3	1	0	19.56	7.70		de Blok et al. (2001)

Table 10 Continued.

Galaxy	Profile	α	β	γ	δ	r_s kpc	ρ_s $10^{-3}M_\odot \cdot pc^{-3}$	Additional info	References
	ISO	2	2	0	0	1.60	130.00		Kun et al. (2017)
	EIN	n=1.91	-	-	-	12.49	1.64		
	NFW	1	3	1	0	13.00	8.60		
	soliton+NFW	-	-	-	-	9.31	25.4		Bernal et al. (2018)
UGC 11557	ISO	2	2	0	0	5.48 ± 0.55	15.2 ± 0.9		de Blok et al. (2001)
	NFW	1	3	1	0	566.80	0.054		de Blok et al. (2001)
	ISO	2	2	0	0	3.35	20.00		Swaters et al. (2003)
	NFW	1	3	1	0	532.08	0.054		Swaters et al. (2003)
	ISO	2	2	0	0	5.0	18.0		Spano et al. (2008)
	NFW	1	3	1	0	37.0	1.0		Spano et al. (2008)
	BUR	2	3	1	1	5.52	10.51		Wang & Chen (2021)
	NFW	1	3	1	0	108.6	0.06		
	soliton+NFW	-	-	-	-	2.26	146		Bernal et al. (2018)
UGC 11583	ISO	2	2	0	0	0.63 ± 0.08	117.8 ± 16.5		de Blok et al. (2001)
	NFW	1	3	1	0	24.88	1.36		de Blok et al. (2001)
	soliton+NFW	-	-	-	-	0.86	732		Bernal et al. (2018)
UGC 11616	ISO	2	2	0	0	1.45 ± 0.05	208.9 ± 11.6		de Blok et al. (2001)
	NFW	1	3	1	0	13.06	12.62		de Blok et al. (2001)
	ISO	2	2	0	0	1.40	61.00		Kun et al. (2017)
	EIN	n=0.89	-	-	-	6.70	3.10		
	NFW	1	3	1	0	9.70	5.30		
	soliton+NFW	-	-	-	-	4.21	86.0		Bernal et al. (2018)
UGC 11648	ISO	2	2	0	0	1.95 ± 0.25	104.9 ± 20.7		de Blok et al. (2001)
	NFW	1	3	1	0	24.37	4.07		de Blok et al. (2001)
	soliton+NFW	-	-	-	-	11.5	12.1		Bernal et al. (2018)
UGC 11748	ISO	2	2	0	0	0.36 ± 0.15	8540 ± 6661		de Blok et al. (2001)
	NFW	1	3	1	0	3.18	502.39		de Blok et al. (2001)
	ISO	2	2	0	0	1.12	1010		Kun et al. (2017)
	EIN	n=1.33	-	-	-	6.57	30.50		
	NFW	1	3	1	0	6.47	117.00		
	soliton+NFW	-	-	-	-	2.60	803		Bernal et al. (2018)
UGC 11819	ISO	2	2	0	0	2.93 ± 0.14	88.2 ± 5.2		de Blok et al. (2001)
	NFW	1	3	1	0	52.69	2.40		de Blok et al. (2001)
	ISO	2	2	0	0	1.43	23.40		Kun et al. (2017)
	EIN	n=0.35	-	-	-	3.82	4.41		
	NFW	1	3	1	0	7.39	3.18		
	soliton+NFW	-	-	-	-	8.98	27.5		Bernal et al. (2018)
ESO-LV 014-0040	ISO	2	2	0	0	2.55 ± 0.18	249.5 ± 27.0		de Blok et al. (2001)
	NFW	1	3	1	0	16.14	25.50		de Blok et al. (2001)
	soliton+NFW	-	-	-	-	7.87	90.7		Bernal et al. (2018)
ESO-LV 084-0411	ISO	2	2	0	0	6.41 ± 0.56	5.2 ± 0.3		de Blok et al. (2001)
	NFW	1	3	1	0	241.33	0.054		de Blok et al. (2001)
	soliton+NFW	-	-	-	-	4.42	19.0		Bernal et al. (2018)

Table 10 Continued.

Galaxy	Profile	α	β	γ	δ	r_s kpc	ρ_s $10^{-3} M_\odot \cdot pc^{-3}$	Additional info	References
ESO-LV 120-0211	ISO	2	2	0	0	0.57 ± 0.08	45.5 ± 9.2		de Blok et al. (2001)
	NFW	1	3	1	0	5.73	2.40		de Blok et al. (2001)
	soliton+NFW	-	-	-	-	1.18	30.2		Bernal et al. (2018)
ESO-LV 187-0510	ISO	2	2	0	0	0.97 ± 0.05	53.5 ± 3.2		de Blok et al. (2001)
	NFW	1	3	1	0	32.84	0.74		de Blok et al. (2001)
	soliton+NFW	-	-	-	-	0.73	330		Bernal et al. (2018)
ESO-LV 206-0140	ISO	2	2	0	0	1.17 ± 0.05	231.1 ± 16.9		de Blok et al. (2001)
	NFW	1	3	1	0	8.13	19.80		de Blok et al. (2001)
	soliton+NFW	-	-	-	-	3.28	139		Bernal et al. (2018)
ESO-LV 302-0120	ISO	2	2	0	0	1.90 ± 0.09	53.6 ± 3.4		de Blok et al. (2001)
	NFW	1	3	1	0	19.90	2.58		de Blok et al. (2001)
	soliton+NFW	-	-	-	-	1.20	908		Bernal et al. (2018)
ESO-LV 305-0090	ISO	2	2	0	0	2.09 ± 0.14	27.3 ± 1.8		de Blok et al. (2001)
	NFW	1	3	1	0	431.46	0.054		de Blok et al. (2001)
	soliton+NFW	-	-	-	-	1.70	134		Bernal et al. (2018)
ESO-LV 425-0180	ISO	2	2	0	0	4.41 ± 0.75	30.0 ± 6.6		de Blok et al. (2001)
	NFW	1	3	1	0	129.72	0.47		de Blok et al. (2001)
	soliton+NFW	-	-	-	-	2.13	229		Bernal et al. (2018)
ESO-LV 488-0490	ISO	2	2	0	0	1.63 ± 0.04	101.1 ± 3.1		de Blok et al. (2001)
	NFW	1	3	1	0	57.03	1.30		de Blok et al. (2001)
	soliton+NFW	-	-	-	-	1.13	1090		Bernal et al. (2018)
U 5750	ISO	2	2	0	0	5.00	7.90		de Blok & Bosma (2002)
	NFW	1	3	1	0	102.26	0.17		de Blok & Bosma (2002)
	ISO	2	2	0	0	4.0	9.1		de Blok & McGaugh (1997)
	BUR	2	3	1	1	6.73	11.5		Rodrigues et al. (2017)
	ISO	2	2	0	0	5.7 ± 0.4	7.1 ± 0.3		Kuzio de Naray et al. (2006)
	NFW	1	3	1	0	867.18	0.018		Kuzio de Naray et al. (2006)
	constrainedNFW	1	3	1	0	9.98	5.38		Kuzio de Naray et al. (2006)
	ISO	2	2	0	0	5.7 ± 0.4	7.1 ± 0.3		Kuzio de Naray et al. (2008)
	NFW	1	3	1	0	867.18	0.018		Kuzio de Naray et al. (2008)
	ISO	2	2	0	0	4.25 ± 0.39	10.6 ± 1.0		de Blok et al. (2001)
	NFW	1	3	1	0	63.13	0.33		de Blok et al. (2001)
	ISO	2	2	0	0	40.97	0.54		Kun et al. (2017)
	EIN	n=0.15	-	-	-	19.00	0.47		
	NFW	1	3	1	0	2000	0.0012		
U 5005	ISO	2	2	0	0	4.70	11.50		de Blok & Bosma (2002)
	NFW	1	3	1	0	50.35	0.54		de Blok & Bosma (2002)
	ISO	2	2	0	0	2.2	40.1		de Blok & McGaugh (1997)
	BUR	2	3	1	1	11.66	5.31		Rodrigues et al. (2017)
U 1230	ISO	2	2	0	0	1.50	103.50		de Blok & Bosma (2002)
	BUR	2	3	1	1	3.53	77.7		Rodrigues et al. (2017)
	NFW	1	3	1	0	9.52	11.18		
	ISO	2	2	0	0	3.7	14.2		de Blok & McGaugh (1997)

Table 10 Continued.

Galaxy	Profile	α	β	γ	δ	r_s kpc	ρ_s $10^{-3} M_\odot \cdot pc^{-3}$	Additional info	References
	ISO	2	2	0	0	7.19	4.53		Kun et al. (2017)
	EIN	n=1.38	-	-	-	34.17	0.16		
	NFW	1	3	1	0	290	0.042		
	ISO	2	2	0	0	3.7	14.2		de Blok & McGaugh (1997)
U 731	ISO	2	2	0	0	0.60	333.90		de Blok & Bosma (2002)
	BUR	2	3	1	1	5.86	6.87		Rodrigues et al. (2017)
	NFW	1	3	1	0	3.81	33.04		de Blok & Bosma (2002)
	NFW	1	3	1	0	4.34	22.53		van den Bosch & Swaters (2001)
	NFW	1	3	1	0	5.17	14.69		van den Bosch & Swaters (2001)
	ISO	2	2	0	0	0.87	163.0		Swaters et al. (2003)
	NFW	1	3	1	0	7.11	10.95		Swaters et al. (2003)
U 4173	ISO	2	2	0	0	3.50	7.30		de Blok & Bosma (2002)
	BUR	2	3	1	1	4.12	8.88		Rodrigues et al. (2017)
	NFW	1	3	1	0	4262	0.0024		de Blok & Bosma (2002)
UGC 477	ISO	2	2	0	0	2.2 ± 0.1	57.0 ± 2.0		Kuzio de Naray et al. (2006)
	NFW	1	3	1	0	23.57	2.78		Kuzio de Naray et al. (2006)
	constrainedNFW	1	3	1	0	17.14	4.31		Kuzio de Naray et al. (2006)
U 4325	ISO	2	2	0	0	2.70	100.10		de Blok & Bosma (2002)
	BUR	2	3	1	1	4.32	104		Rodrigues et al. (2017)
	BUR	2	3	1	1	1.45	309		Rodrigues et al. (2017)
	NFW	1	3	1	0	44428.10	0.0024		de Blok & Bosma (2002)
	NFW	1	3	1	0	2.31	123.11		van den Bosch & Swaters (2001)
	NFW	1	3	1	0	2.73	76.07		van den Bosch & Swaters (2001)
	BUR	2	3	1	1	1.77	231.00		Marchesini et al. (2002)
	NFW	1	3	1	0	8.08	13.89		Marchesini et al. (2002)
	ISO	2	2	0	0	3.3 ± 0.2	91.0 ± 4.0		Kuzio de Naray et al. (2006)
	constrainedNFW	1	3	1	0	48.90	2.78		Kuzio de Naray et al. (2006)
	ISO	2	2	0	0	0.94	263.0		Swaters et al. (2003)
	NFW	1	3	1	0	7.48	18.50		Swaters et al. (2003)
	ISO	2	2	0	0	4.1 ± 0.3	88 ± 3.0		Kuzio de Naray et al. (2008)
	NFW	1	3	1	0	48.90	2.78		Kuzio de Naray et al. (2008)
	ISO	2	2	0	0	1.9	121.0		Spano et al. (2008)
	NFW	1	3	1	0	2.7	1.0		Spano et al. (2008)
	ISO	2	2	0	0	1.95	64.57		Rodríguez-Meza (2012)
UGC 4499	NFW	1	3	1	0	8.61	5.41		van den Bosch & Swaters (2001)
	NFW	1	3	1	0	109.60	0.13		van den Bosch & Swaters (2001)
	BUR	2	3	1	1	2.52	59.1		Rodrigues et al. (2017)
	BUR	2	3	1	1	2.28	90.00		Marchesini et al. (2002)
	NFW	1	3	1	0	10.61	5.12		Marchesini et al. (2002)
	ISO	2	2	0	0	2.08	37.4		Swaters et al. (2003)
	NFW	1	3	1	0	44.45	0.78		Swaters et al. (2003)
	ISO	2	2	0	0	2.2	43.0		Spano et al. (2008)
	NFW	1	3	1	0	4.3	19.0		Spano et al. (2008)

Table 10 Continued.

Galaxy	Profile	α	β	γ	δ	r_s kpc	ρ_s $10^{-3}M_\odot \cdot pc^{-3}$	Additional info	References
UGC 5721	ISO	2	2	0	0	0.39	874.0		Swaters et al. (2003)
	BUR	2	3	1	1	1.24	307		Rodrigues et al. (2017)
	NFW	1	3	1	0	2.85	69.34		Swaters et al. (2003)
	ISO	2	2	0	0	1.0	408.0		Spano et al. (2008)
	NFW	1	3	1	0	2.6	84.0		Spano et al. (2008)
	BUR	2	3	1	1	1.05	448.49		Wang & Chen (2021)
	NFW	1	3	1	0	4.71	22.29		
UGC 5414	NFW	1	3	1	0	> 338.19	< 0.054		van den Bosch & Swaters (2001)
	NFW	1	3	1	0	> 171.76	< 0.054		van den Bosch & Swaters (2001)
	BUR	2	3	1	1	5.51	9.17		Rodrigues et al. (2017)
UGC 6446	NFW	1	3	1	0	3.99	27.88		van den Bosch & Swaters (2001)
	NFW	1	3	1	0	11.34	2.96		van den Bosch & Swaters (2001)
	BUR	2	3	1	1	4.53	15.3		Rodrigues et al. (2017)
UGC 7232	NFW	1	3	1	0	36.83	0.92		van den Bosch & Swaters (2001)
	NFW	1	3	1	0	> 79.48	< 0.054		van den Bosch & Swaters (2001)
UGC 7323	NFW	1	3	1	0	36.69	1.18		van den Bosch & Swaters (2001)
	NFW	1	3	1	0	> 258.57	< 0.054		van den Bosch & Swaters (2001)
	BUR	2	3	1	1	6.91	13.0		Rodrigues et al. (2017)
	ISO	2	2	0	0	7.7	12.0		Spano et al. (2008)
	NFW	1	3	1	0	20.0	3.0		Spano et al. (2008)
UGC 7399	NFW	1	3	1	0	3.63	57.69		van den Bosch & Swaters (2001)
	NFW	1	3	1	0	6.22	19.79		van den Bosch & Swaters (2001)
	BUR	2	3	1	1	3.97	52.0		Rodrigues et al. (2017)
	BUR	2	3	1	1	1.57	296.49		Wang & Chen (2021)
	NFW	1	3	1	0	11.59	7.01		
UGC 7524	NFW	1	3	1	0	11.28	4.71		van den Bosch & Swaters (2001)
	NFW	1	3	1	0	22.92	1.24		van den Bosch & Swaters (2001)
	BUR	2	3	1	1	0.68	167		Rodrigues et al. (2017)
	BUR	2	3	1	1	3.59	18.7		Rodrigues et al. (2017)
	ISO	2	2	0	0	3.4	24.0		Spano et al. (2008)
	NFW	1	3	1	0	19.0	2.0		Spano et al. (2008)
UGC 7577	BUR	2	3	1	1	INF	0.825		Rodrigues et al. (2017)
UGC 7559	NFW	1	3	1	0	128.97	0.098		van den Bosch & Swaters (2001)
	NFW	1	3	1	0	150.13	0.074		van den Bosch & Swaters (2001)
	BUR	2	3	1	1	0.88	106		Rodrigues et al. (2017)
UGC 8837	BUR	2	3	1	1	INF	19.1		Rodrigues et al. (2017)
UGC 7603	NFW	1	3	1	0	21.31	1.69		van den Bosch & Swaters (2001)
	NFW	1	3	1	0	> 289.78	< 0.054		van den Bosch & Swaters (2001)
	BUR	2	3	1	1	3.57	28.1		Rodrigues et al. (2017)
	BUR	2	3	1	1	1.94	78.3		Rodrigues et al. (2017)
	BUR	2	3	1	1	2.09	80.00		Marchesini et al. (2002)
	NFW	1	3	1	0	17.93	1.91		Marchesini et al. (2002)
UGC 8490	NFW	1	3	1	0	2.77	65.07		van den Bosch & Swaters (2001)

Table 10 Continued.

Galaxy	Profile	α	β	γ	δ	r_s kpc	ρ_s $10^{-3}M_\odot \cdot pc^{-3}$	Additional info	References
	NFW	1	3	1	0	5.65	14.69		van den Bosch & Swaters (2001)
	BUR	2	3	1	1	2.88	50.7		Rodrigues et al. (2017)
	ISO	2	2	0	0	0.56	424.0		Swaters et al. (2003)
	NFW	1	3	1	0	3.85	36.80		Swaters et al. (2003)
	ISO	2	2	0	0	1.90	95.0		Spano et al. (2008)
	NFW	1	3	1	0	4.50	26.0		Spano et al. (2008)
	BUR	2	3	1	1	1.58	184.84		Wang & Chen (2021)
	NFW	1	3	1	0	6.39	11.31		
UGC 9211	NFW	1	3	1	0	3.18	31.70		van den Bosch & Swaters (2001)
	NFW	1	3	1	0	4.01	18.50		van den Bosch & Swaters (2001)
	BUR	2	3	1	1	1.74	100		Rodrigues et al. (2017)
	BUR	2	3	1	1	2.36	51.9		Rodrigues et al. (2017)
UGC 11707	NFW	1	3	1	0	6.85	13.63		van den Bosch & Swaters (2001)
	NFW	1	3	1	0	7.97	9.23		van den Bosch & Swaters (2001)
	BUR	2	3	1	1	INF	0.692		Rodrigues et al. (2017)
	ISO	2	2	0	0	1.81	62.30		Swaters et al. (2003)
	NFW	1	3	1	0	18.67	2.96		Swaters et al. (2003)
	ISO	2	2	0	0	2.4	84.0		Spano et al. (2008)
	NFW	1	3	1	0	6.1	19.0		Spano et al. (2008)
UGC 11861	NFW	1	3	1	0	8.86	22.53		van den Bosch & Swaters (2001)
	NFW	1	3	1	0	10.73	12.12		van den Bosch & Swaters (2001)
	BUR	2	3	1	1	5.81	60.00		Marchesini et al. (2002)
	NFW	1	3	1	0	28.47	3.38		Marchesini et al. (2002)
	ISO	2	2	0	0	2.92	69.40		Swaters et al. (2003)
	NFW	1	3	1	0	25.55	4.45		Swaters et al. (2003)
UGC 11820	ISO	2	2	0	0	1.1 ± 0.1	274.0 ± 21.0		Kuzio de Naray et al. (2008)
UGC 128	ISO	2	2	0	0	2.3 ± 0.1	66.0 ± 0.6		Kuzio de Naray et al. (2008)
	NFW	1	3	1	0	16.90	5.10		Kuzio de Naray et al. (2008)
	ISO	2	2	0	0	6.74	6.95		Kun et al. (2017)
	EIN	n=1.48	-	-	-	37.49	0.19		
	NFW	1	3	1	0	420	0.037		
	ISO	2	2	0	0	4.0	21.7		de Blok & McGaugh (1997)
UGC 191	ISO	2	2	0	0	1.7 ± 0.1	138.0 ± 10.0		Kuzio de Naray et al. (2008)
UGC 1551	ISO	2	2	0	0	1.3 ± 0.2	57.0 ± 5.0		Kuzio de Naray et al. (2008)
UGC 1206	NFW	1	3	1	0	1.80	165.77		van den Bosch & Swaters (2001)
	NFW	1	3	1	0	2.55	65.77		van den Bosch & Swaters (2001)
UGC 12632	NFW	1	3	1	0	4.92	16.09		van den Bosch & Swaters (2001)
	NFW	1	3	1	0	5.44	12.37		van den Bosch & Swaters (2001)
	BUR	2	3	1	1	INF	1.17		Rodrigues et al. (2017)
UGC 12732	NFW	1	3	1	0	8.75	7.51		van den Bosch & Swaters (2001)
	NFW	1	3	1	0	14.38	2.77		van den Bosch & Swaters (2001)
	BUR	2	3	1	1	12.51	4.24		Rodrigues et al. (2017)
	ISO	2	2	0	0	1.77	54.70		Swaters et al. (2003)

Table 10 Continued.

Galaxy	Profile	α	β	γ	δ	r_s kpc	ρ_s $10^{-3}M_\odot \cdot pc^{-3}$	Additional info	References
	NFW	1	3	1	0	17.65	2.78		Swaters et al. (2003)
UGC 3060	BUR	2	3	1	1	13.47	6.66		Rodrigues et al. (2017)
UGC 3851	BUR	2	3	1	1	1.06	173		Rodrigues et al. (2017)
U 628	ISO	2	2	0	0	1.50	151.90		de Blok & Bosma (2002)
	NFW	1	3	1	0	10.46	13.11		de Blok & Bosma (2002)
U 1281	ISO	2	2	0	0	2.20	28.00		de Blok & Bosma (2002)
	NFW	1	3	1	0	10468.30	0.0024		de Blok & Bosma (2002)
	ISO	2	2	0	0	2.6 ± 0.1	23.0 ± 1.0		Kuzio de Naray et al. (2006)
	constrainedNFW	1	3	1	0	8.45	5.67		Kuzio de Naray et al. (2006)
U 3137	ISO	2	2	0	0	2.00	61.20		de Blok & Bosma (2002)
	NFW	1	3	1	0	11.76	6.99		de Blok & Bosma (2002)
U 10310	ISO	2	2	0	0	2.50	27.20		de Blok & Bosma (2002)
	NFW	1	3	1	0	92.99	0.33		de Blok & Bosma (2002)
	ISO	2	2	0	0	4.8	10.0		Spano et al. (2008)
	NFW	1	3	1	0	14.0	3.0		Spano et al. (2008)
	ISO	2	2	0	0	18000	13.00		Kun et al. (2017)
	EIN	n=0.99	-	-	-	38.00	1.70		
	NFW	1	3	1	0	210.00	0.041		
UGC 6614	ISO	2	2	0	0	1.86 ± 0.49	218.4 ± 102.5		de Blok et al. (2001)
	BUR	2	3	1	1	12.96	18.7		Rodrigues et al. (2017)
	NFW	1	3	1	0	21.98	7.52		de Blok et al. (2001)
	ISO	2	2	0	0	2.50	93.60		Kun et al. (2017)
	EIN	n=3.09	-	-	-	59.89	0.114		
	NFW	1	3	1	0	24.00	6.40		
U 5999	ISO	2	2	0	0	4.1	40.8		de Blok & McGaugh (1997)
UGC 10981	NFW	1	3	1	0	8.0 ± 2.9	19.20		Frigerio Martins (2009)
	ISO	2	2	0	0	1.57	647.22		Rodríguez-Meza (2012)
UGC 2034	ISO	2	2	0	0	184.0	1.0		Spano et al. (2008)
	NFW	1	3	1	0	10.0	1.0		Spano et al. (2008)
UGC 2455 (NGC 1156)	ISO	2	2	0	0	30.0	5.0		Spano et al. (2008)
	NFW	1	3	1	0	5.8	1.0		Spano et al. (2008)
UGC 2503 (NGC 1169)	ISO	2	2	0	0	188.0	1.0		Spano et al. (2008)
	NFW	1	3	1	0	57.0	1.0		Spano et al. (2008)
UGC 3876	ISO	2	2	0	0	100.0	23.0		Spano et al. (2008)
	NFW	1	3	1	0	33.0	5.0		Spano et al. (2008)
UGC 4276	ISO	2	2	0	0	3.4	49.0		Spano et al. (2008)
	NFW	1	3	1	0	6.8	19.0		Spano et al. (2008)
UGC 4274	ISO	2	2	0	0	1.0	253.0		Spano et al. (2008)
	NFW	1	3	1	0	2.3	60.0		Spano et al. (2008)
UGC 4456	ISO	2	2	0	0	15.0	1.0		Spano et al. (2008)
	NFW	1	3	1	0	14.0	2.0		Spano et al. (2008)
UGC 4555 (NGC 2649)	ISO	2	2	0	0	100.0	5.0		Spano et al. (2008)
	NFW	1	3	1	0	20.0	14.0		Spano et al. (2008)

Table 10 Continued.

Galaxy	Profile	α	β	γ	δ	r_s kpc	ρ_s $10^{-3}M_\odot \cdot pc^{-3}$	Additional info	References
	ISO	2	2	0	0	0.84 ± 0.13	676.08		Martinsson et al. (2013)
	NFW	1	3	1	0	8.38	18.44		
UGC 5175 (NGC 2977)	ISO	2	2	0	0	2.0	200.0		Spano et al. (2008)
	NFW	1	3	1	0	3.8	54.0		Spano et al. (2008)
UGC 5272	ISO	2	2	0	0	25.0	14.0		Spano et al. (2008)
	NFW	1	3	1	0	25.0	1.0		Spano et al. (2008)
UGC 5279 (NGC 3026)	ISO	2	2	0	0	3.2	95.0		Spano et al. (2008)
	NFW	1	3	1	0	35.0	3.0		Spano et al. (2008)
UGC 5789 (NGC 3319)	ISO	2	2	0	0	7.4	11.0		Spano et al. (2008)
	NFW	1	3	1	0	35.0	1.0		Spano et al. (2008)
UGC 5842 (NGC 3346)	ISO	2	2	0	0	1.7	251.0		Spano et al. (2008)
	NFW	1	3	1	0	5.0	43.0		Spano et al. (2008)
UGC 6537 (NGC 3726)	ISO	2	2	0	0	4.7	8.0		Spano et al. (2008)
	NFW	1	3	1	0	16.0	12.0		Spano et al. (2008)
	BUR	2	3	1	1	18.10	5.20		Wang & Chen (2021)
	NFW	1	3	1	0	269.35	0.06		
UGC 6778 (NGC 3893)	ISO	2	2	0	0	2.8	282.0		Spano et al. (2008)
	NFW	1	3	1	0	5.8	95.0		Spano et al. (2008)
	BUR	2	3	1	1	3.77	138.49		Wang & Chen (2021)
	NFW	1	3	1	0	17.68	6.76		
UGC 7699	ISO	2	2	0	0	2.7	29.0		Spano et al. (2008)
	NFW	1	3	1	0	15.0	2.0		Spano et al. (2008)
UGC 7876 (NGC 4635)	ISO	2	2	0	0	1.60	239.0		Spano et al. (2008)
	NFW	1	3	1	0	9.30	18.0		Spano et al. (2008)
UGC 7901 (NGC 4651)	ISO	2	2	0	0	5.80	48.0		Spano et al. (2008)
	NFW	1	3	1	0	4.0	179.0		Spano et al. (2008)
UGC 9219 (NGC 5608)	ISO	2	2	0	0	1.80	40.0		Spano et al. (2008)
	NFW	1	3	1	0	5.0	6.0		Spano et al. (2008)
UGC 9248 (NGC 5622)	ISO	2	2	0	0	1.70	75.0		Spano et al. (2008)
	NFW	1	3	1	0	1.0	10.0		Spano et al. (2008)
UGC 8508	NFW	1	3	1	0	9.50	3.71		Oh et al. (2015)
	ISO	2	2	0	0	1.95 ± 0.21	45.29 ± 2.38		Oh et al. (2015)
UGC 9465 (NGC 5727)	ISO	2	2	0	0	13.0	10.0		Spano et al. (2008)
	NFW	1	3	1	0	61.0	1.0		Spano et al. (2008)
UGC 10075 (NGC 6015)	ISO	2	2	0	0	2.80	182.0		Spano et al. (2008)
	NFW	1	3	1	0	11.0	16.0		Spano et al. (2008)
	BUR	2	3	1	1	5.37	43.54		Wang & Chen (2021)
	NFW	1	3	1	0	14.69	7.01		
UGC 12060	ISO	2	2	0	0	4.60	26.0		Spano et al. (2008)
	BUR	2	3	1	1	23.55	1.08		Rodrigues et al. (2017)
	NFW	1	3	1	0	14.0	5.0		Spano et al. (2008)
UGC 00089	ISO	2	2	0	0	$36.2^{+93.8}_{-35.7}$	$75.0^{+24.0}_{-35.0}$		Korsaga et al. (2018)

Table 10 Continued.

Galaxy	Profile	α	β	γ	δ	r_s kpc	ρ_s $10^{-3} M_\odot \cdot pc^{-3}$	Additional info	References
	NFW	1	3	1	0	2.15	1537.61		Korsaga et al. (2018)
UGC 00094	ISO	2	2	0	0	$0.6^{+0.2}_{-0.1}$	$750.0^{+1.0}_{-650.0}$		Korsaga et al. (2018)
	NFW	1	3	1	0	2.74	404.05		Korsaga et al. (2018)
UGC 00508	ISO	2	2	0	0	$4.9^{+1.0}_{-4.4}$	$250.0^{+49.0}_{-20.0}$		Korsaga et al. (2018)
	NFW	1	3	1	0	24.42	42.93		Korsaga et al. (2018)
UGC 00528	ISO	2	2	0	0	$0.5^{+9.5}_{-0.1}$	$0.0^{+1.0}_{-1.0}$		Korsaga et al. (2018)
	NFW	1	3	1	0	24.25	1.69		Korsaga et al. (2018)
UGC 00763	ISO	2	2	0	0	$1.9^{+0.3}_{-1.4}$	$70.0^{+29.0}_{-20.0}$		Korsaga et al. (2018)
	NFW	1	3	1	0	11.89	7.88		Korsaga et al. (2018)
UGC 01317	ISO	2	2	0	0	$17.2^{+0.8}_{-16.7}$	$5.0^{+10.0}_{-5.0}$		Korsaga et al. (2018)
	NFW	1	3	1	0	11.09	19.79		Korsaga et al. (2018)
UGC 01437	ISO	2	2	0	0	$0.8^{+0.1}_{-0.3}$	$750.0^{+1.0}_{-550.0}$		Korsaga et al. (2018)
	NFW	1	3	1	0	2.38	520.38		Korsaga et al. (2018)
UGC 01736	ISO	2	2	0	0	$2.6^{+0.6}_{-2.1}$	$138.0^{+67.0}_{-38.0}$		Korsaga et al. (2018)
	NFW	1	3	1	0	148.17	1.07		Korsaga et al. (2018)
114 new objects	ISO								Korsaga et al. (2018)
	NFW								Korsaga et al. (2018)
UGC 463	ISO	2	2	0	0	1.16 ± 0.21	676.1		Westfall et al. (2011)
	NFW	1	3	1	0	7.75	33.34		
	ISO	2	2	0	0	1.06 ± 0.21	707.95		
	NFW	1	3	1	0	7.17	33.96		
	ISO	2	2	0	0	1 ± 0.21	501.18		Martinsson et al. (2013)
	NFW	1	3	1	0	9.25	15.52		
UGC 448	ISO	2	2	0	0	0.35 ± 0.08	4168.7		Martinsson et al. (2013)
	NFW	1	3	1	0	7	30.88		
UGC 1081	ISO	2	2	0	0	1.75 ± 0.67	120.23		Martinsson et al. (2013)
	NFW	1	3	1	0	21.03	2.53		
UGC 1087	ISO	2	2	0	0	1.12 ± 0.14	380.19		Martinsson et al. (2013)
	NFW	1	3	1	0	10.2	11.95		
UGC 1529	ISO	2	2	0	0	0.37 ± 0.12	3890.45		Martinsson et al. (2013)
	NFW	1	3	1	0	5.55	48.75		
UGC 1635	ISO	2	2	0	0	0.89 ± 0.08	524.81		Martinsson et al. (2013)
	NFW	1	3	1	0	7.86	17.53		
UGC 1862	ISO	2	2	0	0	0.8 ± 0.14	288.4		Martinsson et al. (2013)
	NFW	1	3	1	0	12.53	4.34		
UGC 1908	ISO	2	2	0	0	4.56 ± 1.35	52.48		Martinsson et al. (2013)
	NFW	1	3	1	0	62.92	0.92		
UGC 3091	ISO	2	2	0	0	1.12 ± 0.13	389.05		Martinsson et al. (2013)
	NFW	1	3	1	0	9.59	13.66		
UGC 3140	ISO	2	2	0	0	0.39 ± 0.17	3162.28		Martinsson et al. (2013)
	NFW	1	3	1	0	8.7	19.06		
UGC 3701	ISO	2	2	0	0	2.62 ± 0.24	46.77		Martinsson et al. (2013)

Table 10 Continued.

Galaxy	Profile	α	β	γ	δ	r_s kpc	ρ_s $10^{-3}M_\odot \cdot pc^{-3}$	Additional info	References
	NFW	1	3	1	0	28.81	1.064		
UGC 3997	ISO	2	2	0	0	1.01 ± 0.14	398.11		Martinsson et al. (2013)
	NFW	1	3	1	0	10.64	9.95		
UGC 4036	ISO	2	2	0	0	1.5 ± 0.25	263.03		Martinsson et al. (2013)
	NFW	1	3	1	0	16.26	6.3		
UGC 4107	ISO	2	2	0	0	0.97 ± 0.12	489.78		Martinsson et al. (2013)
	NFW	1	3	1	0	8.27	16.94		
UGC 4256	ISO	2	2	0	0	5.43 ± 0.49	38.02		Martinsson et al. (2013)
	NFW	1	3	1	0	75.41	0.66		
UGC 4368	ISO	2	2	0	0	2.24 ± 0.25	87.1		Martinsson et al. (2013)
	NFW	1	3	1	0	21.85	2.44		
UGC 4380	ISO	2	2	0	0	1.78 ± 0.22	229.09		Martinsson et al. (2013)
	NFW	1	3	1	0	18.72	5.7		
UGC 4458	ISO	2	2	0	0	0.3 ± 0.1	4897.79		Martinsson et al. (2013)
	NFW	1	3	1	0	5.84	48.18		
UGC 4622	ISO	2	2	0	0	1.4 ± 0.14	467.74		Martinsson et al. (2013)
	NFW	1	3	1	0	18.32	7.82		
UGC 6903	ISO	2	2	0	0	3.19 ± 0.34	67.61		Martinsson et al. (2013)
	NFW	1	3	1	0	57.48	0.82		
UGC 6918	ISO	2	2	0	0	0.46 ± 0.05	1819.7		Martinsson et al. (2013)
	NFW	1	3	1	0	5.18	39.17		
UGC 7244	ISO	2	2	0	0	6.6 ± 1.09	12.59		Martinsson et al. (2013)
	NFW	1	3	1	0	69.88	0.29		
UGC 7917	ISO	2	2	0	0	2.59 ± 0.55	151.36		Martinsson et al. (2013)
	NFW	1	3	1	0	20.89	5.99		
UGC 8196	ISO	2	2	0	0	15.5 ± 1.5	4.37		Martinsson et al. (2013)
	NFW	1	3	1	0	305.94	0.051		
UGC 9177	ISO	2	2	0	0	1.3 ± 0.14	436.52		Martinsson et al. (2013)
	NFW	1	3	1	0	13.79	10.59		
UGC 9837	ISO	2	2	0	0	1.68 ± 0.11	177.83		Martinsson et al. (2013)
	NFW	1	3	1	0	18.56	4.09		
UGC 9965	ISO	2	2	0	0	1.36 ± 0.11	281.84		Martinsson et al. (2013)
	NFW	1	3	1	0	13.13	8.18		
UGC 11318	ISO	2	2	0	0	0.97 ± 0.58	676.08		Martinsson et al. (2013)
	NFW	1	3	1	0	11.27	13.92		
UGC 12391	ISO	2	2	0	0	2.03 ± 0.31	107.15		Martinsson et al. (2013)
	NFW	1	3	1	0	27.21	1.88		
ESO 563-G021	BUR	2	3	1	1	8.25	109.59		Wang & Chen (2021)
	NFW	1	3	1	0	191.6	0.27		
F571-8	BUR	2	3	1	1	7.81	32.65		Wang & Chen (2021)
	NFW	1	3	1	0	440.9	0.072		
	ISO	2	2	0	0	7.0	21.00		de Blok & McGaugh (1997)
	BUR	2	3	1	1	5.15	65.00		Marchesini et al. (2002)

Table 10 Continued.

Galaxy	Profile	α	β	γ	δ	r_s kpc	ρ_s $10^{-3} M_\odot \cdot pc^{-3}$	Additional info	References
	NFW	1	3	1	0	21.09	4.85		Marchesini et al. (2002)
	ISO	2	2	0	0	2.12 ± 0.19	106.9 ± 14.0		de Blok et al. (2001)
	NFW	1	3	1	0	28.0	3.83		de Blok et al. (2001)
NGC 0289	BUR	2	3	1	1	14.89	8.03		Wang & Chen (2021)
	NFW	1	3	1	0	50.69	0.72		
NGC 1003	BUR	2	3	1	1	11.75	6.76		Wang & Chen (2021)
	NFW	1	3	1	0	81.17	0.18		
	soliton+NFW	-	-	-	-	128^{30}_{-50}	0.13		Bernal et al. (2018)
NGC 2915	BUR	2	3	1	1	2.05	137.93		Wang & Chen (2021)
	NFW	1	3	1	0	10.08	5.59		
NGC 3769	BUR	2	3	1	1	5.49	33.22		Wang & Chen (2021)
	NFW	1	3	1	0	22.39	2.05		
NGC 3877	BUR	2	3	1	1	2.78	180.33		Wang & Chen (2021)
	NFW	1	3	1	0	15.9	6.04		
NGC 3917	BUR	2	3	1	1	4.69	55.17		Wang & Chen (2021)
	NFW	1	3	1	0	110.03	0.20		
NGC 3949	BUR	2	3	1	1	3.39	91.39		Wang & Chen (2021)
	NFW	1	3	1	0	81.99	0.55		
NGC 3953	BUR	2	3	1	1	3.21	159.32		Wang & Chen (2021)
	NFW	1	3	1	0	14.14	7.14		
NGC 3972	BUR	2	3	1	1	3.83	74.31		Wang & Chen (2021)
	NFW	1	3	1	0	164.25	0.20		
NGC 4051	BUR	2	3	1	1	2.47	110.15		Wang & Chen (2021)
	NFW	1	3	1	0	8.43	7.66		
NGC 4085	BUR	2	3	1	1	5.01	55.92		Wang & Chen (2021)
	NFW	1	3	1	0	247.71	0.15		
NGC 4088	BUR	2	3	1	1	6.33	33.22		Wang & Chen (2021)
	NFW	1	3	1	0	166.11	0.12		
NGC 4100	BUR	2	3	1	1	3.34	182.96		Wang & Chen (2021)
	NFW	1	3	1	0	14.09	8.78		
NGC 4559	BUR	2	3	1	1	7.67	15.20		Wang & Chen (2021)
	NFW	1	3	1	0	29.0	1.22		
NGC 5371	BUR	2	3	1	1	3.74	197.04		Wang & Chen (2021)
	NFW	1	3	1	0	11.79	19.28		
UGC 6923	BUR	2	3	1	1	3.36	42.79		Wang & Chen (2021)
	NFW	1	3	1	0	116.53	0.17		
UGC 7690	BUR	2	3	1	1	0.70	392.19		Wang & Chen (2021)
	NFW	1	3	1	0	3.08	19.52		
UGC 9037	BUR	2	3	1	1	11.61	11.75		Wang & Chen (2021)
	NFW	1	3	1	0	338.73	0.05		
UGC 12506	BUR	2	3	1	1	5.35	147.68		Wang & Chen (2021)
	NFW	1	3	1	0	19.65	9.99		

Table 10 Continued.

Galaxy	Profile	α	β	γ	δ	r_s kpc	ρ_s $10^{-3} M_\odot \cdot pc^{-3}$	Additional info	References
MUSE 3	DC14	1.47	2.71	0.83	0	12.0	16.67		Bouché et al. (2022)
MUSE 15	DC14	0.86	2.85	1.09	0	11.75	15.15		Bouché et al. (2022)
MUSE 37	DC14	2.31	2.53	0.28	0	21.71	5.63		Bouché et al. (2022)
MUSE 912	DC14	2.61	2.5	0.24	0	8.99	53.74		Bouché et al. (2022)
MUSE 919	DC14	2.47	2.51	0.24	0	8.96	52.24		Bouché et al. (2022)
MUSE 937	NFW	1	3	1	0	17.77	3.47		Bouché et al. (2022)
MUSE 943	DC14	0.58	2.93	1.2	0	13.28	5.87		Bouché et al. (2022)
MUSE 982	DC14	2.53	2.51	0.23	0	29.51	6.26		Bouché et al. (2022)
MUSE 1002	DC14	2.01	2.61	0.61	0	19.00	5.29		Bouché et al. (2022)
EGS3_10098 /EGS4_30094	gNFW	-	-	0.1	-	29.86	2.85		Genzel et al. (2020)
U3_21388	gNFW	-	-	0.88	-	20.14	2.76		Genzel et al. (2020)
EGS4_21351	gNFW	-	-	0.06	-	21.18	2.41		Genzel et al. (2020)
EGS4_11261	gNFW	-	-	0.05	-	33.79	2.25		Genzel et al. (2020)
GS4_13143	gNFW	-	-	1.47	-	17.69	2.17		Genzel et al. (2020)
U3_05138	gNFW	-	-	0.71	-	20.46	2.17		Genzel et al. (2020)
GS4_03228	gNFW	-	-	1.56	-	15.69	2.17		Genzel et al. (2020)
GS4_32796	gNFW	-	-	1.63	-	23.08	2.17		Genzel et al. (2020)
COS4_01351	gNFW	-	-	1.3	-	34.92	2.17		Genzel et al. (2020)
COS3_22796	gNFW	-	-	0.89	-	17.71	1.87		Genzel et al. (2020)
U3_15226	gNFW	-	-	0.09	-	26.89	1.87		Genzel et al. (2020)
GS4_05881	gNFW	-	-	1.72	-	17.17	1.80		Genzel et al. (2020)
COS3_16954	gNFW	-	-	1.37	-	23.93	1.87		Genzel et al. (2020)
COS3_04796	gNFW	-	-	1.31	-	34.10	1.87		Genzel et al. (2020)
EGS_13035123	gNFW	-	-	0.07	-	30.00	1.80		Genzel et al. (2020)
EGS_13004291	gNFW	-	-	0.12	-	21.17	1.80		Genzel et al. (2020)
EGS_13003805	gNFW	-	-	0.19	-	39.49	1.73		Genzel et al. (2020)
EGS4_38153	gNFW	-	-	1.7	-	33.40	1.18		Genzel et al. (2020)
EGS4_24985	gNFW	-	-	1.3	-	28.80	1.18		Genzel et al. (2020)
zC_403741	gNFW	-	-	0.1	-	20.6	1.18		Genzel et al. (2020)
D3a_6397	gNFW	-	-	1.18	-	30.00	1.18		Genzel et al. (2020)
EGS_13011166	gNFW	-	-	0.49	-	27.80	1.18		Genzel et al. (2020)
GS4_43501/GK_2438	gNFW	-	-	1.17	-	24.60	1.18		Genzel et al. (2020)
GS4_14152	gNFW	-	-	0.93	-	44.40	1.18		Genzel et al. (2020)
K20_ID9-GS4_27404	gNFW	-	-	1.04	-	25.75	0.72		Genzel et al. (2020)
zC_405501	gNFW	-	-	0.59	-	19.00	0.72		Genzel et al. (2020)
SSA22_MD41	gNFW	-	-	0.79	-	13.50	0.72		Genzel et al. (2020)
Q2343_BX389	gNFW	-	-	1.53	-	28.25	0.72		Genzel et al. (2020)
zC_407302	gNFW	-	-	1.02	-	21.25	0.72		Genzel et al. (2020)
GS3_24273	gNFW	-	-	0.07	-	22.75	0.72		Genzel et al. (2020)
zC_406690	gNFW	-	-	0.15	-	22.75	0.72		Genzel et al. (2020)
Q2343_BX610	gNFW	-	-	0.86	-	24.50	0.72		Genzel et al. (2020)

Table 10 Continued.

Galaxy	Profile	α	β	γ	δ	r_s kpc	ρ_s $10^{-3} M_\odot \cdot pc^{-3}$	Additional info	References
K20_ID7-GS4_29868	gNFW	-	-	1.3	-	24.00	0.72		Genzel et al. (2020)
K20_ID6-GS3_ _22466-GS4_33689	gNFW	-	-	0.11	-	20.75	0.72		Genzel et al. (2020)
zC_400569	gNFW	-	-	0.14	-	26.50	0.72		Genzel et al. (2020)
Q2346-BX482	gNFW	-	-	0.81	-	22.00	0.72		Genzel et al. (2020)
COS4_02672	gNFW	-	-	1.05	-	22.75	0.72		Genzel et al. (2020)
D3a_15504	gNFW	-	-	0.23	-	27.75	0.72		Genzel et al. (2020)
D3a_6004	gNFW	-	-	0.3	-	35.50	0.72		Genzel et al. (2020)
GS4_37124	gNFW	-	-	1.17	-	20.50	0.72		Genzel et al. (2020)
GS4_42930/GK_2363	gNFW	-	-	0.17	-	17.50	0.72		Genzel et al. (2020)
ESO 381-G20	ISO	2	2	0	0	2.4	28.0		Côté et al. (2000)
ESO 444-G84	ISO	2	2	0	0	1.5	116.0		Côté et al. (2000)
ESO 325-G11	ISO	2	2	0	0	2.8	11.0		Côté et al. (2000)
ESO 059-G001	ISO	2	2	0	0	1.48	67.08 ± 3.18		van Eymeren et al. (2009)
	NFW	1	3	1	0	9.70	5.53		van Eymeren et al. (2009)
ESO 215-G009	ISO	2	2	0	0	1.27	77.74 ± 10.73		van Eymeren et al. (2009)
	NFW	1	3	1	0	14.95	5.24		van Eymeren et al. (2009)
ESO 215G39	ISO	2	2	0	0	1.26	280		Kun et al. (2017)†
	EIN	n=2.9	-	-	-	18.85	0.804		
	NFW	1	3	1	0	10.74	18.0		
ESO 322G76	ISO	2	2	0	0	0.9	580		Kun et al. (2017)
	EIN	n=6.1	-	-	-	120	0.012		
	NFW	1	3	1	0	7.27	37.4		
ESO 322G77	ISO	2	2	0	0	0.42	2150		Kun et al. (2017)
	EIN	n=6.5	-	-	-	76	0.027		
	NFW 1	3	1	0		2.90	189		
ESO 322G82	ISO	2	2	0	0	0.38	2010		Kun et al. (2017)
	EIN	n=4.01	-	-	-	15.97	0.716		
	NFW	1	3	1	0	3.19	137		
ESO 323G25	ISO	2	2	0	0	0.19	7400		Kun et al. (2017)
	EIN	n=9.6	-	-	-	120	0.0036		
	NFW	1	3	1	0	2.2	280		
ESO 374G02	ISO	2	2	0	0	0.90	767		Kun et al. (2017)
	EIN	n=5.6	-	-	-	55.7	0.0783		
	NFW	1	3	1	0	5.35	91.9		
ESO 375G12	ISO	2	2	0	0	0.17	1.5410^4		Kun et al. (2017)
	EIN	n=3.58	-	-	-	13.98	1.66		
	NFW	1	3	1	0	3.32	202		
ESO 376G02	ISO	2	2	0	0	1.09	343		Kun et al. (2017)
	EIN	n=1.74	-	-	-	8.28	5.33		
	NFW	1	3	1	0	6.09	43.1		
ESO 383G02	ISO	2	2	0	0	0.54	1410		Kun et al. (2017)
	EIN	n=2.92	-	-	-	13.36	1.62		

Table 10 Continued.

Galaxy	Profile	α	β	γ	δ	r_s kpc	ρ_s $10^{-3}M_\odot \cdot pc^{-3}$	Additional info	References
	NFW	1	3	1	0	4.5	84.8		
ESO 383G88	ISO	2	2	0	0	0.40	906		Kun et al. (2017)
	EIN	n=1.5	-	-	-	5.32	6.01		
	NFW	1	3	1	0	2.94	75.4		
ESO 445G19	ISO	2	2	0	0	1.16	278		Kun et al. (2017)
	EIN	n=4.9	-	-	-	60	0.046		
	NFW	1	3	1	0	8.23	23.5		
ESO 446G01	ISO	2	2	0	0	1.11	472		Kun et al. (2017)
	EIN	n=6.5	-	-	-	150	0.0087		
	NFW	1	3	1	0	8.38	35.6		
ESO 502G02	ISO	2	2	0	0	1.49	8.43		Kun et al. (2017)
	EIN	n=0.08	-	-	-	1.2	47.0		
	NFW	1	3	1	0	0.42	126		
ESO 509G80	ISO	2	2	0	0	2.24	185		Kun et al. (2017)
	EIN	n=2.4	-	-	-	22	1.3		
	NFW	1	3	1	0	14.41	18.3		
ESO 569G17	ISO	2	2	0	0	1.21	229		Kun et al. (2017)
	EIN	n=2.9	-	-	-	11	1.3		
	NFW	1	3	1	0	13.03	11.0		
F 561-1	ISO	2	2	0	0	1.40	16.0		Kun et al. (2017)
	EIN	n=0.39	-	-	-	3.57	3.53		
	NFW	1	3	1	0	9.04	1.50		
F 563-1	ISO	2	2	0	0	9.73	3.36		Kun et al. (2017)
	EIN	n=0.14	-	-	-	11.54	1.80		
	NFW	1	3	1	0	160	0.099		
	ISO	2	2	0	0	1.5	111.2		de Blok & McGaugh (1997)
	BUR	2	3	1	1	19.59	3.53		Rodrigues et al. (2017)
	BUR	2	3	1	1	16.23	3.5		Rodrigues et al. (2017)
	ISO	2	2	0	0	2.1 ± 0.1	67.0 ± 2.0		Kuzio de Naray et al. (2006)
	NFW	1	3	1	0	18.41	3.71		Kuzio de Naray et al. (2006)
	constrainedNFW	1	3	1	0	16.29	4.44		Kuzio de Naray et al. (2006)
	ISO	2	2	0	0	2.1 ± 0.1	67.0 ± 2.0		Kuzio de Naray et al. (2008)
	NFW	1	3	1	0	18.41	3.71		Kuzio de Naray et al. (2008)
	ISO	2	2	0	0	1.72 ± 0.23	91.9 ± 21.6		de Blok et al. (2001)
	NFW	1	3	1	0	11.60	8.25		de Blok et al. (2001)
F 5631	ISO	2	2	0	0	2.0	70.4		de Blok & Bosma (2002)
	NFW	1	3	1	0	18.26	3.83		de Blok & Bosma (2002)
F 568-3	ISO	2	2	0	0	2.92	19.40		Kun et al. (2017)
	EIN	n=0.13	-	-	-	4.70	10.00		
	NFW	1	3	1	0	80.24	0.30		
	ISO	2	2	0	0	3.4	28.2		de Blok & McGaugh (1997)
	BUR	2	3	1	1	4.42	43.6		Rodrigues et al. (2017)
	ISO	2	2	0	0	3.8 ± 0.2	27.0 ± 1.0		Kuzio de Naray et al. (2006)

Table 10 Continued.

Galaxy	Profile	α	β	γ	δ	r_s kpc	ρ_s $10^{-3} M_\odot \cdot pc^{-3}$	Additional info	References
	constrainedNFW	1	3	1	0	18.18	4.19		Kuzio de Naray et al. (2006)
	ISO	2	2	0	0	2.50	480.00		Swaters et al. (2000)
	ISO	2	2	0	0	3.23	35.30		Swaters et al. (2003)
	NFW	1	3	1	0	849.46	0.054		Swaters et al. (2003)
	ISO	2	2	0	0	3.8 ± 0.2	27.0 ± 1.0		Kuzio de Naray et al. (2008)
	NFW	1	3	1	0	18.18	4.19		Kuzio de Naray et al. (2008)
	ISO	2	2	0	0	2.92 ± 0.36	36.6 ± 5.4		de Blok et al. (2001)
	NFW	1	3	1	0	89.42	0.51		de Blok et al. (2001)
	ISO	2	2	0	0	3.93 ± 0.75	30.2 ± 5.6		de Blok et al. (2001)
	NFW	1	3	1	0	656.77	0.07		de Blok et al. (2001)
F 569-V1	ISO	2	2	0	0	0.46	805.0		Kun et al. (2017)
	EIN	n=2.90	-	-	-	8.13	1.87		
	NFW	1	3	1	0	3.13	72.40		
F 583-1	ISO	2	2	0	0	2.76	26.00		Kun et al. (2017)
	EIN	n=0.99	-	-	-	9.22	2.03		
	NFW	1	3	1	0	38.57	0.87		
	ISO	2	2	0	0	2.8	21.8		de Blok & McGaugh (1997)
	BUR	2	3	1	1	3.77	38.7		Rodrigues et al. (2017)
	BUR	2	3	1	1	4.23	35.00		Marchesini et al. (2002)
	NFW	1	3	1	0	22.72	1.62		Marchesini et al. (2002)
	ISO	2	2	0	0	2.7 ± 0.1	35.0 ± 2.0		Kuzio de Naray et al. (2006)
	NFW	1	3	1	0	38.34	1.14		Kuzio de Naray et al. (2006)
	constrainedNFW	1	3	1	0	12.93	4.83		Kuzio de Naray et al. (2006)
	ISO	2	2	0	0	2.5 ± 0.1	30.0 ± 2.0		Kuzio de Naray et al. (2008)
	NFW	1	3	1	0	36.13	1.04		Kuzio de Naray et al. (2008)
	ISO	2	2	0	0	2.44 ± 0.06	33.0 ± 1.1		de Blok et al. (2001)
	NFW	1	3	1	0	27.87	1.42		de Blok et al. (2001)
	ISO	2	2	0	0	2.8	21.8		de Blok & McGaugh (1997)
F 730-V1	ISO	2	2	0	0	1.21	198.00		Kun et al. (2017)
	EIN	n=1.67	-	-	-	8.03	3.76		
	NFW	1	3	1	0	9.83	13.00		
	soliton+NFW	-	-	-	-	4.62	86.3		Bernal et al. (2018)
	ISO	2	2	0	0	1.46 ± 0.06	215.8 ± 14.2		de Blok et al. (2001)
	NFW	1	3	1	0	14.85	10.51		de Blok et al. (2001)
individual analysis	soliton+NFW	-	-	-	-	-	-		Bernal et al. (2018)
NGC 7814	soliton+NFW	-	-	-	-	$5.17^{0.67}_{-0.93}$	121.48		Bernal et al. (2018)
CVnldwA	ISO	2	2	0	0	2.01 ± 0.52	8.19 ± 1.62		Oh et al. (2015)
	NFW	1	3	1	0	2.44	5.66		Oh et al. (2015)
DDO 43	NFW	1	3	1	0	9.63	1.70		Oh et al. (2015)
	ISO	2	2	0	0	0.94 ± 0.18	33.22 ± 8.78		Oh et al. (2015)
DDO 46	NFW	1	3	1	0	4.43	32.45		Oh et al. (2015)
	ISO	2	2	0	0	0.51 ± 0.04	517.82 ± 65.46		Oh et al. (2015)
DDO 50	NFW	1	3	1	0	0.94	50.42		Oh et al. (2015)

Table 10 Continued.

Galaxy	Profile	α	β	γ	δ	r_s kpc	ρ_s $10^{-3}M_\odot \cdot pc^{-3}$	Additional info	References
	ISO	2	2	0	0	0.15 ± 0.08	379.64 ± 381.14		Oh et al. (2015)
DDO 161	ISO	2	2	0	0	3.3	26.0		Côté et al. (2000)
DDO 154	ISO	2	2	0	0	197.00	0.0016		Begeman et al. (1991)
	ISO	2	2	0	0	2.69 ± 0.24	9.0 ± 1.1		de Blok et al. (2008)
	NFW	1	3	1	0	26.67	0.58		de Blok et al. (2008)
	ISO	2	2	0	0	1.7	21.1		de Blok & McGaugh (1997)
	ISO	2	2	0	0	3.0	16.0		Carignan & Freeman (1988)
	ISO	2	2	0	0	1.3 ± 0.1	28.5 ± 2.5		Chemin et al. (2011)
	NFW	1	3	1	0	21.09	0.84		Chemin et al. (2011)
	EIN	n=2.2 ± 0.3	-	-	-	5.9 ± 0.8	1.5 ± 0.3		Chemin et al. (2011)
	ISO	2	2	0	0	1.5 ± 0.1	26.2 ± 3.0		Jovanović (2017)
	NFW	1	3	1	0	$11.85^{+1.21}_{-1.07}$	$0.56^{+0.07}_{-0.07}$		Jovanović (2017)
	NFW	1	3	1	0	14.5	1.59		de La Macorra et al. (2011)
	BDM					3.6	19.95	$r_c = 1.3$kpc	de La Macorra et al. (2011)
	NFW	1	3	1	0	10.31	2.33		Oh et al. (2015)
	ISO	2	2	0	0	0.95 ± 0.03	53.21 ± 3.19		Oh et al. (2015)
	BUR	2	3	1	1	4.31	10.3		Rodrigues et al. (2017)
DDO 168	ISO	2	2	0	0	1.5	51.2		de Blok & McGaugh (1997)
	ISO	2	2	0	0	2.81 ± 0.83	39.81 ± 6.37		Oh et al. (2015)
	NFW	1	3	1	0	9.41	5.53		Oh et al. (2015)
DDO 170	ISO	2	2	0	0	2.04	24.13		Begeman et al. (1991)
	ISO	2	2	0	0	1.6	35.4		de Blok & McGaugh (1997)
	ISO	2	2	0	0	2.4	17.12		Lake et al. (1990)
	ISO	2	3	0	0	4.9	9.89		Lake et al. (1990)
	ISO	2	4	0	0	7.1	7.18		Lake et al. (1990)
DDO 185	ISO	2	2	0	0	INF	22.40		de Blok & Bosma (2002)
	NFW	1	3	1	0	10461.6	0.0024		
DDO 189	ISO	2	2	0	0	1.0	97.90		de Blok & Bosma (2002)
	NFW	1	3	1	0	7.98	6.82		de Blok & Bosma (2002)
DDO 47	ISO	2	2	0	0	2.10	47.50		de Blok & Bosma (2002)
	NFW	1	3	1	0	17769.40	0.0024		de Blok & Bosma (2002)
	NFW	1	3	1	0	176.0 ± 10.0	0.18		Frigerio Martins (2009)
	BUR	2	3	1	1	7.0	20.68		Salucci et al. (2003), Gentile et al. (2005)
	ISO	2	2	0	0	3.72 ± 0.48	12.15 ± 1.49		Oh et al. (2015)
	NFW	1	3	1	0	7.56	5.53		Oh et al. (2015)
	ISO	2	2	0	0	2.983	23.71		Rodríguez-Meza (2012)
DDO 64	ISO	2	2	0	0	1.20	72.70		de Blok & Bosma (2002)
	NFW	1	3	1	0	15763.80	0.0024		de Blok & Bosma (2002)
	ISO	2	2	0	0	4.4 ± 0.9	38.0 ± 3.0		Kuzio de Naray et al. (2006)
	constrainedNFW	1	3	1	0	9.13	5.53		Kuzio de Naray et al. (2006)
	ISO	2	2	0	0	3.3 ± 0.5	43.0 ± 3.0		Kuzio de Naray et al. (2008)
	NFW	1	3	1	0	9.13	5.53		Kuzio de Naray et al. (2008)

Table 10 Continued.

Galaxy	Profile	α	β	γ	δ	r_s kpc	ρ_s $10^{-3} M_\odot \cdot pc^{-3}$	Additional info	References
DDO 52	ISO	2	2	0	0	0.70	123.80		de Blok & Bosma (2002)
	NFW	1	3	1	0	13215.40	0.0024		
	NFW	1	3	1	0	15.97	2.08		Oh et al. (2015)
	ISO	2	2	0	0	1.33 ± 0.07	48.81 ± 3.63		Oh et al. (2015)
DDO 53	ISO	2	2	0	0	2.22 ± 1.95	25.10 ± 5.63		Oh et al. (2015)
	NFW	1	3	1	0	3.62	7.45		Oh et al. (2015)
DDO 70	ISO	2	2	0	0	0.51 ± 0.11	119.95 ± 34.69		Oh et al. (2015)
	NFW	1	3	1	0	5.08	7.28		Oh et al. (2015)
DDO 87	ISO	2	2	0	0	2.46 ± 0.11	13.91 ± 0.77		Oh et al. (2015)
	NFW	1	3	1	0	5.81	5.97		Oh et al. (2015)
DDO 101	NFW	1	3	1	0	2.38	68.58		Oh et al. (2015)
	ISO	2	2	0	0	0.32 ± 0.01	849.14 ± 77.23		Oh et al. (2015)
DDO 126	ISO	2	2	0	0	1.33 ± 0.10	21.59 ± 2.00		Oh et al. (2015)
	NFW	1	3	1	0	4.21	6.94		Oh et al. (2015)
DDO 133	NFW	1	3	1	0	20.60	1.26		Oh et al. (2015)
	ISO	2	2	0	0	0.83 ± 0.06	73.69 ± 7.61		Oh et al. (2015)
DDO 216	BUR	2	3	1	1	$0.3^{+0.3}_{-0.1}$	$125.89^{+125.3}_{-62.79}$		Gammaldi et al. (2021)
	NFW	1	3	1	0	0.7	19.95		Gammaldi et al. (2021)
	NFW	1	3	1	0	0.90	13.45		Oh et al. (2015)
	ISO	2	2	0	0	0.15 ± 0.03	127.02 ± 43.35		Oh et al. (2015)
DDO 210	BUR	2	3	1	1	$0.5^{+0.9}_{-0.2}$	$100.0^{+25.89}_{-37.7}$		Gammaldi et al. (2021)
	NFW	1	3	1	0	1.0	15.85		Gammaldi et al. (2021)
	ISO	2	2	0	0	0.20 ± 0.05	116.43 ± 23.05		Oh et al. (2015)
	NFW	1	3	1	0	1.38	11.05		Oh et al. (2015)
WLM	BUR	2	3	1	1	$1.3^{+0.2}_{-0.1}$	$63.10^{+12.98}_{-16.33}$		Gammaldi et al. (2021)
	NFW	1	3	1	0	2.8	10.0		Gammaldi et al. (2021)
	ISO	2	2	0	0	55.38 ± 32.11	0.57 ± 0.22		Ianjamasimanana et al. (2020)
	NFW	1	3	1	0	$4.14^{+7.01}_{-2.31}$	$4.67^{+8.06}_{-3.76}$		Ianjamasimanana et al. (2020)
	NFW	1	3	1	0	41.01	0.43		Oh et al. (2015)
	ISO	2	2	0	0	0.74 ± 0.01	57.46 ± 1.57		Oh et al. (2015)
Haro 29	NFW	1	3	1	0	1.63	36.12		Oh et al. (2015)
	ISO	2	2	0	0	0.23 ± 0.04	414.68 ± 137.20		Oh et al. (2015)
Haro 36	ISO	2	2	0	0	8.40 ± 12.17	16.99 ± 2.78		Oh et al. (2015)
	NFW	1	3	1	0	6.69	6.29		Oh et al. (2015)
Phoenix	BUR	2	3	1	1	0.2	31.62		Gammaldi et al. (2021)
	NFW	1	3	1	0	0.2	7.94		Gammaldi et al. (2021)
KK98 250	ISO†	2	2	0	0	1.5 ± 0.2	37.6 ± 1.2		Begum & Chengalur (2004)
	ISO	2	2	0	0	1.4 ± 0.04	39.0 ± 1.0		Begum & Chengalur (2004)
KK98 251	ISO	2	2	0	0	2.8 ± 0.5	18.5 ± 1.0		Begum & Chengalur (2004)
K 124	ISO	2	2	0	0	4.4	13.5		de Blok & Bosma (2002)
	NFW	1	3	1	0	4408	0.0053		de Blok & Bosma (2002)
F 563-V2	ISO	2	2	0	0	1.9	80.9		de Blok & McGaugh (1997)

Table 10 Continued.

Galaxy	Profile	α	β	γ	δ	r_s kpc	ρ_s $10^{-3}M_\odot \cdot pc^{-3}$	Additional info	References
	ISO	2	2	0	0	1.5 ± 0.1	119.0 ± 6.0		Kuzio de Naray et al. (2006)
	NFW	1	3	1	0	22.52	3.6		Kuzio de Naray et al. (2006)
	constrainedNFW	1	3	1	0	22.30	3.83		Kuzio de Naray et al. (2006)
	ISO	2	2	0	0	0.94	283.00		Swaters et al. (2000)
	ISO	2	2	0	0	1.13	231.0		Swaters et al. (2003)
	NFW	1	3	1	0	8.52	17.27		Swaters et al. (2003)
	ISO	2	2	0	0	1.5 ± 0.1	119.0 ± 6.0		Kuzio de Naray et al. (2008)
	NFW	1	3	1	0	22.52	3.60		Kuzio de Naray et al. (2008)
	ISO	2	2	0	0	1.69 ± 0.17	131.2 ± 19.4		de Blok et al. (2001)
	NFW	1	3	1	0	27.22	3.49		de Blok et al. (2001)
F564-V3	NFW	1	3	1	0	3.29	8.18		Oh et al. (2015)
	ISO	2	2	0	0	0.55 ± 0.20	74.24 ± 40.17		Oh et al. (2015)
F 565-V2	ISO	2	2	0	0	2.8	8.4		de Blok & McGaugh (1997)
F 568-1	ISO	2	2	0	0	2.0	82.2		de Blok & McGaugh (1997)
	ISO	2	2	0	0	1.50	181.00		Swaters et al. (2000)
	ISO	2	2	0	0	1.95	115.0		Swaters et al. (2003)
	NFW	1	3	1	0	16.71	7.52		Swaters et al. (2003)
	ISO	2	2	0	0	2.22 ± 0.10	97.2 ± 6.2		de Blok et al. (2001)
	NFW	1	3	1	0	40.54	2.40		de Blok et al. (2001)
F 568-V1	ISO	2	2	0	0	3.1	35.0		de Blok & McGaugh (1997)
	ISO	2	2	0	0	1.20	188.00		Swaters et al. (2000)
	ISO	2	2	0	0	1.43	150.0		Swaters et al. (2003)
	NFW	1	3	1	0	9.05	15.24		Swaters et al. (2003)
	ISO	2	2	0	0	1.45 ± 0.11	153.0 ± 18.2		de Blok et al. (2001)
	NFW	1	3	1	0	8.40	17.89		de Blok et al. (2001)
F 571-V1	ISO	2	2	0	0	2.5	18.6		de Blok & McGaugh (1997)
F 571-V2	ISO	2	2	0	0	0.8	75.5		de Blok & McGaugh (1997)
F 574-1	ISO	2	2	0	0	7.5	7.5		de Blok & McGaugh (1997)
	ISO	2	2	0	0	1.50	920.00		Swaters et al. (2000)
	ISO	2	2	0	0	1.66	86.30		Swaters et al. (2003)
	NFW	1	3	1	0	12.92	6.33		Swaters et al. (2003)
	ISO	2	2	0	0	1.83 ± 0.06	71.5 ± 3.7		de Blok et al. (2001)
	NFW	1	3	1	0	15.79	4.45		de Blok et al. (2001)
F578-1	BUR	2	3	1	1	5.30	64.2		Rodrigues et al. (2017)
F 579-V1	ISO	2	2	0	0	0.67 ± 0.02	574.8 ± 37.3		de Blok et al. (2001)
	BUR	2	3	1	1	0.93	640		Rodrigues et al. (2017)
	NFW	1	3	1	0	5.00	44.57		de Blok et al. (2001)
F 583-4	ISO	2	2	0	0	4.7	7.8		de Blok & McGaugh (1997)
	BUR	2	3	1	1	0.42	114		Rodrigues et al. (2017)
	ISO	2	2	0	0	1.3 ± 0.1	67.0 ± 2.0		Kuzio de Naray et al. (2006)
	NFW	1	3	1	0	22.67	1.64		Kuzio de Naray et al. (2006)
	constrainedNFW	1	3	1	0	9.98	5.38		Kuzio de Naray et al. (2006)
	ISO	2	2	0	0	1.3 ± 0.1	67.0 ± 2.0		Kuzio de Naray et al. (2008)

Table 10 Continued.

Galaxy	**Profile**	α	β	γ	δ	r_s **kpc**	ρ_s $10^{-3}M_\odot \cdot pc^{-3}$	**Additional info**	**References**
	NFW	1	3	1	0	22.67	1.64		Kuzio de Naray et al. (2008)
	ISO	2	2	0	0	1.10 ± 0.13	85.50 ± 15.80		de Blok et al. (2001)
	NFW	1	3	1	0	20.94	1.83		de Blok et al. (2001)
FGC 1540	ISO	2	2	0	0	0.61 ± 0.06	337 ± 61		Kurapati et al. (2018)
SDSS J2141	gNFW	-	-	0.82	-	38.05	4.82		Barnabè et al. (2012)
AGC 114905	Reads	-	-	-	-	23.82	0.17	$r_c = 6.74$kpc	Kong et al. (2022)
	DPL	1	2.05	0.09	0	4.15	1.78		Kong et al. (2022)
AGC 122966	Reads	-	-	-	-	9.29	1.29	$r_c = 0.59$kpc	Kong et al. (2022)
	DPL	1	2.17	0.85	0	1.34	21.88		Kong et al. (2022)
AGC 219533	Reads	-	-	-	-	12.78	0.93	$r_c = 0.57$kpc	Kong et al. (2022)
	DPL	1	2.17	0.85	0	1.61	19.50		Kong et al. (2022)
AGC 248945	Reads	-	-	-	-	15.73	0.30	$r_c = 0.85$kpc	Kong et al. (2022)
	DPL	1	2.15	0.59	0	1.94	7.08		Kong et al. (2022)
AGC 334315	Reads	-	-	-	-	22.35	0.21	$r_c = 0.62$kpc	Kong et al. (2022)
	DPL	1	2.14	0.5	0	3.01	4.27		Kong et al. (2022)
AGC 749290	Reads	-	-	-	-	18.15	0.25	$r_c = 0.91$kpc	Kong et al. (2022)
	DPL	1	2.14	0.49	0	2.52	4.89		Kong et al. (2022)
AGC 242019	Reads	-	-	-	-	47.12	0.12	$r_c = 0.26$kpc	Kong et al. (2022)
	DPL	1	2.11	0.5	0	5.24	2.75		Kong et al. (2022)
AGC 242019	Reads	-	-	-	-	24.14	0.30	$r_c = 3.15$kpc	Kong et al. (2022)
	DPL	1	2.13	0.24	0	5.73	3.24		Kong et al. (2022)
N 4310	gNFW	-	-	0.4	-	1.78	178.27		Cooke et al. (2022)
N 4451	gNFW	-	-	0.6	-	2.25	235.61		Cooke et al. (2022)
N 4701	gNFW	-	-	0.4	-	1.44	322.23		Cooke et al. (2022)
N 5692	gNFW	-	-	0.7	-	1.63	341.67		Cooke et al. (2022)
10K galaxies	NFW								Zhu et al. (2023)
	constrainedNFW								Zhu et al. (2023)
	gNFW								Zhu et al. (2023)
22K galaxies	NFW								Yasin et al. (2023)
	BUR								Yasin et al. (2023)

.

References

Aartsen, M. G., Abraham, K., Ackermann, M., et al. 2015, European Physical Journal C, 75, 492
Abbasi, R., Abdou, Y., Abu-Zayyad, T., et al. 2011, Phys. Rev. D, 84, 022004
Abdallah, H., Abramowski, A., Aharonian, F., et al. 2018, Phys. Rev. Lett., 120, 201101
Abdo, A. A., Ackermann, M., Ajello, M., et al. 2010, The Astrophysical Journal, 712, 147–158
Abramowski, A., Acero, F., Aharonian, F., et al. 2012a, ApJ, 750, 123
Abramowski, A., Acero, F., Aharonian, F., et al. 2012b, ApJ, 750, 123
Abramowski, A., Acero, F., Aharonian, F., et al. 2011, Phys. Rev. Lett., 106, 161301
Abramowski, A. et al. 2014, Phys. Rev. D, 90, 112012
Acciari, V. A., Arlen, T., Aune, T., et al. 2010, The Astrophysical Journal, 720, 1174–1180
Acharyya, A., Adam, R., Adams, C., et al. 2021, J. Cosmology Astropart. Phys., 2021, 057
Ackermann, M., Ajello, M., Allafort, A., et al. 2010, Journal of Cosmology and Astroparticle Physics, 2010, 025–025
Ackermann, M., Ajello, M., Atwood, W. B., et al. 2012, ApJ, 761, 91
Agrawal, P., Batell, B., Fox, P. J., & Harnik, R. 2015, J. Cosmology Astropart. Phys., 2015, 011
Aharonian, F., Akhperjanian, A., Aye, K.-M., et al. 2004, Astroparticle Physics, 22, 109–125
Aharonian, F., Akhperjanian, A. G., Anton, G., et al. 2009, A&A, 503, 817
Aharonian, F., Akhperjanian, A. G., Bazer-Bachi, A. R., et al. 2006, ApJ, 636, 777
Aharonian, F., Akhperjanian, A. G., Bazer-Bachi, A. R., et al. 2008, Astroparticle Physics, 29, 55
Aharonian, F., Akhperjanian, A. G., Bazer-Bachi, A. R., et al. 2006, Physical Review Letters, 97
Albert, A., Anderson, B., Bechtol, K., et al. 2017, The Astrophysical Journal, 834, 110
Albert, J., Aliu, E., Anderhub, H., et al. 2008, The Astrophysical Journal, 679, 428–431
Aleksić, J., Antonelli, L. A., Antoranz, P., et al. 2010, ApJ, 710, 634
Aleksić, J., Antonelli, L. A., Antoranz, P., et al. 2010, The Astrophysical Journal, 710, 634–647
Aliu, E., Anderhub, H., Antonelli, L. A., et al. 2009, The Astrophysical Journal, 697, 1299–1304
Allen, S. W., Schmidt, R. W., & Fabian, A. C. 2001, MNRAS, 328, L37
Allingham, J. F. V., Jauzac, M., Lagattuta, D. J., et al. 2023, MNRAS, 522, 1118
Amodeo, S., Ettori, S., Capasso, R., & Sereno, M. 2016, A&A, 590, A126
Amorisco, N. C., Agnello, A., & Evans, N. W. 2013, MNRAS, 429, L89
Andersson, K. E. & Madejski, G. M. 2004, The Astrophysical Journal, 607, 190
Ando, S. & Nagai, D. 2012, J. Cosmology Astropart. Phys., 2012, 017
ANTARES Collaboration. 2015, J. Cosmology Astropart. Phys., 2015, 068
Arabadjis, J. S., Bautz, M. W., & Garmire, G. P. 2002, ApJ, 572, 66
Athanassoula, E., Bosma, A., & Papaioannou, S. 1987a, A&A, 179, 23
Athanassoula, E., Bosma, A., & Papaioannou, S. 1987b, A&A, 179, 23
Babyk, I. V., Del Popolo, A., & Vavilova, I. B. 2014, Astronomy Reports, 58, 587
Bahcall, J. N. & Soneira, R. M. 1980, ApJS, 44, 73
Balestra, I., Mercurio, A., Sartoris, B., et al. 2016, ApJS, 224, 33
Bardeau, S., Kneib, J. P., Czoske, O., et al. 2005, A&A, 434, 433
Bardeau, S., Soucail, G., Kneib, J. P., et al. 2007, A&A, 470, 449
Barnabè, M., Dutton, A. A., Marshall, P. J., et al. 2012, MNRAS, 423, 1073
Barrena, R., Biviano, A., Ramella, M., Falco, E. E., & Seitz, S. 2002, A&A, 386, 816
Battaglia, G., Helmi, A., Morrison, H., et al. 2005, MNRAS, 364, 433
Battaglia, G., Helmi, A., Tolstoy, E., et al. 2008, ApJ, 681, L13
Battaglia, G., Tolstoy, E., Helmi, A., et al. 2011, MNRAS, 411, 1013
Baumgardt, H. & Hilker, M. 2018, MNRAS, 478, 1520
Begeman, K. G. 1989, A&A, 223, 47
Begeman, K. G., Broeils, A. H., & Sanders, R. H. 1991, MNRAS, 249, 523
Begeman, K. K. G. 1987, PhD thesis, University of Groningen, Netherlands
Begum, A. & Chengalur, J. N. 2004, A&A, 424, 509
Bergström, L., Ullio, P., & Buckley, J. H. 1998, Astroparticle Physics, 9, 137
Bernal, T., Fernández-Hernández, L. M., Matos, T., & Rodríguez-Meza, M. A. 2018, MNRAS, 475, 1447
Bernal, T., Robles, V. H., & Matos, T. 2017, MNRAS, 468, 3135
Binney, J. & Tremaine, S. 1987, Galactic dynamics
Biviano, A., Pizzuti, L., Mercurio, A., et al. 2023, ApJ, 958, 148
Biviano, A., Rosati, P., Balestra, I., et al. 2013, A&A, 558, A1
Blais-Ouellette, S., Carignan, C., Amram, P., & Côté, S. 1999, AJ, 118, 2123
Boardman, N. F., Weijmans, A.-M., van den Bosch, R., et al. 2016, MNRAS, 460, 3029
Bonnivard, V., Combet, C., Daniel, M., et al. 2015, MNRAS, 453, 849
Borriello, E., Longo, G., Miele, G., et al. 2010, ApJ, 709, L32
Borukhovetskaya, A., Navarro, J. F., Errani, R., & Fattahi, A. 2022, MNRAS, 512, 5247
Bosma, A. 1981, AJ, 86, 1791
Bouché, N. F., Bera, S., Krajnović, D., et al. 2022, A&A, 658, A76
Boyarsky, A., Ruchayskiy, O., Iakubovskyi, D., Maccio', A. V., & Malyshev, D. 2009, arXiv e-prints, arXiv:0911.1774
Bradač, M., Allen, S. W., Treu, T., et al. 2008a, ApJ, 687, 959
Bradač, M., Schrabback, T., Erben, T., et al. 2008b, ApJ, 681, 187
Bringmann, T., Doro, M., & Fornasa, M. 2009, J. Cosmology Astropart. Phys., 2009, 016
Broadhurst, T., Benítez, N., Coe, D., et al. 2005a, ApJ, 621, 53
Broadhurst, T., Takada, M., Umetsu, K., et al. 2005b, ApJ, 619, L143
Broadhurst, T., Umetsu, K., Medezinski, E., Oguri, M., & Rephaeli, Y. 2008, ApJ, 685, L9
Broeils, A. H. 1992, PhD thesis, University of Groningen, Netherlands
Brownsberger, S. R. & Randall, L. 2021, MNRAS, 501, 2332
Brownstein, J. R. 2009, PhD thesis, University of Waterloo, Canada
Buote, D. A. 2004, in Dark Matter in Galaxies, ed. S. Ryder, D. Pisano, M. Walker, & K. Freeman, Vol. 220, 149
Buote, D. A. 2017, ApJ, 834, 164
Buote, D. A. & Barth, A. J. 2019, ApJ, 877, 91
Buote, D. A., Humphrey, P. J., & Stocke, J. T. 2005, ApJ, 630, 750
Buote, D. A., Jeltema, T. E., Canizares, C. R., & Garmire, G. P. 2002, ApJ, 577, 183
Buote, D. A. & Lewis, A. D. 2004, ApJ, 604, 116
Burkert, A. 1995, ApJ, 447, L25
Bustamante-Rosell, M. J., Noyola, E., Gebhardt, K., et al. 2021, ApJ, 921, 107
Calabrese, E. & Spergel, D. N. 2016, MNRAS, 460, 4397
Caminha, G. B., Grillo, C., Rosati, P., et al. 2017, A&A, 607, A93
Carignan, C., Frank, B. S., Hess, K. M., et al. 2013, AJ, 146, 48
Carignan, C. & Freeman, K. C. 1985, ApJ, 294, 494
Carignan, C. & Freeman, K. C. 1988, ApJ, 332, L33
Carignan, C., Sancisi, R., & van Albada, T. S. 1988, AJ, 95, 37
Carrasco, E. R., Verdugo, T., Motta, V., et al. 2021, ApJ, 918, 61
Caso, J. P. 2022, MNRAS, 511, 5314
Chang, L. J. & Necib, L. 2021, MNRAS, 507, 4715
Chemin, L., Carignan, C., Drouin, N., & Freeman, K. C. 2006, AJ, 132, 2527
Chemin, L., de Blok, W. J. G., & Mamon, G. A. 2011, AJ, 142, 109
Chiu, I. N., Umetsu, K., Sereno, M., et al. 2018, ApJ, 860, 126
Cholis, I., Dobler, G., Finkbeiner, D. P., et al. 2009, The Fermi gamma-ray spectrum of the inner galaxy: Implications for annihilating dark matter
Cirelli, M., Corcella, G., Hektor, A., et al. 2011, J. Cosmology Astropart. Phys., 2011, 051
Cirelli, M., Corcella, G., Hektor, A., et al. 2011, Journal of Cosmology and Astroparticle Physics, 2011, 051–051
Clowe, D. 2003, in Astronomical Society of the Pacific Conference Series, Vol. 301, Matter and Energy in Clusters of Galaxies, ed. S. Bowyer & C.-Y. Hwang, 271
Clowe, D., Bradač, M., Gonzalez, A. H., et al. 2006, ApJ, 648, L109
Clowe, D., Gonzalez, A., & Markevitch, M. 2004, ApJ, 604, 596
Clowe, D. & Schneider, P. 2001a, A&A, 379, 384
Clowe, D. & Schneider, P. 2001b, A&A, 379, 384
Clowe, D. & Schneider, P. 2002a, A&A, 395, 385
Clowe, D. & Schneider, P. 2002b, A&A, 395, 385
Comerford, J. M., Meneghetti, M., Bartelmann, M., & Schirmer, M. 2006, ApJ, 642, 39
Comerford, J. M. & Natarajan, P. 2007, MNRAS, 379, 190

Contenta, F., Balbinot, E., Petts, J. A., et al. 2018, MNRAS, 476, 3124
Cooke, L. H., Levy, R. C., Bolatto, A. D., et al. 2022, MNRAS, 512, 1012
Corbelli, E. 2003, MNRAS, 342, 199
Corbelli, E. 2003, Monthly Notices of the Royal Astronomical Society, 342, 199
Corless, V. L., King, L. J., & Clowe, D. 2009, MNRAS, 393, 1235
Côté, S., Carignan, C., & Freeman, K. C. 2000, AJ, 120, 3027
Cote, S., Carignan, C., & Sancisi, R. 1991, AJ, 102, 904
Dahle, H. 2006, ApJ, 653, 954
Darragh-Ford, E., Mantz, A. B., Rasia, E., et al. 2023, MNRAS, 521, 790
Daylan, T., Finkbeiner, D. P., Hooper, D., et al. 2016, Physics of the Dark Universe, 12, 1
de Blok, W. J. G. & Bosma, A. 2002, A&A, 385, 816
de Blok, W. J. G. & McGaugh, S. S. 1997, Monthly Notices of the Royal Astronomical Society, 290, 533
de Blok, W. J. G. & McGaugh, S. S. 1997, MNRAS, 290, 533
de Blok, W. J. G., McGaugh, S. S., & Rubin, V. C. 2001, AJ, 122, 2396
de Blok, W. J. G., Walter, F., Brinks, E., et al. 2008, AJ, 136, 2648
de la Macorra, A. 2010a, Astroparticle Physics, 33, 195
de la Macorra, A. 2010b, Astroparticle Physics, 33, 195
de La Macorra, A., Mastache, J., & Cervantes-Cota, J. L. 2011, Phys. Rev. D, 84, 121301
Dehnen, W. 1993, MNRAS, 265, 250
Démoclès, J., Pratt, G. W., Pierini, D., et al. 2010, A&A, 517, A52
Di Cintio, A., Brook, C. B., Dutton, A. A., et al. 2014, MNRAS, 441, 2986
Di Mauro, M., Hou, X., Eckner, C., Zaharijas, G., & Charles, E. 2019, Phys. Rev. D, 99, 123027
Donnarumma, A., Ettori, S., Meneghetti, M., & Moscardini, L. 2009, MNRAS, 398, 438
Dumont, A., Seth, A. C., Strader, J., et al. 2023, arXiv e-prints, arXiv:2306.11786
Eichner, T., Seitz, S., Suyu, S. H., et al. 2013, ApJ, 774, 124
Einasto, J. 1965, Trudy Astrofizicheskogo Instituta Alma-Ata, 5, 87
Elagali, A., Staveley-Smith, L., Rhee, J., et al. 2019, MNRAS, 487, 2797
Elson, E. C., de Blok, W. J. G., & Kraan-Korteweg, R. C. 2013, MNRAS, 429, 2550
Ettori, S., De Grandi, S., & Molendi, S. 2002, A&A, 391, 841
Ettori, S., Gastaldello, F., Leccardi, A., et al. 2010, A&A, 524, A68
Ettori, S., Ghirardini, V., Eckert, D., Dubath, F., & Pointecouteau, E. 2017, MNRAS, 470, L29
Ettori, S., Ghirardini, V., Eckert, D., et al. 2019, A&A, 621, A39
Evrard, A. E., Metzler, C. A., & Navarro, J. F. 1996, ApJ, 469, 494
Fardal, M. A., Guhathakurta, P., Babul, A., & McConnachie, A. W. 2007, MNRAS, 380, 15
Finner, K., Randall, S. W., Jee, M. J., et al. 2023, ApJ, 942, 23
Forestell, A. D. & Gebhardt, K. 2010, ApJ, 716, 370
Frigerio Martins, C. 2009, PhD thesis, -
Gammaldi, V., Pérez-Romero, J., Coronado-Blázquez, J., et al. 2021, Phys. Rev. D, 104, 083026
Gastaldello, F., Buote, D. A., Humphrey, P. J., et al. 2007, ApJ, 669, 158
Gavazzi, R. 2005, A&A, 443, 793
Gavazzi, R., Adami, C., Durret, F., et al. 2009, A&A, 498, L33
Gavazzi, R., Fort, B., Mellier, Y., Pelló, R., & Dantel-Fort, M. 2003, A&A, 403, 11
Geehan, J. J., Fardal, M. A., Babul, A., & Guhathakurta, P. 2006, MNRAS, 366, 996
Gentile, G., Baes, M., Famaey, B., & van Acoleyen, K. 2010, MNRAS, 406, 2493
Gentile, G., Burkert, A., Salucci, P., Klein, U., & Walter, F. 2005, ApJ, 634, L145
Gentile, G., Salucci, P., Klein, U., & Granato, G. L. 2007a, MNRAS, 375, 199
Gentile, G., Salucci, P., Klein, U., Vergani, D., & Kalberla, P. 2004, MNRAS, 351, 903
Gentile, G., Tonini, C., & Salucci, P. 2007b, A&A, 467, 925
Genzel, R., Price, S. H., Übler, H., et al. 2020, ApJ, 902, 98
Geringer-Sameth, A., Koushiappas, S. M., & Walker, M. 2015, ApJ, 801, 74
Gilmore, G., Wilkinson, M. I., Wyse, R. F. G., et al. 2007, ApJ, 663, 948
Goerdt, T., Moore, B., Read, J. I., Stadel, J., & Zemp, M. 2006, MNRAS, 368, 1073
Gómez-Vargas, G. A., Sánchez-Conde, M. A., Huh, J.-H., et al. 2013, J. Cosmology Astropart. Phys., 2013, 029
Gopika, K. & Desai, S. 2021, Physics of the Dark Universe, 33, 100874
Gopika, K. & Desai, S. 2023, Physics of the Dark Universe, 42, 101291
Gruen, D., Brimioulle, F., Seitz, S., et al. 2013, MNRAS, 432, 1455
Gruen, D., Seitz, S., Brimioulle, F., et al. 2014, MNRAS, 442, 1507
Gunn, J. E. & Gott, J. Richard, I. 1972, ApJ, 176, 1
H. E. S. S. Collaboration, Abdalla, H., Abramowski, A., et al. 2018, A&A, 612, A1
H. E. S. S. Collaboration, Abdallah, H., Adam, R., et al. 2021, arXiv e-prints, arXiv:2105.04325
H. E. S. S. Collaboration, Abramowski, A., Acero, F., et al. 2011, Astroparticle Physics, 34, 608
Halkola, A., Seitz, S., & Pannella, M. 2006, MNRAS, 372, 1425
Hayashi, K. & Chiba, M. 2012, ApJ, 755, 145
Hayashi, K. & Chiba, M. 2014, ApJ, 789, 62
Hayashi, K., Chiba, M., & Ishiyama, T. 2020, ApJ, 904, 45
Hayashi, K., Hirai, Y., Chiba, M., & Ishiyama, T. 2023, ApJ, 953, 185
Hayashi, K., Ichikawa, K., Matsumoto, S., et al. 2016, MNRAS, 461, 2914
Hernquist, L. 1990, ApJ, 356, 359
High, F. W., Stalder, B., Song, J., et al. 2010, ApJ, 723, 1736
Hoekstra, H., Franx, M., Kuijken, K., & van Dokkum, P. G. 2002, MNRAS, 333, 911
Huang, Z., Radovich, M., Grado, A., et al. 2011, A&A, 529, A93
Humphrey, P. J., Buote, D. A., Gastaldello, F., et al. 2006, ApJ, 646, 899
Humphrey, P. J., Buote, D. A., O'Sullivan, E., & Ponman, T. J. 2012, ApJ, 755, 166
Ianjamasimanana, R., Namumba, B., Ramaila, A. J. T., et al. 2020, MNRAS, 497, 4795
Jee, M. J., Dawson, W. A., Stroe, A., et al. 2016, ApJ, 817, 179
Jee, M. J., Hughes, J. P., Menanteau, F., et al. 2014, ApJ, 785, 20
Jee, M. J., Ko, J., Perlmutter, S., et al. 2017, ApJ, 847, 117
Jee, M. J., Rosati, P., Ford, H. C., et al. 2009, ApJ, 704, 672
Jee, M. J. & Tyson, J. A. 2009, ApJ, 691, 1337
Jee, M. J., White, R. L., Benítez, N., et al. 2005, ApJ, 618, 46
Jimenez, R., Verde, L., & Oh, S. P. 2003, MNRAS, 339, 243
Jobin, M. & Carignan, C. 1990, AJ, 100, 648
Jovanović, M. 2017, MNRAS, 469, 3564
Karwin, C., Murgia, S., Tait, T. M. P., Porter, T. A., & Tanedo, P. 2017, Phys. Rev. D, 95, 103005
Kazantzidis, S., Mayer, L., Mastropietro, C., et al. 2004, ApJ, 608, 663
Kelson, D. D., Zabludoff, A. I., Williams, K. A., et al. 2002, ApJ, 576, 720
Kent, S. M. 1986, AJ, 91, 1301
Kent, S. M. 1987, AJ, 93, 816
Khoperskov, S. A., Moiseev, A. V., Khoperskov, A. V., & Saburova, A. S. 2014, MNRAS, 441, 2650
Khosroshahi, H. G., Jones, L. R., & Ponman, T. J. 2004, MNRAS, 349, 1240
Kim, J., Jee, M. J., Hughes, J. P., et al. 2021, ApJ, 923, 101
Kim, M., Jee, M. J., Finner, K., et al. 2019, ApJ, 874, 143
King, I. 1962, AJ, 67, 471
King, I. R. 1966, AJ, 71, 64
King, L. J., Clowe, D. I., Lidman, C., et al. 2002a, A&A, 385, L5
King, L. J., Clowe, D. I., & Schneider, P. 2002b, A&A, 383, 118
Kirihara, T., Miki, Y., & Mori, M. 2014, PASJ, 66, L10
Kling, T. P., Dell'Antonio, I., Wittman, D., & Tyson, J. A. 2005, ApJ, 625, 643
Klop, N., Zandanel, F., Hayashi, K., & Ando, S. 2017, Phys. Rev. D, 95, 123012
Klypin, A., Kravtsov, A. V., Bullock, J. S., & Primack, J. R. 2001, ApJ, 554, 903
Kneib, J.-P., Hudelot, P., Ellis, R. S., et al. 2003, ApJ, 598, 804
Komatsu, E., Dunkley, J., Nolta, M. R., et al. 2009, ApJS, 180, 330
Kong, D., Kaplinghat, M., Yu, H.-B., Fraternali, F., & Mancera Piña, P. E. 2022, ApJ, 936, 166
Korsaga, M., Carignan, C., Amram, P., Epinat, B., & Jarrett, T. H. 2018, MNRAS, 478, 50
Kubo, J. M., Stebbins, A., Annis, J., et al. 2007, ApJ, 671, 1466
Kun, E., Keresztes, Z., Simkó, A., Szűcs, G., & Gergely, L. Á. 2017, A&A, 608, A42
Kurapati, S., Banerjee, A., Chengalur, J. N., et al. 2018, MNRAS, 479, 5686
Kuzio de Naray, R., McGaugh, S. S., & de Blok, W. J. G. 2008, ApJ, 676, 920
Kuzio de Naray, R., McGaugh, S. S., de Blok, W. J. G., & Bosma, A. 2006, ApJS, 165, 461

Lake, G. & Feinswog, L. 1989, AJ, 98, 166
Lake, G., Schommer, R. A., & van Gorkom, J. H. 1990, AJ, 99, 547
Lane, R. R., Salinas, R., & Richtler, T. 2015, A&A, 574, A93
Lemze, D., Barkana, R., Broadhurst, T. J., & Rephaeli, Y. 2008, MNRAS, 386, 1092
Lerchster, M., Seitz, S., Brimioulle, F., et al. 2011, MNRAS, 411, 2667
Lewis, A. D., Buote, D. A., & Stocke, J. T. 2003, ApJ, 586, 135
Li, P., Lelli, F., McGaugh, S., & Schombert, J. 2020, ApJS, 247, 31
Li, P., Lelli, F., McGaugh, S. S., Starkman, N., & Schombert, J. M. 2019, MNRAS, 482, 5106
Liang, J., Jiang, F., Danieli, S., Benson, A., & Hopkins, P. 2023, arXiv e-prints, arXiv:2304.14431
Limousin, M., Richard, J., Jullo, E., et al. 2007, ApJ, 668, 643
López Fune, E., Salucci, P., & Corbelli, E. 2017, MNRAS, 468, 147
Macciò, A. V., Stinson, G., Brook, C. B., et al. 2012, ApJ, 744, L9
MAGIC Collaboration, Ahnen, M. L., Ansoldi, S., et al. 2016, J. Cosmology Astropart. Phys., 2016, 039
Marchesini, D., D'Onghia, E., Chincarini, G., et al. 2002, ApJ, 575, 801
Markevitch, M., Vikhlinin, A., Forman, W. R., & Sarazin, C. L. 1999, ApJ, 527, 545
Marsh, D. J. E. & Pop, A.-R. 2015, Monthly Notices of the Royal Astronomical Society, 451, 2479
Martinet, N., Clowe, D., Durret, F., et al. 2016, A&A, 590, A69
Martinez, G. D., Bullock, J. S., Kaplinghat, M., Strigari, L. E., & Trotta, R. 2009, J. Cosmology Astropart. Phys., 2009, 014
Martinsson, T. P. K., Verheijen, M. A. W., Westfall, K. B., et al. 2013, A&A, 557, A131
Mashchenko, S., Sills, A., & Couchman, H. M. 2006, ApJ, 640, 252
Mathews, W. G. 2021, MNRAS, 506, 2030
McCleary, J., dell'Antonio, I., & Huwe, P. 2015, ApJ, 805, 40
McDaniel, A., Jeltema, T., & Profumo, S. 2021, J. Cosmology Astropart. Phys., 2021, 020
McInnes, R. N., Menanteau, F., Heavens, A. F., et al. 2009, MNRAS, 399, L84
McLaughlin, D. E. 1999, The Astrophysical Journal, 512, L9–L12
Medezinski, E., Broadhurst, T., Umetsu, K., et al. 2007, ApJ, 663, 717
Medezinski, E., Umetsu, K., Nonino, M., et al. 2013, ApJ, 777, 43
Medezinski, E., Umetsu, K., Okabe, N., et al. 2016, ApJ, 817, 24
Melchior, P., Suchyta, E., Huff, E., et al. 2015, MNRAS, 449, 2219
Merritt, D., Graham, A. W., Moore, B., Diemand, J., & Terzić, B. 2006, AJ, 132, 2685
Merten, J., Meneghetti, M., Postman, M., et al. 2015, ApJ, 806, 4
Michailidis, M., Marafatto, L., Malyshev, D., et al. 2023, J. Cosmology Astropart. Phys., 2023, 073
Michailidis, M. et al. 2024, A&A
Mitzkus, M., Cappellari, M., & Walcher, C. J. 2017, MNRAS, 464, 4789
Miyatake, H., Nishizawa, A. J., Takada, M., et al. 2013, MNRAS, 429, 3627
Mo, W., Gonzalez, A., Jee, M. J., et al. 2016, ApJ, 818, L25
Moore, B., Quinn, T., Governato, F., Stadel, J., & Lake, G. 1999, MNRAS, 310, 1147
Munari, E., Biviano, A., & Mamon, G. A. 2014, A&A, 566, A68
Murphy, J. D., Gebhardt, K., & Adams, J. J. 2011, ApJ, 729, 129
Namumba, B., Carignan, C., Passmoor, S., & de Blok, W. J. G. 2017, MNRAS, 472, 3761
Napolitano, N. R., Romanowsky, A. J., Capaccioli, M., et al. 2011, MNRAS, 411, 2035
Napolitano, N. R., Romanowsky, A. J., Coccato, L., et al. 2009, MNRAS, 393, 329
Navarro, J. F., Frenk, C. S., & White, S. D. M. 1997, ApJ, 490, 493
Navarro, J. F., Hayashi, E., Power, C., et al. 2004, MNRAS, 349, 1039
Navarro, J. F., Ludlow, A., Springel, V., et al. 2010, MNRAS, 402, 21
Nesti, F. & Salucci, P. 2013, J. Cosmology Astropart. Phys., 2013, 016
Newman, A. B., Treu, T., Ellis, R. S., & Sand, D. J. 2013a, ApJ, 765, 25
Newman, A. B., Treu, T., Ellis, R. S., et al. 2013b, ApJ, 765, 24
Newman, A. B., Treu, T., Ellis, R. S., et al. 2009, ApJ, 706, 1078
Oakes, L., Armand, C., Charles, E., et al. 2019, Combined Dark Matter searches towards dwarf spheroidal galaxies with Fermi-LAT, HAWC, HESS, MAGIC and VERITAS
Oguri, M., Bayliss, M. B., Dahle, H., et al. 2012, MNRAS, 420, 3213
Oguri, M., Schrabback, T., Jullo, E., et al. 2013, MNRAS, 429, 482
Oguri, M., Takada, M., Okabe, N., & Smith, G. P. 2010, MNRAS, 405, 2215
Oh, S.-H., de Blok, W. J. G., Walter, F., Brinks, E., & Kennicutt, Robert C., J. 2008, AJ, 136, 2761
Oh, S.-H., Hunter, D. A., Brinks, E., et al. 2015, AJ, 149, 180
Okabe, N., Bourdin, H., Mazzotta, P., & Maurogordato, S. 2011, ApJ, 741, 116
Okabe, N., Futamase, T., Kajisawa, M., & Kuroshima, R. 2014, ApJ, 784, 90
Okabe, N., Okura, Y., & Futamase, T. 2010a, ApJ, 713, 291
Okabe, N., Takada, M., Umetsu, K., Futamase, T., & Smith, G. P. 2010b, PASJ, 62, 811
Okabe, N., Umetsu, K., Tamura, T., et al. 2016, MNRAS, 456, 4475
Paiano, S., Lombardi, S., Doro, M., Nieto, D., & Fornasa, M. 2011, arXiv e-prints, arXiv:1110.6775
Paulin-Henriksson, S., Antonuccio-Delogu, V., Haines, C. P., et al. 2007, A&A, 467, 427
Pearson, S., Price-Whelan, A. M., Hogg, D. W., et al. 2022, ApJ, 941, 19
Peng, E. W., Ford, H. C., & Freeman, K. C. 2004, ApJ, 602, 685
Pieri, L., Lavalle, J., Bertone, G., & Branchini, E. 2011, Phys. Rev. D, 83, 023518
Pierre, M., Siegal-Gaskins, J. M., & Scott, P. 2014, J. Cosmology Astropart. Phys., 2014, 024
Planck Collaboration, Aghanim, N., Akrami, Y., et al. 2018, arXiv e-prints, arXiv:1807.06209
Puche, D. & Carignan, C. 1991, ApJ, 378, 487
Puche, D., Carignan, C., & Bosma, A. 1990, AJ, 100, 1468
Puche, D., Carignan, C., & Wainscoat, R. J. 1991, AJ, 101, 447
Pullen, A. R., Chary, R.-R., & Kamionkowski, M. 2007, Phys. Rev. D, 76, 063006
Radovich, M., Puddu, E., Romano, A., Grado, A., & Getman, F. 2008, A&A, 487, 55
Ragozzine, B., Clowe, D., Markevitch, M., Gonzalez, A. H., & Bradač, M. 2012, ApJ, 744, 94
Read, J. I., Agertz, O., & Collins, M. L. M. 2016, MNRAS, 459, 2573
Refregier, A. 2003, ARA&A, 41, 645
Regis, M., Richter, L., & Colafrancesco, S. 2017, J. Cosmology Astropart. Phys., 2017, 025
Relatores, N. C., Newman, A. B., Simon, J. D., et al. 2019, ApJ, 887, 94
Richardson, T. & Fairbairn, M. 2014, MNRAS, 441, 1584
Richtler, T., Dirsch, B., Gebhardt, K., et al. 2004, AJ, 127, 2094
Rines, K., Geller, M. J., Diaferio, A., & Kurtz, M. J. 2013, ApJ, 767, 15
Rines, K., Geller, M. J., Diaferio, A., Kurtz, M. J., & Jarrett, T. H. 2004, AJ, 128, 1078
Rines, K., Geller, M. J., Kurtz, M. J., & Diaferio, A. 2003, AJ, 126, 2152
Rix, H.-W., de Zeeuw, P. T., Cretton, N., van der Marel, R. P., & Carollo, C. M. 1997, ApJ, 488, 702
Rodrigues, D. C., del Popolo, A., Marra, V., & de Oliveira, P. L. C. 2017, MNRAS, 470, 2410
Rodrigues, D. C., Hernandez-Arboleda, A., & Wojnar, A. 2023, Physics of the Dark Universe, 41, 101230
Rodríguez-Meza, M. A. 2012, in American Institute of Physics Conference Series, Vol. 1473, IX Workshop of the Gravitation and Mathematical Physics Division of the Mexican Physical Society, ed. L. A. Uren-López, R. Becerril-Bárcenas, & R. Linares-Romero, 74–84
Roelfsema, P. R. & Allen, R. J. 1985, A&A, 146, 213
Romano, A., Fu, L., Giordano, F., et al. 2010, A&A, 514, A88
Romanowsky, A. J., Strader, J., Spitler, L. R., et al. 2009, AJ, 137, 4956
Rubin, V. C. 1983, Scientific American, 248, 96
Runge, J., Walker, S. A., & Mirakhor, M. S. 2022, MNRAS, 509, 2647
Rzepecki, J., Lombardi, M., Rosati, P., Bignamini, A., & Tozzi, P. 2007, A&A, 471, 743
Salinas, R., Richtler, T., Bassino, L. P., Romanowsky, A. J., & Schuberth, Y. 2012, A&A, 538, A87
Salucci, P., Walter, F., & Borriello, A. 2003, A&A, 409, 53
Samurović, S. 2010, A&A, 514, A95
Samurović, S. 2012, A&A, 541, A138
Samurović, S. 2014, A&A, 570, A132
Samurović, S. 2016a, Ap&SS, 361, 199
Samurović, S. 2016b, Serbian Astronomical Journal, 192, 9
Samurović, S. 2017, Serbian Astronomical Journal, 195, 9
Samurović, S., Vudragović, A., & Jovanović, M. 2015, MNRAS, 451, 4073
Sánchez-Conde, M. A., Cannoni, M., Zandanel, F., Gómez, M. E., & Prada, F. 2011, J. Cosmology Astropart. Phys., 2011, 011
Sánchez-Conde, M. A., Prada, F., Łokas, E. L., et al. 2007, Phys. Rev. D, 76, 123509
Sand, D. J., Treu, T., Ellis, R. S., Smith, G. P., & Kneib, J.-P. 2008, ApJ, 674, 711

Sartoris, B., Biviano, A., Rosati, P., et al. 2020, A&A, 637, A34
Saturni, F. G., Rodríguez-Fernández, G., & Morselli, A. 2019, in European Physical Journal Web of Conferences, Vol. 209, European Physical Journal Web of Conferences, 01024
Schaller, M., Frenk, C. S., Bower, R. G., et al. 2015, MNRAS, 452, 343
Schive, H.-Y., Chiueh, T., & Broadhurst, T. 2014, Nature Physics, 10, 496
Schmidt, R. W. & Allen, S. W. 2007, MNRAS, 379, 209
Schmidt, R. W., Allen, S. W., & Fabian, A. C. 2001, MNRAS, 327, 1057
Schrabback, T., Schirmer, M., van der Burg, R. F. J., et al. 2018, A&A, 610, A85
Schuberth, Y., Richtler, T., Dirsch, B., et al. 2006, A&A, 459, 391
Seigar, M. S. 2011, ISRN Astronomy and Astrophysics, 2011, 725697
Sereno, M., Lubini, M., & Jetzer, P. 2010, A&A, 518, A55
Sereno, M. & Zitrin, A. 2012, MNRAS, 419, 3280
Sicotte, V. & Carignan, C. 1997, AJ, 113, 609
Simionescu, A., Allen, S. W., Mantz, A., et al. 2011, Science, 331, 1576
Simon, J. D. & Geha, M. 2007, ApJ, 670, 313
Sin, S.-J. 1994, Phys. Rev. D, 50, 3650
Smith, R. J., Lucey, J. R., & Edge, A. C. 2017, MNRAS, 471, 383
Smoot, G. F., Bennett, C. L., Kogut, A., et al. 1992, ApJ, 396, L1
Sofue, Y. 2015, PASJ, 67, 75
Spano, M., Marcelin, M., Amram, P., et al. 2008, MNRAS, 383, 297
Strigari, L. E., Koushiappas, S. M., Bullock, J. S., & Kaplinghat, M. 2007, Phys. Rev. D, 75, 083526
Sun, M., Voit, G. M., Donahue, M., et al. 2009, ApJ, 693, 1142
Swaters, R. A., Madore, B. F., & Trewhella, M. 2000, ApJ, 531, L107
Swaters, R. A., Madore, B. F., van den Bosch, F. C., & Balcells, M. 2003, ApJ, 583, 732
Tamm, A., Tempel, E., Tenjes, P., Tihhonova, O., & Tuvikene, T. 2012, A&A, 546, A4
Tan, W. S., Abidin, Z. Z., & Hashim, N. 2022, Indian Journal of Physics, 96, 671
Tempel, E., Tamm, A., & Tenjes, P. 2007, arXiv e-prints, arXiv:0707.4374
Thanjavur, K., Crampton, D., & Willis, J. 2010, ApJ, 714, 1355
Thorpe-Morgan, C., Malyshev, D., Stegen, C.-A., Santangelo, A., & Jochum, J. 2021, MNRAS, 502, 4039
Tully, R. B. 2023, arXiv e-prints, arXiv:2305.11950
Umetsu, K. & Broadhurst, T. 2008, ApJ, 684, 177
Umetsu, K., Medezinski, E., Broadhurst, T., et al. 2010, ApJ, 714, 1470
Umetsu, K., Medezinski, E., Nonino, M., et al. 2014, ApJ, 795, 163
Umetsu, K., Medezinski, E., Nonino, M., et al. 2012, ApJ, 755, 56
Umetsu, K., Sereno, M., Medezinski, E., et al. 2015, ApJ, 806, 207
Umetsu, K., Zitrin, A., Gruen, D., et al. 2016, ApJ, 821, 116
van den Bosch, F. C. & Swaters, R. A. 2001, MNRAS, 325, 1017
van Eymeren, J., Trachternach, C., Koribalski, B. S., & Dettmar, R. J. 2009, A&A, 505, 1
Verdugo, T., Limousin, M., Motta, V., et al. 2016, A&A, 595, A30
Viana, A., Medina, M. C., Peñarrubia, J., et al. 2012, ApJ, 746, 77
Viana, A., Schoorlemmer, H., Albert, A., et al. 2019, J. Cosmology Astropart. Phys., 2019, 061
Voigt, L. M. & Fabian, A. C. 2006, MNRAS, 368, 518
Walker, M. G., Mateo, M., Olszewski, E. W., et al. 2009, ApJ, 704, 1274
Walsh, D., Carswell, R. F., & Weymann, R. J. 1979, Nature, 279, 381
Wang, L. & Chen, D.-M. 2021, Research in Astronomy and Astrophysics, 21, 271
Wasserman, A., Romanowsky, A. J., Brodie, J., et al. 2018, ApJ, 863, 130
Weijmans, A.-M., Cappellari, M., Bacon, R., et al. 2009, MNRAS, 398, 561
Weijmans, A.-M., Krajnović, D., van de Ven, G., et al. 2008, MNRAS, 383, 1343
Weldrake, D. T. F., de Blok, W. J. G., & Walter, F. 2003, MNRAS, 340, 12
Westfall, K. B., Bershady, M. A., Verheijen, M. A. W., et al. 2011, ApJ, 742, 18
Westmeier, T., Braun, R., & Koribalski, B. S. 2011, MNRAS, 410, 2217
Widrow, L. M. & Dubinski, J. 2005, ApJ, 631, 838
Wilkinson, M. I. & Evans, N. W. 1999, MNRAS, 310, 645
Wolf, J. & Bullock, J. S. 2012, arXiv e-prints, arXiv:1203.4240
Wood, M., Blaylock, G., Bradbury, S., et al. 2008, The Astrophysical Journal, 678, 594–605
Wood, M., Buckley, J., Digel, S., et al. 2013, arXiv e-prints, arXiv:1305.0302
Yang, M., Zhu, L., Weijmans, A.-M., et al. 2020, MNRAS, 491, 4221
Yapici, T. & Smith, A. J. 2017, Dark Matter Searches with HAWC
Yasin, T., Desmond, H., Devriendt, J., & Slyz, A. 2023, MNRAS, 526, 5861
Zaharijas, G., Conrad, J., Cuoco, A., & Yang, Z. 2013, Nuclear Physics B Proceedings Supplements, 239, 88
Zappacosta, L., Buote, D. A., Gastaldello, F., et al. 2006, ApJ, 650, 777
Zhang, Z., Xu, H., Wang, Y., et al. 2007, ApJ, 656, 805
Zhao, H. 1996, MNRAS, 278, 488
Zhu, K., Lu, S., Cappellari, M., et al. 2023, MNRAS, 522, 6326
Zhu, L., Romanowsky, A. J., van de Ven, G., et al. 2016a, MNRAS, 462, 4001
Zhu, L., van de Ven, G., Watkins, L. L., & Posti, L. 2016b, MNRAS, 463, 1117
Zitrin, A., Broadhurst, T., Umetsu, K., et al. 2010, MNRAS, 408, 1916
Zitzer, B. & Collaboration, V. 2017, The VERITAS Dark Matter Program
Zohren, H., Schrabback, T., Bocquet, S., et al. 2022, A&A, 668, A18
Zwicky, F. 1933, Helvetica Physica Acta, 6, 110

Chapter 5

Results and discussion

This chapter highlights and summarizes the main findings of the research conducted during the two and a half years of Doctoral studies as collected from the individual publications listed above.

5.1 SNR studies

5.1.1 Scientific questions

The main scientific questions asked in this project are:

- Is it possible to identify the SNR nature of Galactic objects using eROSITA in conjunction with multiwavelength surveys?
- Is it possible to identify the non-thermal (electron) particles through X-ray synchrotron in light of the new eROSITA data?
- Overall, is it possible to identify and possibly constrain the nature of both the HE particle population (seen in X-rays) through (non) detection of X-ray synchrotron, as well as VHE particle population (leptonic and/or hadronic components) through γ-ray detection. Could the study of the HE population through eROSITA assist the interpretation of the VHE γ-ray radiation?

Larger goals that are being pursued:

- Increase the sample of SNRs with signatures of particle acceleration
- Understand the obstacles in finding more SNRs for this study
- Interpret the sources as leptonic or hadronic (or explore what is necessary to distinguish between the particle populations)
- Ultimately: Is the hypothesis that SNRs contribute substantially to Galactic CRs consistent/challenged by the data?

5.1.2 General overview/Scientific context

As for the missing problem of Galactic SNRs, and their multiwavelength study (with emphasis given on those SNRs that are interesting targets for CR Physics, i.e., those that exhibit non-thermal features - detection of a non-thermal component in the X-ray energy range and/or detection of γ-ray emission (GeV and/or TeV) originating from the SNR): With eROSITA we have managed to detect several tens of prominent non-thermal targets. In particular, we detected 30 new shell-type objects (see Tab. 6.1), with prominent non-thermal features (X-ray and γ-ray signatures) out of which 12 are known SNRs that we detected for the first time in X-rays, and 18 are new SNRs candidates that need to be further studied across the entire EM spectrum to confirm their nature. It is noteworthy, that the locations of SNRs that have confirmed TeV counterparts (and/or the locations of unidentified TeV objects as cataloged in the TeVcat[1]and as collected from the inspection of the significance map of the H.E.S.S. Galactic Plane Survey (HGPS)), that have not been detected in previous X-ray studies, do not exhibit any significant X-ray emission, as confirmed after detailed inspection of the eRASS:4 data. In addition, we have detected several tens more SNR candidates, but they lack evidence of non-thermal particle populations and thus they have not been examined in the context of this work.

In this dissertation, we particularly focus on an extensive study of four individual targets of interest that are not included in the pool of new SNR candidates mentioned above. The thorough screening of the first four eRASS surveys (eRASS:4) that we conducted has revealed four new locations of interest (i.e., new X-ray shell-type structures) that we either initially classified as SNR candidates and subsequently, we confirmed their SNR nature through exhaustive multiwavelength studies or we classified them as X-ray counterparts of known SNRs since they were spatially coincident with well-established Galactic SNRs (mainly from radio studies) i.e., they are known SNRs that we detected for the first time in X-rays. Individual studies for all four cases of the aforementioned SNRs are reported in the publication list and have been extensively studied across the entire EM spectrum. Of those four new findings, three are embedded in the category of known SNRs of which we detected for the first time X-ray emission (G279.0+01.1, the Spaghetti nebula, and G309.8+00.0) and one that has been studied before as a SNR candidate that we confirm its SNR nature in our study (HESS J1614-518). With this study, we have managed to detect X-ray emission from

[0]http://tevcat.uchicago.edu/

all four SNRs (but also radio emission for the case of HESS J1614-518 and confirm the detection of γ-ray emission for all four objects) that were missed by previous studies on those wavelengths mainly due to their faint appearance (low surface brightness both in radio and X-ray wavelengths) and/or their location close to the Galactic Plane (highly absorbed SNRs in X-rays and/or SNRs located in complex regions) and the background contamination (both in radio (nearby MCs) and X-rays (diffuse X-ray emission from the Galactic plane originating from a population of unresolved X-ray sources)) and/or their large angular extension in X-rays (lack of a highly sensitive instrument that has performed an all-sky coverage in X-rays before eROSITA).

Many SNRs (especially those with low surface brightness) are difficult to detect because they are located at complex regions of high background emission (HESS J1614-518 is a showcase example of this class of objects). Others are subject to strong absorption features (e.g., G309.8+00.0). In the last two decades, technological advancement has resulted in higher sensitivity instruments in X-rays, γ-rays, and radio (eROSITA, *Fermi*-LAT, H.E.S.S., the GaLactic and Extragalactic All-sky MWA Survey (GLEAM), the Australian Square Kilometre Array Pathfinder (ASKAP)). In particular, the G279.0+01.1, the Spaghetti nebula, the G309.8+00.0, and the HESS J1614-518 SNRs (all four SNRs investigated in this work) have been detected for the first time in X-rays and γ-rays (GeV energies) with eROSITA and *Fermi*-LAT, respectively. HESS J1614-518 has been detected in TeV γ-rays with the H.E.S.S. ground-based observatory. The latter SNR has also been detected for the first time in radio with the GLEAM radio survey. The radio morphology of the G279.0+01.1 has been refined using Parkes-MIT-NRAO (PMN) and ASKAP data. The increased number of the known population of Galactic SNRs emitting in X-rays (with eROSITA) and the recent studies with GLEAM (e.g., Hurley-Walker et al. (2019)) and ASKAP radio data (e.g., Ball et al. (2023)) that revealed several tens of new Galactic SNRs points towards the fact that a significant fraction of the missing number of Galactic SNRs could be the result that the whole sky has not been properly covered in all distinct wavelengths that SNRs are observable (mainly radio, IR, optical, X-rays, and γ-rays) and that the sensitivity of the surveys that have provided full-sky coverage is limited (e.g., ROSAT in X-rays). The findings presented in this work indirectly contribute toward closing the gap between the detected number of Galactic SNRs and the expected number of Galactic SNRs, however, a large discrepancy still remains. Quantifying such a discrepancy remains a difficult task. Taking into consideration that a certain

number of SNRs might never be able to be detected due to detection limits that both the local background and the instrument itself introduce and that a certain number of SN explosions (CC) leave behind a black-hole (BH) as their legacy that would not result to an observable SNR, we might never be able to explore the whole population of Galactic SNR but only to gradually close the gap between the number of Galactic SNRs that have been observed and the number that is estimated to exist at any given moment as more sensitive instruments allow us to perform deeper studies.

5.1.3 Individual targets investigation

G279.0+01.1 & Spaghetti nebula:

The angular size of SNRs varies based on their distance from Earth and their evolutionary state. More distant SNRs (tens of kpc) and/or younger SNRs usually have angular sizes of a few arcmin whereas Earth-adjacent SNRs (tens of hundreds of parsecs (pc) away from us) at the latest stages of their evolution can reach degree scale sizes (e.g., Vela SNR). Both the G279.0+01.1 and the Spaghetti nebula SNR belong to the closed group (only a handful of such SNRs have been detected in the MW) with angular sizes of several degrees. Both remnants have an angular size of ~ 3.0 deg. However, the angular size is not the only common feature that those two remnants share. Both SNRs have been detected in radio synchrotron and optical (Hα) wavelengths and as of recently (in the last decade) they have been classified as extended GeV sources in the 4FGL-DR4 (Abdollahi et al., 2022; Ballet et al., 2023) *Fermi*-LAT catalog (γ-ray emitters). Therefore, they exhibit prominent non-thermal signatures and thus are interesting targets for CR Physics. Exploiting ~ 14.5 years of *Fermi*-LAT data we confirm the detection of both SNRs in the GeV-band and we provide updated imaging (residual count maps and test statistic (TS) maps) and spectral analysis results. With eROSITA we detected the X-ray counterparts of both SNRs for the first time. Looking back to eROSITA's predecessor (i.e., ROSAT data) we made an aposteriori detection of X-ray emission from the two remnants (after the initial detection in the eROSITA data), however, the quality of data is insufficient to exploit and analyze the remnants' X-ray properties. Unpublished (in terms of diffuse X-ray emission) *XMM-Newton* observations that happen to cover small portions of those two remnants were also exploited and provided nicely confirmatory results to eROSITA. The spectra of both remnants, based on eROSITA data, are characterized by faint X-ray emission of purely thermal nature (expected due to their evolved stage –

both are considered to be among the most evolved Galactic SNRs according to the literature) and the majority of the X-ray emission is soft, found in $\sim 0.3-1.1$ keV, while both remnants remain totally undetected above 2.0 keV. Thus those two SNRs do not efficiently accelerate electrons to TeV energies at their current evolutionary stage while there is no direct evidence they did in the past. Consequently, leptonically induced γ-rays are highly unlikely to be detected. Both SNRs are also located close to the Galactic Plane ($\pm 1.5^{\circ}$, where massive stars are most abundant) and thus a potential pulsar association is highly likely. The shape of the X-ray spectrum of both remnants also exhibits similar features. It is characterized by a high Oxygen-to-Iron ratio (O/Fe$\gg$1) and it is dominated by light element emission lines (mainly OVII, OVIII, NeIX+X, and Mg XI). Thus, the characteristics of their spectral shape in combination with their location along the Galactic disk (dense areas), which also increases the probability for hadronic γ-ray emission observed from both remnants, are consistent with CC SNRs enhancing the probability for a pulsar association. The morphology of both remnants is also hugely impacted by the presence of nearby MCs and dust clouds ("responsible" for X-ray and optical absorption as well as enhancing the probability for γ-ray emission of hadronic origin which is consistent with the modeling of the GeV spectral energy distribution (SED) of both remnants and their expected old age). According to the spatial anticorrelation between X-ray and IR data from localized structures in both SNRs, dust destruction features are also highly likely to be present. Both SNRs are considered to be among the oldest Galactic SNRs with ages exceeding 10^5 yrs, given their large size and distances ($\sim$ 1.3 kpc for the Spaghetti nebula and $\sim$ 2.7 kpc for the G279.0+01.1 according to the literature). Thus, G279.0+01.1 appears to have double, i.e., $\sim$ 140 pc the actual (linear) size of the Spaghetti nebula, $\sim$ 70 pc, and thus it has been considered to be the largest and oldest SNR in our galaxy. Whereas the distance estimate for the Spaghetti nebula is well-established and supported by its associated pulsar J0538+2817 kinematic distance measurements, the G279.0+01.1 distance has been derived from either empirical relations (optical extinction data) or potential association with nearby dust clouds and, therefore, it could carry large uncertainties. Large uncertainty in the G279.0+01.1 distance estimate is also supported by the detection of X-ray emission from the SNR with eROSITA down to 0.3 keV, which indicates that it is not subject to strong absorption characteristics that might be expected at a distance of $\sim$ 2.7 kpc. In contrast to the fact that both SNRs are considered to be evolved, the X-ray spectral fitting

provides a multi-temperature thermal plasma (even if the total remnant's spectrum can be well-fitted with a single temperature plasma with a gas temperature of kT $= 0.22^{+0.02}_{-0.03}$ keV, and an absorption column density of $N_H = 0.30^{+0.04}_{-0.03} \cdot 10^{22}$ cm^{-2} for the Spaghetti nebula and a two-temperature thermal plasma of kT ~ 0.3 keV and kT ~ 0.6 keV, and an absorption column density of $N_H \sim 0.3$ cm^{-2} for the G279.0+01.1 SNR) in non-equilibrium ionization as the best model to describe the spectral characteristics of both remnants. In addition, the detection of γ-ray emission from such old SNRs is uncommon and triggers the question of up to what age SNRs can efficiently accelerate particles to the highest energies and if the γ-ray emission is the result of ongoing hadronic acceleration from such old SNRs (which could be explored by the hints of rapid variability (sudden brightening and decay of γ-ray spots at the shockfront) that, however, we do not have the means to inspect with *Fermi*-LAT – but still such a possibility seems unlikely since the acceleration time for protons for typical hadronic CR energies and typical SNR magnetic fields does not commonly exceed $10^3 - 10^4$ yrs) or the result of the interaction of "sea CRs" with nearby dense gas.

In light of the eROSITA X-ray data that lend support to younger SNR scenarios for both SNRs, we examine different modeling scenarios that appear to be better aligned with the observational data from both objects.

i) Spaghetti nebula: historically, two substantially different assumptions on the age of the Spaghetti nebula have been discussed. The first one is a natural consequence of the remnant's large physical size, which, for typical explosion energy of $\sim 10^{51}$ erg and reasonable parameters of the ISM, suggests $t_{age} \sim 10^5$ yr (Silk & Wallerstein, 1973). This would make Spaghetti nebula one of the oldest supernova remnants in the Galaxy. Another, shorter age estimate, $t_{age} \sim 3 \times 10^4$ yr came up after the discovery of a pulsar in the remnant and measurements of its proper motions (Romani & Ng, 2003; Chatterjee et al., 2009). Given this dichotomy, it is necessary to confront both assumptions with the eROSITA data and discuss what additional data might help differentiate between these scenarios. To keep the discussions of both scenarios focused, such analysis has been split into two parts. In Michailidis et al. (2024b), we consider the high-age scenario which is consistent with the obtained best-fit X-ray spectral parameters but contradicts the young pulsar kinematic age, while in Khabibullin et al. (2024) we pursue the low-age version (a younger SNR scenario which is the byproduct of a SN explosion expanding in low-density material (as a result of the strong stellar winds of the progenitor massive star that largely disturbed the surrounding ISM),

i.e., wind-blown-bubble, which found to be broadly consistent with the newly derived eROSITA X-ray data. Such a scenario justifies a younger SNR age and the large angular size of the SNR and is better in line with the pulsar's kinematic age estimate. We note that due to the large physical and angular sizes, both models do not fully address the question of how the large-scale inhomogeneities of the ISM might affect the observed properties of S147. The presented studies demonstrate clearly the complicated multiphase structure of the Spaghetti nebula and provide guidelines for future work, including taking advantage of more sensitive X-ray data.

ii) G279.0+01.1: the results obtained in this work cast some doubt on the so far prevailing interpretation that G279.0+01.1 is located at a distance of $\sim$ 2.7 kpc and has an age of $\sim$ 1 Myr (the largest and oldest Galactic SNR scenario). In particular, the distance of the G279.0+01.1 SNR is highly uncertain. Throughout the years a number of different associations to the remnant have been proposed (mainly associations with MCs and red clump stars optical extinction measurements) placing the remnant at a distance of $\sim$ 3 kpc. Nevertheless, all distance estimates are based on empirical relations with substantial scatter, and a critical assessment may be justified. In light of the new X-ray data, two possible scenarios emerged. The first scenario yields a consistent picture with the literature (the latest optical extinction measurements favor a distance of 2.7 kpc (Shan et al., 2019)) of a remnant at a distance of $\sim$ 2.5 kpc based on the absorption column density values derived from the X-ray spectral fitting of the eROSITA data. An alternative different scenario emerges through the inspection of nearby pulsars. A potential pulsar association, as suggested by the shape and the characteristics of the X-ray spectrum of the remnant as well as the remnant's location on the Galactic plane, with any of the pulsars detected within 3° from the remnant's center, would place the remnant at a much closer distance of $\sim$ 0.4 kpc changing totally our knowledge about its specifics. The latter result is supported by the updated distances as derived by the updated electron density model (the default electron density model adopted since 2016 (Yao et al., 2017)) which favors largely reduced dispersion-measure based distances of all pulsars in projected vicinity to G279.0+01.1 by typically a factor of $\sim$ 8. Such a closer distance, which yields a $\sim$ 20 pc linear diameter and an age well below 10^6 yrs, provides a more consistent picture with the non-equilibrium best-fit model of the X-ray spectrum and with the morphological-associated GeV counterpart of the remnant. In the latter case, the GeV emission is more likely to be associated with the SNR rather than being co-located with the remnant by

chance due to sea CRs interacting with nearby dense gas.

HESS J1614-518:

HESS J1614-518 was initially proposed as SNR candidate purely based on its shell-type appearance (with an angular extension of 0.8°) in the TeV energy range, as detected with the H.E.S.S. ground-based observatory. An extended GeV source had previously been detected with *Fermi*-LAT with position, extension, and spectral characterization that makes it a clear counterpart of HESS J1614-518. Three *XMM-Newton* observations were requested and granted towards this exciting object, however, no firm results were derived mainly due to the stray-light contamination due to the presence of the RCW 103 nearby SNR and the large systematic uncertainties on the derived results. HESS J1614-518 is placed onto the Galactic Plane in an extremely complex region, being surrounded by the extremely bright in X-rays RCW 103 SNR, the LMXB 4U 1608-52, and most importantly a diffuse extended soft X-ray emission component potentially originating from unresolved X-ray emitting sources on the Galactic Plane, mainly confined below 1.3 keV. In the broadband, i.e., 0.3-5.0 keV energy range, this soft background and/or foreground emission component is an inhibitory factor for detecting X-ray emission from this exciting TeV object. Only after filtering out this soft emission component, which heavily contaminates the X-ray signal from the location of the object, and restricting the analysis $>$ 1.3 keV, extended diffuse X-ray excess which is spatially coincident with the TeV object becomes clearly apparent. The majority of the X-ray emission is confined in the 1.3-2.5 keV energy band and by properly modeling the soft background and/or foreground emission component (which appears to be best described by a two-temperature thermal plasma model), we obtained a purely non-thermal X-ray spectrum which is best described by a powerlaw with an index of ~ 1.8, as the best-fit model to the data. Additionally, we examined the ~ 14.5 yrs of *Fermi*-LAT data refining the morphology of the object's GeV counterpart and readdressing its GeV-TeV spectrum in view of the fact that more *Fermi*-LAT data and updated analysis methods have become available. However, Galactic objects are usually classified as SNRs based on the detection of radio synchrotron emission, as discussed in sec 1.1.3. Therefore, we exploited the newly collected GLEAM radio data, which provides a radio wavelength coverage of the sky at low frequencies (80-300 MHz), and we report the first discovery of a radio-continuum emitting shell in morphological agreement with the TeV and X-ray shells, confirming the SNR nature of the source. Modeling

the non-thermal spectral components of the remnant's multiwavelength SED (i.e., radio synchrotron emission, X-ray synchrotron emission, GeV emission, and TeV emission) we provide constraints on the properties of the remnant such as its magnetic field which is estimated to be 25 μG, and the origin of the γ-ray emission which appears to be leptonic induced. Finally, purely based on the absorption column density values derived from the X-ray spectral fitting of the remnant we report the first distance estimate of this remnant using data from the object itself since all distance measurements reported to date come from potential remnant's associations resulting in an uncertainty range 1.2-10 kpc. The obtained distance was found to be of the order of $3.5^{+1.76}_{-0.88}$, thus likely placing the remnant at the Scutum-Crux spiral arm. Given the location of the remnant, i.e., Galactic Plane, we also searched for potential pulsar associations. Among the pulsars that fall in projection near the remnant we singled out three J1613-5211, J1615-5137 (4FGL J1615.3-5136), and J1616-5017, as the most probable candidates mainly taking into account their estimated characteristic age and by computing the transverse velocities required for each pulsar to reach its present location assuming that it started its journey from the remnant's re-defined center (which we studied in detail using all three wavelengths, i.e., radio, X-rays, GeV to TeV γ-rays). Finally, exploiting Leahy & Williams (2017) evolutionary models for SNRs we computed the remnant's age to be of the order of $\sim 4 \cdot 10^4$ yrs.

G309.8+00.0:

Finally, the SNR G309.8+00.0, with its center coinciding with a galactic latitude of 0°, has a small angular size of $0.43° \times 0.32°$ but it is likely the most distant SNR, among the four examined SNRs in this work, with an estimated distance of the order of 3 kpc according to the literature. The SNR has only been detected in the radio band, and classified as a SNR with a shell-type morphology of elliptical shape. In this work, we report the detection of its X-ray counterpart. The remnant is subjected to strong absorption features resulting in the detection of X-ray emission originating from the remnant which is solely restricted in the 1-2 keV energy band, thus mimicking a hard spectral appearance which could be misinterpreted as a non-thermal X-ray spectrum. The soft X-ray emission component (< 1 keV) is totally absorbed, while only ~ 300 X-ray photons have been detected from this source with eROSITA, making it one of the faintest Galactic SNRs ever detected in X-rays ($F_{\rm total} = 1.42^{+0.87}_{-0.51} \cdot 10^{-11}$ erg/cm^2/s in the 1-2 keV energy range). Its X-ray spectral analysis reveals a purely thermal SNR in X-rays

which exhibits Mg emission in the 1.33-1.47 keV and Si (XIII) emission in the 1.7-1.9 keV energy band. However, the limited photon statistics do not allow us to derive firm conclusions about its spectral classification, while the strong absorption of the X-ray emission at softer X-rays does not permit us to inspect its spectrum for the presence of lighter elements (i.e., O and Ne). Therefore, we have no means to compare elemental abundance fractions and consequently disentangle between a type-Ia event and a CC SNR. However, the X-ray absorption column density values derived from the X-ray spectral fit when combined with optical extinction data toward the remnant direction favor a much larger remnant distance above 6 kpc, and of the order of 10 kpc, which contradicts the 3 kpc distance reported in the literature and which is also supported from the estimated distances of nearby pulsars in the remnant's near vicinity that could be potentially associated with the remnant. Based on the analysis of nearby pulsars' properties (age, distance, and transverse velocity), J1350-6225 (4FGL J1350.6-6224) and J1358-6025 (4FGL J1358.3-6026) would be most likely to be associated with the remnant in case of a CC SN progenitor origin. If the remnant is of type Ia SN progenitor origin then this would be a surprising and rare finding especially given the location of the remnant on the Galactic plane. Typical type Ia SNe occur at high galactic latitudes since the explosion is triggered by the thermonuclear runaway of a white dwarf in a close binary system and thus is connected with low-mass stars rather than massive stars at the end of their life that are most abundant along the Galactic disk. No optical counterpart has been found to date that could provide further insight into how the progenitor of the SNR shaped the surrounding medium. Therefore, due to the lack of sufficient evidence, we are planning to request a deep X-ray follow-up observation from the remnant's location to examine its X-ray spectrum in detail and gain valuable information about its progenitor. We also examined the unidentified uncertain 4FGL J1349.5-6206c γ-ray source which seems to extend at and around the remnant's location. After a detailed spatial analysis of the latter source, we argue that it can be decomposed into four point-like sub-components. We note that modeling the latter components as extended sources is only marginally preferred. However, the limited photon statistics > 5 GeV in combination with the large PSF size of the *Fermi*-LAT instrument ~ 1 GeV does not allow us to investigate the nature of the spatial distribution of the γ-ray emission from the four sub-components in detail (i.e., if of point-like or extended nature). Among the latter components, the one that is spatially coincident with the SNR is detected with a 5.8σ significance

> 1 GeV. Therefore, given that no prominent γ-ray point sources have been detected from the direction of the SNR, we argue that the G309.8+00.0 SNR accounts for at least a significant part of the emission from the source.

5.1.4 Discussion

Concluding, the four individual cases of SNRs reported in this work showcase that although eROSITA was not intended to study nonthermal Galactic SNRs as its primary objective, a different survey strategy covering harder X-ray energies with a higher sensitivity may be the most optimal approach for the goals of our study, it provides a unique opportunity to discover and investigate SNRs in X-rays (either thermal or non-thermal (especially when working complementary to GeV/TeV instruments such as H.E.S.S. and *Fermi*-LAT) but also highly absorbed SNRs that are located at complex regions) since it offers an all-sky coverage with unprecedented sensitivity below 2 keV and the first true imaging survey of the sky in the 2.0-10 keV energy band. The increasing number of Galactic SNRs detected in X-rays also points toward the conclusion that the missing number of Galactic SNRs is largely dependent on the limited sensitivity of current instruments observing across different energy bands of the EM spectrum but it is also dependent on the lack of the complete coverage of the sky across the entire EM spectrum. In addition, the new findings outline how eROSITA can work complementary to GeV-TeV surveys for studies of those SNRs that are interesting targets for CR Astrophysics (e.g., provide distances and ages of the SNRs that can accelerate particles up to the highest energies), and how a complete SNR population study (that falls beyond the capabilities of the findings in this work) in high and very high energies (X-rays and γ-rays), in the near future, can help address important questions of Modern Astrophysics such as up to what ages SNRs can efficiently accelerate particles, what is the contribution of the SNRs to the total CR spectrum, and what is the total contribution of the Galactic SNRs to the total CR spectrum? To date, only $\sim$ 10 % of the Galactic SNR have been found to exhibit non-thermal signatures. This does not come as a surprise since thermal X-rays from SNRs come as a natural consequence due to heating mechanisms whereas sufficient particle acceleration (X-ray synchrotron radiation and γ-rays) depends on the individual properties of the SNR and its progenitor origin. With the exception of the HESS J1614-518 which appears to be non-thermal in X-rays, the majority of the targets investigated in this study (including the targets listed for future in-depth analysis) do not exhibit non-thermal features in

X-rays, indicating the difficulty of finding suitable targets for further research into acceleration mechanisms in these objects. An interesting finding (an observational result that is consistent with theoretical predictions), is that the three SNRs (G279.0+01.1, the Spaghetti nebula, and G309.8+00.0), which we confirmed their GeV counterpart and characterized its spectrum as hadronic, do not exhibit a non-thermal component in X-rays (or it is essentially weak to be detected). This does not come as a surprise since the origin of the GeV emission is likely hadronic and thus it does not originate from TeV electrons that could emit X-ray synchrotron. However, assuming that the Spaghetti nebula does not evolve as a SNR-in-cavity scenario (and thus it is old) and that the G279.0+01.1 is not associated with any of the nearby pulsars, thus it could indeed be located at a distance of 2.7 kpc and being perhaps the oldest Galactic SNR, it could be the case that the γ-ray emission originates from the interaction of "sea" CRs with high-density gas instead of high-density CRs accelerated in the SNRs. Likewise, for the case of the HESS J1614-518 SNR from which we detect non-thermal X-ray synchrotron emission; the characterization of the GeV SED favors a leptonic origin of the spectrum which means that the remnant efficiently accelerates electrons up to TeV energies that can emit in X-rays through synchrotron and in γ-rays through IC. Such a result showcase a tendency, even if not universally confirmed yet, that the absence of a non-thermal component in the X-ray spectrum of Galactic SNRs is accompanied by the detection of γ-ray emission of hadronic origin (or lack of γ-ray emission originating from the SNR, i.e, either γ-ray emission steaming from "sea CRs" interacting with high density gas from the nearby location of the remnant, or total absence of γ-ray emission), while leptonically induced γ-rays usually accompany non-thermal X-rays. To this end, we observe an excellent spatial correlation of X-ray synchrotron emission and γ-ray emission of leptonic origin from HESS J1614-518 (the X-ray emission fills the entire shell of the observed TeV and GeV emission from this SNR), whereas for the rest three SNRs, that appear thermal in X-rays and their γ-ray emission is likely hadronically induced, there is no overall spatial coincidence of X-ray and γ-ray emission across the remnants' area. However, more sensitive γ-ray facilities (e.g., CTA) are necessary to constrain theoretical models that account for physics acceleration and different radiation processes, and consequently confidently disentangle between hadronic and leptonic γ-rays detected from SNRs. Finally, with this work, we indirectly contribute toward shortening the gap between the total number of Galactic SNRs and the number of Galactic SNRs detected in

X-rays, as well as gradually closing the gap between the expected and detected number of Galactic SNRs (in light of the Galactic SNR candidates listed for further examination), and gaining further insight and a crucial understanding of the production and energy density of Galactic cosmic rays and the overall energy budget of the interstellar medium (ISM) that a full Galactic SNR population characterization can provide.

5.2 DM studies

5.2.1 Scientific questions

The main goals pursued in this project are:

- The expected CTA sensitivity toward annihilating DM signals from not that frequently observed objects for DM studies that will be observed with CTA in the future
- Nature and effect of uncertainties on the derived sensitivity prospects
- Provide the most comprehensive catalog of DM density profiles of objects spanning a wide range of mass orders, from dSphs to Galaxy clusters
- Is there a universal scaling law observed by matter distributions of all sizes?

5.2.2 Indirect DM studies with CTA

As for the problem of the missing mass of the Universe (unseen mass or DM): The CTA observatory comes with an improved set of attributes, such as an improved angular resolution, a wide energy coverage, a full sky coverage, and a larger effective area compared the current IACTs, motivating the expectation for higher sensitivity and therefore making it a promising instrument for DM searches.

In our work, we focus on a detailed assessment of the CTA sensitivity to potential DM signals from WIMPs annihilation in nearby galaxies (M31 and M33). To this aim, we consider the planned observational strategy reported in Acharya et al. (2019) and we use the latest available IRFs – prod3b-v2 and prod5b respectively. This study is based on 100 hours sets of data simulation of M31 and M33 nearby spiral galaxies expected to be promising DM candidates due to their large angular size, proximity, and sideways view. We modeled the DM halo of each galaxy with different hypothetical DM profiles collected from the literature, paying special attention to the various

sources of uncertainties that impact the DM sensitivity of the CTA detection: i) uncertainties connected to the astrophysical background contamination, ii) uncertainties connected to the presence of DM substructures, iii) uncertainties connected to the imperfect knowledge of the instrument itself, and iv) uncertainties connected to the unknown DM density distribution of the targets. As a result of the simulation, we present the expected sensitivity of CTA for the detection of annihilating WIMP signal from M 31 and M 33 in the form of "CTA limits", so to say the limits (on the weighted velocity annihilation cross-section) that CTA could provide in the case of no signal detection.

In the absence of a significant detection of the DM annihilation signal for both targets, we present which constraints are to be expected with CTA for 95 % confidence level for the weighted velocity annihilation cross section for $\tau\bar{\tau}$, $b\bar{b}$, and W^+W^- channels. Our studies resulted in the most constraining value of the level of $5 \cdot 10^{-25}$ cm^3 s^{-1} at energies $\sim$ 0.3 TeV for the $\tau^+\tau^-$ annihilation channel when observing M31. Although the obtained upper limits are far from the thermal relic value, they are at least by a factor of 5 more constraining than the latest VERITAS stacked dSphs analysis and MAGIC deep observations towards Segue 1. What is more exciting, though, is that the expected CTA sensitivity towards annihilating WIMP signal from M 31 exceeds by an order of magnitude the HAWC sensitivity towards annihilating WIMP signal from the same target (when considering the same DM density profile). Additionally, most recent predictions of CTA GC simulations might provide better constraints, however, they were obtained based on substantially larger amounts of data (254 hours of observation) and are focusing on a DM target of much higher DM density.

As for the different classes of uncertainties that could largely affect our upper limit results we have examined in detail their impact.

i) The Astrophysical background contamination: since there are no known TeV sources inside the FoV of CTA for both DM targets, we focused on possible astrophysical sources emitting GeV radiation as reported in the literature, that contribute to DM signal contamination and therefore result in sensitivity loss. Thus, we listed all sources included in the 4FGL and 3FHL *Fermi*-LAT catalogs (both point-like sources and extended sources) and derived our upper limits results both in the presence and absence of the latter sources. Our results show that the extended (Inner M 31) and all point sources collectively appear to be too faint to affect the derived upper limits. Additionally, we considered the spectral breaking of the Inner M31

γ-ray spectrum, as detected by *Fermi*-LAT, at $\sim$ 5 GeV (as indicated by the flat spectral points). A simple powerlaw spectral fit assuming that the Inner M31 spectrum extends at energies above 0.3 TeV resulted in a $\sim$ 2.4 or harder powerlaw index value so that the Inner M 31 astrophysical source can be detectable by CTA.

ii) The presence of DM substructures: Using the CLUMPY software package we performed an additional set of analyses in the presence of DM substructures for M 31. The derived improvement of the upper limits results is connected to the spatial scale of the DM template. The J-factor values, which represent the DM density distribution and are used for the construction of the DM source templates, appear to increase when we include sub-halos in the analysis in comparison to the smooth J-factor values, but only at larger distances. Still, the improvement in the upper limits, when we include substructures, appears to be negligible even when we extend the radius of our DM templates at values where the J-factor is significantly enhanced by the substructures boosting. The substructures boosting is extensively discussed in Han et al. (2016), where the authors attribute this behavior to the fact that the fraction of the mass bound into substructures is expected to decrease towards the center of the given galaxy (M 31 in our case), as sub-halos are tidally disrupted by the strong gradient of the gravitational potential (they are suffering from tidal stripping). This negligible contribution of the DM sub-halos to the upper limits results, for the CTA instrument, is consistent with the results that were reported in Hütten et al. (2016). In particular, Hütten et al. (2016) report that for the angular resolution of CTA at E $>$ 0.03 TeV (same E_{min} as we are considering in our analysis) the substructure contribution appears negligible. The upper limit results in the presence of substructures should be considered preliminary, as the nature of the DM sub-halos has not yet been revealed. Further details regarding the true nature of those substructures (i.e., mass, spatial distribution, and DM distribution within each halo) will be required to obtain results of higher precision.

iii) The systematic uncertainties: an important element of the sensitivity loss, considered in this study, is connected to systematic uncertainties. We study the systematic uncertainty impact in the case of M 31. For the estimated CTA systematic uncertainty at the level of 3–10%, we collate the outcomes of two approaches to systematics treatment. The first strategy is contingent on modifying the log-likelihood function used to fit the model to the data, whereas the second is based on limiting the observational time so that the margin of the statistical uncertainty is similar to the systematics level.

Although the strategies employed were distinctive, they both brought about similar sensitivity loss compared to the no systematic case. In both cases, losses tend to affect low DM masses, whose limits are strongly dominated by low-energy data, where systematics are the most important factor. Whereas the modification of the log-likelihood function introducing scaling parameters is not a new technique used to account for systematic uncertainties (i.e., it has been introduced in Silverwood et al. (2015)), the main concept behind the new idea of constraining the exposure time is is that different observation times can be assigned to different energy bands. Therefore we splitted the analysis energy range (0.03 to 100 TeV) in log-equal energy bins of 10% width (CTA energy resolution). We selected the energy bins where the systematic uncertainty exceeds the statistical, by counting the number of photons in each energy bin, and we proceeded with a "time-cut" in those energy bins, so that the two types of uncertainties become equal. As a final step, we implemented a joint likelihood analysis of those (40) energy bins from which we derived the upper limits results. The derived results show that the systematic uncertainties dominate at low energies, while they only weakly affect the upper limits at higher energy ranges. Such treatment of systematic uncertainties allows us to propose a high-precision observation mode for CTA, i.e., the target can be observed by different types of telescopes (SST/MST/LST) for a specific time without entering the systematic-dominated regime. LSTs will observe for the shortest exposures since they are operating in the lowest energy range, MSTs will observe longer since they are operating in the "middle energy range", and SSTs will observe the longest since they are operating in the highest energy range of CTA. At the same time, such an approach allows to "free" some CTA time which can be dedicated to observations of other sources. To sum up, the upper limit results that we obtained correspond to one of the worst-case sensitivity scenarios and show that a whole observation campaign can be very significantly affected by factors attributed to the instrument itself.

iv) The lack of knowledge of the actual DM density distribution of the DM targets: For both DM targets, more than a single profile are reported in the literature. Therefore, we collected all available DM profiles for both objects and examined how much our upper limits are affected, if eventually, the DM density distribution appears to be significantly less or more peaked towards the target's center. We conclude that a large flat core in the DM distribution (e.g, Burkert profile) can severely worsen the CTA sensitivity by at least a factor of 5 and up to an order of magnitude compared to more

cuspy profiles (e.g., NFW, Moore, Einasto). We conclude that for the DM density profiles exploited in this work the corresponding uncertainty can reach an order of magnitude for certain annihilation channels, thus introducing the most important cause of uncertainties. Thus, a thorough testing of the reliability of DM density profiles is necessary.

5.2.3 DM$_\rho$cat: a catalog of DM density profiles

Driven by the result that the uncertainties on the DM profiles provide the highest uncertainty in the derived prospects among all examined classes of uncertainties, we argue that future studies that will provide further insight and more accurate assessments into how DM distributes in all targets (more accurate simulations of the Dark matter component (e.g., determination of a dynamical profile of each particle rather than traditional binning of particles on the basis of their instant positions (Muni et al., 2024)) in conjunction with baryonic effects, e.g., supernova feedback and enhanced dynamical friction, that can largely impact usual dark-matter-only simulations), broadly considered for DM searches, are crucial for the precise appraisal of DM annihilation detection within these objects. On that note, we collate and summarise the vast number of DM profiles for different categories of objects in literature spanning all orders of masses. In particular, we summarise profiles for dSphs, Dwarf galaxies, Spiral galaxies, Elliptical Galaxies, Galaxy groups, Galaxy Clusters as well as displaying differing profiles for the GC. We present differing profiles, of the order of several thousands, for a few thousands of objects. Such a comprehensive catalog of DM density profiles can serve as a tool for future DM studies providing more realistic constraints on the DM parameter space compared to past studies that employed a single (statistically favored to be far from reality) DM density profile. We furthermore exploit this vast pool of profiles to investigate the correlation between several fitting parameters such as Virial mass as well as investigating the J/D-factors of these profiles aiming to confirm the universal relation discussed in Boyarsky et al. (2009), which appears to be satisfied by matter distributions at all observed scales and is hard to explain in the absence of DM, thus providing further proof for its existence. The latter effort is still ongoing.

Chapter 6

Future projects

In light of the many open questions regarding Galactic SNRs and DM, I briefly outline below some of the future research endeavors I plan to undertake during my first postdoctoral years.

A new ERA of Galactic population studies: With an average rate of 1-2 SNe per century (Keane & Kramer, 2008) a total of ∼1200 SNRs are expected to be observable in the Milky Way (MW) at any given moment. Despite the rough estimation of a few thousand SNe, up-to-date findings result in a much lower number of identified SNRs ∼ 300 (Green, 2019), with the majority of those discovered in radio. Therefore, it is necessary to use novel survey methods to address the problem of the missing number of SNRs. In this regard, a promising method includes the application of machine learning techniques for image classification in all-sky survey data (mainly eROSITA and *Fermi*-LAT) with an objective of adding new findings, obtained from the Artificial intelligence (AI) applications on the newly collected eROSITA and *Fermi*-LAT data that were probably missed by eye-inspection, to the existing pool of objects, i.e., the 30 new shell-type objects in the eROSITA data with prominent γ-ray counterparts as discussed in sec. 5 that are selected as prominent targets for further inspection (as shown in Tab. 6.1). SNR's age and the sensitivity of our instruments play a key role in their detection since fainter remnants would not be observable. The size, which is a function of the distance, of each remnant is also an unavoidable factor in the proper instrument selection (pointing observations versus all-sky surveys). In particular, the size of evolved SNRs in close proximity to Earth (hundreds of parsecs) can reach degree-scale numbers. Current imaging X-ray instruments, such as *XMM-Newton*, *Chandra*, *Suzaku*, and NuSTAR have a limited field of view (FoV), making them difficult to study in X-rays. As confirmed by

the study conducted in my Doctoral program but also from current radio surveys (e.g., GLEAM and ASKAP), as mentioned above, a large fraction of the missing number of Galactic SNRs is a result of not having properly covered the whole sky in all distinct energy bands that SNRs are detectable. In addition, most of the newly detected diffuse X-ray sources (likely SNRs), have low surface brightness. In many cases, imaging survey data is the only option. Indeed, many new remnants have been detected with eROSITA (still an ongoing process). Knowing where to search for remnants gives a unique opportunity to propose numerous and deep *Chandra* and *XMM-Newton* follow-up observations toward the direction of those new remnants (the sample of SNR candidates collected from my Doctoral program + the results that will be obtained from the application of machine learning techniques on HE and VHE All-Sky Survey data) aiming at their detailed X-ray and γ-ray imaging and spectral analysis, given the experience and expertise acquired during my Doctoral studies on *XMM-Newton*, *Chandra*, and *Fermi*-LAT data analysis. High-energy resolution data from the forthcoming missions like XRISM (and in the near future LEM and Athena) will also provide detailed measurements of X-ray emission line velocities, and thus one will be able to gain more insight into the physical processes of those objects. However, searching all-sky survey maps manually (i.e., by eye) for potential targets is neither the only nor a highly accurate option. Applying machine learning techniques for image classification on All-Sky Survey data with unprecedented sensitivity (e.g., eROSITA in X-rays and *Fermi*-LAT in γ-rays) based on size and shape of known remnants (AI algorithms (i.e., neural networks) can effectively recognize patterns in images where the majority of pixels contain unrelated - background and/or foreground - contamination) gives the opportunity to reveal numerous hidden structures (potential SNRs located at complex regions) which will shorten the gap between the expected and detected number of Galactic SNRs. To this end, and having used applications of AI in Astrophysics to obtain a vast pool of SNRs, I plan to use my programming skills and multiwavelength data analysis knowledge of SNRs in an effort to develop software for combined multiwavelength data analysis of the latter objects in the concept of the Multi-Mission Maximum Likelihood framework (3ML) (Vianello et al., 2015) during my Postdoctoral research at the Kavli Institute of Particle Physics and Cosmology (KIPAC) Stanford.

Table 6.1: Selected targets for further inspection in increasing galactic longitude order. The question mark (?) symbol marks new findings that we classified as SNR candidates based on morphological criteria. ✓ and **x** symbols mark the detection and lack of detection, respectively.

SNR name	**Radio**	**Optical**	**X-rays (eROSITA)**	**GeV (*Fermi*-LAT)**	**H.E.S.S.** Significance
[redacted]	✓	✓	X-ray detection in eRASS:4 (> 1 keV)	Confirm detection	Not observed
[redacted]	✓	✓	First X-ray detection in eRASS:4	First Detection	Not observed
[redacted]	✗ (hints from GLEAM)	✗	First X-ray detection in eRASS:4 (> 1 keV)	Uncertain detection	Not observed
[redacted]	✓	✗ (hints from SHASSA)	First X-ray detection in eRASS:4	No detection	Not observed
[redacted]	✓	✓	First X-ray detection in eRASS:4	First detection	3.4σ
[redacted]	✗ (hints from GLEAM)	✗	First X-ray detection in eRASS:4	No detection	3.5σ?
[redacted]	✗ (hints from GLEAM/GB6)	✗ (hints from SHASSA)	First X-ray detection in eRASS:4 (> 1 keV)	Uncertain detection	No detection
[redacted]	✗ (hints from GLEAM/GB6)	✗ (hints from SHASSA)	First X-ray detection in eRASS:4 (> 1 keV)	First detection	No detection
[redacted]	✗ (hints from GLEAM/GB6)	✗ (hints from SHASSA)	First X-ray detection in eRASS:4	Uncertain detection	3.6σ?
[redacted]	✗ (hints from GLEAM/GB6)	✗ (hints from SHASSA)	First X-ray detection in eRASS:4 (> 1 keV)	No detection	No detection
[redacted]	✓	✗	X-ray detection in eRASS:4 (> 1 keV)	Already detected	0.7σ
[redacted]	✗ (hints from GLEAM/GB6)	✗	First X-ray detection in eRASS:4 (> 1 keV)	No detection	No detection
[redacted]	✗	✗	First X-ray detection in eRASS:4 (> 1 keV)	Uncertain	Uncertain
[redacted]	✓	✓	First X-ray detection in eRASS:4	First detection	No detection
[redacted]	✓	✗	First X-ray detection in eRASS:4 (> 1 keV)	Uncertain	0.5σ

Table 6.1 Continued.

SNR name	Radio	Optical	X-rays (eROSITA)	GeV (*Fermi*-LAT)	H.E.S.S. Significance
[redacted]	✓	✗	First X-ray detection in eRASS:4 (> 1 keV)	No detection	No detection
[redacted]	✗	✗	First X-ray detection in eRASS:4 (> 1 keV)	Already detected	[redacted]
[redacted]	✗ (hints from GLEAM/GB6)	✗ (hints from SHASSA)	First X-ray detection in eRASS:4 (> 1 keV)	Uncertain	No detection
[redacted]	✗ (hints from GLEAM/GB6)	✗ (hints from SHASSA)	First X-ray detection in eRASS:4	Not detected	No detection
[redacted]	✗ (hints from GLEAM/GB6)	✗ (hints from SHASSA)	First X-ray detection in eRASS:4 (> 1 keV)	Uncertain	No detection
[redacted]	✓	✓	First X-ray detection in eRASS:4 (> 1 keV)	No detection	No detection
[redacted]	✗	✗ (hints from SHASSA)	First X-ray detection in eRASS:4 (> 1 keV)	No detection	No detection
[redacted]	✗ (hints from GLEAM/GB6)	✗	First X-ray detection in eRASS:4 (> 1 keV)	No detection	No detection
[redacted]	✓	✗	First X-ray detection in eRASS:4 (> 1 keV)	Already detected	[redacted]
[redacted]	✗ (hints from GLEAM/GB6)	✗	First X-ray detection in eRASS:4 (> 1 keV)	Already detected	[redacted]
[redacted]	✓	✓	First complete X-ray coverage in eRASS:4 (> 1 keV)	Uncertain	0.3σ
[redacted]	✗ (hints from GLEAM/GB6)	✗ (hints from SHASSA)	First X-ray detection in eRASS:4	Uncertain	3.5σ?
[redacted]	✓	✗	First X-ray detection in eRASS:4 (> 1 keV)	First detection	1.8σ
[redacted]	✓	✗	First X-ray detection in eRASS:4 (> 1 keV)	Uncertain detection	1.9σ
[redacted]	✗	✗	First X-ray detection in eRASS:4 (> 1 keV)	Uncertain	No detection

In addition, SNRs are believed to be the sources for the generation of Galactic CRs (gin, 2013; Berezhko & Krymskiĭ, 1988; Reynolds, 2008) and are considered to be capable of accelerating particles up to 10^{15} ev-PeV energies, PeVatrons (Krymskii, 1977; Bell, 1978; Völk et al., 2008). Whereas surveys across the entire EM spectrum can identify the leptonic cosmic-ray component, the hadronic component is only traceable by high energy (GeV) and very high energy (TeV) γ-ray emission. The latter component is of great importance since the direction of charged particles cannot be traced back to their original location of production given the numerous galactic magnetic fields. Therefore, aiming to search their production location it is necessary to use γ-ray instruments such as *Fermi*-LAT, and H.E.S.S., as they detect the neutral secondary products of cosmic-ray acceleration, as well as X-ray instruments (eROSITA, *Chandra*, and *XMM-Newton*) towards prominent targets of non-thermal nature. A good example to start with is HESS J1614-518, an object just recently identified as an SNR in our study, and which is believed to be purely non-thermal in X-rays. However, the low statistics of that low surface brightness SNR in X-rays, and the stray light contamination issue of the three existing *XMM-Newton* observations towards the remnant, demand the proposal of an optimized pointing strategy with *Chandra* and/or *XMM-Newton* for deep follow-up observations aiming at unraveling the nature of its X-ray population particles (a work that tops my priority list). Another object that certainly "deserves" a deep X-ray follow-up observation with a pointing instrument is the SNR G309.8+00.0; aiming at detecting detailed characteristics of its X-ray spectrum which would either further support or waiver indications (i.e., presence of Si) of a type Ia progenitor origin. In addition, Cosmic rays (CRs) are vital "life" (not by its biological meaning) indicators in our Galaxy. It is known that the energy density of these CRs is comparable to the magnetic field of our Galaxy, to its gas, and to its starlight. Thus, the underlying processes driving these parameters must be intimately related. CRs also heavily contribute to the ionization of the gas in our Galaxy, resulting in astro-chemistry, chemical enrichment of the surrounding ISM, and formation and/or enhancement of the magnetic fields. As a result, CRs are linked to star formation, and subsequently to the evolution of galaxies. They are composed of high-energy charged particles: protons, nuclei (but electrons as well in a smaller abundance) with corresponding energies that can reach from 1 PeV up to 100 PeV. As mentioned above their paths are strongly bent by magnetic fields, however, secondary γ-ray signals produced due to their interaction with ISM are traceable. Recent

TeV γ-ray searches at and around the Galactic Center revealed PeV energy particles, as well as objects in the Galactic Center region which accelerate ultra-relativistic CRs (PeVatrons), e.g., HESS Collaboration et al. (2016). However, TeV-emitting sources and PeVatrons have also been investigated by X-ray studies (Uchiyama et al., 2007). Further studying of the latter objects can give the answer to the fundamental question of the origin of the highest energy CRs in our Galaxy, and up to which energies Galactic CRs contribute to the total CR spectrum. To address this one needs to employ currently operating advanced γ-ray telescopes (*Fermi*-LAT, H.E.S.S.) which when combined with X-ray searches (eROSITA, *Chandra*, and *XMM-Newton*), can probe the origin of TeV/PeV-emitting sources and consequently of Galactic CRs. The propagation of CRs from the production location to the ISM (gas) can then be modeled (model γ-ray maps and spectra) and be compared with radio and X-rays (X-ray synchrotron emission well constrains electrons and magnetic field properties (e.g., Kavanagh et al. (2019)), and traced back their path all the way to their accelerator.

The results of such a study, which I intend to pursue in the near future, would be essential to better understanding the nature of Galactic SNRs and it would be evident of the importance of using AI applications in Astrophysics to give answers to fundamental yet unanswered questions of Modern Astrophysics by analyzing vast amounts of multiwavelength data in reasonable time-frames.

Probing Dark Matter with state-of-the-art X-ray and optical surveys of Galaxy Clusters. eROSITA All-Sky X-ray Survey is sensitive enough to provide robust estimates of mass proxies (e.g., gas mass, the product of gas mass and temperature) and Fe-line-based redshifts for Galaxy Clusters up to z=2 (redshift estimates based on the Fe-K 6.7 keV line in X-ray spectra with a $\Delta z \leq 0.01$ precision when at least 10^3 counts are available (Yu et al., 2011)). Given that a significant number of the X-ray-detected Galaxy Clusters, with eROSITA, exceeds a few hundred to thousands of X-ray photons, only the fainter and/or peculiar cases of Galaxy Clusters require a deep follow-up observation with *XMM-Newton* and/or *Chandra*. Such cases have been identified (and more cases will appear in the near future) and follow-up data will be requested.

Once again, by applying machine learning techniques for image classification on all-sky survey and wide-field survey data with unprecedented sensitivity (e.g., eROSITA in X-rays, and Dark Energy Survey (DES), Euclid

in optical) based on size, shape, and brightness of known Clusters (AI algorithms (i.e., neural networks) can effectively recognize patterns in images offering the opportunity to reveal numerous hidden structures (potential Galaxy Clusters)). To this end, the software development for combined multiwavelength data (3ML) can be employed for the purposes of this study.

In addition, using a complete sample of hundreds of thousands of Galaxy Cluster at $z<2$, and attempting to reconstruct the large-scale power spectrum (full shape and amplitude) is at the top of my priority list and will definitely provide more robust results compared to a similar work that employed 1000 nearby clusters at $z<0.2$ detected by ROSAT (Balaguera-Antolínez et al., 2011). Such a result will allow to compare measurements from the power spectrum to the predictions of the ΛCDM cosmological model and put further constraints on cosmological parameters.

eROSITA allows us to observe Galaxy Clusters in X-rays, of which we already know the direction and brightness. Follow-up by optical instruments such as DES, Euclid, and JWST can help us determine their distance with high accuracy (for cases where a Fe-K line distance measurement is not available) and thus their mass (with small intrinsic scatter). Ultimately, depending on the distance of the Cluster, one can obtain the Universe's density at a specific time. In such a way, we can determine how the density of the Universe alters throughout the eons, allowing us to derive cosmological parameters and constrain DE models.

Finally, using weak-lensing measurements, one can infer the total mass of a Galaxy Cluster and compare it with the (baryonic) hot gas mass from X-ray observations as computed above. Such a study will allow us to determine the missing mass (DM) of Galaxy Clusters at different epochs, and thus provide tighter constraints on the nature of the unseen mass in our Universe.

Acknowledgements

As a final note, I would like to express my sincere gratitude to all those who played a significant role in the successful completion of my Doctoral program. First and foremost I would like to thank my two supervisors Dr. Gerd Pühlhofer and Prof.Dr. Andrea Santangelo. I am above all thankful to them for the guidance they gave me, I very much appreciate their support throughout this journey and their patience in dealing with my numerous questions and doubts. I am also thankful to them for challenging me to come to a better understanding not only of various aspects of the analysis that we conducted but of physics in general. I am thankful for their open door and willingness to help me clarify any doubts throughout the whole procedure. A special thanks to Dr. Gerd Pühlhofer who has daily been a collaborator and consultant. I consider myself lucky that both my supervisors are exceptional leaders but at the same time also exceptional mentors who generously shared with me their expertise, ideas, and time.

I would also like to thank Dr Denys Malyshev, Dr. Victor Doroshenko, and Dr. Lorenzo Ducci for all the fruitful discussions. An additional thanks to Dr. Denys Malyshev for his constant and flawless IT support. Individual projects have also benefited from the contributions of many more people, all co-authors who made our publications possible, and who are included in my publication list. The least I can do is thank them for their contributions to our conversations, thoughts, opinions, and ideas on my publication efforts by including a shout-out for them in this section.

Those people alongside my parents and friends, who I also thank for their support, sacrifice, and love, are the persons who deserve my deepest gratitude.

Bibliography

Abdalla H., et al., 2018, A&A, 612, A1

Abdo A. A., et al., 2011, ApJ, 734, 28

Abdollahi S., et al., 2022, ApJS, 260, 53

Abeysekara A. U., et al., 2018, J. Cosmology Astropart. Phys., 2018, 049

Acero F., et al., 2010, A&A, 516, A62

Acero F., et al., 2016, ApJS, 224, 8

Acharya B. S., et al., 2019, Science with the Cherenkov Telescope Array, doi:10.1142/10986.

Ackermann M., et al., 2013, Science, 339, 807

Aharonian F., et al., 2001, A&A, 370, 112

Aharonian F. A., et al., 2004, Nature, 432, 75

Akrami Y., et al., 2020, Astronomy & Astrophysics, 641, A7

Albert A., et al., 2018a, ApJ, 853, 154

Albert A., et al., 2018b, J. Cosmology Astropart. Phys., 2018, 043

Allen G. E., et al., 1997, ApJ, 487, L97

Araya M., 2020, MNRAS, 492, 5980

Aschenbach B., 1998, Nature, 396, 141

Atwood W. B., et al., 2009, ApJ, 697, 1071

Baer H., Choi K.-Y., Kim J. E., Roszkowski L., 2015, Physics Reports, 555, 1

Bahcall J. N., Soneira R. M., 1980, ApJS, 44, 73

Balaguera-Antolínez A., Sánchez A. G., Böhringer H., Collins C., Guzzo L., Phleps S., 2011, MNRAS, 413, 386

Ball B. D., et al., 2023, MNRAS, 524, 1396

Ballet J., Bruel P., Burnett T. H., Lott B., The Fermi-LAT collaboration 2023, arXiv e-prints, p. arXiv:2307.12546

Becker W., Hurley-Walker N., Weinberger C., Nicastro L., Mayer M. G. F., Merloni A., Sanders J., 2021, A&A, 648, A30

Bell A., 1978, Monthly Notices of the Royal Astronomical Society, 182, 147

Berezhko E. G., Krymskiĭ G., 1988, Soviet Physics Uspekhi, 31, 27

Bertone G., Hooper D., Silk J., 2005, Phys. Rep., 405, 279

Boyarsky A., Ruchayskiy O., Iakubovskyi D., Maccio' A. V., Malyshev D., 2009, arXiv e-prints, p. arXiv:0911.1774

Bradač M., Allen S. W., Treu T., Ebeling H., Massey R., Morris R. G., von der Linden A., Applegate D., 2008, ApJ, 687, 959

Burkert A., 1995, ApJ, 447, L25

Carignan C., Freeman K. C., 1985, ApJ, 294, 494

Carrigan S., Brun F., Chaves R. C. G., Deil C., Donath A., Gast H., Marandon V., Renaud M., 2013, in International Cosmic Ray Conference. p. 952 (arXiv:1307.4690), doi:10.48550/arXiv.1307.4690

Chatterjee S., et al., 2009, ApJ, 698, 250

Chemin L., de Blok W. J. G., Mamon G. A., 2011, AJ, 142, 109

Chen Y., Jiang B., 2013, Scientia Sinica Physica, Mechanica & Astronomica, 43, 1

Cirelli M., et al., 2011, Journal of Cosmology and Astroparticle Physics, 2011, 051–051

Clark D. H., Caswell J. L., Green A. J., 1973, Nature, 246, 28

Clowe D., Bradač M., Gonzalez A. H., Markevitch M., Randall S. W., Jones C., Zaritsky D., 2006, ApJ, 648, L109

Coronado-Blázquez J., Sánchez-Conde M. A., 2020, Galaxies, 8, 5

Cowie L. L., Hu E. M., Taylor W., York D. G., 1981, ApJ, 250, L25

Einasto J., 1965, Trudy Astrofizicheskogo Instituta Alma-Ata, 5, 87

Einasto J., 1968, Publications of the Tartu Astrofizica Observatory, 36, 414

Esposito J. A., Hunter S. D., Kanbach G., Sreekumar P., 1996, ApJ, 461, 820

Feng J. L., Kumar J., 2008, Phys. Rev. Lett., 101, 231301

Ferrand G., Safi-Harb S., 2012, Advances in Space Research, 49, 1313

Frail D. A., Goss W. M., Whiteoak J. B. Z., 1994, ApJ, 437, 781

Giuliani A., et al., 2011, ApJ, 742, L30

Green D. A., 2019, Journal of Astrophysics and Astronomy, 40, 36

H. E. S. S. Collaboration et al., 2018, A&A, 612, A8

HESS Collaboration et al., 2016, Nature, 531, 476

Han J., Cole S., Frenk C. S., Jing Y., 2016, Monthly Notices of the Royal Astronomical Society, 457, 1208–1223

Hayashi K., Chiba M., 2014, ApJ, 789, 62

Helder E. A., Vink J., Bykov A. M., Ohira Y., Raymond J. C., Terrier R., 2012, Space Sci. Rev., 173, 369

Hurley-Walker N., et al., 2019, PASA, 36, e045

Hütten M., Combet C., Maier G., Maurin D., 2016, J. Cosmology Astropart. Phys., 2016, 047

Jee M. J., Dawson W. A., Stroe A., Wittman D., van Weeren R. J., Brüggen M., Bradač M., Röttgering H., 2016, ApJ, 817, 179

Kapteyn J. C., 1922, ApJ, 55, 302

Katagiri H., et al., 2011, ApJ, 741, 44

Kavanagh P. J., et al., 2019, Astronomy & Astrophysics, 621, A138

Keane E. F., Kramer M., 2008, Monthly Notices of the Royal Astronomical Society, 391, 2009

Kesteven M. J., Caswell J. L., 1987, A&A, 183, 118

King I. R., 1966, AJ, 71, 64

Koyama K., Petre R., Gotthelf E. V., Hwang U., Matsuura M., Ozaki M., Holt S. S., 1995, Nature, 378, 255

Krymskii G., 1977, in Akademiia Nauk SSSR Doklady. pp 1306–1308

Kuijken K., Gilmore G., 1989, MNRAS, 239, 651

Leahy D. A., Williams J. E., 2017, AJ, 153, 239

Lee B. W., Weinberg S., 1977, Phys. Rev. Lett., 39, 165

Lelli F., McGaugh S. S., Schombert J. M., 2016, AJ, 152, 157

Merloni A., et al., 2012, arXiv e-prints, p. arXiv:1209.3114

Merloni A., et al., 2023, A&A

Merritt D., Graham A. W., Moore B., Diemand J., Terzić B., 2006, AJ, 132, 2685

Milgrom M., 1983, ApJ, 270, 365

Moore B., Quinn T., Governato F., Stadel J., Lake G., 1999, MNRAS, 310, 1147

Muni C., Pontzen A., Sanders J. L., Rey M. P., Read J. I., Agertz O., 2024, MNRAS, 527, 9250

Navarro J. F., Frenk C. S., White S. D. M., 1997, ApJ, 490, 493

Navarro J. F., et al., 2010, MNRAS, 402, 21

Oliva E., Moorwood A. F. M., Danziger I. J., 1989, A&A, 214, 307

Oort J. H., 1932, Bull. Astron. Inst. Netherlands, 6, 249

Pavlinsky M., et al., 2021, A&A, 650, A42

Predehl P., et al., 2021, A&A, 647, A1

Profumo S., 2013, arXiv e-prints, p. arXiv:1301.0952

Ragozzine B., Clowe D., Markevitch M., Gonzalez A. H., Bradač M., 2012, ApJ, 744, 94

Reynolds S. P., 2008, Annu. Rev. Astron. Astrophys., 46, 89

Romani R. W., Ng C. Y., 2003, ApJ, 585, L41

Rubin V. C., 1983, Scientific American, 248, 96

Sedov L. I., 1959, Similarity and Dimensional Methods in Mechanics

Shan S.-S., Zhu H., Tian W.-W., Zhang H.-Y., Yang A.-Y., Zhang M.-F., 2019, Research in Astronomy and Astrophysics, 19, 092

Shull P. J., Dyson J. E., Kahn F. D., West K. A., 1985, MNRAS, 212, 799

Silk J., Wallerstein G., 1973, ApJ, 181, 799

Silverwood H., Weniger C., Scott P., Bertone G., 2015, J. Cosmology Astropart. Phys., 2015, 055

Sturner S. J., Dermer C. D., 1995, A&A, 293, L17

Sunyaev R., et al., 2021, A&A, 656, A132

Tanaka T., et al., 2011, ApJ, 740, L51

Taylor G., 1950, Proceedings of the Royal Society of London Series A, 201, 159

Thompson D. J., Baldini L., Uchiyama Y., 2012, Astroparticle Physics, 39, 22

Tsunemi H., Inoue H., 1980, PASJ, 32, 247

Uchiyama Y., Aharonian F. A., Tanaka T., Takahashi T., Maeda Y., 2007, Nature, 449, 576

Vianello G., et al., 2015, arXiv e-prints, p. arXiv:1507.08343

Vink J., 2012, A&A Rev., 20, 49

Voges W., et al., 1999, A&A, 349, 389

Völk H., Berezhko E., Ksenofontov L., 2008, Astronomy & Astrophysics, 483, 529

Weiler K. W., Sramek R. A., 1988, ARA&A, 26, 295

Woltjer L., 1972, ARA&A, 10, 129

Yao J. M., Manchester R. N., Wang N., 2017, ApJ, 835, 29

Yu H., Tozzi P., Borgani S., Rosati P., Zhu Z. H., 2011, A&A, 529, A65

Zasov A. V., Saburova A. S., Khoperskov A. V., Khoperskov S. A., 2017, Physics Uspekhi, 60, 3

Zhao H., 1996, MNRAS, 278, 488

Zwicky F., 1933, Helvetica Physica Acta, 6, 110

Zwicky F., 1937, ApJ, 86, 217

Zyla P., et al., 2020, PTEP, 2020, 083C01

2013, The origin of cosmic rays. Elsevier

List of Figures

List of Tables